

---

METALS  
AND SUPERCONDUCTORS

---

# Generation of Coherent Off-Diagonal Raman-Active Phonons by Femtosecond Laser Pulses in High-Temperature Superconductor $\text{YBa}_2\text{Cu}_3\text{O}_{7-x}$

O. V. Misochko and M. V. Lebedev

*Institute of Solid-State Physics, Russian Academy of Sciences, Chernogolovka, Moscow oblast, 142432 Russia*

*e-mail: misochko@issp.ac.ru*

Received October 4, 2000

**Abstract**—The time-resolved optical response from various crystallographic planes of a  $\text{YBa}_2\text{Cu}_3\text{O}_{7-x}$  monocrystal is investigated. In such measurements of temporal behavior, the phonon system is driven by an ultrashort (subpicosecond) pulse into a coherent state and is probed by a second ultrashort pulse with a given temporal delay. A comparison of the Fourier transforms of the temporal responses with the spontaneous Raman scattering spectra shows that the contribution to a temporal response comes not only from fully symmetric phonons, but also from off-diagonal modes. The mechanism of generation of coherent phonons in high-temperature superconductors is discussed. © 2001 MAIK “Nauka/Interperiodica”.

Basic information on the dynamics of long-wavelength even-parity phonons in high-temperature superconductors (HTSCs) is obtained from investigations of the Raman scattering (RS) of light [1]. A characteristic feature of most HTSCs is the domination of fully symmetric phonons in the RS spectrum, whereas the phonons of lower symmetry ( $E_g$  in the case where the lattice belongs to the tetragonal point group  $D_{4h}$ ) are considerably less intensive (as is the case with  $\text{YBa}_2\text{Cu}_3\text{O}_{7-x}$  [2]) or are not revealed in the spectrum at all, as in  $\text{Bi}_2\text{Sr}_2\text{CaCu}_2\text{O}_{8+x}$  [3] and in systems of the type  $\text{Tl-Ba-Ca-Cu-O}$  [4]. An exception is the system  $\text{Hg-Ba-Ca-Cu-O}$ , where the off-diagonal phonons dominate in the RS spectrum at room temperature; however, even in this system in the superconducting state, the contribution from fully symmetric phonons becomes comparable to that from off-diagonal phonons [5].

Due to progress in the development of laser technology, laser pulse duration can be as short as several femtoseconds, which opens up various new research opportunities, in particular, a real-time study of lattice vibrations. If the pulse duration is shorter than the inverse frequency of lattice vibrations, phonons can be prepared and investigated not only in a thermal state, which is usually investigated by RS spectroscopy, but also in a coherent state. Real-time investigations (one typical example of which is the method of excitation of a phonon state with its subsequent probing by two laser pulses separated in time) are now being actively carried out for condensed systems [6]. High-temperature superconductors were among the first opaque crystalline media in which coherent phonons were observed. The first observation was made on semiconducting  $\text{YBa}_2\text{Cu}_3\text{O}_{6+x}$  with  $x < 0.4$  [7], which was followed by

investigations of coherent phonons in superconducting samples both in normal and superconducting states [8, 9]. In all these investigations, subpicosecond laser pulses excited low-energy fully symmetric phonons. The full symmetry of the excited modes led one to draw on the displacive mechanism [10] for explaining the generation of coherent phonons in HTSCs. The displacive mechanism adapted to the superconducting state [11] did not only explain phenomenologically the excitation of coherent lattice vibrations but also described the temperature anomaly, which consists in a change in polarity and an increase in the photo-induced response in the superconducting state. However, it is necessary to note that the earliest research into coherent phonons was carried out on  $c$ -oriented films [7–9] and  $ab$  planes of monocrystals [12, 13]. Therefore, the geometry of the experiments excluded the possibility of observing the off-diagonal  $E_g$  phonons. Ascertainment of the real mechanism of excitation of coherent phonons is necessary in order to understand the numerous interesting anomalies of the time-resolved optical response, one of which is the phase-dependent noise of coherent phonons [12].

The generation and detection of coherent phonons was carried out by the method of excitation with subsequent probing by subpicosecond light pulses. The reflection was measured using phase-sensitive detection and pulses of a titanate sapphire laser ( $\lambda = 780$  nm) with a duration of 35 fs. A train of pulses was divided into two beams with orthogonal polarizations, and the probing beam was approximately 100 times weaker in power (of the order 1 mW) than the pumping beam. The relative delay between the beams was varied using a step drive, which changes the optical path of one of the beams in steps of 1  $\mu\text{m}$ . The modulation of the pumping

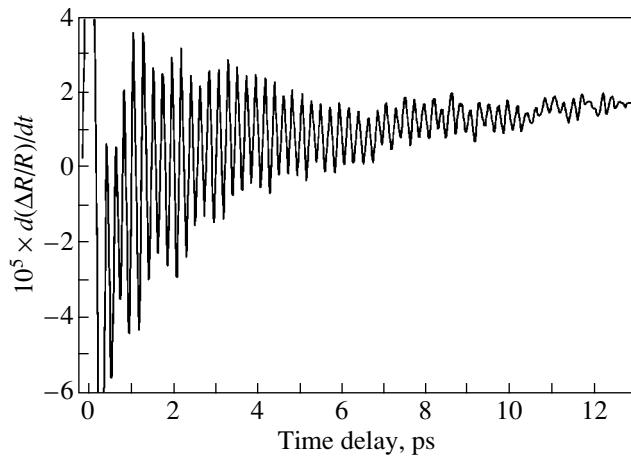


**Fig. 1.** Time-resolved normalized reflection for the basal  $ab$  plane of the monocrystal  $\text{YBa}_2\text{Cu}_3\text{O}_{7-x}$ .

beam was realized by rocking a retroreflector with a frequency of 550 Hz and an amplitude not exceeding the duration of light pulses used. The RS investigations were carried out in the back-scattering geometry with the line  $\lambda = 514$  nm of an  $\text{Ar}^+$  laser using a triple spectrometer equipped with a multichannel detector. A detailed description of the equipment used for measuring the time-resolved optical responses and the spontaneous RS spectra can be found in [12, 13].

The measurements were carried out at room temperature on the  $ab$  and  $ac$  faces of the monocrystal  $\text{YBa}_2\text{Cu}_3\text{O}_{7-x}$ . The investigated  $\text{YBa}_2\text{Cu}_3\text{O}_{7-x}$  crystal had a superconducting transition temperature  $T_c = 92$  K. Since the crystal was twinned, we could not distinguish the crystallographic directions  $a$  and  $b$ , which we assumed equivalent.

The typical optical response in the case of excitation and subsequent probing of the  $ab$  plane of the crystal  $\text{YBa}_2\text{Cu}_3\text{O}_{7-x}$  by ultrashort pulses is shown in Fig. 1. The excited state of the crystal relaxes to the equilibrium state in a time of the order of 1–2 ps. Fast oscillations generated by coherent phonons are superimposed on this electronic relaxation. The coherent oscillations decay according to an exponential law, which testifies to the excitation of a single mode. In the case of modified geometry of the experiment for measuring the optical response of the  $ac$  plane, the character of oscillations is changed. In Fig. 2, the optical responses obtained in identical conditions, except for the geometry of the experiment, are presented. The upper oscillatory curve corresponds to the geometry  $\mathbf{E}_e \parallel \mathbf{c}$  and  $\mathbf{E}_p \parallel \mathbf{a}$ , the middle curve corresponds to the geometry  $\mathbf{E}_e \parallel \mathbf{a}$  and  $\mathbf{E}_p \parallel \mathbf{c}$  (where  $\mathbf{E}_e$  and  $\mathbf{E}_p$  are the electrical field vectors of the exciting and the probing beams, respectively), and the lower curve is obtained from the basal plane with  $\mathbf{E}_e \perp \mathbf{c}$ ,  $\mathbf{E}_p \perp \mathbf{c}$ , and  $\mathbf{E}_e \perp \mathbf{E}_p$ . In the optical response of the  $ac$  plane, a slight manifestation of beats is observed instead of decaying oscillations, which

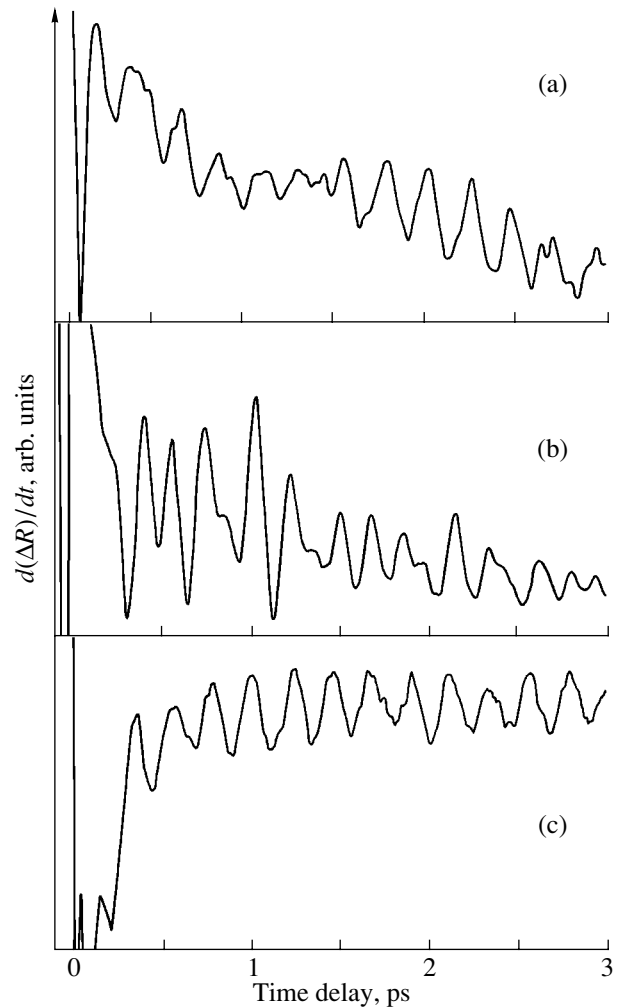


**Fig. 2.** Time-resolved reflection from various crystallographic faces. The oscillatory curves correspond (a) to  $\mathbf{E}_e \parallel \mathbf{c}$  and  $\mathbf{E}_p \parallel \mathbf{a}$ , (b) to  $\mathbf{E}_e \parallel \mathbf{a}$  and  $\mathbf{E}_p \parallel \mathbf{c}$ , and (c) to reflection from the basal  $ab$  plane for  $\mathbf{E}_e \perp \mathbf{c}$ ,  $\mathbf{E}_p \perp \mathbf{c}$ , and  $\mathbf{E}_e \perp \mathbf{E}_p$ .

indicates the presence of several phonon modes. The character of oscillations depends on the orientation of the polarization of the exciting laser pulse with respect to the crystallographic axes. In order to verify that the temporal oscillations observed in various geometries of the experiment correspond to the Raman-active phonon modes of the crystal, the Fourier transforms (FTs) of the measured time-dependent responses were numerically calculated. The typical calculated power spectra (periodograms) are presented in Figs. 3a–3c, and the RS spectra of the  $zz$ ,  $xx$ , and  $zx$  polarizations of the same crystal are shown in Figs. 3d–3f. Since the fully symmetric RS tensors for a tetragonal crystal are diagonal,

$$\begin{pmatrix} a & & \\ & a & \\ & & b \end{pmatrix}, \text{ and the } E_g \text{ tensors have the form } \begin{pmatrix} & c \\ & c \\ c & c \end{pmatrix},$$

comparison of the RS-polarization data allows one to

identify the modes observed in a temporal response. In the polarized  $xx$  and  $zz$  spectra, the two pronounced peaks at frequencies 3.6 (120  $\text{cm}^{-1}$ ) and 4.5 THz (150  $\text{cm}^{-1}$ ) correspond to the fully symmetric phonon modes that involve displacements of Ba and Cu ions, whereas the peak at 10.1 THz (337  $\text{cm}^{-1}$ ) is caused by out-of-phase displacements of oxygen ions of the cuprate plane. The latter mode has the  $B_{1g}$  symmetry for the tetragonal group, which excludes its observation in the  $zz$  spectrum; however, the symmetry of the mode becomes as high as  $A_g$  for the orthorhombic group  $D_{2h}$ , which is the true group of symmetry for  $\text{YBa}_2\text{Cu}_3\text{O}_{7-x}$ . In the depolarized ( $zx$ ) RS spectrum, there are  $E_g$  modes ( $B_{2g}$  and  $B_{3g}$  in the orthorhombic-group notation); they correspond to the peaks at frequencies 2.0, 6.3, and 9.3 THz in the investigated spectral range shown in Fig. 3. Comparison of the relative intensities of the two higher frequency modes with the data obtained on an untwinned monocrystal [2] reveals that there are both  $B_{3g}$  and  $B_{2g}$  components in the spectrum; this is due to twinning of the crystal. These two modes involve  $y$  and  $x$  displacements of the bridge oxygen. The lower frequency  $E_g$  mode corresponds to displacements of the Ba ion that are polarized in the basal plane [14]. In the periodogram shown in Fig. 3a, there is a mode at a frequency of 6.3 THz (210  $\text{cm}^{-1}$ ) which involves  $y$  displacements of the bridge oxygen from the BaO plane and has  $E_g$  symmetry ( $B_{3g}$  for the orthorhombic group). It is necessary to note that the spontaneous  $E_g$  Raman spectra are approximately one order less intensive than the fully symmetric RS spectra. However, in the periodogram presented in Fig. 3a, the fully symmetric and off-diagonal modes observed in the temporal response have approximately equal intensities. A plausible explanation for this discordance is the different resonance conditions realized in the frequency domain and the time domain. In the former case, the spectra are obtained using light beams with  $\lambda = 514$  nm, whereas in the latter case, the wavelength of laser radiation was considerably greater,  $\lambda = 780$  nm. Strictly speaking, comparison of the relative intensities should be carried out only for identical resonance conditions. It is known that the fully symmetric phonon modes of optimum doped  $\text{YBa}_2\text{Cu}_3\text{O}_{7-x}$  become less intensive for an increased wavelength of laser light [15]; however, resonance dependences of the off-diagonal modes are unknown to date.

The displacive mechanism [10] allows us to explain the generation of coherent phonons in opaque crystalline media only for fully symmetric modes. This theory implies that the electronic system is quickly thermalized, acquiring full symmetry, and that the condition for applicability of the theory is  $\tau_{e-e} \ll \tau_{e-l}$ ; i.e., the electron–electron relaxation time  $\tau_{e-e}$  is significantly shorter than the electron–lattice relaxation time  $\tau_{e-l}$ . The observation of the off-diagonal phonon mode in the temporal response indicates that the lattice ions

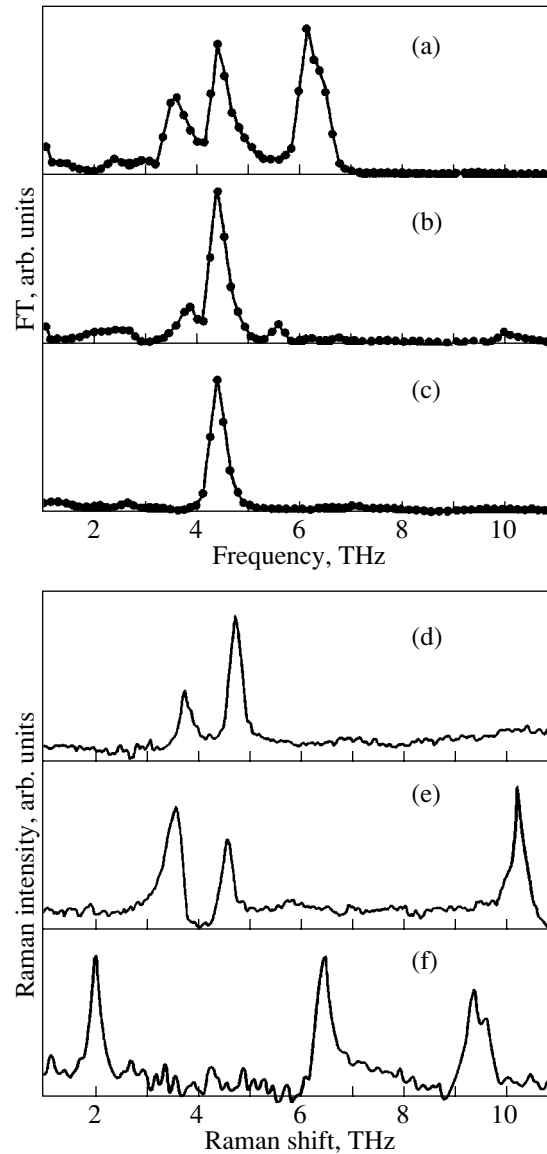


**Fig. 3.** Fourier-transformed temporal response: (a)  $\mathbf{E}_e \parallel \mathbf{c}$  and  $\mathbf{E}_p \parallel \mathbf{a}$ ; (b)  $\mathbf{E}_e \parallel \mathbf{a}$  and  $\mathbf{E}_p \parallel \mathbf{c}$ ; and (c)  $\mathbf{E}_e \perp \mathbf{c}$ ,  $\mathbf{E}_p \perp \mathbf{c}$ , and  $\mathbf{E}_e \perp \mathbf{E}_p$ ; and spontaneous RS spectrum in various polarizations: (d)  $x(zz)x$ , (e)  $z(xx)z$ , and (f)  $y(xz)y$ .

have time to react to the initial electronic distribution, which has lower symmetry. Perhaps the reason for the violation of the inequality  $\tau_{e-e} \ll \tau_{e-l}$  is the van Hove singularity, which is inherent to HTSCs and causes the movement of electrons in some directions of the cuprate plane to be slower than the movement of lattice ions [16]. It is also necessary to note that off-diagonal coherent Raman-active phonons were recently detected in a number of systems [6, 17, 18] for which only fully symmetric modes were initially registered in the time domain. This fact was interpreted as being due to the generation of coherent lattice phonons by stimulated RS. Moreover, it was shown that the displacive mechanism can be reduced to one of the special cases of res-

onant stimulated RS [6]. Microscopically, coherent oscillations are due to macroscopic filling of the  $\mathbf{q} = 0$  phonon mode, which makes the situation similar to Bose condensation [19]. We note that the Bogolyubov transformation, which is used for the description of superfluidity, can also be applied in describing compressed phonon states [20]. These states were detected in crystals of perovskite structure, similar to the structure of HTSCs [21], and in  $\text{YBa}_2\text{Cu}_3\text{O}_{7-x}$  [12].

In summary, we carried out an optical investigation on various faces of the monocrystal  $\text{YBa}_2\text{Cu}_3\text{O}_{7-x}$  in frequency and time domains and found that the off-diagonal phonons contribute to the temporal response. The excitation of the off-diagonal phonon modes casts some doubt on the displacement mechanism as the main mechanism of generation of coherent phonon modes in  $\text{YBa}_2\text{Cu}_3\text{O}_{7-x}$ . An alternative explanation might be the mechanism of stimulated RS. We believe that this mechanism is capable of describing not only the generation of coherent phonons but also their exotic statistical properties.

#### ACKNOWLEDGMENTS

This work was supported by the Alexander von Humboldt Foundation (Germany) and the Kansai Advance Research Center (Japan).

#### REFERENCES

1. R. Feile, *Physica C (Amsterdam)* **159**, 1 (1989); C. Thomsen, in *Light Scattering in Solids*, Ed. by M. Cardona and G. Güntherodt (Springer-Verlag, Berlin, 1991), Vol. VI, p. 285.
2. V. D. Kulakovskii, O. V. Misochko, and V. B. Timofeev, *Fiz. Tverd. Tela (Leningrad)* **31** (9), 220 (1989) [*Sov. Phys. Solid State* **31**, 1599 (1989)].
3. R. Liu, M. V. Klein, P. D. Han, and D. A. Payne, *Phys. Rev. B* **45**, 7392 (1992).
4. L. V. Gasparov, V. D. Kulakovskii, O. V. Misochko, and V. B. Timofeev, *Zh. Éksp. Teor. Fiz.* **96**, 2115 (1989) [*Sov. Phys. JETP* **69**, 1196 (1989)].
5. A. Sacuto, A. Lebon, D. Colson, *et al.*, *Physica C (Amsterdam)* **259**, 209 (1996); A. Sacuto, R. Combescot, N. Bontemps, *et al.*, *Phys. Rev. B* **58**, 11721 (1998); X. Zhou, M. Cardona, D. Colson, and V. Viallet, *Phys. Rev. B* **55**, 12770 (1997).
6. R. Merlin, *Solid State Commun.* **102**, 207 (1997).
7. J. M. Chwalek, C. Uher, J. F. Whitaker, *et al.*, *Appl. Phys. Lett.* **58**, 980 (1991).
8. W. Albrecht, Th. Kruze, and H. Kurz, *Phys. Rev. Lett.* **69**, 1451 (1992); A. Kutt, W. Albrecht, and H. Kurz, *IEEE J. Quantum Electron.* **QE-28**, 2434 (1992).
9. O. V. Misochko, K. Kisoda, K. Sakai, and S. Nakashima, *Phys. Rev. B* **61**, 4305 (2000).
10. H. J. Zeiger, J. Vidal, T. K. Cheng, *et al.*, *Phys. Rev. B* **45**, 768 (1992).
11. I. I. Mazin, A. I. Liechtenstein, O. Jepsen, *et al.*, *Phys. Rev. B* **49**, 9210 (1994).
12. O. V. Misochko, *Phys. Lett. A* **269**, 97 (2000).
13. O. V. Misochko, *Fiz. Tverd. Tela (St. Petersburg)* **42**, 1169 (2000) [*Phys. Solid State* **42**, 1204 (2000)].
14. W. Kress, U. Schroder, J. Prade, *et al.*, *Phys. Rev. B* **38**, 2906 (1988).
15. O. V. Misochko, *Fiz. Tverd. Tela (Leningrad)* **31** (11), 280 (1989) [*Sov. Phys. Solid State* **31**, 1998 (1989)]; O. V. Misochko and E. Ya. Sherman, *Zh. Éksp. Teor. Fiz.* **99**, 330 (1991) [*Sov. Phys. JETP* **72**, 185 (1991)]; O. V. Misochko, E. Ya. Sherman, and V. B. Timofeev, *Physica C (Amsterdam)* **185–189**, 1025 (1991).
16. R. S. Markiewicz, *J. Phys. Chem. Solids* **58**, 1179 (1997).
17. G. A. Garrett, T. F. Albrecht, J. F. Whitaker, and R. Merlin, *Phys. Rev. Lett.* **77**, 3661 (1996).
18. M. Hase, K. Mizoguchi, H. Harima, *et al.*, *Appl. Phys. Lett.* **69**, 2474 (1996).
19. A. V. Kuznetsov and C. J. Stanton, *Phys. Rev. Lett.* **73**, 3243 (1994).
20. M. M. Nieto, in *Frontiers of Nonequilibrium Statistical Physics*, Ed. by G. T. Moore and M. O. Scully (Plenum, New York, 1986), p. 287.
21. G. A. Garrett, J. F. Whitaker, A. K. Sood, and R. Merlin, *Opt. Express* **1**, 385 (1997); G. A. Garrett, A. G. Rojo, A. K. Sood, *et al.*, *Science* **275**, 1638 (1997); A. Bartels, T. Dekorsy, and H. Kurz, *Phys. Rev. Lett.* **84**, 2981 (2000).

*Translated by O. Ivanov*

---

---

**METALS  
AND SUPERCONDUCTORS**

---

---

## **Resistive State of Superconducting Structures with Fractal Clusters of a Normal Phase**

**Yu. I. Kuzmin**

*Ioffe Physicotechnical Institute, Russian Academy of Sciences, Politekhnicheskaya ul. 26, St. Petersburg, 194021 Russia*

*e-mail: yurk@shuv.ioffe.rssi.ru*

*e-mail: iourk@usa.net*

Received October 10, 2000; in final form, November 13, 2000

**Abstract**—The effect of morphologic factors on magnetic flux trapping and critical currents in a superconducting structure, which presents a type II percolation superconductor with pinning centers, is considered. The role of pinning centers is played by fractal clusters of the normal phase. The properties of these clusters are analyzed in detail: their statistics is studied, the distribution of critical currents of depinning is found, and the dependences of the main statistical parameters on the fractal dimension are obtained. The effect of fractal clusters of the normal phase on the electric field caused by the motion of the magnetic flux after the vortices have been broken away from pinning centers is considered. The current–voltage characteristics of superconducting structures in a resistive state are obtained for an arbitrary fractal dimension. It is found that the fractality of the boundaries of normal-phase clusters forces magnetic flux trapping, thereby increasing the critical current. © 2001 MAIK “Nauka/Interperiodica”.

### 1. INTRODUCTION

An important property of clusters of a normal phase located in a superconducting medium is their ability to trap magnetic flux. While preventing vortices from moving under the action of the Lorentz force, these clusters can act as effective pinning centers [1–4]. This property is widely used in creating composite superconducting materials with high critical current values [5, 6]. The morphologic characteristics of clusters of a normal phase essentially influences the dynamics of trapped magnetic flux, especially in the case when the clusters have fractal boundaries [7–9]. In the present work, we consider in detail the geometric and probability properties of these fractal clusters and their influence on the critical current and dynamics of trapped magnetic flux upon transition of the superconductor into a resistive state.

### 2. FRACTAL GEOMETRY OF THE CLUSTERS OF NORMAL PHASE AND THE DISTRIBUTION OF CRITICAL CURRENTS

We consider a superconductor which contains fragments of a normal phase. Let the dimension of these fragments along one direction significantly exceed the other dimensions. Similar columnar defects are of great interest in creating artificial pinning centers [5, 10–12]. If this superconducting structure is cooled in a magnetic field directed along the axis of alignment of these defects below the critical temperature, then the distribution of trapped magnetic flux in clusters of the normal phase will be two-dimensional. This can be espe-

cially easily done with a superconducting film, in which such clusters are formed near defects at the boundary with the substrate during the growing process and are normal to the film plane [5, 12]. Let the relative filling of the film surface with the normal phase be less than the percolation threshold for the transfer of magnetic flux (i.e., less than 50% for 2D percolation [13]). In this case, the fraction of the superconducting phase exceeds the percolation threshold and, in the film plane, there is a superconducting percolation cluster capable of conducting a transport current. This kind of structure provides for the effective pinning, thereby raising the critical current, as the magnetic flux is trapped in isolated clusters of the normal phase and vortices cannot leave them without crossing the surrounding superconducting space. As the current increases, the trapped flux will remain unchanged until the vortices begin to break away from those clusters for which the pinning force is less than the Lorentz force caused by the transport current. When the magnetic flux is breaking away from the pinning centers, each vortex must cross the infinite superconducting cluster. In this case, the vortices will move primarily along the weak links that connect the clusters of the normal phase to each other [3, 14–17]. These weak links are especially easily formed in high-temperature superconductors (HTSCs), which are characterized by a small coherence length [5, 16]. Structural defects, which could serve simply as scattering centers at a large coherence length, create weak links in HTSCs. There is a large variety of weak links in a wide range of spatial scales in HTSCs [5, 14–18]. On the atomic level, weak links are created by structural point defects, primarily by oxygen vacancies [16, 19]. On a

mesoscopic scale, weak links are efficiently formed on twin boundaries [15, 16, 18, 20]. Twins can be located at a distance of several tens of nanometers from each other; therefore, even a single crystal can have a fine substructure created by twins. Finally, on a macroscopic scale, weak links are created by various structural defects, such as boundaries of grains and crystallites or barriers arising due to secondary decomposition of a nonstoichiometric crystal into regions with a high and a low oxygen content [17–19]. Moreover, upon exposure to a magnetic field, the coherence length further decreases [21], which also facilitates the formation of weak links. In conventional low-temperature superconductors showing large coherence lengths, weak links are formed due to the proximity effect at sites where the distance between neighboring clusters of the normal phase is minimal.

Thus, irrespective of their origin, weak links form channels for the transport of vortices in which the pinning force is less than the Lorentz force caused by the transport current. According to its configuration, each cluster of the normal phase will possess a characteristic value of the depinning critical current which makes its own contribution to the overall statistical distribution. Upon exposure to a transport current, vortices will be broken away first from clusters of a smaller pinning force and, accordingly, a smaller critical current. Consequently, the change in the trapped magnetic flux  $\Delta\Phi$  will be proportional to the number of clusters of the normal phase in which the critical current is less than the specified value  $I$ . Therefore, the relative change in the flux can be expressed through the function of cumulative probability  $F = F(I)$  for the distribution of critical currents of the clusters:

$$\frac{\Delta\Phi}{\Phi} = F(I),$$

where

$$F(I) = \Pr\{\forall I_j < I\}. \quad (1)$$

The right-hand part of Eq. (1) is the probability of the critical current  $I_j$  of any  $j$ th cluster being less than the specified upper limit  $I$ . On the other hand, the magnetic flux trapped in a single cluster is proportional to its area  $A$ . Therefore, the change in the trapped flux can be expressed through the function of cumulative probability  $W = W(A)$  for the area distribution of normal-phase clusters, which is a measure of the number of clusters whose area does not exceed the specified value  $A$ :

$$\frac{\Delta\Phi}{\Phi} = 1 - W(A),$$

where

$$W(A) = \Pr\{\forall A_j < A\}. \quad (2)$$

Generally, the distribution of cluster areas can be described by the gamma distribution, for which the

function of cumulative probability has the form

$$W(A) = \frac{\gamma(g+1, A/A_0)}{\Gamma(g+1)}, \quad (3)$$

where  $\gamma(v, z)$  is the incomplete gamma function,  $\Gamma(v)$  is the Euler gamma function, and  $A_0$  and  $g$  are the parameters of the gamma distribution which determine the average area of the cluster  $\bar{A} = (g+1)A_0$  and its standard deviation  $\sigma_A = A_0\sqrt{g+1}$ . The form of the distribution function of cluster areas can be found from the results of geometric probability analyses of electron photomicrographs of superconducting films [8, 11, 12]. For example, in the case of practically important YBCO film structures which contain columnar defects [12], exponential distribution is realized; this is a particular case of the gamma distribution in Eq. (3) with  $g = 0$ .

To clarify how the transport current affects the trapped magnetic flux, one should find the relationship between the distribution of critical currents of clusters in Eq. (1) and the distribution of their areas in Eq. (2). The larger the normal-phase cluster size, the more weak links arise from its perimeter bordering with the surrounding superconducting space, and, consequently, the smaller is the critical current at which the magnetic flux breaks away from this cluster. If the concentration of weak links per unit length of the perimeter is the same for all clusters and all clusters of equal perimeters have the same pinning force, then the critical current  $I$  will be inversely proportional to the perimeter  $P$  of a normal-phase cluster,  $I \propto 1/P$ , because the larger the perimeter, the higher the probability of the presence of a weak link there. It is suggested here that if a vortex, which is subjected to the action of the Lorentz force, encounters a weak link connecting normal-phase clusters to each other, then the vortex has a 100% chance of passing through it. In this case, the magnetic flux is transferred through the superconducting medium by Josephson vortices. The probability of trapping the vortex when it moves through the weak link under the action of the Lorentz force is negligible, as the Josephson penetration depth in the materials under consideration significantly exceeds the sizes of possible irregularities along the weak link. In accordance with these assumptions, in order to find the distribution function in Eq. (1), one should know the relation between the perimeter and the area of a cluster. As was first established in [8], fractal properties of the boundaries of normal-phase clusters essentially affect the dynamics of magnetic flux in superconductors. For fractal clusters, the relationship between their perimeter and area has the form [22]

$$P \propto A^{\frac{D}{2}}, \quad (4)$$

where  $D$  is the fractal dimension of the cluster boundary.

Relation (4) agrees with the generalized Euclidean theorem [23], according to which the ratios of the corresponding measures are equal when they are reduced to the same dimension. Consequently,  $P^{1/D} \propto A^{1/2}$ , which is valid both for Euclidean clusters (for which the Hausdorff–Besikovich dimension of the perimeter is equal to the topological dimension of a line,  $D = 1$ ) and for fractal clusters (for which the Hausdorff–Besikovich dimension of the boundary strictly exceeds the topological dimension,  $D > 1$ ).

Note that it is the statistical distribution of cluster areas, not of their perimeters, that is fundamental in the following determination of the distribution of critical currents. As long as the Hausdorff–Besikovich dimension of a fractal line exceeds unity, the perimeter of a fractal cluster is not a well-defined quantity, because it diverges with an infinite increase in the precision of measurement [22]. At the same time, the topological dimension of the cluster area coincides with the Hausdorff–Besikovich dimension (both are equal to 2). Therefore, the area of a surface confined by a fractal curve is a finite, well-defined quantity.

When analyzing the geometric characteristics of normal-phase clusters, we consider the cross sections of extended columnar defects according to the plane in which the transport current flows. Therefore, though a normal-phase cluster is a self-affine fractal [24], we can consider its geometric probability properties in the plane of its cross section, where the boundaries of clusters are statistically self-similar.

Now, using relation (4) between the fractal perimeter and area, together with the assumption of inverse proportionality of the critical current of a cluster to its perimeter, we arrive at the following expression relating the critical current and the area of the cluster:  $I = \alpha A^{-D/2}$ , where  $\alpha$  is a form factor. In the general case of the gamma distribution of cluster areas (3), in accordance with initial relations (1) and (2), the distribution of critical currents has the form

$$F(i) = \frac{\Gamma\left(g+1, Gi^{-\frac{2}{D}}\right)}{\Gamma(g+1)}, \quad (5)$$

where

$$G \equiv \frac{\theta^{\frac{2}{D}(g+1)+1}}{\left(\theta^{g+1} - \frac{D}{2} e^{\theta} \Gamma(g+1, \theta)\right)^{\frac{2}{D}}},$$

$$\theta \equiv \frac{D}{2} + g + 1,$$

$\Gamma(v, z)$  is the complementary incomplete gamma function,  $i \equiv II_c$  is the dimensionless electric current, and  $I_c = \alpha(A_0 G)^{-\frac{D}{2}}$  is the critical current for the transition

into a resistive state. The function of cumulative probability in Eq. (5) found by us gives a complete description of the effect of the transport current on the trapped magnetic flux. Using this function, one can easily find the probability density  $f(i) \equiv dF/di$  of the distribution of depinning critical currents, which, in the general case, has the form

$$f(i) = \frac{2G^{g+1}}{D\Gamma(g+1)} i^{-\frac{2}{D}(g+1)-1} \exp\left(-Gi^{-\frac{2}{D}}\right). \quad (6)$$

The probability density is normalized to unity over all possible positive values of the critical current. The relative change in the trapped flux  $\Delta\Phi/\Phi$ , which can be directly calculated by using Eq. (5), also determines the density of vortices  $n$  broken away from pinning centers by the current  $i$ :

$$n(i) = \frac{B}{\Phi_0} \int_0^i f(i') di' = \frac{B \Delta\Phi}{\Phi_0 \Phi}, \quad (7)$$

where  $B$  is the magnetic field and  $\Phi_0 \equiv hc/(2e)$  is the quantum of magnetic flux ( $h$  is Planck's constant,  $c$  is the velocity of light, and  $e$  is the electron charge).

In Fig. 1, we show how the parameter of the gamma distribution  $g$  affects the distribution of the critical currents of clusters. As an example, we used a value of the fractal dimension  $D = 1.5$ , which is rather close to the value of  $D = 1.44 \pm 0.02$  of the fractal dimension of the boundaries of normal-phase clusters, which play the

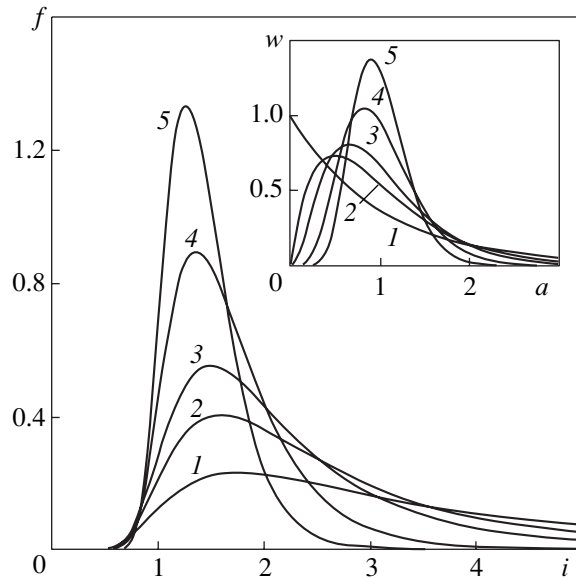


**Fig. 1.** Distribution of the critical currents for various values of the parameter  $g$  of the gamma distribution at a fixed fractal dimension of the cluster boundaries ( $D = 1.5$ ):  $g = (1) 0$ ,  $(2) 1$ ,  $(3) 2$ ,  $(4) 5$ , and  $(5) 10$ . In the inset: gamma distribution of the areas of normal-phase clusters.

role of pinning centers in YBCO film structures [8]. On the other hand, the value  $D = 1.5$  is intermediate between the limiting values  $D = 1$  for the Euclidean clusters and  $D = 2$  for the clusters of boundary with the maximum fractality. When the fractal dimension differs from unity so noticeably, the fractal properties of the cluster structure of a superconductor are of great importance. In the inset of Fig. 1, the area distribution of clusters is presented. The corresponding probability density has the form

$$w(a) = \frac{(g+1)^{g+1}}{\Gamma(g+1)} a^g e^{-(g+1)a}, \quad (8)$$

where  $a \equiv A/\bar{A}$  is the dimensionless cluster area, with  $\bar{a} = 1$  and  $\sigma_a = 1/\sqrt{g+1}$ . The function of cumulative probability for the dimensionless area is related with function (8) by the formula  $W(a) = \int_0^a w(a') da'$  and can be written in the form

$$W(a) = \frac{\gamma(g+1, (g+1)a)}{\Gamma(g+1)}.$$

As is seen from Fig. 1, when the parameter  $g$  decreases, the distribution  $f = f(i)$  spreads to the right side, covering progressively larger values of the critical currents. It might be expected that the greatest current-carrying ability of the superconductor is achieved in the limiting case of  $g = 0$ , when the gamma distribution in Eq. (8) is reduced to an exponential one,  $w(a) = \exp(-a)$ . In this case, small clusters make a maximal contribution to the resulting distribution (curve 1 in the

inset of Fig. 1). With  $g = 0$ , expressions (5) and (6) are simplified

$$F(i) = \exp\left(-\left(\frac{2+D}{2}\right)^{\frac{2}{D}+1} i^{-\frac{2}{D}}\right), \quad (9)$$

$$f(i) = \frac{2}{D} \left(\frac{2+D}{2}\right)^{\frac{2}{D}+1} i^{-\left(\frac{2}{D}+1\right)} \times \exp\left(-\left(\frac{2+D}{2}\right)^{\frac{2}{D}+1} i^{-\frac{2}{D}}\right), \quad (10)$$

where, as before,  $i \equiv I/I_c$  and the critical current for the resistive transition can be calculated using a simpler

$$\text{formula: } I_c = \left(\frac{2}{2+D}\right)^{\frac{2+D}{2}} \alpha(A_0)^{\frac{D}{2}}.$$

In Fig. 2, we show how the fractal dimension of the boundaries of clusters influences the distribution of the depinning critical currents in Eq. (10). As is clearly seen from the figure, with increasing fractal dimension, the distribution of critical currents spreads and shifts to larger values of current. Quantitatively, this shift is characterized by the dependences of the average critical current  $\bar{i}$  and of the mode of depinning current distribution on the fractal dimension, as is shown in the inset of Fig. 2. The distribution mode, i.e., the value of the critical current at which the probability density in Eq. (10) achieves its maximum, varies linearly with the fractal dimension, mode  $f(i) = (2+D)/2$ . The mathematical expectation obeys a much stronger superlinear law, which is governed by the gamma function

$$\bar{i} = \left(\frac{2+D}{2}\right)^{\frac{2+D}{2}} \Gamma\left(1 - \frac{D}{2}\right). \quad (11)$$

Thus, the geometric probability properties of normal-phase clusters determine the statistical distribution of depinning currents. Knowing this distribution, in accordance with Eq. (1), one can find the relative change in the trapped flux under the action of the transport current.

### 3. DYNAMICS OF MAGNETIC FLUX TRAPPED IN NORMAL-PHASE CLUSTERS WITH FRACTAL BOUNDARIES

The effect of the transport current on the trapped magnetic flux is demonstrated in Fig. 3. The change in the trapped flux was calculated from Eq. (1) for the exponential-hyperbolic distribution of critical currents in Eq. (9). Curves 1 and 5 in Fig. 3 correspond to the limiting cases of the Euclidean clusters ( $D = 1$ ) and the clusters of maximum fractal dimension ( $D = 2$ ), respec-

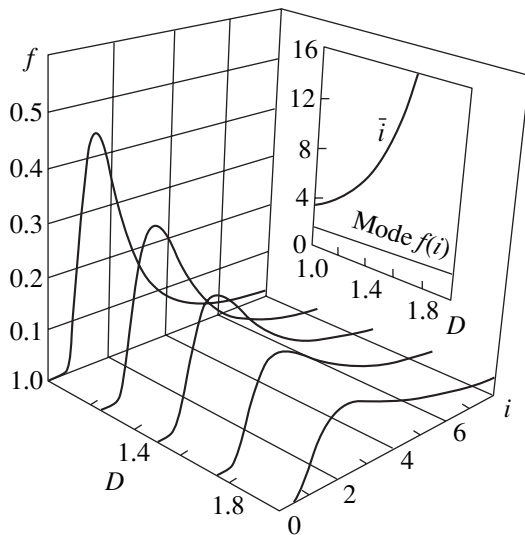


**Fig. 2.** Effect of the fractal dimension of the boundaries of normal-phase clusters on the distribution of the critical currents at  $g = 0$ . In the inset, we show how the average critical current and the mode of this distribution depend on the fractal dimension.



tively; they confine the region of changes in the trapped flux for all possible values of the fractal dimension. The function  $F = F(i)$  reveals one important property; namely, it is very flat near the origin of coordinates. It can easily be shown that all its derivatives become zero at the point  $i = 0$ :

$$\frac{d^k}{di^k} F(0) = 0 \text{ for any value of } k.$$

Therefore, even the expansion of the function into a Taylor series in the vicinity of the origin of coordinates converges to zero value but not to the quantity  $F$  itself. This mathematical property has a clear physical sense: so small transport current does not cause any effect on the trapped magnetic flux, because there are no pinning centers with such small critical currents in the statistical distribution. The change in the magnetic flux becomes noticeable only in the vicinity of the resistive transition point ( $i = 1$ ). Using the exponential-hyperbolic distribution of critical currents (9) naturally excludes the uncertainty caused by truncation of non-physical negative values of the depinning currents, as, for instance, in the case of the normal distribution [25–27].

As is seen from Fig. 3, the breaking of the vortices away is observed mainly at  $i > 1$ , when the sample undergoes a transition into a resistive state. Figure 3 demonstrates the practically important property of a superconducting structure with fractal normal-phase clusters: the fractality favors magnetic flux trapping by making its breaking away from pinning centers more difficult and thereby increasing the critical current below which the sample remains in the superconducting state. Indeed, the transport current of the value  $i = 2$  causes the 43% of the total trapped magnetic flux to break away from the usual Euclidean clusters ( $D = 1$ , curve 1), whereas this value equals only 13.5% for the fractal normal-phase clusters of the greatest possible perimeter dimension ( $D = 2$ , curve 5). This is equivalent to the pinning increase of 218% in the latter case. The enhancement of pinning due to fractality can be characterized by the gain factor,

$$k_\Phi \equiv 20 \log \frac{\Delta\Phi(D=1)}{\Delta\Phi(D)}, \text{ dB},$$

which is equal to the relative decrease in the fraction of the magnetic flux broken away from the fractal clusters of dimension  $D$  in comparison with the Euclidean clusters ( $D = 1$ ). In the inset of Fig. 3, the dependences of the pinning gain factor on the transport current and on the fractal dimension are presented. The maximal gain is achieved when the boundaries of clusters have the greatest possible fractal dimension ( $D = 2$ ):  $\max_D k_\Phi = \exp((4i - 3.375)/i^2)$ , with the maximum on the transport-current dependence of  $k_\Phi$  at  $i = 1.6875$ . Note that the pinning gain factor characterizes the properties of the superconductor in the region of transport currents

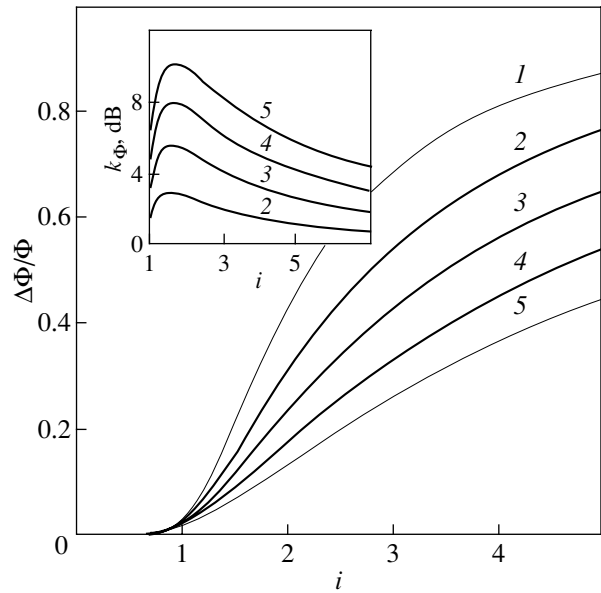


**Fig. 3.** Effect of a transport current on the magnetic flux trapped in fractal normal-phase clusters ( $g = 0$ ).  $D = (1)$  1, (2) 1.25, (3) 1.5, (4) 1.75, and (5) 2. In the inset: the pinning gain factor at different values of the fractal dimension of the cluster boundaries.

corresponding to the resistive state ( $i > 1$ ). With smaller currents, the trapped magnetic flux virtually does not change, because there are no pinning centers with such small critical currents (Figs. 1, 2) and the breaking of vortices away has still not begun. In the presence of a finite resistance, current flow is accompanied by energy dissipation. As for any hard superconductor (of type II, with pinning centers) the energy dissipation in the resistive state does not indicate destruction of the phase coherence yet. Some dissipation accompanies any motion of the magnetic flux; this can be observed in a hard superconductor even for small transport currents. Therefore, the critical current in such materials cannot be determined as the greatest nondissipative current. The superconducting state collapses only when the dissipation increases in an avalanche-like manner as a result of the thermal magnetic instability.

The reason for the pinning gain due to the cost of fractality of the boundaries of normal-phase clusters lies in the fundamental properties of the statistical distribution of critical currents (Fig. 2). In the case of Euclidean clusters, the average value of the critical current calculated in accordance with Eq. (11) is equal to  $\bar{i} (D = 1) = (3/2)^{3/2} \sqrt{\pi} = 3.2562$ , whereas for the clusters of boundary with the maximum fractality, it is  $\bar{i} (D = 2) \rightarrow \infty$ . As is seen from Fig. 2, as the fractal dimension increases, the contribution made by the clusters with large depinning critical currents to the overall statistical distribution increases, which results in an increase in magnetic flux trapping.

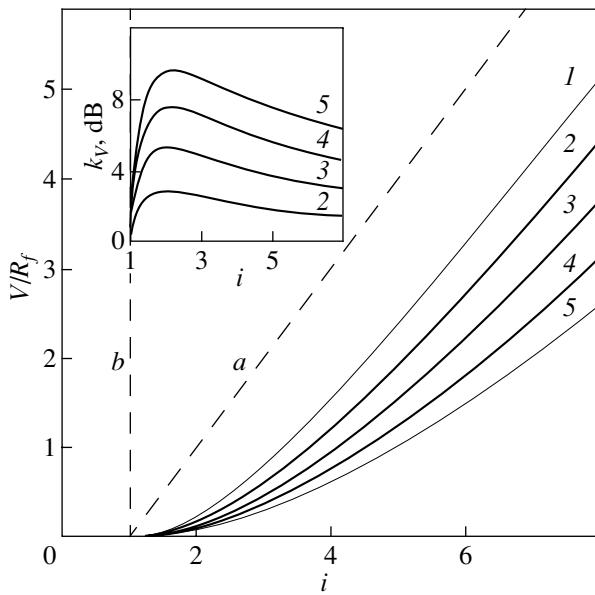


**Fig. 4.** Current–voltage characteristics of superconducting structures with fractal normal-phase clusters ( $g = 0$ ).  $D = (1)$  1,  $(2)$  1.25,  $(3)$  1.5,  $(4)$  1.75, and  $(5)$  2. Dashed line  $a$  corresponds to viscous flow of a magnetic flux for the case of  $\delta$ -like distribution of the critical currents, and dashed line  $b$  describes the superconductor in the critical state. In the inset: attenuation factor of dissipation at different values of the fractal dimension of the cluster boundaries.

In a resistive state, a hard superconductor is adequately described by its current–voltage characteristics. Knowing the fractal distribution of the critical currents in Eq. (6), one can find the electric field caused by magnetic flux motion after the vortices have been broken away from pinning centers. Inasmuch as each cluster of the normal phase contributes to the overall distribution of the critical currents, the voltage across the superconductor  $V = V(i)$  is a response to the sum of effects made by contribution from each cluster. This response can be expressed as a convolution integral

$$V = R_f \int_0^i (i - i') f(i') di', \quad (12)$$

where  $R_f$  is the flux flow resistance. This representation for the voltage across the sample is often used to consider the pinning of bunches of vortex lines in a superconductor [28] and to analyze the critical scaling of current–voltage characteristics [27], i.e., in all cases when the distribution of depinning critical currents is present. In the subsequent analysis, we focus on the results stemming from the properties of the exponential-hyperbolic distribution in Eq. (10); we will not consider questions associated with the possible dependence of the resistance for the flux flow  $R_f$  on the transport current.

In the simplest case, when all pinning centers have the same critical current  $i_c$ , all vortices are released

simultaneously at  $i = i_c$  and their density, in accordance with Eq. (7), has the form

$$n = \frac{B}{\Phi_0} \int_0^i \delta(i' - i_c) di' = \frac{B}{\Phi_0} h(i - i_c),$$

where  $\delta(i)$  is the Dirac  $\delta$  function and  $h(i) \equiv \begin{cases} 1, & i \geq 0 \\ 0, & i < 0 \end{cases}$  is the Heaviside function. The trapped flux would change at once by 100% in this case,  $\Delta\Phi/\Phi = h(i - i_c)$ .

Thus, in accordance with Eq. (12), for the  $\delta$ -like distribution of the critical currents in the regime of viscous flow of the magnetic flux, the voltage across the superconductor is governed by a simple linear dependence,  $V = R_f(i - i_c)h(i - i_c)$ . The corresponding current–voltage characteristics is indicated in Fig. 4 by the dashed line  $a$ . In the same figure, the current–voltage characteristics of the superconductor in a still simpler approximation (a critical-state model) is represented by the dashed curve  $b$ . In this case, the response upon any external action resulting in the appearance of an electric field in the hard superconductor is the flowing of a current, which is equal to the critical current  $i = i_c$ , regardless of the value of the voltage across the sample. (The dimensionless critical current is equal to unity due to the normalization chosen earlier,  $i \equiv I/I_c$ .)

For the fractal distribution of the critical currents, the situation changes drastically, because now the vortices are being broken away in a wide range of transport currents. We shall consider the case of the exponential area distribution of clusters ( $g = 0$ ), in which the current-carrying ability of the superconductor is maximal. After substitution of the distribution (10) into Eq. (12) followed by integration, the voltage across the sample can be expressed through the function of cumulative probability in Eq. (9):

$$V = R_f \int_0^i F(i') di'.$$

After integration, we arrive at

$$V = R_f \left[ i \exp \left( - \left( \frac{2+D}{2} \right)^{\frac{2}{D}+1} i^{\frac{2}{D}} \right) - \left( \frac{2+D}{2} \right)^{\frac{2+D}{2}} \times \Gamma \left( 1 - \frac{D}{2}, \left( \frac{2+D}{2} \right)^{\frac{2}{D}+1} i^{\frac{2}{D}} \right) \right]. \quad (13)$$

In the limiting cases of  $D = 1$  and 2, Eq. (13) can be simplified.

For the Euclidean clusters ( $D = 1$ ), the voltage across the superconductor has the form

$$\frac{V}{R_f} = \left[ i \exp\left(-\frac{3.375}{i^2}\right) - \sqrt{3.375\pi} \operatorname{erfc}\left(\frac{\sqrt{3.375}}{i}\right) \right], \quad (14)$$

where the complementary incomplete gamma function is expressed through the complementary error function

$$\Gamma(1/2, z) = \sqrt{\pi} \operatorname{erfc}(\sqrt{z}).$$

For clusters of boundary with the maximum fractality ( $D = 2$ ), after substitution of the representation for the complementary incomplete gamma function  $\Gamma(0, z) = -\operatorname{Ei}(-z)$ , Eq. (13) for the voltage takes the final form

$$V = R_f \left[ i \exp\left(-\frac{4}{i}\right) + 4 \operatorname{Ei}\left(-\frac{4}{i}\right) \right], \quad (15)$$

where  $\operatorname{Ei}(z)$  is the exponential integral function.

Figure 4 presents the current–voltage characteristics of a superconductor containing fractal clusters of the normal phase. A noticeable drop in voltage across the sample is observed for all values of the fractal dimension, starting from the value of the transport current  $i = 1$ ; this coincides with the value that was found earlier from the distributions of the critical currents in Eqs. (5) and (9) for the current at which the transition into the resistive state occurs. Equations (14) and (15) describe the dependences of the voltage on the transport current for the limiting values of the fractal dimension. Whatever the geometric probability properties of the normal-phase clusters, the current–voltage characteristics of a superconductor with these clusters will lie in the region confined by these dependences (curves 1, 5 in Fig. 4). As is seen from the figure, the fractality significantly reduces the electric field induced in the superconductor by magnetic flux motion. In the inset of Fig. 4, the dependences of the attenuation factor of dissipation

$$k_V \equiv 20 \log \frac{V(D=1)}{V(D)}, \text{ dB}$$

on the transport current at various values of the fractal dimension of cluster boundaries are presented. The decrease in the electric field with increasing fractal dimension is especially appreciable in the region of currents  $1 < i < 3$ , where the pinning gain also has a maximum (Fig. 3). Both of these effects have the same nature: they are due to the fractal distribution of the depinning critical currents. As is seen from Fig. 2, an increase in the fractal dimension leads to considerable spreading of the tail of the distribution,  $f = f(i)$ . This means that more and more clusters of small sizes, which are able to trap the magnetic flux most efficiently, are being involved in the game. As a result, the density of vortices broken away from pinning centers by the Lorentz force decreases and the smaller part of

the magnetic flux can flow, creating, therefore, a lower electric field. In turn, the smaller the electric field, the smaller the energy dissipated when the transport current passes through the sample; the decrease in heat release, which can cause a transition into the normal state, leads to an increase in the current-carrying ability of the superconductor containing such fractal clusters.

Thus, both Figs. 4 and 3 clearly demonstrate the most practically important result: the fractality of the boundaries of normal-phase clusters, which act as pinning centers, prevents destruction of the superconductivity by the transport current and, consequently, increases the critical current that the superconductor can withstand.

The fractal properties of normal-phase clusters essentially influence the dynamics of the magnetic flux trapped in the superconductor. This influence is due to a crucial change in the distribution of the depinning critical currents with an increasing fractal dimension of the cluster boundaries. The most important result is that the fractality of the boundaries of normal-phase clusters strengthens pinning and slows down destruction of the superconductivity by the transport current, thereby increasing the current-carrying ability of the superconductor. This opens crucially new prospects for increasing the critical currents of composite superconductors by optimization of their geometric morphological properties.

## REFERENCES

1. T. Higuchi, S. I. Yoo, and M. Murakami, *Phys. Rev. B* **59**, 1514 (1999).
2. L. Krusin-Elbaum, G. Blatter, J. R. Thompson, *et al.*, *Phys. Rev. Lett.* **81**, 3948 (1998).
3. S. N. Dorogovtsev and Yu. I. Kuzmin, *Phys. Lett. A* **170**, 245 (1992).
4. R. Surdeanu, R. J. Wijngaarden, B. Dam, *et al.*, *Phys. Rev. B* **58**, 12467 (1998).
5. E. Mezzetti, R. Gerbaldo, G. Ghigo, *et al.*, *Phys. Rev. B* **60**, 7623 (1999).
6. M. R. Beasley, in *Percolation, Localization and Superconductivity*, Ed. by A. M. Goldman and S. A. Wolf (Plenum, New York, 1984); NATO ASI Ser., Ser. B **109**, 115 (1984).
7. C. J. Olson, C. Reichhardt, and F. Nori, *Phys. Rev. Lett.* **80**, 2197 (1998).
8. Yu. I. Kuzmin, *Phys. Lett. A* **267**, 66 (2000).
9. Yu. I. Kuzmin, *Pis'ma Zh. Tekh. Fiz.* **26** (17), 81 (2000) [*Tech. Phys. Lett.* **26**, 791 (2000)].
10. L. Krusin-Elbaum, L. Civale, G. Blatter, *et al.*, *Phys. Rev. Lett.* **72**, 1914 (1994).
11. Yu. I. Kuz'min and I. V. Pleshakov, *Pis'ma Zh. Tekh. Fiz.* **25** (12), 30 (1999) [*Tech. Phys. Lett.* **25**, 475 (1999)].
12. Yu. I. Kuz'min, I. V. Pleshakov, and S. V. Razumov, *Fiz. Tverd. Tela (St. Petersburg)* **41**, 1739 (1999) [*Phys. Solid State* **41**, 1594 (1999)].
13. D. Stauffer, *Phys. Rep.* **54**, 2 (1979).

14. V. V. Bryksin, A. V. Goltsev, S. N. Dorogovtsev, *et al.*, J. Phys.: Condens. Matter **4**, 1791 (1992).
15. M. J. M. E. De Nivelte, G. J. Gerritsma, and H. Rogalla, Phys. Rev. Lett. **70**, 1525 (1993).
16. D. J. Scalapino, Phys. Rep. **250**, 329 (1995).
17. R. Haslinger and R. Joynt, Phys. Rev. B **61**, 4206 (2000).
18. H. R. Kerchner, D. P. Norton, A. Goyal, *et al.*, Phys. Rev. B **60**, 6878 (1999).
19. A. I. Rykov, S. Tajima, F. V. Kusmartsev, *et al.*, Phys. Rev. B **60**, 7601 (1999).
20. I. Maggio-April, C. Renner, A. Erb, *et al.*, Nature **390**, 487 (1997).
21. J. E. Sonier, R. F. Kiefl, J. H. Brewer, *et al.*, Phys. Rev. B **59**, R729 (1999).
22. B. B. Mandelbrot, *Fractals: Form, Chance, and Dimension* (Freeman, San Francisco, 1977).
23. B. B. Mandelbrot, *The Fractal Geometry of Nature* (Freeman, San Francisco, 1982).
24. B. B. Mandelbrot, in *Fractals in Physics*, Ed. by L. Pietronero and E. Tosatti (North Holland, Amsterdam, 1986; Mir, Moscow, 1988).
25. Yu. I. Kuzmin, A. P. Paugurt, I. V. Pleshakov, and S. V. Rasumov, Supercond. Sci. Technol. **7**, 41 (1994).
26. R. Wördenweber, Phys. Rev. B **46**, 3076 (1992).
27. B. Brown, Phys. Rev. B **61**, 3267 (2000).
28. W. H. Warnes and D. C. Larbalestier, Appl. Phys. Lett. **48**, 1403 (1986).

*Translated by N. Kovaleva*

---

**METALS  
AND SUPERCONDUCTORS**

---

## Nonlinear Stationary Waves with Transport Current in Superconductors

N. A. Tailanov and U. T. Yakhshiev

*Research Institute of Applied Physics, State University of Uzbekistan,  
Universitetskaya ul. 95, Vuzgorodok, Tashkent, 700174 Uzbekistan*

Received November 13, 2000

**Abstract**—The profile of a nonlinear stationary thermomagnetic wave in the resistive state of superconductors is studied at different transport currents. It is proved that the thermomagnetic wave has an oscillating profile at relatively high values of the transport current in the sample. A shock wave with a monotonic structure corresponds to comparatively weak transport currents. The wave propagation velocity and the wave front width in a superconductor are estimated. © 2001 MAIK “Nauka/Interperiodica”.

The problem of thermal suppression of the superconducting state in the presence of transport current is topical in the practical use of superconducting magnetic systems (see [1]). External fluctuations of various physical natures (thermal, magnetic, mechanical, etc.) can lead to the formation of resistive-phase regions in a superconductor. The ohmic heating of these regions under a transport current with density  $j_{tr}$  can bring about an increase in the temperature  $T$  above the critical point ( $T > T_c$ ) and, hence, the emergence of a vortex electric field  $\mathbf{E}$  in the sample. It was shown earlier [2] that, together with dispersive and nonlinear effects, the dissipative processes induced under ohmic heating in a superconductor lead to the formation of stable structures, thermoelectromagnetic  $\mathbf{E}$  and  $\mathbf{H}$  waves, depending on the conditions at the sample surface.

In the present work, we studied the qualitative pattern of the dynamics of nonlinear thermomagnetic dissipative structures in the resistive state of a superconductor.

The dynamics of thermomagnetic waves, which move at a constant velocity  $v$  along the  $x$  axis in a superconductor, is described in terms of self-simulated variables  $\xi(x, t) = x - vt$  by the nonlinear heat conduction equation [2–4]

$$-v\nu\frac{dT}{d\xi} = \frac{d}{d\xi}\left[\kappa\frac{dT}{d\xi}\right] + jE, \quad (1)$$

a set of Maxwell equations

$$\frac{dE}{d\xi} = -\frac{4\pi v}{c^2}j, \quad (2)$$

$$E = \frac{v}{c}H, \quad (3)$$

and their related equation of the critical state

$$j = j_c(T, H) + j_r(E) + j_{tr}. \quad (4)$$

Here,  $\nu$  and  $\kappa$  are the heat capacity and thermal conductivity coefficients, respectively;  $j_c(T) = j_0 - a(T - T_0)$  is the critical current density in the Bean model

( $\frac{dj_c}{dH} = 0$ ) [5] (where  $T_0$  and  $T_c$  are the initial and critical temperatures of the superconductor, respectively,

and the quantity  $a = \left.\frac{dj_c}{dT}\right|_{T=T_0}$  describes the thermally

activated weakening of the Abrikosov vortex pinning by lattice defects);  $j_r(E)$  is the resistive current density; and  $j_{tr}$  is the transport current density.

In the weak-heating approximation ( $T - T_0 \ll (T_c - T_0)$ ) for the viscous flow region ( $E > E_f$ , where  $E_f$  is the boundary of the linear section in the current–voltage characteristics of hard superconductors [6]), the dependence of the resistive current density  $j_r$  on the electric field  $E$  is linear; i.e.,  $j_r \approx \sigma_f E$  ( $\sigma_f$  is the effective conductivity). In weak fields ( $E < E_f$ ), the dependence  $j_r(E)$  is essentially nonlinear and is most likely determined by the thermally activated motion of the magnetic flux (flux creep [6]). Here, we will consider a perturbation with a sufficiently high amplitude ( $E > E_f$ ) and use the linear dependence  $j_r(E)$ .

The appropriate thermal and electrodynamic boundary conditions for Eqs. (1)–(4) have the form

$$T(\xi \rightarrow +\infty) = T_0, \quad \frac{dT}{d\xi}(x \rightarrow -\infty) = 0, \quad (5)$$

$$E(\xi \rightarrow +\infty) = 0, \quad E(\xi \rightarrow -\infty) = E_e,$$

where  $E_e$  is the external electric field.

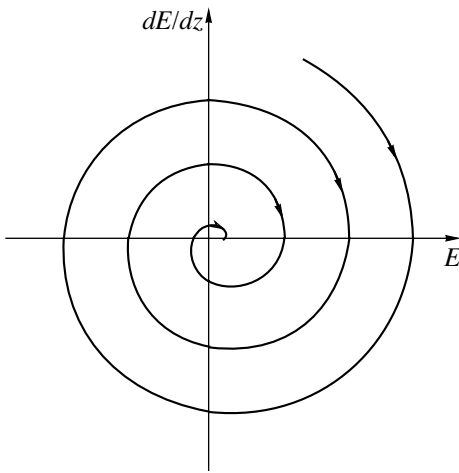


Fig. 1. Phase portrait of Eq. (7) at  $\beta(1 + \tau)E_\kappa > E_j$ .

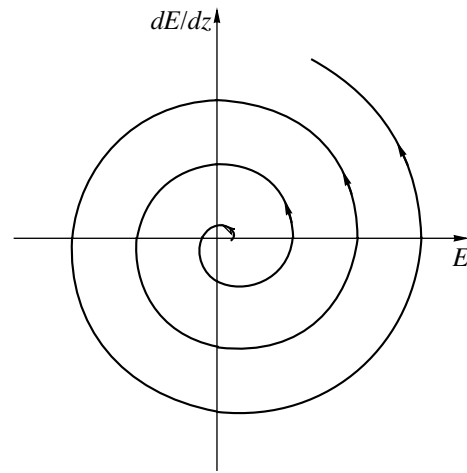


Fig. 2. Phase portrait of Eq. (7) at  $\beta(1 + \tau)E_\kappa < E_j$ .

By solving the set of Eqs. (1)–(4) with boundary conditions (5), we obtain the following equation for the distribution of the nonlinear  $E$  wave:

$$\frac{d^3 E}{dz^3} + \beta(1 + \tau) \frac{d^2 E}{dz^2} + \beta^2 \tau \left[ \frac{dE}{dz} + \frac{E_j}{E_\kappa} E \right] = 0. \quad (6)$$

$$\text{Here, } z = \frac{\xi}{L}, \beta = \frac{vt_k}{L}, \tau = \frac{4\pi\kappa\sigma_f}{c^2\nu}, E_j = \frac{j_{tr}}{\sigma_f}, E_\kappa = \frac{\kappa}{aL^2},$$

$L = \frac{cH_e}{4\pi j_0}$  is the depth of the magnetic field penetration

into the bulk of the superconductor,  $t_\kappa = \frac{\nu L^2}{\kappa}$  is the thermal

time of the problem, and  $H_e$  is the external magnetic field.

By analyzing the roots of the characteristic equation [7]

$$\lambda(\lambda + \beta)(\lambda + \beta\tau) = -\beta^2\tau \frac{E_j}{E_\kappa}, \quad (7)$$

we can easily verify that the problem considered has solutions that oscillate about the origin of the coordinates ( $E_0 = 0$ ) of the phase diagram with decreasing and increasing amplitudes. The oscillations appear at  $E_j >$

$\frac{\beta\tau}{2(1 + \tau)} E_\kappa$ , attenuate at  $\beta(1 + \tau)E_\kappa > E_j > \frac{\beta\tau}{2(1 + \tau)} E_\kappa$ , and increase at  $\beta(1 + \tau)E_\kappa < E_j$ . This means that, at a sufficiently high transport current  $j_{tr}$ , the roots of the characteristic equation (7) are complex, the integral curves are helical, and the origin  $E_0 = 0$  is a singular point (focus). If the coefficients  $\beta$  and  $\tau$  are assumed to be universally positive, the representative point approaches the origin of coordinates, which is a stable equilibrium position (Fig. 1). In the opposite case, when  $\beta(1 + \tau)E_\kappa < E_j$ , the focus becomes unstable and

the representative point goes to infinity (Fig. 2). Note that the final value of the transport current  $j_{tr}$  leads to a displacement of singular points and, correspondingly, of the boundary conditions.

At sufficiently weak transport currents, when the condition  $\frac{dE}{dz} \gg \beta^2\tau E_j$  is satisfied (high-amplitude waves), Eq. (6) is an integrable equation and the corresponding model can be considered a damped linear oscillator owing to the friction force, that is,

$$F_t = -\beta(1 + \tau) \frac{dE}{dz}, \quad (8)$$

where  $z$  is an analogue of time and  $E$  is the coordinate of the “material” point. The potential well equation has the form

$$U(E) = -\frac{E^3}{6E_\kappa} + \beta^2\tau \frac{E^2}{2}. \quad (9)$$

Analysis of the phase plane  $\left(\frac{dE}{dz}, E\right)$  described by Eq. (6) shows that it has two equilibrium points:  $E_0$  is a stable node and  $E_1 = 2\beta^2\tau E_\kappa$  is a saddle. The two equilibrium states ( $E_0, E_1$ ) are separated by the separatrix  $AB$  in the phase plane (Fig. 3). The material point is located at the point  $E_1$  at  $z \rightarrow \infty$  and goes over into the point  $E_0$  at  $z \rightarrow -\infty$ . The change-over from one equilibrium state to the other occurs only monotonically.

Within the approximation  $\tau \ll 1$ , the solution of Eq. (6) is represented as

$$E(z) = \frac{E_1}{2} \left[ 1 - \tanh\left(\frac{\beta}{2}(z - z_0)\right) \right]. \quad (10)$$

The condition  $\tau = \frac{D_t}{D_m} \ll 1$  means that the magnetic flux is redistributed much faster than the heat is transferred. Here,  $D_t = \frac{\kappa}{\nu}$  and  $D_m = \frac{c^2}{4\pi\sigma_f}$  are the thermal and magnetic diffusion coefficients, respectively [6]. Hence, the spatial scale  $L_E$  for the magnetic flux penetration is substantially greater than the corresponding thermal scale  $L_T$ . Therefore, the spatial derivatives  $\frac{d^n E}{dz^n}$

will contain a small parameter  $\left[\frac{L_T}{L_E}\right] \ll 1$ . We can easily check the validity of this approximation by the direct differentiation of Eq. (6), that is,

$$\frac{d^2 E}{dz^2} \left( \beta \frac{dE}{dz} \right)^{-1} = \tau \ll 1. \quad (11)$$

The maximum error of this approximation is of the order  $\frac{\tau}{(1+\tau)^2}$ . For example, the error is equal to 25% at  $\tau = 1$  and is vanishingly small in the limiting case  $\tau \rightarrow 0$ . Relationship (10) describes the profile of a shock thermomagnetic wave propagating into the bulk of the superconductor. The wave structure is shown in Fig. 4. At the boundary condition  $E(z \rightarrow -\infty) = E_e$ , we can easily determine the velocity  $v_E$  of the wave with an amplitude  $E_e$  in the form

$$v_E = \frac{L}{t_\kappa} \left[ \frac{E_e}{2\tau E_\kappa} \right] \quad (12)$$

and the wave front width  $\delta z$ ,

$$\delta z = 16 \frac{1+\tau}{\tau^{1/2}} \left[ \frac{E_\kappa}{E_e} \right]. \quad (13)$$

The numerical estimates yield the values  $v_E = 1-10^2$  cm/s and  $\delta z = 10^{-1}-10^{-2}$  for  $\tau = 1$ .

In conclusion, we note that the results obtained make it possible to describe the nonlinear stage of evolution of the thermomagnetic instability in the resistive state of superconductors. In the initial stage, we observe an exponential increase in the perturbations of  $T$ ,  $E$ , and  $H$  with the increment  $\lambda$  determined from the linear theory (see [8]). The linear stage of the instability evolution lasts for the period  $t_j = \frac{t_\kappa}{\lambda}$ . In the latter stage of the instability evolution, the stationary  $\mathbf{E}$  or  $\mathbf{H}$  wave (depending on whether the  $\mathbf{E}$  or  $\mathbf{H}$  quantity is fixed on the sample surface during the wave motion) propagates into the bulk of the sample. The velocity of the wave is determined by formula (12), and the time of its motion

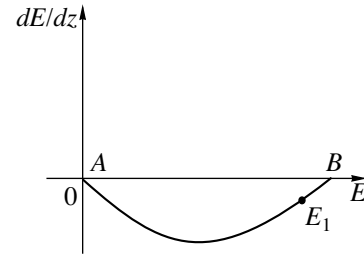


Fig. 3. Phase portrait of Eq. (7) for low values of the transport current  $\frac{dE}{dz} \gg \beta^2 \tau E_j$ .

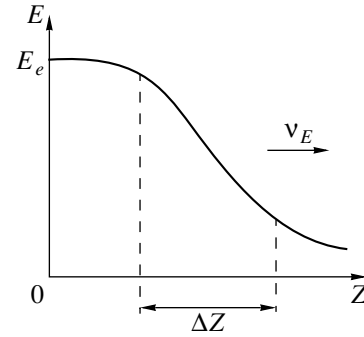


Fig. 4. Structure of the shock thermomagnetic wave.

in the sample with thickness  $2l$  is given by

$$\Delta t = \frac{l}{v_E}. \quad (14)$$

Hence, it follows that the transition from the superconducting to the normal state can occur through the propagation of a stationary thermomagnetic wave whose structure essentially depends on dispersive and dissipative effects.

## REFERENCES

1. V. R. Romanovskii, Dokl. Akad. Nauk **365** (1), 44 (1999) [Dokl. Phys. **44**, 137 (1999)].
2. I. L. Maksimov, Yu. N. Mastakov, and N. A. Taïlanov, Fiz. Tverd. Tela (Leningrad) **28** (8), 2323 (1986) [Sov. Phys. Solid State **28**, 1300 (1986)].
3. N. A. Taïlanov, Metallofizika (Kiev) **13** (9), 713 (1991).
4. N. A. Taïlanov and S. Kuchkarov, Fiz. Tverd. Tela (Leningrad) **33** (6), 1873 (1991) [Sov. Phys. Solid State **33**, 1052 (1991)].
5. C. P. Bean, Phys. Rev. Lett. **8** (6), 250 (1962).
6. R. G. Mints and A. L. Rakhmanov, *Instability in Superconductors* (Nauka, Moscow, 1984).
7. V. I. Karpman, *Non-Linear Waves in Dispersive Media* (Nauka, Moscow, 1973; Pergamon, Oxford, 1975).
8. V. A. Al'tov, V. B. Zenkevich, M. G. Kremlev, and V. V. Sychev, *Stabilization of Superconducting Magnetic Systems* (Énergoatomizdat, Moscow, 1984).

Translated by M. Lebedkin

---

METALS  
AND SUPERCONDUCTORS

---

## Peculiarities of Magnetic Flux Penetration and Trapping in Monocrystalline ( $\text{YBa}_2\text{Cu}_3\text{O}_{7-x}$ and $\text{Bi}_2\text{Sr}_2\text{CaCu}_2\text{O}_{8+x}$ ) and Polycrystalline ( $\text{YBa}_2\text{Cu}_3\text{O}_{7-x}$ ) Samples

V. N. Gubankov and Kh. R. Rostami

*Institute of Radio Engineering and Electronics, Russian Academy of Sciences,  
ul. Mokhovaya 11, Moscow, 103907 Russia*

*e-mail: vip@ire216.msk.su*

Received July 3, 2000; in final form, November 24, 2000

**Abstract**—A comparative analysis of the magnetic flux trapping in monocrystalline and polycrystalline HTSC samples is carried out, and the possibility of employing the dependence of the trapped magnetic flux on the external magnetic field for obtaining comparative estimates of the effect of pinning centers is determined. © 2001 MAIK “Nauka/Interperiodica”.

1. In spite of the large number of publications devoted to magnetic flux penetration and trapping (MFT) in monocrystalline and polycrystalline HTSC samples (see, for example, [1–4] and the references therein), no systematic comparative analysis of the experimental data on MFT has been carried out to date on a unified basis for a variety of structures. At the same time, such an analysis makes it possible to reveal some features of the penetration and trapping of the magnetic flux, whose comparison might provide information on the dynamics of flux penetration under various conditions (e.g., those depending on the past history of the sample), the energy spectrum of pinning centers, etc. The present work aims at filling this gap. We simultaneously consider the magnetic-field dependences of the magnetic flux trapped in monocrystalline and polycrystalline samples and investigate the possibility of using these dependences for obtaining comparative estimates of the effect of pinning centers on the magnetic properties of materials.

2. For our investigations, we chose  $\text{YBa}_2\text{Cu}_3\text{O}_{7-x}$  single crystals with a superconducting transition temperature  $T_c \approx 91$  K and  $\sim 1 \times 1 \times 0.5$  mm,  $2 \times 1 \times 0.05$  mm, and  $0.8 \times 0.7 \times 0.05$  mm in size;  $\text{Bi}_2\text{Sr}_2\text{CaCu}_2\text{O}_{8+x}$  single crystals with  $T_c \approx 90.2$  K  $\sim 1.2 \times 1.1 \times 0.15$  mm,  $4 \times 4 \times 0.1$  mm, and  $4 \times 10 \times 0.6$  mm in size; and polycrystals (partially molten ceramic samples) of  $\text{YBa}_2\text{Cu}_3\text{O}_{7-x}$  with  $T_c \approx 91.5$  K in the form of a disk of radius  $R = 4.5$  mm and thickness  $h = 3$  mm; and with  $R = 3$  mm and  $h = 2$  mm. The superconducting transition temperature of the samples was determined from the temperature dependence of the high-frequency inductance.

The trapped magnetic flux was measured at liquid nitrogen temperature in static magnetic fields up to 1 kG by a Hall probe with a working area of  $0.15 \times$

$0.45$  mm and a sensitivity of  $10 \mu\text{V G}^{-1}$ . The Hall probe ensured a field recording with a sensitivity not worse than  $10^{-2}$  G and could be displaced from the center along the ( $z$ ) axis and to the sample periphery. The trapped magnetic field  $B_{\text{tr}}(0)$  was measured at the centers of the samples as a function of the external magnetic field  $B_0$ ; the axial coordinate distributions of the maximum trapped field  $B_{\text{tr}}^{\text{max}}(z)$  as a function of coordinate  $z$  were also measured. For our measurements, we used regimes of sample cooling in a magnetic field (FC), as well as in zero magnetic field (ZFC). The field was directed at right angles to the plane of the sample. The experimental technique is described in detail in [5].

3. Figure 1 shows typical dependences of  $B_{\text{tr}}(0)$  on the external magnetic field  $B_0$  for the samples under investigation in the FC and ZFC modes. These dependences indicate the initial increase in the value of  $B_{\text{tr}}(0)$  with a smooth transition to the saturation region upon further increase in  $B_0$ . The following differences are typically observed in the curves: in the values of the lower critical field  $B_{c1}$ , in the saturation field  $B_0^*$  for which  $B_{\text{tr}}(0)$  attains the saturation region, and in the maximum trapped field  $B_{\text{tr}}^{\text{max}}(0)$  corresponding to the saturation region. In the ZFC mode, these values were 50, 95, and 0.29 G, respectively, for the YBCO single crystal, while for the BSCCO single crystals, these values were 4.5, 30, and 2.1 G, respectively. The same values for the polycrystalline YBCO sample were 0.1, 500, and 29.8 G (the values of these fields for each group of crystals varied within 15%). A comparison of these values leads to the following conclusions: (a) the intervals of fields  $B_0$  in which an increase in  $B_{\text{tr}}(0)$  is observed amounts to several tens of gauss for YBCO and BSCCO single crystals, but for the latter single



crystals, this interval is shifted to the region of lower fields due to the smaller values of the lower critical field  $B_{c1}$  and the saturation field  $B_0^*$ ; (b) the maximum trapped field  $B_{tr}^{max}(0)$  of the BSCCO single crystal is a few times higher than the value of  $B_{tr}(0)$  for the YBCO single crystal; and (c) the field interval in which the increase in  $B_{tr}(0)$  is observed in polycrystalline YBCO crystals is much larger due to the smaller value of the lower critical field  $B_{c1}$  and the larger value of the saturation field  $B_0^*$  (the value of  $B_{tr}^{max}(0)$  for a polycrystalline sample is more than two orders of magnitude larger than the field trapped in the YBCO single crystal).

The above difference in the behavior of monocrystalline and polycrystalline YBCO samples are natural and correspond to earlier results [5] of investigations into MFT for YBCO ceramic samples. Comparison of the behavior of YBCO and BSCCO single crystals is of greater interest.

Figure 2 shows the typical dependences of the normalized quantities  $B_{tr}(0)/B_{tr}^{max}(0)$  on the external normalized magnetic field  $B_0/B_0^*$  for the same samples. It can be seen from this figure that in the ZFC mode, the magnetic field penetrates into BSCCO single crystals relatively more easily and rapidly, while the pattern observed in the case of FC is different: the field penetrates into YBCO single crystals relatively more easily and rapidly. These dependences can be qualitatively interpreted as follows.

The dynamics of magnetic field penetration into the samples under investigation is mainly determined by the following two factors: the magnetic field screening by the superconducting currents induced in the sample and the presence of pinning centers. In the case of ZFC, both factors are present, while the second factor dominates in the FC mode. According to Bean's model [6], the thinner the sample and the smaller its critical current, the shorter the time required for the magnetic field to reach the center of the sample. The experimentally estimated [7] value of the critical current for the YBCO single crystal was  $8.6 \times 10^3 \text{ A cm}^{-2}$ . It was several times higher than the critical current for the BSCCO sample ( $2.02 \times 10^3 \text{ A cm}^{-2}$ ) and more than two orders of magnitude higher than the critical current in the polycrystalline YBCO sample. This difference explains the relatively slow penetration of the magnetic field observed in the YBCO single crystal in the ZFC mode. In this case, the value of the maximum trapped magnetic field  $B_{tr}^{max}(0)$  itself indicates that the influence of pinning centers in the YBCO single crystals used was the least significant.

In the FC mode, when the dynamics of magnetic field penetration into the samples was in fact determined by the interaction of the magnetic flux with pin-

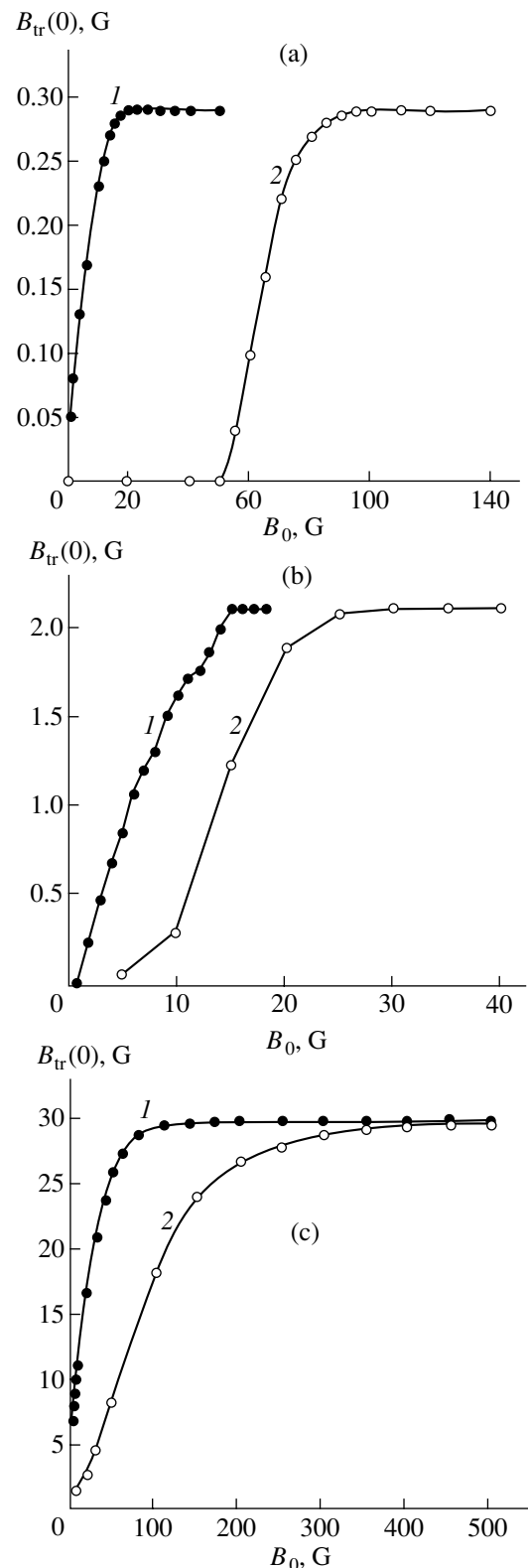


**Fig. 1.** Magnetic-field dependences of the trapped magnetic field at the center of the sample,  $B_{tr}(0)$  ( $B_0$ ): (a) YBCO, monocrystalline sample of size  $1 \times 1 \times 0.05$  mm; (b) BSCCO, monocrystalline sample ( $4 \times 4 \times 0.1$  mm); and (c) YBCO, polycrystalline sample (of radius  $R = 3$  mm and thickness  $h = 2$  mm); curves 1 were recorded in the FC mode and curves 2 in the ZFC mode. The temperature is 77.4 K.

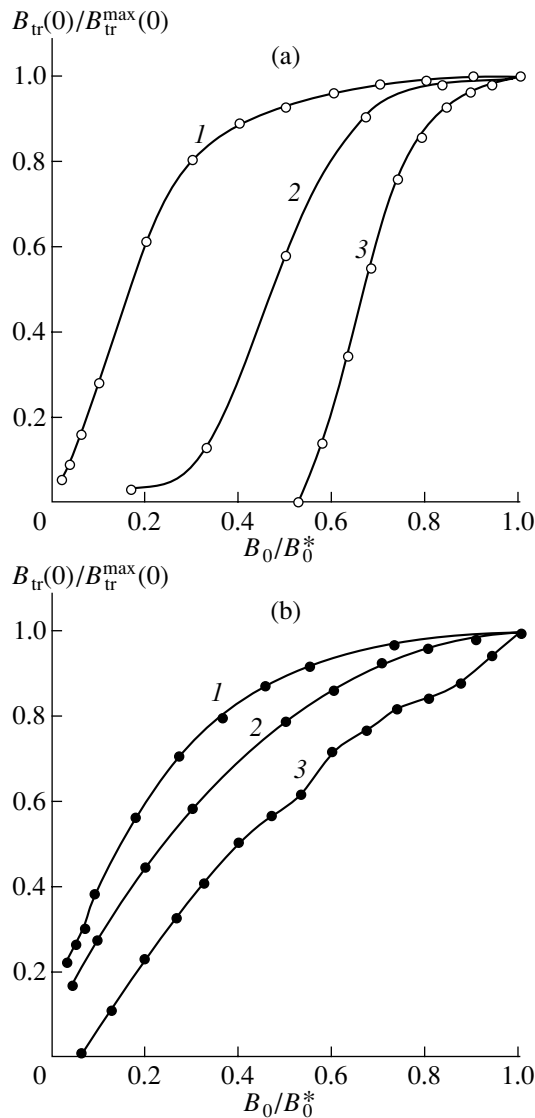


**Fig. 2.** Dependence of normalized values of  $B_{tr}(0)/B_{tr}^{max}(0)$  on  $B_0/B_0^*$ : YBCO, polycrystalline sample (curve 1); BSCCO, monocrystalline sample (curve 2); and YBCO, monocrystalline sample (curve 3) (a) for ZFC and (b) FC. The samples are the same as in Fig. 1. The temperature is 77.4 K.

ning centers (since the effects of magnetic field screening by superconducting currents are virtually eliminated), a relatively more rapid arrival of the magnetic field to the center of the sample is observed for YBCO single crystals. The bulk pinning force estimated in accordance with [8] by using the known formula  $a = J_c B_{tr}^{max}(0)$  amounted to  $4.32 \times 10^2$  and  $2.67 \times 10^2$  dyn cm<sup>-3</sup> for BSCCO and YBCO single crystals, respectively. This means that the increase in the magnetic field in BSCCO single crystals in the FC regime occurs at a slower rate. This conclusion is in accordance with the estimates

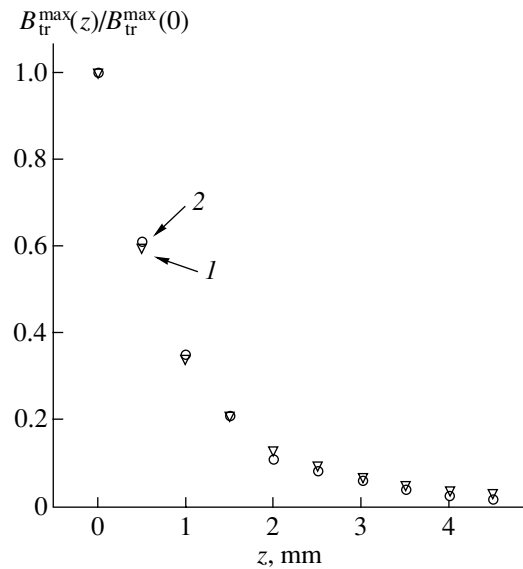


**Fig. 3.** Axial distribution of the normalized maximum trapped magnetic field  $B_{tr}^{max}(z)/B_{tr}^{max}(0)$  for a monocrystalline BSCCO sample for (1) FC and (2) ZFC. The sample is the same as in Figs. 1 and 2. The temperature is 77.4 K.

obtained for the values of  $B_{tr}^{max}(0)$  for YBCO and BSCCO single crystals.

**4.** Figure 3 shows the axial distribution of the normalized trapped magnetic field  $B_{tr}^{max}(z)/B_{tr}^{max}(0)$  for a monocrystalline BSCCO sample in the ZFC and FC modes. The coincidence of the experimental points obtained in these two regimes of measurement indicates the identity of MFT topologies in the ZFC and FC modes. In other words, the same pinning centers participate in the MFT irrespective of the past history of the sample. In HTSC ceramics, no such coincidence is observed up to high values of the magnetic fields; i.e., the MFT topology is different in view of the strong spatial inhomogeneity of the sample and the wider energy spectrum of pinning centers responsible for the MFT as compared to that in single crystals.

Thus, a comparative analysis of the MFT in different modes makes it possible to draw conclusions on the main reasons determining the dynamics of penetration of the magnetic field into the samples and to estimate the effect of pinning centers. In particular, it was found that the effect of pinning centers, in the batch of samples under investigation, was less significant in YBCO single crystals than in BSCCO single crystals.

## REFERENCES

1. A. A. Elistratov and I. L. Maksimov, *Fiz. Tverd. Tela* (St. Petersburg) **42**, 196 (2000) [*Phys. Solid State* **42**, 201 (2000)].

2. V. N. Zabenkin, L. A. Aksel'rod, A. A. Vorob'ev, *et al.*, *Pis'ma Zh. Éksp. Teor. Fiz.* **70**, 771 (1999) [JETP Lett. **70**, 787 (1999)].
3. R. Khasanov, Yu. I. Talanov, W. Assmus, and G. B. Teitelbaum, *Phys. Rev. B* **54** (18), 13339 (1996).
4. M. Benkrouda and J. R. Clem, *Phys. Rev. B* **53** (9), 5716 (1996).
5. Kh. R. Rostami, V. V. Mantorov, and V. I. Omel'chenko, *Fiz. Nizk. Temp.* **22**, 736 (1996) [*Low Temp. Phys.* **22**, 565 (1996)].
6. C. P. Bean, *Rev. Mod. Phys.* **36**, 31 (1964).
7. Kh. R. Rostami, *Fiz. Nizk. Temp.* **27** (17), 18 (2001) [*Low Temp. Phys.* **27** (1), 79 (2001)].
8. A. M. Campbell and J. E. Evetts, *Critical Currents in Superconductors* (Taylor and Francis, London, 1972; Mir, Moscow, 1975).

*Translated by N. Wadhwa*

# Kinetics of Optical Thermal Breakdown of a Thin Semiconducting Film

R. D. Vengrenovich and Yu. V. Gudyma

Chernovtsy National University, Chernovtsy, 58012 Ukraine

Received September 21, 2000; in final form, November 28, 2000

**Abstract**—The kinetics of various stages of the optical thermal breakdown in a semiconducting wafer is considered on a unified basis. The evolution of the radius of a new-phase nucleus in the space of nucleus sizes is studied in analogy with the decomposition of a supersaturated solid solution. © 2001 MAIK “Nauka/Interperiodica”.

## 1. INTRODUCTION

Analysis of physical processes associated with laser-induced destruction is the most reliable method of solving practical problems associated with the development of the technology of optically stable materials. Indeed, the destruction of transparent elements in lasers under the action of intrinsic radiation restricts their maximum power. The phenomenon of optical breakdown in transparent hard materials was discovered in 1964 [1, 2] after the creation of giant-pulse lasers. The highest output power with a satisfactory monochromaticity of the beam is attained for CO<sub>2</sub> continuous-wave lasers. The lasing wavelength for such lasers (10.6 μm) lies in the relatively distant infrared region in which germanium has a high transparency.

Reversible optical thermal breakdown is an example of the nonlinear optical effects in systems excited by coherent light. A distinguishing feature of such systems is the formation of multiple stable states after the system parameters exceed certain critical values in the absence of external feedback [3]. The physical origin of this phenomenon is associated with the rapid (exponential) increase in the light absorption coefficient by free charge carriers (the energy of a light quantum is slightly smaller than the band gap width) upon semiconductor heating by absorbed radiation and is manifested in a drastic increase in the semiconductor temperature when the light intensity (extrinsic parameter) exceeds the breakdown threshold. The interest in optical thermal breakdown as an example of the formation of a dissipative structure in an open system far from thermodynamic equilibrium is due to the fact that this phenomenon was observed experimentally [4] and explained theoretically [5]. The model of this phenomenon was used to demonstrate the features of hysteresis in distributed systems and to prove the existence of switching waves between the states corresponding to different branches of the hysteresis loop. Thus, almost all non-equilibrium effects observed in optical heat-induced breakdown, including the emergence of fluctuational

bursts and their independent growth [6, 7], have been described. At the same time, the late stages in the optical heat-induced breakdown have been insufficiently studied. Moreover, no unified approach has been worked out for all stages of the nonequilibrium transition. In this work, the kinetics of various stages of optical thermal breakdown in a semiconducting wafer are considered on a unified basis using a differential equation simulating this physical phenomenon.

## 2. PHYSICAL MODEL AND BASIC EQUATIONS

It should be noted that the system under investigation is a convenient object for experimental investigation since the intensity of incident light (extrinsic parameter) can easily be varied over a wide range. We will assume that the incident laser beam is homogeneous in the transverse directions. In this case, the thermal balance equation for a semiconducting wafer has the form [3]

$$cd\frac{\partial T}{\partial t} = \chi\left(\frac{\partial^2 T}{\partial x^2} + \frac{\partial^2 T}{\partial y^2}\right) \quad (1)$$

$$+ G\{1 - \exp(-\alpha(T)l)\}/l - H(T - T_0)/l,$$

where  $G$  is the intensity of the wide incident beam of light,  $c$  is the specific heat of the semiconducting material,  $d$  is the surface density of the substance,  $l$  is the plate thickness,  $H$  is the heat transfer factor equal to the ratio of the specific heat to the density of the material per unit length,  $T_0$  is the temperature of the thermostat,  $\chi$  is the transverse thermal conductivity,

$$\alpha(T) = \alpha_0 \exp(-E_g/2kT) \quad (2)$$

is the coefficient of light absorption by free carriers, and  $E_g$  is the band gap width of the semiconductor. The temperature dependence of the absorption coefficient  $\alpha_0$  at high temperatures is usually disregarded.

We can easily write Eq. (1) in dimensionless variables:

$$\begin{aligned} \frac{\partial \theta}{\partial \tau} &= \frac{\partial^2 \theta}{\partial \rho^2} + \beta \{ 1 - \exp(-\eta \exp(\gamma - \gamma/\theta)) \} \\ -(\theta - 1) &\equiv \frac{\partial^2 \theta}{\partial \rho^2} + f(\theta), \end{aligned} \quad (3)$$

where  $\theta = T/T_0$ ,  $\tau = tH/cdl$ ,  $\rho = H^{1/2}\chi^{-1/2}l^{-1/2}r_{\perp}$ ,  $\gamma = E_g/2kT_0$ ,  $\eta = \alpha(T_0)l$ , and  $\beta = GH^{-1}T_0^{-1}$ .

### 3. NUCLEATION

In the stationary homogeneous case, Eq. (3) has one to three solutions, depending on the controlling parameter  $\beta$  (Fig. 1). In the last case, the system has two stationary homogeneous states characterized by temperatures  $\theta_1$  and  $\theta_3$  and an unstable state with a temperature  $\theta_2$  lying between these temperatures. The low-temperature state with  $\theta_1$  on the left of  $\theta_2$  is stable, while the high-temperature state with  $\theta_3$  is metastable; to the right of this value, the opposite situation takes place. Consequently, each stable state can be put in correspondence to a certain physical phase. Each phase is characterized by the corresponding absorption coefficient  $\eta$ .

It is convenient to carry out the subsequent analysis by writing the initial equation (3) in an equivalent form:

$$\frac{\partial \theta}{\partial \tau} = -\frac{\delta \Phi[\theta]}{\delta \theta(\rho, \tau)}, \quad (4)$$

where

$$\Phi[\theta] = \int \left[ \frac{1}{2} \left( \frac{\partial \theta}{\partial \rho} \right)^2 + F(\theta) \right] d\rho. \quad (5)$$

In accordance with the basic concepts of the thermodynamics of nonequilibrium processes [8], the rate of variation of the order parameter is proportional to the conjugate thermodynamic force for a small deviation from equilibrium. Equation (4) is in complete agreement with this statement. Such a similarity allows one to introduce a generalized free energy  $\Phi[\theta]$  and a generalized scalar order parameter  $\theta$  [9]. In the case at hand, the density of the generalized free energy  $\Phi[\theta]$  is defined as

$$F(\theta) = -\int_{\theta_1}^{\theta} f(u) du. \quad (6)$$

It has one or two minima (Fig. 2). The states of the substance corresponding to each of these two minima are locally stable and equilibrium states. A change in the extrinsic parameter (luminous flux level  $\beta$ ) causes a change in the mutual positions of the minima on the curves. The luminous flux level  $\beta_c$  for which the ener-

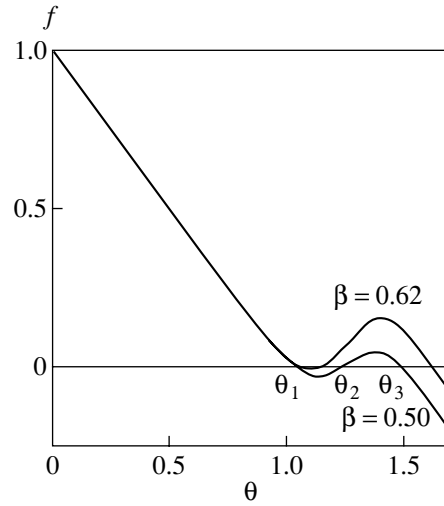


Fig. 1. Plot of the  $f(\theta)$  dependence.

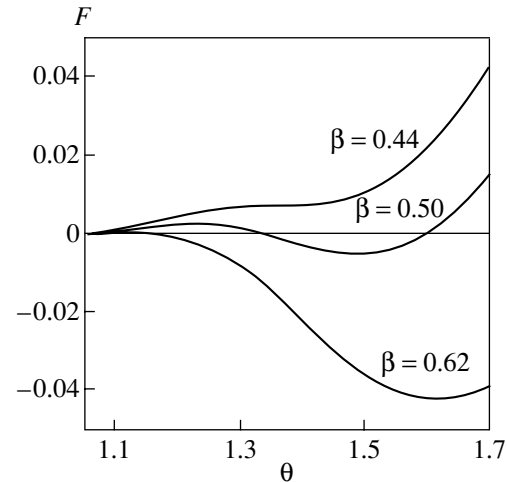


Fig. 2. Dependence of the generalized free energy density  $F(\theta)$  on the dimensionless light intensity  $\beta$ .

gies at the minima coincide corresponds to the phase transition point. Thus, in a certain interval of luminous flux  $\beta$ , both (low- and high-temperature) phases coexist. The phase corresponding to a higher free energy is metastable.

The transition from the metastable to the stable phase occurs through the fluctuation-induced formation of small aggregates of the new phase (nuclei) in a homogeneous medium. The probability of the formation of a state of the system with a single nucleus, which is determined by the minimum work that must be done for creating a nucleus of a given size on the water plane [10], is

$$A_{\min} = \varphi S + \alpha P, \quad (7)$$

where  $S = 4\pi R^2$  and  $P = 2\pi R$  are the area and the perimeter of the nucleus, respectively;  $\varphi$  is the free energy per unit area; and  $\alpha$  is the energy per unit length of the interface.

For a nucleus which is in equilibrium with the ambient, we have

$$\left. \frac{dA_{\min}}{dR} \right|_{R_c} = 0, \quad (8)$$

whence

$$\varphi = -\frac{\alpha}{4R_c}. \quad (9)$$

Taking into account the last relation, we can write

$$A_{\min} = -\frac{\pi\alpha}{R_c}R^2 + 2\pi\alpha R. \quad (10)$$

If we disregard the displacement of the nucleus as a unit and assume that it is stable to changes in its shape, the local size distribution function for nuclei is determined by the peak of the function  $A_{\min}(R)$ , which can be considered the potential barrier that hampers the formation of a critical nucleus:

$$f_0(R) = f_0(R_c) \exp\left\{ \frac{\pi\alpha}{DR_c} (R - R_c)^2 \right\}, \quad (11)$$

$$f_0(R_c) = C \exp\left\{ -\frac{\pi\alpha}{D} R_c \right\}, \quad (11a)$$

$D$  being the noise intensity of the medium.

It is well known that the preexponential factor in  $f_0(R_c)$  associated with the frequency of transition of particles from the initial to the new phase cannot be expressed in terms of only the macroscopic parameters of the phases [11]. The fluctuational evolution of nuclei in the critical size range of width  $\delta R \approx (DR_c/\pi\alpha)^{1/2}$  around the critical value  $R = R_c$  can transfer them back to the subcritical region; however, the nuclei whose size has passed through the critical range will inevitably evolve into the new phase. The thermodynamic approach, however, cannot be used to determine the processes associated with the transition to a new phase state. Indeed, the theory of nucleation must independently describe the process of surmounting the energy barrier by nuclei and the variation of the barrier parameters as a result of depletion of the metastable phase. In this case, kinetic analysis of the nucleus evolution is required.

Before we go over to such a description, we note that Eq. (11) also implies that, in the metastable region, for

$$\pi\alpha(R - R_c)^2/DR_c \gg 1, \quad (12)$$

temperature fluctuations are not significant [12] for description of the thermodynamics of optical thermal breakdown. Inequality (12) can be written in the form of the well-known Ginzburg–Levanyuk criterion for the applicability of the self-consistent-field approximation in the theory of phase transitions:

$$N_{Gi} = \frac{D}{\pi\alpha R_c (R/R_c - 1)^2} \ll 1 + O(\varepsilon). \quad (13)$$

From this relation, it follows that the nonfluctuational approach is justified in the case of low-intensity external noise or when  $R_c$  tends to zero. As will be clear from subsequent analysis, the latter condition means that the relevant physical processes occur in the region of existence of standing switching waves (small deviations from metastability) in the system.

#### 4. INDEPENDENT GROWTH OF PRECIPITATES OF A NEW PHASE

Let us determine the law of propagation of a circular front whose radius  $R$  is larger than the width  $\Delta\rho$  of the transient layer.<sup>1</sup> In the polar system of coordinates, taking into account the axial symmetry, Eq. (3) can be written in the form

$$\frac{\partial\theta}{\partial\tau} = f(\theta) + \frac{1}{\rho} \frac{\partial\theta}{\partial\rho} + \frac{\partial^2\theta}{\partial\rho^2}. \quad (14)$$

In fact, derivative  $\partial\theta/\partial\rho$  differs from zero only within a narrow transient layer in the vicinity of  $\rho = R$ . Consequently, in the second term on the right-hand side of Eq. (14), we can approximately put  $\rho = R$ . It should be noted that any convex nucleus of the new phase formed on the plane has a tendency to acquire a perfectly circular shape [13, 14].

Let  $V(R)$  be the instantaneous velocity of propagation of a circular front of radius  $R$ . Under the assumptions made above, such a front corresponds to the self-similar solution

$$\theta = \theta(\xi), \quad \xi = \rho - V(R)\tau \quad (15)$$

of the differential equation

$$-V(R)\theta' = f(\theta) + R^{-1}\theta' + \theta'' \quad (16)$$

with the boundary conditions

$$\begin{aligned} \theta &\rightarrow \theta_1 \text{ for } \xi \rightarrow +\infty, \\ \theta &\rightarrow \theta_3 \text{ for } \xi \rightarrow -\infty. \end{aligned} \quad (17)$$

It should be noted that Eq. (13) coincides with the equation for a plane switching wave propagating at a velocity  $V$ , which is connected with the velocity  $V(R)$  of

<sup>1</sup> Here and below,  $R$  indicates a dimensionless quantity normalized to the diffusion length  $L \approx (\chi^l/cdH)^{1/2}$ .

propagation of the front with radius  $R$  through the relation

$$V(R) = V - R^{-1}. \tag{18}$$

On the other hand, multiplying both sides of Eq. (16) by the derivative  $d\theta/d\xi$ , integrating with respect to  $\xi$  between  $-\infty$  and  $+\infty$ , and taking into account the boundary conditions, we obtain

$$V = V(R) + R^{-1} \equiv A \left( \int_{-\infty}^{+\infty} \left( \frac{d\theta}{d\xi} \right)^2 d\xi \right)^{-1}, \tag{19}$$

where  $A = \int_{\theta_1}^{\theta_3} [\beta\{1 - \exp(-\eta \exp(\gamma - \gamma/\theta))\} / l - (\theta - 1)] d\theta$ . Thus, Eq. (14) leads to an important class of dissipative structures, viz., switching waves. For  $\beta \rightarrow \beta_0$ , the value of  $A$  tends to zero, which corresponds to a standing switching wave.

If we consider, as before, a stationary nucleus, we have  $V(R) = dR/d\tau$ . From this equality and from Eq. (18), it follows that

$$\frac{dR}{d\tau} = V - R^{-1}. \tag{20}$$

This equation indicates that, in fact, the processes at the interface are regarded as quite rapid, such that local equilibrium sets in at each point of the interface. The steady-state condition for the critical value of  $R$  implies that

$$R_c = V^{-1} \equiv A^{-1} \int_{-\infty}^{+\infty} \left( \frac{d\theta}{d\xi} \right)^2 d\xi, \tag{21}$$

which indicates that the quantity  $A$  has the meaning of the degree of supersaturation [15] of the metastable phase in a bistable system. It should also be noted that, writing again Eq. (21) in the dimensional form and comparing it with Eq. (9), we can establish a formal analogy between the physical parameters of the problem and the quantities appearing in Eq. (9).

By substituting Eq. (21) into Eq. (20), we obtain

$$\frac{dR}{d\tau} = \frac{1}{R_c} - \frac{1}{R}. \tag{22}$$

For  $R < R_c$ , we have  $dR/d\tau < 0$  and plane nuclei of radius  $R$  are dissolved in the metastable phase, while for  $R > R_c$ , we have  $dR/d\tau > 0$  and plane nuclei grow. The nuclei of critical radius  $R_c$  are in equilibrium with the medium and neither grow nor dissolve.

At the stage of independent growth of supercritical nuclei, their mean size is much larger than  $R_c$ . In addition, at the initial stage of growth, we can disregard the decrease in the supersaturation level while determining the nucleus growth rate. In this case, from Eq. (22), we obtain the following expression for the time depen-

dence of the radius of nuclei whose size is noticeably larger than the critical radius:

$$R(\tau) = R(0) + R_c^{-1} \tau. \tag{23}$$

The noticeable difference between this result and that obtained in [16] is due to the fact that, in our case, the kinetics of the growth of nuclei is determined by the attachment and detachment of particles at the two-dimensional interface rather than by diffusion in the solution.

### 5. BEHAVIOR OF AN ENSEMBLE OF NEW-PHASE NUCLEI AT LATER STAGES OF OPTICAL THERMAL BREAKDOWN

At the later stages of the first-order phase transition, the growth of coarser nuclei of the new phase occurs at the expense of dissolution of smaller nuclei [17, 18]. For a photo-induced phase transition, Ostwald ageing begins when the supersaturation level  $A$  tends to zero. This condition resembles the well-known Maxwell rule which determines the possibility of coexistence of liquid and gaseous phases in space [8] and, in the case at hand, implies a stationary front of the switching between the two states. In other words, a well-developed surface is formed between the phases in the non-equilibrium system and the appearance of this surface is associated with the stage of Ostwald ageing [14]. It should be noted that the fluctuation-induced nucleation at this stage is virtually ruled out since critical sizes are large.

Equation (22) describing the growth rate of a drop of the enriched phase can be written as

$$\frac{dR}{d\tau} = \frac{1}{R} \left[ \frac{R}{R_c} - 1 \right]. \tag{24}$$

This expression is completely analogous to that describing the control of the nucleus growth by the boundary kinetics [18].

Following Greenwood [19], we determine the maximum possible size  $R_g$  to which nuclei can grow from the equation for the specific growth rate (in the form proposed in [20]):

$$\frac{d}{dR} \left( \frac{\dot{R}}{R} \right)_{R=R_g} = 0. \tag{25}$$

This equation gives  $R_g = 2R_c$ . Using Eq. (24), we can easily find the time dependence of  $R_g$ :

$$R_g^2 - R_{g0}^2 = 2(\tau - \tau_0). \tag{26}$$

This equation makes it possible to estimate the size of the nuclei formed as a result of thermal breakdown at the stage of Ostwald ageing. Indeed, returning successively from the dimensionless to dimensional variables, we obtain

$$R_g^2 - R_{g0}^2 = 2k(t - t_0),$$

where  $k = \chi/c^2d^2$  is the thermal diffusivity, which amounts to  $0.36 \text{ cm}^2/\text{s}$  for Ge crystals.

Considering that  $dR/d\tau$  is the velocity of a nucleus in the size space, we can write the continuity equation in this space in the form

$$\frac{\partial g}{\partial \tau} + \frac{\partial}{\partial R} \left( g \frac{\partial R}{\partial \tau} \right) = 0. \quad (27)$$

The size distribution function for nuclei is normalized so that

$$N(\tau) = \int_0^{\infty} g(\tau, R) dR \quad (28)$$

is the number of nuclei per unit volume.

Equation (27) should also be supplemented with the temperature balance equation

$$\Delta\theta(\tau) + \pi\theta_3 \int_0^{\infty} R^2 g(\tau, R) dR = \Delta\theta_0, \quad (29)$$

where  $\Delta\theta_0$  is the difference between the transition temperature  $\theta_2$  and the temperature  $\theta_0$  of the medium at the beginning of Ostwald ageing and  $\Delta\theta(\tau)$  is the difference between the transition temperature  $\theta_2$  and the temperature  $\theta(\tau)$  of the medium at instant  $\tau$ . The last term reflects the filling of the plane of the semiconducting wafer with a phase having temperature  $\theta_3$ .

Equations (24), (27), and (29) form the complete system of equations for the problem under investigation. Substituting Eq. (24) into Eq. (27), we obtain the distribution function in the form in which it was obtained earlier for island-type films [21]:

$$g(u) = Cu(2-u)^{-4} \exp\left(-\frac{4}{2-u}\right), \quad (30)$$

where  $u = R/R_c$ .

The normalization constant  $C$  can be determined from Eq. (29).

Obviously, the size distribution function for nuclei presented above does not exhaust all the possible mechanisms of coarsening of the new phase. However, in order to include these mechanisms (e.g., diffusion from the ambient), we have to make assumptions that do not follow directly from the model described in section 3.

## 6. CONCLUSION

Thus, we have succeeded in presenting the process of nucleation, as well as of later stages (i.e., Ostwald ageing), in a strongly nonequilibrium system on a unified basis in the case of a reversible optical heat-induced breakdown of a semiconducting wafer. No additional assumptions besides those underlying the physical model that reflects the properties of the given system were made for studying the kinetics of the non-

equilibrium phase transition. The proposed approach makes it possible to study the kinetics of a wide class of nonequilibrium systems. It is well known that modern advances in the theory of self-organizing systems are primarily due to the fact that the thermodynamically nonequilibrium systems that are in a steady state with detailed balance are formally indistinguishable from equilibrium systems [22], which can be analyzed on the basis of a detailed mathematical apparatus [8]. The physical state of a thermodynamic system that is far from equilibrium is determined by its characteristic function, viz., the generalized thermodynamic potential [9, 23, 24]. The kinetics of phase transformations of the above systems is described by the Landau–Khalatnikov equation describing the relaxation of the phase variable to a new state which is more advantageous from the point of view of energy.

However, such an algorithm is inapplicable to most physically significant situations in nonequilibrium kinetics (e.g., within the model described by Eq. (3)) in view of the complexity of constructing the generalized thermodynamic potential in an analytic form. The approach developed above makes it possible to describe the evolution of a strongly nonequilibrium system on the basis of a formal analogy with the decomposition of a supersaturated solid solution without using the specific analytic form of the generalized thermodynamic potential.

## REFERENCES

1. C. R. Giuliano, *Appl. Phys. Lett.* **5** (7), 137 (1964).
2. J. H. Cullom and R. W. Waynant, *Appl. Opt.* **3** (8), 989 (1964).
3. N. N. Rozanov, *Optical Bistability and Hysteresis in Distributed Nonlinear Systems* (Moscow, 1997).
4. P. A. Young, *Appl. Opt.* **10** (3), 638 (1971).
5. É. M. Épshteĭn, *Izv. Vyssh. Uchebn. Zaved., Radiofiz.* **15** (1), 33 (1972).
6. N. N. Rozanov and G. V. Kholodova, *Kvantovaya Élektron.* (Moscow) **13** (2), 368 (1986).
7. A. V. Subashiev and I. M. Fishman, *Zh. Éksp. Teor. Fiz.* **93** (6), 2264 (1987) [*Sov. Phys. JETP* **66**, 1293 (1987)].
8. L. D. Landau and E. M. Lifshitz, *Statistical Physics* (Nauka, Moscow, 1995; Pergamon, Oxford, 1980), Part 1.
9. R. Graham and T. Tel, *Phys. Rev. A* **42**, 4661 (1990).
10. E. A. Brener, V. I. Marchenko, and S. V. Meshkov, *Zh. Éksp. Teor. Fiz.* **85** (6), 2107 (1983) [*Sov. Phys. JETP* **58**, 1223 (1983)].
11. E. M. Lifshitz and L. P. Pitaevskĭĭ, *Physical Kinetics* (Nauka, Moscow, 1979; Pergamon, Oxford, 1981).
12. V. G. Boiko, V. M. Sysoev, and A. V. Chalyĭ, *Zh. Éksp. Teor. Fiz.* **97** (3), 842 (1990) [*Sov. Phys. JETP* **70**, 472 (1990)].
13. Yu. E. Kuzovlev, T. K. Soboleva, and A. É. Fillipov, *Zh. Éksp. Teor. Fiz.* **103** (5), 1742 (1993) [*JETP* **76**, 858 (1993)].



14. B. Meerson and P. V. Sasorov, *Phys. Rev. E* **53** (4), 3491 (1996).
15. I. M. Lifshits and V. V. Slezov, *Zh. Éksp. Teor. Fiz.* **35** (2), 479 (1959) [*Sov. Phys. JETP* **8**, 331 (1959)].
16. V. I. Marchenko, *Pis'ma Zh. Éksp. Teor. Fiz.* **64** (1), 61 (1996) [*JETP Lett.* **64**, 66 (1996)].
17. I. M. Lifshits and V. V. Slezov, *J. Phys. Chem. Solids* **19** (1/2), 35 (1961).
18. C. Wagner, *Z. Elektrochem.* **65** (7/8), 581 (1961).
19. G. W. Greenwood, in *The Mechanism of Phase Transformation in Crystalline Solids: Proceedings of an International Symposium, 1968* (Inst. of Metals for the Metals and Metallurgy Trust, London, 1969).
20. R. D. Vengrenovich, *Acta Metall.* **20**, 1079 (1982).
21. R. D. Vengrenovich, *Ukr. Fiz. Zh.* **22** (2), 219 (1977).
22. Al. S. Mikhailov, *Foundations of Synergetics*, Vol. 1: *Distributed Active Systems* (Springer-Verlag, Berlin, 1994).
23. A. Hagberg and E. Meron, *Phys. Rev. Lett.* **72** (15), 2494 (1994).
24. G. Izus, R. Deza, O. Ramírez, *et al.*, *Phys. Rev. E* **52** (1), 129 (1995).

*Translated by N. Wadhwa*

## Indirect Interaction of Mössbauer Nuclei

A. R. Kessel' and V. A. Popov

Zavoiskii Physicotechnical Institute, Kazan Scientific Center, Russian Academy of Sciences,  
Sibirskii trakt 10/7, Kazan, 420029 Tatarstan, Russia

e-mail: vladimir@dionis.kfti.knc.ru

Received December 4, 2000

**Abstract**—An expression is deduced for the operator of the indirect interaction of nuclei via the electromagnetic field. The properties of Mössbauer nuclei are described within the pseudospin formalism, which is usually used in the theory of optical two-level systems. The indirect interaction of pseudospins is derived by a method adopted from the theory of superconductivity. It is found that the potentials of this interaction involve terms decreasing as  $r^{-3}$ ,  $r^{-2}$ , and  $r^{-1}$ . The estimates demonstrate that the two-particle interaction can contribute significantly to the width of the resonance line, for example, in crystals whose cells contain thulium nuclei. © 2001 MAIK "Nauka/Interperiodica".

### 1. INTRODUCTION

Traditionally, the interaction of nuclei with each other is ignored in the theory of the Mössbauer effect. It is believed that the nuclear interaction reduces solely to the magnetic dipole–dipole interaction [1], which is considerably weaker than the coupling of the nucleus with the electron shell of the atom. The cooperative effects related to this interaction also manifest themselves only slightly, because its potential decreases as  $r^{-3}$ .

It is known from quantum optics [2, 3] that indirect interactions of localized particles via transfer fields can contain terms that decrease more slowly with an increase in the distance (as  $r^{-2}$  or  $r^{-1}$ ) and, thus, have a greater effect on the physical properties.

A greater contribution associated with indirect interaction can be expected in Mössbauer spectroscopy due to the higher (than in optics) resonance frequencies and relative narrowness (high  $Q$ -factor) of the resonance lines. In this work, we calculated the indirect interaction of Mössbauer nuclei via the vacuum electromagnetic field.

The problem on the degrees of freedom of indirect interaction is not a trivial one. It is solved by introduction of the pseudospin  $S = 1/2$ , which can always be associated with any two energy levels sufficiently separated from other states. A similar formalism is widely used in optics and has the universally accepted abbreviation TLS, a two-level system [4, 5].

The operator of the indirect interaction is deduced by a method that has been successfully used in the theory of superconductivity since the Fröhlich derivation of the operator for the electron interaction [6, 7] in the Bardeen–Cooper–Schrieffer theory.

### 2. A GENERAL SCHEME OF DEDUCTION OF THE PAIR INTERACTION OPERATOR

In the general case, the structure of the Hamiltonian of two interacting subsystems can be represented in the form

$$\mathcal{H} = \mathcal{H}_s + \mathcal{H}_f + V_{sf}, \quad (1)$$

where  $\mathcal{H}_s$  is the Hamiltonian of the dynamic subsystem composed of noninteracting particles,  $\mathcal{H}_f$  is the Hamiltonian of the field which transfers the interaction, and  $V_{sf}$  is the operator of interaction between the particles of two subsystems.

The method of calculation of the indirect interactions [7] consists of two stages and rests on the assumption that the matrix elements of the operators obey the following inequality:

$$|V_{sf}| \ll |\mathcal{H}_s| + |\mathcal{H}_f|.$$

The first stage is the change-over to a new representation via the unitary transformation  $U = \exp\{-L\}$ . Here,  $L$  is a skew-Hermitian operator which satisfies the condition

$$V_{sf} + [\mathcal{H}_s + \mathcal{H}_f, L] = 0. \quad (2)$$

As a consequence, the Hamiltonian  $\mathcal{H}$  in the new representation takes the form

$$\mathcal{H} \rightarrow \tilde{\mathcal{H}} = \mathcal{H}_s + \mathcal{H}_f + \frac{1}{2}[V_{sf}, L] + O(V_{sf}^3). \quad (3)$$

As follows from relationship (3), the Hamiltonian loses the terms linear with respect to  $V_{sf}$  because it is assumed that the generator of the unitary transforma-

tion is  $L \sim |V_{sf}|(|\mathcal{H}_s| + |\mathcal{H}_f|)$ . The solution to the operator equation (2) is given by

$$L = \frac{1}{i\hbar} \lim_{\varepsilon \rightarrow 0} \int_{-\infty}^0 dt e^{\varepsilon t} V_{sf}(t), \quad (4)$$

$$V_{sf}(t) = \exp\{i(\mathcal{H}_s + \mathcal{H}_f)t/\hbar\} V_{sf} \\ \times \exp\{-i(\mathcal{H}_s + \mathcal{H}_f)t/\hbar\}.$$

The second stage consists in averaging expression (3) for  $\tilde{\mathcal{H}}$  over the states of the interaction transfer field, so that the second-order term of the perturbation theory,

$$W = \frac{1}{2} \langle [V_{sf}, L] \rangle, \quad (5)$$

in expansion (3) ceases to be dependent on the variables of the electromagnetic field but remains dependent on the pseudospin operators of different particles and, hence, takes on the meaning of the operator of their indirect interaction. Running a little ahead, it should be noted that, in a number of cases, including the case we consider here, this averaging can be executed, because the second-order terms in expansion (3) do not contain field operators.

### 3. THE CHANGE-OVER TO AN EFFECTIVE TWO-LEVEL HAMILTONIAN

As a rule, Mössbauer transitions take place between the states of a nucleus with different spins. In this case, each of these states is usually degenerate with respect to the projection of the spin. The interaction with the internal local electric and magnetic fields can result in degeneracy relieving. This brings about the formation of a hyperfine structure of the nuclear levels.

Let us calculate the interaction of identical Mössbauer nuclei, which is projected onto a particular pair of the  $|I_g m_g\rangle$  and  $|I_e m_e\rangle$  states of the hyperfine structure where the Mössbauer transition takes place. The first state corresponds to the ground energy level with spin  $I_g$  and its projection  $m_g$ , and the second state corresponds to the excited state with spin  $I_e$  and projection  $m_e$ . Then, the following operator can be chosen as a basic Hamiltonian of the dynamic subsystem:

$$\mathcal{H}_s = \hbar \omega_0 \sum_j S_j^z, \quad (6)$$

where  $\omega_0$  is the frequency of the transition under consideration and  $S_j^z$  is the operator of the pseudospin of a single nucleus, which is determined at the specified levels [4].

As a field transferring the interaction, we will consider the electromagnetic field whose Hamiltonian has a standard form

$$\mathcal{H}_f = \hbar \sum_{\mathbf{k}\sigma} \omega_k \left( a_{\mathbf{k}\sigma}^\dagger a_{\mathbf{k}\sigma} + \frac{1}{2} \right), \quad (7)$$

where  $a_{\mathbf{k}\sigma}^\dagger$  and  $a_{\mathbf{k}\sigma}$  are the operators of production and annihilation of a photon with wave vector  $\mathbf{k}$ , frequency  $\omega_k$ , and polarization  $\sigma$ .

The Hamiltonian of the interaction between the nuclei and the electromagnetic field has the form

$$V_{\text{int}} = -\frac{1}{c} \sum_j \mathbf{j}_j \mathbf{A}(\mathbf{R}_j). \quad (8)$$

Here,  $\mathbf{j}_j$  is the current of the  $j$ th nucleon and the potential of the electromagnetic field is represented in the form of an expansion in terms of the operators of the production and annihilation of photons, that is,

$$\mathbf{A}(\mathbf{R}_j) = \sum_{\mathbf{k}\sigma} \left( \frac{2\pi\hbar c}{V k} \right)^{1/2} (a_{\mathbf{k}\sigma} \mathbf{e}_\sigma e^{i\mathbf{k}\mathbf{R}_j} + a_{\mathbf{k}\sigma}^\dagger \mathbf{e}_\sigma^* e^{-i\mathbf{k}\mathbf{R}_j}), \quad (9)$$

where  $\mathbf{e}_{\pm 1}$  are the vectors of the right and left-hand circular polarization;  $\mathbf{R}_j = \mathbf{r}_j + \mathbf{x}_j$  and  $\mathbf{r}_j$ ,  $\mathbf{x}_j$  are the radius vectors of the nucleus in the laboratory system of coordinates and the nucleon in the nucleus system of coordinates, respectively; and  $V$  is the volume of the electromagnetic field quantization. Generally speaking, the summation should be carried out over all nucleons of the nucleus. However, as a first approximation, we can assume that the properties of the nucleus are determined by the last unpaired nucleon. Then, the subscript  $j$  can be considered as running through the nuclei.

Now, we change over from Hamiltonian (8) to the effective two-level Hamiltonian. For this purpose, it is necessary to determine the matrix elements of Hamiltonian (8) for the vectors of the  $|I_g m_g\rangle$  and  $|I_e m_e\rangle$  states. The matrix elements for the operators related to both the nuclei and the electromagnetic field are calculated individually. The procedure of changing-over to the pseudospins becomes more descriptive in the rotary wave approximation of [2, 4]. In this case, the terms  $S^+ a^\dagger$  and  $S^- a$  are eliminated from the effective Hamiltonian. These terms oscillate with frequencies equal to the sum of the frequency  $\omega_0$  of the transition and the frequency of a photon  $\omega_k = ck$ . The terms which remain in the Hamiltonian correspond to the processes of photon emission in the transition  $|I_e m_e\rangle \rightarrow |I_g m_g\rangle$  and photon absorption in the transition  $|I_g m_g\rangle \rightarrow |I_e m_e\rangle$ . Thus, we should calculate only the matrix elements  $\langle I_g m_g,$

$\mathbf{k}\sigma|V_{\text{int}}|I_e m_e\rangle$  and  $\langle I_e m_e|V_{\text{int}}|I_g m_g, \mathbf{k}\sigma\rangle$ , which should coincide with the matrix elements of the two-level Hamiltonian:

$$\begin{aligned}\langle g|V_{ge}|e\rangle &\equiv \langle I_g m_g, \mathbf{k}\sigma|V_{\text{int}}|I_e m_e\rangle \\ &= \left(\frac{2\pi\hbar c}{Vk}\right)^{1/2} e^{-i\mathbf{k}\mathbf{r}_j} \langle I_g m_g| \\ &- \frac{1}{c} \mathbf{j}_j \mathbf{e}_\sigma^* e^{-i\mathbf{k}\mathbf{x}_j} |I_e m_e\rangle \equiv g_{k\sigma}^* \langle g|S_j^-|e\rangle, \\ \langle e|V_{ge}|g\rangle &\equiv \langle I_e m_e|V_{\text{int}}|I_g m_g, \mathbf{k}\sigma\rangle \\ &= \left(\frac{2\pi\hbar c}{Vk}\right)^{1/2} e^{i\mathbf{k}\mathbf{r}_j} \langle I_e m_e| \\ &- \frac{1}{c} \mathbf{j}_j \mathbf{e}_\sigma e^{i\mathbf{k}\mathbf{x}_j} |I_g m_g\rangle \equiv g_{k\sigma} \langle e|S_j^+|g\rangle.\end{aligned}$$

In the calculation of the matrix elements of Hamiltonian (8), we assumed that the magnetic dipole transition  $M1$  ( $I_g = 1/2$ ,  $m_g = 1/2 \rightarrow I_e = 3/2$ ,  $m_e = 3/2$ ) [1] takes place.

In these designations, the effective Hamiltonian of the interaction of the pseudospins with the electromagnetic field has the form

$$\begin{aligned}V_{ge} &= \sum_j \sum_{\mathbf{k}\sigma} (g_{k\sigma} S_j^+ a_{\mathbf{k}\sigma} e^{i\mathbf{k}\mathbf{r}_j} + g_{k\sigma}^* S_j^- a_{\mathbf{k}\sigma}^\dagger e^{-i\mathbf{k}\mathbf{r}_j}), \\ g_{k\sigma} &= i \left(\frac{12\pi^2 \hbar c}{Vk}\right)^{1/2} \sigma \mathcal{D}_{1\sigma}^1(\hat{\mathbf{z}} \rightarrow \hat{\mathbf{k}}) \left\langle \frac{1}{2} \middle| M1 \middle| \frac{3}{2} \right\rangle^*,\end{aligned}\quad (10)$$

where  $\mathcal{D}_{1\sigma}^1(\hat{\mathbf{z}} \rightarrow \hat{\mathbf{k}})$  is the rotation matrix of the angular momentum eigenfunctions upon the change-over from the laboratory system of coordinates to the coordinate system in which the  $z$  axis coincides with vector  $\mathbf{k}$  [1] and  $\left\langle \frac{1}{2} \middle| M1 \middle| \frac{3}{2} \right\rangle$  is the reduced matrix element of the transition under consideration.

#### 4. THE INTERACTION OF MÖSSBAUER NUCLEI

The operator of the unitary transformation in the pseudospin representation, which corresponds to operators (6), (7), and (10), can be determined from formula (4) as follows:

$$\begin{aligned}L &= \frac{1}{\hbar} \sum_j \sum_{\mathbf{k}\sigma} \left( g_{k\sigma} S_j^+ a_{\mathbf{k}\sigma} \frac{e^{i\mathbf{k}\mathbf{r}_j}}{\omega_k - \omega_0 + i\varepsilon} \right. \\ &\left. + g_{k\sigma}^* S_j^- a_{\mathbf{k}\sigma}^\dagger \frac{e^{-i\mathbf{k}\mathbf{r}_j}}{\omega_k - \omega_0 - i\varepsilon} \right).\end{aligned}\quad (11)$$

Then, the operator of the indirect interaction of Mössbauer nuclei takes the form

$$\begin{aligned}W &= \frac{1}{2} \langle [\mathcal{H}', L] \rangle \\ &= -\frac{1}{\hbar} \sum_{ij} \sum_{\mathbf{k}\sigma} |g_{k\sigma}|^2 \left( S_i^+ S_j^- \frac{e^{i\mathbf{k}\mathbf{r}_{ij}}}{\omega_k - \omega_0 + i\varepsilon} \right. \\ &\left. + S_i^- S_j^+ \frac{e^{-i\mathbf{k}\mathbf{r}_{ij}}}{\omega_k - \omega_0 - i\varepsilon} \right).\end{aligned}\quad (12)$$

Since  $\sigma^2 = 1$  and

$$\begin{aligned}\sum_{\sigma} |\mathcal{D}_{1\sigma}^1(\hat{\mathbf{z}} \rightarrow \hat{\mathbf{k}})|^2 &= \left(\frac{1 + \cos\theta}{2}\right)^2 + \left(\frac{1 - \cos\theta}{2}\right)^2 \\ &= \frac{1}{2}(1 + \cos^2\theta),\end{aligned}$$

we have

$$\sum_{\sigma} |g_{k\sigma}|^2 = \frac{6\pi^2 \hbar c}{Vk} (1 + \cos^2\theta) \left\langle \frac{1}{2} \middle| M1 \middle| \frac{3}{2} \right\rangle^2, \quad (13)$$

where  $\theta$  is the angle between the  $z$  axis and vector  $\mathbf{k}$ .

Let us change over from the summation over  $k$  to the integration

$$\sum_{\mathbf{k}} \rightarrow \frac{V}{(2\pi)^3} \int d\mathbf{k}.$$

Now, we expand the exponent in the spherical functions [8] and perform integration with respect to the angles:

$$\begin{aligned}\int d\Omega (1 + \cos^2\theta) e^{i\mathbf{k}\mathbf{r}} \\ = \frac{4\pi}{3} [4j_0(kr) - (3\cos^2\vartheta - 1)j_2(kr)],\end{aligned}\quad (14)$$

where  $\vartheta$  is the angle between the  $z$  axis and the radius vector  $\mathbf{r}$  and  $j_j(x)$  are spherical Bessel functions. As a result, the transformed Hamiltonian of the interaction takes the following form:

$$\begin{aligned}W &= -\frac{1}{2} \sum_{ij} (S_i^+ S_j^- + S_i^- S_j^+) \int_0^\infty \frac{k}{k - k_0} [4j_0(kr_{ij}) \\ &- (3\cos^2\vartheta_{ij} - 1)j_2(kr_{ij})] \left\langle \frac{1}{2} \middle| M1 \middle| \frac{3}{2} \right\rangle^2 dk,\end{aligned}\quad (15)$$

where  $k_0 = \omega_0/c$ .

In order to calculate integral (15), it is necessary to know the functional dependence of the reduced matrix element on  $k$ . We assume that the nuclear potential has the form of an oscillator well. Then, as a first approxi-

mation, the reduced matrix element for the magnetic dipole transition can be written as

$$\left\langle \frac{1}{2} \left| M1 \right| \frac{3}{2} \right\rangle = Akae^{-(k\rho)^2/4}, \quad (16)$$

where  $A$  is a constant independent of  $k$  and  $\rho$  is the nuclear radius. The partial width of  $\gamma$ -radiation at the frequency of the transition is given by

$$\begin{aligned} \Gamma_\gamma(k_0) &\equiv \Gamma_\gamma = \frac{8\pi k_0}{2I_e + 1} \left\langle \frac{1}{2} \left| M1(k_0) \right| \frac{3}{2} \right\rangle^2 \\ &\approx 2\pi A^2 k_0^3 \rho^2, \end{aligned} \quad (17)$$

because  $k_0\rho \ll 1$ . Thus, we can write

$$\left\langle \frac{1}{2} \left| M1 \right| \frac{3}{2} \right\rangle^2 = \frac{\Gamma_\gamma k^2}{2\pi k_0^3} e^{-(k\rho)^2/2}. \quad (18)$$

By substituting expression (18) into Eq. (15), we obtain

$$W = \frac{1}{2} \sum_{ij} A_{ij} (S_i^+ S_j^- + S_i^- S_j^+). \quad (19)$$

The potentials  $A_{ij}$  are determined by the expression

$$A_{ij} = -\frac{\Gamma_\gamma}{4\pi} [4\Phi_0(\beta_{ij}, p) \quad (20)$$

$$- (3 \cos^2 \vartheta_{ij} - 1) \Phi_2(\beta_{ij}, p)],$$

$$\Phi_l(\beta, p) \equiv \int_0^\infty \frac{q^3 e^{-p^2 q^2}}{q-1} j_l(\beta q) dq, \quad l = 0, 2, \quad (21)$$

where  $p = k_0\rho/\sqrt{2}$  and  $\beta = k_0r$ . We failed to obtain the exact analytical form of the functional dependence for  $\Phi_l$ . In the Appendix, it will be shown how expressions (21) can be approximately integrated having in mind the small value of the  $p$  parameter. In this case, the  $\Phi_l$  function is virtually independent of  $p$ ,

$$\Phi_0(\beta) = \pi \frac{\cos \beta}{\beta} - 3 \frac{\cos 2\beta}{\beta^2} + \frac{\sin 2\beta}{\beta^3} - \frac{f(\beta)}{\beta}, \quad (22)$$

$$\begin{aligned} \Phi_2(\beta) &= -\pi \frac{\cos \beta}{\beta} + 3\pi \frac{\sin \beta}{\beta^2} + 3 \frac{\cos 2\beta}{\beta^2} + 3\pi \frac{\cos \beta}{\beta^3} \\ &\quad - 4 \frac{\sin 2\beta}{\beta^3} + \frac{f(\beta)}{\beta} - 3 \frac{g(\beta)}{\beta^2} - 3 \frac{f(\beta)}{\beta^3}, \end{aligned} \quad (23)$$

$$f(\beta) = \sin \beta \text{Ci}(\beta) - \cos \beta \left( \text{Si}(\beta) - \frac{\pi}{2} \right),$$

$$g(\beta) = -\cos \beta \text{Ci}(\beta) - \sin \beta \left( \text{Si}(\beta) - \frac{\pi}{2} \right),$$

where  $\text{Si}(\beta)$  and  $\text{Ci}(\beta)$  are the integral sine and cosine, respectively. Functions  $f(\beta)$  and  $g(\beta)$  monotonically decrease as  $\beta$  increases. These functions can be approximated by the simpler dependences  $f(\beta) \sim 1/\beta$  and  $g(\beta) \sim 1/\beta^2$  for large values of the argument.

## 5. DISCUSSION

In order to demonstrate interaction (19) experimentally, it is convenient to measure its contribution to the shift and width of the absorption line of the signal. In the low-temperature approximation ( $\hbar\omega_0 \ll kT$ ,  $\langle S_i^z \rangle = -1/2$ ), the first and second moments of the absorption line for a system of particles whose interaction is described by operator (19) have the following form [9]:

$$M_1 = \frac{1}{N} \sum_{ij} A_{ij}, \quad M_2 = \frac{1}{N} \sum_i \left( \sum_j A_{ij} \right)^2. \quad (24)$$

For the potentials [see Eq. (20)] considered in this work, the calculation of the sum in formulas (24) is a rather difficult problem. This is due to the fact that the gamma-radiation wavelength is less than the interatomic distance and the conventional (in these situations) change-over from the summation to the integration cannot be carried out because of the existence of oscillating functions. Moreover, the systems with a regular arrangement of Mössbauer nuclei call for different computational methods than the materials with a small concentration of Mössbauer nuclei. The qualitative estimation for the materials with a small concentration  $n$  of Mössbauer isotopes (a sample with a spherical form of radius  $R$ ) demonstrates that the moments are determined only by the last term in formula (22) and the contribution of the oscillating terms can be disregarded. The broadening of the resonance line, which, in these estimates, is described by the second moment  $M_2$ , is determined by the relationship

$$\Gamma_{ss} = \Gamma_\gamma R n k_0^{-2}. \quad (25)$$

For a  $^{57}\text{Fe}$  isotope, whose fraction under usual conditions is 2% and  $\hbar\omega_0 = 14.4$  keV, the ratio  $\Gamma_{ss}/\Gamma_\gamma$  is  $\sim 10^{-3}$ . For the enriched samples, this ratio can be as much as  $10^{-1}$ . This estimate agrees well with the fact that a single-particle model works well for the Mössbauer line of iron, even though the two-particle interaction, apparently, also contributes to the line broadening.

According to formula (25), interaction (19) can be most pronounced in materials for which the concentration of Mössbauer isotopes is large and the magnitude of the transition is relatively small. These conditions are satisfied in the case of  $^{169}\text{Tm}$  with a hundred percentage of Mössbauer nuclei and  $\hbar\omega_0 = 8.4$  keV. The contribution to the line width for this material, which was estimated according to formula (25), is of an order of the natural width of the line  $\Gamma_\gamma$ . In these cases, the experimental investigations into the dependence of the line shape on the nucleus concentration or sample size can serve as a tool for the detection of the two-particle interactions of the Mössbauer nuclei.

Thus, we considered the indirect interaction of only a single pair of the spin sublevels of Mössbauer nuclei.

The result represented by relationships (19)–(23) is readily generalized to the case of several sublevels:

$$W = \frac{1}{2} \sum_{ij} \sum_{m_g m_e} A_{m_g m_e}^{ij} (P_{m_g m_e}^i P_{m_e m_g}^j + P_{m_g m_e}^j P_{m_e m_g}^i), \quad (26)$$

where  $P_{m_g m_e}^i$  are the projective operators with a single nonzero matrix element corresponding to the transition  $|I_g m_g\rangle \rightarrow |I_e m_e\rangle$  and the  $A_{m_g m_e}^{ij}$  potentials have a form similar to that described by Eq. (20) for each of the allowed transitions  $|I_g m_g\rangle \rightarrow |I_e m_e\rangle$ . They differ from expression (20) only by a numerical factor related to the calculation of the matrix element and by the frequency of the transition that appears in functions (22) and (23). Note that expression (26) corresponds to the so-called secular part of the two-particle interaction, which manifests itself most dramatically in resonance spectroscopy.

## APPENDIX

### CALCULATION OF THE INTEGRALS

In order to determine the analytical dependence of the potential of the indirect interaction (19) on the distance between the nuclei, it is necessary to calculate integrals of the form (21). Exact integration fails. However, taking into account that parameter  $p \sim 10^{-4}$ , an approximate integration can be carried out with a high degree of accuracy.

Let us consider, for example, the function  $\Phi_0(\beta)$ . Integral  $\Phi_2$  can be calculated in a similar manner. First, we replace the variables  $\xi = q - 1$  and then break the integration range into two intervals:

$$\Phi_0 = \left( \int_{-1}^1 + \int_1^{\infty} \right) \frac{(\xi + 1)^2 e^{-p^2(\xi + 1)^2}}{\xi} \sin(\beta[\xi + 1]) d\xi. \quad (27)$$

In the first integral, we can set  $\exp(-p^2[\xi + 1]^2) \approx 1$ . Then, we obtain

$$\begin{aligned} & \int_{-1}^1 \frac{(\xi + 1)^2}{\xi} \sin(\beta[\xi + 1]) d\xi \\ &= \frac{1}{\beta} - 3 \frac{\cos 2\beta}{\beta} + \frac{\sin 2\beta}{\beta^2} - 2\text{Si}(\beta) \cos \beta. \end{aligned} \quad (28)$$

Now, we divide the second integral into three terms, two of which can be calculated exactly,

$$\begin{aligned} & \int_1^{\infty} \xi e^{-p^2(\xi + 1)^2} \sin(\beta[\xi + 1]) d\xi \\ &= -\frac{\sqrt{\pi}}{2p} \exp\left\{-\frac{\beta^2}{4p^2}\right\} \left(\frac{\beta}{p^2} - \text{erfi}\left(\frac{\beta}{2p}\right)\right), \end{aligned} \quad (29)$$

$$\begin{aligned} & 2 \int_1^{\infty} e^{-p^2(\xi + 1)^2} \sin(\beta[\xi + 1]) d\xi \\ &= -\frac{\sqrt{\pi}}{p} \exp\left\{-\frac{\beta^2}{4p^2}\right\} \text{erfi}\left(\frac{\beta}{2p}\right). \end{aligned} \quad (30)$$

Their sum is an expression which behaves as  $-1/\beta$  when  $p \ll 1$ . The function  $\text{erfi}(z)$  is the imaginary error integral,  $\text{erfi}(z) = -i \text{erf}(iz)$ .

The numerical estimate of the remaining integral demonstrated that it can be approximated by the following expression with an accuracy of the order of  $10^{-6}$ :

$$\begin{aligned} & \int_1^{\infty} e^{-p^2(\xi + 1)^2} \sin(\beta[\xi + 1]) \frac{d\xi}{\xi} \approx \int_1^{\infty} \sin(\beta[\xi + 1]) \frac{d\xi}{\xi} \\ &= \cos \beta \left( \frac{\pi}{2} - \text{Si}(\beta) \right) - \sin \beta \text{Ci}(\beta). \end{aligned} \quad (31)$$

Summing expressions (28)–(30), we obtain the form of potential (22).

It should be noted that, for the parameters specific to this problem, comparison of expressions (22) and (23) with the results of the numerical integration gives a difference of the order of  $10^{-6}$ .

## REFERENCES

1. M. A. Andreeva and R. N. Kuz'min, *Mössbauer Gamma Optics* (Mosk. Gos. Univ., Moscow, 1982).
2. P. W. Milonni and P. L. Knight, *Phys. Rev. A* **10** (4), 1096 (1974).
3. Y. Ben-Aryeh, C. M. Bowden, and J. C. Englund, *Phys. Rev. A* **34** (5), 3917 (1986).
4. L. Allen and J. H. Eberly, *Optical Resonance and Two-Level Atoms* (Wiley, New York, 1975; Mir, Moscow, 1978).
5. G. S. Agarwal, in *Springer Tracts in Modern Physics*, Vol. 70: *Quantum Statistic Theories of Spontaneous Emission and Their Relation to Other Approaches* (Springer-Verlag, Berlin, 1974).
6. H. Fröhlich, *Phys. Rev.* **79** (2), 845 (1950).
7. H. Fröhlich, H. Pelzer, and S. Zienau, *Philos. Mag.* **41** (314), 221 (1950).
8. L. D. Landau and E. M. Lifshitz, *Course of Theoretical Physics*, Vol. 3: *Quantum Mechanics: Non-Relativistic Theory* (Nauka, Moscow, 1989, 4th ed.; Pergamon, New York, 1977, 3rd ed.).
9. A. Abragam and M. Goldman, *Nuclear Magnetism: Order and Disorder* (Clarendon Press, Oxford, 1982; Mir, Moscow, 1984), Vol. 2.

Translated by O. Moskalev

---

---

SEMICONDUCTORS  
AND DIELECTRICS

---

---

# Electrical Properties of Nanocomposites Subjected to Deformation

E. Z. Meĭlikhov

*Institute of Molecular Physics, Russian Research Centre Kurchatov Institute,  
pl. Akademika Kurchatova 1, Moscow, 123182 Russia*

*e-mail: meĭlikhov@imp.kiae.ru*

Received November 27, 2000

**Abstract**—The electrophysical properties of a new type of nanocomposites are considered. In these materials, the metallic granules are distributed in a rubberlike matrix. Nanocomposites exhibit either metallic or hopping conduction, depending on the bulk concentration of the metallic granules. The effect of pressure (for hydrostatic compression and for uniaxial deformation) upon the resistance of such composites is studied in both conduction regimes. The practically important extremely strong dependence of their resistance upon pressure in the hopping conduction regime is a consequence of the exponentially strong dependence of the probability of intergranule electron tunneling on the distance between the granules. © 2001 MAIK “Nauka/Interperiodica”.

## 1. INTRODUCTION

Metallic nanocomposites are two-phase systems consisting of metallic nanometer-sized particles distributed in an insulating matrix. The properties of such systems are critically dependent upon the bulk concentration  $x$  of the metallic phase. For  $x > x_c \approx 0.5$ , a metallic percolation cluster spreading over the entire sample occurs. It looks like a branching network consisting of metallic particles in mutual contact. Clearly, the conductivity of such a system has a metallic character. When the fraction of the metallic phase is small ( $x < x_c$ ), such an infinite cluster is not formed and the conduction is due to the charge carriers tunneling between the separate particles (granules) of the nanocomposite. Due to the small sizes of such granules, the Coulomb blockade is of fundamental importance in this process; this means that tunnel transitions between electrically neutral and charged granules become energetically unfavorable. For this reason, the conduction of such a system is determined fundamentally by tunnel transitions between pairs of granules, one of which is charged and the other is neutral. The conduction  $G$  of the system is thermally activated and usually described by the so-called 1/2 law:  $G \propto \exp[-(T_0/T)^{1/2}]$ , where  $T_0$  is a characteristic temperature dependent on  $x$  [1]. The origin of the 1/2 law is connected with the fact that there is a large dispersion of metallic-granule sizes in real nanocomposites. A considerable contribution to conductivity is due only to the tunnel transitions between granules of the so-called optimal (or close to it) size. This size falls exponentially with increasing temperature [1].

The properties of nanocomposites containing granules of ferromagnetic metals are of considerable interest. For  $x > x_c$ , a sample contains an infinite ferromag-

netic cluster and its magnetic properties are similar to those of a bulk metal. In particular, a well-defined Curie temperature is observed [2]. In the opposite case ( $x < x_c$ ), it is essential that for quite small sizes of granules (not exceeding values of ~10–100 nm, depending on the material), they have a single-domain structure. The direction of their magnetic moment is determined by the balance of the orientational action of the external magnetic field and the stabilizing action of magnetic anisotropy, crystalline or geometrical (due to the non-spherical form of granules). For this reason, the magnetic properties of such a nanocomposite are quite unusual and they strongly depend on the temperature and the magnetic field [3].

The galvanomagnetic properties of materials with  $x < x_c$  are also unusual. The probability of the intergranule tunnel transitions depends on the mutual orientation of the granule magnetic moments. This orientation can be controlled by an external magnetic field. This leads to the so-called giant magnetoresistance effect, i.e., a considerable (compared to that in usual metals) relative change in the resistance of such nanocomposites in a magnetic field. This change normally attains several dozen percent [4].

Thus, one can effectively (i.e., considerably and in a reversible manner) change different properties of nanocomposites by changing the temperature or the magnetic field. This, in principle, opens some possibilities for their practical application. However, one can also influence the properties of nanocomposites by means of their deformation. This possibility has not yet been discussed. Recently, the development of a new type of nanocomposite material was reported [5]. This material is a fine disperse metallic powder incorporated into an insulating matrix of the elastomer type (a plastic with a

relatively sparse network of bonds between polymer chains). It was pointed out that the conductivity of this material changes strongly (by several orders of magnitude) under the action of various deformations (compression, twist, or stretching). This phenomenon, connected with the physical nature of the tunnel conductivity of nanocomposites and having considerable promise for practical applications, will be the subject of discussion of this paper.

From what has been said above, it is clear that the conduction mechanisms in metallic ( $x > x_c$ ) and insulating ( $x < x_c$ ) nanocomposites are completely different. In the former case, it is the metallic conductivity through the intergranule contacts, while in the latter case, we have hopping conduction due to electron tunneling between granules. We will consider the effect of deformation on the properties of nanocomposites with these two types of conduction separately.

## 2. METALLIC NANOCOMPOSITES

The conduction in metallic nanocomposites is realized through the infinite cluster of metallic granules and is determined by the properties of the intergranule contacts. Each such contact is a microscopic narrow constriction in the electric conductive circuit. Its simplest model is a hole in an insulating, infinitely thin membrane between two conducting half-spaces. There exist two regimes of the current flow through such a contact [6]. If the contact radius  $r$  is large relative to the mean free path of electrons  $l$ , then its resistance equals  $R = \rho/2r$  (the Holm resistance), where  $\rho$  is the conductivity of the material of the electrodes (granules). In the opposite case ( $r \ll l$ ), we have  $R = (\rho/2r)(l/2r)$  (the

Sharvine resistance). The general relation for the resistance of the contact, which is valid for any ratio between  $r$  and  $l$ , has the form [6]

$$R(r/l) = (\rho/2l)(l/2r)[1 + (4/\pi)(r/l)\arctan(r/l)]. \quad (1)$$

The model considered above is applicable for describing two contacting spherical granules. To calculate the response of such contacts to pressure, one can use the solution to the problem on the contact of two balls having a diameter  $D$  and compressed by an external force  $F$  [7]. The radius  $r$  of the circular contact area depends on the effective pressure  $P = F(\pi D^2/4)$ , and, for elastic deformations, it is equal to

$$r = \alpha(D/2)P^{1/3}, \quad \alpha = [3(1 - \nu^2)/4E]^{1/3}.$$

For real metallic nanocomposites, the last relation should be written in a slightly modified form:

$$\begin{aligned} r(D) &= \alpha(D/2)(P + P_0)^{1/3} \\ &= \alpha P_0^{1/3}(D/2)(1 + P/P_0)^{1/3}. \end{aligned} \quad (2)$$

This formula takes into account that even in the absence of external pressure, the granules are already slightly deformed in the vicinity of the contact (in the course of their formation in the specific technological process). The seeding pressure  $P_0$  determines the value of this deformation.

Due to an increase in the contact area, the hydrostatic compression leads to a decrease in the resistance. Assuming, in the simplest approximation, that all initial ( $P = 0$ ) contacts are identical and that their number remains unchanged with increasing pressure, we find that  $R(P) = R[r(P)/l]$ , where the functions  $R(r/l)$  and  $r(P)$  are given by Eqs. (1) and (2). In the two limit cases, we have  $R(P) \propto (1 + P/P_0)^{-1/3}$  for the Holm contacts ( $r \gg l$ ) and  $R(P) \propto (1 + P/P_0)^{-2/3}$  for the Sharvine contacts ( $r \ll l$ ).

Figure 1 shows the dependence of  $R(P)$  on the pressure for different values of the parameter  $\beta = (\alpha D P_0^{1/3})/l \approx (D/l)(P_0/E)^{1/3}$ , which is determined by the ratio between the size of a granule  $D$  and the mean free path of electrons  $l$ , as well as by the seeding pressure  $P_0$ . This pressure determines the radius of the intergranule contact area in the absence of external pressure,  $r(P_0) = \alpha(D/2)(P_0)^{1/3} \approx (D/2)(P_0/E)^{1/3}$ . To estimate the parameter  $\beta$ , we note that the electron-microscopic investigations of metallic nanocomposites show that the sizes of intergranule contacts are, on average, one order of magnitude smaller than the sizes of the granules themselves. This corresponds to  $P_0/E \sim 10^{-3}$ . The mean free path of electrons in typical metals is 10–100 nm; thus,  $D/l \sim 0.1$ –1 for granules with a size of  $\sim 10$  nm. Thus, typical values of  $\beta$  are of the order unity. For such values, as is clear from Fig. 1, one should expect a considerable (one to two orders of magnitude)

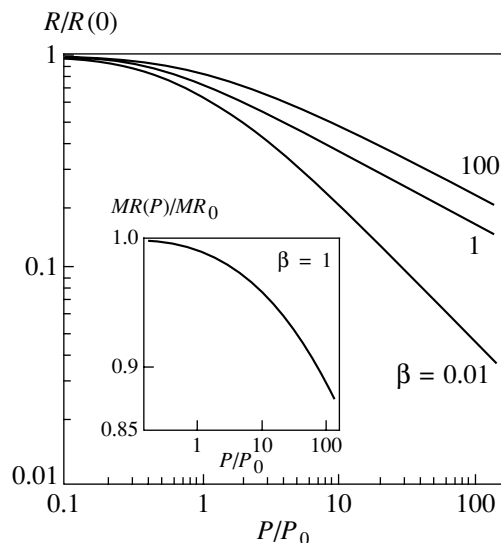


**Fig. 1.** Dependences of the resistivity  $R(P)$  of a metallic nanocomposite upon pressure for different values of the parameter  $\beta$ . The inset shows the dependence of the magnetoresistance upon pressure for  $\beta = 1$ .



change in the nanocomposite resistance at pressures of  $P \sim 100P_0 \sim 0.1E$ .

It is also of interest to find out how the pressure influences the giant magnetoresistance of the nanocomposite containing ferromagnetic granules. The issue of the magnetoresistance  $MR$  of a separate nanocontact between some ferromagnetic materials was considered in [8]. The quantity  $MR = (R_{\uparrow\downarrow} - R_{\uparrow\uparrow})/R_{\uparrow\uparrow}$  was determined as the relative change in contact resistance when one goes over from the high-resistance configuration with antiparallel magnetic moments of the contacting granules ( $\uparrow\downarrow$ ) to the lower resistance configuration with parallel magnetic moments ( $\uparrow\uparrow$ ). The quasi-classical theory of [8] predicts that, in going from the ballistic regime ( $l \gg r$ ) to the diffusion regime ( $l \ll r$ ), the magnetoresistance is decreased by about half and the  $MR(r/l)$  dependence itself can be approximated by the relation

$$MR(r/l) = MR_0[1 - (1/\pi)\arctan(2r/l)], \quad (3)$$

where the ballistic magnetoresistance  $MR_0$  depends upon the spin polarization of the conduction electrons in the ferromagnetic metal, and can be as large as unity [9].

Substituting Eq. (2) into Eq. (3), we find the dependence of the magnetoresistance upon the pressure,

$$MR(P)/MR_0 = 1 - (1/\pi)\arctan[\beta(1 + P/P_0)^{1/3}]. \quad (4)$$

The maximum changes in the magnetoresistance with pressure take place at  $\beta \approx 1$ . The corresponding dependence is shown in the inset to Fig. 1.

### 3. INSULATING NANOCOMPOSITES

In insulating nanocomposites, we deal with hopping conduction. In this case, the problem is reduced to calculations for an equivalent Miller–Abrahams resistor network with resistances  $R_{ij} = R_{ij}^0 \exp \xi_{ij}$  [10]. In this network, the sites are located at random. In our case, the sites are the granule centers. For the tunnel intergranule transitions, we have  $\xi_{ij} = \delta_{ij}/\lambda + \varepsilon_{ij}/kT$ , where  $\lambda \sim \hbar/(mW)^{1/2}$  is the electron wavelength in the dielectric matrix ( $W$  is the height of the tunnel barrier, which is virtually equal to the half-width of the energy band gap of the dielectric);  $\varepsilon_{ij}$  is the Coulomb energy of the transition (the change in the energy of the system in the electron transition  $i \rightarrow j$ ); and  $\delta_{ij} = r_{ij} - (a_i - a_j)$  is the spacing between the  $i$ th and  $j$ th granules having radii  $a_i$  and  $a_j$ , respectively (the distance between their centers is equal to  $r_{ij}$ ).

As was already pointed out, most important are the transitions between neighboring granules where one granule is charged and the other is electrically neutral. For spherical granules of the same size ( $a_i = a_j = D/2$ ), we have  $\varepsilon_{ij} = 0$ .<sup>1</sup> Therefore,  $\xi_{ij} = \delta_{ij}/\lambda = (r_{ij} - D)/\lambda$ ,  $R_{ij} = R_{ij}^0 \exp[(r_{ij} - D)/\lambda]$  and the problem is reduced to the problem of spheres [10]. In this case, the resistivity of

the system is determined by the well-known relation  $\rho = \rho_0 \exp[(r_c - D)/\lambda]$ , where  $r_c = 0.865 N_0^{1/3}$ , with  $N_0 = (6x/\pi)/\langle D^3 \rangle$  being the concentration of granules whose mean volume is  $(\pi/6)\langle D^3 \rangle$  in the absence of external pressure. If the deformation does not break the isotropy of the system (for instance, in the case of hydrostatic compression), then its action is equivalent to changing the granule concentration and can easily be taken into account by including its pressure dependence  $N(P)$ . Assuming that the deformation of the metallic granules of the nanocomposite is negligible in comparison with the deformation of its soft matrix, we find  $N(P) = N_0[x + (1-x)(1 - P/E)^3]^{-1}$ , where  $E$  is Young's modulus. Thus,

$$\begin{aligned} \rho(P)/\rho(0) &= \exp \left\{ \frac{0.865([x + (1-x)(1 - P/E)^3]^{1/3} - 1)}{N_0^{1/3}\lambda} \right\} \\ &= \exp \left\{ \left( \frac{\bar{D}}{\lambda} \right) \left( \frac{0.35}{x} \right)^{1/3} ([x + (1-x)(1 - P/E)^3]^{1/3} - 1) \right\}, \end{aligned} \quad (5)$$

where  $\bar{D} = \langle D^3 \rangle^{1/3}$ .

However, generally speaking, deformations break the system isotropy. For example, for uniaxial compression, the relative deformation  $u(\phi)$  in the direction making an angle  $\phi$  with the direction of the compression depends on this angle and equals [11]

$$u(\phi) = -(1/E)[(1 + \nu)\cos^2\phi - \nu]P, \quad (6)$$

where  $P$  is the compression pressure and  $E$  and  $\nu$  are Young's modulus and Poisson's ratio of the material, respectively.<sup>2</sup> In accordance with Eq. (6), the uniaxial compression is accompanied by stretching in the transverse (relative to the compression) direction; that is, the system becomes anisotropic: the intergranule spacings along the directions which are close to the compression direction are shortened, while the spacings along the transverse direction are lengthened. In terms of the percolation theory of hopping conduction, this is equivalent to the case of anisotropic wave functions for which [10]

$$\xi_{ij} = \left( \frac{x_{ij}^2 + y_{ij}^2}{\lambda_{\perp}} + \frac{z_{ij}^2}{\lambda_{\parallel}} \right)^{1/2}, \quad (7)$$

where  $x_{ij}$ ,  $y_{ij}$ , and  $z_{ij}$  are the components of vector  $\mathbf{r}_{ij}$  along the axes  $x$ ,  $y$ , and  $z$  (the direction of compression),

<sup>1</sup> In the general case,  $\varepsilon_{ij} \neq 0$ . However, this influences only the temperature dependence of the conductivity of the system. In this paper, we consider only the deformation dependence of the conductivity at a fixed temperature.

<sup>2</sup> We mean plastic and rubberlike materials for which  $E \sim 10^9$ – $10^{10}$  dyn/cm<sup>2</sup> (fluoroplastic, polyethylene, kapron resin) or  $E \sim 10^6$ – $10^7$  dyn/cm<sup>2</sup> (rubber).

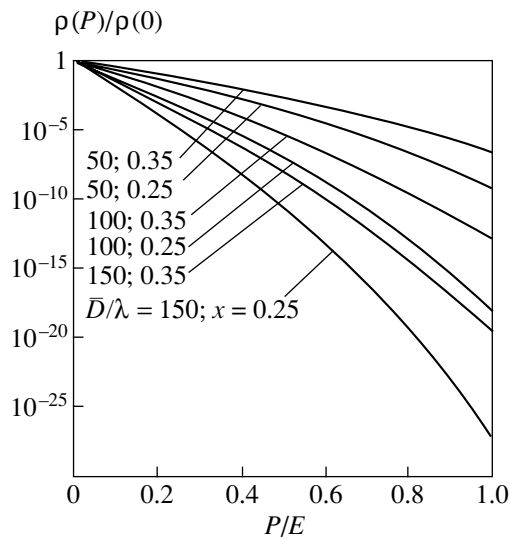


**Fig. 2.** Dependences of the resistivity  $\rho(P)$  of the insulating nanocomposite upon pressure for different values of the parameters  $\bar{D}/\lambda$  and  $x$ .

respectively. Here,  $\lambda_{\perp}$  and  $\lambda_{\parallel}$  are the characteristic sizes of the equivalent wave function in the corresponding directions.

For simplicity, we will consider only the case where  $x \ll 1$  and, therefore, the granule concentration is equal to  $N(P) = N_0[(1 - P/E)(1 + \nu P/E)^2]^{-1}$ . As is clear from Eq. (7), the action of the pressure which decreases (increases) the distance between the granules is equivalent to increasing (decreasing) the electron wavelength. Therefore,

$$\lambda_{\parallel} = \lambda/(1 - P/E), \quad \lambda_{\perp} = \lambda/(1 + \nu P/E). \quad (8)$$

Taking into account the fact that in the case of Eq. (7) the anisotropy of the resistivity is determined by the relation  $\rho_{zz}/\rho_{xx} = (\lambda_{\perp}/\lambda_{\parallel})^2$  [10], we find that for  $P < E$  the anisotropy of the resistivity of the uniaxially compressed nanocomposite is small:  $\rho_{zz}/\rho_{xx} = [(1 - P/E)(1 + \nu P/E)]^2 \sim 1$ . In this case, the weakly anisotropic resistivity of the uniaxially deformed nanocomposite is equal to  $\rho = \rho_0 \exp(0.865/N_0^{1/3} \lambda^*)$ , where  $\lambda^* = (\lambda_{\perp}^2 \lambda_{\parallel})^{1/3}$  [10]. Thus, the dependence of the resistance on the pressure has the form

$$\rho(P) = \rho(0) \exp \left[ \frac{0.865(1 - P/E)^{1/3} (1 + \nu P/E)^{2/3}}{N_0^{1/3} \lambda} \right]. \quad (9)$$

Let us evaluate the sensitivity of the insulating nanocomposite with granules of diameter  $D = 5\text{--}15$  nm to pressure. For a typical value of  $\lambda \sim 0.2$  nm, the dependences of the resistivity on the pressure are represented in Fig. 2. It can be seen that, for  $x = 0.25\text{--}0.35$ , even low pressures ( $P \ll E$ ) lead to a colossal change in the system resistivity.<sup>3</sup>

Thus, the electric properties of insulating nanocomposites with a rubberlike matrix are extremely sensitive to pressure. This is obviously the consequence of the exponentially strong dependence of the probability of the intergranule electron tunneling on the distance between the granules. A number of other physical characteristics of these materials (in particular, their optical, acoustical, and thermal properties) should be subjected to strong changes under pressure. The magnetic properties of such nanocomposites with ferromagnetic granules can strongly depend on the pressure due to a changed intergranule magnetic interaction. All these issues require special consideration.

## REFERENCES

1. E. Z. Meĭlikhov, Zh. Ėksp. Teor. Fiz. **115**, 1484 (1999) [JETP **88**, 819 (1999)].
2. A. Gavrin and C. L. Chein, J. Appl. Phys. **73**, 6949 (1993).
3. E. Z. Meĭlikhov, Zh. Ėksp. Teor. Fiz. **116**, 2182 (1999) [JETP **89**, 1184 (1999)].
4. J. S. Moodera, L. R. Kinder, T. M. Wong, and R. Meservey, Phys. Rev. Lett. **74**, 3273 (1995).
5. <http://www.peratech.co.uk>.
6. A. Mikrajuddin, F. G. Shi, H. K. Kim, and K. Okuyama, Mater. Sci. Semicond. Process. **2**, 321 (1999).
7. L. D. Landau and E. M. Lifshitz, *Course of Theoretical Physics, Vol. 7: Theory of Elasticity* (Nauka, Moscow, 1987; Pergamon, New York, 1986).
8. B. P. Vodop'yanov and L. R. Tagirov, in *Proceedings of the XXXII All-Russia Conference on Low Temperature Physics, Kazan, 2000*, Report NS o16.
9. J. S. Moodera and G. Mathon, J. Magn. Magn. Mater. **200**, 248 (1999).
10. B. I. Shklovskii and A. L. Efros, *Electronic Properties of Doped Semiconductors* (Nauka, Moscow, 1979; Springer-Verlag, New York, 1984).
11. L. M. Brekhovskikh and V. V. Goncharov, *An Introduction to the Mechanics of Continuous Media* (Nauka, Moscow, 1982).

Translated by A. Sonin

<sup>3</sup> For a rubberlike matrix, the condition  $P/E \sim 1$  is fulfilled at a pressure of  $P \sim 1$  atm.

# Temperature Dependence of the Radiation-Stimulated Conductivity of CsI Crystals upon Picosecond Excitation by Electron Beams

B. P. Aduiev, É. D. Aluker, V. M. Fomchenko, and V. N. Shvayko

Kemerovo State University, ul. Krasnaya 6, Kemerovo, 650043 Russia

e-mail: lira@kemsu.ru

Received October 17, 2000

**Abstract**—The temperature dependence of the pulse conductivity for CsI crystals upon excitation with an electron beam (0.2 MeV, 50 ps, 400 A/cm<sup>2</sup>) at a time resolution of 150 ps is investigated. Under experimental conditions, the time of bimolecular recombination of electrons and holes ( $V_k$  centers) is directly measured in the temperature range 100–300 K. This made it possible to calculate the temperature dependence of the effective recombination cross section  $S(T) = 7.9 \times 10^{-8} T^2$  cm<sup>2</sup>. The temperature dependence of the conductivity  $\sigma(T)$  is interpreted within the model of the separation of genetically bound electron–hole pairs. The activation energy of this process is found to be  $E_G = 0.07$  eV. © 2001 MAIK “Nauka/Interperiodica”.

## 1. INTRODUCTION

Investigation of the radiation-stimulated conductivity of nonmetallic materials is a direct method of providing information on the energy relaxation of band charge carriers and their interaction with structural and radiation-induced defects before recombination and deep trapping. For alkali halide crystals, the lifetime of band charge carriers is short. The hole lifetime is restricted by the autolocalization time ( $\sim 10^{-12}$  s), and the electron lifetime is limited by the recombination or deep trapping time ( $\sim 10^{-9}$ – $10^{-12}$  s). For this reason, the quasi-stationary excitation mode is usually used for measuring the radiation-stimulated conductivity with the help of both stationary and pulse excitation sources. In this case, a certain effective quantity  $\mu_d \tau$ , i.e., the product of the drift mobility  $\mu_d$  by the charge-carrier lifetime  $\tau$ , is measured. The last two quantities can be associated with multiple trapping in different-type attachment levels. Hence the required information on the mechanism of relaxation of band charge carriers and their fundamental characteristics, such as the microscopic (Hall) mobility  $\mu_H$  or the recombination cross section  $S$ , is difficult to obtain from these experiments.

In this respect, a promising trend consists in decreasing the excitation pulse duration  $\tau_p$  and increasing the time resolution of the reading instruments. With the proviso that  $\tau_p < \tau$ , the situation changes qualitatively. In this case, the instantaneous excitation mode is used and the lifetime  $\tau$  and other microscopic characteristics of charge carriers can be directly measured in the experiment.

This situation was realized in the present work.

## 2. EXPERIMENTAL TECHNIQUE

A needle-gap electron accelerator [1] was used as an excitation source. The parameters of the excitation pulse were as follows: the maximum electron energy was 0.2 MeV, the beam current density was 10<sup>3</sup> A/cm<sup>2</sup>, and the pulse duration was 50 ps. The technique for measuring the conduction current pulses was described in [2]. The direct time resolution of the technique was 150 ps. Pure-grade CsI crystals were used in the measurements. The experiment was carried out in the temperature range 100–300 K.

Oscillograms of conduction current pulses are shown in Fig. 1. The investigation of pure-grade crystals, which were taken from different batches, revealed that either an increase in the pulse decay or flattening at the pulse top are observed for some samples (see, for

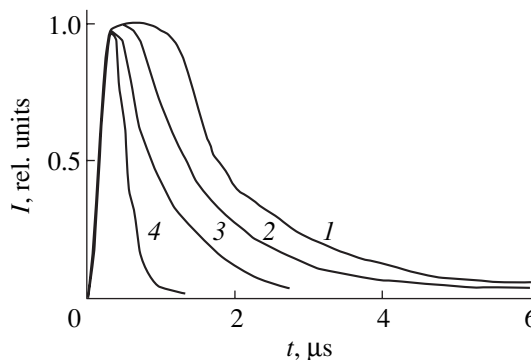


**Fig. 1.** Oscillograms of the conduction current pulses for CsI crystal samples: (1) sample 1 and (2–4) sample 2.  $T$ , K: (1, 2) 300, (3) 150, and (4) 15.

example, oscillogram 1 in Fig. 1 for sample 1). Such a shape of pulses indicates the presence of uncontrollable attachment centers for band electrons [3], which leads to a decrease in the drift mobility  $\mu_d$  with respect to the Hall mobility  $\mu_h$ . For samples of the second batch (CsI, sample 2), the front of the conduction current pulse corresponds to the integral of the excitation pulse followed by hyperbolic decay. It seems likely that no attachment centers occur in these samples. For this reason, these samples were used in our experiments; in further calculations, we assumed that  $\mu_d = \mu_h$ . Note that, at temperatures  $T \leq 100$  K, the duration of the conduction current pulse decay becomes shorter than the time resolution of the equipment; i.e., the instantaneous excitation mode was realized only at  $T > 100$  K. Consequently, it was in this temperature range that the results of kinetic measurements were further processed.

The current–voltage characteristics, which were measured at the instant of completion of the excitation pulse, are linear over the entire temperature range under investigation.

### 3. PROCESSING OF THE RESULTS AND THEIR DISCUSSION

The resistance of the sample was determined from the slope of the current–voltage characteristic, and the specific conductivity  $\sigma$  was calculated. The temperature dependence of  $\sigma$  is shown in Fig. 2.

Earlier [4, 5], we demonstrated that the hyperbolic decay of the conduction current pulses in pure CsI crystals at room temperature is due to bimolecular recombination of coherent conduction-band electrons and autolocalized holes ( $V_k$  centers).

In this connection, further oscillogram processing was carried out according to the hyperbolic decay for which the following expression is valid:

$$j(t) = \frac{j_0}{1 + \alpha j_0 t}, \quad (1)$$

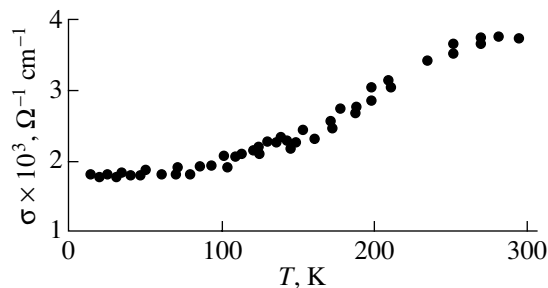


**Fig. 2.** Temperature dependence of the conductivity for the CsI crystal at an excitation density of  $400 \text{ A/cm}^2$ .

where  $j_0$  is the conduction current density at the instant of completion of the excitation pulse. It was shown [4, 5] that the parameter  $\alpha$  is related to the cross section of the  $e-V_k$  recombination  $S$  and the drift mobility  $\mu_d$  by the equation

$$\frac{S}{\mu_d} = \frac{\alpha e E}{v}, \quad (2)$$

where  $e$  is the elementary charge,  $E$  is the strength of the external electric field,  $v = (3kT/m^*)^{1/2}$  is the thermal velocity of electrons, and  $m^* \approx 0.5m_0$  is the effective electron mass. Oscillogram processing for different temperatures allowed us to calculate the  $\alpha$  parameters and, consequently, the dependence of  $S/\mu_d$  on  $T$ . The result for  $S/\mu_d$  is shown in Fig. 3.

For further analysis, we used the available data [6] for  $\mu_h$  and calculated the experimental values of  $S$  by assuming that  $\mu_d = \mu_h$  for these samples. Unfortunately, the  $\mu_h$  values available in the literature are appropriate only for the temperature range 150–350 K. For this reason, our data were processed for this temperature range. The corresponding curve is depicted in Fig. 4.

The electron capture cross section for a Coulomb center is usually approximated by an exponential law [7, 8]. Hence, we accepted the following expression for  $S$ :

$$S = CT^\beta, \quad (3)$$

where  $C$  and  $\beta$  are constants. The solid curve in Fig. 4 was constructed according to formula (3) for  $C = 7.9 \times 10^{-8} \text{ cm}^2 \text{ K}^{-2}$  and  $\beta = 2$ . Then, the  $C$  and  $\beta$  values obtained and the experimental data presented in Fig. 3 were used to calculate the Hall mobility  $\mu_h$  in the temperature range 100–150 K (Fig. 5). By using the  $\mu_h$  values and the data presented in Fig. 2, we obtained the

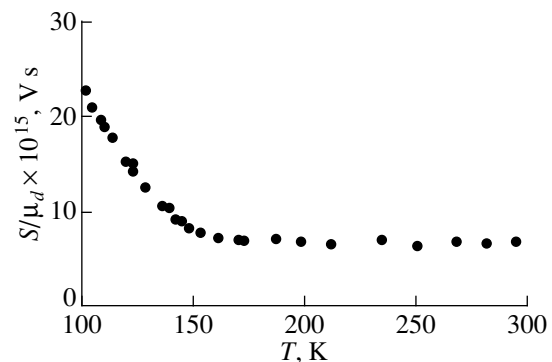


**Fig. 3.** Temperature dependence of the ratio of the effective recombination cross section  $S$  to the drift mobility  $\mu_d$ .

temperature dependence of the concentration of conduction band electrons from the formula

$$n = \frac{\sigma}{e\mu_h}. \quad (4)$$

The result of calculation is shown in Fig. 6. It is seen that  $n$  monotonically decreases with a decrease in temperature and approaches a constant value. We interpreted this result in the framework of the model of recombination in correlated (genetic) pairs [9]. This model was used in our recent work [10] for the interpretation of the results of measuring the temperature dependence of the conductivity for crystals with a NaCl-type lattice. In essence, the model is as follows. For a long mean free path, the genetically bound electron and hole fly far apart, so that the particles formed as a result of different ionizing events are "mixed up." In this case, the genetic coupling between the partners is lost and the recombination process is described by the bimolecular scheme. Hereafter, these mixed-up particles will be referred to as statistical particles. For a short mean free path, the components of an electron-hole pair fly apart for short distances during relaxation, which substantially decreases the probability of mixing-up the particles created in different ionizing events. In this case, the probability of the recombination of a genetically bound electron and hole (genetic pair) is rather high. This can be responsible for the considerable contribution of the monomolecular constituent to the recombination. As applied to our case, we can conclude that the statistical pairs only can contribute to the conductivity. However, a certain probability exists of an electron leaving its genetic partner (hole) due to thermal fluctuations. Let us denote the activation energy of the separation of genetic pairs as  $E_G$ .

For the electron concentration in the conduction band at the instant of completion of the excitation pulse, we can write

$$n = n_S + n_G e^{-E_G/kT}, \quad (5)$$

where  $n_S$  and  $n_G$  are the concentrations of electron-hole pairs generated in the lattice in statistic and genetic ways, respectively. The solid curve in Fig. 6 was constructed at the following parameters:  $n_S = 0.36 \times 10^{14} \text{ cm}^{-3}$ ,  $n_G/n_S = 180$ , and  $E_G = 0.07 \text{ eV}$ . Consequently, in the framework of the model considered, the majority of charge carriers is thermalized in genetic pairs. From the calculated  $E_G$  value, we can estimate the effective distance at which the genetically bound electron and hole undergo thermalization, that is,

$$r = \frac{1}{4\pi\epsilon\epsilon_0 E_G}. \quad (6)$$

The calculation gives the value  $R \approx 17 \text{ \AA}$ .

In the temperature range  $T < 100 \text{ K}$ , in which the instantaneous excitation mode changes over to the quasi-stationary mode, the conductivity is temperature

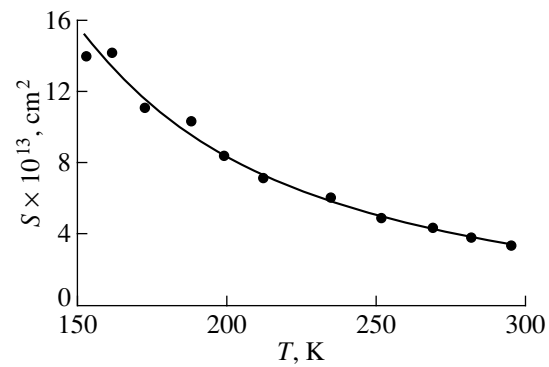


**Fig. 4.** Temperature dependence of the effective recombination cross section. Points correspond to calculations from the experimental data, and the solid line represents the approximation by formula (3) for  $C = 7.9 \times 10^{-8} \text{ cm}^2 \text{ K}^{-2}$  and  $\beta = 2$ .

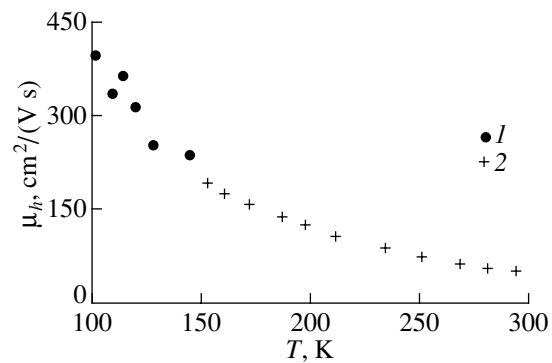


**Fig. 5.** Temperature dependence of the Hall mobility  $\mu_h$  according to (1) the data taken from [3] and (2) calculations from the experimental data shown in Fig. 3.

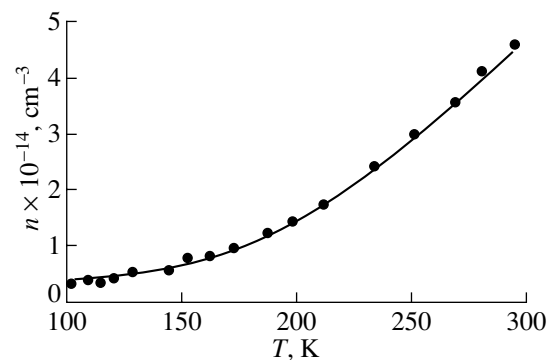


**Fig. 6.** Temperature dependence of the concentration of conduction band electrons at the instant of completion of the excitation pulse. Points correspond to the calculation by formula (4) using the experimental data for  $\sigma$  (Fig. 2) and  $\mu_h$  (Fig. 5), and the solid line represents the approximation by formula (5) for  $n_G/n_S = 180$  and  $E_G = 0.07 \text{ eV}$ .

independent (Fig. 2). This result can be interpreted qualitatively in the following way. In the quasi-stationary approximation, the expression for the conductivity

$\sigma$  can be written in the form [11]

$$\sigma = G\tau e\mu, \quad (7)$$

where  $G$  is the generation rate of electron–hole pairs and  $\tau$  is the charge-carrier lifetime.

According to [12], for electron trapping by a Coulomb center, the lifetime is determined by the expression

$$\tau = \frac{\varepsilon\varepsilon_0}{Ne\mu}, \quad (8)$$

where  $N$  is the concentration of trapping (recombination) centers. In this case, according to formula (7), the electrical conductivity  $\sigma$  is temperature independent at constant  $G$ , which was observed experimentally.

#### ACKNOWLEDGMENTS

This work was supported by the Ministry of Education of the Russian Federation.

#### REFERENCES

1. B. P. Aduiev and V. G. Shpak, *Prib. Tekh. Éksp.*, No. 2, 49 (1990).
2. B. P. Aduiev, É. D. Aluker, G. M. Belokurov, *et al.*, in *Proceedings of the I All-Russia Symposium "Solid-State Ionizing-Radiation Detectors, TTD-97," Yekaterinburg, 1998*, p. 126.
3. K. Weaver, J. K. Shtis, and R. E. Faw, *J. Appl. Phys.* **48**, 2762 (1977).
4. B. P. Aduiev, A. V. Igolinskiĭ, and V. N. Shvayko, *Fiz. Tverd. Tela (St. Petersburg)* **38** (3), 948 (1996) [*Phys. Solid State* **38**, 525 (1996)].
5. B. P. Aduiev, E. D. Aluker, G. M. Belokurov, and V. N. Shvayko, *Phys. Status Solidi B* **208**, 137 (1998).
6. C. H. Scager and D. Emin, *Phys. Rev. B* **2**, 3421 (1970).
7. P. V. Meĭklyar, *Physical Processes during Formation of Latent Photographic Images* (Nauka, Moscow, 1972).
8. V. L. Bonch-Bruevich and E. G. Landsberg, *Phys. Status Solidi B* **29**, 9 (1968).
9. É. D. Aluker, D. Yu. Lusic, and S. A. Chernov, *Electron Excitations and Radioluminescence in Alkali Halide Crystals* (Zinatne, Riga, 1979).
10. B. P. Aduiev, V. M. Fomchenko, and V. N. Shvayko, *Fiz. Tverd. Tela (St. Petersburg)* **41** (3), 429 (1999) [*Phys. Solid State* **41**, 384 (1999)].
11. S. M. Ryvkin, *Photoelectric Effects in Semiconductors* (Fizmatgiz, Leningrad, 1963; Consultants Bureau, New York, 1964).
12. S. I. Pekar, *Research on Electron Theory of Crystals* (Gostekhizdat, Moscow, 1951).

*Translated by N. Korovin*

## Relaxation of Electronic Excitations in Beryllium Oxide: A Time-Resolved Vacuum-UV Spectroscopy Study

V. A. Pustovarov\*, V. Yu. Ivanov\*, M. Kirm\*\*, A. V. Kruzhalov\*,  
A. V. Korotaev\*, and G. Zimmerer\*\*

\* Ural State Technical University, ul. Mira 19, Yekaterinburg, 620002 Russia

\*\* II Institute of Experimental Physics, Hamburg University, D22761 Hamburg, Germany

e-mail: ivy@dpt.ustu.ru

Received November 13, 2000

**Abstract**—Beryllium oxide crystals are studied by time-resolved optical and luminescence vacuum-UV spectroscopy. The low-temperature luminescence spectra and the luminescence decay kinetics (2.5–10 eV, 1–500 ns) upon selective photoexcitation, and also the luminescence excitation and reflectivity spectra (8–35 eV), are analyzed for BeO crystals with the optic axis aligned parallel and perpendicular to the electric vector of exciting polarized synchrotron radiation. It is found that the radiative relaxation of electronic excitations proceeds through a large number of channels. The excited states of self-trapped excitons are characterized by different multiplicity depending on the excitation energy and the sample orientation. © 2001 MAIK “Nauka/Interperiodica”.

### 1. INTRODUCTION

Self-trapped excitons in wide-gap oxide systems were discovered twenty years ago. However, the mechanisms responsible for the formation of excited states and models of self-trapped excitons remain a subject of discussion to the present day. It is found that the self-trapping of excitons is characteristic of oxide compounds with a low local symmetry of oxygen sites ( $\text{SiO}_2$ ,  $\alpha\text{-Al}_2\text{O}_3$ ,  $\text{YAlO}_3$ ,  $\text{Y}_3\text{Al}_5\text{O}_{12}$ , etc.) [1]. As a rule, the excitonic structure of the fundamental absorption edge for these compounds is weakly pronounced or is absent entirely. By contrast, the self-trapping of excitons is not observed in high-symmetry oxide matrices ( $\text{MgO}$  and  $\text{CaO}$ ) with a well-developed structure of anionic excitons in the optical constant spectra. As a consequence, the luminescence excitation spectra for oxide systems in the range of fundamental absorption appear little informative in analyzing the mechanisms responsible for the formation of excited states of self-trapped excitons. At the same time, the efficiency of this analysis for alkali halide crystals was demonstrated by Matsumoto *et al.* [2, 3]. A comparative analysis of the time-resolved emission and luminescence excitation spectra of alkali halide crystals made it possible to separate and systematize three types of self-trapped excitons (which differ in the degree of displacement of two-halide hole nucleus from the regular to the interstitial site) and to determine the multiplicity of their excited states [2–4].

Beryllium oxide crystals have a hexagonal structure of the wurtzite type and the widest band gap ( $E_g = 10.63$  eV) among oxides. As regards the local symme-

try of oxygen sites, these crystals are intermediate between high-symmetry ( $\text{MgO}$ ) and low-symmetry ( $\text{Al}_2\text{O}_3$ ) matrices. The existence of a preferred optic axis in BeO (unlike alkali halide crystals) allows the use of orientational spectroscopic techniques. The well-developed excitonic edge structure was first observed by Roessler *et al.* [5] in the reflectivity spectra of BeO and, more recently, was thoroughly investigated using synchrotron radiation and oriented samples [6–8]. In our earlier work [9], the broad bands at 4.9 and 6.7 eV in the luminescence spectra of BeO were attributed to the radiative decay of self-trapped excitons of two types, which differ in the configuration of a hole nucleus, i.e., a small-radius polaron of the  $\text{O}^-$  ion type in a local crystal lattice fragment. In alkali halide crystals, the luminescence of triplet self-trapped excitons can occur through a pure excitonic mechanism due to exciton self-trapping and as a result of the recombination of electrons and self-trapped holes [1, 4]. However, recent investigations [10–12] revealed the branching of the radiative relaxation of electronic excitations into different channels for some crystals of the Group III metal and complex oxides. In a number of experimental works dealing with BeO [9, 11, 13, 14], there is also indirect evidence that excited states of self-trapped excitons in BeO exhibit a wide variety of relaxation channels and different multiplicities.

The present work is a continuation of our earlier investigations into the relaxation of electronic excitations in BeO [9, 15]. With the aim of elucidating the mechanisms responsible for the formation of excited states of self-trapped excitons, we experimentally studied the time-resolved luminescence spectra and the

luminescence decay kinetics in the UV and vacuum-UV ranges upon selective photoexcitation and the time-resolved luminescence excitation spectra of oriented beryllium oxide crystals. The results reported were obtained at  $T = 10$  K, because all types of radiative relaxation of electronic excitations in BeO can be realized only at a low temperature.

## 2. SAMPLES AND EXPERIMENTAL TECHNIQUE

Crystals were grown from a solution in the sodium tungstate melt by V.A. Maslov according to the procedure described in [16]. The impurity contents in samples were checked by laser mass spectrography and did not exceed 140 ppm Na, 10 ppm Li, 70 ppm Mg, 7 ppm Zn, 16 ppm B, and 2 ppm Al. Single crystals (prisms or plates) with natural growth or polished faces oriented parallel or perpendicular to the crystal optic axis  $\mathbf{C}$  were used as samples. In the case of crystals with a preferred optic axis, there are two orientations that are alternative to the  $\mathbf{E} \parallel \mathbf{C}$  orientation. One orientation is realized when the axis of a luminescence recording system is aligned along the crystal optic axis  $\mathbf{C}$ . Hereafter, this orientation will be designated as  $\mathbf{E} \perp \mathbf{C}_0$ . In the other case, the crystal optic axis is perpendicular to the recording axis; this mutual orientation will be denoted as  $\mathbf{E} \perp \mathbf{C}$ .

Measurements were performed on a SUPERLUMI station (HASYLAB Laboratory, DESY, Hamburg) [17]. The luminescence in the range 6–35 eV was excited by a 2-m vacuum monochromator with changeable gratings. The luminescence excitation spectra were normalized to an equal number of photons incident on the crystal with the use of sodium salicylate. The luminescence spectra were analyzed in the range 2.5–6.0 eV by using a B&M monochromator (the Czerny–Turner scheme) and a R2059 photomultiplier tube (Hamamatsu) and in the range 4–10 eV with a second 0.5-m vacuum monochromator and a R6836 solar-insensitive photomultiplier tube. The emission and luminescence excitation spectra were measured for the time-integrated luminescence and the luminescence recorded in time windows (with the width  $\Delta_t$ ), which were correlated with respect to an exciting synchrotron radiation pulse (with the delay time  $\delta_t$  after initiation of the synchrotron radiation pulse). Reasoning from the decay kinetics, the values of  $\Delta_t$  and  $\delta_t$  were taken equal to 2.2 and 8.2 ns for the fast component and 23 and 111 ns for the slow component, respectively. The luminescence spectra (shown in the figures) for the fast components of the luminescence decay kinetics were obtained by subtracting the luminescence spectra for the slow component (with the corresponding coefficient) from the experimental luminescence spectra measured in a fast time window. The parameters of the decay kinetics were determined by the convolution integral method. The reflectivity spectra (the angle of incidence of synchrotron radiation was  $17.5^\circ$ ) were recorded simultaneously with the luminescence excita-

tion spectra. In order to exclude the luminescence contribution to the reflectivity spectra, they (like the luminescence excitation spectra) were taken in a separate fast time window ( $\Delta_t = 22.5$  ns and  $\delta_t = 2.0$  ns) with the recording of a signal from sodium salicylate. The measurements were carried out at  $T = 10$  K in a cryostat that provided a vacuum of no worse than  $2 \times 10^{-10}$  Torr, which ensured the purity of the crystal surface in low-temperature experiments. The check measurements of the orientation dependences were performed using the same natural growth face of the prismatic sample.

## 3. THE TIME-RESOLVED EMISSION AND LUMINESCENCE SELECTIVE-EXCITATION SPECTRA

The time-resolved emission and luminescence selective-photoexcitation spectra of BeO exhibit a pronounced orientation dependence. In the case when the  $\mathbf{E}$  vector of exciting synchrotron radiation is aligned along the crystal optic axis  $\mathbf{C}$  ( $\mathbf{E} \parallel \mathbf{C}$ ), the early stage of the UV luminescence decay involves, at least, two components depending on the exciting radiation energy [band maxima at 4.0 and 5.0 eV; full widths at half-maximum (FWHM)  $\sim 1.0$  eV] (Fig. 1). A gradual increase in the energy of exciting synchrotron radiation in the range of the fundamental absorption edge and the initial range of interband transitions leads to a shift in the spectrum of the early stage of luminescence decay toward the long-wavelength range. In this case, in the excitation spectrum of fast luminescence components, the band at 4.0 eV is most efficiently excited in the range corresponding to the  $E_{n=2}$  and  $E_{n=3}$  maxima of excitonic reflection, whereas the 5.0-eV luminescence is most efficiently excited at 10.2–10.3 eV, which is considerably less than the energy  $E_{n=1}$  of the first maximum of excitonic reflection (Fig. 2a). For comparison, note that the band at 10.38 eV in the excitation spectrum of the slow 4.7-eV luminescence component is immediately adjacent to the energy  $E_{n=1}$  (Fig. 2b).

The decay time of fast luminescence at 4.0 eV upon photon excitation within the range of  $E_{n=2}$  is equal to 2.2 ns, and the fast luminescence at 5.0 eV upon excitation within the range of  $E_{n=1}$  has a decay time of 4.4 ns (Fig. 3). It should be noted that this result confirms the data obtained in our earlier works [13, 14], in which we, for the first time, measured the spectrum of the fast UV luminescence in BeO upon excitation with x-ray synchrotron radiation and determined the parameters of the decay kinetics ( $\tau = 2.0$  ns) and the degree of linear polarization ( $P = +70\%$ ) of this luminescence. (In [13, 14], the degree of linear polarization was calculated by the formula  $P = (I_{\parallel} - I_{\perp}) / (I_{\parallel} + I_{\perp})$ , where  $I_{\parallel}$  is the luminescence intensity measured for the analyzer (a Rochon prism) axis parallel to the crystal optic axis  $\mathbf{C}$  and  $I_{\perp}$  is the luminescence intensity measured for the crossed axes.) However, we failed to reveal the fast luminescence in the range of 5.0 eV upon this excita-



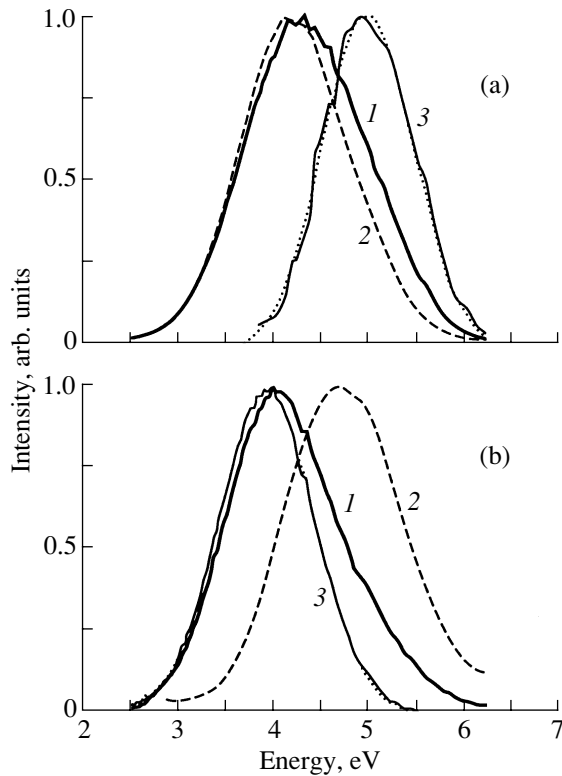


**Fig. 1.** Time-resolved photoluminescence spectra of BeO ( $T = 10$  K) for the crystal orientation  $\mathbf{E} \parallel \mathbf{C}$  at excitation energies of (a) 10.25 and (b) 10.7 eV: (1) fast and (2) slow time windows. (3) Difference spectra and their approximation by Gaussian lines.

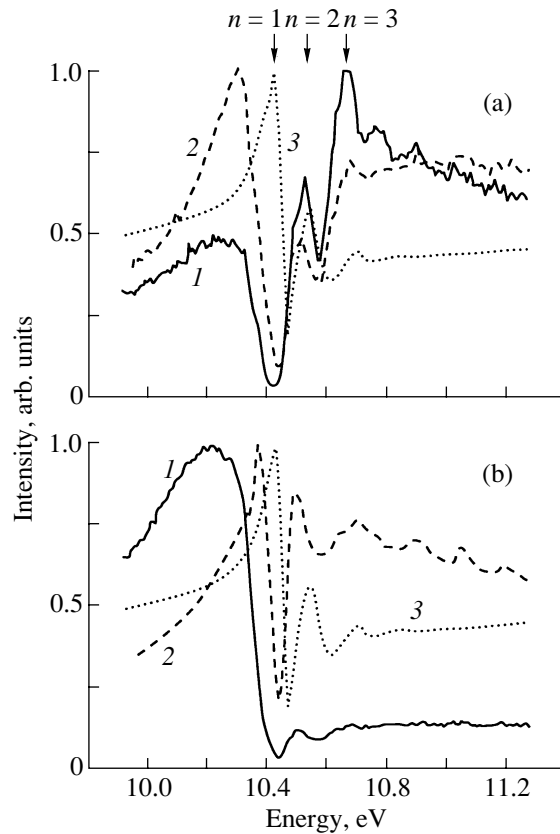


**Fig. 2.** Excitation spectra of the UV luminescence at (1) 3.35 and (2) 4.75 eV and (3) reflectivity spectra of BeO ( $T = 10$  K) for the crystal orientation  $\mathbf{E} \parallel \mathbf{C}$ : (a) fast and (b) slow time windows.

tion in our earlier works [13, 14]. As is now clear from the luminescence excitation spectra, this is explained by the narrow range of its efficient selective excitation.

The slow stage of the UV luminescence decay at  $\mathbf{E} \parallel \mathbf{C}$  is also characterized by two components in the luminescence spectrum (Fig. 1): bands with maxima at 4.2 and 4.7 eV (depending on the excitation energy). Upon selective photon excitation with  $E_{\text{exc}} = 9.5$  eV, the characteristic decay time of the 4.2-eV luminescence is equal to 34 ns. The luminescence at 4.2 eV is evidently associated with the relaxation of electronic excitations localized near impurity or intrinsic crystal defects, since its excitation spectrum predominantly manifests itself in the range 9.5–10.2 eV (Fig. 2b) and is rather typical of impurity luminescence in BeO (see, for example, the luminescence excitation spectrum of BeO–Zn in [15]). The excitation spectrum of the slow luminescence component at 4.7 eV (its kinetics can be described by a two-component exponential dependence with  $\tau_1 = 54$  ns and  $\tau_2 = 36$   $\mu$ s; in this case, the latter component accounts for up to 95% of the total light sum) is very similar to the excitation spectrum of the fast luminescence component at 5.0 eV: the 4.7-eV luminescence is most efficiently excited in the energy range of 10.38 eV, which is immediately adjacent to

$E_{n=1}$  (Fig. 2). The degree of linear polarization  $P$  of the slow component upon excitation with x-ray synchrotron radiation is negative and equal to  $-50\%$  at  $T = 80$  K [13, 14].

For the crystal orientation  $\mathbf{E} \perp \mathbf{C}$ , the fast UV luminescence component (the band at 4.0 eV) at the same excitation energies is considerably less pronounced. This is clearly seen from Fig. 3, which shows the luminescence decay kinetics for BeO in the 4.0- and 5.0-eV spectral ranges (corresponding to the fast luminescence components) as a function of the characteristic excitation energy and the crystal orientation. The orientation dependence of the decay kinetics is independently confirmed by the luminescence excitation spectra displayed in Figs. 4a and 4b and also by the data obtained in [13, 14] on the orientation dependence of the fast UV luminescence for BeO upon excitation with x-ray synchrotron radiation. For this orientation, the fast luminescence at 5.0 eV is not observed upon excitation into the range of excitonic absorption and the initial range of interband transitions, and the luminescence spectrum measured in the fast time window remains virtually unchanged (maximum at 3.9 eV; FWHM = 1.0 eV) (Fig. 4b). As for the  $\mathbf{E} \parallel \mathbf{C}$  orientation, the fast luminescence is most efficiently excited in the range of the

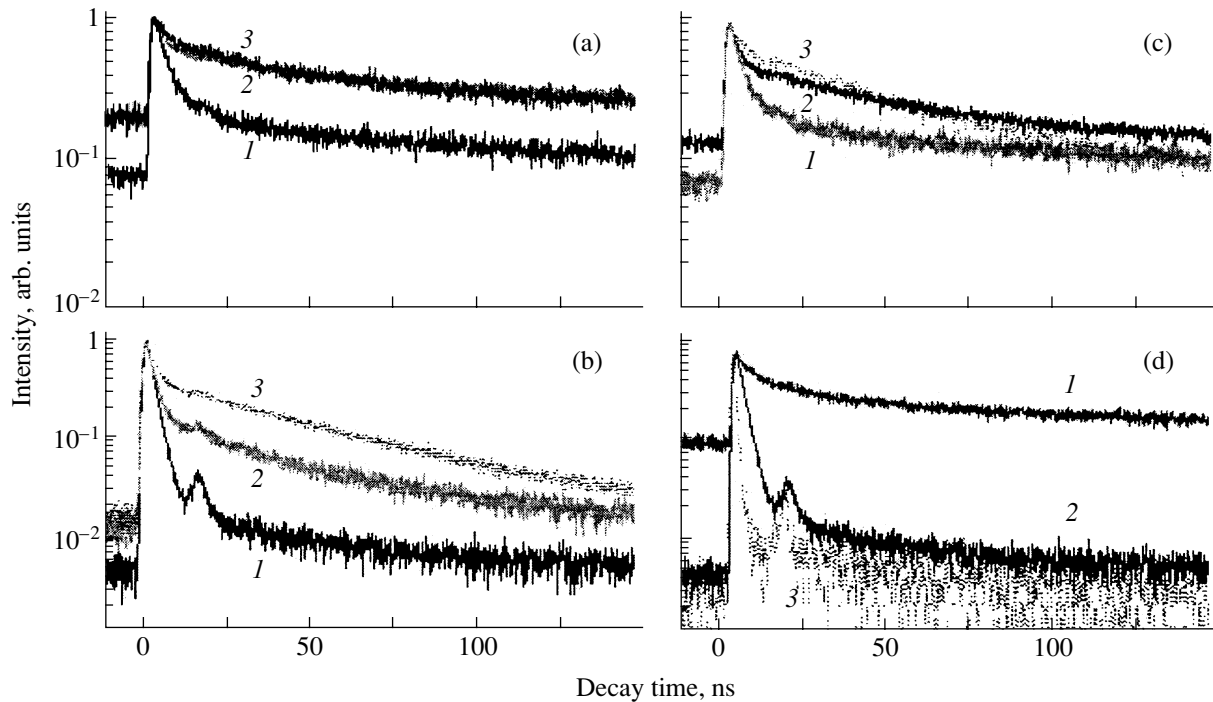


**Fig. 3.** Kinetics of luminescence decay in BeO at  $T = 10$  K: (a)  $E_{\text{emiss}} = 5.0$  eV and  $E_{\text{exc}} = 10.24$  eV at (1)  $\mathbf{E} \parallel \mathbf{C}$ , (2)  $\mathbf{E} \perp \mathbf{C}$ , and (3)  $\mathbf{E} \perp \mathbf{C}_0$ ; (b)  $E_{\text{emiss}} = 3.35$  eV and  $E_{\text{exc}} = 10.67$  eV at (1)  $\mathbf{E} \parallel \mathbf{C}$ , (2)  $\mathbf{E} \perp \mathbf{C}$ , and (3)  $\mathbf{E} \perp \mathbf{C}_0$ ; (c)  $\mathbf{E} \parallel \mathbf{C}$  and  $E_{\text{emiss}} = 5.0$  eV at  $E_{\text{exc}} =$  (1) 10.24, (2) 10.67, and (3) 11.27 eV; and (d)  $\mathbf{E} \parallel \mathbf{C}$  and  $E_{\text{emiss}} = 3.35$  eV at  $E_{\text{exc}} =$  (1) 10.24 and (2) 10.67 eV, and (3) instrument function of excitation pulse. The systematic instrumental peak observed was taken into account in analyzing the kinetic parameters and choosing the time windows  $\Delta_t$ .

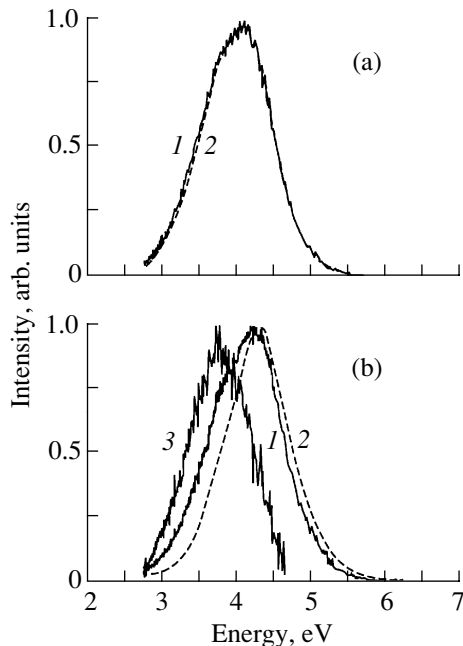


**Fig. 4.** Time-resolved photoluminescence spectra of BeO ( $T = 10$  K) for the crystal orientation  $\mathbf{E} \perp \mathbf{C}$  at excitation energies of (a) 10.2 and (b) 10.6 eV: (1) fast and (2) slow time windows. (3) Difference spectrum and its approximation by a Gaussian line.

$E_{n=2}$  and  $E_{n=3}$  excited exciton states (Fig. 5a). The band at 4.5 eV ( $\tau = 52$  ns) predominates in the spectrum of the slow component at this orientation (Fig. 4b), and its luminescence excitation spectrum differs from that of the fast component at 3.9 eV by a higher excitation efficiency in the range of 10.4 eV, which is immediately adjacent to the  $E_{n=1}$  energy (Fig. 5b, curve 2).

In the vacuum-UV range, the luminescence spectrum of BeO at  $T < 160$  K exhibits a band at 6.7 eV (FWHM  $\sim 0.8$  eV) [9]. Fast components are not observed in the decay kinetics of vacuum-UV luminescence (6.7 eV) in BeO upon photoexcitation. As was noted in our previous works (see, for example, [9]), this kinetics is predominantly described by an exponential component with  $\tau = 340$   $\mu\text{s}$ . At the crystal orientation  $\mathbf{E} \parallel \mathbf{C}$ , the 6.7-eV vacuum-UV luminescence (the degree of polarization  $P = -75\%$ , according to the x-ray luminescence data at  $T = 80$  K [9]) is excited in the range of the  $E_{n=1}$  ground and (more efficiently)  $E_{n=2}$  and  $E_{n=3}$  excited exciton states and also in the range of formation of separate electron-hole pairs (Fig. 6, curve 1). Note that the efficiency of the luminescence excitation in the interband absorption range ( $E_{\text{exc}} > E_g$ ) is higher than that in the excitonic range. At  $\mathbf{E} \perp \mathbf{C}$ , the excitation spectrum of the luminescence at 6.7 eV changes radically: the luminescence is excited most

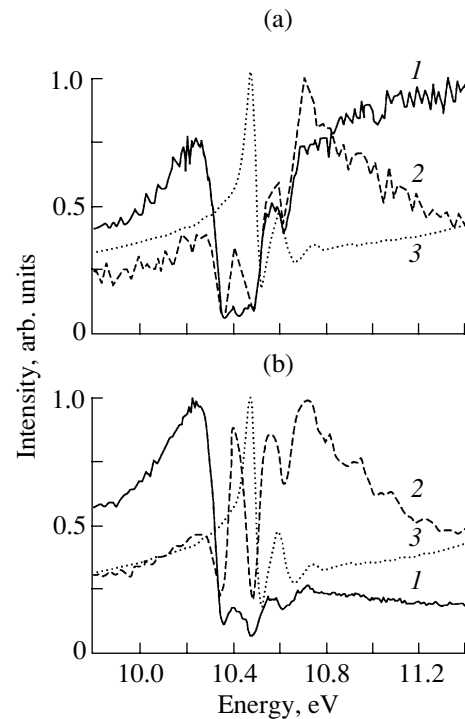
efficiently in the range of  $E_{n=1}$  and substantially less efficiently in the ranges of the excited exciton states and interband transitions at  $E_{exc} > E_g$  (Fig. 6, curve 2).

Figure 7 depicts the steady-state (without time resolution) luminescence excitation spectra at 4.8 and 6.7 eV for the BeO crystals in the range  $E_{exc} = 8\text{--}35$  eV. It is clearly seen that there is a considerable difference in the excitation efficiencies of these luminescence components in the excitonic range and the range of the threshold of the electronic excitation multiplication at  $E_{exc} > 20$  eV. The threshold energy  $E_{pm}$  of the multiplication of electronic excitations for the 6.7-eV luminescence falls in the range of the formation of secondary excitons  $E_{pm} \approx 2E_{n=1}$ , whereas this energy for the luminescence at 4.8 eV lies in the range of the generation of secondary electron-hole pairs at  $E_{pm} > 2E_g$  ( $E_{pm} = 24$  eV).

#### 4. BRANCHING OF RELAXATION OF ELECTRONIC EXCITATIONS (DISCUSSION OF THE RESULTS)

The time-resolved luminescence spectra of BeO crystals upon selective photoexcitation are characterized by several luminescence types, namely, the fast luminescence components with band maxima at 4.0 and 5.0 eV and the slow luminescence components with band maxima at 4.2–4.7 and 6.7 eV. It is of fundamental importance to elucidate the nature of the luminescence components observed: whether they are caused by the radiative relaxation of electronic states in the regular lattice (intrinsic luminescence) or are associated with structural defects in the crystal. It seems likely that the time-resolved luminescence excitation spectra are most informative in solving this problem.

Actually, from the excitation spectrum of the fast luminescence at 5.0 eV (Figs. 2a, 5a, curves 2), it follows that this luminescence is most efficiently excited at 10.2–10.3 eV, which is 120–200 meV less than the energy corresponding to the first peak of the excitonic reflection (compare with curves 2 in Figs. 2b, 5b). This indicates that the radiative relaxation of electronic excitations occurs near structural defects in the crystal. A different situation is observed for the fast luminescence at 4.0 eV. Although the luminescence excitation spectrum of this band in the fast time window also contains a maximum at 10.2–10.3 eV (Figs. 2a, 5a, curves 1), this maximum is determined by the slow components, which are undeniably dominant in this range in the luminescence excitation spectrum measured in the slow time window (Figs. 2b, 5b, curves 1). The fact that the fast luminescence at 4.0 eV is not actually excited at 10.2–10.3 eV is supported by the absence of the fast component in the luminescence kinetics upon excitation into the 10.24-eV band (Fig. 3d, curves 1, 2). This suggests that the fast luminescence at 4.0 eV is excited only in the ranges of the  $E_{n=2}$  and  $E_{n=3}$  exciton states and interband transitions; i.e., it is intrinsic in nature.



**Fig. 5.** Excitation spectra of the UV luminescence at (1) 3.35 and (2) 5.05 eV and (3) reflectivity spectra of BeO ( $T = 10$  K) for the crystal orientation  $\mathbf{E} \perp \mathbf{C}$ : (a) fast and (b) slow time windows.

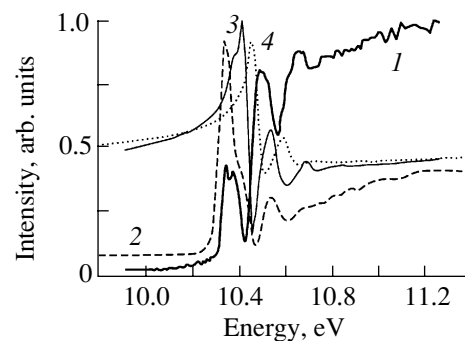


**Fig. 6.** (1, 2) Excitation spectra of the vacuum-UV luminescence at 6.7 eV and (3, 4) reflectivity spectra of BeO ( $T = 9.6$  K) for the crystal orientations (1, 3)  $\mathbf{E} \parallel \mathbf{C}$  and (2, 4)  $\mathbf{E} \perp \mathbf{C}$ .

The nature of the slow luminescence components in BeO is also different. The luminescence at 4.2 eV is efficiently excited in the range 10.2–10.3 eV (Fig. 2a, curve 2) and, hence, corresponds to the radiative annihilation of electronic excitations near defects. By contrast, the luminescence with a maximum at 4.4–4.7 eV (depending on the orientation) is intrinsic, because it is excited in the range immediately adjacent to the peaks

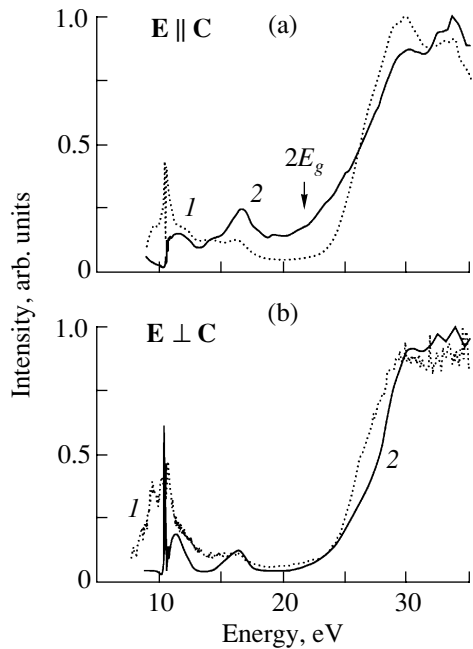


**Fig. 7.** Luminescence excitation spectra of BeO crystals ( $T = 10$  K) at  $E_{\text{emiss}} = (1)$  4.8 and (2) 6.7 eV for different crystal orientations.

of excitonic reflection and in the range of interband transitions ( $E_{\text{exc}} > E_g$ ) (Fig. 2b, curve 2).

The vacuum-UV luminescence band at 6.7 eV does not overlap with other luminescence bands, and the decay kinetics of this luminescence involves a sole component. The excitation spectrum of this luminescence (Fig. 6) indicates its intrinsic character. This confirms the assumption made earlier (see, for example, [9]) that the vacuum-UV luminescence is brought about by the radiative decay of self-trapped excitons.

Therefore, in the oriented BeO crystals at  $T = 10$  K, selective time-resolved vacuum-UV spectroscopy enables us to separate the following intrinsic luminescence components: the fast component at 4.0 eV ( $\tau = 2.2$  ns) and the slower components at 4.4–4.7 eV ( $\tau_1 = 54$  ns and  $\tau_2 = 36$   $\mu$ s) and 6.7 eV ( $\tau = 340$   $\mu$ s). The other luminescence bands in the luminescence spectrum should be attributed to the radiative decay of electronic excitations near structural defects in the crystal. Analysis of the dependence of the luminescence excitation spectrum demonstrates that the efficiency of the intrinsic luminescence excitation in the energy ranges of the ground ( $E_{n=1}$ ) and excited ( $E_{n=2}$  and  $E_{n=3}$ ) exciton states depends on the crystal orientation. In particular, the excitation spectrum of the self-trapped exciton luminescence at 6.7 eV (Fig. 6, curves 1, 2) suggests the orientation dependence of the exciton relaxation from the ground and excited states into the self-trapped state. Previously, for low-symmetry oxide crystals ( $\alpha$ - $\text{Al}_2\text{O}_3$ ,  $\text{YAlO}_3$ , and  $\text{Y}_3\text{Al}_5\text{O}_{12}$ ), Kuznetsov *et al.* [10]

found that the exciton relaxation into the self-trapped state and the recombination formation of small-radius excitons lead to the generation of different luminescence centers. In the present work, for wide-gap crystals, we pioneered the observation of the orientation-induced branching of the exciton relaxation with the formation of different radiative centers.

As follows from the experimental data, the fast intrinsic luminescence at 4.0 eV in BeO considerably differs in spectral, kinetic, orientational, and polarization characteristics from the previously studied luminescence of self-trapped excitons in BeO (see, for example, [7, 9]). The electronic structure of BeO [18] gives no reason to assign this luminescence to the valence core transitions responsible for characteristic fast luminescence in a number of crystals. The excitation spectrum of the 4.0-eV luminescence confirms the assumption made in [13, 14] that it is associated with the luminescence of singlet self-trapped excitons. In BeO, the exciton relaxation predominantly occurs from the  $E_{n=2}$  and  $E_{n=3}$  excited states into the singlet radiative level of self-trapped excitons, which was also earlier observed for alkali iodides [2, 3].

It is known that, in alkali halide crystals, the luminescence of triplet self-trapped excitons is polarized perpendicular to the axis of a two-halide hole nucleus in a self-trapped exciton and that the luminescence of singlet self-trapped excitons is polarized parallel to this axis [1, 4]. At present, the fact that the transitions responsible for the vacuum-UV band in the luminescence spectrum of BeO occur from the triplet state is beyond question. Moreover, in our earlier work [9], we proposed the model for the 6.7-eV luminescence center, which is treated as a self-trapped exciton with a hole nucleus—a small-radius polaron of the  $\text{O}^-$  ion type with an axial configuration of a local tetrahedron in the crystal structure. Of crucial importance in interpreting the fast luminescence at 4.0 eV in BeO is its lower energy as compared to that of the luminescence associated with triplet self-trapped excitons. A similar situation is also realized in NaI and NaBr crystals [2]: the band of singlet self-trapped excitons in the luminescence spectrum is shifted toward the long-wavelength range with respect to the band of triplet self-trapped excitons (the shift is equal to several tens of meV). Within the model of adiabatic curves of the potential energy, this is explained by the fact that the potential energy of a singlet self-trapped exciton at a minimum has the configurational coordinate  $Q_2$  that is substantially larger than the coordinate  $Q_1$  of the triplet state [2]. For BeO, the observed difference between the energies of the triplet and singlet states is appreciably larger. However, it should be taken into account that the crystal structure of beryllium oxide has a lower symmetry ( $C_{3v}$ ). Local lattice distortion caused by exciton self-trapping results in a further lowering of the local crystal symmetry. For this reason, the relative shift of

the coordinates of the triplet and singlet states can be larger than that in alkali halide crystals.

For alkali halide crystals, Matsumoto *et al.* [2, 3] found that the radiative decay of self-trapped excitons with different degrees of displacement of two-halide hole nuclei from regular to interstitial ion sites leads to the appearance of different luminescence bands. The luminescence band of self-trapped excitons with the largest displacement is characterized by the maximum Stokes shift. In BeO, the Stokes shift is largest for the 4.0-eV luminescence. It can be supposed that the corresponding short-lived luminescence centers are formed under the maximum local crystal deformation. By analogy with alkali halide crystals, we can assume that BeO also exhibits a tendency to the displacement of anions toward interstitial sites. Then, the arising luminescence center can be represented as a short-lived defect of the  $F^+$ -center type. The fact that the crystal structure of wide-band oxides actually undergoes a considerable deformation during the relaxation of electronic excitations was proved by Itoh *et al.* [19], who directly measured the short-term change in volume of an  $\alpha$ - $\text{Al}_2\text{O}_3$  crystal (in which, like in BeO, the self-trapping of excitons is realized [20]) after excitation by an electron pulse. The increase observed in the crystal volume in [19] turned out to be comparable to that typical of alkali halide crystals. This is also confirmed by the observation of the luminescence associated with  $F^-$ - and  $F^+$ -centers in nominally pure  $\alpha$ - $\text{Al}_2\text{O}_3$  [21] and BeO crystals upon pulsed excitation by electrons with prethreshold energies, which is not accompanied by the creation of stable Frenkel defects. Note that stable  $F^+$ -centers in beryllium oxide are characterized by the luminescence band with a maximum at 3.92 eV (FWHM = 0.5 eV) and a decay time of less than 1 ns [22, 23]. The luminescence at 4.0 eV is caused by the relaxation of excitons from excited states. In a number of alkali halide crystals (NaCl and KI), it is this predominant relaxation from the excited states with  $n = 2$  that results in the prethreshold defect formation [24]. Therefore, according to spectral and polarization characteristics (results obtained in [13, 14] and the present work), the fast luminescence at 4.0 eV should be attributed to axial singlet self-trapped excitons.

In the range of the electron-hole pair formation by photons with  $E_{\text{exc}} > 11$  eV, the increase in the excitation energy leads to a considerable difference in the luminescence excitation spectra at 4.7 and 6.7 eV. According to the electron-hole pair hot disintegration theory [25], this indicates different migration losses. Self-trapped excitons responsible for the 6.7-eV luminescence are formed without migration losses, and the points of self-trapping and generation of electronic excitation virtually coincide. This is confirmed by the large exciton-phonon coupling constant  $\sigma_0 = 0.6$ , which was determined from analysis of the Urbach rule in BeO [5]. At the same time, self-trapped excitons

responsible for the luminescence at 4.7 eV are formed after the migration of electronic excitations.

## ACKNOWLEDGMENTS

We would like to thank V.A. Maslov for supplying the samples and for his long-term cooperation and also G.N. Kulipanov and É.I. Zinin for their assistance in the performance of research at the Siberian Center of Synchrotron Radiation, which stimulated the present work.

This work was supported by the Russian Foundation for Basic Research (project no. 02-16206), the Ministry of Education of the Russian Federation (project no. 992886), and Deutsche Forschungsgemeinschaft (grant ZI-159/4-1).

## REFERENCES

1. Ch. B. Lushchik, *Excitons* (Nauka, Moscow, 1985), pp. 362–385.
2. T. Matsumoto, T. Kawata, A. Miyamoto, and K. Kan'no, *J. Phys. Soc. Jpn.* **61** (11), 4229 (1992).
3. T. Matsumoto, M. Shirai, and K. Kan'no, *J. Phys. Soc. Jpn.* **64** (3), 987 (1995).
4. K. S. Song and R. T. Williams, *Self-Trapped Excitons* (Springer-Verlag, Berlin, 1993).
5. D. M. Roessler, W. C. Walker, and E. Loh, *J. Phys. Chem. Solids* **30** (1), 157 (1969).
6. J. L. Freeouf, *Phys. Rev. B* **7**, 3810 (1973).
7. V. Yu. Ivanov, V. A. Pustovarov, A. V. Kruzhalov, and B. V. Shulgin, *Nucl. Instrum. Methods Phys. Res. A* **282**, 559 (1989).
8. E. Feldbach, W. Laasch, D. Varding, and G. Zimmerer, *Phys. Status Solidi B* **170**, 623 (1992).
9. V. Yu. Ivanov, V. A. Pustovarov, S. V. Gorbunov, and A. V. Kruzhalov, *Fiz. Tverd. Tela (St. Petersburg)* **36** (9), 2634 (1994) [*Phys. Solid State* **36**, 1436 (1994)].
10. A. I. Kuznetsov, V. N. Abramov, V. V. Mürk, and B. R. Namozov, *Fiz. Tverd. Tela (Leningrad)* **33** (7), 2000 (1991) [*Sov. Phys. Solid State* **33**, 1126 (1991)].
11. V. Mürk, B. Namozov, and N. Yaroshevich, *Radiat. Meas.* **24** (4), 371 (1995).
12. B. R. Namozov, M. É. Fominich, V. V. Mürk, and R. I. Zakharchenya, *Fiz. Tverd. Tela (St. Petersburg)* **40** (5), 910 (1998) [*Phys. Solid State* **40**, 837 (1998)].
13. V. A. Pustovarov, V. Yu. Ivanov, A. V. Kruzhalov, and É. I. Zinin, *Fiz. Tverd. Tela (St. Petersburg)* **36** (5), 1523 (1994) [*Phys. Solid State* **36**, 833 (1994)].
14. V. A. Pustovarov, V. Yu. Ivanov, A. V. Kruzhalov, and É. I. Zinin, *Zh. Prikl. Spektrosk.* **60** (5–6), 443 (1994).
15. V. Yu. Ivanov, V. A. Pustovarov, S. V. Gorbunov, *et al.*, *Fiz. Tverd. Tela (St. Petersburg)* **38** (11), 3333 (1996) [*Phys. Solid State* **38**, 1818 (1996)].
16. V. A. Maslov, G. M. Rylov, V. G. Mazurenko, and A. V. Kruzhalov, in *Extended Abstracts of the VI International Conference on Crystal Growth, Moscow, 1980*, Vol. 3.
17. G. Zimmerer, *Nucl. Instrum. Methods Phys. Res. A* **308**, 178 (1991).

18. V. A. Lobach, I. R. Rubin, and A. V. Kruzhalov, *Fiz. Tverd. Tela (Leningrad)* **29** (9), 2610 (1987) [*Sov. Phys. Solid State* **29**, 1506 (1987)].
19. C. Itoh, K. Tanimura, and N. Itoh, *J. Phys. C* **19** (35), 6887 (1986).
20. M. Kirm, G. Zimmerer, E. Feldbach, *et al.*, *Phys. Rev. B* **60** (1), 502 (1999).
21. V. I. Baryshnikov, E. F. Martynovich, T. A. Kolyasnikova, and L. I. Shchepina, *Fiz. Tverd. Tela (Leningrad)* **30** (5), 1505 (1988) [*Sov. Phys. Solid State* **30**, 868 (1988)].
22. S. V. Gorbunov, A. V. Kruzhalov, and M. J. Springis, *Phys. Status Solidi B* **141**, 293 (1987).
23. V. A. Pustovarov, M. Kirm, A. V. Kruzhalov, *et al.*, Annual Report, DESY, HASYLAB (Hamburg, 1999), p. 331.
24. Ch. B. Lushchik and A. Ch. Lushchik, *Decay of Electronic Excitations in Solids* (Nauka, Moscow, 1989).
25. A. N. Vasil'ev, V. V. Mikhaïlin, and I. V. Ovchinnikova, *Izv. Akad. Nauk SSSR, Ser. Fiz.* **49**, 2044 (1985).

*Translated by O. Borovik-Romanova*

---

SEMICONDUCTORS  
AND DIELECTRICS

---

## Parameters and Properties of Crystals of Ionic Compounds Obtained by Centrifugal Separation of Supersaturated Aqueous Solutions

V. N. Gurin\*, S. P. Nikanorov\*, A. P. Nechitailov\*\*, L. I. Derkachenko\*, M. M. Korsukova\*,  
V. N. Osipov\*, I. N. Zimkin\*, Z. I. Uspenskaya\*\*\*, and L. L. Regel\*\*\*\*

\* Ioffe Physicotechnical Institute, Russian Academy of Sciences, ul. Politekhnicheskaya 26, St. Petersburg, 194021 Russia  
e-mail: vladimir.gurin@pop.ioffe.rssi.ru

\*\* Joint-Stock Company All-Russia Aluminum–Magnesium Institute, St. Petersburg, 199106 Russia

\*\*\* Institute of Cytology, Russian Academy of Sciences, Tikhoretskii pr. 4, St. Petersburg, 194021 Russia

\*\*\*\* International Center of Gravitational Material Science and Applications,  
Clarkson University, 13699-5814 Potsdam, USA

Received November 23, 2000; in final form, November 29, 2000

**Abstract**—The change in the chemical composition, structural parameters, and properties of  $\text{Ba}(\text{NO}_3)_2$ ,  $\text{PbCl}_2$ , and  $\text{KI}$  crystals and the binary alkali-halide systems  $\text{LiCl-KCl}$  (eutectic) and  $\text{LiCl-NaCl}$  and  $\text{KCl-KI}$  (solid solutions) after centrifugal separation under acceleration  $(1.3, 6.2, 11.8) \times 10^3 g$  is investigated. The composition variation was monitored by the methods of chemical gravimetric and titration analyses, as well as of flame-photometric and spectrophotometric analyses. Acceleration causes a change in the chemical composition, lattice parameter, refractive index, and microhardness in all systems as compared to the initial values. It is found that centrifugation affects the systems with different masses of cations more strongly than the systems with different masses of anions. A criterion of the ratio of the masses of ions (cations and anions)  $\text{rat } i/i$  is proposed for predicting the effect of centrifugation on the change in the chemical composition and properties of compounds and their systems (a larger value of this ratio leads to a stronger variation of the composition and properties). The crystals of all compounds and solid solutions display an increase in microinclusions (visible only in transmitted light) upon an increase in the acceleration. The lattice parameters and microhardness measured in  $\text{KCl}$  and  $\text{KBr}$  crystals four years after their fabrication by using centrifugal separation indicate a considerable return to their initial values. © 2001 MAIK “Nauka/Interperiodica”.

### 1. INTRODUCTION

In our earlier publications [1, 2], we established for the first time the change in the chemical composition, structure, and properties of crystals of binary alkali-halide compounds as a result of centrifugation of their supersaturated aqueous solutions. In order to verify the existence of this phenomenon in more complex compounds and systems, we subjected the compounds with more complex anions to centrifugation, as well as the systems consisting of two binary alkali-halide compounds (solid solutions and eutectic).

### 2. EXPERIMENTAL TECHNIQUE

We studied the products of crystallization resulting from centrifugation of the binary compounds  $\text{Ba}(\text{NO}_3)_2$ ,  $\text{PbCl}_2$ , and  $\text{KI}$  and of eutectics and solid solutions of binary systems of the alkali-halide compounds  $\text{LiCl-KCl}$ ,  $\text{KCl-KI}$ , and  $\text{LiCl-NaCl}$ . The systems were chosen so that they contained different cations for the same anion and vice versa. The experiments were made in a centrifuge K24D (with an arm of length 70 mm) under an acceleration of  $(1.3, 6.2, 11.8)$

$\times 10^3 g$  and lasted 30 min. The maximum supersaturation was attained in the centrifuge whose working volume was automatically cooled to  $-10^\circ\text{C}$ . The solutions were saturated at  $40-50^\circ\text{C}$  and overheated to  $70-80^\circ\text{C}$  before they were placed in the centrifuge. The volume of the solutions subjected to centrifugation was 40–60 ml. Overheated solutions of two compositions were balanced in two special polyethylene test tubes intended for centrifugal separation. The test tubes were sealed and placed in a rotor mounted in the centrifuge and subjected to centrifugation under appropriate conditions. After the termination of the process, the unsaturated solution over the crystalline precipitate formed at the bottom of the polyethylene test tubes was poured into separate vessels. In most cases, precipitates stuck to the bottom of the test tubes and were extracted with the help of metallic spatulas and scalpels. After extraction, the precipitates were dried in a drying chamber (at  $\sim 100^\circ\text{C}$ ) and subjected to chemical gravimetric analysis and titration followed by flame-photometric and spectrophotometric analyses and investigation of their properties. All analyses and measurements of properties were made according to standard techniques. Since

the crystals in the LiCl–KCl and LiCl–NaCl systems were strongly wetted in air (which virtually ruled out the study of various properties in these crystals), the microhardness and refractive index were measured only in Ba(NO<sub>3</sub>)<sub>2</sub>, PbCl<sub>2</sub>, and KI crystals and in the KCl–KI system.

### 3. DISCUSSION OF RESULTS

The results of our experiments are presented in Tables 1–4 (in all tables except Table 1, the results are given in mol %; all experimental data are reduced to 100%) and in Figs. 1 and 2.

The results of the chemical analysis of the centrifugation products for the above-mentioned systems presented in Tables 1–4 completely confirm our earlier results concerning the considerable change in chemical composition of the crystals of ionic compounds formed as a result of centrifugal separation [1]. It can be seen that the crystals obtained from the initial composition with an excess of the lighter component contain a considerable excess of the heavier component (ion) after centrifugation. This points to a considerable difference in the results of sedimentation for ions with different masses. The concentration of heavier ions near the

growing surfaces in the solution is higher than the concentration of lighter ions; consequently, the concentration of the heavier ions becomes excessive as compared to the initial (stoichiometric) composition. In order to characterize and predict this effect for centrifugal separation, we chose the ratio of the atomic mass of heavier ions to that of lighter ions [in the general case, we denote it as  $\text{rat } i/i$ , while in the case of cations and anions, we denote this ratio as  $\text{rat } k/a$  (or  $a/k$ , or  $k/k$ , or  $a/a$  in a compound or in a more complex system)] [2]. If this ratio is greater than two (e.g.,  $\text{rat } a/k = 2.04$  for KBr), this produces a noticeable effect, changing the composition and properties of the compounds [3]. Consequently, this ratio may serve as an approximate quantitative indicator for choosing the objects of investigation (naturally, if other factors, such as strong wetting in air for Li salts or low solubility for some Ba and Pb salts, do not hamper the choice of a given object). Additionally, we chose systems with identical cations and different anions and vice versa in order to compare the effect of different origins of the ions on the results of centrifugation.

Table 1 contains the data on the change in the chemical composition, lattice parameter, refractive index, and microhardness of the crystals of binary ionic com-

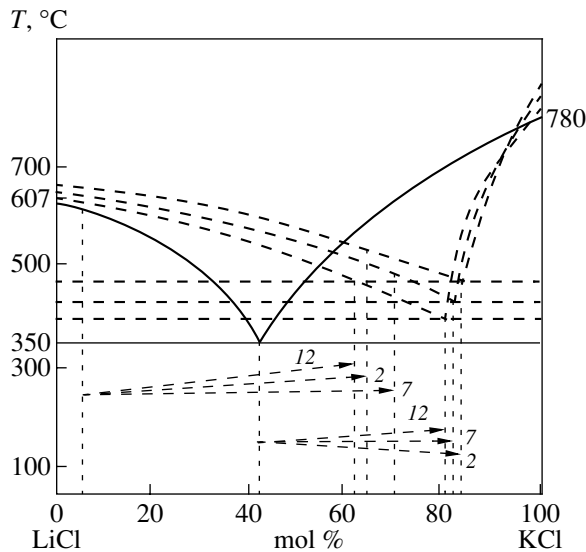


**Fig. 1.** Schematic diagram illustrating the change in the initial chemical composition of crystals (or conditional displacement of figurative points) in the eutectic system LiCl–KCl obtained from supersaturated aqueous solutions upon centrifugation. The solid curve is the equilibrium eutectic diagram of state, while the dotted curves are the initial compositions and the compositions obtained after centrifugation (the arrows indicate the shifts in the eutectic and hyper-eutectic compositions under various accelerations), and the dashed lines are the presumed schemes of variation of the eutectic diagram after centrifugation under (2, 7, 12)  $\times 10^3$  g (the values of the acceleration are rounded and reduced by a factor of  $10^3$  for convenience).

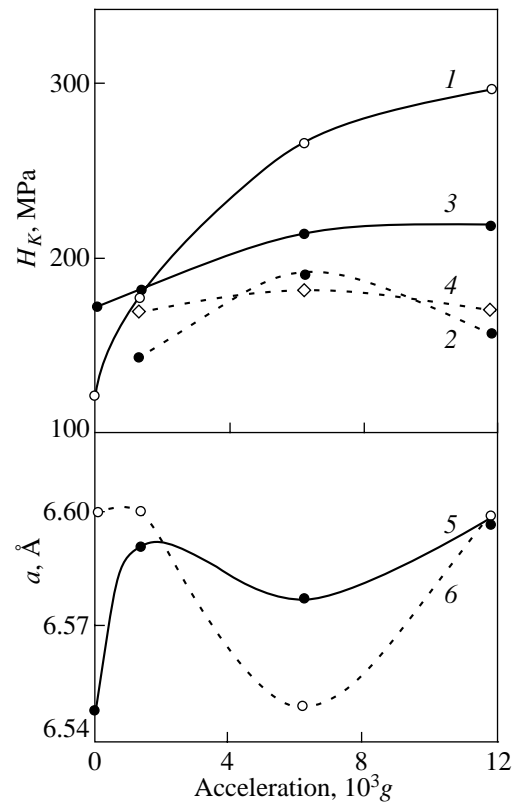


**Fig. 2.** Relaxation of the lattice parameter and microhardness of (1, 2) KCl and (3–6) KBr crystals obtained as a result of centrifugation. Curves 1, 3, and 5 correspond to the initial data and 2, 4, and 6 correspond to the data obtained 4 years after centrifugation.



**Table 1.** Variation of the chemical composition (wt %), lattice parameter ( $a$ ), refractive index ( $n$ ), and microhardness ( $H_K$ ) of the crystals of ionic compounds upon centrifugation

Parameter	Acceleration			
	1 g	$1.3 \times 10^3$ g	$6.2 \times 10^3$ g	$11.8 \times 10^3$ g
Ba(NO <sub>3</sub> ) <sub>2</sub> , rat Ba <sup>2+</sup> /2(NO <sub>3</sub> ) = 1.11				
Ba <sup>2+</sup> , wt %	51.5	52.1	52.4	52.5
$a$ , Å	8.1166(4)	8.1169(4)	8.1218(4)	8.1224(4)
$n$	1.5710(3)	1.5712(3)	1.5738(3)	1.5700(3)
Calculated $n_t$	1.5711	1.57107	1.57055	1.57049
$H_K$ , MPa ( $P = 19.62$ mN)	703	867	1016	1255
PbCl <sub>2</sub> , rat Pb <sup>2+</sup> /2Cl <sup>-</sup> = 2.92				
Cl <sup>-</sup> , g/l	6.7	6.3	5.4	6.8
$H_K$ , MPa ( $P = 19.62$ mN)	–	2285 (  001) (on prism)	2628 (  [001]) (on prism) 1804 (  [100]) (on tetrahedron)	2251 (  [001]) (on prism) or (  [100]) (on lateral surface of prism)
KI, rat I <sup>-</sup> /K <sup>+</sup> = 3.25				
K <sup>+</sup> , wt %	25.1	25.0	24.6	25.1
$a$ , Å	7.0663(5)	7.0641(5)	7.0666(5)	7.0666(5)
$n$	1.6656(3)	1.6660(3)	1.6656(3)	1.6658(3)
Calculated $n_t$	1.6656	1.6657	1.6656	1.6656
$H_K$ , MPa ( $P = 98.1$ mN)	–	100	109	133

**Table 2.** Variation of the ratio of components in solid solutions of the binary systems KCl–KI and LiCl–NaCl upon centrifugation (the calculated values are given in parentheses)

Acceleration, g	Binary systems of alkali-halide compounds							
	KCl–KI (rat $a/a(I/Cl^-) = 3.25$ )				LiCl–NaCl (rat $k/k(Na^+/Li^+) = 3.31$ )			
	excess KCl		excess KI		excess LiCl		excess NaCl	
	KCl	KI	KI	KCl	LiCl	NaCl	NaCl	LiCl
1	(95.07)	(4.93)	(80.15)	(19.85)	(92.5)	(7.5)	(86.69)	(13.31)
	98.5	1.5	89.06	10.94	–	–	–	–
$1.3 \times 10^3$	95.24	4.76	83.33	16.67	29.03	70.97	98.3	1.7
$6.2 \times 10^3$	96.12	3.88	77.94	22.06	14.6	85.4	96.5	3.5
$11.8 \times 10^3$	96.12	3.88	98.36	1.64	–	–	–	–

pounds after centrifugation. It can be seen that the values of these quantities undergo considerable changes in many cases. However, as the ratio of ionic masses increases, no general tendency is observed in the variation of the compositions and lattice parameters. This can be attributed to the different origins, structures, and masses of the cations and anions, as well as to different viscosities of the solutions and, hence, different hydrodynamic fluxes in the centrifuge. Only the microhardness displays a general tendency to increase with overloading, while the refractive index varies symbatically with the change in the lattice parameter.

It follows from Table 2 that the mass ratio for the cations and anions in the KCl–KI and LiCl–NaCl systems is approximately the same. However, the results of centrifugation are quite different. For example, the tendency to a change in the composition towards the component with the larger mass of the anion (KI) in the KCl–KI system (the anions have different masses) can be visualized only in comparison with the experimental data obtained for 1g and only for an excess of KCl (as well as for an excess of KI for  $11.8 \times 10^3$  g). On the contrary, the calculated data do not confirm this tendency in the case of an excess of KCl, while for an excess of

**Table 3.** Variation of the lattice parameter ( $a$ ), refractive index ( $n$ ), and microhardness ( $H_K$ ) of the crystals of solid solutions in the KCl–KI system after centrifugation for the initial excess (see Table 2) of each of the components

Acceleration, $g$	KCl–KI (excess KCl)				KI–KCl (excess KI)			
	$H_K$ , MPa ( $P = 49.05$ mN)	$a$ , Å	$n$ ( $\pm 0.0006$ )	$n_t$	$H_K$ , MPa ( $P = 49.05$ mN)	$a$ , Å	$n$ ( $\pm 0.0006$ )	$n_t$
$1.3 \times 10^3$	173	6.2925	1.4883	1.4898	212	7.0629	KI – 1.6668 KCl – 1.4890	KI – 1.6674
$6.2 \times 10^3$	182	6.2920	1.4888	1.4899	171	7.0636	KI – 1.6659 KCl – 1.4890	KI – 1.6673
$11.8 \times 10^3$	218	6.2934	1.4873	1.4892	108–132	7.0636	KI – 1.6657 KCl – 1.4890	KI – 1.6673

KI, this tendency is confirmed for  $1.3 \times 10^3 g$  and  $11.8 \times 10^3 g$ . The variation in the ratio of KCl and KI under different acceleration does not display any regularity. On the contrary, this tendency is strongly manifested in the LiCl–NaCl system with different masses of cations (for the initial excess amounts of the lighter compound LiCl, as well as the heavier compound NaCl). It can only be noted that upon an increase in the overload, an excess of LiCl in the system enhances this tendency, while no such enhancement is observed for an excess of NaCl.

Thus, binary alkali-halide systems with different cations and anions display different behaviors under centrifugation. In systems with different anions (Cl<sup>−</sup> and I<sup>−</sup>), the tendency towards composition variation is weakly pronounced and is observed mainly for the initial excess of the component with the heavier anion. However, this tendency is strongly manifested in systems with different cations (Li<sup>+</sup> and Na<sup>+</sup>), where the composition can change by more than 70 mol % towards the component with the heavier cation (Na<sup>+</sup>) for the initial excess of the component with the lighter cation (Li<sup>+</sup>).

**Table 4.** Variation of the ratio of components in the LiCl–KCl eutectic upon centrifugation (the calculated initial values are indicated in parentheses)

Acceleration, $g$	Compositions, %			
	eutectic point: LiCl – 58.25, KCl – 41.75, rat $k/k(K^+/Li^+) = 5.64$		hypereutectic point: LiCl – 94.03, KCl – 5.97	
	LiCl	KCl	excess LiCl	KCl
1	27.93	72.07	(94.03)	(5.97)
$1.3 \times 10^3$	16.16	83.84	36.48	63.52
$6.2 \times 10^3$	18.71	81.29	29.87	70.13
$11.8 \times 10^3$	20.41	79.59	37.5	62.5

Such a situation undoubtedly affects the properties of the crystals under investigation also. In the KCl–KI system, we measured the microhardness and the refractive index for two compositions (with an excess of each component) (Table 3). In the case when KCl is in excess, the microhardness increases with overloading (this increase is slightly smaller than for pure KCl [1], indicating the formation of the crystals of solid solutions), while the refractive index varies in accordance with the change in the lattice parameter of the solid solution. However, a slightly different pattern is observed when KI is in excess. In this case, the microhardness attains its maximum value only for  $1.3 \times 10^3 g$  and then decreases considerably for  $6.2 \times 10^3 g$  and  $11.8 \times 10^3 g$  (for  $P = 19.62$  and  $98.1$  mN). The refractive indices have two values close to those for pure KCl and KI. This indicates that two types of solid solutions are formed in this system with an excess of KI. For a smaller overloading ( $1.3 \times 10^3 g$ ), these solutions contain a larger amount of KCl (the microhardness is comparatively large; see Table 3), while upon an increase in the acceleration, the KI phase with a small admixture of KCl (judging from the small differences in the values of the lattice parameter, microhardness, and refractive index from those for pure KI; see Tables 1, 3) becomes predominant. Unfortunately, this assumption cannot be confirmed by the results of direct chemical analysis since it is impossible to distinguish and select the crystals of these solid solutions under a reflection microscope.

It follows from Table 2 that systems with different cations and anions demonstrate different behaviors under centrifugal separation. This may be due to the different hydrations of cations and anions. The cations, possessing a simple spherical shape, smaller volume, and coordination number, are subjected to sedimentation during centrifugation more easily, while the anions having a larger volume and sometimes a much more complex configuration and hydration system have a weaker tendency to sedimentation and experience more complex transformations under centrifugation.

The displacements of the points characterizing the composition for the eutectic system LiCl–KCl under investigation with a large difference in the masses of the cations (rat  $K^+/Li^+ = 5.64$ ) are most striking. We studied two compositions: eutectic and hypereutectic on the LiCl side (90 wt % or 94.03 mol % LiCl), both with a definite large excess of the lighter component LiCl. The results of investigations are presented in Table 4. It can be seen that both points (eutectic and especially hypereutectic) are strongly displaced toward the heavier component KCl (with the heavier cation  $K^+$ ). An inexplicable tendency is observed in this case: a certain increase in the LiCl concentration is observed instead of its expected decrease at the eutectic point upon an increase in acceleration from  $1.3 \times 10^3 g$  to  $11.8 \times 10^3 g$ . The same tendency is preserved at the hypereutectic point for  $1.3 \times 10^3 g$  and  $11.8 \times 10^3 g$ , while for  $6.2 \times 10^3 g$ , the decrease in the concentration of the lighter component becomes stronger. However, at both points (starting from the acceleration  $1.3 \times 10^3 g$ ), a strong decrease in the concentration of the lighter component (and, accordingly, an increase in the concentration of the heavier component) as compared to the initial concentration is observed (see the diagram of composition displacements in Fig. 1).

Analyzing the data presented above, we must emphasize that the features of the behavior of ionic compounds during their formation from supersaturated aqueous solutions subjected to centrifugation are far from having been explained (especially upon a change in overloading). However, we have established an undisputable fact: the crystals of solid solutions and eutectics obtained as a result of centrifugation strongly change their composition as compared to the initial ratio of components prior to centrifugation. This is visually illustrated on the schematic diagram of states (Fig. 1) showing the displacement of the points corresponding to the crystal composition, or the so-called figurative composition points [4], toward the compound with a heavier ion (cation).

It should be noted that the change in the composition of the systems was taken into account only for crystals obtained as a result of centrifugation, while the composition of the solution remaining after crystallization (having, accordingly, the opposite ratio of the components) was disregarded (in other words, we did not consider the entire amount of the substance subjected to centrifugation).

In this work, it is established that an increase in the acceleration leads to a certain increase in the amount of microscopic inclusions in the crystals of the compounds under investigation. The crystals had a size up to 1–2 mm, while inclusions were of the order of  $10 \mu m$  in size; were spherical, oval, columnar, or prismatic in shape; and were arranged, as a rule, parallel to the cleavage planes and edges of the crystals. Their size increased with acceleration, and the faceting acquired new forms. According to qualitative estimates, the

amount of inclusions reaches 5–10% of the volume of the crystal under investigation. Such inclusions are also present in the crystals of the initial substances, but they have a smaller size and a less pronounced faceting. Microscopic inclusions may be observed only in transmitted light (as in the study of the refractive index in this work). Their origin is connected in all probability with turbulent flows emerging in supersaturated aqueous solutions subjected to rapid cooling under ordinary conditions or during centrifugation. The presence of liquid flows with different temperatures (and, accordingly, different supersaturation, densities, surface tension, etc.) in rapidly cooled solutions leads to the formation of tiny spherical drops which preserve their shape for a certain time since their surface tension differs slightly from that of the ambient solution. They can be trapped in the crystals being formed. It is quite difficult to determine their composition and structure since it is virtually impossible to separate them from the crystals or to study them in the crystals in transmitted light in view of their small amounts and tiny sizes [5]. Such inclusions change the microscopic structure of the crystals and create a sort of composite material possessing an elevated hardness (for example,  $H_K$  for KBr increases by a factor of 2.4; see [1, table]). At the same time, the value of  $H_K$  can also increase as a result of an increase in the dislocation density upon an increase in the acceleration. However, the dislocation density has not been investigated in this case.

In the present work, we measured for the first time the microhardness of KCl and KBr crystals 4 years after their fabrication with the help of centrifugation [1]. We observed the ageing and microhardness relaxation upon the ageing of these crystals; their microhardness noticeably decreased as compared to the initial value (Fig. 2), although complete recovery was not observed. The values of  $H_K$  for an acceleration of  $6.2 \times 10^3 g$  were slightly higher than for other values of the acceleration. The value of  $H_K$  for KCl returned to the values corresponding to the stoichiometric compound [1]. We again measured the lattice parameter for KBr, which also relaxed, for the overload  $6.2 \times 10^3 g$ , to the initial value for the stoichiometric composition. For other values of the acceleration, it was even slightly higher. Thus, we may conclude that the crystals grown under centrifugation and having a composition differing strongly from the stoichiometric one are in an unstable (metastable) state.

#### 4. CONCLUSIONS

The main results of this research can be formulated as follows.

For the first time, a considerable variation in the chemical composition (as compared to the initial composition) of the crystals obtained with the help of centrifugation from supersaturated aqueous solutions of binary ionic compounds and binary alkali-halide sys-

tems (solid solutions and eutectics) is established. It is shown for the first time that a stronger change in the composition and properties occurs upon an increase in the ratio of the atomic masses of cations and anions of ionic compounds, their solid solutions, and eutectics (rat  $i/i = 2$  to 5 and greater). Binary systems with different anions display a smaller change in the composition upon centrifugation as compared to systems with different cations.

The microhardness of the crystals strongly increases with acceleration in all cases.

The refractive index varies in accordance with the lattice parameter, while the latter may increase or decrease upon a change in the acceleration for various compounds.

It is found that the amount of microinclusions increases in all crystals of all substances whose supersaturated solutions were subjected to centrifugation. Microinclusions form a composite structure of the crystal and cause an increase in its microhardness.

For the first time, it was found that after 4 years of ageing of crystals of ionic alkali-halide compounds

(KCl, KBr), a noticeable relaxation of their lattice parameters and microhardness took place.

#### REFERENCES

1. V. N. Gurin, S. P. Nikanorov, M. M. Korsukova, *et al.*, *Fiz. Tverd. Tela* (St. Petersburg) **39** (10), 1792 (1997) [*Phys. Solid State* **39**, 1599 (1997)].
2. V. N. Gurin, S. P. Nikanorov, A. P. Nechitailov, *et al.*, in *Centrifugal Materials Processing IV: 4th International Workshop on Materials Processing at High Gravity*, Clarkson Univ., Potsdam, 2000.
3. V. N. Gurin, S. P. Nikanorov, L. L. Regel, and L. I. Derkachenko, in *Centrifugal Materials Processing*, Ed. by Z. L. Regel and W. R. Wilcox (Plenum, New York, 1997), p. 197.
4. V. Ya. Anosov, M. I. Ozerova, and Yu. Ya. Fialkov, *An Introduction to the Physicochemical Analysis* (Nauka, Moscow, 1976), p. 49.
5. S. P. Nikanorov, V. N. Gurin, L. I. Derkachenko, *et al.*, in *Centrifugal Materials Processing IV: 4th International Workshop on Materials Processing at High Gravity*, Clarkson Univ., Potsdam, 2000.

*Translated by N. Wadhwa*

---

---

**DEFECTS, DISLOCATIONS,  
AND PHYSICS OF STRENGTH**

---

---

# The Energy and Peierls Barrier of a Frenkel–Kontorova Dislocation (Kink)

O. V. Usatenko\*, A. V. Gorbach\*, and A. S. Kovalev\*\*

\* *Kharkov National University, Kharkov, 61077 Ukraine*

\*\* *Verkin Institute for Low Temperature Physics and Engineering, National Academy of Sciences of Ukraine, Kharkov, 61164 Ukraine*

Received September 11, 2000; in final form, November 9, 2000

**Abstract**—The energy of the potential relief and of the Peierls barrier for a topological excitation (kink) in the Frenkel–Kontorova model is calculated in the continual limit to the second order of perturbation theory. A new method is proposed for analysis of the problem in a strongly discrete limit. Analytical results are compared with the results of numerical calculations. © 2001 MAIK “Nauka/Interperiodica”.

## 1. INTRODUCTION

Interest in the effect of discreteness on the properties of solutions to nonlinear equations has increased considerably in recent years. A large number of publications are devoted to analysis of the structure and dynamics of a kink in discrete systems [1–9]. The sine-Gordon equation (SGE) and the  $\Phi^4$  model are the most frequently studied one-dimensional nonlinear equations permitting solutions in the form of a topological defect (kink). The well-known Frenkel–Kontorova model [10] can be reduced to the SGE in the long-wave limit. This model was repeatedly used for theoretical analysis of dislocations in crystals [11, 12], the motion of crowdions [13], fluxons in Josephson junctions, domain walls in magnetically ordered media [14], etc.

The inclusion of the discreteness of a dynamic system leads to several qualitatively new properties of the kink movement. First, the potential energy of a kink becomes a function of the position of its center. A periodic potential with a period equal to the lattice constant and associated with the discreteness of the system is called the Peierls potential, and the difference between the maximum and minimum energies of the kink is referred to as the Peierls barrier (PB). Thus, if the kink does not possess the energy required for surmounting the PB, it is “locked” between two adjacent maxima of the Peierls potential and oscillates. Second, if the kink has a sufficiently high energy, it loses its energy in the course of motion and ultimately becomes locked [8, 9].

A transition from the continual to the discrete model and back can be made using one of several existing methods [1, 2, 4]. As a rule, certain methods of perturbation theory are used for describing such a transition. Typical models like the SGE and the  $\Phi^4$  model have a parameter that allows one to transform discrete systems into corresponding continual systems in the so-called continual limit. All the methods mentioned above lead

to good results in estimating some parameters of the kink, such as the energy and mass. However, these methods are ineffective in analyzing finer effects like the Peierls barrier.

In this work, the correction to the energy of the well-known Frenkel–Kontorova solution is calculated, using the Frenkel–Kontorova model, to the second order of perturbation theory in a small parameter equal to the ratio of the nonlinear potential relief amplitude to the energy of interaction between particles [10]. Comparison with numerical results shows that the second-order correction to energy gives a more exact result, while the correction to the PB noticeably degrades the result obtained in the previous step in perturbation theory. This means that the coincidence of the analytical and numerical expressions for the PB in the first order of perturbation theory is accidental [2]. Moreover, the second-order correction to the PB is of the same order in the small parameter as the first-order term. This discrepancy confirms the earlier assumptions that all the terms in perturbation theory make contributions to the PB of the same order of magnitude [2, 3]. For this reason, the applicability of perturbation theory to calculating the PB is disputable. The reason behind the inapplicability of perturbation theory lies in the exponentially small value of the barrier. For this reason, in order to obtain the value of the PB, we must take into account all the terms in the asymptotic expression or apply some other method.

We will also consider the limit of weak interatomic coupling in the Frenkel–Kontorova model and present an asymptotic method of calculating the kink energy based on a combination of exact (at the dislocation core) and approximate linearized (on the dislocation tails) solutions to the equation of motion.

## 2. FORMULATION OF THE PROBLEM

Let us consider a one-dimensional monatomic chain (the mass of the atoms is  $m$  and the interatomic spacing is  $a = 1$ ) with a harmonic interaction potential between the particles,

$$U(\xi_n) = \frac{\alpha}{2}(v_n - v_{n-1})^2, \quad (1)$$

which is placed in a periodic external field

$$V(x_n) = U_0(1 - \cos x_n), \quad (2)$$

where  $x_n$  is the spatial coordinate of the  $n$ th atom and  $x_n = x_n^0 + v_n$ ,  $v_n$  being the displacement of the  $n$ th atom from its position  $x_n^0 = 2\pi n$  for  $n \leq 0$  and  $x_n^0 = 2\pi(n+1)$  for  $n > 0$ .

We introduce variables  $u_n$  specifying the displacements of the particles from their positions  $x_n^0 = 2\pi n$  for negative, as well as positive, values of  $n$  ( $u_n = v_n$  for  $n \leq 0$  and  $u_n = 2\pi + v_n$  for  $n > 0$ ). The static displacements  $u_n$  are determined by the system of difference equations

$$K(2u_n - u_{n+1} - u_{n-1}) + \sin u_n = 0, \quad (3)$$

where the parameter  $K = \alpha/U_0$  characterizes the ratio of the interaction energy between the atoms of the chain and the energy of interaction with the substrate.

## 3. CONTINUAL LIMIT ( $K \gg 1$ )

For a strong coupling between the atoms ( $K \gg 1$ ), the displacements of atoms in the chain are smooth functions of the coordinate, which allows us to go over from the discrete equations (3) to the continual limit. Instead of displacements  $u_n$ , we introduce the function  $u(x)$  of the continuous coordinate  $x$ . Displacements  $u_{n\pm 1}$  can be expanded in the vicinity of  $u_n$  into a power series in the small parameter  $1/L$ , where  $L$  is the characteristic scale of variation of the function  $u(x)$ . From Eq. (3), it follows that  $L \sim \sqrt{K}$ . In the first-order perturbation theory,  $u_{n\pm 1}$  can be expanded to within second-order terms in the small parameter  $1/\sqrt{K}$ . This leads to a continual analog of Eq. (3), i.e., to the SGE

$$-Ku'' + \sin u = 0. \quad (4)$$

The solution to this equation satisfying the boundary conditions  $u(-\infty) = 0$ ,  $u(\infty) = 2\pi$ ,  $u'(-\infty) = 0$ , and  $u'(\infty) = 0$  and corresponding to a kink has the form

$$u(x) = U_0 \equiv 4 \arctan \left[ \exp \left( \frac{x - x_0}{\sqrt{K}} \right) \right], \quad (5)$$

where  $x_0$  determines the arbitrary position of the center of the kink.

The discreteness of the system leads to the dependence of the energy of the kink on its position, i.e., on the value of constant  $x_0$  [15]:

$$E \cong 8\sqrt{K} + \frac{1}{2}\Delta_P \cos(2\pi x_0), \quad (6)$$

where the first term describes the kink energy in the zeroth approximation in the small parameter  $1/\sqrt{K}$  and the second term is an additional periodic potential known as the Peierls potential. The kink possesses a maximum energy at  $x_0 = 0$  and a minimum energy at  $x_0 = 1/2$ . The quantity  $\Delta_P$  characterizes the difference between the maximum and minimum energies of the kink and is equal to the PB.

In the first step of perturbation theory, the value of the PB was obtained by Indenbom [15]:

$$\Delta_{P,I} = 64\pi^2 K \exp(-\pi^2 \sqrt{K}). \quad (7)$$

It is interesting to compare the analytical result  $\Delta_{P,I}$  obtained by Indenbom and the result  $\Delta_{P,num}$  of numerical calculations. For  $K = 10$ , we have

$$\Delta_{P,I} = 1.762 \times 10^{-10}, \quad \Delta_{P,num} = 1.747 \times 10^{-10}.$$

From the data presented above, it can be seen that Eq. (7) gives a quite exact expression for the PB. However, the calculation of the maximum and minimum energy of the kink for the same value of  $K = 10$  revealed that the error in the kink energy defined by Eqs. (6) and (7) is of the order of  $10^{-2}$ , which is many times larger than the value of the PB.

This problem can be analyzed by calculating the next correction to the kink energy and, accordingly, to the PB. For this purpose, we must use more exact equations of motion in the continual approximation; i.e., in them, we must retain higher order terms in  $1/\sqrt{K}$  upon a transition to the continual limit in the equation of motion (3) for a discrete chain. The standard procedure based on the replacement of the displacements of neighboring atoms by the derivatives of function  $u(x)$  with respect to the coordinate has a serious drawback: on each next step in perturbation theory, we must retain the derivatives of the higher order. This necessitates a search for additional boundary conditions that are generally absent in the initial discrete problem. In the present work, we used the two different asymptotic methods developed in [1, 2]. Both methods are free from the above drawback and lead to the same solution for the function  $u(x)$  to within second-order terms in the small parameter  $1/\sqrt{K}$ :

$$u(x) = U_0(x) + U_1(x), \quad (8)$$

where  $U_0(x)$  is the solution obtained in the lowest order of perturbation theory [Eq. (5)] and the function  $U_1(x)$  has the form

$$U_1(x) = \frac{3 \tanh[(x-x_0)/\sqrt{K}] - (x-x_0)/\sqrt{K}}{12K \cosh[(x-x_0)/\sqrt{K}]} \quad (9)$$

Using expressions (8) and (9) found in [1, 2], we can calculate the kink energy to within  $1/\sqrt{K}$ :

$$E = 8\sqrt{K} \left(1 - \frac{1}{72K}\right) + \frac{1}{2} \Delta_p \cos 2\pi x_0, \quad (10)$$

where

$$\Delta_p = \left[ \left(64\pi^2 + \frac{32\pi^4}{9}\right)K - \frac{8}{3}\pi^3\sqrt{K} + \frac{16\pi^2}{9} \right] \times \exp(-\pi^2/\sqrt{K}). \quad (11)$$

For  $K = 10$ , expressions (10) and (11) give more exact values for the kink energy as compared to expression (6); the error in the calculated value of the kink energy is now of the order of  $10^{-4}$ . This justifies the application of the methods of perturbation theory in the above model proposed for calculating the kink energy. However, the result for the PB does not become closer to the numerical value:

$$\Delta_p = 9.33611 \times 10^{-10}.$$

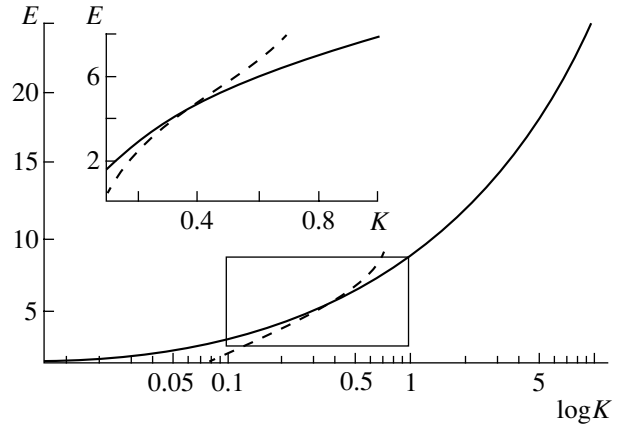
Moreover, it becomes even worse; i.e., the error has become larger than the error in the previous step of perturbation theory as compared to the exact result of numerical calculations. According to Eqs. (7) and (11), the values of the PB obtained in the two successive steps of perturbation theory differ even in the lowest order in parameter  $1/\sqrt{K}$ . This contradicts the basic premises of the perturbation theory. It was proved earlier [2, 3] that the terms of different orders of the perturbation theory make comparable the contributions to the PB. Our results confirm this statement.

The figure shows the dependence of the minimum kink energy on coefficient  $K$ . The solid curve corresponds to numerical calculations, while the dashed curves correspond to the values given by formulas (10) and (11). It can be seen from the inset to the figure that, for values of  $K \leq 0.3$ , the results of numerical calculations and the analytical results following from Eqs. (10) and (11) begin to diverge.

#### 4. LIMIT OF WEAK INTERATOMIC COUPLING ( $K \ll 1$ )

In the weak interatomic coupling limit ( $K \ll 1$ ), the kink becomes narrow and essentially discrete. In fact, only for a few atoms located in the vicinity of the kink center do the displacements from the equilibrium positions differ from 0 or  $2\pi$ . In this case, it is convenient to return to the variables  $v_n$  introduced above:

$$\begin{aligned} v_n &= u_n, & n \leq 0, \\ v_n &= 2\pi - u_n, & n > 0. \end{aligned} \quad (12)$$



Dependence of the minimum energy of the kink on the ratio of the interaction energy between particles and the energy of their interaction with the substrate ( $K = \alpha/U_0$ ). The solid curve corresponds to numerical calculations, the dashed curves correspond to the analytical expression obtained in the limit of strong interatomic coupling [Eqs. (10), (11)], and the dotted curves describe the analytical expression obtained in the limit of weak atomic coupling, Eq. (28).

Assuming that the displacements from the equilibrium positions  $v_n$  are small, as the first approximation, we linearize the system of equations (3):

$$(2K + 1)v_n - K(v_{n-1} + v_{n+1}) = 0. \quad (13)$$

In contrast to the previous limiting case (of strong interatomic coupling), here we disregard the nonlinearity but preserve the initial discreteness of the problem. The general solution to system (13) has the form

$$v_n = A_1 \lambda_1^n(K) + A_2 \lambda_2^n(K), \quad (14)$$

where coefficients  $A_1$  and  $A_2$  are arbitrary and functions  $\lambda_1$  and  $\lambda_2$  are defined by the relations

$$\begin{aligned} \lambda_1 &= 1 + \frac{1}{2K} + \sqrt{\frac{1}{K} + \frac{1}{4k^2}} \cong \frac{1}{K}, \\ \lambda_2 &= 1 + \frac{1}{2K} - \sqrt{\frac{1}{K} + \frac{1}{4k^2}} \cong \frac{1}{K}. \end{aligned} \quad (15)$$

In order to make the solution bounded at infinity, we must choose  $A_2 = 0$  for  $n > 0$  and  $A_1 = 0$  for  $n < 0$ . Returning to the initial variables  $u_n$ , we obtain an approximate solution to the system of equations (3) for  $K \ll 1$  in the form

$$\begin{aligned} u_n &= 2\pi - A\lambda_2^n, & n > 0, \\ u_n &= B\lambda_1^n, & n < 0, \end{aligned} \quad (16)$$

where coefficients  $A$  and  $B$  are determined by the specific configuration of the kink, i.e., by the position of its center, and also by the joining condition for  $n = 0$ . For the kink with a maximum energy (the center of the kink lies at the site with index  $n = 0$ ), these coefficients are

$A = B = \pi$ , while for the kink with a minimum energy (whose center lies between the sites with  $n = 0$  and 1), we have  $A = 2\pi(1 + \lambda_2)$  and  $B = 2\pi\lambda_2/(1 + \lambda_2)$ .

The obtained solutions make it possible to determine the maximum and minimum energies of the kink in the limit  $K \ll 1$ :

$$E_{\max} = 2 + \frac{\pi^2}{2} \left[ \frac{K(1 - \lambda_2)^2 + \lambda_2^2}{1 - \lambda_2^2} + \frac{K(1 - \lambda_1)^2 + 1}{\lambda_1^2 - 1} \right], \quad (17)$$

$$E_{\min} = \frac{\pi^2 \lambda_2^2}{(1 + \lambda_2)^2} \left[ \frac{K(1 - \lambda_2)^2 + \lambda_2^2}{(1 - \lambda_2^2)\lambda_2^2} + \frac{K(1 - \lambda_1)^2 + \lambda_1^2}{\lambda_1^2 - 1} \right]. \quad (18)$$

For small  $K$ , approximate values for  $\lambda_1$  and  $\lambda_2$  are given by  $\lambda_1 \cong K^{-1}$  and  $\lambda_2 \cong K$ . Taking into account these expressions, Eqs. (17) and (18) are simplified as

$$E_{\max} = 2 + \frac{\pi^2 K(1 - K + K^2)}{1 - K^2}, \quad (19)$$

$$E_{\min} = \frac{2\pi^2 K(1 + 2K^2 - 2K^3 + K^4)}{(1 + K)^2(1 - K^2)}. \quad (20)$$

Comparison of the energies  $E_{\max}$  and  $E_{\min}$  obtained from Eqs. (19) and (20) with the results of numerical calculations for  $K = 0.05$  gives

$$\Delta E_{\max} = E_{\max} - E_{\max, \text{num}} \cong 2.5 \times 10^{-4}, \quad (21)$$

$$\Delta E_{\min} = E_{\min} - E_{\min, \text{num}} \cong 1.2 \times 10^{-3}.$$

As a next approximation in perturbation theory, one can expand the nonlinear term  $\sin u_n$  in Eq. (3) in small displacements up to cubic-order terms. Here, we use a different approach based on the combination of exact solutions to nonlinear discrete equations (3) at the center of the kink with solutions (16) on its tails. New values of constants  $A$  and  $B$  in expressions (16) are determined from the conditions of joining with the solution to nonlinear equations at the kink center and depend on the number of particles whose displacements can be calculated exactly.

The exact inclusion of the displacements of three central particles in the case when the kink possesses a maximum energy (the kink center is at the site with index  $n = 0$ ) leads to the following expressions for coefficients  $A$  and  $B$  in solution (16):  $A = B = A(K)$ , where function  $A(K)$  is defined by the transcendental equation

$$K(\pi - 2AK + AK^2) - \sin(AK) = 0. \quad (22)$$

In this case, the approximate solution to system (3) in the limit of small  $K$  for the kink with a maximum

energy assumes the form

$$u_n = 2\pi - A(K)K^n, \quad n > 0, \\ u_n = \pi, \quad n = 0, \quad (23)$$

$$u_n = A(K) \left( \frac{1}{K} \right)^n, \quad n < 0.$$

On account of the smallness of  $K$ , we obtain from Eq. (22)  $A(K) \cong 2\pi/(1 + 2K)$ .

The maximum kink energy, exactly taking into account the displacement of central particles, has the form

$$E_{\max}^* = 2 + \frac{A^2 K^3 (1 - K + K^2)}{1 - K^2} + K(\pi - AK)^2 + 2[1 - \cos(AK)]. \quad (24)$$

For  $K = 0.05$ , the difference between the maximum energies obtained from Eq. (24) and by a numerical method is

$$\Delta E_{\max}^* = E_{\max}^* - E_{\max, \text{num}} \cong 4.5 \times 10^{-7}. \quad (25)$$

Similarly, we obtain a more exact solution to system (3) for the kink possessing a minimum energy (the kink center lies between the zeroth and first particles, whose displacements we determine exactly):

$$u_n = 2\pi - B(K)K^n, \quad n > 0, \\ u_n = B(K) \left( \frac{1}{K} \right)^{n-1}, \quad n \leq 0, \quad (26)$$

where  $B(K)$  is defined by the equation

$$K(2\pi - 3BK + BK^2) - \sin(BK) = 0. \quad (27)$$

An approximate expression for  $B(K)$  has the form  $B(K) \cong 2\pi/(1 + 3K)$ .

The minimum kink energy is defined by the formula

$$E_{\min}^* = \frac{B^2 K^3 (1 - K + K^2)}{1 - K^2} + 2[1 - \cos(BK)] + 2K(\pi - BK)^2. \quad (28)$$

For  $K = 0.05$ , we obtain the following value for  $\Delta E_{\min}^* = E_{\min}^* - E_{\min, \text{num}}$ :

$$\Delta E_{\min}^* = E_{\min}^* - E_{\min, \text{num}} \cong 3.1 \times 10^{-9}. \quad (29)$$

A comparison of Eq. (21) with Eqs. (25) and (29) for  $\Delta E$  shows that the proposed method of calculating the kink energy in the limit of weak interatomic coupling considerably increases the accuracy of the analytical approach.

The dotted curves in the figure represent the dependence of the minimum energy of the kink on coefficient  $K$  defined by Eq. (28). The curves show that the set of



formulas (10), (11), (24), and (28) obtained in the limits of large and small values of  $K$  gives a fairly exact expression for the kink energy in the entire range of values of the coefficient characterizing the ratio of the interaction energy between particles in the chain and the energy of their interaction with the substrate.

It should be noted that the error in the calculation of the kink energy based on the method described above is determined by the error in the calculation of displacements of tail (noncentral) particles. In order to improve the accuracy of calculating the energy, we must either increase the number of particles whose displacements were determined exactly or improve the accuracy of calculation for the remaining particles.

## 5. CONCLUSION

Thus, the Frenkel–Kontorova model is considered in the limits of strong and weak interatomic coupling. The energies of the kink and the Peierls barrier are calculated in the continual limit in the second-order perturbation theory. In the discrete limit, a new method of obtaining a solution is proposed, which involves the exact inclusion of the nonlinearity of interaction between a small number of particles in the kink core and the solution to linearized equations outside the core. A comparison of analytical results with results of numerical calculations shows that the expressions obtained for the kink energy in the case of a strong, as well as a weak, interatomic coupling give quite exact results. At the same time, analysis of the expression for the PB in the limit of a strong interatomic coupling reveals a considerable discrepancy with the results of numerical calculations. This is due to the fact that, in accordance with Eqs. (7) and (11), the PB in this limit is an exponentially small quantity and all the terms in the expansion in perturbation theory must be taken into account in order to estimate it.

## ACKNOWLEDGMENTS

This work was partly supported by the INTAS-99 project, grant no. 167, and the MNOP program, grant USU 082087.

## REFERENCES

1. P. Rosenau, *Phys. Lett. A* **118** (5), 222 (1986).
2. S. Flach and K. Kladko, *Phys. Rev. E* **54** (3), 2912 (1996).
3. S. Flach and C. R. Willis, *Phys. Rev. E* **47** (6), 4447 (1993).
4. Y. Ishimory and T. Munakata, *J. Phys. Soc. Jpn.* **51** (10), 31367 (1982).
5. M. Peyrard and M. D. Kruskal, *Physica D (Amsterdam)* **14** (1), 88 (1984).
6. T. Munakata, *Phys. Rev. A* **45** (2), 1230 (1992).
7. J. M. Speight and R. S. Ward, *Nonlinearity* **7** (2), 475 (1994).
8. R. Boesch, C. R. Willis, and M. El-Batanouny, *Phys. Rev. B* **40** (4), 2284 (1989).
9. E. Majernikova and G. Drobny, *Phys. Rev. E* **47** (5), 3677 (1993).
10. Ya. I. Frenkel' and T. A. Kontorova, *Zh. Éksp. Teor. Fiz.* **8** (12), 1340 (1938).
11. I. R. Sagdeev and V. M. Vinokur, *J. Phys. (Paris)* **48** (9), 1395 (1987).
12. N. Flytzanis, S. Crowley, and V. Celli, *Phys. Rev. Lett.* **39** (14), 891 (1977).
13. A. M. Kosevich and A.S. Kovalev, *Theory of Dynamic Crowdions. Radiation and Others Effects in Solids* (Tbilisi, 1973); in *Proceedings of the School on Radiation and Others Defects in Solids, Tbilisi, 1974*, Vol. 1, p. 186.
14. M. J. Ablowitz and H. Segur, *Solitons and the Inverse Scattering Transform* (SIAM, Philadelphia, 1981; Mir, Moscow, 1987).
15. V. L. Indenbom, *Kristallografiya* **3** (2), 197 (1958) [*Sov. Phys. Crystallogr.* **3**, 193 (1959)].

*Translated by N. Wadhwa*

## DEFECTS, DISLOCATIONS, AND PHYSICS OF STRENGTH

# Magnetically Stimulated Variation of Dislocation Mobility in Plastically Deformed *n*-Silicon

A. M. Orlov, A. A. Skvortsov, and L. I. Gonchar

Ul'yanovsk State University, ul. L'va Tolstogo 42, Ul'yanovsk, 432700 Russia

Received July 18, 2000; in final form, November 20, 2000

**Abstract**—The acoustic emission method is employed for an experimental investigation of the effect of a magnetic field on the mobility of edge dislocations in a plastically deformed *n*-silicon sample carrying a current. It is found that the preliminary treatment of a dislocated crystal in a constant magnetic field ( $B < 1$  T) changes the intensity of its acoustic response depending on the magnetic induction. The observed effect is associated with spin-dependent magnetosensitive reactions of defects occurring in the vicinity of the dislocation core, which facilitate the detachment of the dislocations from the stoppers and, hence, increase the mobility of dislocations and the acoustic response of the dislocation structure. © 2001 MAIK “Nauka/Interperiodica”.

## 1. INTRODUCTION

The effect of a magnetic field on the properties of plastically deformed ionic crystals and semiconductors has become an object of intense investigation in recent years. It is generally accepted that the dominating mechanism explaining the observed variations in the mobility of dislocations in a magnetic field is that of spin-dependent reactions of defects [1–6]. At the same time, the effect of a magnetic field on the state of defects in doped semiconductors has not been studied comprehensively, although this problem is important in connection with improvement of the reliability of microelectronic devices subjected to the action of external electric and magnetic fields. The present work aims at analyzing the effect of a weak magnetic field on the mobility of linear defects in a doped semiconductor.

## 2. EXPERIMENT

The samples were prepared from *n*-Si wafers doped with phosphorus, oriented in the [111] direction, at a concentration  $N_d = 10^{23} \text{ m}^{-3}$ . The sample size was  $40 \times 0.35 \times 10 \text{ mm}$ . Dislocations were introduced through plastic deformation of the samples according to the three-point scheme at  $T = 1273 \text{ K}$  for 25 min. The detection of dislocations was carried out from etch pits by using the standard selective etchant SR-4. The mean density of dislocations introduced in the detection region was not lower than  $10^9 \text{ m}^{-2}$ .

The combined effect of magnetic and electric fields on the dislocation mobility was studied by the acoustic emission method [7, 8]. The samples were placed in the setup presented in Fig. 1. Acoustic emission in silicon was excited by the simultaneous action on a sample of a constant electric current  $j = 3 \times 10^5 \text{ A/m}^2$ , directed in the plane of the sample, and an external constant magnetic field  $B = 0.3 \text{ T}$ . The magnetic induction vector was

also in the plane of the sample, but was at right angles to the electric field. We assume that the action of the Ampère force on the current-carrying sample affects the relative motion of dislocations in the sample insignificantly, since the current along a dislocation is negligibly small under our experimental conditions in view of its perpendicular orientation relative to the electric field.

Ohmic contacts with Si controlled from the current-voltage characteristic were created using a liquid (In–Ga) eutectic. The possible effect of the magnetic field on the contact regions and the contacts themselves (both electric and acoustic) was controlled by a complex of special experiments intended to estimate the spectral characteristic of the system of contacts under electrical and mechanical effects in the presence of a magnetic field. The reliability of the obtained results

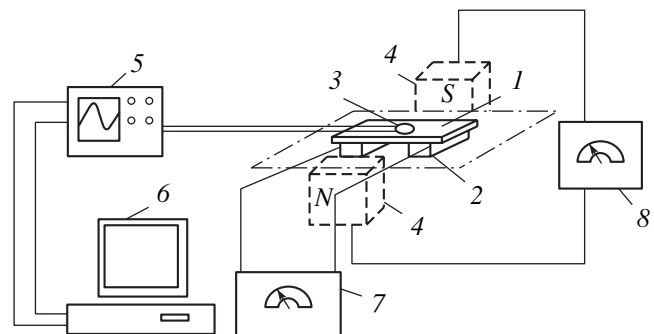


**Fig. 1.** Schematic diagram of the experimental setup: (1) Si sample, (2) ohmic contacts, (3) AE detector, (4) poles of magnet, (5) storage oscilloscope, (6) computer, (7) dc power supply, and (8) power supply for the electromagnet.

rules out the possibility of magnetically stimulated distortion of the acoustic emission spectra.

A TsTS-19 piezoelectric ceramic wafer was used as a detector of acoustic emission (AE) signals. The acoustic contact between the sample and the detector was improved by using vacuum oil VM-6. The signal from the detector was fed to a digital storage oscilloscope and then (through an interface) to a computer, where the spectral analysis of the AE signal was carried out by processing the response with the help of a program based on the standard algorithm of the fast Fourier transform.

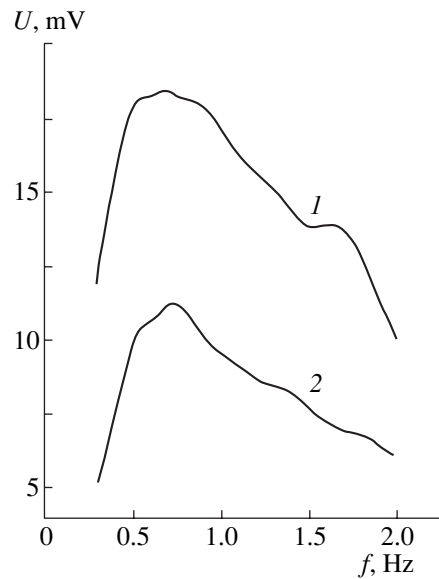
As a result of numerous experiments, it was found that the spectrum of the AE signal carries information on the dislocation dynamics in the sample under investigation. The visual observation of the motion of dislocations was carried out from etch pits and was clearly detected in the case of electric and mechanical actions. The electrically stimulated changes in the mean velocity of the directional drift of dislocations and of the characteristic frequency of the acoustic emission spectrum are found to be well correlated. For instance, we associated the clearly manifested peak in the acoustic emission spectrum observed at a frequency of 0.1 Hz with the characteristic frequency of the detachment of a dislocation (or its fragment) from stoppers and its transition to the next metastable state [8]. Consequently, the variation of the spectrum of the acoustic emission signal can be used as an indicator of the state of linear defects in a semiconductor subjected to the action of electric and magnetic fields.

### 3. RESULTS

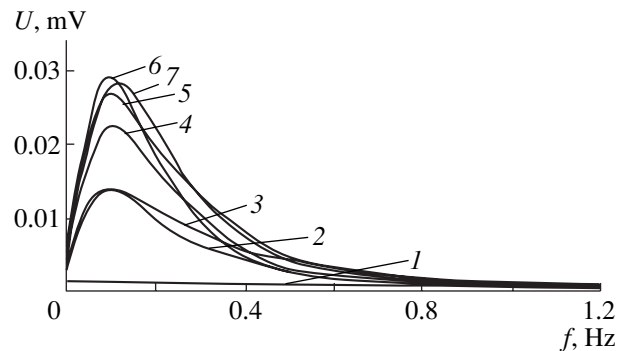
We investigated the change in the acoustic response of the sample under the simultaneous action of electric and magnetic fields, as well as when the actions were separated by a time interval.

Figure 2 shows the experimental acoustic emission spectra in the case of combined electric and magnetic effects (curve 1), as well as the spectrum of a reference sample carrying only an electric current in a zero magnetic field (curve 2). It can be seen that the combined action of the magnetic and electric fields leads not only to a 50% increase in the AE signal  $U$  from the material under investigation but also to the emergence of a spike on the detector signal at a frequency of 1.6 Hz in addition to the clearly manifested peak in the frequency region  $f = 0.5\text{--}1$  Hz.

The magnetic field energy is much lower than the thermal energy and even lower in respect to the energy of atomic coupling. For this reason, we should not expect its direct effect on the transport properties of dislocations or their fragments weighted by impurity atoms. However, the emergence of the new peak in the high-frequency region unambiguously indicates the selective response of some types of dislocations experiencing a lower resistance and, hence, having a higher



**Fig. 2.** Experimental AE spectra for dislocated silicon wafers (1) under the combined action of electric and magnetic fields and (2) under the action of electric current alone:  $j = 3 \times 10^5$  A/m<sup>2</sup>,  $B = 0.3$  T (curve 1) and  $j = 3 \times 10^5$  A/m<sup>2</sup>,  $B = 0$  (curve 2).



**Fig. 3.** Variation of the acoustic emission spectra for samples carrying current  $j = 5 \times 10^5$  A/m<sup>2</sup> after exposure to a magnetic field with various values of magnetic induction  $B$ , T: (2) 0, (3) 0.1, (4) 0.2, (5) 0.3, (6) 0.6, and (7) 1.0. Curve 1 is the acoustic emission spectrum in zero electric and magnetic fields.

frequency of transition in the field of internal stresses induced by a constant electric field.

At the same time, the results of experiments proved that the removal of the magnetic field acting on the sample for constant current density  $j = 3 \times 10^5$  A/m<sup>2</sup> flowing through the sample does not lead to its complete recovery to the initial state, which completely agrees with our earlier results [9], as well as with the results obtained by other authors [10].

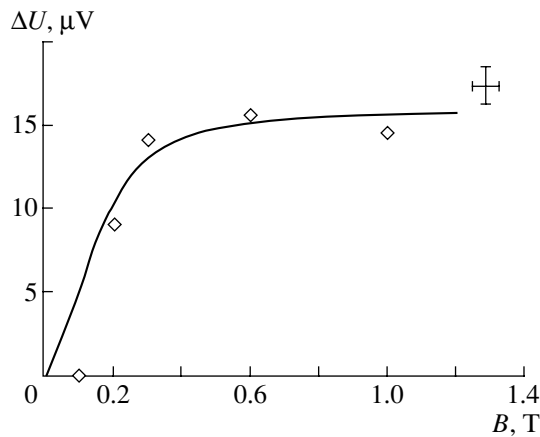


**Fig. 4.** Experimental magnetic-field dependence of the increment to the intensity corresponding to the acoustic emission peak at frequency 0.1 Hz. The solid curve is calculated using Eq. (2).

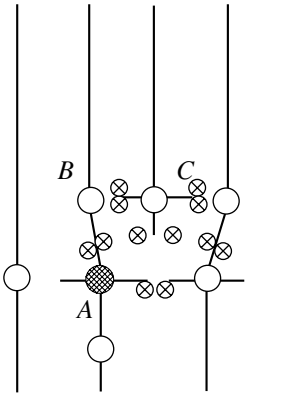


**Fig. 5.** Model of a deformed region in the crystal.

If, however, we pass an electric current through a deformed sample after exposing it to a magnetic field, an increase in the dislocation mobility as compared to the reference samples will be observed. Figure 3 shows the acoustic emission spectra for samples subjected to the action of a current after exposure to a magnetic field. Curve 1 corresponds to the acoustic emission of samples in the absence of a current and magnetic field and characterizes the background acoustic noise. Curves 2–7 reflect the change in the acoustic signal spectrum associated with an increase in the dislocation mobility in samples held preliminarily for 30 min in a weak constant magnetic field with various values of magnetic induction  $B$ . It can be seen that the position of the characteristic peak of the acoustic emission spectrum on the frequency axis virtually does not change with increasing  $B$ , while the peak amplitude increases.

The field dependence of the magnetically stimulated increment in the acoustic emission intensity obtained as a result of experimental investigations at a frequency of 0.1 Hz is depicted in Fig. 4. We observed the existence of a threshold value of magnetic induction (amounting to 0.1 T) above which the effect of the magnetic field on the acoustic emission intensity becomes noticeable. A similar effect was also observed for ionic crystals [10].

#### 4. DISCUSSION OF RESULTS

For analysis of the obtained results, we used the mechanism of spin-dependent reactions of magneto-sensitive defects, which was worked out for ionic crystals [1, 12] and modified by us in view of the fact that the Cottrell impurity cloud existing in a doped semiconductor in the vicinity of the dislocation core must be taken into account. Figure 5 shows the crystal structure in the vicinity of a dislocation core in real doped  $n$ -Si. It should be noted that, among the silicon atoms in lattice sites, the most sensitive to the action of the magnetic field are those which have an unpaired electron, i.e., silicon atoms at the edge of the damaged atomic plane (atom  $C$  in Fig. 5). Another type of point defect sensitive to the magnetic field is the impurity ions at the lattice sites that are localized near a dislocation core, i.e., phosphorus atoms in the present case (atom  $A$  in Fig. 5). These ions possess paramagnetic properties and are in the singlet state [13]. Thus, when a dislocated sample is placed in a weak magnetic field, the spin system of atom  $C$  at the dislocation core might be transformed from the triplet to the singlet state as a result of the interaction between the orbital and spin magnetic moments; as a result, the probability of reaction of defects between this atom and the paramagnetic impurity ion  $A$  becomes higher.

In this case, the role of the electric field is reduced to bringing the magnetically sensitive defects  $A$  and  $C$  to the critical distance [14] permitting transition of the dislocation or its fragment to a new fixed position. This reaction will result in the breaking of the  $A$ – $B$  bond and the formation of the  $A$ – $C$  bond, which corresponds to a displacement of the dislocation to a new position in which atom  $B$  becomes its core. The presence of a strongly deformed region in the vicinity of a dislocation leads to the diffusion of paramagnetic centers to a new position of the dislocation core.

The above mechanism of the combined action of magnetic and electric fields on the mobility of dislocations in doped Si provides a satisfactory explanation of the emergence of the second peak in the  $U(f)$  spectrum, which reflects the emergence of dislocations that can perform displacements more frequently due to the removal of spin prohibition.

The experimental evidence we obtained regarding the fact that the sample does not completely recover its initial properties after the removal of the magnetic field acting on it indicates that the configuration of bonds in

the dislocation core which is formed during exposure to the magnetic field is preserved for quite a long time. The mechanism responsible for the observed “magnetic memory” effect is not completely clear. However, the existence of such a memory is manifested in an increase in the amplitude of the acoustic emission signal peak in a current-carrying sample after its exposure to a weak magnetic field (Fig. 4). As the value of  $B$  increases further, the acoustic emission intensity first increases and then attains a constant value (to within the confidence interval). The observed increment to the acoustic emission signal is proportional to the number  $N$  of dislocations that can be displaced from their previous position as a result of the spin-dependent reaction that occurs between magnetosensitive defects (such as an atom in the dislocation core or a paramagnetic impurity ion) and is localized in the Cottrell cloud in the vicinity of the dislocation core. In turn, the number of detached dislocations is determined by the frequency  $T_1^{-1}$  at which the spin magnetization component along the applied magnetic field of the particles participating in the reaction takes its equilibrium value. In addition,  $\Delta U$  depends on the energy  $\Omega$  of the wave packet detected by the sensor. Consequently, we can write

$$\Delta U \sim N\Omega \sim T_1^{-1}\Omega. \quad (1)$$

Thus, the experimentally obtained field dependence of  $\Delta U$  qualitatively coincides with the dependence of  $T_1^{-1}$  on the magnetic induction and, hence, is nonlinear.

Since, in accordance with the concepts of the theory of magnetosensitive chemical reactions, the frequency of singlet–triplet ( $S$ – $T$ ) transitions occurring due to the difference in the Zeeman frequencies ( $\Delta g$  mechanism) and due to the isotropic hyperfine interaction of unpaired electrons with magnetic nuclei (HFI mechanism) displays a linear dependence on the external magnetic field, we may logically assume that the experimentally obtained nonlinear field dependence indicates the predominance of the relaxation mechanism of  $S$ – $T$  transitions in the spin system of an interacting pair of defects. The frequency of such transitions is connected with the change in their Zeeman energy in the external magnetic field and displays the following dependence on the magnetic induction [14]:

$$\begin{aligned} T_1^{-1} &= 0.33aB^2/(1 + bB^2), \\ a &= \overline{\Delta g^2} \beta_e^2 \hbar^{-2} \tau_b, \\ b &= \mu_e^2 \hbar^{-2} \tau_b^2, \end{aligned} \quad (2)$$

where  $\overline{\Delta g^2}$  characterizes the anisotropy scale of the  $g$  tensor,  $\beta_e$  is Bohr’s magneton,  $\mu_e$  is the magnetic moment of the electron, and  $\tau_b$  is the characteristic time.

The approximation of the obtained experimental dependence  $\Delta U(B)$ , taking into account Eqs. (1) and (2), made it possible to estimate the value of  $\Omega$  characterizing the energy of the wave packet emitted as a result of the magnetically stimulated detachment of dislocations in the sample under investigation:  $\Omega \approx 10^{-6}$  J.

## 5. CONCLUSION

Thus, it is found that the action of a weak magnetic field combined with the action of an electric current on a deformed sample of doped  $n$ -Si leads to a change in the dislocation mobility. The model used for describing the mechanism of action of the magnetic and electric fields on the mobility of dislocations in doped silicon makes it possible to explain the formation of dislocations capable of performing displacements in the sample more frequently, which is manifested in the formation of a second peak in the acoustic emission spectrum. It is shown that the preliminary exposure of the samples of deformed doped  $n$ -Si to a constant weak magnetic field leads to a change in the height of the acoustic emission peak upon passage of the current through the sample; this change depends on the magnetic induction of the applied field. The obtained effect is associated with the spin-dependent magnetic-field-sensitive reactions of defects occurring in the vicinity of the dislocation core and suppressing the retarding action of paramagnetic stoppers, which is manifested in an increase in the dislocation mobility. Analysis of the field dependence made it possible to estimate the energy of the wave packet emitted during the magnetically stimulated detachment of dislocations in the sample under investigation.

## ACKNOWLEDGMENTS

This work was supported by the program “Degradation Processes in Multilayered Thin-Film Structures” and by the Russian Foundation for Basic Research, project no. 98-02-03335.

## REFERENCES

1. Yu. I. Golovin and R. B. Morgunov, Zh. Éksp. Teor. Fiz. **115** (2), 605 (1999) [JETP **88**, 332 (1999)].
2. V. I. Al’shits, E. V. Darinskaya, and O. L. Kazakova, Zh. Éksp. Teor. Fiz. **111** (2), 615 (1997) [JETP **84**, 338 (1997)].
3. Yu. I. Golovin and R. B. Morgunov, Fiz. Tverd. Tela (St. Petersburg) **40** (11), 2065 (1998) [Phys. Solid State **40**, 1870 (1998)].
4. Yu. I. Golovin and R. B. Morgunov, Fiz. Tverd. Tela (St. Petersburg) **39** (4), 630 (1997) [Phys. Solid State **39**, 550 (1997)].
5. V. I. Al’shits, E. V. Darinskaya, and O. L. Kazakova, Fiz. Tverd. Tela (St. Petersburg) **40** (1), 81 (1998) [Phys. Solid State **40**, 70 (1998)].

6. E. V. Darinskaya, E. A. Petrzhik, S. A. Erofeeva, and V. P. Kisel', *Pis'ma Zh. Éksp. Teor. Fiz.* **70** (4), 298 (1999) [*JETP Lett.* **70**, 309 (1999)].
7. V. A. Kalitenko, I. Ya. Kucherov, and V. M. Perga, *Fiz. Tekh. Poluprovodn. (Leningrad)* **22** (4), 578 (1988) [*Sov. Phys. Semicond.* **22**, 361 (1988)].
8. A. M. Orlov, A. A. Skvortsov, and V. A. Frolov, *Pis'ma Zh. Tekh. Fiz.* **25** (3), 28 (1999) [*Tech. Phys. Lett.* **25**, 95 (1999)].
9. A. A. Skvortsov, A. M. Orlov, V. A. Frolov, *et al.*, *Fiz. Tverd. Tela (St. Petersburg)* **42** (10), 1814 (2000) [*Phys. Solid State* **42**, 1861 (2000)].
10. Yu. V. Golovin, R. B. Morgunov, V. E. Ivanov, and A. A. Dmitrievskii, *Fiz. Tverd. Tela (St. Petersburg)* **41** (10), 1778 (1999) [*Phys. Solid State* **41**, 1631 (1999)].
11. Yu. I. Golovin and R. B. Morgunov, *Fiz. Tverd. Tela (St. Petersburg)* **40** (12), 2184 (1998) [*Phys. Solid State* **40**, 1981 (1998)].
12. V. I. Al'shits, E. V. Darinskaya, and E. Yu. Mikhina, *Fiz. Tverd. Tela (St. Petersburg)* **38** (8), 2426 (1996) [*Phys. Solid State* **38**, 1333 (1996)].
13. U. Gerstmann, M. Amkreutz, and H. Overhof, *Phys. Status Solidi B* **217**, 667 (2000).
14. A. L. Buchachenko, R. Z. Sagdeev, and K. M. Salikhov, *Magnetic and Spin Effects in Chemical Reactions* (Nauka, Novosibirsk, 1978).

*Translated by N. Wadhwa*

## MAGNETISM AND FERROELECTRICITY

# Dynamics of a Néel Domain Wall with a Fine Structure in Rare-Earth Orthoferrites

E. G. Ekomasov and M. A. Shabalin

*Bashkortostan State University, ul. Frunze 32, Ufa, 450074 Bashkortostan, Russia*

*e-mail: EkomasovEG@bsu.bashedu.ru*

Received June 1, 2000

**Abstract**—The dynamics of an isolated domain wall (DW) with a fine structure moving at a supersonic velocity in a rare-earth orthoferrite is studied. A set of nonlinear equations of motion of the center of a DW structure line is derived. A steady-state solution to these equations adequately describes the experimental data for yttrium orthoferrite. The effect of an external magnetic field on the steady-state velocity of a DW with structural lines is investigated. © 2001 MAIK “Nauka/Interperiodica”.

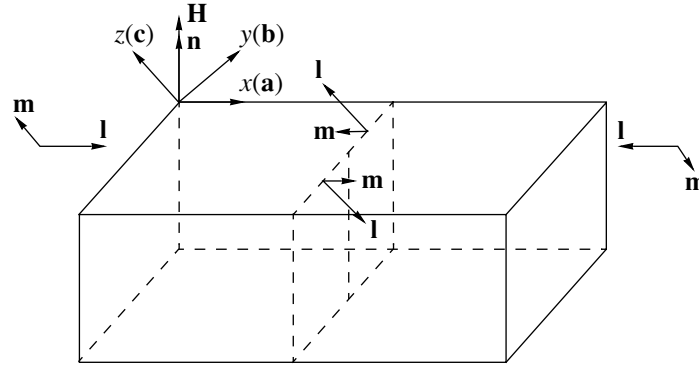
The static and dynamic properties of domain walls (DWs) with a fine structure (vertical and horizontal Bloch lines, etc.) in ferromagnets (e.g., garnet ferrites) have been well studied experimentally and theoretically, and such DWs have found application in a number of devices [1, 2]. However, the situation is different for weak ferromagnets (e.g., rare-earth orthoferrites, REOs). Although the existence of DWs with a fine structure has long since been predicted theoretically [3], the experiments indicating the occurrence of dynamic lines in the structure of a Néel DW moving at a supersonic velocity in yttrium orthoferrite have been performed only quite recently [4, 5]. Perhaps such lines are difficult to observe in REOs, because the ferromagnetism ( $\mathbf{m}$ ) and antiferromagnetism ( $\mathbf{l}$ ) vectors only slightly deflect (under the action of an external magnetic field  $\mathbf{H}$ ) from the plane of their rotation in the DW in both static and dynamic cases [6]. It was also shown theoretically [7–9] that the dynamic characteristics of DWs with structural lines in REOs differ essentially from those of DWs with vertical Bloch lines in ferromagnets. For example, the gyrotropic term in the dynamic force acting on the line in an REO appears when an external magnetic field is perpendicular to the plane of rotation of the vector  $\mathbf{l}$ ; this term can be comparable in magnitude to the viscous-damping and inertial terms. It should also be noted that the experiments reported in [4, 5, 10, 11] were performed under fairly specific conditions which have not been considered theoretically.

In this paper, we theoretically investigate the dynamics of an isolated Néel DW with structural lines, which moves at a supersonic velocity in an infinite plate of an REO in the high-temperature magnetic phase. The plate is cut perpendicularly to the optical axis and placed in an external magnetic field perpendicular to the plane of the plate.

The equations describing the motion of the DW in the REO plate can be expressed in terms of the angular variables of the ferromagnetism vector  $\mathbf{l} = \mathbf{l}(\cos\theta, \sin\theta\sin\varphi, \sin\theta\cos\varphi)$  and have the form [8]

$$\begin{aligned} & A(\Delta\theta - c^{-2}\ddot{\theta}) - \{K_{ab} - K_{cb}\cos^2\varphi \\ & + A[(\nabla\varphi)^2 - c^{-2}\dot{\varphi}^2]\} \sin\theta\cos\theta \\ = & -2\gamma A c^{-2} \sin^2\theta f(H)\dot{\varphi} - m_c H_z \sin\theta + 2\alpha M_0 \gamma^{-1} \dot{\theta}, \\ & \sin^2\theta \{A(\Delta\varphi - c^{-2}\ddot{\varphi}) - K_{cb}\sin\varphi\cos\varphi\} \\ = & -A \sin 2\theta (\nabla\varphi \nabla\theta - c^{-2}\dot{\varphi}\dot{\theta}) \\ & + 2\gamma A c^{-2} \sin^2\theta f(H) + 2\alpha M_0 \gamma^{-1} \sin^2\theta \dot{\varphi}, \end{aligned} \quad (1)$$

where  $c = \gamma\sqrt{aA}/2M_0$ ;  $m_c = -2M_0 d/a$ ;  $f(H) = H_y \sin\varphi + H_z \cos\varphi$ ;  $a$  and  $A$  are the homogeneous and inhomogeneous exchange constants, respectively;  $M_0$  is the magnetic moment of the sublattices;  $\gamma$  is the gyromagnetic ratio;  $\alpha$  is the dimensionless damping parameter;  $d$  is the Dzyaloshinskii interaction constant; and  $K_{ab}$  and  $K_{cb}$  are the effective anisotropy constants in the  $ab$  and  $cb$  planes, respectively. If the right-hand sides of Eqs. (1) are equal to zero, these equations are known to have a steady-state solution  $\theta = \theta_0(x - v_{DW}t)$ ,  $\varphi = \varphi_0(\eta - v_\eta t)$ , where  $x$  is the coordinate along the direction perpendicular to the DW plane and  $\eta$  is the coordinate along the direction perpendicular to the structural line. This solution describes the Néel DW fine structure in which the vector  $\mathbf{m}$  is rotated (figure). From Eq. (1), by eliminating the secular terms [6, 7], one can derive a set of nonlinear equations of motion for the center of the  $i$ th line (in much the same way as in the case of a Bloch-type DW [8];  $x_i$  and  $\eta_i$  are the coordinates of the cen-



Néel domain wall with a fine structure in an infinite plate (cut perpendicular to the optical axis) of the REO in the high-temperature magnetic phase (schematic).

ter):

$$\begin{aligned} \frac{d(m_x \dot{x}_i)}{dt} + \tau^{-1} m_x \dot{x}_i - \frac{\pi M_0 H_y}{\gamma H_E} \dot{\eta}_i &= m_c \lambda H_z, \\ \frac{d(m_{l\eta} \dot{\eta}_i)}{dt} + m_{l\eta} \tau^{-1} \dot{\eta}_i + \frac{\pi M_0 H_y}{\gamma H_E} \dot{x}_i &= 0, \end{aligned} \quad (2)$$

where

$$\begin{aligned} m_x &= [m_{\text{DW}x} \lambda + m_{lx}], \quad m_{\text{DW}x} = m_{\text{DW}} (1 - \dot{x}_i^2/c^2)^{-1/2}, \\ m_{lx} &= m_l (1 - \dot{\eta}_i^2/c^2)^{1/2} (1 - \dot{x}_i^2/c^2)^{-1/2}, \\ m_{l\eta} &= m_l (1 - \dot{x}_i^2/c^2)^{1/2} (1 - \dot{\eta}_i^2/c^2)^{-1/2}, \\ m_{\text{DW}} &= \frac{M_0}{\gamma^2 \delta_0 H_E}, \quad m_l = \frac{2M_0 \delta_0}{\gamma^2 \Lambda_0 H_E}, \\ H_E &= \frac{a}{4M_0}, \quad \delta_0 = \left[ \frac{A}{K_{ab} - K_{cb}} \right]^{1/2}, \\ \Lambda_0 &= \left( \frac{A}{K_{cb}} \right)^{1/2}, \end{aligned} \quad (3)$$

and  $\lambda$  is the period of the fine DW structure. The range of applicability of equations similar to Eq. (2) is discussed in detail in [7].

In Eq. (2), as in [1], we separate the dynamic reaction force (per unit length of the line):

$$\mathbf{F}_i = \frac{d\mathbf{P}_i}{dt} + \tau^{-1} \mathbf{P}_i - \frac{\pi M_0 H_y [\mathbf{t}, \dot{\mathbf{r}}_i]}{\gamma H_E}, \quad (4)$$

where  $\mathbf{P}_i = (m_{lx} \dot{x}_i, m_{l\eta} \dot{\eta}_i, 0)$  and  $\mathbf{t} = \nabla\varphi \times \nabla\theta / |\nabla\varphi \times \nabla\theta|$  is a unit vector tangent to the  $i$ th line at its geometric center. The gyroscopic force acting on the line [the last term in Eq. (4)] reverses its direction when  $H_y$  changes its sign. It should also be noted that this force should be taken into account when one considers the equation of motion of a DW curved because of the presence of the structural line [9]. In the steady-state case, the velocity

of the structural line moving along the DW  $v_l^*$  is found from Eq. (2) to be

$$v_l^* = \frac{v_{\text{DW}} [(a_0^2 - 1)(1 - v_{\text{DW}}^2/c^2)]^{1/2}}{[1 + (a_0^2 - 1)v_{\text{DW}}^2/c^2]^{1/2}}, \quad (5)$$

where  $a_0 = \pi Q^{1/2} H_y / 4\alpha H_E$ ,  $Q = (\Lambda_0/\delta_0)^2$ , and  $v_{\text{DW}}$  is the DW velocity, which can be found from the equation

$$\begin{aligned} \left\{ 1 + \frac{m_l}{m_{\text{DW}} \lambda} \left[ 1 - \frac{a_0^2 v_{\text{DW}}^2/c^2}{[1 + (a_0^2 - 1)v_{\text{DW}}^2/c^2]} \right]^{1/2} \right\} \\ \times (1 - v_{\text{DW}}^2/c^2)^{-1/2} \frac{v_{\text{DW}}}{c} \\ + \frac{a_1 v_{\text{DW}}^2/c^2}{[1 + (v_{\text{DW}}/c)^2 (a_0^2 - 1)]^{1/2}} = -\frac{\mu_0 H_z}{c}, \end{aligned} \quad (6)$$

where  $a_1 = a_0^2 2\delta_0^2 / \Lambda_0 \lambda$  and  $\mu_0 = \gamma \delta_0 d / \alpha a$ . Equation (5) adequately describes the experimental data [4, 5] if one assumes that  $a_0^2 \gg 1$ . In this case, this equation takes a simpler form,

$$v_l^* \cong c(1 - v_{\text{DW}}^2/c^2)^{1/2}, \quad (7)$$

corresponding to the experimental situation where the total velocity of the line is close to the limit velocity of the DW. For the experimental data from [5] ( $H \cong 100$  Oe,  $Q \cong 1.5$ ,  $H_E \cong 10^6$  Oe,  $\alpha \cong 10^{-5}$ ,  $\lambda \cong 100$   $\mu\text{m}$ ), we obtain  $a_0 \cong 10$  and  $a_1 \cong 10^{-1}$ . When  $a_0 \gg 1$  and  $a_1 \ll 1$ , Eq. (6) also takes a simpler form and its solution is

$$\frac{v_{\text{DW}}}{c} = \frac{v_0}{(1 + v_0^2)^{1/2}}, \quad (8)$$

where  $v_0 = \mu_0 H_z / c - a_1 / a_0$ ; therefore, the presence of the structural lines causes the DW mobility to decrease only slightly.



It will be recalled that in the case in question the line can move even when the DW is at rest if the component  $H_x$  of the external magnetic field is nonzero [8]. When the component  $H_x$  is taken into account,  $a_0$  and  $a_1$  in Eqs. (5) and (6) are replaced by  $a_0\zeta$  and  $a_1\zeta$ , respectively, where

$$\zeta = \left\{ 1 + 2(\mu_l H_x c / a_0 v_{DW}) (1 - v_{DW}^2 / c^2)^{-1/2} + (\mu_l H_x c / a_0 v_{DW})^2 \right\}^{1/2}, \quad (9)$$

with  $\mu_l = \pi\mu_0 Q^{1/2}/2$ . It can be seen that, by changing the sign of the field component  $H_x$ , one can both accelerate and slow down the motion of the line in the DW, whose velocity decreases and increases, respectively, in that case. It is of interest to test this prediction experimentally; at  $H_x \sim 100$  Oe, the second and third terms in Eq. (9) can be as large as several tenths.

#### ACKNOWLEDGMENTS

The authors are grateful to M.V. Chetkin and A.K. Zvezdin for useful discussions.

#### REFERENCES

1. A. P. Malozemov and J. C. Slonczewskii, *Domain Walls in Bubble Materials* (Academic, New York, 1979).
2. V. G. Barjaktar, M. V. Chetkin, B. A. Ivanov, and S. N. Gadetskiy, in *Tracts in Modern Physics*, Vol. 129:

*Dynamic of Topological Magnetic Solitons: Experiment and Theory* (Springer-Verlag, Berlin, 1994).

3. M. M. Farztdinov, M. A. Shamsutdinov, and A. A. Khalifina, *Fiz. Tverd. Tela (Leningrad)* **21** (5), 1522 (1979) [*Sov. Phys. Solid State* **21**, 878 (1979)].
4. M. V. Chetkin, Yu. N. Kurbatova, and A. I. Akhutkina, *J. Appl. Phys.* **79** (8), 6132 (1996).
5. M. V. Chetkin, Yu. N. Kurbatova, and B. N. Filatov, *Pis'ma Zh. Éksp. Teor. Fiz.* **65** (10), 760 (1997) [*JETP Lett.* **65**, 797 (1997)].
6. A. K. Zvezdin, A. A. Mukhin, and A. F. Popkov, Preprint No. 108, *Fiz. Inst. Akad. Nauk SSSR im. N. P. Lebedeva (Lebedev Institute of Physics, Academy of Sciences of USSR, Moscow, 1982)*.
7. E. G. Ekomasov, M. M. Farztdinov, and M. A. Shamsutdinov, Available from VINITI, No. 6462-85 (1985).
8. M. M. Farztdinov, M. A. Shamsutdinov, and E. G. Ekomasov, *Fiz. Tverd. Tela (Leningrad)* **30** (6), 1866 (1988) [*Sov. Phys. Solid State* **30**, 1076 (1988)].
9. E. G. Ekomasov, M. A. Shamsutdinov, and M. M. Farztdinov, *Fiz. Tverd. Tela (Leningrad)* **32** (5), 1542 (1990) [*Sov. Phys. Solid State* **32**, 902 (1990)].
10. M. V. Chetkin, Yu. N. Kurbatova, A. I. Akhutkina, and T. B. Shapaeva, *Zh. Éksp. Teor. Fiz.* **115** (6), 2160 (1999) [*JETP* **88**, 1179 (1999)].
11. M. V. Chetkin and Yu. N. Kurbatova, *Phys. Lett. A* **260** (108), 127 (1999).

*Translated by Yu. Epifanov*

## MAGNETISM AND FERROELECTRICITY

# Dipole Contribution of Fe<sup>3+</sup> Ions in 12*k* Positions to the Anisotropy Energy Constant of the BaFe<sub>12</sub>O<sub>19</sub> Hexaferrite

A. A. Bezlepkin and S. P. Kuntsevich

Kharkov National University, pl. Svobody 4, Kharkov, 61077 Ukraine

Received October 9, 2000

**Abstract**—The anisotropy of local fields on <sup>57</sup>Fe nuclei of Fe<sup>3+</sup> ions located in the 12*k* positions of the BaFe<sub>12</sub>O<sub>19</sub> ferrite is studied at low temperatures. The contributions of the anisotropy of the dipole and hyperfine fields to the anisotropy of local fields are separated. The contribution of Fe<sup>3+</sup> ions in the 12*k* positions to the anisotropy energy constant  $K_1$  is calculated in the case of the interionic magnetic dipole–dipole interaction. This contribution comprises more than one-half the experimental  $K_1$  value. © 2001 MAIK “Nauka/Interperiodica”.

### 1. INTRODUCTION

Hexaferrites of the structural type M, namely,  $MeFe_{12}^{3+}O_{19}$  (where  $Me$  is  $Pb^{2+}$ ,  $Ba^{2+}$ ,  $Si^{2+}$ , and  $Ca^{2+}$ ), contain only one type of magnetoactive ions, Fe<sup>3+</sup>. The anisotropy energy constants for these ferrites are two orders of magnitude larger than those for garnet- and spinel-type ferrites, which also contain only the same type of Fe<sup>3+</sup> magnetoactive ions. By virtue of their large anisotropy constants and, correspondingly, high anisotropy fields, the M-type hexaferrites have wide technical applications. In this respect, the elucidation of the physical mechanisms responsible for the high-anisotropy properties of these ferrites is of considerable scientific and practical interest.

In the M-type hexaferrites, Fe<sup>3+</sup> ions are distributed over five crystallographically nonequivalent positions, thus forming five sublattices: 12*k*(*a*), 2*a*(*b*), 2*b*(*e*), 4*f*<sub>1</sub>(*c*), and 4*f*<sub>2</sub>(*d*). Among the twelve iron ions in the formula unit  $MeFe_{12}O_{19}$ , six ions occupy the 12*k* positions (the *a* sublattice). Hence, the calculation of the contribution of these positions to the anisotropy energy constant and, correspondingly, the anisotropy energy is of special interest. In this work, we proposed a method for calculating the sublattice contributions of the dipole–dipole interaction of Fe<sup>3+</sup> ions from the NMR data on the anisotropy of local fields on <sup>57</sup>Fe nuclei. Using the BaFe<sub>12</sub>O<sub>19</sub> (BaM) ferrite as an example, we calculated the low-temperature contribution of the dipole–dipole interaction to the anisotropy energy constant  $K_1$  of Fe<sup>3+</sup> ions in the 12*k* positions.

### 2. SAMPLES AND EXPERIMENTAL TECHNIQUES

The samples were BaM single crystals grown from the BaO · B<sub>2</sub>O<sub>3</sub> melt by the solution technique. The

crystals were synthesized in the temperature range 1420–1300 K. The samples were enriched to 95% with a <sup>57</sup>Fe isotope. The phase composition of crystals was controlled by the x-ray diffraction technique. The crystal lattice constants at room temperature are as follows:  $a = 0.589$  nm and  $c = 2.319$  nm. The NMR frequency was determined using an incoherent spin echo spectrometer. The anisotropy of the local NMR frequencies was calculated as the difference between the frequencies of the spin echo spectra, which were measured in a magnetic field exceeding the sample saturation field and applied along the hexagonal axis (the *c* axis) and in the basal plane.

### 3. RESULTS AND DISCUSSION

Earlier [1], we studied thoroughly the dependence of the <sup>57</sup>Fe NMR frequency on the magnetization orientation in BaM single crystals. In particular, we revealed a strong anisotropy of local frequencies for nuclei in the 12*k* positions upon reorientation of the magnetization (and, therefore, the magnetic moments of Fe<sup>3+</sup> ions) of the sample both from the *c* axis to the basal plane and within the basal plane. The local NMR frequency is unambiguously determined by the local field on the nuclei. This makes it possible to determine the anisotropy of the local fields from the orientation dependences of the frequency. Points in the figure represent the orientation dependences of the anisotropy  $\Delta H_l$  of local fields on <sup>57</sup>Fe nuclei of Fe<sup>3+</sup> ions in the *a* sublattice (12*k* positions), which were obtained using the data taken from [1] and the formula

$$\Delta H_l(\varphi) = \gamma[v^\perp(\varphi) - v^\parallel]. \quad (1)$$

Here,  $\gamma = 0.1377$  kOe/MHz is the gyromagnetic ratio for the <sup>57</sup>Fe nuclei,  $v^\perp(\varphi)$  is the NMR frequency in a magnetic field applied at an angle  $\varphi$  to the *a*<sub>1</sub> axis in the

basal plane, and  $\nu^{\parallel}$  is the NMR frequency in a magnetic field of the same magnitude but applied along the  $\mathbf{c}$  axis. As follows from this figure, there are three groups of nuclei which have different anisotropies  $\Delta H_l$  of local fields when the magnetization vector lies in the basal plane.

It is known that the anisotropy  $\Delta H_l$  of a local field on a nucleus can be represented as the sum of the contributions from the anisotropy  $\Delta H_d$  of dipole fields and the anisotropy  $\Delta H_{\text{hf}}$  of the hyperfine field [2]:

$$\Delta H_l = \Delta H_d + \Delta H_{\text{hf}}. \quad (2)$$

The dependences  $\Delta H_l(\varphi)$  shown in the figure can be described by the relationship

$$\Delta H_l(\varphi) = \Delta H_{\text{hf}} + \Delta H_d^{\varphi} [1 - \cos 2(\varphi + n\pi/3)], \quad (3)$$

where  $n = 0, 1$ , or  $2$  designates the number of the nuclear group.

The dependences  $\Delta H_l(\varphi)$ , which were constructed according to relationship (3) and the values  $\Delta H_{\text{hf}} = -5.3$  kOe and  $\Delta H_d^{\varphi} = -6.0$  kOe, are shown by solid lines in the figure.

Stepankova *et al.* [3] calculated the anisotropy of dipole fields for the 12k positions in the M-type structure upon spin reorientation of the Fe<sup>3+</sup> ions from the basal plane to the hexagonal  $\mathbf{c}$  axis at  $T = 0$ . It was shown that in the case when the magnetization of spins of the Fe<sup>3+</sup> ions is oriented in the basal plane (perpendicular to the  $\mathbf{c}$  axis), an assembly of Fe<sup>3+</sup> ions in the  $a$  sublattice (12k positions) breaks up into three groups with an identical number of ions for which the anisotropy of dipole fields depends on the orientation of magnetization in this plane with respect to the  $\mathbf{a}_1$  axis of the basis. Formal mathematical transformations of the relationship derived in [3] for dipole fields in the 12k positions permit us to obtain the following expression for  $\Delta H_d^n$  for each of the three nuclear groups of Fe<sup>3+</sup> ions:

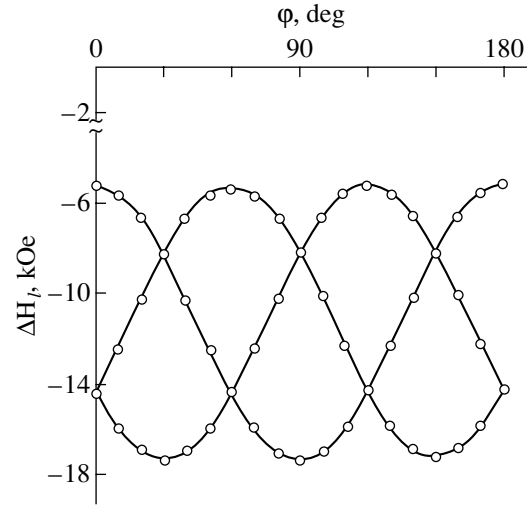
$$\Delta H_d^n = \Delta H^c + \Delta H_d^{\varphi} [1 - \cos 2(\varphi - n\pi/3)], \quad (4)$$

where  $n = 0, 1$ , or  $2$ ;  $\Delta H^c$  is the constant component of the dipole field; and  $\Delta H_d^{\varphi}$  is the component of the dipole field that depends on the magnetization orientation in the basal plane.

As follows from the data obtained in [3],  $|\Delta H^c| \ll |\Delta H_d^{\varphi}|$ . Therefore, expression (4) can be approximated by the relationship

$$\Delta H_d^n \approx \Delta H_d^{\varphi} [1 - \cos 2(\varphi + n\pi/3)]. \quad (5)$$

Expressions (2)–(4) suggest that the value  $\Delta H_{\text{hf}} = -5.3$  kOe at 77 K should be interpreted as the anisotropy of the hyperfine field. According to the experi-



Anisotropy of local fields on <sup>57</sup>Fe nuclei in the  $a$  sublattice as a function of the magnetization orientation in the basal plane of the BaFe<sub>12</sub>O<sub>19</sub> ferrite in an external magnetic field of 21.3 kOe at a temperature of 77 K.

mental data, this anisotropy has an identical magnitude for all three groups of nuclei in the 12k positions.

In the model assuming that the anisotropy of the dipole field on nuclei of the Fe<sup>3+</sup> ions differs insignificantly from that in the region of localization of their electron-magnetic moments, we can calculate the contribution  $K_{1a}^d$  of the Fe<sup>3+</sup> ions in the 12k positions to the anisotropy energy constant  $K_1$  due to the interionic dipole–dipole interaction. The expression relating  $K_{1a}^d$  and  $\Delta H_d^{\varphi}$  for a specific angle  $\varphi$  has the form

$$K_{1a}^d = -(1/2) \sum_n J_a^n \Delta H_d^{\varphi} [1 - \cos 2(\varphi + n\pi/3)], \quad (6)$$

where  $J_a^n$  is the specific magnetization of the  $n$ th group of Fe<sup>3+</sup> ions in the 12k positions. Since the number of iron ions is the same in all three groups, we obtain  $3J_a^n = J_a$ , where  $J_a$  is the specific magnetization of the  $a$  sublattice. The specific magnetization of the sublattice is considered to mean the magnetic moment of the sublattice per unit volume. Its magnitude can be determined by the procedure described in [4], provided that the saturation magnetization of the ferrite is known. The saturation magnetization  $J_s$  of the crystals under study is equal to 550 G at 77 K. In this case, according to [4], we have  $J_a = 825$  G and  $J_a^n = 275$  G. Using the values  $\Delta H_d^{\varphi} = -6.0$  kOe and  $J_a^n = 275$  G and expression (6), we obtain  $K_{1a}^d = 2.55 \times 10^6$  erg/cm<sup>3</sup> at 77 K for the angle  $\varphi = 0$ .

Since the trigonometric functions in expression (6) satisfy the relationship

$$\cos 2\varphi + \cos 2(\varphi + \pi/3) + \cos 2(\varphi + \pi/3) = \text{const},$$

the calculated value of  $K_{1a}^d$  is independent of the angle  $\varphi$ .

The value obtained,  $K_{1a}^d = 2.55 \times 10^6 \text{ erg/cm}^3$ , agrees satisfactorily with the value  $K_{1a}^d = 2.7 \times 10^6 \text{ erg/cm}^3$  for the same temperature, which was determined earlier in [5] from the data on the temperature dependence of the anisotropy constant  $K_1$  for the BaM ferrite. The anisotropy energy constant of this ferrite is equal to  $4.4 \times 10^6 \text{ erg/cm}^3$  at 77 K.

The calculations reported in the present work and in [5] demonstrated that, at low temperatures, the contribution of  $\text{Fe}^{3+}$  ions in the 12k positions of the BaM ferrite due to the interionic dipole-dipole interaction comprises more than one-half the anisotropy energy constant  $K_1$ .

## ACKNOWLEDGMENTS

The work was supported by the Ministry of Education of Ukraine.

## REFERENCES

1. A. A. Bezlepkin, S. P. Kuntsevich, and Yu. A. Popkov, *Fiz. Nizk. Temp.* **15** (8), 875 (1989) [*Sov. J. Low Temp. Phys.* **15**, 484 (1989)].
2. E. A. Turov and M. P. Petrov, *Nuclear Magnetic Resonance in Ferro- and Antiferromagnets* (Nauka, Moscow, 1969; Wiley, New York, 1972).
3. H. Stepankova, J. Englich, and B. Sedlak, *Czech. J. Phys., Sect. B* **33**, 816 (1983).
4. S. P. Kuntsevich and A. A. Bezlepkin, *Fiz. Tverd. Tela (Leningrad)* **29** (9), 2595 (1987) [*Sov. Phys. Solid State* **29**, 1497 (1987)].
5. S. P. Kuntsevich, *Vestn. Khar'k. Gos. Univ., Ser. Fiz.* **440** (3), 125 (1999).

*Translated by M. Lebedkin*

## MAGNETISM AND FERROELECTRICITY

# Stochastic Resonance in Low-Disperse Magnets: Mechanism of Subbarrier Magnetization Reversal

A. G. Isavnin

Kama Polytechnical Institute, Naberezhnye Chelny, 423810 Russia

e-mail: Isavnin@mail.ru

Received October 25, 2000

**Abstract**—The phenomenon of stochastic resonance is studied theoretically in a system of single-domain particles with an “easy-axis”-type magnetic anisotropy at temperatures close to absolute zero, for which the tunneling of the magnetic moment vector between stable states dominates. Calculations are made on the basis of the master equation in the model of discrete orientations in the quasi-adiabatic approximation. The dynamic magnetic susceptibility components of the system under the action of a weak rf field are calculated. The critical temperature at which a transition from the above-the-barrier mechanism of magnetization reversal to the subbarrier mechanism occurs is estimated. © 2001 MAIK “Nauka/Interperiodica”.

1. The phenomenon of stochastic resonance, in which the response of a multistable system (having several stable states) to a weak external periodic signal passes through a clearly manifested peak upon a uniform increase in the noise in the system, has been studied extensively both theoretically [1, 2] and experimentally [3]. For a system of small magnetic uniaxial particles, each of which is a bistable element whose two stable states correspond to two opposite orientations of the magnetic moment vector along the easy axis, this effect was considered in the case of the thermal activation of the system [4, 5]. In this case, the internal noise in the system was attributed to thermally induced hopping of the magnetization vector above the potential barrier separating two energy minima. The components of the dynamic magnetic susceptibility regarded as the response of the system to a weak external rf field had a nonmonotonic bell-shaped temperature dependence typical of stochastic resonance.

Later, stochastic resonance was studied theoretically in this system at absolute zero temperature, where the heat-induced jumps above the barrier are ruled out completely and the magnetization reversal of a particle occurs via the subbarrier tunneling of the magnetic moment [6]. Macroscopic quantum tunneling of magnetization from metastable states was predicted theoretically [7] and soon after confirmed experimentally [8]. In contrast to the case of a thermally activated system [4, 5], quantum transitions require the application of an additional constant magnetic field perpendicular to the easy axis of the particle. The presence of such a field distorts the axial symmetry of the Hamiltonian of the system, which makes possible the tunneling of magnetization [7]. By varying the magnitude of this field, it is possible to control the average rate of quantum switching of the magnetic moment and, hence, to vary the level of intrinsic noise in the system.

In this work, we consider the situation of combined operation of above-the-barrier and subbarrier mechanisms of magnetization reversal in uniaxial finely dispersed particles. Stochastic resonance in such systems is considered at low temperatures (near 0 K), when both mechanisms of magnetization reversal are operating.

2. The energy of a particle in spherical coordinates has the form

$$E(t) = K\nu\sin^2\theta - \mu_0HM\nu\sin\theta\cos\varphi + \mu_0AM\nu\cos\theta\sin(\Omega t). \quad (1)$$

Here,  $K$  is the magnetic anisotropy constant;  $\nu$  is the particle volume;  $H$  is the constant magnetic field strength applied at right angles to the easy axis; and  $A$  and  $\Omega$  are the amplitude and frequency of a weak modulating rf field applied along the easy axis. In order to simplify calculations, we go over to the following steady-state potential [6], which is the averaging of expression (1) over half the modulation period for  $\varphi = 0$ :

$$U = K\nu\sin^2\theta - \mu_0HM\nu\sin\theta + \mu_0H_1M\nu\cos\theta, \quad (2)$$

where  $H_1 = 2A/\pi$ . This model presumes a jumpwise variation of the system energy. The potential has the form depicted in Fig. 1 for a half-period of modulation, while in the next half-period, the pattern changes to its opposite (the sign of the last term in Eq. (2) is reversed): the lower minimum is located on the left and the upper minimum is on the right, and so on. The rate of magnetization tunneling attains noticeable values for  $H$  close to  $H_c = 2K/(\mu_0M)$  [7], such that it is convenient to go over in our calculations to the angle  $\delta = \pi/2 - \theta \ll 1$ . The extrema of expression (2) can be found from the condition  $dU/d\theta = 0$ :

$$\delta^3 - (H_1/H_c)\delta^2 - 2\epsilon\delta + 2H_1/H_c = 0, \quad (3)$$

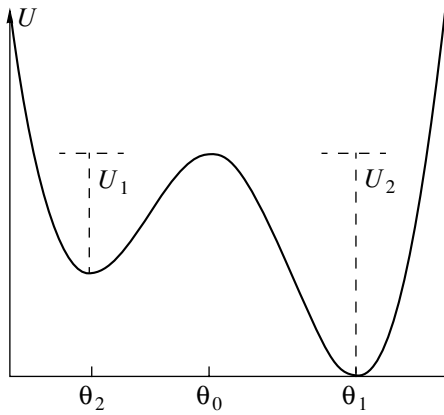


**Fig. 1.** Bistable potential in Eq. (2) of the system found by averaging Eq. (1) over the modulation half-period  $1/\Omega$ . Angles  $\theta_n = \pi/2 - \delta_n$ .

where  $\varepsilon = 1 - H/H_c \ll 1$ . For  $H_1/H_c \ll 1$ , the solution to this cubic equation has the form

$$\delta_n = H_1/(3H_c) + 2(2\varepsilon/3)^{1/2} \cos((\phi + 2\pi n)/3),$$

$$n = 0, 1, 2, \quad (4)$$

$$\cos \phi \approx -H_1/(H_c(2\varepsilon/3)^{3/2}),$$

where  $\delta_1$  and  $\delta_2$  correspond to two minima and  $\delta_0$  corresponds to the maximum energy of the system. A system having potential (2) is bistable if  $H < H_{c1} = (1 - 3/2[H_1/H_c]^{2/3})H_c$ . If this condition is violated, only one minimum survives. The rate of magnetization tunneling is usually represented in the form  $W = \omega_0 \exp(-S_E/\hbar)$  [7], and in the case of a parabolic potential barrier, the WKB exponent is connected with the barrier height  $U_0$  through the relation [9]

$$\frac{S_E}{\hbar} \approx \frac{2\pi U_0}{\hbar \omega_0}. \quad (5)$$

Here,  $\omega_0$  is the attempt frequency, which is determined by the curvature of the curve at the potential minimum and is usually approximately equal to the frequency of the Larmor precession about the corresponding effective field  $\omega_0 \sim \mu_0 \gamma H / \cos \delta_2$  ( $\gamma$  is the gyromagnetic ratio), which amounts approximately to  $10^9 - 10^{10} \text{ s}^{-1}$ . In [6], the case of  $T = 0 \text{ K}$  was considered; i.e., magnetization tunneling was possible only from the very bottom of the potential well. At temperatures above absolute zero, one must take into account the possibility of tunneling from the higher energy levels  $E_n = (1/2 + n)\hbar\omega_0$  also. In this case, the rates of tunneling  $W_+$  and  $W_-$  from the upper minimum of potential (2) (left minimum in Fig. 1) and from the lower (right) minimum, respec-

tively, will be defined as

$$W_+ = \frac{1}{Z_0} \sum_{n=0}^{\infty} W(E_n) \exp(-E_n/kT),$$

$$Z_0 = \sum_{n=0}^{\infty} \exp(-E_n/kT), \quad (6)$$

$$W_- = \frac{1}{Z_0} \sum_{n=N}^{\infty} W(E_n) \exp(-E_n/kT).$$

Here,

$$W(E_n) = \omega_0 [1 + \exp(-2\pi(E_n - U_0)/\hbar\omega_0)]^{-1} \quad (7)$$

is the rate of tunneling from the metastable level  $E_n$  through a parabolic barrier [9]. Using Eq. (7) for the extreme cases  $E_n \ll U_0$  and  $E_n \gg U_0$ , we write the rates of magnetization tunneling in the form

$$W_+ \cong \frac{\omega_0}{Z_0} \left\{ \sum_{n=0}^{M-1} \exp\left(-2\pi\left(\frac{U_1}{\hbar\omega_0} - \left(\frac{1}{2} + n\right)\right)\right) \times \exp\left(-\frac{\left(\frac{1}{2} + n\right)\hbar\omega_0}{kT}\right) + \left(1 + \exp\left(-2\pi\left(\frac{1}{2} + M - \frac{U_1}{\hbar\omega_0}\right)\right)\right)^{-1} \times \exp\left(-\frac{\left(\frac{1}{2} + M\right)\hbar\omega_0}{kT}\right) + \sum_{n=M+1}^{\infty} \exp\left(-\frac{\left(\frac{1}{2} + n\right)\hbar\omega_0}{kT}\right) \right\}$$

$$= \omega_0 \left\{ \left(1 - \exp\left(-\frac{\hbar\omega_0}{kT}\right)\right) \times \left[ \frac{\exp\left(-\frac{2\pi U_1}{\hbar\omega_0} + \pi\right) - \exp\left(-\frac{U_1}{kT} + \frac{\hbar\omega_0}{2kT}\right)}{1 - \exp\left(2\pi - \frac{\hbar\omega_0}{kT}\right)} + \frac{1}{2} \exp\left(-\frac{U_1}{kT} + \frac{\hbar\omega_0}{2kT}\right) + \exp\left(-\frac{U_1}{kT} + \frac{\hbar\omega_0}{2kT}\right) \right] \right\},$$

$$\begin{aligned}
 W_- \equiv \frac{\omega_0}{Z_0} & \left\{ \sum_{n=N}^{N+M-1} \exp\left(-2\pi\left(\frac{U_2}{\hbar\omega_0} - \left(\frac{1}{2} + n\right)\right)\right) \right. & (8) \\
 & \times \exp\left(-\frac{\left(\frac{1}{2} + n\right)\hbar\omega_0}{kT}\right) \\
 & + \left(1 + \exp\left(-2\pi\left(\frac{1}{2} + M + N\frac{U_2}{\hbar\omega_0}\right)\right)\right)^{-1} \\
 & \times \exp\left(-\frac{\left(\frac{1}{2} + M + N\right)\hbar\omega_0}{kT}\right) \\
 & + \left. \sum_{n=M+N+1}^{\infty} \exp\left(-\frac{\left(\frac{1}{2} + n\right)\hbar\omega_0}{kT}\right) \right\} \\
 & = \omega_0 \left\{ \left(1 - \exp\left(-\frac{\hbar\omega_0}{kT}\right)\right) \right. \\
 & \times \left[ \frac{\exp\left(-\frac{2\pi U_1}{\hbar\omega_0} - \frac{U_2 - U_1}{kT} + \frac{\hbar\omega_0}{kT}\right) - \exp\left(-\frac{U_2}{kT} + \frac{\hbar\omega_0}{2kT}\right)}{1 - \exp\left(2\pi - \frac{\hbar\omega_0}{kT}\right)} \right. \\
 & \left. \left. + \frac{1}{2} \exp\left(-\frac{U_2}{kT} + \frac{\hbar\omega_0}{2kT}\right) \right] + \exp\left(-\frac{U_2}{kT} + \frac{\hbar\omega_0}{2kT}\right) \right\}.
 \end{aligned}$$

Here,  $U_1 = (1/2 + M)\hbar\omega_0$  and  $U_2 = (1/2 + M + N)\hbar\omega_0$  are the depths of the potential wells for the upper and lower minima, respectively (Fig. 1). For the dynamic tunneling rate in the case of external periodic modulation of the system by an rf field, it is convenient to use the following model expression verified by numerical calculations for  $T = 0$  K [6]:

$$\begin{aligned}
 W(t) &= (W_1 + W_2 \sin \Omega t)/2, \\
 W_1 &= W_+ + W_-, \quad W_2 = W_+ - W_-.
 \end{aligned} \quad (9)$$

3. We consider the dynamic magnetic susceptibility as the response of the system to a weak rf field. The solution of the corresponding master equation for the transition rates and for the population of stable states in

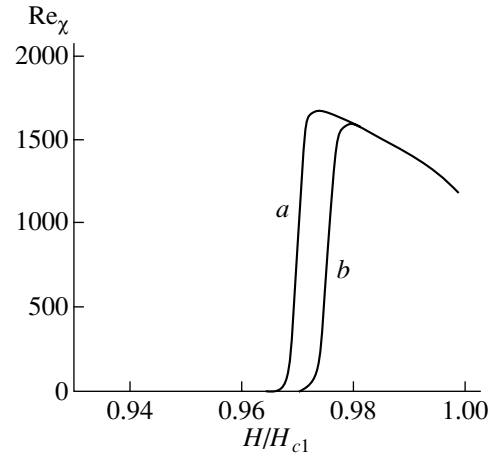


**Fig. 2.** Real component of the dynamic magnetic susceptibility for an iron particle ( $K = 4 \times 10^4$  J/m<sup>3</sup>,  $M = 1.72 \times 10^6$  A/m,  $v = 10^{-26}$  m<sup>3</sup>) at temperature  $T = 0.005$  K,  $\Omega = 10^5$  s<sup>-1</sup>, and  $H_1/H_c = 0.01$ . Curve *a* is plotted taking into account quantum and thermal fluctuations of magnetization, while curve *b* corresponds to the thermal mechanism of magnetization reversal alone.

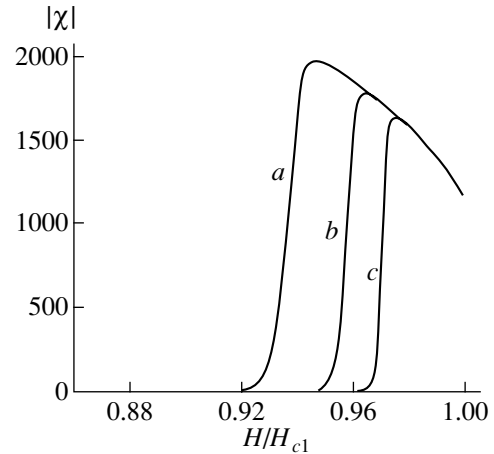


**Fig. 3.** Magnetic susceptibility for an iron particle ( $K = 4 \times 10^4$  J/m<sup>3</sup>,  $M = 1.72 \times 10^6$  A/m,  $v = 10^{-26}$  m<sup>3</sup>,  $\Omega = 10^5$  s<sup>-1</sup>,  $H_1/H_c = 0.01$ ) at low temperatures. Curve *a* corresponds to  $T = 0.02$  K; curve *b*, to 0.01 K; and curve *c*, to 0.001 K.

the approximation of discrete orientations in the quasi-adiabatic limit has the form [1, 4, 6]

$$\begin{aligned}
 \text{Re } \chi &= \frac{M \sin \delta_2 W_1 W_2}{H_1 (W_1^2 + \Omega^2)}, \quad \text{Im } \chi = \frac{M \sin \delta_2 W_2 \Omega}{H_1 (W_1^2 + \Omega^2)}, \\
 |\chi| &= \frac{M \sin \delta_2 W_2}{H_1 (W_1^2 + \Omega^2)^{1/2}}.
 \end{aligned} \quad (10)$$

Figure 2 shows the real component of the dynamic magnetic susceptibility varying in phase with the exter-

nal varying magnetic field. The contribution of the tunnel mechanism of magnetization reversal (curve *a*) for the system at nonzero temperatures can be seen clearly. Curve *b* is plotted without taking into account quantum corrections associated with the possibility of subbarrier tunnel transitions, i.e., by using only the last terms in Eq. (8), which are connected with transitions above the barrier. Figure 3 depicts the susceptibility of the system which takes into account the thermal and quantum mechanisms at various low temperatures. The effects of the macroscopic quantum tunneling of magnetization are manifested most clearly below a certain temperature  $T_c$  (the crossover temperature [7]), which can be estimated from the relation  $T_c \sim \hbar\omega_0/(2\pi k)$  obtained by equating the exponents of the tunneling rate in Eq. (5) and of the Kramers rate  $W_K \sim \exp(-U_0/kT)$  of thermal above-the-barrier transitions. The values of this critical temperature are of the order of 0.01 K. At temperatures higher than  $T_c$ , above-the-barrier transitions dominate; i.e., the thermal mechanism of magnetization reversal prevails.

4. In conclusion, it may be noted that the effect under investigation has a high resolution from the viewpoint of the possible observation of stochastic resonance in the quantum mode; for example,  $\delta_2 = 31^\circ$  for  $H_1/H_c = 0.01$  and  $H/H_{c1} = 0.9$ . Since the potential barrier height  $U_0$  is usually proportional to the particle volume  $v$ , it is convenient to choose finer particles for attaining higher tunneling rates. However, for particles with a high Curie point ( $T_C \sim 500\text{--}1000$  K), ferromagnetism as a cooperative effect is destroyed for the particle size  $d_0 \sim 1$  nm. This lower limit set for choosing the particle size is determined by comparing the zero-point energy and the magnetic-ordering energy:

$$\Delta\varepsilon_0 \cong \frac{(\Delta p)^2}{2m} \cong \frac{\hbar^2}{2md_0^2}, \quad \Delta\varepsilon_M \cong kT_C. \quad (11)$$

Modern SQUID-based experimental setups make it possible to detect jumps of the magnetic moment vector

of a single isolated particle at temperatures close to 0 K [10]. In this paper, we disregarded the effect of dissipation processes on the magnetization dynamics [11]. Such processes can be the result of interaction with phonons, nuclear spins, Stoner perturbations, and vortex currents in magnets.

#### ACKNOWLEDGMENTS

This work was supported in part by the International Science Foundation (ISF), grant no. NNT300.

#### REFERENCES

1. B. McNamara and K. Wiesenfeld, *Phys. Rev. A* **39** (9), 4854 (1989).
2. P. Jung and P. Hanggi, *Phys. Rev. A* **44** (12), 8032 (1991).
3. A. N. Grigorenko, P. I. Nikitin, A. N. Slavin, and P. Y. Zhou, *J. Appl. Phys.* **76** (10), 6335 (1994).
4. É. K. Sadykov and A. G. Isavnin, *Fiz. Tverd. Tela (St. Petersburg)* **36** (11), 3473 (1994) [*Phys. Solid State* **36**, 1843 (1994)].
5. É. K. Sadykov and A. G. Isavnin, *Fiz. Tverd. Tela (St. Petersburg)* **38** (7), 2104 (1996) [*Phys. Solid State* **38**, 1160 (1996)].
6. É. K. Sadykov, A. G. Isavnin, and A. B. Boldenkov, *Fiz. Tverd. Tela (St. Petersburg)* **40** (3), 516 (1998) [*Phys. Solid State* **40**, 474 (1998)].
7. E. M. Chudnovsky and L. Gunther, *Phys. Rev. Lett.* **60** (8), 661 (1988).
8. J. Tejada, X. X. Zhang, and L. Balcells, *J. Appl. Phys.* **73** (10), 6709 (1993).
9. I. Affleck, *Phys. Rev. Lett.* **46** (6), 388 (1981).
10. W. Wernsdorfer, K. Hasselbach, D. Mailly, *et al.*, *J. Magn. Magn. Mater.* **145** (1–2), 33 (1995).
11. A. Garg, *J. Appl. Phys.* **76** (10), 6168 (1994).

*Translated by N. Wadhwa*



---

## MAGNETISM AND FERROELECTRICITY

---

# Thermopower and Electrical Resistivity of $\text{La}_{1-x}\text{Sr}_x\text{MnO}_3$ Single Crystals under Hydrostatic Pressure

E. S. Itskevich and V. F. Kraidenov

Vereshchagin Institute of High-Pressure Physics, Russian Academy of Sciences,  
Troitsk, Moscow oblast, 142092 Russia

Received July 28, 2000; in final form, November 13, 2000

**Abstract**—The thermopower  $\alpha$  and the electrical resistivity  $\rho$  of  $\text{La}_{1-x}\text{Sr}_x\text{MnO}_3$  single crystals with a strontium content  $x = 0.125$ , which corresponds to the stoichiometric composition of the new charge-ordered (CO) phase, are measured in the temperature range 77–300 K at pressures up to 12 kbar. The dependence  $\alpha(T)$  exhibits two maxima. The first low-temperature maximum is associated with the formation of the charge-ordered phase. The second high-temperature maximum is attributed to the  $O \rightarrow O'$  structural transition between the orthorhombic phases and the formation of ferromagnetic clusters. It is found that the phase transition observed at  $P > 9.2$  kbar is accompanied by a substantial shift of both maxima toward the low-temperature range. © 2001 MAIK “Nauka/Interperiodica”.

## 1. INTRODUCTION

Investigations into the properties of perovskite structures of high-temperature superconductors and manganates gave rise to a great variety of physical theories based on the experimental results. Recent studies of the thermopower and the electrical resistivity as functions of temperature have provided a considerable amount of valuable information for a better understanding of the mechanisms of the physical processes occurring in the normal state of high-temperature superconductors and in manganates with a giant magnetoresistance. The use of pressure in these experiments furnishes better results [1, 2] and, in particular, makes possible a comparative analysis of the behavior of these two systems.

The  $\text{La}_{1-x}\text{Sr}_x\text{MnO}_3$  system is among the most interesting systems. Yamada *et al.* [3] investigated this system at  $x = 0.10$ – $0.15$  by neutron diffraction and revealed that a new charge-ordered (CO) phase is formed in the temperature range 100–200 K. As the strontium content  $x$  decreases in the specified range, the second-order transition transforms into the first-order transition. It is quite probable that the crossover between different-type transitions occurs at the content  $x = 0.125$  (1/8), which corresponds to the stoichiometric composition of the new charge-ordered phase. Zhou *et al.* [4] measured the thermopower  $\alpha$  and the electrical resistivity  $\rho$  under pressures up to 18 kbar in samples with  $x = 0.12$ , 0.14, and 0.15. The fact that the electronic structure of these samples undergoes a substantial transformation at intermediate  $x$  is confirmed by a sixfold change in the thermopower in the vicinity of the low-temperature maximum associated with the formation of the charge-ordered phase. In this respect, we performed compression measurements of the ther-

mopower of  $\text{La}_{0.875}\text{Sr}_{0.125}\text{MnO}_3$  samples ( $x = 0.125$ ) in order to obtain new information on the formation of the charge-ordered phase.

## 2. SAMPLE PREPARATION AND COMPRESSION MEASUREMENT TECHNIQUE

The procedures used for preparing single-crystal samples and checking the content  $x$  and the single-crystal state were described earlier in [5]. The sample was prepared in the form of a trapezoidal plate with a height of 2.5 mm, a thickness of 1.3 mm, and base lengths of 1.5 and 2.0 mm. The initial resistivity  $\rho(300)$  at atmospheric pressure was equal to 12  $\Omega$  cm. A heater together with a thermocouple were cemented to the upper surface of the sample with the use of a silver paste, followed by drying at 60°C for a few hours. This paste was also used to cement the sample to a copper washer on an obturator of a high-pressure chamber and to connect potential leads for measuring the electrical resistivity  $\rho$  of the sample. The distance between the leads was 0.3 mm.

The thermopower was measured in the temperature range 77–300 K at a pressure up to 12.5 kbar. Measurements were performed by the method of a longitudinal thermal flux at a constant power delivered by the heater [6]. The temperature gradient was measured by a (Cu + 0.1% Fe + 0.01% Li)–Cu thermocouple, and the absolute temperature  $T$  was determined with a (Cu + 0.15% Fe)–Cu thermocouple. The temperature gradient across the sample at a constant heater power varied from 0.09 to 0.045 K with an increase in the pressure from 0 to 12 kbar. The thermopower of the sample was determined with respect to copper. The results obtained were corrected according to the data available in the literature and our measurements of the thermopower for

copper with respect to the Y-123 superconductor. The pressure dependence of the thermopower for copper was ignored because of the smallness of the correction.

### 3. EXPERIMENTAL RESULTS

**3.1. Thermopower.** The experimental data on the thermopower  $\alpha$  of the  $\text{La}_{0.875}\text{Sr}_{0.125}\text{MnO}_3$  sample are presented in Fig. 1. All four curves at different pressures in the temperature range  $T = 80\text{--}300$  K exhibit three extrema: two maxima at  $T_{\alpha 1 \text{max}} \sim 130$  K and  $T_{\alpha 2 \text{max}} = 225\text{--}255$  K and one minimum at  $T_{\alpha \text{min}} = 177\text{--}185$  K. It is seen that  $\alpha > 0$  over the entire temperature range. Note that, unlike the samples with  $x = 0.18$  [7], the temperatures of the extrema in the dependences of the thermopower  $\alpha(T)$  and the electrical resistivity  $\rho(T)$  for the given sample do not coincide. The first extremum of the  $\alpha$  thermopower at  $T_{\alpha 1 \text{max}}$  is observed in the range of the transition to the ordered phase [3]. In our opinion, the onset of this transition corresponds to  $\sim 130$  K.

As the pressure increases, the thermopower  $\alpha_{1 \text{max}}$  at the first maximum initially increases, then slightly decreases at the pressure  $P = 9.2$  kbar, and drastically increases at  $P = 12.5$  kbar. The temperature  $T_{\alpha 1 \text{max}}$  also depends nonmonotonically on the pressure:  $T_{\alpha 1 \text{max}}$  increases with an increase in the pressure  $P$  to 9.2 kbar and, at  $P = 12.5$  kbar, returns to its initial (at  $P = 0$ ) value. At the temperature  $T_{\alpha 2 \text{max}} \sim 250$  K, the thermopower  $\alpha_{2 \text{max}}$  at the second maximum is nearly twice as large as  $\alpha_{1 \text{max}}$  in the pressure range  $P < 10$  kbar. The second maximum  $\alpha_{2 \text{max}}$  is observed at temperatures above  $T_C$  ( $\sim 200$  K), which was determined from the data on electrical resistivity. According to the phase

diagram [8], this maximum corresponds to the paramagnetic insulating phase. Compared to  $\alpha_{1 \text{max}}$ , the  $\alpha_{2 \text{max}}$  thermopower varies inversely with the pressure. As the pressure  $P$  increases to 9.2 kbar, the  $\alpha_{2 \text{max}}$  thermopower decreases in magnitude and shifts toward the low-temperature range. At  $P = 12.5$  kbar, the value of  $\alpha_{2 \text{max}}$  remains unchanged compared to that at  $P = 9.2$  kbar, but its temperature decreases by approximately 20 K. The thermopower minimum  $\alpha_{\text{min}}$  is observed at the midpoint between  $T_{\text{CO}}$  and  $T_C$ . This is the sole extremum whose parameters monotonically depend on the pressure:  $\alpha_{\text{min}}$  and  $T_{\alpha \text{min}}$  increase, i.e.,  $dT_{\alpha \text{min}}/dP = 1.7$  K/kbar and  $d\alpha_{\text{min}}/dP = 2.1$  ( $\mu\text{V/K}$ )/kbar. The main features of the  $\alpha(T)$  curve at a pressure of 12.5 kbar are similar to those of the  $\alpha(T)$  curves at lower pressures. However, the magnitude of  $\alpha(T)$  at  $P = 12.5$  kbar differs significantly from that at a lower pressure and the  $\alpha_{2 \text{max}}$  extremum is shifted considerably to the low-temperature range. Only a weak feature is seen at the temperature of the expected extremum.

The transition observed at  $T = 282$  K in the  $\rho(T)$  curve at atmospheric pressure is rather weak and does not manifest itself in the  $\alpha(T)$  curves.

**3.2. Electrical resistivity.** The experimental data on the electrical resistivity  $\rho$  of the sample as a function of temperature and pressure are shown in Fig. 2. As the temperature decreases from 300 K to  $T_{\text{max}}(\rho) = 202\text{--}212$  K, the electrical resistivity  $\rho$  increases at all the pressures studied and exhibits a semiconductor behavior. As a rule, the temperature  $T_{\text{max}}(\rho)$  is taken as the Curie point  $T_C$ , which corresponds to the onset of the ferromagnetic ordering. At  $T < T_C$ , the resistivity  $\rho$  decreases (as in the case of ferromagnets) to the temperature of a diffuse minimum  $T_{\text{min}}(\rho) \approx 150\text{--}155$  K.

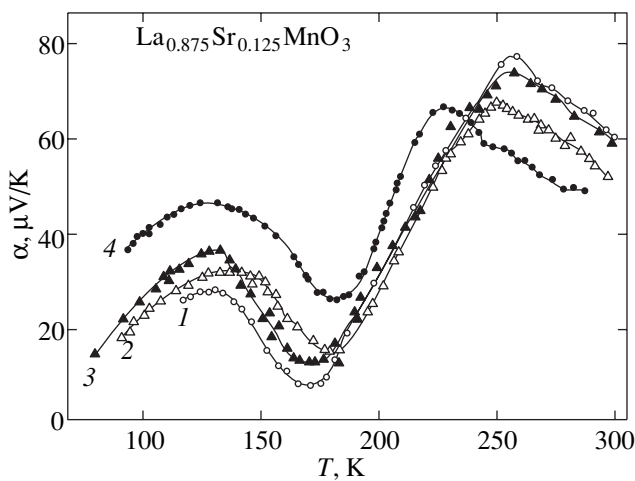


**Fig. 1.** Temperature dependences of the thermopower of  $\text{La}_{0.875}\text{Sr}_{0.125}\text{MnO}_3$  at different pressures  $P$ : (1) 0, (2) 4.3, (3) 9.5, and (4) 12.5 kbar.

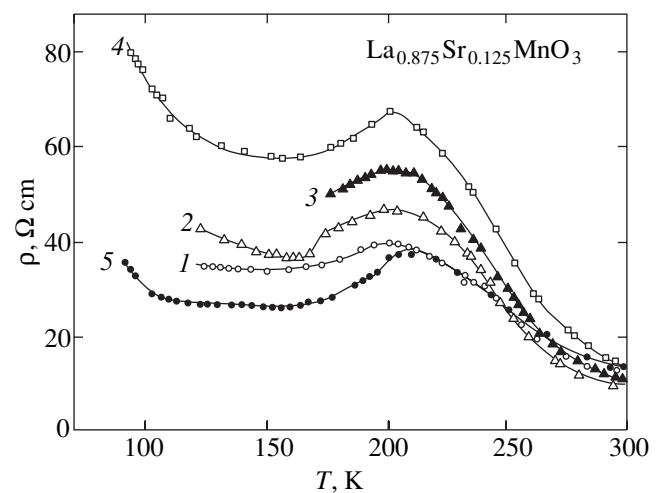


**Fig. 2.** Temperature dependences of the electrical resistivity of  $\text{La}_{0.875}\text{Sr}_{0.125}\text{MnO}_3$  at different pressures  $P$ : (1) 0, (2) 4.3, (3) 4.3 (after 3 days), (4) 4.3 (after 6 days), and (5) 9.2 kbar.

This point is treated as a charge-orbital ordering temperature  $T_{CO}$  [4]. We retain this designation and assume that the actual ordering, as will be shown below, occurs at the temperature  $T_{\alpha 1 \max} \approx 130$  K. At  $T < T_{CO}$ , the resistivity  $\rho$  also has a semiconductor behavior. Under pressure,  $\rho$  decreases and  $T_C$  shifts toward the high-temperature range at a mean rate  $dT_C/dP = 1.6$  K/kbar.

Since the curve  $\rho(T)$  has a diffuse minimum, the shift of  $T_{CO}$  with a change in the pressure is difficult to determine. It should be noted that the holding of the studied sample under a pressure  $P = 4.3$  kbar for two weeks resulted in a continuous increase in the resistivity  $\rho(T)$ , which was especially pronounced in the range  $T < T_C$ . In this case, the temperatures  $T_C$  and  $T_{CO}$  remained constant.

A small jump in the resistivity  $\rho$  (by  $\sim 0.1\%$  with a jump width of  $\sim 0.1$  K) is observed at the pressure  $P = 4.3$  kbar and  $T = 282$  K. The transition is characterized by a small ( $\sim 0.1$  K) temperature hysteresis with a shift of the temperature gradient toward the low-temperature range upon heating. We failed to reveal reliably the transition at high pressures due to its considerable smearing in temperature.

At temperatures close to  $T_{\alpha 2 \max}$ , a small anomaly in the resistivity  $\rho$  is clearly seen in Fig. 3. Figure 3 shows the dependences of the logarithm of the electrical resistivity  $\ln\rho(T)$  and the temperature gradient  $\Delta T$  across the sample at atmospheric pressure and a constant power delivered by the heater. It can be seen that, at temperatures close to  $T_{\alpha 2 \max} \approx 250$  K, an increase in the resistivity  $\rho$  is attended by an increase in the temperature gradient  $\Delta T$  across the sample, which is proportional to the thermal resistance  $R_T$ . However, at temperatures below the anomaly,  $\rho$  continues to increase, whereas  $R_T$  decreases and reaches a minimum at  $T_C$ . A similar situation is observed only at  $P = 0$  when the thermal resistance  $R_T$  of the sample is not shunted by a pressure-transferring medium.

#### 4. DISCUSSION

In general, our curves for the thermopower  $\alpha(T)$  with two maxima and one minimum in the temperature range 80–300 K (Fig. 1) are similar to the curves obtained for samples with  $x = 0.12, 0.14,$  and  $0.15$  [4] and  $x = 0.18$  [7]. In our opinion, the large difference between the  $\alpha(T)$  magnitudes determined in the present work and those obtained in [4] for  $x = 0.12$  is primarily associated with the fact that our sample corresponds to the stoichiometric composition of a specific ordered phase. In the phase diagram of the La–Sr–Mn–O system, the composition with  $x = 0.125$  plays a special role due to the formation of a new ordered cell that is commensurate with the crystal lattice. It should be noted that  $x = 0.125 = 1/8$  is a special concentration in high-temperature perovskite cuprates [9].

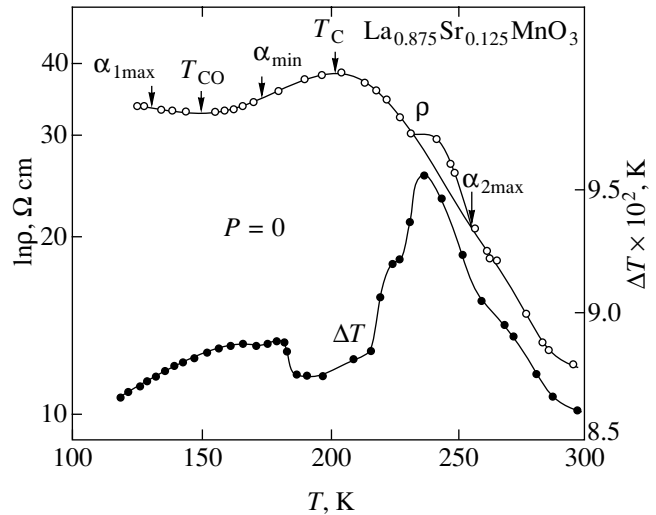


**Fig. 3.** Temperature dependences of the logarithm of the electrical resistivity  $\rho$  and the temperature gradient  $\Delta T$  across the sample of  $\text{La}_{0.875}\text{Sr}_{0.125}\text{MnO}_3$  at the pressure  $P = 0$ .

According to Kawano *et al.* [10], the sample with  $x = 0.125$  at  $T = 160$  K undergoes a structural transition  $O' \rightarrow O^*$  to the orthorhombic phase with small Jahn–Teller distortions. Endoh *et al.* [11] studied the sample with  $x = 0.12$  by resonance x-ray scattering and revealed orbital ordering with a structural modulation along the  $c$  axis at the temperature  $T = 145$  K, which corresponds to the structural phase transition  $O' \rightarrow O^*$ . The charge ordering observed by Yamada *et al.* [3] in the (001) plane was not found. Mizokawa *et al.* [12] calculated several variants of the charge ordering, which could not be observed in the experimental work [11] due to the small difference in the numbers of  $3d$  electrons on  $\text{Mn}^{3+}$  and  $\text{Mn}^{4+}$  ions.

The large difference between the temperature of the second thermopower maximum and the Curie point is of particular interest. The temperature of the second thermopower maximum ( $T_{\alpha 2 \max} = 256$  K) at atmospheric pressure is substantially higher than the Curie point  $T_C = 202$  K. A similar situation was observed for the sample with  $x = 0.12$  [4]. On the other hand, close values of  $T_{\alpha 2 \max}$  and  $T_C$  were obtained in experiments for samples with  $x = 0.15$  [4] and  $0.18$  [7]. Although the maximum under consideration corresponds to the paramagnetic insulating phase, its origin is closely allied to the transition to the ferromagnetic state at  $T_C$ . As follows from the theoretical [13, 14] and experimental [15] data, ferromagnetic clusters (polarons  $\sim 12$  Å in size) nucleate at  $T \sim 1.8T_C$ . As the temperature decreases, they increase in size and, at  $T_C$ , merge together to form a continuous charge flow [13, 14]. However, these clusters affect the thermopower at temperatures far above the Curie point.

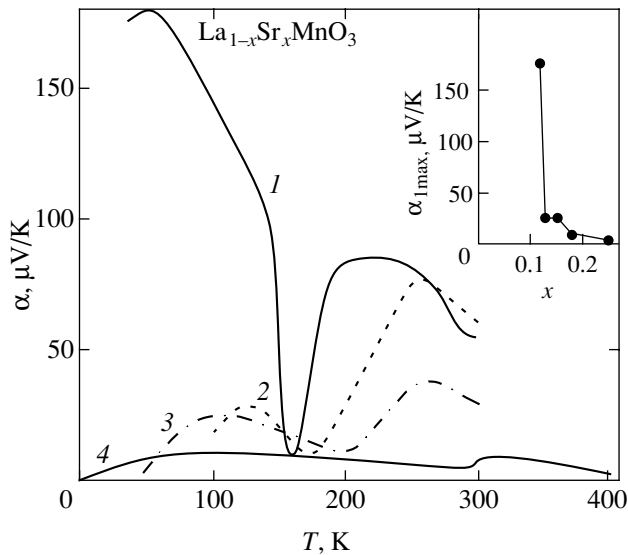


**Fig. 4.** Temperature dependences of the thermopower  $\alpha$  at atmospheric pressure for  $\text{La}_{1-x}\text{Sr}_x\text{MnO}_3$  at different contents  $x$ : (1) 0.12 [4], (2) 0.125 (this work), (3) 0.15 [4], and (4) 0.18 [7]. The inset shows the dependence of  $\alpha_{1\text{max}}$  on  $x$  for the specified compositions.

The fact that ferromagnetic clusters can exist at  $T > T_C$  is confirmed by the experimental data on small-angle neutron scattering and magnetic susceptibility [15]. According to the neutron diffraction data [10], as the temperature decreases, the  $\text{La}_{1-x}\text{Sr}_x\text{MnO}_3$  compound with  $x = 0.125$  at  $T_H = 260$  K undergoes a structural phase transition from the orthorhombic (pseudocubic) phase  $O$  to the orthorhombic phase  $O'$ , which is characterized by large Jahn–Teller lattice distortions. It is quite possible that the anomalies observed in the electrical resistivity and the thermal resistance at  $T_{\alpha 2\text{max}}$  (Fig. 3) and the thermopower maximum  $\alpha_{2\text{max}}$  at  $T = 256$  K are explained by this phase transition. It is most likely that this transition contributes significantly to the formation of ferromagnetic clusters. Hence, the decrease in  $\alpha$  at  $T < T_{\alpha 2\text{max}}$  is observed at temperatures substantially higher than  $T_C$  and the clusters gradually merge together. According to the assumption made by Kawano *et al.* [10], the ferromagnetic ordering severely hinders the Jahn–Teller distortions, which leads to the  $O' \rightarrow O^*$  structural transition at  $T_L = 160$  K.

As a result of this transition, the Curie temperature  $T_C$  in our experiments occurs at the midpoint of the temperature range of the  $O'$  phase and the boundary temperature  $T_L$  of this phase virtually coincides with the temperature  $T_{\text{CO}} \approx 150\text{--}155$  K, which is attributed to the formation of the ordered phase [3, 11].

The temperature of the thermopower minimum  $T_{\alpha\text{min}} = 175$  K lies between  $T_{\text{CO}}$  and  $T_C$  and, quite probably, can be associated with the magnetic ordering. Within the limits of experimental error, no anomalies

are observed in the  $\alpha(T)$  curves at  $T_{\text{CO}}$ . It can be assumed that a magnetic transition, rather than the formation of a charge-ordered phase, occurs at  $T_{\text{CO}}$ . For example, Ghosh *et al.* [16] studied the  $\text{La}_{1-x}\text{Sr}_x\text{MnO}_3$  compound with  $x = 0.1$  at  $T = 100\text{--}110$  K and revealed a new phase with an increased magnetic susceptibility strongly dependent on the magnetic field. We believe that the transition to the new ordered orthorhombic phase occurs at the temperature  $T_{\alpha 1\text{max}} \approx 130$  K. For this phase, a decrease in the temperature is accompanied by a decrease in the thermopower  $\alpha$  and a steep increase in the electrical resistivity  $\rho$ . In the temperature range  $T_{\alpha 1\text{max}}\text{--}T_{\text{CO}}$ , the resistivity  $\rho$  shows a weak semiconductor behavior. Thus, the new phase in this range exhibits specific features of a ferromagnetic insulating phase.

Under pressure, the  $T_C$  temperature, which was determined from the  $\rho(T)$  dependence (Fig. 2), and the  $T_{\alpha 2\text{max}}$  temperature become closer to each other in magnitude:  $T_C$  increases and  $T_{\alpha 2\text{max}}$  decreases. The value of  $T_C$  obtained by the extrapolation of the resistivity data to the pressure  $P = 12.5$  kbar is very close to  $T_{\alpha 2\text{max}}$ . It can be assumed that, at the pressure  $P = 12.5$  kbar, the system under investigation is very close to the phase transition to the ferromagnetic metallic state, for which both maxima coincide [4, 7]. The  $P$ – $T$  phase diagram for the sample with  $x = 0.14$  [4] also indicates that the phase transition can occur under pressure. Apparently, the transition to the ferromagnetic metallic phase at  $P > 11$  kbar and, then, the metal–insulator transition with a decrease in the temperature can be responsible for a sharp temperature shift of both maxima of the thermopower  $\alpha$  and a change in their magnitudes.

Figure 4 depicts the temperature dependences of the thermopower at atmospheric pressure for the  $\text{La}_{1-x}\text{Sr}_x\text{MnO}_3$  samples with different contents  $x$  according to the data taken from [4, 7] and those obtained in the present work. It is clearly seen that the magnitudes of  $\alpha(T)$  at both maxima decrease with an increase in the strontium content  $x$ . The temperatures of the maxima variously depend on  $x$ . An increase in  $x$  leads to an increase in the  $T_{\alpha 2\text{max}}$  temperature, whereas  $T_{\alpha 1\text{max}}$  changes nonmonotonically. The thermopower  $\alpha_{\text{min}}$  only slightly depends on  $x$ . The  $T_{\alpha\text{min}}$  temperature with an increase in  $x$  shifts toward the high-temperature range in the same way as the  $T_C(x)$  temperature. According to our assumptions, the stoichiometry of the composition with  $x = 0.125$  should manifest itself in the temperature range  $T < T_{\alpha 1\text{max}}$ . This is illustrated by the dependence  $\alpha_{1\text{max}}(x)$  shown in the inset in Fig. 4. A sharp jump in  $\alpha_{1\text{max}}$  by a factor of more than six when passing from  $x = 0.125$  to  $x = 0.12$  suggests that the stoichiometric charge-ordered phase is formed when the  $x$  value is sufficiently close to the composition of our sample.

All the main differences between the results obtained by Zhou *et al.* [4] and our data can be associated with the different phase states of samples with  $x =$

0.12 and 0.125. The results of many works dealing with perovskite cuprates and perovskite manganates were explained in terms of the phase transitions at  $x = N/8$ , where  $N$  is an integer (see, for example, [17]).

It is of interest to investigate how the dependence  $\rho(T)$  at a pressure of 4.3 kbar varies with time. Sequential measurements performed for different time intervals revealed a continuous increase in the resistivity  $\rho$ , which was especially pronounced at temperatures below 200 K. After holding the samples under pressure for two months, the resistivity  $\rho$  increased by more than 50%, whereas the  $T_C$  and  $T_{CO}$  temperatures remained constant. Note that the change in the thermopower  $\alpha(T)$  did not exceed the experimental error. In our opinion, this can be explained by the fact that the impurities scattering holes are ordered with time. In this case, the correlation between the scattering centers becomes stronger, the scattering probability  $\sim 1/\tau$  increases, and hence, the electrical resistivity also increases. At the same time, the thermopower is most likely determined not by the magnitude of the time constant  $\tau$  but by its energy dependence  $\tau(E)$ , which changes only slightly. Since the dependence  $\rho(T)$  was measured after holding under pressure for a certain time, we could not elucidate how the pressure affects the electrical resistivity  $\rho$ .

At  $T > T_{\max}(\rho)$ , the sample undergoes a transition from the ferromagnetic to the paramagnetic state and the dependence  $\rho(T)$  exhibits a semiconductor behavior. The dynamic Jahn–Teller distortions are observed in samples with  $x = 0.1–0.3$ . A decrease in  $\rho(T)$  in the temperature range  $T > T_{\max}(\rho)$  is consistent with a band gap of 0.2 eV at 300 K, which was found by Chainemi *et al.* [18] for samples with  $x = 0–0.4$ . This band gap corresponds to the Mott transition mechanism [14]. As follows from the Mott criterion,  $\rho$  is proportional to  $\alpha$  and decreases under pressure.

According to [14], strontium-doped  $\text{LaMnO}_3$  at  $T > T_C$  is characterized by the band dielectric spectrum which is split into four branches when the superstructure is superposed on the cubic lattice due to the Jahn–Teller distortions of  $\text{MnO}_6$  octahedra. As the hole concentration increases, the superstructure becomes energetically unfavorable. This leads to the first-order transition, which, in turn, brings about the formation of coexisting clusters enriched and depleted in holes. This process can be responsible for the transition observed in [4] and in the present work at  $T = 282$  K.

As was noted in [13, 14], one hole formed by one Sr ion can be localized in eight equivalent  $\text{Mn}^{4+}$  sites and the wave function of the hole extends outside the cell. As a result, there appears a correlation between the sites, which brings about the ferromagnetic magnetization of the spins of the manganese ions surrounding the  $\text{Sr}^{2+}$  ion. At a threshold value of  $x$ , bivalent  $\text{Sr}^{2+}$  ions of the adjacent sites begin to form an infinite conducting cluster. It can be assumed that the decrease in  $\rho(T)$  and  $\rho_{\max}$  (which was observed in [4] and in the present work

at  $T_{CO} < T < T_C$ ) over a temperature range of  $\sim 50$  K corresponds to the percolation of carriers along the bonds between the sites. Thus, the sample consists of the dielectric phase and the conducting ferromagnetic phase involving charge transfer paths [13, 14]. The formation of two-phase states is characteristic of the doping mechanisms for both manganates and high-temperature cuprates.

## 5. CONCLUSIONS

The results of the investigation performed can be summarized as follows.

(1) The pressure dependences of  $\alpha(T)$  and  $\rho(T)$  were measured for the  $\text{La}_{1-x}\text{Sr}_x\text{MnO}_3$  sample with  $x = 0.125$ , which corresponds to the stoichiometric ( $N/8$ ) composition of the specific ordered orthorhombic phase.

(2) Two maxima were revealed in the  $\alpha(T)$  dependence. The first low-temperature maximum was attributed to the formation of the ferromagnetic insulating phase. The second high-temperature maximum was associated with the  $O \rightarrow O'$  structural phase transition and the formation of ferromagnetic clusters.

(3) The assumption was made that the particular ferromagnetic phase with a weak localization of carriers and an increased magnetic susceptibility exists in the temperature range  $T_{\alpha 1 \max} - T_{CO}$ .

(4) The pressure and temperature dependences of the thermopower  $\alpha$  and the electrical resistivity  $\rho$  were discussed in terms of the models proposed in [13, 14]. It was assumed that the phase transition from the ferromagnetic polaron state to the ferromagnetic metallic state occurs in the pressure range 9–12 kbar.

(5) The electrical resistivity jump, which was observed at temperature  $T = 282$  K and pressure  $P = 4.3$  kbar, was explained by the segregation into hole-enriched and hole-depleted regions.

## ACKNOWLEDGMENTS

We are grateful to É.L. Nagaev for useful remarks and L.I. Koroleva for her participation in discussions of the results.

This work was supported by the Russian Foundation for Basic Research (project no. 00-02-16019), the “High-Temperature Superconductivity” Program of the Russian Federation, and the International Association of Assistance for the promotion of cooperation with scientists from the New Independent States of the former Soviet Union (project INTAS no. 99-1136).

## REFERENCES

1. E. S. Itskevich, V. F. Kraidenov, and I. G. Kuzemskaya, *Zh. Éksp. Teor. Fiz.* **118** (3), 647 (2000) [*JETP* **91**, 562 (2000)].
2. J.-S. Zhou and J. B. Goodenough, *Phys. Rev. Lett.* **77** (1), 151 (1996).

3. Y. Yamada, O. Hino, S. Nohdo, *et al.*, Phys. Rev. Lett. **77** (5), 904 (1996).
4. J.-S. Zhou, J. B. Goodenough, A. Asamitsu, and Y. Tokura, Phys. Rev. Lett. **79** (17), 3234 (1997); J.-S. Zhou and J. B. Goodenough, Phys. Rev. B **62** (6), 3834 (2000).
5. A. M. Balbashov and S. K. Egorov, J. Cryst. Growth **52** (2), 498 (1981).
6. S. L. Bud'ko, A. G. Gapotchenko, E. S. Itskevich, and V. F. Kraïdenov, Prib. Tekh. Éksp., No. 5, 189 (1986); V. F. Kraïdenov and E. S. Itskevich, Fiz. Nizk. Temp. **22** (9), 1028 (1996) [Low Temp. Phys. **22**, 784 (1996)].
7. A. Asamitsu, Y. Morimoto, and Y. Tokura, Phys. Rev. B **53** (6), 2952 (1996).
8. A. Urushibara, Y. Morimoto, T. Arima, *et al.*, Phys. Rev. B **51** (20), 14103 (1995).
9. A. Bianconi and M. Missuri, Solid State Commun. **91** (4), 287 (1994).
10. H. Kawano, R. Kajimoto, V. Kubota, and H. Yoshizawa, Phys. Rev. B **53** (5), 2202 (1996); Phys. Rev. B **53** (22), 14709 (1996).
11. J. Endoh, K. Hirota, S. Ishibara, *et al.*, Phys. Rev. Lett. **82** (21), 4328 (1999).
12. T. Mizokawa, D. I. Khomskii, and G. A. Sawatzky, Phys. Rev. B **61** (6), R3776 (2000).
13. É. D. Nagaev, Usp. Fiz. Nauk **166** (8), 833 (1996) [Phys. Usp. **39**, 781 (1996)].
14. L. P. Gor'kov, Usp. Fiz. Nauk **168** (6), 665 (1998) [Phys. Usp. **41**, 589 (1998)].
15. J. M. de Teresa, M. R. Ibarra, P. A. Algarabel, *et al.*, Nature (London) **386**, 256 (1997).
16. K. Ghosh, R. L. Green, S. T. Loflanad, *et al.*, Phys. Rev. B **58** (13), 8206 (1998).
17. *Abstracts of the Second International Conference on Stripes, Rome, 1998.*
18. A. Chainemi, H. Mathew, and D. Sarma, Phys. Rev. B **47**, 15397 (1993).

*Translated by O. Borovik-Romanova*

---

## MAGNETISM AND FERROELECTRICITY

---

# Specific Features in Thermal Expansion of $R\text{Fe}_{11}\text{Ti}$ Single Crystals

V. V. Zubenko, I. S. Tereshina, I. V. Telegina, E. A. Tereshina,  
D. O. Luchev, and N. Yu. Pankratov

Moscow State University, Vorob'evy gory, Moscow, 119899 Russia

e-mail: irina@rem.phys.msu.su

Received November 15, 2000

**Abstract**—Thermal expansion and its anomalies in the vicinity of spin-reorientation phase transitions in single crystals of  $R\text{Fe}_{11}\text{Ti}$  ( $R = \text{Y, Tb, Dy, Ho, and Er}$ ) compounds are investigated by the tensometric technique in the temperature range 77–400 K. The temperature dependences of the thermal expansion coefficient  $\alpha(T)$  are obtained. It is found that the  $\text{YFe}_{11}\text{Ti}$  and  $\text{HoFe}_{11}\text{Ti}$  uniaxial magnetic materials exhibit pronounced anomalies in the  $\alpha$  coefficient at  $T = 200$  and 290 K. For the  $\text{TbFe}_{11}\text{Ti}$  single crystal, the  $\alpha$  coefficient is close to zero in the vicinity of the spin-reorientation phase transition (at  $T = 325$  K). For the  $\text{DyFe}_{11}\text{Ti}$  single crystal, which is characterized by two spin-reorientation phase transitions (at  $T = 120$  and 250 K), no features in the  $\alpha(T)$  dependence are revealed in the region of the low-temperature spin-reorientation phase transition. In the  $\text{ErFe}_{11}\text{Ti}$  single crystal, the specific feature of thermal expansion is observed at  $T \sim 220$  K. © 2001 MAIK “Nauka/Interperiodica”.

## 1. INTRODUCTION

Iron compounds with rare-earth metals ( $R\text{Fe}_{11}\text{Ti}$ ) are convenient model objects owing to the specific features of their crystal and magnetic structures. Compounds  $R\text{Fe}_{11}\text{Ti}$  have a crystal structure of the  $\text{ThMn}_{12}$  type with the space symmetry group  $I4/mmm$  and a tetragonal body-centered Bravais cell ( $a \sim 8.5$  Å,  $c \sim 4.8$  Å, and  $c/a \sim 0.56$ ). A cell involves two formula units. Rare-earth atoms  $R$  are located in the  $[0\ 0\ 0]$  and  $[1/2\ 1/2\ 1/2]$  positions. Iron and titanium atoms occupy three general eightfold positions  $8f$ ,  $8i$ , and  $8j$  with displacement parameters  $x \sim 0.3$  and the symmetries  $2/m$ ,  $mm$ , and  $mm$ , respectively. These three positions of iron atoms can be nonequivalent due to the difference in their symmetries, the predominant occupation of the  $8i$  positions by titanium atoms (the valence configuration of titanium differs from the iron configuration), and the difference in ionic radii. As a consequence, the different positions are characterized by different displacement parameters  $x$ . This parameter also changes when passing from one R atom to another in the series of lanthanides. Making allowance for the above features in the description of the magnetic structure, the lattice can be treated as a result of the interaction between the rare-earth ion sublattice and the sublattices (up to three types) formed by iron ions.

The magnetic structure of  $R\text{Fe}_{11}\text{Ti}$  compounds is collinear ferromagnetic for yttrium and light rare-earth elements and ferrimagnetic for heavy rare-earth metals. The magnetic anisotropy of the iron sublattice is comparable in magnitude to that of the rare-earth sublattice. The main contribution to the magnetic anisotropy is made by the rare-earth metal sublattice at low tempera-

tures and by the iron sublattice at high temperatures. This explains the great diversity of magnetic structures and spin-reorientation transitions observed in these compounds.

The magnetic anisotropy and spin-reorientation phenomena in  $R\text{Fe}_{11}\text{Ti}$  compounds have been investigated in many works [1–5].

Analysis of the data available in the literature on  $R\text{Fe}_{11}\text{Ti}$  compounds shows that there is a disagreement regarding the phase transition temperatures. This situation for  $\text{DyFe}_{11}\text{Ti}$  and  $\text{TbFe}_{11}\text{Ti}$  single crystals was described in detail in [6–8].

Andreev *et al.* [9] revealed that the external magnetic field applied to the studied sample strongly affects the spin-reorientation temperature. This temperature changed by 70–80 K depending on the strength of the applied field.

The aim of the present work was to investigate the anomalies of the thermal expansion (the field-free method) in the vicinity of spin-reorientation phase transitions in the  $R\text{Fe}_{11}\text{Ti}$  single crystals (where  $R = \text{Y, Tb, Dy, Ho, and Er}$ ) under conditions when a change in the temperature leads to a gradual or jumpwise deviation of the magnetic moment from the crystallographic direction  $[001]$  (the tetragonal symmetry axis).

## 2. SAMPLE PREPARATION AND EXPERIMENTAL TECHNIQUE

Single-crystal samples of the  $R\text{Fe}_{11}\text{Ti}$  ( $R = \text{Y, Tb, Dy, Ho, and Er}$ ) alloys in the form of plates  $7\text{--}10 \times 5\text{--}8 \times 1\text{--}1.5$  mm in size were used in the measurements.

The alloys were prepared according to the technique described earlier in [10]. When developing the technique (the choice of the appropriate temperature–time schedules and the ratio between the batch components), the composition and the distribution of elements were checked by x-ray fluorescence probe microanalysis. The final testing of the surfaces of single-crystal samples was performed at the Trzebiatowski Institute of Low Temperature and Structure Research (Wroclaw, Poland). The distribution of elements and the composition were determined from the ratio between the intensities of the Fe and Ti  $K_{\alpha}$  lines and the  $L_{\alpha}$  lines of rare-earth elements. The composition was derived by the standard method with ZAF corrections. The largest deviations of the iron-to-titanium content ratio (up to 0.9 instead of the calculated value of 1.0) were observed for single crystals with  $R = \text{Tb}$ ,  $\text{Dy}$ , and  $\text{Er}$ .

In the course of the preparation of single-crystal plates, we determined the crystal lattice type and the unit cell parameters and checked their correspondence to the space group by x-ray diffraction analysis. The parameters obtained are in good agreement with the available data [11]. The samples were cut from an ingot according to the orientation of the crystallographic axes with respect to the surface. The plates prepared were investigated by x-ray topography.

The plates chosen for our investigations contained aggregates of large-sized single-crystal blocks (three or four blocks) with a misorientation of no more than  $2^{\circ}$ . According to the estimates, the surface of single crystals was of good quality. As a rule, the two opposite surfaces of the plate had a virtually identical block character. Strain gauges were cemented to the surface of the single-crystal sample along the [001] and [110] crystallographic directions.

The thermal expansion was measured by the tensorimetric technique. The strain gauges used in the measurements were fabricated from a strain-sensitive wire without a noticeable galvanomagnetic effect. The nominal length of the strain gauges was 5 mm, and their resistance was equal to about 100  $\Omega$ . The strain gauge factor  $S$  was equal to 2.15 over the entire temperature range. In the measurements, one of the strain gauges was cemented to the sample and the other (temperature-compensating) gauge was cemented to a thin quartz plate that was kept against the sample. Both gauges were connected across the opposite arms of a Wheatstone bridge. The resistances of the operating and temperature-compensating strain gauges differed by no more than 1%. The circuit was calibrated by measuring the signal of the out-of-balance bridge when a standard resistor of 0.1  $\Omega$  was connected in the circuit. Polycrystalline nickel was used as a reference sample.

Since the main purpose of the present work is to investigate the transformation of the magnetic structure in the vicinity of spin-reorientation transitions in the studied compounds, and since the reorientation mecha-

nism is associated primarily with the deviation of the magnetic moments from the [001] crystallographic direction, this paper presents the results of measurements of the thermal expansion only along the [001] direction in the sample plane. The temperature dependences measured along the [110] direction do not provide radically new information and will not be discussed in this work. The samples to be measured were preliminarily cooled to a temperature of 80 K. Then, the samples were heated at a rate of less than 1 K/min. The measurements were performed in the temperature range 80–400 K. The sample in a cryostat was mounted in an electromagnet gap, which allowed us to measure the thermostriction and magnetostriction in the temperature range 80–400 K in magnetic fields up to 12 kOe.

The error in measurements of the elongation per unit length did not exceed 3%. The absolute error in the measurements was determined by the accuracy of measuring the current of the out-of-balance bridge and was approximately equal to  $10^{-5}$  (8%).

The thermal elongation of a macroscopic sample (the change in the nominal length of the strain gauge) can be strongly affected by accidental temperature and instrumental errors or undetectable defects in the sample. In order to avoid these blunders, the elongations were measured upon repeated mounting of the strain gauge to the sample and replacement of the given sample by another (the measurements were performed for at least two different plate samples). In different series of measurements, the absolute elongations varied insignificantly but the character of the thermal expansion remained unchanged.

The temperature dependence of the linear thermal expansion coefficient  $\alpha(T)$  was obtained by numerical differentiation of the temperature dependence of the thermal expansion  $\Delta l/l(T)$ , that is,

$$\alpha(T) = \frac{1}{l} \frac{d}{dT} l(T).$$

According to our estimates, the error in determination of the thermal expansion coefficient did not exceed 10%.

### 3. RESULTS AND DISCUSSION

**3.1.  $\text{YFe}_{11}\text{Ti}$ .** In this work, particular emphasis was placed on the  $\text{YFe}_{11}\text{Ti}$  compound. Yttrium ions have no localized magnetic moments. This makes it possible to investigate the specific features of thermal expansion of the iron sublattice in  $R\text{Fe}_{11}\text{Ti}$  compounds. The  $\text{YFe}_{11}\text{Ti}$  compound possesses uniaxial magnetic anisotropy of the easy magnetization axis (EMA) type over the entire temperature range of magnetic ordering. The temperature dependence  $\Delta l/l(T)$  for the  $\text{YFe}_{11}\text{Ti}$  single crystal is depicted in Fig. 1. The inset in Fig. 1 shows the temperature dependence of the linear thermal expansion coefficient  $\alpha(T)$ . Both dependences exhibit two clearly pronounced features at  $T \approx 200$  and  $\approx 290$  K. According to



Bordyakov and Nikitin [12], the dependence of the Young's modulus  $E$  for this compound also shows a kneelike inflection of the relaxation type in the temperature range 170–300 K, which is accompanied by a characteristic broad maximum of the internal friction  $Q^{-1}$ .

The complex behavior of the  $\alpha(T)$  dependence can be explained by the fact that iron ions in the lattice of  $\text{YFe}_{11}\text{Ti}$  compounds occupy three crystallographically nonequivalent positions ( $8i$ ,  $8j$ , and  $8f$ ) and can be treated as ions forming three sublattices. Note that the magnetic moments localized on iron atoms occupying different crystallographic positions in  $\text{YFe}_{11}\text{Ti}$  considerably differ from each other in magnitude and are equal to 1.92 ( $8i$ ), 2.28 ( $8j$ ), and 1.8 ( $8f$ ) [13]. It is known that iron atoms can interact ferromagnetically and antiferromagnetically when the distance between them is larger and smaller than 2.4 Å, respectively. The Fe–Fe distance in particular pairs is less than the critical value, and they can undergo negative exchange interactions. The temperature dependences of the magnetization for particular iron sublattices can have a different shape, which leads to the features observed in the thermal expansion of the  $\text{YFe}_{11}\text{Ti}$  single crystal.

**3.2.  $\text{TbFe}_{11}\text{Ti}$ .** The  $\text{TbFe}_{11}\text{Ti}$  compound undergoes an EMA plane–EMA spin-reorientation transition at  $T_{\text{SR}} = 325$  K. The temperature dependence of the thermal expansion  $\Delta l/l$  for the  $\text{TbFe}_{11}\text{Ti}$  single crystal is displayed in Fig. 2. It can be seen that the thermal expansion  $\Delta l/l$  increases with a rise in temperature over the entire temperature range studied. The dependence  $\Delta l/l(T)$  deviates from the monotonic behavior at temperatures  $T > 300$  K: the slope of the curve changes substantially. It should be noted that the slope of the thermal expansion curve for the  $\text{TbFe}_{11}\text{Ti}$  single crystal also slightly changes at  $T = 140$  K and the curve has a weakly pronounced bend at  $T = 240$  K. These features are more clearly seen in the temperature dependence of the linear thermal expansion coefficient  $\alpha(T)$  (see the inset in Fig. 2). According to Andreev and Zadvorkin [11], distortions of the crystal structure (of the orthorhombic type) occur at  $T < 240$  K. It seems likely that the constant  $\alpha$  value observed in our work at  $T < 240$  K is associated with the crystal lattice deformation which compensates for the elastic thermal expansion of the lattice. The coefficient  $\alpha$  is close to zero in the vicinity of the spin-reorientation transition (at  $T_{\text{SR}} = 325$  K). In this case, the temperature dependence of the thermal expansion  $\Delta l/l(T)$  is attended by a considerable temperature hysteresis, which is characteristic of a first-order phase transition.

**3.3.  $\text{DyFe}_{11}\text{Ti}$ .** In our earlier work [6], we demonstrated that the  $\text{DyFe}_{11}\text{Ti}$  compound is characterized by the following two spin-reorientation transitions. (1) The second-order spin-reorientation transition of the EMA cone–EMA type occurs at  $T_{\text{SR1}} = 250$  K; upon cooling, the magnetic moment gradually deviates from the  $\mathbf{c}$  axis in the (010) plane and the  $\theta_0$  angle becomes

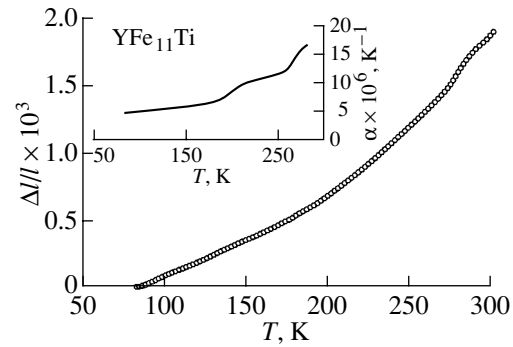


**Fig. 1.** Temperature dependence of the thermal expansion  $\Delta l/l$  along the  $\mathbf{c}$  axis for the  $\text{YFe}_{11}\text{Ti}$  single crystal. The inset shows the temperature dependence of the linear thermal expansion coefficient for the  $\text{YFe}_{11}\text{Ti}$  single crystal.

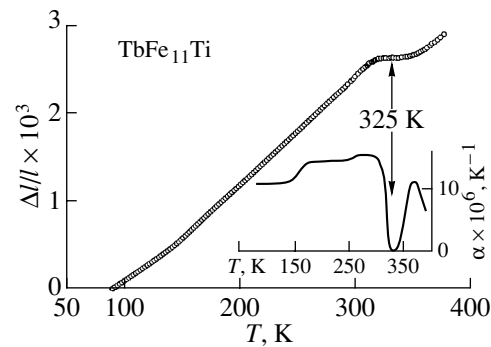


**Fig. 2.** Temperature dependence of the thermal expansion  $\Delta l/l$  along the  $\mathbf{c}$  axis for the  $\text{TbFe}_{11}\text{Ti}$  single crystal. The inset shows the temperature dependence of the linear thermal expansion coefficient for the  $\text{TbFe}_{11}\text{Ti}$  single crystal.

as large as  $45^\circ$ . (2) The jumpwise reorientation of the magnetic moment in the basal plane (the first-order phase transition) is observed at  $T_{\text{SR2}} = 122$  K. Surprisingly, we revealed neither features of thermal expansion in the low-temperature range (Fig. 3) nor the hysteresis that usually accompanies first-order phase transitions. This surprising fact was also noted by Andreev and Zadvorkin [11], who studied the temperature dependence of the lattice parameters of this compound. Upon heating of the sample, the thermal expansion coefficient  $\alpha(T)$  exhibits a feature associated with the iron sublattice in the range of  $T \approx 200$  K (see the inset in Fig. 3), passes through a weak local minimum at  $T \approx 250$  K (in the range of the spin-reorientation transition), and then increases.

**3.4.  $\text{HoFe}_{11}\text{Ti}$ .** The  $\text{HoFe}_{11}\text{Ti}$  compound, like  $\text{YFe}_{11}\text{Ti}$ , is a uniaxial material, even though, in this case, the spin-reorientation phenomenon could be expected, because  $\text{Ho}^{3+}$  ions have a negative Stevens factor ( $\alpha_J < 0$ ). The temperature dependence of the thermal expansion  $\Delta l/l$  for the  $\text{HoFe}_{11}\text{Ti}$  single crystal is plotted in Fig. 4. It can be seen that the thermal

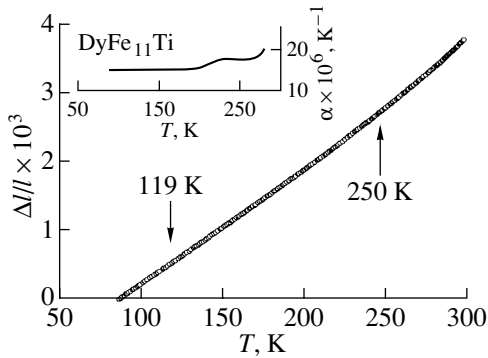


**Fig. 3.** Temperature dependence of the thermal expansion  $\Delta l/l$  along the  $c$  axis for the  $\text{DyFe}_{11}\text{Ti}$  single crystal. The inset shows the temperature dependence of the linear thermal expansion coefficient for the  $\text{DyFe}_{11}\text{Ti}$  single crystal.

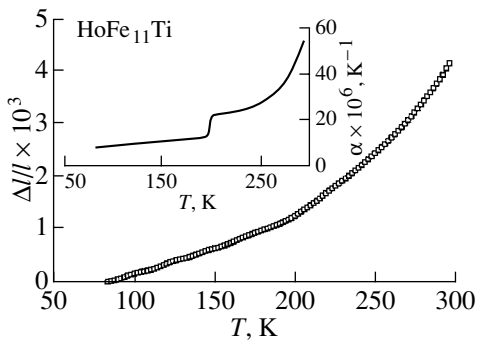


**Fig. 4.** Temperature dependence of the thermal expansion  $\Delta l/l$  along the  $c$  axis for the  $\text{HoFe}_{11}\text{Ti}$  single crystal. The inset shows the temperature dependence of the linear thermal expansion coefficient for the  $\text{HoFe}_{11}\text{Ti}$  single crystal.

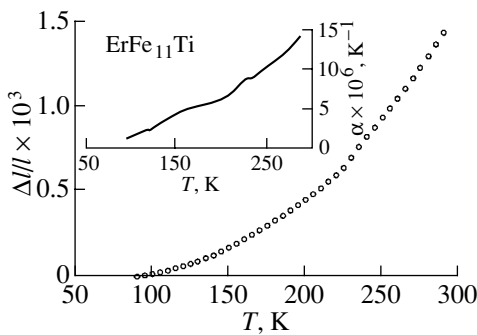


**Fig. 5.** Temperature dependence of the thermal expansion  $\Delta l/l$  along the  $c$  axis for the  $\text{ErFe}_{11}\text{Ti}$  single crystal. The inset shows the temperature dependence of the linear thermal expansion coefficient for the  $\text{ErFe}_{11}\text{Ti}$  single crystal.

expansion  $\Delta l/l$  increases with a rise in temperature over the entire temperature range covered. However, the dependence of the thermal expansion deviates from the monotonic behavior at a temperature  $T \approx 200$  K: the

slope of the curve changes considerably. This feature also clearly manifests itself in the temperature dependence of the linear thermal expansion coefficient  $\alpha(T)$  (see the inset in Fig. 4). In order to elucidate whether this feature is caused by the spin-reorientation transition, we performed similar measurements in a magnetic field of 10 kOe. At  $T < 200$  K, the curves obtained in the absence and in the presence of the magnetic field coincide to within reasonable accuracy. The slope of the  $\Delta l/l(T)$  curve measured in the magnetic field also changes at  $T \approx 200$  K. At temperatures above 200 K, this curve lies below the dependence obtained in the absence of a magnetic field. The temperature dependences  $\Delta l/l(T)$  and  $\alpha(T)$  for the  $\text{YFe}_{11}\text{Ti}$  and  $\text{HoFe}_{11}\text{Ti}$  single crystals have a similar behavior. This allows us to make the inference that the above features are associated with the iron sublattice.

**3.5.  $\text{ErFe}_{11}\text{Ti}$ .** In the  $\text{ErFe}_{11}\text{Ti}$  compound, the  $\text{Er}^{3+}$  ion, as well as  $\text{Sm}^{3+}$  and  $\text{Tm}^{3+}$  ions, has a positive Stevens factor ( $\alpha_j > 0$ ), and, hence, the spin-reorientation phenomenon should not be observed. However, the  $\text{ErFe}_{11}\text{Ti}$  compound undergoes a second-order spin-reorientation transition of the EMA cone–EMA type at temperature  $T_{\text{SR}} = 55$  K. Our measurements were performed in the temperature range 77–300 K, in which this compound is a uniaxial material. Consequently, only one feature at  $T \approx 220$  K is revealed in the temperature dependences of thermal expansion  $\Delta l/l(T)$  and the linear thermal expansion coefficient  $\alpha(T)$  (Fig. 5). This feature can be explained by the presence of the iron sublattice.

The anomaly associated with the deviation of the magnetic moment from the tetragonal axis  $c$  in the  $\text{ErFe}_{11}\text{Ti}$  compound at low temperatures and the absence of spin-reorientation transitions in the  $\text{HoFe}_{11}\text{Ti}$  compound were explained by Abadia *et al.* [14] in terms of the single-ion anisotropy theory with inclusion of higher-order (fourth and sixth) terms in the crystal-field Hamiltonian.

## ACKNOWLEDGMENTS

We would like to thank K.P. Skokov for growing the single crystals, K.D. Nierzewski for his assistance in the characterization of the samples, and S.A. Nikitin for helpful discussions of the results.

This work was supported by the State Program of Support for Leading Scientific Schools of the Russian Federation (project no. 00-15-96695) and the Russian Foundation for Basic Research (project no. 99-02-17821).

## REFERENCES

1. A. G. Savchenko and A. E. Kolchin, *Magnetic Properties of New Ternary Intermetallic Compounds Based on Fe with  $\text{ThMn}_{12}$ -Type Structure*, in *Reference Collection*

- of All-Russia Institute of Scientific and Technical Information* (VINITI, Moscow, 1990), Vol. 7.
2. H. S. Li and J. M. D. Coey, in *Handbook of Magnetic Materials*, Ed. by K. H. J. Buschow (North-Holland, Amsterdam, 1991), Vol. 6, pp. 1–84.
  3. J. J. M. Franse and R. J. Radwanski, in *Rare-Earth Iron Permanent Magnets*, Ed. by J. M. D. Coey (Clarendon Press, Oxford, 1996), pp. 178–215.
  4. L. Schultz and M. Katter, in *Supermagnets: Hard Magnetic Materials*, Ed. by G. J. Long and F. Grandjean (Kluwer Academic, Dordrecht, 1991); NATO ASI Ser., Ser. C **331**, 227 (1991).
  5. X. C. Kou, T. S. Zhao, R. Grossianger, *et al.*, *Phys. Rev. B* **47** (6), 3231 (1993).
  6. I. S. Tereshina, I. V. Telegina, and K. P. Skokov, *Fiz. Tverd. Tela* (St. Petersburg) **40** (4), 699 (1998) [*Phys. Solid State* **40**, 643 (1998)].
  7. S. A. Nikitin, T. I. Ivanova, V. V. Zubenko, *et al.*, *Fiz. Tverd. Tela* (St. Petersburg) **37** (2), 561 (1995) [*Phys. Solid State* **37**, 306 (1995)].
  8. J. Wang, G. Wu, N. Tang, *et al.*, *Appl. Phys. Lett.* **76**, 1170 (2000).
  9. A. V. Andreev, N. V. Kudrevatykh, S. M. Razgonyaev, and E. N. Tarasov, *Physica B* (Amsterdam) **183**, 379 (1993).
  10. I. S. Tereshina, S. A. Nikitin, T. I. Ivanova, and K. P. Skokov, *J. Alloys Compd.* **275–277**, 625 (1998).
  11. A. V. Andreev and S. M. Zadvorkin, *Philos. Mag. B* **77** (1), 147 (1998).
  12. V. Yu. Bodryakov and S. A. Nikitin, *Fiz. Met. Metallogr.* **80** (4), 62 (1995).
  13. Y. C. Yang, H. Sun, and L. S. Kong, *J. Appl. Phys.* **64** (10), 5968 (1988).
  14. C. Abadia, P. A. Algarabel, B. García-Landa, *et al.*, *J. Phys.: Condens. Matter* **10**, 349 (1998).

*Translated by O. Borovik-Romanova*

## MAGNETISM AND FERROELECTRICITY

# Transition to the Quasi-Two-Dimensional Magnetic State in Pd–Fe Films

R. M. Mirzababaev

Gaziantep University, 27310 Gaziantep, Turkey

e-mail: mirza@gantep.edu.tr

Received August 3, 2000; in final form, November 24, 2000

**Abstract**—The Mössbauer spectra of Pd–Fe films with different thicknesses and iron concentrations are measured. In these films, the spin fluctuations associated with the transition to a quasi-two-dimensional magnetic state are observed over a wide range of temperatures. The dependences of the magnetic field strength and the Curie temperature on the film thickness are quite consistent with the scaling theory. Owing to the long-range exchange coupling, the films containing 14.4 and 7.8 at. % Fe undergo a transition to the quasi-two-dimensional state at a film thickness of several thousand angstroms. © 2001 MAIK “Nauka/Interperiodica”.

### 1. INTRODUCTION

It is well known that no spontaneous magnetization is observed in isotropic two-dimensional Heisenberg magnets at temperatures  $T > 0$  [1]. By contrast, a magnetic order exists in real sufficiently thick three-dimensional films. As a rule, the properties of quasi-two-dimensional films, i.e., intermediate systems, are not associated with spin fluctuations throughout the quasi-two-dimensional system as a whole. For this reason, the relaxation phenomena observed in these objects with the use of the Mössbauer effect either remain only qualitatively described without their interpretation [2], are explained by the presence of foreign phases [3], or, most frequently, are ascribed to imperfect techniques used in film preparation under the assumption that uncoupled superparamagnetic clusters are formed in these films (see, for example, [4, 5]).

The present paper reports the results of Mössbauer investigations of Pd–Fe films with different thicknesses and iron concentrations. Owing to the specific features of a Pd–Fe alloy, the films prepared from this material at a sufficiently large thickness which excludes the presence of individual microcrystalline formations behave like ultrafine magnetic films.

### 2. THEORY

In the absence of an external magnetic field, the magnetization vector of a three-dimensional magnet is aligned with its easy axis. As one of the crystal sizes decreases, the anisotropy energy decreases and, at a sufficiently small thickness  $L$ , can become equal to the thermal fluctuation energy  $kT$  even at room temperature. In this case, the magnetization along the easy axis is not constant but fluctuates with the frequency  $\tau_s^{-1}$ ,

which depends on the sample thickness [6]:

$$\tau_s = \tau_0 \exp(KL/kT), \quad (1)$$

where  $\tau_0 \approx 10^{-9}$ – $10^{-11}$  s,  $k$  is the Boltzmann constant, and  $K$  is the anisotropy constant.

For a film, the magnetization averaged over a time much longer than the relaxation time,  $t \gg \tau_s$ , is equal to zero [7]. However, if  $t \leq \tau_s$ , the measured magnetization is determined by the expression

$$M(L, T) \cong M_s(1 - kT/2KL), \quad (2)$$

where  $M_s$  is the magnetization of a three-dimensional magnet.

In this case, the magnetization and, hence, the Curie temperature  $T_C$  depend on the film thickness. The time scale  $t$ , which is characteristic of the Mössbauer effect, is specified by the Larmor precession frequency  $1/\tau_L = \omega_L = -\mu H/I$  and the lifetime  $\tau$  of excited nuclei [8].

According to the scaling theory, the distance scale in the critical region is defined by the correlation length  $\xi(T)$  of the spin fluctuation [9]:

$$\xi(T) = \xi_0[(T - T_C)/T_C]^{-\nu}, \quad (3)$$

where  $\xi_0$  is the correlation length amplitude and  $\nu$  is the critical exponent.

The onset of critical phenomena is taken to be the instant of time at which the correlation length becomes approximately equal to the physical thickness of films, i.e.,  $\xi(T) \approx L$ . The dimension and the properties of films are governed by the ratio between the thickness  $L$  and the correlation amplitude  $\xi_0$ , which, in turn, depends on the character of the spin–spin interaction. This implies that the critical phenomena can be induced in different ways.

If the radius of an exchange interaction is so large that  $\xi_0 \geq L$ , even a sufficiently thick film behaves like a quasi-two-dimensional system. In the case of a short-range exchange interaction, the film thickness should be considerably reduced to the point where the inequality  $\xi(T) > L$  is fulfilled. The shift in the ordering temperature of a film serves as an indicator of a transition from the three-dimensional to the quasi-two-dimensional state [9]:

$$[T_C(\infty) - T_C(L)]/T_C(\infty) = C/L^\lambda, \quad (4)$$

where  $\lambda$  is the shift index.

The Pd-Fe alloys belong to disordered magnets in which impurity iron atoms are distributed in a random way. They magnetize the palladium matrix and, thus, produce the ferromagnetic potential whose effective range is larger than the lattice constant [10], that is,

$$V(T) = V_0 \frac{R(T)}{r} \exp\left(-\frac{r}{R(T)}\right) + V_1 \frac{\cos(2K_F r)}{(K_F r)^3}, \quad (5)$$

where  $r$  is the distance between magnetic impurities,  $V_0$  and  $V_1$  are the scale factors,  $K_F$  is the Fermi wave vector, and  $R(T)$  is the polarization radius.

The lower the temperature, the larger the radius  $R(T)$ . At a sufficiently low temperature, the exponential term becomes larger than the oscillating term and impurity atoms undergo ferromagnetic ordering. Despite a random distribution of atoms over the matrix, the strengths of magnetic fields on all iron nuclei are identical [11]. This means that the polarization radius is substantially larger than the mean distance between impurities. Therefore, the transition to the quasi-two-dimensional state in a Pd-Fe alloy should occur at a larger thickness compared to that of ordered magnets.

### 3. EXPERIMENTAL TECHNIQUE

The width of the emission line of the  $^{57}\text{Co}(\text{Cr})$  source was equal to  $2\Gamma$ . Measurements were performed in the range from 4.2 K to room temperature. The temperature was maintained to within  $\pm 1$  K in the range 150–185 K and to within  $\pm 0.1$  K otherwise. The transition temperatures were determined from the Mössbauer measurements. The widths of the Mössbauer spectra were calculated using a computer according to the model proposed by Window [12].

The Pd-Fe films were obtained in two stages. At the first stage, we prepared samples of the Pd-Fe alloys which were enriched to 92% in a  $^{57}\text{Fe}$  isotope and had iron concentrations of  $14.40 \pm 0.05$  at. % and  $7.85 \pm 0.05$  at. % [13]. At the second stage, the films were evaporated from the prepared alloys [14]. All in all, we obtained eleven films of different thicknesses and concentrations. The iron concentrations in the films were equal to  $14.4 \pm 0.5$  and  $7.8 \pm 0.5$  at. %, respectively. These values closely coincided with iron concentrations in the initial samples.

### 4. RESULTS AND DISCUSSION

Let us compare the Mössbauer spectra of a bulk Pd-Fe alloy (Fig. 1) and a Pd-Fe film 3480 Å thick (Fig. 2) which have the same iron concentration (7.85 at. %). As the temperature increases, the Mössbauer spectra of the bulk sample becomes narrower and the spectral lines shift toward the center due to a decrease in the magnetization. In the vicinity of the transition, the spectra contain only a slightly broadened single line which is a superposition of unresolved Zeeman lines. Similar results were obtained for the alloy containing 14.4 at. % Fe.

The spectra of films radically differ from the spectra of bulk samples. The spectra of films are characterized by lower magnetic fields and transition temperatures. In a temperature range of several tens of degrees, the spectra represent a superposition of poorly resolved paramagnetic and Zeeman lines. An increase in the temperature leads to a decrease in the intensity of magnetic lines and an increase in the intensity of the paramagnetic component.

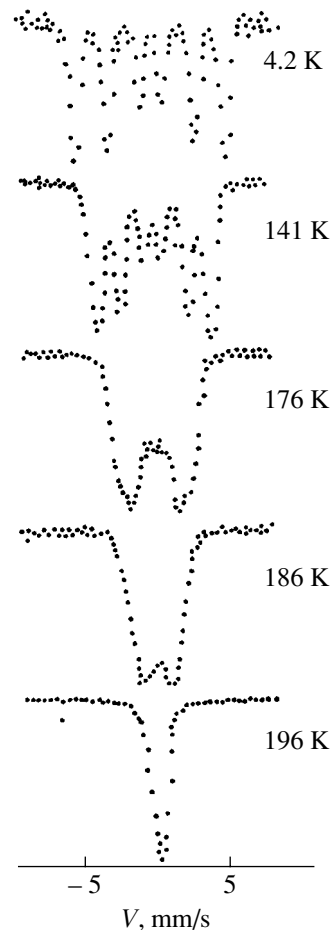
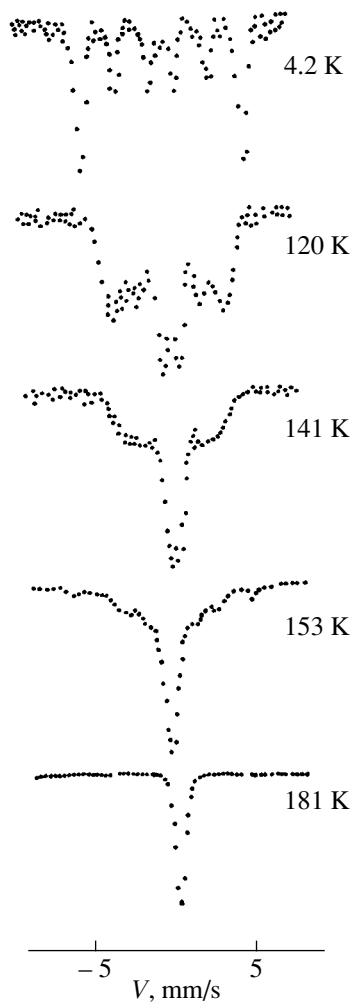
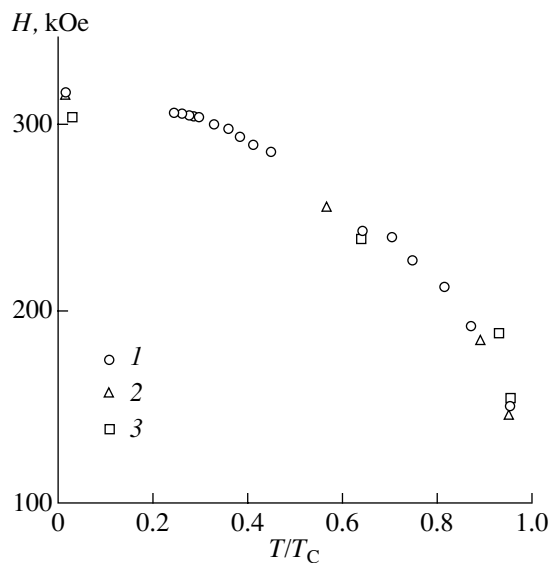


Fig. 1. Mössbauer spectra of the bulk Pd-Fe alloy at an iron concentration of 7.85 at. %.



**Fig. 2.** Mössbauer spectra of the Pd-Fe film 3480 Å thick at an iron concentration of 7.85 at. %.



**Fig. 3.** Temperature dependences of the spectrum width (hyperfine magnetic splitting) for (1) the bulk sample and (2, 3) films. Film thickness, Å: (2) 120 and (3) 350. The iron concentration is 14.4 at. %.

One of the necessary conditions for the observation of magnetic splitting, namely,  $\tau\omega_L \geq 1$ , is determined by the physical nuclear constants of a Mössbauer isotope and does not depend on the dimension of the magnetic system [15]. The second condition,  $\tau_s\omega_L \geq 1$ , implies that the nuclear moment should make several turns about the direction of the magnetic field for the time  $\tau_s$  during which this direction remains unchanged [8]. As follows from relationship (1), the second condition depends on the dimension of the magnetic system.

In three-dimensional systems, the condition  $\xi(T) \geq L$  for the onset of critical phenomena is fulfilled only at  $T \rightarrow T_c$ . Hence, the difference between the  $T_c$  values obtained by different methods is small. For ordered magnets, we have  $T - T_c = 10^{-2} - 10^{-3}$  K. To put it differently, the transition temperatures are constants. In quasi-two-dimensional systems, the condition  $\xi(T) \geq L$  is met at temperatures below  $T_c$ . The thinner the film and the larger the exchange interaction radius, the wider the temperature range  $T - T_c$  in which the critical phenomena occur, and, correspondingly, the lower the transition temperature determined from measurements.

At low temperatures ( $\tau_s\omega_L \geq 1$ ), the spectra of the films contain only the lines of magnetic splitting. The spectra have a shape similar to that as though the spins were frozen, as is the case in three-dimensional systems. The occurrence of spin fluctuations at these temperatures is confirmed by the fact that, for the same films, the transition temperatures measured by the magnetic susceptibility technique differ by several tens of degrees from the transition temperatures determined by

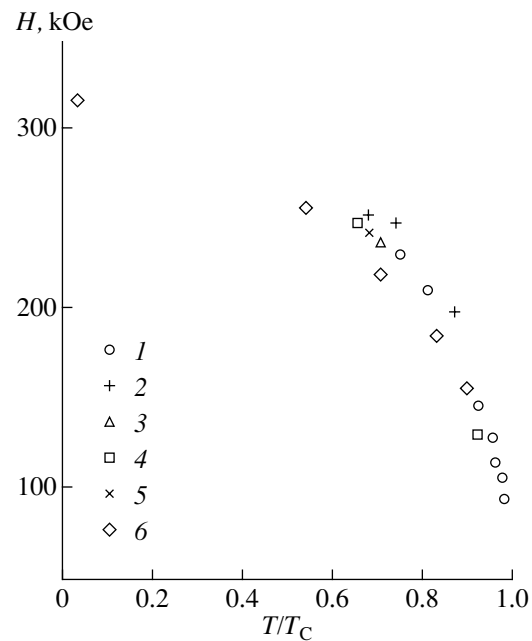


**Fig. 4.** Temperature dependences of the spectrum width (hyperfine magnetic splitting) for (1) the bulk sample and (2–6) films. Film thickness, Å: (2) 920, (3) 1100, (4) 1390, (5) 1620, and (6) 3480. The iron concentration is 7.85 at. %.

the Mössbauer method [2]. Since the time scale of magnetic measurements covers several seconds, the condition  $\tau_s \omega_L \geq 1$  is fulfilled at other temperatures.

An increase in the temperature results in the equalization of the frequencies ( $\tau_s \omega_L \approx 1$ ) and the appearance of the paramagnetic lines. In the case when  $\tau_s \omega_L \ll 1$ , the magnetic splitting disappears and only the paramagnetic line is observed.

The temperature dependences of the spectrum width (the magnetic field on nuclei) are displayed in Figs. 3 and 4. It can be seen that, irrespective of the film thickness, the magnetic fields for all films with the same iron concentration vary in a similar way with a change in the reduced temperature and coincide with those for the bulk sample. Therefore, the shift of the transition temperatures and the changes in the magnetic fields have the same origin, namely, spin fluctuations, which, in turn, arise from the transition to the quasi-two-dimensional state in the films. It is evident that the character of exchange couplings, the polarization radius  $R$ , and the amplitude  $\xi_0$  are independent of the magnet dimension.

A comparison of Figs. 3 and 4 shows that the above parameters depend on the iron concentration. An increase in the iron concentration leads to a decrease in the values of  $R$  and  $\xi_0$ . As a result, the critical thicknesses that correspond to the onset of the transition to the quasi-two-dimensional state also decrease. Note that these results indicate a high evaporation quality.

Figure 5 depicts the dependences of the magnetic phase transition temperature on the film thickness. These results are adequately described by expression (4), which relates the temperature  $T_c$  and the thickness  $L$  in the case of the transition to the quasi-two-dimensional magnetic state. The extrapolation of the obtained data by the least-squares technique gave the following parameters of films:  $\lambda_1 = 0.86$  and  $C_1 = 33.9 \text{ \AA}$  for an iron concentration of 14.4 at. % and  $T_c(\infty) = 193 \pm 7 \text{ K}$ ,  $\lambda_2 = 0.95 \pm 0.15$ , and  $C_2 = 255 \pm 5 \text{ \AA}$  for an iron concentration of 7.8 at. %.

The temperature  $T_c$ , which was calculated from the results for thin films at  $n = 7.8$  at. %, is very close to  $T_c = 192 \pm 0.1 \text{ K}$ , which was determined from the experimental data for the bulk alloy. This also confirms the validity of the model described by relationship (4).

The experimental shift indices  $\lambda$  are close to the theoretical values, which are derived within the mean-field model and are equal to unity [9]. These indices are quite inconsistent with both the index  $\lambda = 1.56$ , which was calculated in the framework of the Ising model, and the indices  $\lambda = 1.6$ – $1.7$ , which were experimentally determined for iron and nickel films [5, 16]. This can be explained by the specific features of the nature of ferromagnetism in the Pd–Fe system, specifically by the long-range couplings associated with the matrix polarization. These couplings are in better agreement with the mean-field model as compared to the Ising model in

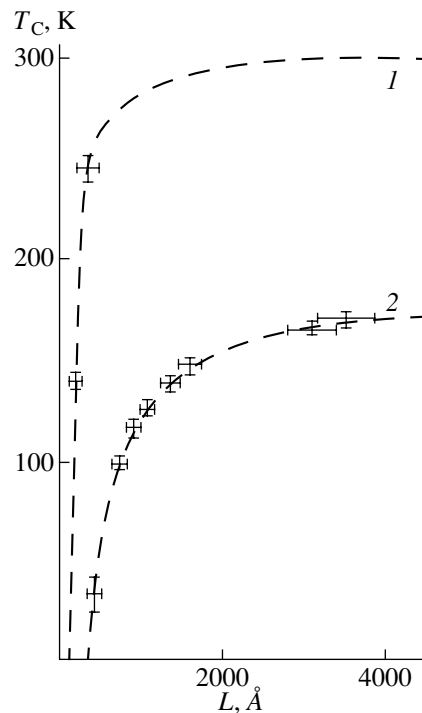


Fig. 5. Dependences of the magnetic phase transition temperature on the thickness of the Pd–Fe films containing (1) 14.4 and (2) 7.85 at. % Fe.

which only the nearest neighbors in the lattice are taken into consideration.

## 5. CONCLUSION

Thus, the transition to the quasi-two-dimensional state in the Pd–Fe films occurs at a thickness of several thousand angströms. This is explained by the fact that the radius of exchange interactions exceeds the lattice constant. The films possess superparamagnetic properties, as is the case in quasi-zero-dimensional microcrystals. The spin fluctuations are associated with the nature of quasi-two dimensional magnetic systems rather than with the presence of inhomogeneities in the structure.

## REFERENCES

1. N. D. Mermin and H. Wagner, Phys. Rev. Lett. **17**, 1133 (1966).
2. J. R. Long and R. W. Mattozzi, J. Appl. Phys. **55** (6), 2359 (1984).
3. R. D. McGrath, A. Levy, and J. C. Walker, Hyperfine Interact. **10**, 801 (1981).
4. S. Shinjo, J. Cunningham, R. Du, *et al.*, J. Magn. Magn. Mater. **54**, 773 (1986).
5. S. Duncan, A. H. Owens, R. J. Semper, and J. C. Walker, Hyperfine Interact. **4**, 886 (1978).

6. P. F. García and A. D. Meinhardt, *Appl. Phys. Lett.* **47**, 178 (1985).
7. S. Morup, *Hyperfine Interact.* **60**, 959 (1990).
8. I. P. Suzdalev, *Dynamic Effects in Mössbauer Spectroscopy* (Atomizdat, Moscow, 1979).
9. M. E. Fisher, *J. Vac. Sci. Technol.* **10** (5), 665 (1973).
10. I. Ya. Korenblit and E. F. Shender, *Usp. Fiz. Nauk* **126** (2), 233 (1978) [*Sov. Phys. Usp.* **21**, 832 (1978)].
11. P. Craig and B. Mozer, *Phys. Rev. Lett.* **14** (22), 895 (1965).
12. B. Window, *J. Phys. E* **4** (5), 401 (1971).
13. R. M. Mirzababaev, *Izv. Akad. Nauk, Met.*, No. 2, 121 (1994).
14. R. M. Mirzababaev, *Neorg. Mater.* **30** (2), 192 (1994).
15. A. M. Afanas'ev and Yu. M. Kagan, *Zh. Éksp. Teor. Fiz.* **45** (5), 1660 (1963) [*Sov. Phys. JETP* **18**, 1139 (1963)].
16. H. Lutz, O. D. Gunton, H. K. Shumann, *et al.*, *Solid State Commun.* **14** (11), 1075 (1974).

*Translated by O. Borovik-Romanova*



---

**MAGNETISM  
AND FERROELECTRICITY**

---

## Spectral Dependence of Photoinduced Optical Absorption in Doped Yttrium Iron Garnet Single Crystals

**R. A. Doroshenko and M. D. Nadezhdin**

*Institute of Molecular and Crystal Physics, Russian Academy of Sciences,  
Ufa, 450075 Bashkortostan, Russia*

*e-mail: dar@anrb.ru*

*e-mail: imcp@anrb.ru*

Received in final form December 20, 2000

**Abstract**—The photoinduced optical absorption  $\alpha$  of doped yttrium iron garnets (YIG) is investigated. It is found that the optical absorption  $\alpha$  at a wavelength of 1.1  $\mu\text{m}$  depends on the wavelength of irradiating light in the range 0.6–1.9  $\mu\text{m}$ . It is demonstrated that, in the  $\text{Y}_3\text{Fe}_5\text{O}_{12}$  crystal with an acceptor Ba impurity, the photoinduced increase in  $\alpha$  is due to the formation of  $\text{Fe}^{4+}$  ions in octahedral sites. The charge transfer occurs through photoexcitation of the  ${}^6A_{1g}({}^6S) \rightarrow {}^4T_{1g}({}^4G)$  and  ${}^6A_{1g}({}^6S) \rightarrow {}^4T_{2g}({}^4G)$  transitions of octahedral  $\text{Fe}^{3+}$  ions. In the crystal with a donor Si impurity, the increase in  $\alpha$  is caused by the formation of  $\text{Fe}^{2+}$  ions upon photoionization of silicon. © 2001 MAIK “Nauka/Interperiodica”.

### 1. INTRODUCTION

Investigation of changes in the optical properties of magnetically ordered materials under exposure to light is not only of considerable interest but also of importance in obtaining new information on photoinduced magnetic phenomena in yttrium iron garnets (YIG), which have been extensively studied in recent years [1, 2]. Gyorg *et al.* [3] observed an increase in optical absorption at the wavelength  $\lambda = 1.1 \mu\text{m}$  for  $\text{Y}_3\text{Fe}_5\text{O}_{12}$  samples doped with  $\text{Ca}^{2+}$  and bleaching for samples doped with  $\text{Si}^{4+}$ . Hisatake *et al.* [4, 5] analyzed the change in the optical absorption for undoped YIG single crystals in the spectral range 0.7–2.0  $\mu\text{m}$  after exposure to light pulses. In our recent work [6], we found that photoinduced changes in the optical absorption depend on the spectral composition and the sequence of exposure to light at different wavelengths. Under illumination, the optical density increases in YIG:Ba and decreases in YIG:Si (the main impurity is given after the colon). Note that the maximum effect was observed under illumination through IKS-7 for YIG:Si and KS-17 for YIG:Ba.

Earlier [7], we studied the photosensitivity spectrum at a wavelength of 1.1  $\mu\text{m}$  with the use of narrow-band light filters. In the present work, we experimentally investigated the photoinduced changes in the optical absorption coefficient  $\alpha$  at a wavelength of 1.1  $\mu\text{m}$  upon exposure to monochromatic light in the wavelength range 0.6–1.9  $\mu\text{m}$ . In order to elucidate the specific features of the photoinduced changes in  $\alpha$  in the course of sequential exposure to light, we examined the

time dependences of  $\alpha$  under irradiation with light at characteristic wavelengths.

### 2. SAMPLES AND EXPERIMENTAL TECHNIQUE

Measurements were performed with single crystals grown from different solvents. The YIG single crystals doped with silicon (YIG:Si) were grown from a  $\text{PbO-PbF}_2$  lead solvent, and the single crystals with a barium impurity (YIG:Ba) were grown from a  $\text{BaO-Ba}_2\text{O}_3$  solvent [8]. The barium ions were identified by secondary ion mass spectrometry. In the silicon-doped  $\text{Y}_3\text{Fe}_{5-x}\text{Si}_x\text{O}_{12}$  samples, the as-batched silicon content  $x$  was equal to 0.04. The samples used in the investigation were prepared in the form of polished single-crystal disks 0.5 mm thick.

A tungsten incandescent lamp with a power of 400 W was used as a light source. The monochromatic radiation was obtained using an MDR-12 grating monochromator. The spectral widths  $\Delta\lambda$  at the output of the monochromator were as follows:  $\Delta\lambda = 20 \text{ nm}$  in the range 0.6–1  $\mu\text{m}$  and  $\Delta\lambda = 40 \text{ nm}$  in the range 1–1.9  $\mu\text{m}$ . The light intensity  $P_0$  was maintained equal to 15 and 33  $\text{mW/cm}^2$  in the ranges 0.6–1 and 1–1.9  $\mu\text{m}$ , respectively. As follows from the experimental dependence of the optical absorption at a wavelength of 1.1  $\mu\text{m}$  on the elapsed time from the switching-on of the probing light with an intensity of  $\sim 10 \mu\text{W}$ , the probing light does not affect the optical absorption.

The optical effect was measured at a constant wavelength of 1.1  $\mu\text{m}$  after irradiation with light at different wavelengths in the range 0.6–1.9  $\mu\text{m}$ . In order to

improve the sensitivity and stability of the measuring system, we used the amplitude modulation of the probing beam followed by synchronous detection with the time constant  $\tau = 0.3$  s.

The sample was immersed in liquid nitrogen and then was illuminated until the maximum effect was attained. In this case, the intensities of the probing light were measured prior to ( $I_d$ ) and after ( $I_1$ ) exposure to light at the wavelength  $\lambda_{ir}$ . The next measurement of the effect at a new wavelength  $\lambda_{ir}$  was performed after heating the sample to room temperature. The spectral sensitivity of the optical effect, which was normalized to unit area  $\beta = (1/P_0)\ln(I_d/I_1)$  at the wavelength  $\lambda_{ir}$ , was calculated from the measured intensities  $I_d$  and  $I_1$  with due regard for the power density  $P_0$ . By this definition, the spectral sensitivity of the optical effect  $\beta(\lambda_{ir})$  is equal to the change in the absorption coefficient  $\Delta\alpha$  per unit power density [the irradiation intensity  $P_0(\lambda_{ir})$ ] at the wavelength  $\lambda_{ir}$ :  $\beta = \Delta\alpha/P_0 = (\alpha_1 - \alpha_d)/P_0$ , where  $\alpha_d$  and  $\alpha_1$  are the absorption coefficients at a wavelength of 1.1  $\mu\text{m}$  prior to and after illumination of the sample and  $d$  is the sample thickness. The coefficient  $\alpha$  decreases ( $\Delta\alpha < 0$ ) upon exposure to light at wavelengths in the range corresponding to  $\beta(\lambda_{ir}) < 0$ . By contrast,  $\alpha$  increases ( $\Delta\alpha > 0$ ) upon irradiation with light in the wavelength range where  $\beta(\lambda_{ir}) > 0$ .

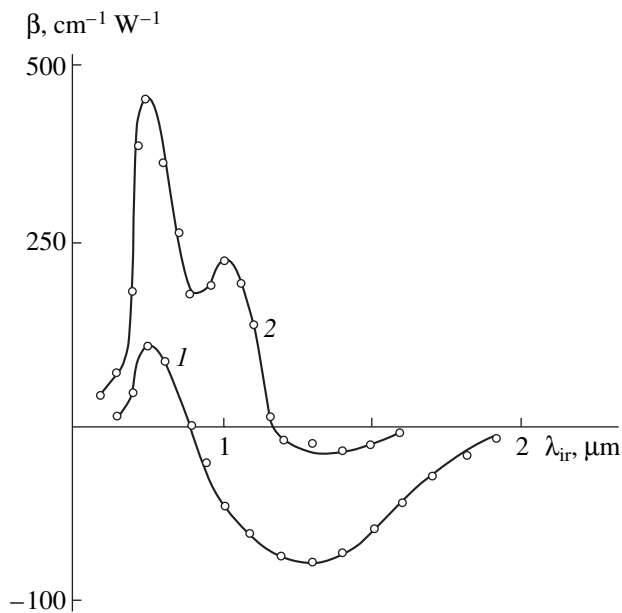


**Fig. 1.** Dependences of the photoinduced change in the optical absorption  $\beta = (\alpha_1 - \alpha_d)/P_0$  at a wavelength of 1.1  $\mu\text{m}$  after exposure to monochromatic light at wavelength  $\lambda_{ir}$  for (1) YIG:Si and (2) YIG:Ba samples.

### 3. RESULTS AND DISCUSSION

Let us consider the photosensitivity spectrum of the photoinduced change in the optical absorption for yttrium iron garnets (Fig. 1). As can be seen from the photosensitivity spectrum of YIG:Si (curve 1), the exposure of the sample to light at wavelengths in the range 0.9–1.9  $\mu\text{m}$  brings about a decrease in  $\alpha_{1.1}$  (the maximum bleaching effect is observed at 1.25  $\mu\text{m}$ ), whereas illumination in the wavelength range 0.6–0.9  $\mu\text{m}$  leads to an increase in  $\alpha_{1.1}$  (the maximum darkening effect is observed at 0.75  $\mu\text{m}$ ). The effect changes sign at a wavelength of 0.9  $\mu\text{m}$ . The photoinduced effects of bleaching and darkening are of the same order of magnitude. In the YIG:Ba crystal, the bleaching effect is induced by light at wavelengths in the range 1.15–1.6  $\mu\text{m}$ , the darkening effect is observed under irradiation with light at wavelengths of 0.6–1.15  $\mu\text{m}$ , and the effect changes sign at a wavelength of 1.15  $\mu\text{m}$  (curve 2). In the range of the darkening effect, there are two features at 0.75 and 1.0  $\mu\text{m}$ . The bleaching effect is one order of magnitude less than the darkening effect.

Now, we analyze the time dependences of the optical absorption coefficient in the course of sequential exposure to monochromatic light at different wavelengths (Fig. 2). Under irradiation with monochromatic light at a wavelength of 1.3  $\mu\text{m}$ , the optical absorption in the YIG:Ba and YIG:Si samples under investigation decreases rapidly (curves 1, 2, portions AB). The effect observed in YIG:Ba is small. At the same time, the effect in YIG:Si is comparable in magnitude to the increase in optical absorption upon exposure to light at a wavelength of 0.8  $\mu\text{m}$ . After switching the light off at a wavelength of 1.3  $\mu\text{m}$ , the optical absorption relaxes insignificantly. After repeated illumination, the optical absorption decreases by a magnitude identical to the change in the absorption in the course of relaxation (curve 2). The initial irradiation with monochromatic light at a wavelength of 0.8  $\mu\text{m}$  brings about an increase in the optical absorption in both samples (curves 1, 2, portion CD). The increase in the optical absorption proceeds more slowly. Note that, after attaining the maximum photoinduced darkening in the YIG:Ba sample, switching-off the light results in a spontaneous increase in the optical absorption (curve 1, portion DF). On the other hand, when the light is switched-off prior to reaching the maximum darkening, the optical absorption retains the magnitude observed at the switching-off instant (curve 1, portion KL). The subsequent irradiation with light at a wavelength of 1.3  $\mu\text{m}$  (points F, D) leads to a reversible decrease in  $\alpha$ . Under exposure to light at wavelengths of 1–1.1  $\mu\text{m}$ , the optical absorption first rapidly decreases and then more slowly increases to a magnitude that corresponds to the darkening effect in YIG:Si and considerably exceeds the dark absorption in YIG:Ba.

The dependence of the optical effect on  $\lambda_{ir}$  was measured at a wavelength of 1.1  $\mu\text{m}$  in the spectral range in which the optical absorption in yttrium iron garnets increases with an increase in the concentration of  $\text{Fe}^{2+}$  ( $\text{Fe}^{4+}$ ) ions [9, 10]. The optical absorption strongly depends on the symmetry distortion (structural distortions), elastic stresses, and charged impurities [11]. Therefore, it can be assumed that the change in the optical absorption coefficient upon exposure to light is associated with the change in the valence of iron ions and the position of  $\text{Fe}^{2+}$  ( $\text{Fe}^{4+}$ ) ions with respect to dopants and other structural distortions. This assumption is also confirmed by the effect of light on the anisotropy and other magnetic properties of these samples [12, 13]. The mechanism of the formation of variable-valence ions depends on the dopant type in the sample. In the YIG:Ba crystal with a *p*-type doping, an increase in  $\alpha$  is caused by the formation of  $\text{Fe}^{4+}$  ions upon photoexcitation of octahedral  $\text{Fe}^{3+}$  ions. For  $\text{Fe}^{3+}$  ions, the energies of the  ${}^6A_{1g}({}^6S) \rightarrow {}^4T_{1g}({}^4G)$  and  ${}^6A_{1g}({}^6S) \rightarrow {}^4T_{2g}({}^4G)$  electronic transitions are equal to 10 800 and 14 200  $\text{cm}^{-1}$ , respectively [9]. These values are close to the energies of the maxima (0.75 and 1  $\mu\text{m}$ ) in the spectrum shown in Fig. 1. The observed difference is explained by the fact that  $\text{Fe}^{4+}$  ions are formed in distorted, energetically favorable, octahedral sites in which long-term localization can occur at liquid-nitrogen temperatures. The peaks in the spectral dependence indicate that the charge transfer to free acceptor levels of barium upon formation of  $\text{Fe}^{4+}$  ions occurs through the photoexcitation of the aforementioned transitions in  $\text{Fe}^{3+}$  ions. As can be seen from the time dependences, the increase in the optical absorption coefficient for YIG:Ba is irreversible. The optical absorption can regain its original value only after heating of the sample. A small reversible decrease in the optical absorption in YIG:Ba (point *F*) can be caused by a decrease in the number of nontrivalent iron ions or by their redistribution from nearest (with respect to doping ions) to distant positions. A comparative analysis of the spectral dependence and the time variations of the optical absorption for YIG:Si allows us to make the following inferences. In the YIG:Si crystal with an *n*-type doping, the increase in  $\alpha$  is associated with the formation of  $\text{Fe}^{2+}$  ions, which are predominantly located in distant (with respect to  $\text{Si}^{4+}$  ions) positions due to the photoionization of silicon and the localization of photoelectrons in the vacant (prior to illumination)  ${}^5E_g$  levels of  $\text{Fe}^{2+}$  ions [10]. The fact that the  $\text{Fe}^{2+}$  ions are formed in distant positions is confirmed by the small magnitude and the reversible character of the subsequent bleaching effect upon exposure to light at a wavelength of 1.3  $\mu\text{m}$  (point *D*). The initial decrease in  $\alpha$  for YIG:Si (portion *AB*) is explained by the redistribution of  $\text{Fe}^{2+}$  ions into energetically favorable distant sites [3], in which the optical absorption has a smaller magnitude because of the weaker structural distortions. As follows

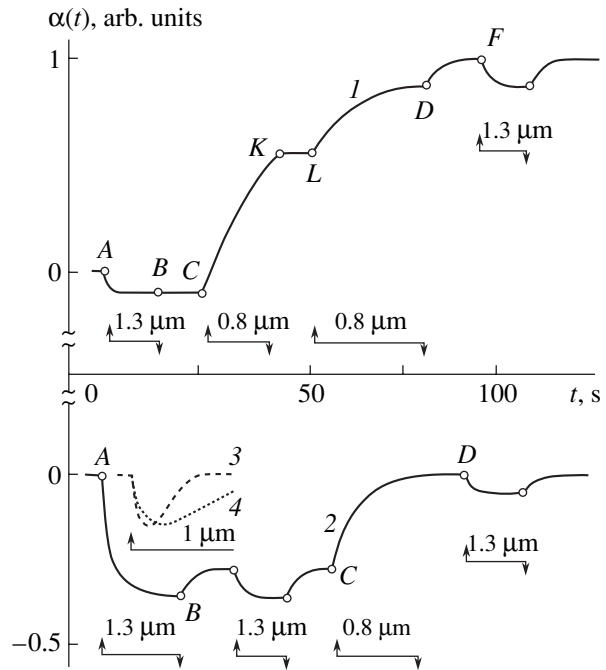


**Fig. 2.** Time dependences of the photoinduced change in the optical absorption coefficient  $\alpha(t)$  at a wavelength of 1.1  $\mu\text{m}$  under exposure to light for (1) YIG:Ba and (2–4) YIG:Si samples. Irradiation intensity  $P_0$ ,  $\text{mW}/\text{cm}^2$ : (3) 40 and (4) 10. Segments with arrows indicate the illumination duration. The upward and downward arrows correspond to the instants of switching-on and switching-off of the light, respectively. Numbers over the horizontal segments are the wavelengths of monochromatic radiation.

from the observed changes in the optical absorption, successive exposures to monochromatic light at different wavelengths do not lead to the inverse redistribution of  $\text{Fe}^{2+}$  ions from distant to nearest sites.

#### ACKNOWLEDGMENTS

This work was supported by the Russian Foundation for Basic Research, project no. 96-02-19255.

#### REFERENCES

1. *Photomagnetism*, Ed. by V. G. Veselago and G. I. Vinogradova (Nauka, Moscow, 1992); Tr. Inst. Obshch. Fiz. Ross. Akad. Nauk **44** (1992).
2. V. F. Kovalenko and É. L. Nagaev, Usp. Fiz. Nauk **148**, 561 (1986) [Sov. Phys. Usp. **29**, 297 (1986)].
3. E. M. Gyorg, J. F. Dillon, and J. P. Remeika, J. Appl. Phys. **42** (4), 1454 (1971).
4. K. Hisatake, I. Matsubara, K. Maeda, *et al.*, J. Magn. Magn. Mater. **140–144**, 2127 (1995).
5. K. Hisatake, I. Matsubara, K. Maeda, *et al.*, J. Magn. Soc. Jpn. **19** (S1), 263 (1995).

6. R. A. Doroshenko and M. D. Nadezhdin, *Fiz. Tverd. Tela (St. Petersburg)* **38** (10), 3075 (1996) [*Phys. Solid State* **38**, 1682 (1996)].
7. R. A. Doroshenko and M. D. Nadezhdin, in *Proceedings of the XIV School–Workshop “New Magnetic Materials of Microelectronics,” Moscow, 1994*, Part 3, p. 58.
8. V. A. Timofeeva, *Crystal Growth from Solutions and Melts* (Nauka, Moscow, 1978).
9. D. L. Wood and J. P. Remeika, *J. Appl. Phys.* **38** (3), 1038 (1967).
10. G. B. Scott and J. L. Page, *Phys. Status Solidi B* **79** (1), 203 (1977).
11. V. V. Randoshkin and A. Ya. Chervonenkis, *Applied Magneto-optics* (Énergoatomizdat, Moscow, 1990).
12. R. A. Doroshenko, M. S. Setchenkov, I. V. Vladimirov, and V. A. Timofeeva, *Fiz. Tverd. Tela (St. Petersburg)* **34**, 377 (1992) [*Sov. Phys. Solid State* **34**, 202 (1992)].
13. R. A. Doroshenko, *Tr. Inst. Obshch. Fiz. Ross. Akad. Nauk* **44**, 105 (1992).

*Translated by O. Borovik-Romanova*

**MAGNETISM  
AND FERROELECTRICITY**

# Topological Destruction of the Phase Transition to the Spin-Glass State in Amorphous Alloys with an Asymmetric Distribution of Exchange Interactions

A. B. Surzhenko and G. A. Takzei

*Institute of Magnetism, National Academy of Sciences of Ukraine, Kiev, 03142 Ukraine*

Received December 26, 2000

**Abstract**—It is shown that an increase in the asymmetry in the distribution of exchange interactions reduces the real magnetic dimension of bulk samples of amorphous spin glasses FeNi and FeMn, which attains its lowest critical value  $D_L = 2.51 \pm 0.12$  near the percolation threshold of infinite ferromagnetic clusters. The experimentally obtained result is in good agreement with calculations made using computer experiments. © 2001 MAIK “Nauka/Interperiodica”.

It is well known [1] that lowering the dimension  $D$  of a magnetic system considerably affects the critical temperature  $T_0$  and the critical indices  $\alpha$ ,  $\beta$ ,  $\delta$ ,  $\gamma$ , etc., of the phase transition occurring in it up to its complete destruction ( $T_0 = 0$  K,  $\beta = \delta^{-1} = 0$ ) after the attainment of the limit  $D \leq D_L$ , where  $D_L$  is the threshold value referred to as the lowest critical dimension of the magnet. It should be noted that  $D_L = 1$  for an Ising ferromagnet (FM),  $D_L = 2$  for a Heisenberg FM (disregarding anisotropy) [2], while for spin glasses (SGs),  $2 < D_L < 3$  [1]. As a rule, the method used to date for obtaining an experimental estimate of  $D_L$  in SG consists in decreasing the geometrical size of the sample; i.e., its Euclidean dimension  $D_E$  was reduced [3]. At the same time, calculations of the fractal aggregates show [4] that a similar result can be obtained in 3D magnetic systems by changing the topology of the Euclidean space itself (for example, by introducing FM pores in SG). According to Nakayama *et al.* [4], the fractal correction  $\Delta = (D_E - D)$  is usually small ( $\Delta \leq 0.5-0.7$ ).

In the present work, an attempt is made to obtain an experimental estimate of the lowest critical dimension of SG on the basis of the results of an investigation into magnetic properties of bulk alloys with predominant FM exchange.

In order to solve this problem, which in fact coincides with the problem of destruction of topological phase transitions, it is important to choose appropriate objects for the investigation. It will be proved that SGs based on amorphous alloys  $(\text{Fe}_C\text{Ni}_{1-C})_{77}\text{B}_{13}\text{Si}_{10}$  ( $C = 0.07$ ) and  $(\text{Fe}_C\text{Mn}_{1-C})_{75}\text{P}_{16}\text{B}_6\text{Al}_3$  ( $C = 0.65$ ) in the vicinity of the critical concentrations for the formation of the long-range FM order are very convenient objects. It should be noted that the alloys for experiments were chosen such that the lowest critical dimension of the magnetic transformation occurring in them was quite

close to the integer value of  $D_E$ , ensuring the validity of the inequality  $(D_E - \Delta) = D \leq D_L < D_E$ . The magnetic structure of amorphous SG has a tendency to the formation of FM clusters screened by a nonmagnetic interlayer from the SG matrix [5, 6]. Owing to this peculiarity, these clusters become natural pores hampering the phase transition to the SG state.

Using the magnetic phase diagram (see inset to Fig. 1) for Ising magnets with the Gaussian distribution  $P(J_{ij}) \sim \exp[-(J_{ij} - J_0)^2/(2J^2)]$  of exchange interactions [1], one can easily prove [7] that the average size  $\xi_{FM}$  of these pores, which satisfies the relation  $\xi_{FM} \sim (T_f/J_0 - 1)^{-\nu} \sim [(1 - \varepsilon)/\varepsilon]^{-\nu}$ , where  $\varepsilon = J_0/J$  and  $\nu \approx 0.8$ , varies significantly along the line  $T_f = J$  ( $J$  is the variance of the exchange interaction energy and  $J_0$  is the average exchange) of the phase transition to the SG state. At the point  $\varepsilon = 0$ , corresponding to the symmetric distribution of exchange interactions of opposite signs, the average pore size is negligibly small. In this case, the SG phase may occupy the entire Euclidean space with  $D = D_E = 3$ . A more complex situation emerges in the vicinity of the percolation threshold  $\varepsilon_p = J_0/J = 1$ , where  $\xi_{FM}(\varepsilon \rightarrow \varepsilon_p) \rightarrow \infty$ . It should be noted that the solution  $D_p = 2.48 \pm 0.09$  to the problem of the fractal dimension  $D_p$  of a critical cluster in the 3D case ( $D_E = 3$ ) is well known [4]. Since this value for SG is smaller than the theoretical estimates of  $D_L$  [7, 8], we can expect that a transition from symmetric SG systems ( $D \approx D_E = 3$ ,  $\beta \approx 1$ ,  $\delta^{-1} \approx 0.3$  [9]) to asymmetric systems ( $\varepsilon \rightarrow \varepsilon_p$ ,  $D \rightarrow D_p$ ) will indeed lead to the destruction of the cooperative phase transformation into the SG state ( $\beta = \delta^{-1} = 0$ ).

Unfortunately, in real alloys [10] (Fig. 1), such a scenario corresponds to a very narrow concentration range, which does not allow us to carry out the required investigations within a quasi-binary cut. For this rea-

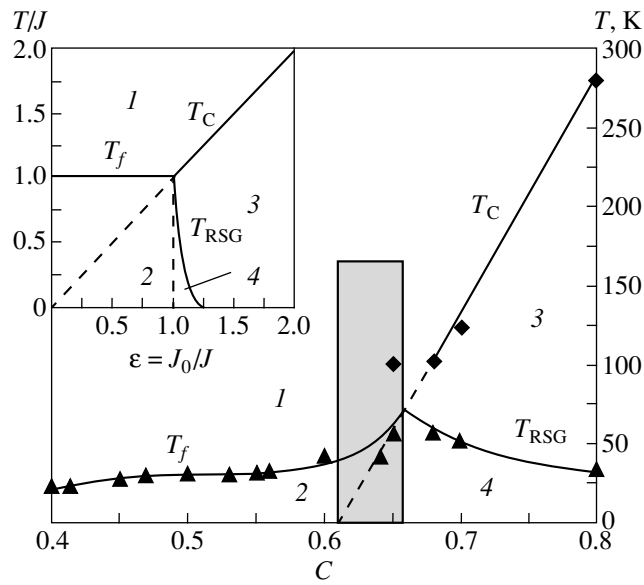


**Fig. 1.** Magnetic phase diagram for amorphous alloys of the quasi-binary cut  $(\text{Fe}_C\text{Mn}_{1-C})_{75}\text{P}_{16}\text{B}_6\text{Al}_3$  [10] and Ising magnets with a Gaussian distribution of exchange interactions [1] (inset). The concentration interval  $0.62 \leq C \leq 0.66$  corresponding to asymmetric SGs ( $0 \leq \varepsilon \leq 1$ ) is hatched: (1) paramagnetic (PM), (2) spin-glass (SG), (3) ferromagnetic (FM), and (4) reentrant SG states;  $T_C$  is the Curie temperature,  $T_f$  is the PM–SG phase-transition temperature, and  $T_{\text{RSG}}$  is the reentrant FM–SG phase-transition temperature.

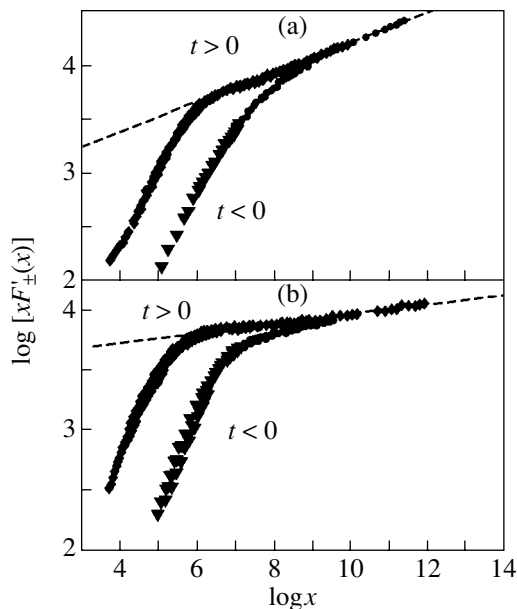


**Fig. 2.** Scaling functions  $x F'_{\pm}(x)$  obtained (a) for the SG  $(\text{Fe}_C\text{Mn}_{1-C})_{75}\text{P}_{16}\text{B}_6\text{Al}_3$  ( $C = 0.65$ ) ( $\varepsilon = 0.49$ ,  $1 \text{ mT} < H < 10 \text{ mT}$ ,  $-0.12 < t < 0.22$ ,  $T_f = 41.61 \text{ K}$ ,  $1/\delta = 0.166$ ,  $\beta = 0.48$ ) and (b) for  $(\text{Fe}_C\text{Ni}_{1-C})_{77}\text{B}_{13}\text{Si}_{10}$  ( $C = 0.07$ ) ( $\varepsilon = 0.76$ ,  $1 \text{ mT} < H < 10 \text{ mT}$ ,  $-0.24 < t < 0.35$ ,  $T_f = 15.63 \text{ K}$ ,  $1/\delta = 0.055$ ,  $\beta = 0.22$ ) with various degrees of asymmetry  $\varepsilon$  in the exchange interaction distribution. The slopes of the dashed lines correspond to  $\delta^{-1}$ .

son, we made a series of test measurements in which samples of amorphous alloys with various degrees of asymmetry of the exchange interaction ( $0 \leq \varepsilon \leq 1$ ) were selected. The measure of its dispersion  $J$  is the temperature corresponding to the maximum of the linear component of the dynamic magnetic susceptibility  $\chi_0(T)$ . The average exchange  $J_0$  was determined from the temperature  $\theta$  of the potential FM ordering [5] (dashed line in Fig. 1) by the processing of the temperature dependences of the magnetic susceptibility  $\chi_0(T) \sim (T - \theta)^{-\lambda}$  ( $T > T_f$ ) by the Cowell–Fisher method in the paramagnetic (PM) region, which ensured correct results for arbitrary values of  $\lambda$  [5]. As a result of the selection carried out by us here, preference was given to bulk samples of amorphous alloys  $(\text{Fe}_{0.65}\text{Mn}_{0.35})_{75}\text{P}_{16}\text{B}_6\text{Al}_3$  and  $(\text{Fe}_{0.07}\text{Ni}_{0.93})_{77}\text{B}_{13}\text{Si}_{10}$  in the form of  $1 \times 1 \times 15 \text{ mm}$  ribbons, for which the value of  $\varepsilon$  was  $0.49 \pm 0.08$  [1, 7] and  $0.76 \pm 0.10$  [7, 11], respectively.

The critical indices of the PM–SG phase transition were determined from the results of analysis of the non-linear response of the sample to a small sinusoidal perturbation by a magnetic field of frequency  $f = 75 \text{ Hz}$  and amplitude  $h_0 = 0.6 \text{ mT}$  in a constant magnetic field  $H \geq h_0$  [12]. Such an approach makes it possible to solve the problem of separation of the singular contribution from the magnetic susceptibility

$$\chi(H, t) = \chi_0(0, t) - t^\beta F'(x) \quad (1)$$

in the most natural way by decomposing it into spectral components. Here,  $F'(x)$  is the scaling function of the variable  $x = H^2/t^{\beta\delta}$  and  $t = |T - T_f|/T_f$  is the reduced temperature. In the case under investigation, the amplitudes of signals detected at the second, third, etc. harmonics of the frequency of the magnetization reversal field carry information on the first  $\chi_1$  [12], second  $\chi_2$ , etc. derivatives of the magnetic susceptibility. For example,

$$\chi_1(H, t) \equiv \frac{d\chi(H, t)}{dH} = -2Ht^{\beta(1-\delta)} \frac{dF'(x)}{dx}. \quad (2)$$

Thus, the problem of determining  $\beta$ ,  $\delta$ , and  $T_f$  is reduced to the standard procedure of their sorting out until the optimal collapse of the experimentally obtained surface  $\chi_1(H, t)$  to the scaling function  $F'(x)$  is obtained. Since a detailed description of such a procedure can be found in [1], we go over to a discussion of the obtained results. For the sake of visualization, they are presented in Fig. 2 in terms of functions  $x F'(x)$ . The two branches of the function  $x F'(x)$  correspond to the temperatures  $T > T_f$  and  $T < T_f$ . This allows us not only to demonstrate the accuracy of the approximation of several hundred points by formula (2) but also to demonstrate the destructive effect of the FM exchange on the critical behavior of amorphous SGs. Indeed, as follows from the above results, the enhancement of the FM exchange is manifested in a decrease in the slope of the dashed lines in Fig. 2, which, in view of the power-

low dependence  $F'(x \rightarrow \infty) \sim x^{1/\delta}$ , corresponds to the reciprocal of the critical isotherm exponent. This indicates the tendency to the destruction of the PM-SG phase transition for  $\varepsilon \rightarrow \varepsilon_p$  due to an increase in the concentration and size of PM pores.

Sounder arguments in favor of the hypothesis of topological destruction of the PM-SG phase transformation follow from the results presented in Fig. 3. In addition to the values of  $\beta$  and  $\delta^{-1}$  obtained in the present work, the figure also presents the results of an investigation of bulk samples ( $D_E = 3$ ) of symmetric SG systems ( $\varepsilon = 0$ ) [9], as well as the alloy  $(\text{Fe}_{0.15}\text{Ni}_{0.85})_{75}\text{P}_{16}\text{B}_6\text{Al}_3$ , which virtually remained the only extensively investigated amorphous SG with an asymmetric distribution of exchange interaction ( $0.4 \leq \varepsilon \leq 0.7$ ) [13] until the present publication.

It is important that the experimental results described above not only confirm the fractal behavior of amorphous SGs but also make it possible to determine their lowest critical dimension. Since the point  $\varepsilon_L = 0.94 \pm 0.06$  of intersection of the straight lines with each other and with the abscissa axis in Fig. 3 almost coincides with the threshold  $\varepsilon_p = 1$  for its setting in the FM order, the value of  $D_L$  must be close to the fractal dimension  $D_p = 2.48 \pm 0.09$  [4] of a critical cluster. Taking into account a small correction, which is equal to  $(\varepsilon_L - \varepsilon_p) \approx (D_E - D_p)$  in the linear approximation, we obtain  $D_L = 2.51 \pm 0.12$ , which is in excellent agreement with the estimate  $D_L = 2.5 \pm 0.2$  obtained for SG by the high-temperature expansion technique [8].

It should be noted that apart from amorphous magnets in which the FM- and SG-order regions can be treated as two independent subsystems [5, 6] and are described by using the theory of fractals, there exist SGs for which this approach is obviously inapplicable. For example, in some alloys of noble and transition metals (AgMn and PdMn [9]), the critical indices remain constant ( $\beta \approx 1$ ,  $\delta \approx 3$ ) in the interval  $0 \leq \varepsilon \leq 0.9$ . Consequently, the behavior of their FM subsystem is completely determined by the behavior of the surrounding SG matrix; i.e., a decrease in the topological dimension of the space is hardly possible. At the same time, the annealing of AuFe alloys accompanied by an increase in the size of FM clusters due to diffusion of iron atoms from the boundary layer leads to the formation of a gold interlayer serving as an insulating PM screen for FM clusters. This should and does result in the destruction of the cooperative nature of SG quenching [1]. This example is very important. Since the critical properties can differ radically even for magnets belonging to the same class, it is premature, on account of the great diversity of SG systems, to regard the value of  $D_L$  obtained above as universal. This problem undoubtedly requires additional investigation.

In conclusion, it should be noted that, in view of the imperfection of the modern technology of synthesis of multicomponent low-dimensional structures, it would

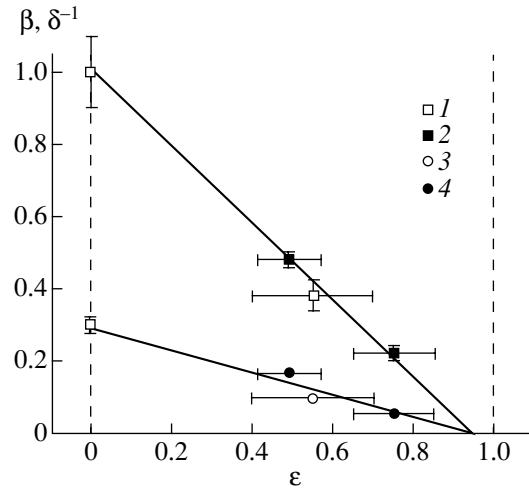


**Fig. 3.** Dependence of (1, 2) the critical indices  $\beta$  and (3, 4)  $\delta^{-1}$  of the PM-SG phase transformation in bulk amorphous alloys  $(\text{Fe}_c\text{Mn}_{1-c})_{75}\text{P}_{16}\text{B}_6\text{Al}_3$  and  $(\text{Fe}_c\text{Ni}_{1-c})_{77}\text{B}_{13}\text{Si}_{10}$  on the degree of asymmetry  $\varepsilon$  in the exchange interaction distribution: (1, 3) are the results obtained in [9, 13], and (2, 4) are our results.

not be inappropriate to doubt the potentialities of the generally accepted approach involving the artificial thinning of the samples. For example, a decrease in the geometrical size of SG samples with the fcc structure of the invar cut  $\text{Fe}_{65}(\text{Ni}_c\text{Mn}_{1-c})_{35}$  to  $\sim 5$  nm (which is required for the emergence of size effects [3]) causes the fcc  $\rightarrow$  bcc structural transformation [14]. Clearly, the study of magnetic phase transitions to the SG state is impossible under such conditions. However, using the bulk samples of asymmetric SGs, in which the size of FM correlations determining their actual dimension is varied due to a change in the atomic composition of the alloys or their thermal treatment, it may be possible to obtain specific results even in the near future.

#### ACKNOWLEDGMENTS

The authors are grateful to E.D. Belokolos and L.P. Gun'ko for fruitful discussions.

This work was financed in part by a joint with Leipzig University (Germany) project 13 no. 6992.

#### REFERENCES

1. K. Binder and A. P. Young, *Rev. Mod. Phys.* **58**, 801 (1986).
2. J. M. Ziman, *Models of Disorder: the Theoretical Physics of Homogeneously Disordered Systems* (Cambridge Univ. Press, Cambridge, 1979; Mir, Moscow, 1982).
3. J. Bass and J. A. Cowen, in *Recent Progress in Random Magnets*, Ed. by W. Ryan (World Sci., Singapore, 1992).

4. T. Nakayama, K. Yakubo, and R. L. Orbach, *Rev. Mod. Phys.* **66**, 381 (1994).
5. V. G. Bar'yakhtar, A. B. Surzhenko, and G. A. TakzeĀ, *Zh. Ėksp. Teor. Fiz.* **102**, 1674 (1992) [*Sov. Phys. JETP* **75**, 905 (1992)].
6. S. N. Kaul, *J. Magn. Magn. Mater.* **53**, 5 (1985).
7. R. R. P. Singh and M. E. Fisher, *J. Appl. Phys.* **63** (8), 3994 (1988).
8. W. L. McMillan, *Phys. Rev. B* **30**, 476 (1984).
9. H. Bouchiat, *J. Phys. (Paris)* **47**, 71 (1986).
10. K. Moorjani and J. M. C. Coey, *Magnetic Glasses* (Elsevier, Amsterdam, 1984).
11. T. Miyazaki, J. Okamoto, Y. Ando, and M. Takahaschi, *J. Phys. F* **18**, 1601 (1988).
12. A. B. Surzhenko, *Pis'ma Zh. Ėksp. Teor. Fiz.* **57**, 690 (1993) [*JETP Lett.* **57**, 702 (1993)].
13. P. Svedlindh, L. Lundgren, P. Nordblad, and H. S. Chen, *Europhys. Lett.* **2**, 805 (1986).
14. B. R. Coles and G. Williams, *J. Phys. F* **18**, 1279 (1988).

*Translated by N. Wadhwa*



## MAGNETISM AND FERROELECTRICITY

# Magnetic Effects in $\text{Co}_{3-x}\text{O}_4$ Defect Films from the Data of Emission Mössbauer Spectroscopy

F. Kh. Chibirova

State Scientific Center of the Russian Federation, Karpov Research Institute of Physical Chemistry,  
ul. Vorontsovo pole 10, Moscow, 103064 Russia  
e-mail: chibir@cc.nifhi.ac.ru

Received October 23, 2000; in final form, December 27, 2000

**Abstract**—The emission Mössbauer spectra of  $\text{Co}_{3-x}\text{O}_4$  defect films are measured in external magnetic fields at strengths of 0.6–3.5 T. It is shown that the memory effect is observed in the spectra of  $\text{Co}_{3-x}\text{O}_4$  defect films after exposure to an external magnetic field. At temperatures above the Néel temperature  $T_N = 26$  K, the memory effect manifests itself in an increase in the relative contribution from the spectral line of the tetrahedral  $A$  sublattice in the spinel structure of  $\text{Co}_{3-x}\text{O}_4$  crystallites ( $[\text{Co}_{0.83}^{2+}]_{\text{tet}}[\text{Co}_{2.20}^{3+}]_{\text{oct}}\text{O}_4$  and  $[\text{Co}_{0.95}^{2+}]_{\text{tet}}[\text{Co}_{2.10}^{3+}]_{\text{oct}}\text{O}_4$  prior to and after the magnetic field treatment, respectively). The isomer shifts  $\delta$  and the quadrupole splitting  $\Delta E$  of the spectral lines for both  $A$  and  $B$  sublattices also change from  $\delta_A = -0.19$  mm/s,  $\delta_B = -0.31$  mm/s, and  $\Delta E_B = 0.83$  mm/s to the values  $\delta_A = -0.24$  mm/s,  $\delta_B = -0.33$  mm/s, and  $\Delta E_B = 0.60$  mm/s, which are close to  $\delta$  and  $\Delta E$  for stoichiometric  $\text{Co}_3\text{O}_4$  oxide. In the low-temperature spectra ( $T < T_N$ ), the memory effect additionally shows itself as a decrease in the hyperfine magnetic field  $H_{hf}$  of the spectral component for the  $A$  sublattice as compared to that in the spectra measured prior to the magnetic field treatment. It is assumed that the concentration of cation vacancies decreases (and, correspondingly, the fraction of reduced  $\text{Co}^{2+}$  cations increases) in the  $\text{Co}_{3-x}\text{O}_4$  defect films under the action of an external magnetic field. A possible mechanism of this process is proposed. © 2001 MAIK “Nauka/Interperiodica”.

### 1. INTRODUCTION

Polycrystalline defect films of  $\text{Co}_{3-x}\text{O}_4$  cobalt oxide, which were prepared by the decomposition of deposited cobalt nitrate solutions at 300°C, were investigated by emission Mössbauer and x-ray photoelectron spectroscopy in our earlier works [1–3]. Stoichiometric  $\text{Co}_3\text{O}_4$  oxide is an antiferromagnet with the Néel temperature  $T_N = 33$  K and the hyperfine magnetic saturation field  $H_{hf} = 43.8$  T [4]. The  $\text{Co}_3\text{O}_4$  compound has a spinel structure in which only the  $A$  sublattice composed of magnetic  $\text{Co}^{2+}$  ions possesses magnetic properties, whereas  $\text{Co}^{3+}$  ions that form the  $B$  sublattice in stoichiometric  $\text{Co}_3\text{O}_4$  oxide have a low-spin nonmagnetic electronic configuration ( $t_{2g}^6 e_g^0$ ). In the  $\text{Co}_{3-x}\text{O}_4$  defect films, the Néel temperature decreases to  $T_N = 26$  K and the hyperfine magnetic saturation field increases to  $H_{hf} = 46.0$  T [2, 3]. The superparamagnetic relaxation observed in the emission spectra of the  $\text{Co}_{3-x}\text{O}_4$  defect films was explained in [2, 3] by the fact that the surface regions of  $\text{Co}_{3-x}\text{O}_4$  crystallites contain clusters (with a mean size of the order of 100 Å) which consist of cation vacancies and magnetic high-spin  $\text{Co}^{3+}$  ions with the  $t_{2g}^4 e_g^2$  electronic configuration. The stabilization of high-spin  $\text{Co}^{3+}$  ions in  $[\text{CoO}_6]$  oxygen octahedra on the surface of  $\text{Co}_{3-x}\text{O}_4$  crystallites was

confirmed by the x-ray photoelectron spectra of the  $\text{Co}_{3-x}\text{O}_4$  films [1].

In [2, 3], we also observed a number of anomalies in the emission Mössbauer spectra measured during and after the exposure of  $\text{Co}_{3-x}\text{O}_4$  defect films to external magnetic fields at strengths  $B = 2.5$  and 3.5 T in the temperature range  $T = 4$ –20 K. Specifically, in the presence of an external magnetic field, the hyperfine magnetic field  $H_{hf}$  in the spectra of the  $\text{Co}_{3-x}\text{O}_4$  films decreased compared to that in the spectra of these films measured prior to the magnetic field treatment. Moreover, the line intensity increased in all the emission Mössbauer spectra recorded after exposure of the  $\text{Co}_{3-x}\text{O}_4$  defect films to the magnetic field. All these findings indicated that the memory effect of the action of an external magnetic field, most likely, manifests itself in the emission Mössbauer spectra of the  $\text{Co}_{3-x}\text{O}_4$  defect films.

Kaleva *et al.* [4] studied another oxide system, namely, yttrium barium cuprate. It was found that exposure of this complex oxide to a magnetic field in the course of its synthesis leads to changes in the structure and the oxygen nonstoichiometry. Special mention should be made of the interesting results obtained by Speriosu *et al.* [5] for the gamma-iron oxide  $\gamma\text{-Fe}_2\text{O}_3$  (a base material for magnetic recording media) prepared by the oxidation of a  $\text{Fe}_3\text{O}_4$  magnetite. These authors

revealed that, after the first test experiments in an external magnetic field, the experimental data obtained for  $\gamma$ - $\text{Fe}_2\text{O}_3$  proved to be typical of the initial  $\text{Fe}_3\text{O}_4$  magnetite. It seems likely that the effect of the magnetic field on the structure of nonstoichiometric oxides has a similar nature.

In the present work, an attempt was made to verify and investigate in greater detail this phenomenon by using Mössbauer spectroscopy. For this purpose, we prepared new defect films of  $\text{Co}_{3-x}\text{O}_4$  doped with a  $^{57}\text{Co}$  isotope. This paper reports the results of our investigation.

## 2. EXPERIMENTAL TECHNIQUE

Samples of the  $\text{Co}_{3-x}\text{O}_4$  defect films suitable for Mössbauer investigations, as in [1–3], were prepared in the form of gamma-ray sources with an activity of 2–5 mCi. For this purpose, the  $^{57}\text{Co}$  isotope in the form of cobalt chloride was added to a cobalt nitrate solution. The solution obtained was deposited onto a quartz substrate and was then heated to 300°C. The emission Mössbauer spectra were recorded on an electrodynamic-type spectrometer operating in the constant-acceleration mode. A resonance counter with an absorber in the form of a thin FeAl alloy foil was used as an absorber and a detector. All the isomer shifts were given with respect to the metallic iron. Measurements of the Mössbauer spectra in the temperature range  $T = 4$ –20 K and in external magnetic fields  $B = 0.3$ –3.5 T were carried out in a helium-flow cryostat with a superconducting solenoid. The magnetic field was applied along the direction of gamma-ray radiation.

## 3. RESULTS AND DISCUSSION

The results obtained in our earlier works [1–3] for the  $\text{Co}_{3-x}\text{O}_4$  defect films were well reproduced with new  $\text{Co}_{3-x}\text{O}_4$  films in a repeated series of emission Mössbauer experiments in external magnetic fields.

Analysis of the emission Mössbauer spectra obtained for new  $\text{Co}_{3-x}\text{O}_4$  films in an external field  $B = 0.3$ –3.5 T at a temperature  $T = 5$ –20 K revealed that, as in [2, 3], the effective hyperfine magnetic field  $H_{\text{eff}}$  in the antiferromagnetically ordered  $A$  sublattice regularly decreases by a magnitude of greater than  $B$ . As in [2, 3], the memory effect of the action of an external magnetic field is observed in the emission Mössbauer spectra of the  $\text{Co}_{3-x}\text{O}_4$  films after the magnetic field treatment. In this case (as in [2, 3]), the intensity of the emission spectrum lines increases after exposure to the magnetic field.

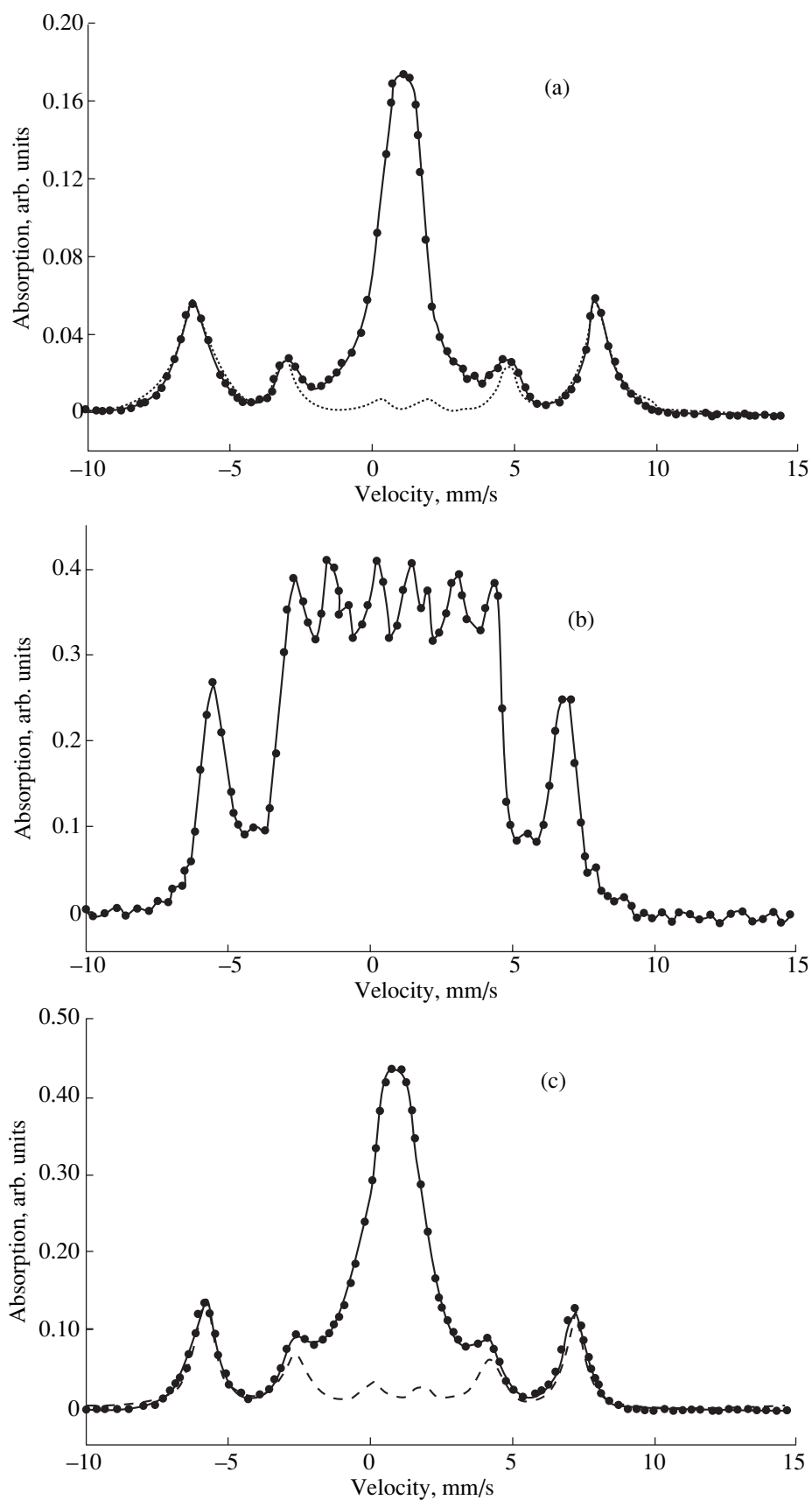
Figure 1 shows the emission Mössbauer spectra measured for the  $\text{Co}_{3-x}\text{O}_4$  films at  $T = 19$  K prior to exposure to the magnetic field, in the external magnetic field  $B = 2.5$  T, and after the magnetic field treatment. The Mössbauer spectrum recorded prior to exposure to the magnetic field is displayed in Fig. 1a. In this spec-

trum, the magnetic sextet with a hyperfine magnetic field  $H_{\text{hf}} = 43.3$  T corresponds to the  $A$  sublattice and a broadened central line is attributed to the  $B$  sublattice. In the external magnetic field  $B = 2.5$  T (Fig. 1b), the central component is split and the hyperfine splitting of the magnetic sextet that corresponds to the  $A$  sublattice decreases by  $\Delta = 4.0$  T. The Mössbauer spectrum of the  $\text{Co}_{3-x}\text{O}_4$  defect film after exposure to an external magnetic field ( $B = 2.5$  T) is depicted in Fig. 1c. A comparison of the initial Mössbauer spectrum of the  $\text{Co}_{3-x}\text{O}_4$  film at  $T = 19$  K (Fig. 1a) and the spectrum of the  $\text{Co}_{3-x}\text{O}_4$  defect film treated in the magnetic field (Fig. 1c) shows that, after exposure to the magnetic field, the hyperfine magnetic field  $H_{\text{hf}}$  decreases by  $\Delta = 3.3$  T and the intensity of spectral lines increases by a factor of more than two.

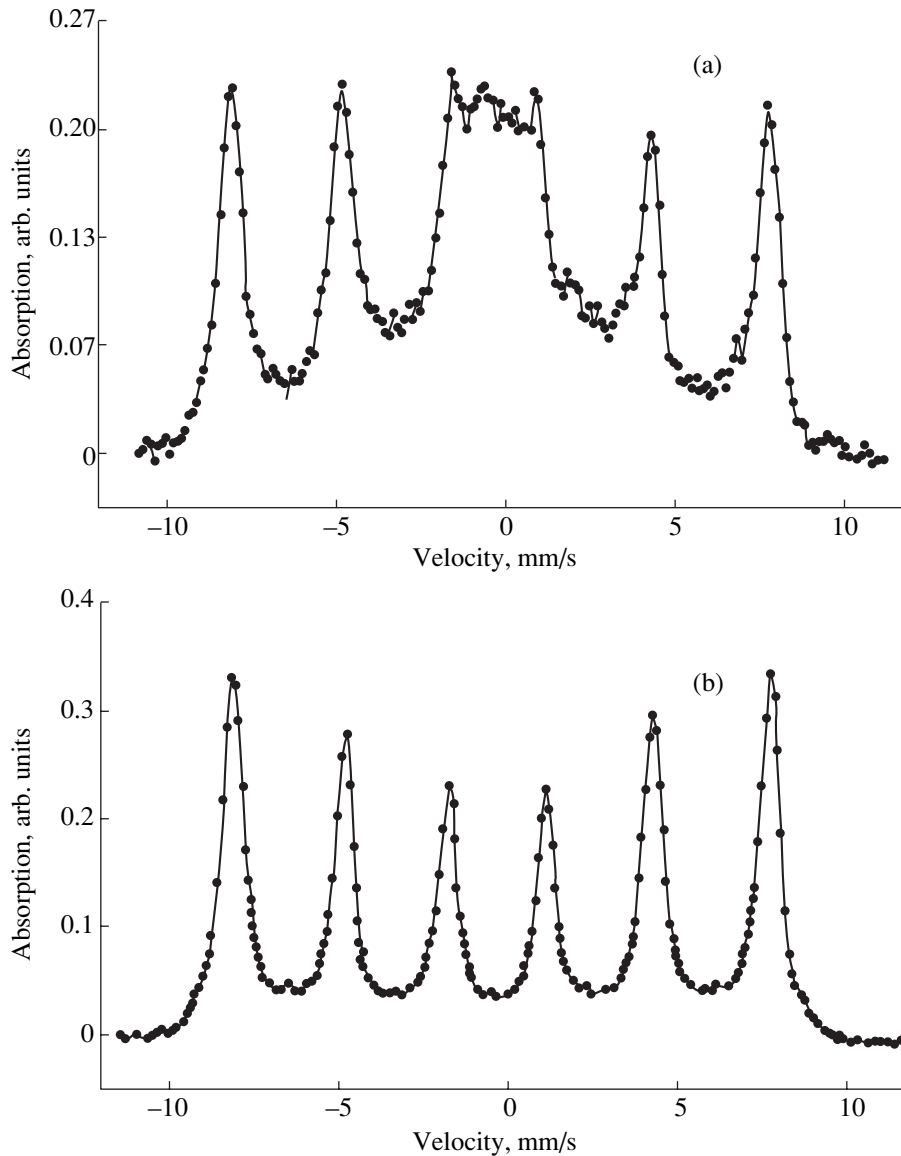
The emission Mössbauer spectra of the  $\text{Co}_{3-x}\text{O}_4$  film after exposure to the external magnetic field  $B = 2.5$  T were also measured in the temperature range from 5 to 297 K. Figure 2 displays the Mössbauer spectra of the  $\text{Co}_{3-x}\text{O}_4$  film at  $T = 5$  K prior to and after exposure to the external magnetic field. As can be seen from this figure, the shape of the spectrum changes considerably after the treatment of the studied film in an external magnetic field. The spectrum of the initial sample (Fig. 2a) represents a magnetic sextet against a broad background, whereas the new spectrum obtained after exposure to the magnetic field  $B = 2.5$  T (Fig. 2b) exhibits a magnetic sextet and a broadened central component.

Figure 3 shows the emission spectra of the  $\text{Co}_{3-x}\text{O}_4$  defect film at temperatures of 30 and 35 K after exposure to the external magnetic field  $B = 2.5$  T. A comparison of these spectra demonstrates that the antiferromagnetic transition temperature  $T_N$  for the  $A$  sublattice of the  $\text{Co}_{3-x}\text{O}_4$  defect film after exposure to the external magnetic field lies in the range from 30 to 35 K, which is higher than the Néel temperature  $T_N = 26$  K for the initial  $\text{Co}_{3-x}\text{O}_4$  defect film and is close to  $T_N = 33$  K for stoichiometric  $\text{Co}_3\text{O}_4$ .

The emission spectra of the  $\text{Co}_{3-x}\text{O}_4$  defect film at 297 K prior to and after exposure to the external magnetic field are depicted in Fig. 4. Both spectra are superpositions of a doublet and a singlet. The isomer shifts  $\delta$  and the quadrupole splittings  $\Delta E$  for these lines in the emission Mössbauer spectra (Figs. 4a, 4b) are listed in the table. The doublet line is assigned to the contribution of the  $B$  sublattice and the singlet line is attributed to the contribution of the  $A$  sublattice of the  $\text{Co}_{3-x}\text{O}_4$  spinel structure [6, 7]. A comparison of the Mössbauer parameters (see table) with the data obtained by Kündig *et al.* [6] for stoichiometric  $\text{Co}_3\text{O}_4$  ( $\delta_A = -0.26$  mm/s,  $\delta_B = -0.34$  mm/s, and  $\Delta E_B = 0.54$  mm/s) and the results reported by Simmons *et al.* [7] for a nonstoichiometric  $\text{Co}_{3-x}\text{O}_4$  compound ( $\delta_A = -0.20$  mm/s,  $\delta_B = -0.33$  mm/s, and  $\Delta E_B = 0.93$  mm/s) shows that the parameters of the Mössbauer spectrum measured for



**Fig. 1.** Emission Mössbauer spectra of  $\text{Co}_{3-x}\text{O}_4$  films at  $T = 19$  K (a) prior to exposure to the magnetic field, (b) in the magnetic field  $B = 2.5$  T, and (c) after exposure to the magnetic field.



**Fig. 2.** Emission Mössbauer spectra of the  $\text{Co}_{3-x}\text{O}_4$  defect film at  $T = 5$  K (a) prior to and (b) after exposure to the magnetic field  $B = 2.5$  T.

the  $\text{Co}_{3-x}\text{O}_4$  film after exposure to the magnetic field  $B = 2.5$  T are close to those for stoichiometric  $\text{Co}_3\text{O}_4$ . By assuming that the probability of the Mössbauer effect for  $^{57}\text{Fe}$  in the tetrahedral environment in the  $A$  sublattice is identical to that in the octahedral environment in the  $B$  sublattice, the degree of stoichiometry of the  $\text{Co}_{3-x}\text{O}_4$  oxide can be estimated from the areas under the curves of the corresponding components in the emission spectra of the  $\text{Co}_{3-x}\text{O}_4$  film (Figs. 4a, 4b) [7]. As follows from the results obtained, the degree of stoichiometry of the initial  $\text{Co}_{3-x}\text{O}_4$  defect film corresponds to the formula  $[\text{Co}_{0.83}^{2+}]_{\text{tet}}[\text{Co}_{2.20}^{3+}]_{\text{oct}}\text{O}_4$ . After the exposure to the magnetic field  $B = 2.5$  T, the contribution from the spectral component of the  $A$  sublattice increases and, correspondingly, the contribution from

the component of the  $B$  sublattice decreases. The new stoichiometric composition of the  $\text{Co}_{3-x}\text{O}_4$  film is described by the formula  $[\text{Co}_{0.95}^{2+}]_{\text{tet}}[\text{Co}_{2.10}^{3+}]_{\text{oct}}\text{O}_4$ .

The temperature dependences of the hyperfine magnetic field  $H_{hf}(T)$  for the  $\text{Co}_{3-x}\text{O}_4$  defect film prior to and after exposure to the external magnetic field  $B = 2.5$  T are plotted in Fig. 5. The temperature dependence  $H_{hf}(T)$  for the  $\text{Co}_{3-x}\text{O}_4$  defect film after the treatment in an external magnetic field is represented by the Brillouin function. According to Kündig *et al.* [6], the same function describes the temperature dependence of the hyperfine magnetic field  $H_{hf}(T)$  for stoichiometric  $\text{Co}_3\text{O}_4$ .

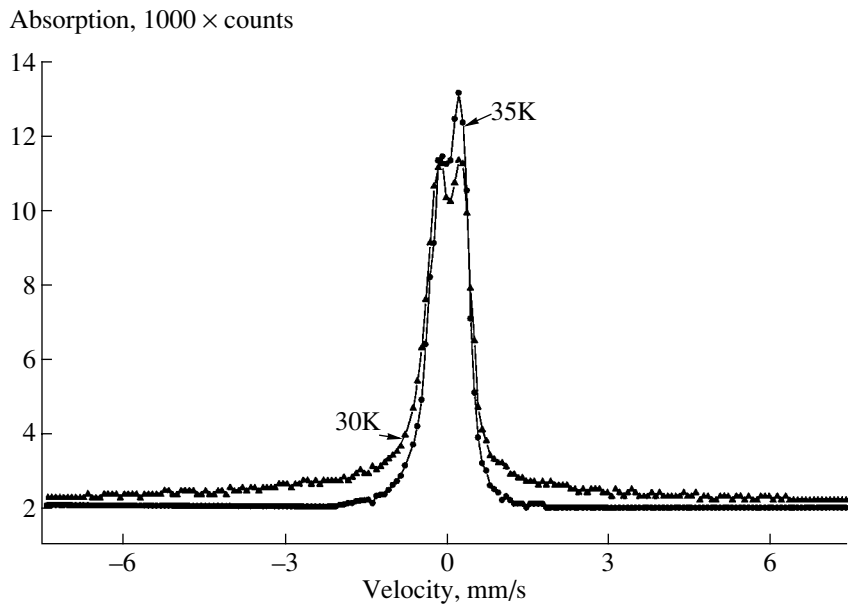


**Fig. 3.** Emission Mössbauer spectra of the  $\text{Co}_{3-x}\text{O}_4$  defect film at  $T = 30$  and  $35$  K after exposure to the magnetic field  $B = 2.5$  T.

Thus, the above experimental results suggest that the structure of the  $\text{Co}_{3-x}\text{O}_4$  defect film can undergo transformations after exposure to the external magnetic field  $B = 2.5$  T. Specifically, the appearance of the central component in the Mössbauer spectrum of the  $\text{Co}_{3-x}\text{O}_4$  defect film ( $T = 5$  K) after the treatment in an external magnetic field (Fig. 2b) can be explained by the increase in the degree of stoichiometry of the  $\text{Co}_{3-x}\text{O}_4$  oxide, i.e., by the larger degree of the magnetic independence of the  $A$  and  $B$  sublattices in the spinel structure, which is observed in stoichiometric  $\text{Co}_3\text{O}_4$  [6]. As was noted above, an increase in the Néel temperature  $T_N$  of the  $\text{Co}_{3-x}\text{O}_4$  films after exposure to the external magnetic field  $B$  (Fig. 3) also indicates an increase in the degree of stoichiometry in these films. Furthermore, an increase in the degree of stoichiometry in the  $\text{Co}_{3-x}\text{O}_4$  defect films after their treatment in an external magnetic field  $B$  is also confirmed by the estimates obtained for the contributions from the  $A$  and  $B$  sublattices of the  $\text{Co}_{3-x}\text{O}_4$  spinel structure to the emission Mössbauer spectra measured at room temperature (Fig. 4). A decrease in the degree of defectiveness of the  $\text{Co}_{3-x}\text{O}_4$  films (or an increase in the degree of their stoichiometry) can be judged from the increase in the spectral line intensity (proportional to the probability  $f$  of the Mössbauer effect), which is observed in all the emission spectra measured after the exposure to external magnetic fields. Finally, the fact that the temperature dependences of the hyperfine magnetic field  $H_{hf}(T)$  for the  $\text{Co}_{3-x}\text{O}_4$  defect film treated in the magnetic field  $B = 2.5$  T coincide with those for stoichiometric  $\text{Co}_3\text{O}_4$  [6] can be explained only by the effect of the external magnetic field on the structural transformations that

lead to changes in the stoichiometry of the  $\text{Co}_{3-x}\text{O}_4$  defect film.

The external magnetic field can affect the possible processes in a solid-state oxide matrix, for example, the creation and destruction of superstructural defects (in our case, cation vacancies), which occur through the formation of charge-transfer states. According to the concepts developed in [8, 9], the magnetic field can affect the formation and destruction of superstructural defects, because these processes (a) involve paramagnetic particles with correlated spins (the charge-transfer state can be treated as an electron-hole pair) and (b) exhibit a nonequilibrium character.

The superstructural cation vacancies are nonequilibrium defects in the structure of  $\text{Co}_{3-x}\text{O}_4$  films. The creation of these defects in the spinel structure of stoichiometric  $\text{Co}_3\text{O}_4$  can be interpreted as the formation of charge-transfer states in the  $A$  sublattice occupied by  $\text{Co}^{2+}$  ions. In this process, the valence electron  $e$  of a  $\text{Co}^{2+}$  ion transfers to a cation vacancy  $\square^e$  with the formation of a bound hole  $p$  of the  $\text{Co}^{2+p}$  ion. The

Mössbauer parameters of the spectral lines for  $A$  and  $B$  sublattices of the  $\text{Co}_{3-x}\text{O}_4$  defect film prior to and after exposure to the magnetic field  $B = 2.5$  T (Fig. 4)

$\text{Co}_{3-x}\text{O}_4$	$\delta_A$ , mm/s (with respect to $\alpha$ -Fe)	$\delta_B$ , mm/s (with respect to $\alpha$ -Fe)	$\Delta E_B$ , mm/s
Prior to magnetic field treatment	$-0.19 \pm 0.01$	$-0.31 \pm 0.01$	$0.83 \pm 0.01$
After magnetic field treatment	$-0.24 \pm 0.01$	$-0.33 \pm 0.01$	$0.60 \pm 0.01$

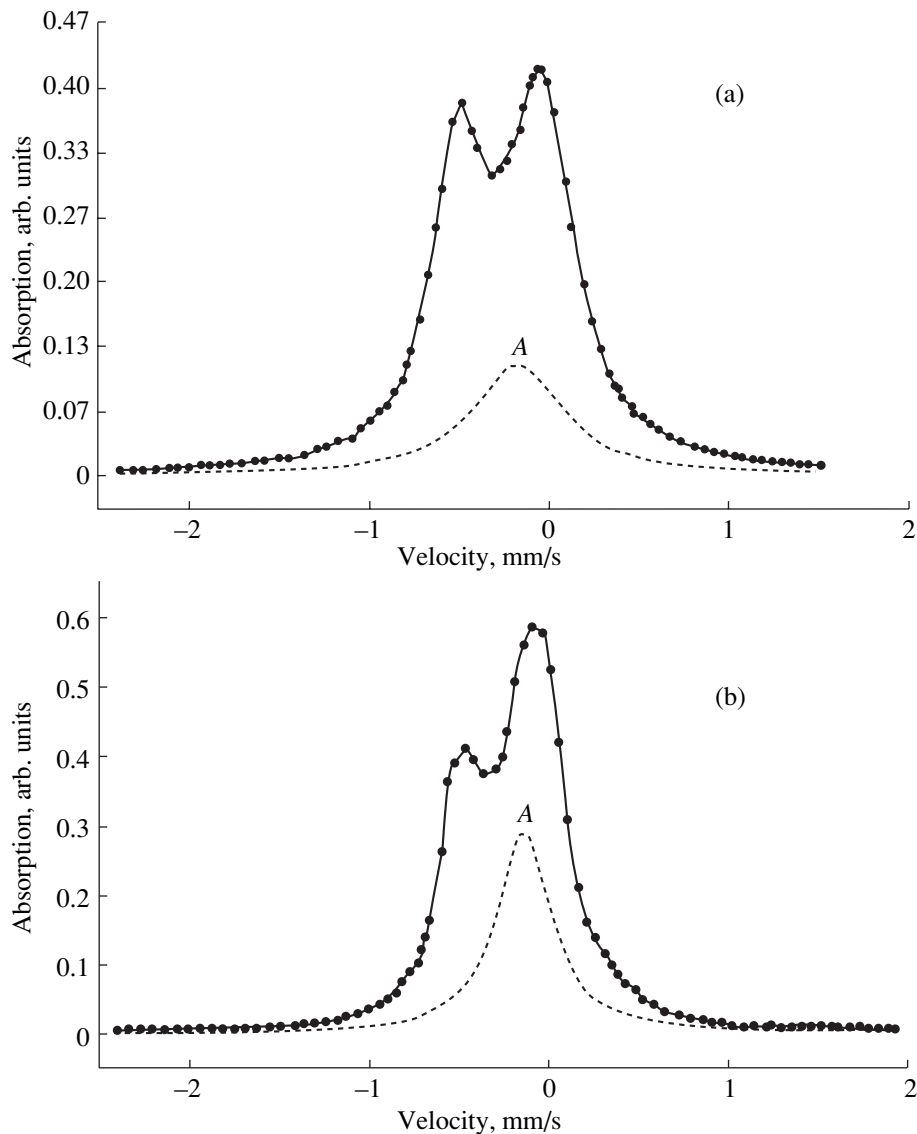


**Fig. 4.** Emission Mössbauer spectra of the  $\text{Co}_{3-x}\text{O}_4$  film at  $T = 297$  K (a) prior to and (b) after exposure to the magnetic field  $B = 2.5$  T. Dashed lines show the contributions of the A sublattice to the spectra of the  $\text{Co}_{3-x}\text{O}_4$  film.

$[\text{Co}^{2+p}\square^e]$  complex thus formed can be treated as an electron-hole pair ( $e + p$ ). Hereafter, these complexes will be referred to as charge-transfer complexes. The  $e + p$  pair possesses correlated spins, and its evolution depends on the spin state. As follows from [8, 9], the pair in a singlet spin state can undergo evolution; i.e., it can either dissociate or annihilate depending on the mobilities of its constituents. For this reason, the charge-transfer complexes in a singlet state are considered short-lived particles. The pair in a triplet spin state does not evolve but waits until the spin dynamics of a different origin brings about a change in its spin state. As a consequence, the triplet charge-transfer complexes are considered long-lived particles. The external magnetic field is one of the factors affecting the spin evolution of triplet pairs [8, 9].

Assumptions of the spin-selective nature of the processes occurring in the  $\text{Co}_{3-x}\text{O}_4$  defect films with the participation of cation vacancies can be indirectly confirmed by the emission of singlet oxygen molecules  $^1\text{O}_2$  upon adsorption of atmospheric oxygen  $^3\text{O}_2$  on the surface of these films at a temperature of  $150^\circ\text{C}$  [10]. The  $\text{Co}_{3-x}\text{O}_4$  defect films studied by Belova *et al.* [10] were identical to those used in the present work but without addition of a  $^{57}\text{Co}$  radioisotope. The experiments performed in [10] allowed these authors to conclude that long-lived charge-transfer metal-oxygen complexes are formed on the surface of the  $\text{Co}_{3-x}\text{O}_4$  films in the presence of high-spin  $\text{Co}^{3+}$  ions, whereas the formation of singlet oxygen  $^1\text{O}_2$  occurs through the energy transfer from an excited surface complex to an adsorbed

molecule of atmospheric triplet oxygen  $^3\text{O}_2$ . According to the inference drawn in [10], the formation of an excited oxygen molecule and its escape into a gaseous phase should be accompanied by the annihilation of an active center on the surface of the  $\text{Co}_{3-x}\text{O}_4$  film. This explains the decrease in the generation of singlet oxygen with time, which was observed in [10].

Belova *et al.* [10] considered the excitation of singlet oxygen on active surface charge-transfer complexes in the presence of high-spin  $\text{Co}^{3+}$  ions with special emphasis made on the energy transfer necessary for the excitation of an adsorbed oxygen molecule. In the case when the excited long-lived charge-transfer complex has a sufficiently high energy ( $\sim 1$  eV) for the excitation of singlet oxygen and occurs in a triplet spin state, there are grounds to propose the mechanism of the triplet-singlet transition in an adsorbed oxygen molecule  $^3\text{O}_2$ . According to the theory developed for magnetic effects in chemical reactions [8, 9], the triplet-singlet transition in an oxygen molecule can proceed through the mechanism of “quenching of the excited triplet by oxygen.” This reaction results in the formation of two singlet states, one of which is an excited state.

As was noted above, the charge-transfer complex on the surface of the  $\text{Co}_{3-x}\text{O}_4$  defect film consists of a  $\text{Co}^{2+}$  ion captured the  $p$  hole and a cation vacancy  $\square^e$  with a transferred electron  $e$ . In the bulk of a crystallite, the cation vacancy is an octahedron whose vertices are occupied by  $\text{O}^{2-}$  ions. This vacancy on the crystallite surface exhibits a specific feature in the form of a surface oxygen atom with a deficit of bonds (and, correspondingly, electrons) on both the solid and gaseous phase sides. As a result, the  $e$  electron transferred to the cation vacancy from the nearest metal ion upon formation of the charge-transfer complex is most likely localized on the surface oxygen atom  $\text{O}^e$ . In this case, the charge-transfer complex  $[\text{Co}^{2+}p\text{O}^e]_{\text{surf}}$ , which corresponds to the cation vacancy formed in the crystallite bulk, transforms into the surface complex  $[\text{Me}^{n+p}\text{O}^e]_{\text{surf}}$  as follows:  $[\text{Me}^{n+p}\square^e] \rightarrow [\text{Me}^{n+p}\text{O}^e]_{\text{surf}}$ . As was shown above, the long-lived charge-transfer complexes are in a triplet spin state. According to the estimates made by Gusev *et al.* [11], the formation of a cation vacancy in metal oxides requires an energy of the order of 1–5 eV. Consequently, the energy of the same order is accumulated in the  $[\text{Me}^{n+p}\text{O}^e]_{\text{surf}}$  complex. Thus, all the necessary and sufficient conditions are met in order for the  $[\text{Co}^{2+}p\text{O}^e]_{\text{surf}}$  charge-transfer complex to become a partner of the  $^3\text{O}_2$  oxygen molecule in the triplet-singlet transition that proceeds through the mechanism of the quenching of the excited triplet by oxygen on the  $\text{Co}_{3-x}\text{O}_4$  crystallite surface. As was already mentioned, the reactants occur in a singlet state: the  $[\text{Co}^{2+}p\text{O}^e]_{\text{surf}}$  charge-transfer complex is in the ground state and the singlet oxygen  $^1\text{O}_2$  is in the

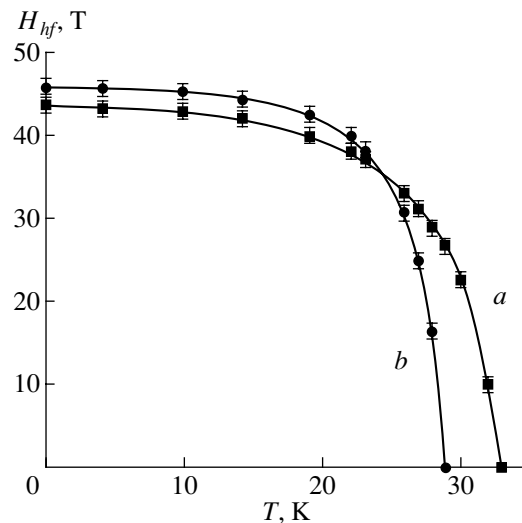


Fig. 5. Temperature dependences of the hyperfine magnetic field on  $^{57}\text{Fe}$  nuclei in the  $\text{Co}_{3-x}\text{O}_4$  defect film (a) prior to and (b) after exposure to the magnetic field  $B = 2.5$  T.

excited state. The singlet oxygen can be desorbed from the surface, and the  $[\text{Co}^{2+p}\text{O}^e]_{\text{surf}}$  complex in the singlet spin state can dissociate into a  $\text{Co}^{2+}$  ion and a surface oxygen radical  $\text{O}^{\bullet}$  due to the annihilation of the  $e + p$  pair. This implies that the surface cation vacancies are destroyed upon desorption of singlet oxygen. Apparently, this process was observed in [10] as the emission of singlet oxygen from the surface of the  $\text{Co}_{3-x}\text{O}_4$  defect film at  $150^\circ\text{C}$ .

Thus, the independent experimental investigation [10] revealed that surface cation vacancies participate in spin-selective excitation of singlet oxygen upon adsorption of atmospheric oxygen on the surface of the  $\text{Co}_{3-x}\text{O}_4$  defect film. This means that the surface cation vacancy is associated with a paramagnetic pair [8, 9], which acts as a partner of an atmospheric oxygen molecule in the triplet-singlet transition. The  $[\text{Co}^{2+p}\text{O}^e]_{\text{surf}}$  charge-transfer complex formed upon creation of the surface cation vacancy can serve as a paramagnetic pair. The spin evolution of the  $[\text{Co}^{2+p}\text{O}^e]_{\text{surf}}$  complex into the singlet state can lead to its dissociation into the  $\text{Co}^{2+}$  ion and the  $\text{O}^{\bullet}$  surface oxygen radical, i.e., to the decay of the cation vacancy, a decrease in the defectiveness, and an increase in the degree of stoichiometry of the  $\text{Co}_{3-x}\text{O}_4$  films. The external magnetic field affects the spin dynamics of paramagnetic pairs (the  $[\text{Co}^{2+p}\text{O}^e]_{\text{surf}}$  charge-transfer complexes). It is quite probable that the external magnetic field promotes their evolution transition to the singlet spin state [8, 9], which is destructive for cation vacancies. The dissociation of the  $[\text{Co}^{2+p}\text{O}^e]_{\text{surf}}$  complexes brings about an increase in the fraction of  $\text{Co}^{2+}$  ions and, correspondingly, an increase in the contribution of the A sublattice

to the emission Mössbauer spectrum of the  $\text{Co}_{3-x}\text{O}_4$  film treated in an external magnetic field. In other words, the external magnetic field is favorable for increasing the degree of stoichiometry of the  $\text{Co}_{3-x}\text{O}_4$  defect films.

However, it is quite possible that the magnetic field only initiates a chain reducing process in the mechanically stressed solid-state matrix of the  $\text{Co}_{3-x}\text{O}_4$  defect film. The chain reducing process in this solid-state matrix can be initiated by the formation of  $\text{O}^\bullet$  radical oxygen atoms in lattice sites under the action of an external magnetic field, as was the case in experiments with a reducing explosion initiated by a shock wave in defect zinc oxide ZnO [12].

Therefore, the effect of the magnetic field on the nonequilibrium structure of the  $\text{Co}_{3-x}\text{O}_4$  defect film, most likely, is not an exclusive property of the oxide system under investigation. In this respect, interesting results, as already mentioned, were obtained by Speriosu *et al.* [5] for the gamma-iron oxide  $\gamma\text{-Fe}_2\text{O}_3$  produced by the oxidation of a  $\text{Fe}_3\text{O}_4$  magnetite. It was found that, after the first test experiments in magnetic fields, the experimental data obtained for  $\gamma\text{-Fe}_2\text{O}_3$  proved to be typical of the initial  $\text{Fe}_3\text{O}_4$  magnetite. The point is that all three oxides ( $\gamma\text{-Fe}_2\text{O}_3$ ,  $\text{Fe}_3\text{O}_4$ , and  $\text{Co}_3\text{O}_4$ ) have a spinel structure; hence, by ignoring the specific structural features of each oxide, the  $\text{Co}_{3-x}\text{O}_4$  defect film can be considered an analogue of the nonstoichiometric oxide  $\gamma\text{-Fe}_2\text{O}_3$  or, what is the same, the nonstoichiometric magnetite  $\text{Fe}_3\text{O}_4$ . Consequently, the effect of the magnetic field on the structure of these oxides apparently should have a similar nature. Under the assumption that, in [5], the oxidation of the  $\text{Fe}_3\text{O}_4$  magnetite resulted in the formation of the nonstoichiometric gamma-iron oxide  $\gamma\text{-Fe}_2\text{O}_3$  (which is quite probable), the effect of the external magnetic field on the nonequilibrium structure of this oxide could lead to its reduction to the initial  $\text{Fe}_3\text{O}_4$  magnetite, as in the case of the  $\text{Co}_{3-x}\text{O}_4$  defect film.

This assumption was verified by the appropriate investigations with the use of Mössbauer spectroscopy. The results obtained in these studies, specifically on the effect of magnetic fields (with different strengths, frequencies, and configurations) on the degree of stoichi-

ometry (or the degree of defectiveness) of  $\text{Fe}_3\text{O}_4$  and  $\gamma\text{-Fe}_2\text{O}_3$ , will be reported in a separate work.

#### ACKNOWLEDGMENTS

I am grateful to S.K. Godovikov and S.I. Reĭman (Laboratory of Nuclear Spectroscopy, Skobeltsyn Research Institute of Nuclear Physics, Moscow State University) for their assistance in this work.

#### REFERENCES

1. F. Kh. Chibirova, I. D. Belova, D. S. Zakhar'in, *et al.*, Fiz. Tverd. Tela (Leningrad) **26** (3), 890 (1984) [Sov. Phys. Solid State **26**, 541 (1984)].
2. F. Kh. Chibirova, D. S. Zaharjin, Yu. E. Roginskaya, *et al.*, in *Proceedings of the International Conference on the Applications of Mössbauer Effect, Alma-Ata, 1983*, p. 274.
3. F. Kh. Chibirova, I. D. Belova, D. S. Zaharjin, and Yu. E. Roginskaya, in *Proceedings of the International Meeting on Highly Dispersed Iron Oxides and Corrosion, Leningrad, 1983*, p. 20.
4. G. M. Kaleva, E. D. Politova, Yu. E. Roginskaya, and F. Kh. Chibirova, Zh. Fiz. Khim. **66** (11), 3052 (1992).
5. V. S. Speriosu, M. M. Chen, and T. Suzuki, IEEE Trans. Magn. **25** (5), 3875 (1989).
6. W. Kündig, M. Kobelt, H. Appel, *et al.*, J. Phys. Chem. Solids **30**, 819 (1969).
7. G. W. Simmons, A. Vertes, M. L. Varsanyi, and H. Leidheiser, J. Electrochem. Soc. **126** (2), 187 (1979).
8. Ya. B. Zel'dovich, A. L. Buchachenko, and E. L. Frankevich, Usp. Fiz. Nauk **155** (1), 3 (1988) [Sov. Phys. Usp. **31**, 385 (1988)].
9. A. L. Buchachenko, R. Z. Sagdeev, and K. M. Salikhov, *Magnetic and Spin Effects in Chemical Reactions* (Nauka, Novosibirsk, 1978).
10. I. D. Belova, S. A. Zav'yalov, and Yu. E. Roginskaya, Zh. Fiz. Khim. **60** (9), 2338 (1986).
11. A. I. Gusev, S. I. Alyamovskii, Yu. G. Zaĭnulin, and G. P. Shveĭkin, Usp. Khim. **55** (12), 2067 (1986).
12. M. Yu. Moiseev, V. A. Onishchenko, and V. P. Shantorovich, Zh. Tekh. Fiz. **55** (7), 1444 (1985) [Sov. Phys. Tech. Phys. **30**, 833 (1985)].

*Translated by O. Borovik-Romanova*



---

**MAGNETISM  
AND FERROELECTRICITY**

---

## Description of Ferroelectric Phase Transitions in Solid Solutions of Relaxors in the Framework of the Random-Field Theory

**M. D. Glinchuk\*, E. A. Eliseev\*, V. A. Stephanovich\*\*, and B. Hilczer\*\*\***

\* *Frantsevich Institute of Materials Science Problems, National Academy of Sciences of Ukraine, ul. Krzhizhanovskogo 3,  
Kiev, 03142 Ukraine*

\*\* *Institute of Mathematics, Opole University, Opole, 45-052 Poland*

\*\*\* *Institute of Molecular Physics, Polish Academy of Sciences, Poznan, 61-614 Poland*

*e-mail: glin@materials.kiev.ua*

Received November 15, 2000

**Abstract**—A model based on the random-field theory is proposed for calculating the properties of solid solutions of ferroelectric relaxors. The electric dipoles randomly distributed in the system are treated as sources of random fields. The random field distribution function is calculated taking into account the contribution of nonlinear and correlation effects and the differences in the dipole orientations for different solid solution components. The dependence of the phase transition temperature  $T_c$  on the concentration of solid solution components is analyzed. Numerical calculations are performed for the lead scandoniobate and lead scandotantalate solid solutions  $(\text{PbSc}_{1/2}\text{Nb}_{1/2}\text{O}_3)_{1-x}(\text{PbSc}_{1/2}\text{Ta}_{1/2}\text{O}_3)_x$  with different degrees of ordering and the lead magnoniobate and lead titanate solid solution  $(\text{PbMg}_{1/3}\text{Nb}_{2/3}\text{O}_3)_{1-x}(\text{PbTiO}_3)_x$ . It is shown that the higher transition temperature for more disordered solid solutions of the composition  $(\text{PbSc}_{1/2}\text{Nb}_{1/2}\text{O}_3)_{1-x}(\text{PbSc}_{1/2}\text{Ta}_{1/2}\text{O}_3)_x$  in the range  $0 \leq x < 0.5$  is associated with the larger nonlinearity coefficient for  $\text{PbSc}_{1/2}\text{Nb}_{1/2}\text{O}_3$  as compared to that for  $\text{PbSc}_{1/2}\text{Ta}_{1/2}\text{O}_3$ . The theory provides a means for calculating the region of the coexistence of the phases with different symmetry groups in the temperature–composition phase diagram of the  $(\text{PbMg}_{1/3}\text{Nb}_{2/3}\text{O}_3)_{1-x}(\text{PbTiO}_3)_x$  solid solution. Numerical calculations with the use of the fitting parameters obtained from the known transition temperatures  $T_c$  for the solid solution components adequately describe the experimental phase diagrams for the aforementioned solid solutions of ferroelectric relaxors. © 2001 MAIK “Nauka/Interperiodica”.

### 1. INTRODUCTION

Solid solutions of different-type ferroelectric relaxors, namely,  $\text{PbMg}_{1/3}\text{Nb}_{2/3}\text{O}_3$  (PMN),  $\text{PbSc}_{1/2}\text{Ta}_{1/2}\text{O}_3$  (PST),  $\text{PbSc}_{1/2}\text{Nb}_{1/2}\text{O}_3$  (PSN), and  $\text{Pb}_{1-x}\text{La}_x\text{Zr}_{0.65}\text{Ti}_{0.35}\text{O}_3$  at  $x = 0.08–0.09$  (PLZT8–9/65/35), have been investigated extensively in recent years [1]. However, the mechanisms responsible for the unusual properties of these materials, such as the Vogel–Fulcher law for the dynamic permittivity, the nonergodic behavior, and the distribution of the maxima of the different properties over a wide temperature range ( $\Delta T \sim 100$  K for the maximum permittivity in PMN), remain unclear. Relaxors are characterized by random fields associated with the disorder in interstices, lead and oxygen vacancies, and impurity atoms. It was demonstrated that making allowance for the local distribution of these fields leads to the Vogel–Fulcher law [2], anomalies of the nonlinear permittivity [3], continuous spectra of the relaxation time, and considerable deviations of the permittivity behavior from the Debye law [4]. A model proposed in [5] for the quantitative description of the properties of relaxor ferroelectrics was based on the assumption that random fields destroy the long-range

order that could appear at the Burns temperature  $T_d$  ( $T_d \sim 600$  K for the majority of relaxors), which results in the formation of a mixed ferroelectric or dipole glass state (both states exhibit a nonergodic behavior). In the case of PLZT, the initial phase is PZT, whose ferroelectric long-range order is destroyed (completely at  $x = 0.07$  or partly at  $x < 0.07$ ) by random fields induced by impurity La ions. The degree of disorder is controlled by a special technological treatment, which leads to a decrease in the number of random-field sources in PST and PSN relaxors and other representatives of the 1 : 1 class. For PMN (a relaxor of the 1 : 2 class), the degree of ordering cannot be increased by a technological treatment. However, this can be achieved with the addition of  $\text{PbTiO}_3$  (PT) (see, for example, [6] and references therein). In particular, according to the experimental data [6], the  $(\text{PMN})_{1-x}(\text{PT})_x$  solid solution undergoes a morphotropic phase transition from the rhombohedral to the tetragonal phase at  $x_c \approx 0.35$ . The usual ferroelectric behavior is observed at  $x > x_c$ . Up to now, there has been no theoretical description of the phase diagram for this solution, which is necessary for the elucidation of the physical nature and mechanisms

responsible for the behavior of ferroelectric relaxors. On the other hand, the solution of these problems is of importance in view of the giant electrostriction associated with a high dielectric response which leads to an extremely large electromechanical coefficient [ $k \sim 0.92$  for (PMN)<sub>0.9</sub>(PT)<sub>0.1</sub> single crystals]. These anomalous properties render solid solutions of ferroelectrics very attractive for use in electromechanical transducers, drives, sonars, etc. [7, 8].

The (PSN)<sub>1-x</sub>(PST)<sub>x</sub> solid solution is also a promising material for these applications [9]. The phase diagram of the solid solution of PSN and PST relaxors (and their behavior) with different degrees of disordering exhibits features that remain unexplained up to now. The most interesting feature is an increase in the transition temperature  $T_c$  in PSN and a decrease in this temperature in PST with an increase in the disorder. As follows from the experimental dependence  $T_c(x)$  at  $0 < x < 1$  for solid solutions of PSN and PST with different degrees of ordering of the components [10–12], the aforementioned feature is observed over a wide range of component concentrations:  $T_c^{\text{dis}}(x) > T_c^{\text{ord}}(x)$  at  $x < 0.5$ . In our recent work [13], we experimentally and theoretically investigated anomalies of the dielectric response (the occurrence of the high-temperature and low-temperature maxima which obey the Vogel–Fulcher and Arrhenius laws, respectively) in PbSc<sub>0.5</sub>(Nb<sub>0.2</sub>Ta<sub>0.3</sub>)O<sub>3</sub> single crystals.

In the present work, we proposed the method for calculating the phase diagrams of similar solid solutions in terms of the random-field theory.

We obtained the theoretical dependences of the transition temperature and the order parameters on the concentration. It was shown that the differences in the behavior of PSN and PST are associated with the contribution made by nonlinear and correlation effects to random fields. The calculated phase diagrams agree reasonably with the experimental phase diagrams for the (PMN)<sub>1-x</sub>(PT)<sub>x</sub> and (PSN)<sub>1-x</sub>(PST)<sub>x</sub> solid solutions.

## 2. MODEL

Relaxors belong to the class of disordered ferroelectrics. In these materials, the electric dipoles arranged randomly tend to order the system through indirect dipole–dipole interactions with the soft mode of the initial phase, whereas other sources of random fields attempt to disorder this system. In the case when these forces are in equilibrium, dipoles aligned in the same direction can appear in the system. The fraction  $L$  of these dipoles can be calculated in the framework of the random-field theory by the equation

$$\mathbf{L} = \int_{-\infty}^{+\infty} \langle \mathbf{l} \rangle f(\mathbf{E}, \mathbf{L}) d\mathbf{E}, \quad (1)$$

where  $f(\mathbf{E}, \mathbf{L})$  is the distribution function of the random field  $\mathbf{E}$ .

In essence,  $L$  is the dimensionless order parameter, which is expressed through the normalized dipole moment  $\langle \mathbf{l} \rangle = \langle \mathbf{d}^* \rangle / d^*$  [where  $d^*$  is the effective dipole moment related to the parameter of the Lorentz field (for more detail, see [14])] averaged over all the possible orientations with the random field distribution function. In the case of two possible directions ( $l_z = \pm 1$ ,  $l_x = l_y = 0$ ),  $\langle l_z \rangle = \tanh(d^* E_z / kT)$  and expression (1) can be rewritten as

$$L_z = \int_{-\infty}^{+\infty} \tanh(d^* E_z / kT) f(E_z, L_z) dE_z. \quad (2)$$

For a completely ordered system that is usually described within the mean-field approximation,  $f(E, L) = \delta(E - E_0 L)$ , where  $E_0$  is the mean field ( $d^* E_0 = kT_{\text{cmf}}$ ). Then, Eq. (2) leads to the well-known relationship for order–disorder type ferroelectrics  $L_{\text{mf}} = \tanh(d^* E_0 L_{\text{mf}} / kT)$  and  $T > T_{\text{cmf}}$  at  $L_{\text{mf}} = 0$ .

In order to describe the  $A_{1-x}B_x$  solid solution composed of two ferroelectric relaxors, we should consider two types of electric dipoles  $d_{1z}^*$  and  $d_{2z}^*$  with different directions with respect to the lattice of the initial phase, which allow for the symmetry of different phases and are determined by the  $z$  and  $z'$  axes, respectively. Dipoles of each type should be described by their own order parameter ( $L_{1z}$  and  $L_{2z'}$ ). The distribution function  $F = f_1(E, L_{1z}, L_{2z'})$  depends on two order parameters, because random fields in the given case are induced by dipoles of both types. Consequently, the equations for the  $L_{1z}$  and  $L_{2z'}$  order parameters can be written in the form of expression (2) with this distribution function and the  $d_{1z}^*$  or  $d_{2z}^*$  dipole, respectively, instead of  $d^*$ .

The majority of the characteristics of the disordered system are included in the random field distribution function  $f(E, L)$ , which is calculated within the statistical theory with due regard for the contribution from electric dipoles, point charges, and dilatation centers [14]. The contribution from nonlinear and spatial correlation effects was taken into account in [15]. By considering all these effects for materials with a cubic symmetry group (see [15]) and electric dipoles as the main sources of a random field, we can obtain the set of equations for the order parameters

$$\begin{aligned} L_1 \equiv L_{1z} &= \int_{-\infty}^{+\infty} \tanh \frac{d_{1z}^* (\epsilon_z + \alpha_3^{(1)} \epsilon_z^{(3)})}{kT} f_1(\epsilon_z, L_1, L_2) d\epsilon_z, \\ L_2 \equiv L_{2z'} &= \int_{-\infty}^{+\infty} \tanh \frac{d_{2z'}^* (\epsilon_{z'} + \alpha_3^{(2)} \epsilon_{z'}^{(3)})}{kT} f_2(\epsilon_{z'}, L_1, L_2) d\epsilon_{z'}. \end{aligned} \quad (3)$$

Here,  $\alpha_3^{(1,2)}$  are the nonlinearity coefficients (with the dimensionality  $\varepsilon^{-2}$ ) of the corresponding initial phases (see [15]), and the distribution functions  $f_{1,2}$  have the form

$$f_1(\varepsilon_z, L_1, L_2) = \frac{1}{2} \int_{-\infty}^{+\infty} \exp(-\rho_z^2 \eta_1) \cos \left[ \rho_z \left( \varepsilon_z - (1-x) \right. \right. \\ \left. \left. \times \frac{T_{\text{cmf}2}}{d_2^*} L_2 \cos(\angle \mathbf{l}_1, \mathbf{l}_2) - x \frac{T_{\text{cmf}1}}{d_1^*} L_1 \right) \right] d\rho_z, \quad (4)$$

$$f_2(\varepsilon_z, L_1, L_2) = \frac{1}{2} \int_{-\infty}^{+\infty} \exp(-\rho_z^2 \eta_2) \cos \left[ \rho_z \left( \varepsilon_z - (1-x) \right. \right. \\ \left. \left. \times \frac{T_{\text{cmf}2}}{d_2^*} L_2 - x \frac{T_{\text{cmf}1}}{d_1^*} L_1 \cos(\angle \mathbf{l}_1, \mathbf{l}_2) \right) \right] d\rho_z,$$

$$\eta_1 = \cos^2(\angle \mathbf{l}_1, \mathbf{l}_2) \xi_1 + \xi_2,$$

$$\eta_2 = \xi_1 + \cos^2(\angle \mathbf{l}_1, \mathbf{l}_2) \xi_2, \quad (5)$$

$$\xi_1 = \frac{16\pi}{15} \frac{d_1^{*2}}{\varepsilon_1 r_{c1}^3} n_1, \quad \xi_2 = \frac{16\pi}{15} \frac{d_2^{*2}}{\varepsilon_2 r_{c2}^3} n_2.$$

In relationship (4),  $\xi_1$  and  $\xi_2$  determine the contributions to the half-widths of the Gaussian distribution functions for dipoles of the first and second types, respectively;  $\varepsilon_{1,2}$  and  $r_{c1,2}$  are the permittivities and the correlation radii of the initial phases of the A and B relaxors; and  $n_1 = \beta_1 x / a_1^3$  and  $n_2 = \beta_2 (1-x) / a_2^3$  are the concentrations of dipoles of the first and second types (here,  $\beta_i$  are the fractions of unit cells containing dipoles and  $a_i$  are the lattice spacings for the initial phases of relaxors). Note that different forms of the  $f_1$  and  $f_2$  distribution functions stem from different dipole orientations, which is reflected by the multiplier  $\cos(\angle \mathbf{l}_1, \mathbf{l}_2)$ . It is evident that, at  $\angle \mathbf{l}_1, \mathbf{l}_2 = 0$ , we have  $f_1 = f_2$ .

The total polarization  $\mathbf{P}$  of the system can be expressed in terms of  $L_1$  and  $L_2$  in the following form:

$$\mathbf{P} = x \frac{\beta_1 \mathbf{d}_1^* L_1}{a_1^3} + x \frac{\beta_2 \mathbf{d}_2^* L_2}{a_2^3}. \quad (6)$$

### 3. PHASE DIAGRAM OF THE SYSTEM

The phase diagram describes the dependence of the transition temperature  $T_c$  on the composition of the system or the mole fraction  $x$  of solid solution components. The  $T_c$  temperatures as a function of  $x$  can be obtained from Eqs. (3) and (4) as the temperatures at which these equations can possess nonzero solutions. As is seen from expression (4), the  $f_1$  and  $f_2$  distribution

functions in the limits  $L_1 \rightarrow 0$  and  $L_2 \rightarrow 0$  can easily be represented as

$$f_{1,2}(\varepsilon_i, L_1, L_2) = f_{01,2}(\varepsilon_i) - k_{1,2} \left( \frac{df_{1,2}}{d\varepsilon_i} \right)_{L_1=L_2=0}, \quad (7)$$

$$i = z, z',$$

$$k_1 = (1-x) \frac{T_{\text{cmf}2} L_2}{d_2^*} \cos(\angle \mathbf{l}_1, \mathbf{l}_2) + x \frac{T_{\text{cmf}1} L_1}{d_1^*}, \quad (8)$$

$$k_2 = (1-x) \frac{T_{\text{cmf}2} L_2}{d_2^*} + x \frac{T_{\text{cmf}1} L_1}{d_1^*} \cos(\angle \mathbf{l}_1, \mathbf{l}_2),$$

$$f_{01,2}(\varepsilon_i) = \frac{1}{2\sqrt{\pi\eta_{1,2}}} \exp\left(-\frac{\varepsilon_i^2}{4\eta_{1,2}}\right). \quad (9)$$

Substituting expressions (7)–(9) into formulas (3) and integrating, we obtain the set of equations for the calculation of  $T_c(x)$

$$L_1 = [(1-x)T_{\text{cmf}2}L_2\Delta \cos(\angle \mathbf{l}_1, \mathbf{l}_2) + xT_{\text{cmf}1}L_1] \frac{1}{kT_c} I_1, \quad (10)$$

$$L_2 = \left[ (1-x)T_{\text{cmf}2}L_2 + x \frac{T_{\text{cmf}1}}{\Delta} L_1 \cos(\angle \mathbf{l}_1, \mathbf{l}_2) \right] \frac{1}{kT_c} I_2,$$

$$I_{1,2} = \int_{-\infty}^{+\infty} f_{01,2}(\varepsilon) \frac{(1 + 3\varepsilon^2 \alpha_3^{(1,2)}) d\varepsilon}{\cosh^2 \frac{d_{1,2}^*}{kT_c} (\varepsilon + \alpha_3^{(1,2)} \varepsilon^3)}, \quad (11)$$

$$\Delta = \frac{d_1^*}{d_2^*}.$$

The  $I_1$  and  $I_2$  integrals depend on the  $T_c$  temperature, the concentrations of the solid solution components, and other material parameters of the system.

The solvability condition (10) gives the following equation for  $T_c$ :

$$T_c^2 - C_2(T_c)T_c + C_1(T_c) = 0, \quad (12)$$

$$C_1(T_c) = (1-x)xI_1I_2T_{\text{cmf}1}T_{\text{cmf}2}[1 - \cos^2(\angle \mathbf{l}_1, \mathbf{l}_2)];$$

$$C_2(T_c) = xI_1T_{\text{cmf}1} + (1-x)I_2T_{\text{cmf}2}. \quad (13)$$

The dependence of the  $C_{1,2}$  coefficients on  $T_c$  is defined by the integrals  $I_{1,2}$  [see formula (11)], so that Eq. (12) is the integral equation for  $T_c$  and can be solved only numerically.

The multiplier  $1 - \cos^2(\angle \mathbf{l}_1, \mathbf{l}_2)$  reflects the dependence on the orientations of the  $\mathbf{d}_1^*$  and  $\mathbf{d}_2^*$  dipoles. For example, this multiplier is equal to  $2/3$  when different-type dipoles are aligned with the [001] and [111] crystallographic directions [i.e.,  $\cos(\angle \mathbf{l}_1, \mathbf{l}_2) = 1/\sqrt{3}$ ] and to zero when the dipoles are aligned identically [i.e.,  $\cos(\angle \mathbf{l}_1, \mathbf{l}_2) = 1$ ]. In the latter case, Eq. (12) is

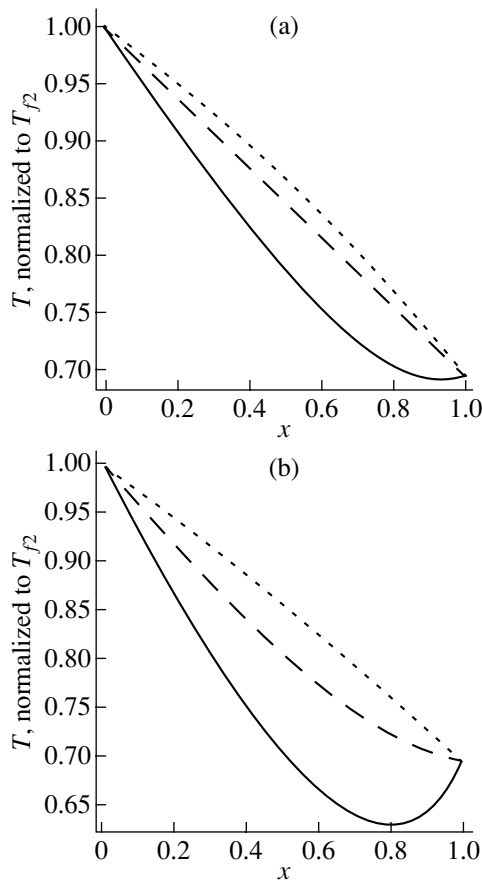


**Fig. 1.** Dependences of the dimensionless transition temperature  $\tau_c = T_c(x)/T_{f2}$  [where  $T_{f2} = T_c(x=0)$ ] on the mole fraction  $x$  for the collinear vectors  $\mathbf{d}_1^*$  and  $\mathbf{d}_2^*$  at the ratios  $d_2^*/d_1^* = 0.6$  (solid lines),  $0.7$  (dashed lines), and  $0.8$  (dotted lines). Nonlinearity coefficients: (a)  $\alpha_0^{(1)} = \alpha_0^{(2)} = 1$  and (b)  $\alpha_0^{(1)} = \alpha_0^{(2)} = 3$ .

reduced to  $T_c = C_2(T_c)$ , because the equation  $T_c = 0$  implies the absence of a phase transition. Evidently, Eq. (12) in the general case is separated into two independent equations for  $T_c(x)$ . It turns out that only the equation that formally corresponds to a “larger” root of Eq. (12) has a real solution.

As can be seen from relationships (9) and (11)–(13), the  $T_c$  temperature depends on several parameters, such as the nonlinearity coefficients, the half-widths of distribution functions, and the dipole moment ratio. In

order to illustrate the influence of particular parameters on the  $T_c(x)$  temperature, we constructed the dependences  $T_c(x)$  for the collinear vectors  $\mathbf{d}_1^*$  and  $\mathbf{d}_2^*$  [i.e.,  $T_c = C_2(T_c)$ ] at several dimensionless parameters (Fig. 1). As is seen from Fig. 1, an increase in the nonlinearity coefficients  $\alpha_0^{(i)}$  and the ratio  $\Delta^{-1} = d_2^*/d_1^*$  leads to an increase in the rate of decrease in  $\tau_c(x)$  with a decrease in the concentration of the second component and the influence of  $\Delta$  is also enhanced.

#### 4. THE $(\text{PSN})_{1-x}(\text{PST})_x$ SOLID SOLUTION OF RELAXORS OF THE 1 : 1 FAMILY

The properties of the components (PSN and PST) of this solid solution differ strongly: as the degree of disorder increases, the transition temperature  $T_c$  increases for PSN and decreases for PST. At first glance, the latter fact is obvious, whereas the properties of PSN seem to be rather strange, because it is believed that random fields in the general case bring about a decrease in the transition temperature  $T_c$ . On the other hand, an increase in the strength of random fields can lead to the necessity of allowing for nonlinear and correlation effects, which should apparently depend on the nonlinearity coefficients of the materials under consideration. Taking into account that PSN and PST contain oxygen octahedra with scandium, niobium, and tantalum, it can be concluded that the nonlinearity coefficient for PSN should be larger than that for PST, since Sepliarsky *et al.* [16] showed that this coefficient for niobium octahedra is several times larger than that for tantalum octahedra.

In order to calculate the  $T_c(x)$  dependences for the  $(\text{PSN})_{1-x}(\text{PST})_x$  solid solutions with different degrees of disorder, we introduce the following parameters:

$$q_i = \frac{\sqrt{\xi_{0i}} d_i^*}{k T_{\text{cmfi}}}, \quad \xi_{0i} = \frac{16\pi d_i^{*2} \beta_i}{15 \varepsilon_i^2 r_{ci}^2 a_i^3}, \quad (14)$$

$$\alpha_0^{(i)} = \alpha_3^{(i)} \left( \frac{k T_{\text{cmfi}}}{d_i^*} \right),$$

where  $q_i$  and  $\alpha_0^{(i)}$  are the dimensionless half-widths and the nonlinearity coefficients of the  $i$ th initial phase, respectively, and  $\xi_{0i}$  are the half-widths independent of the mole fractions of the solid solution components. The transition temperatures  $T_{\text{cmfi}}$  in the mean-field approximation for PST and PSN were taken from [17].

The nonlinearity coefficients  $\alpha_0^{(i)}$  and the half-widths  $q_i$  for PSN and PST were obtained by the fitting of the transition temperatures  $T_c$  calculated by formulas (12) and (13) for PSN ( $x=0$ ) and PST ( $x=1$ ) to the experimental values of  $T_c$  (see, for example, [10, 11] and references therein). Two groups of parameters were applied to two series of samples with different degrees

#### Fitting parameters

Material	PSN		PST	
	$\alpha_0^{(i)}$	$q_i$	$\alpha_0^{(i)}$	$q_i$
Samples				
Ordered	0	0.416	0	0.477
Disordered	0.3	0.425	0.098	0.499

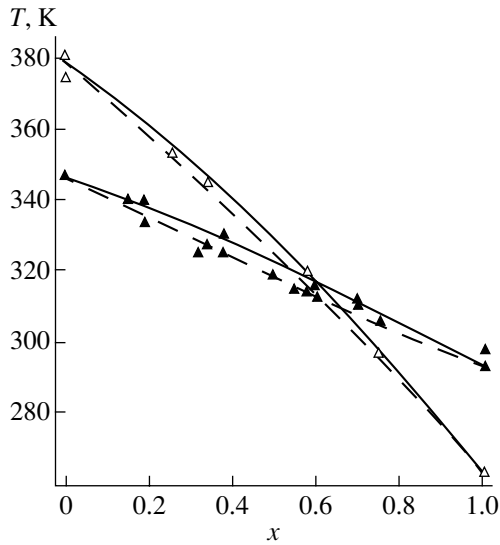


**Fig. 2.** Phase diagrams of the  $(\text{PSN})_{1-x}(\text{PST})_x$  solid solution for less ordered (open triangles) and more ordered (closed triangles) ceramic samples according to the data taken from [10–12]. The solid and dashed lines are the dependences calculated with the following parameters:  $\alpha_0^{(1)} = \alpha_0^{(2)} = 0$  at the ratios  $d_2^*/d_1^* = 0.75$  (solid line) and 0.68 (dashed line) for more ordered samples and  $\alpha_0^{(1)} \approx 0.1$  and  $\alpha_0^{(2)} \approx 0.3$  at the ratios  $d_2^*/d_1^* = 0.8$  (solid line) and 0.7 (dashed line) for less ordered samples.

of disorder. In this case, we accounted for the relationship (obtained in [16]) between the nonlinearity coefficients for less ordered samples. The parameters used are listed in the table.

With due regard for the fact that the parameters of the initial phases for PSN and PST are close to each other, we have the expression  $q_1/q_2 \approx (d_1^*/d_2^*)^2 = \Delta^2$ . Substitution of the parameters from the table to this expression gives  $1/\Delta = 0.92$  for disordered samples and  $1/\Delta = 0.93$  for ordered samples. The parameters thus obtained enable us to calculate the  $T_c(x)$  temperatures for the disordered and ordered  $(\text{PSN})_{1-x}(\text{PST})_x$  solid solutions without additional fitting parameters. For simplicity, we assume that the orientations of the  $\mathbf{d}_1$  and  $\mathbf{d}_2$  dipoles are identical. The calculated and experimental [10–12]  $T_c(x)$  temperatures are compared in Fig. 2. We used two different sets of the  $\Delta$  parameters in order to demonstrate that the concentration  $x_c$  at which  $T_c(\text{disordered}) = T_c(\text{ordered})$  is sensitive to a variation in these parameters. As is seen, the theoretical and experimental data agree sufficiently well considering the fact that different experimental dependences of  $T_c$  were obtained under different experimental conditions (see [10] and references therein).

As follows from calculations of  $L_1$  and  $L_2$  by formulas (3),  $L_2 > L_1$  for both less and more ordered relaxors. Moreover, the order parameters  $L$  for ordered samples

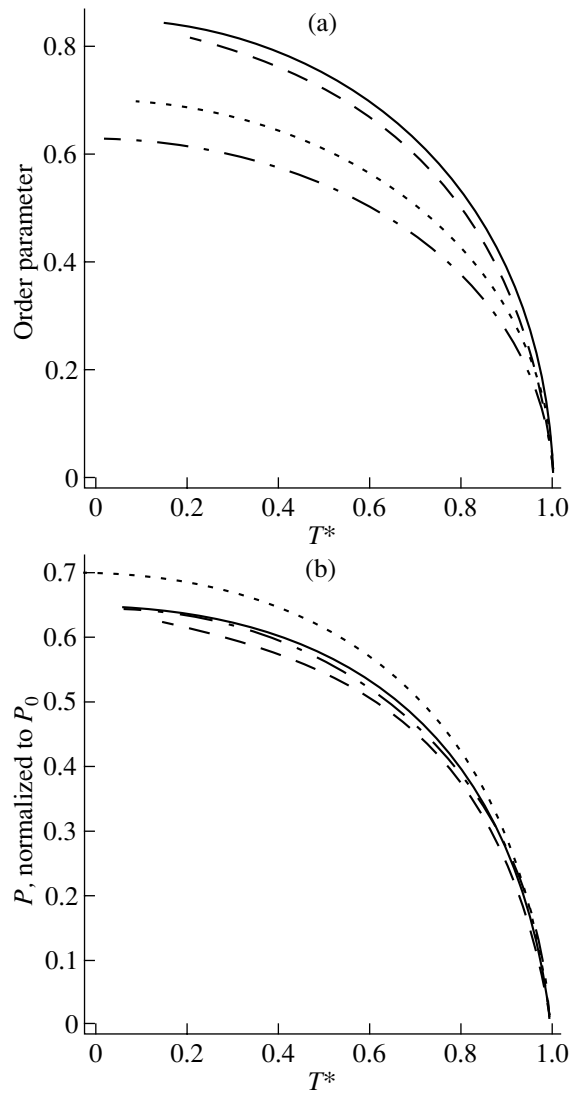


**Fig. 3.** (a) Dependences of the fraction  $L$  of coherently oriented dipoles on the dimensionless temperature  $T^* = T/T_c$  (where  $T_c$  is the concentration-dependent transition temperature) for the  $(\text{PSN})_{1-x}(\text{PST})_x$  solid solutions at  $x = 0$  (PSN) for more ordered (solid line) and less ordered (dashed line) samples and  $x = 1$  (PST) for more ordered (dotted line) and less ordered (dot-and-dash line) samples. (b) Dependences of the polarization  $P/P_0$  (where  $P_0 = \beta_1 d_1^*/a_1^3$ ) on the dimensionless temperature  $T^*$  for the  $(\text{PSN})_{1-x}(\text{PST})_x$  solid solutions at  $x = 0.3$  for more ordered (solid line) and less ordered (dashed line) samples and  $x = 0.8$  for more ordered (dotted line) and less ordered (dot-and-dash line) samples.

are larger than those for disordered samples. The non-zero parameters  $L_1$  and  $L_2$  over the entire range of component concentrations suggest that each component exhibits a mixed ferroelectric glassy state. The results of numerical calculations for certain concentrations of solid solution components are displayed in Fig. 3. Figure 3a shows the temperature dependences of the fraction of coherently oriented dipoles for PSN ( $x = 0$ ) and PST ( $x = 1$ ). This fraction is proportional to the polar-

ization of these materials. By using relationship (6) (at parallel  $\mathbf{d}_1$  and  $\mathbf{d}_2$  dipoles and  $\beta_1 = \beta_2$ ), we calculated the temperature dependences of the dimensionless polarization (normalized to  $P_0 = \beta_1 d_1^* / a_1^3$ ) for the solid solutions of two relaxors at  $x = 0.3$  and  $0.8$  (Fig. 3b). It is seen that an increase in  $x$  brings about an increase in the polarization  $P(x)$ , and the values of  $P(x)$  for more ordered samples are larger than those for less ordered samples.

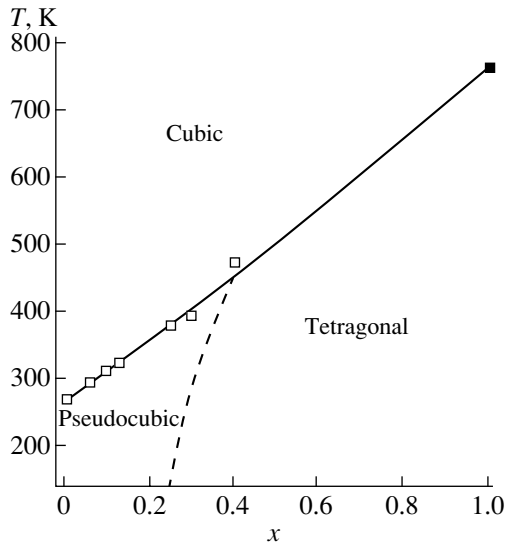


**Fig. 4.** Phase diagram of the  $(\text{PMN})_{1-x}(\text{PT})_x$  solid solution. Open and closed squares correspond to the experimental data taken from [6]. The solid line represents the calculated transition temperature  $T_c(x)$ , and the dashed line is the theoretical curve of the coexistence of two phases.

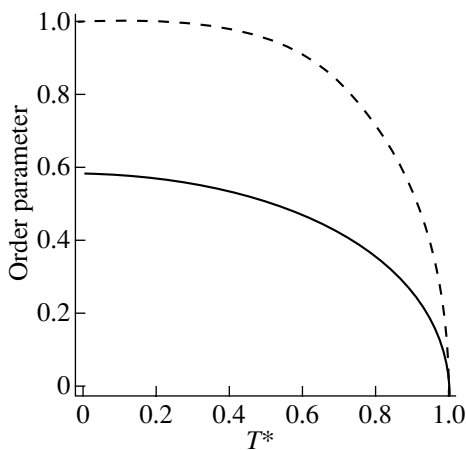


**Fig. 5.** Dependences of the fraction  $L$  of coherently oriented dipoles on the dimensionless temperature  $T^* = T/T_c$  (where  $T_c$  is the concentration-dependent transition temperature) for PMN (solid line) and PT (dashed line) solid solutions.

## 5. THE $(\text{PMN})_{1-x}(\text{PT})_x$ SOLID SOLUTION

This system is the solid solution of the PMN relaxor (component 2) and the  $\text{PbTiO}_3$  (PT) ferroelectric (component 1). The calculation of the phase diagram for this system, for the most part, is similar to that described in the preceding section but involves certain distinguishing features.

For  $\text{PbTiO}_3$ , the transition to the ferroelectric phase at a temperature of 763 K is adequately described within the mean-field approximation. Therefore, we can set  $T_{\text{cmf1}} = 763$  K, treat the random field distribution function for pure PT as a delta function, and assume that the half-width  $\xi_1$  of component 1 [see formula (5)] is equal to 0. Since we suppose that each unit cell of lead titanate contains an electric dipole, the relationship for the dipole concentration can be written as  $n_1 = x/a_1^3$ , where  $a_1$  is the lattice parameter of lead titanate.

The relaxor state of lead magnoniobate PMN was regarded as a mixed ferroelectric glassy phase in which the short-range and long-range orders coexist. This is supported by the features in the nonlinear permittivity of PMN [18]. In our case, dipoles in PMN and PT are aligned with the [111] and [100] crystallographic directions, respectively. Hence, the transition temperatures  $T_c(x)$  were calculated by relationships (12) and (13) at  $\cos(\angle \mathbf{l}_1, \mathbf{l}_2) = 1/\sqrt{3}$ . The nonlinear and correlation effects were ignored in calculations, because their inclusion did not lead to a decrease in the discrepancy between the calculated and experimental dependences  $T_c(x)$ . The results of calculations are shown in Fig. 4. The parameters  $q_2 = 0.51$  and  $\Delta = 1/3$  were obtained from the best fitting of the theoretical dependence  $T_c(x)$  to the experimental data (the choice  $q_1 = 0$  was justified above). It is easy to see that the results of calculations are in reasonable agreement with the experimental phase diagram.

With the aim of elucidating the symmetry of compounds with different compositions and its variation with temperature, we calculated the  $L_1$  and  $L_2$  order parameters at different concentrations of the solid solution components. First, we calculated the order parameters for PMN ( $x = 0$ ) and PT ( $x = 1$ ) with the use of the above parameters (Fig. 5). A comparison of the dependences shown by the solid and dashed lines in Fig. 5 clearly demonstrates the difference in the behavior of the order parameters for the mixed ferroelectric glass (PMN) and the usual ferroelectric material (PT). As can be seen,  $L_2 \approx 0.58$  at  $T = 0$  K; i.e., the contribution from the long-range order for PMN is sufficiently large at low temperatures. The total polarization of the solid solution was calculated by formula (6), in which the first and second terms are the contributions from the corresponding solid solution components:  $\mathbf{P}(x) = \mathbf{P}_1(x) + \mathbf{P}_2(x)$ . The concentration corresponding to  $|\mathbf{P}_1(x)| = |\mathbf{P}_2(x)|$  was attributed to the region in which the compounds with different symmetries coexist, i.e., to

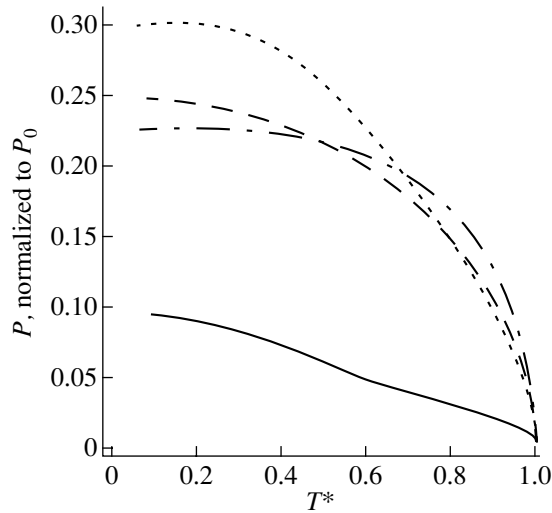


**Fig. 6.** Dependences of the polarization components  $P/P_0$  (where  $P_0 = \beta_1 d_1^*/a_1^3$ ) on the dimensionless temperature  $T^* = T/T_c$  (where  $T_c$  is the concentration-dependent transition temperature) for the  $(\text{PMN})_{1-x}(\text{PT})_x$  solid solution. The solid (dotted) and dashed (dot-and-dash) lines correspond to the components with the rhombohedral and tetragonal symmetry groups at  $x = 0.1$  (0.3), respectively.

the morphotropic region in the phase diagram. The temperature dependences of the polarizations  $|\mathbf{P}_1(x)|$  and  $|\mathbf{P}_2(x)|$  at certain concentrations  $x$  are displayed in Fig. 6.

The most interesting feature of Fig. 6 is the occurrence of the curves intersecting at a certain temperature  $T = T_{cr}(x)$  for  $x = 0.3$  and the nonintersecting curves for  $x = 0.1$ . This means that  $|\mathbf{P}_1| = |\mathbf{P}_2|$  at  $T = T_{cr}(x)$  (morphotropic region),  $|\mathbf{P}_1| > |\mathbf{P}_2|$  at  $T > T_{cr}(x)$  and  $|\mathbf{P}_1| < |\mathbf{P}_2|$  at  $T < T_{cr}(x)$ ; i.e., the symmetry group of the solid solution at these relations corresponds to the symmetry group of the first or second component, respectively. The temperatures  $T_{cr}(x = 0.3) = 275$  K and  $T_{cr}(x = 0.4) = 460$  K were obtained for the  $(\text{PMN})_{1-x}(\text{PT})_x$  solid solution. Consequently, the  $T_{cr}$  temperature increases with an increase in the concentration (Fig. 4, dashed line). On this basis, we assign the appropriate symmetry group (pseudocubic for PMN and tetragonal for PT) to different regions in the phase diagram of the  $(\text{PMN})_{1-x}(\text{PT})_x$  solid solution (see Fig. 4). This assignment is in complete agreement with the experimental data [6].

Since compositions with a low lead titanate concentration ( $\sim 10\%$ ) are of importance for various applications [7, 8], we have constructed the dependences of the fraction of coherently oriented dipoles for each component of the solid solution (Fig. 7a) and the dependences of the corresponding polarization components (Fig. 7b) with tetragonal (solid line) and pseudocubic (rhombohedral) (dashed line) symmetry groups at the temperature  $T = 0$  K. It can easily be seen from Fig. 7b that an increase in the lead titanate fraction  $x$  results in a linear

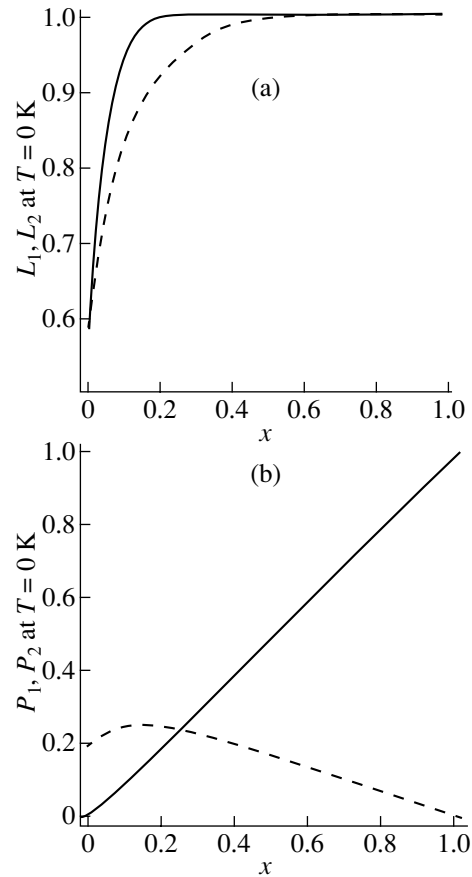


**Fig. 7.** Dependences of (a) the fraction  $L$  of coherently oriented dipoles and (b) the polarization components  $P/P_0$

(where  $P_0 = \beta_1 d_1^*/a_1^3$ ) on the mole fraction  $x$  for the  $(\text{PMN})_{1-x}(\text{PT})_x$  solid solution at  $T = 0$  K. The dashed and solid lines correspond to the components with the rhombohedral and tetragonal symmetry groups, respectively.

increase in the tetragonal component, whereas the rhombohedral component exhibits a maximum at  $x \approx 0.135$ . The appearance of this maximum can be caused by the competition between an increase in the fraction  $L_2$  of coherently oriented dipoles of lead magnoniobate (Fig. 7a, dashed line) and a decrease in its mole fraction  $1 - x$  with an increase in  $x$  [see formula (6)]. This maximum of the pseudocubic polarization component at  $x \approx 0.135$  can explain the observed maxima of the dielectric response and the piezoelectric and electromechanical coefficients at  $x \approx 0.1$  [7, 8], which is only slightly less than 0.135.

## 6. CONCLUSION

Thus, the model for calculating the ferroelectric order parameters and the temperature–concentration phase diagram for solid solutions of relaxors was proposed. The model is based on the theory of random fields and their effect on the properties of the system

under investigation. The electric dipoles randomly distributed in the system were treated as the main source of random fields. The random field distribution function was considered with due regard for the nonlinear and correlation contributions. Numerical calculations were performed for the PSN–PST and PMT–PT solid solutions. For the PSN–PST phase diagram at  $0 < x < 0.5$ , the transition temperature for less ordered samples was found to be higher than that for more ordered samples. This feature was explained by the contribution of the nonlinear effects, which for PSN is larger than that for PST. The obtained dependences of the transition temperature and the polarization of the  $(\text{PMN})_{1-x}(\text{PT})_x$  solid solution indicate the existence of the morphotropic region in the phase diagram, i.e., the region of the coexistence of the pseudocubic and tetragonal phases. The polarization component that corresponds to the pseudocubic component of the solid solution has a maximum at  $x \approx 0.135$ . This can explain the maximum of the electromechanical coupling coefficient at  $x \approx 0.1$ . The outlined theory adequately describes the experimental  $T$ – $x$  phase diagrams for the PSN–PST and PMN–PT solid solutions of relaxors.

#### REFERENCES

1. L. E. Cross, *Ferroelectrics* **150**, 305 (1994).
2. M. D. Glinchuk and V. A. Stephanovich, *J. Appl. Phys.* **85** (10), 1722 (1999).
3. M. D. Glinchuk and V. A. Stephanovich, *J. Phys.: Condens. Matter* **10**, 11081 (1998).
4. M. D. Glinchuk, V. A. Stephanovich, and B. Hilczer, *J. Appl. Phys.* (in press).
5. M. D. Glinchuk and R. Farhi, *J. Phys.: Condens. Matter* **8**, 6985 (1996).
6. E. V. Colla, N. K. Yushin, and D. Viehland, *J. Appl. Phys.* **83** (15), 3298 (1998).
7. S. E. Park and T. R. Shrout, *J. Appl. Phys.* **82** (4), 1804 (1997).
8. C. A. Randal, A. S. Bhalla, T. R. Shrout, and L. E. Cross, *J. Mater. Res.* **5**, 829 (1990).
9. N. K. Yushin, E. I. Smirnova, E. A. Tarakanov, and R. Sommer, *Fiz. Tverd. Tela (St. Petersburg)* **36** (2), 1321 (1994) [*Phys. Solid State* **36**, 721 (1994)].
10. V. Eremkin, V. Smotrakov, E. Gagarina, and I. Raevski, *J. Korean Phys. Soc.* **32** (6), S1597 (1998).
11. N. Setter and L. E. Cross, *J. Appl. Phys.* **51** (6), 4356 (1980).
12. N. Setter and L. E. Cross, *Ferroelectrics* **37**, 551 (1981).
13. M. D. Glinchuk, V. A. Stephanovich, B. Hilczer, *et al.*, *J. Phys.: Condens. Matter* **11**, 6263 (1999).
14. M. D. Glinchuk and V. A. Stephanovich, *J. Phys.: Condens. Matter* **6**, 6317 (1994).
15. M. D. Glinchuk, V. A. Stephanovich, and R. Farhi, *J. Phys.: Condens. Matter* **9**, 10237 (1997).
16. M. Sepliarsky, M. G. Stachiotti, and R. L. Migoni, *Phys. Rev. B* **52** (4), 4044 (1995).
17. O. I. Korshunov, P. A. Markovin, and R. V. Pisarev, *Ferroelectr. Lett. Sect.* **13**, 137 (1992).
18. M. D. Glinchuk and V. A. Stephanovich, *J. Phys.: Condens. Matter* **10**, 11081 (1998).

*Translated by O. Borovik-Romanova*



---

## MAGNETISM AND FERROELECTRICITY

---

# Features of the Shape of Raman Spectra of Disordered Ferroelectrics

M. D. Glinchuk and I. V. Kondakova

Frantsevich Institute of Materials Science Problems, National Academy of Sciences of Ukraine,  
ul. Krzhizhanovskogo 3, Kiev, 03142 Ukraine

e-mail: dep4@materials.kiev.ua

Received November 20, 2000

**Abstract**—A theory of the shape of the first-order Raman scattering (FORS) line is developed in which nonlinear and correlation effects in inhomogeneous broadening and the dynamic mechanism of homogeneous broadening are taken into account. It is shown that the FORS band generally has two peaks and that the shape of the low-frequency peak is determined by homogeneous broadening. Our theory provides an explanation for the features of the observed FORS band of the hard  $TO_2$  mode in KLT and KTN with various concentrations of Li and Nb ions. © 2001 MAIK “Nauka/Interperiodica”.

### 1. INTRODUCTION

The first-order Raman scattering (FORS) in disordered ferroelectrics is known to be a sensitive method for studying critical slowing-down of optical phonons in the vicinity of a ferroelectric phase transition and the dynamics of local fluctuations (see [1, 2] and references therein). Earlier, attempts were made to explain some features of the FORS spectra, such as a sharp increase in the intensity of the scattering peak near  $T_c$  and the special features of the line shape [3]. However, no general model for describing Raman spectra of disordered ferroelectrics in the vicinity of  $T_c$  has been proposed up to now, and there are discrepancies between the values of some physical quantities calculated from the experimental data (see [1, 4]). Such a general model should take into account both inhomogeneous broadening of the FORS lines due to static inhomogeneities and homogeneous broadening due to dynamic effects. Both types of broadening are observed in Raman spectra of  $\text{KTa}_{1-x}\text{Nb}_x\text{O}_3$  (KTN) and  $\text{K}_{1-x}\text{Li}_x\text{TaO}_3$  (KLT) [1–3].

The theory of inhomogeneous broadening of spectral lines in radio-frequency and optical spectroscopy has been developed in detail for dielectric and magnetic systems [5, 6]. In these materials, as a rule, inhomogeneous broadening does not depend on temperature and, therefore, the reason for the temperature dependence of the shape and width of a spectral line can be only homogeneous broadening. The distinctive feature of disordered ferroelectrics is that, as we have shown recently [7], inhomogeneous broadening in them is temperature-dependent because of nonlinear and spatial correlation effects, which are known to be especially significant near  $T_c$ .

In this paper, we develop a theory of the shape of FORS bands, which takes into account both the linear and nonlinear contributions from random fields to inho-

mogeneous broadening, as well as the mechanisms of homogeneous broadening. The theory explains the main features of the FORS spectra observed in KLT with 1 and 4% Li [3] and KTN with 15.7% Nb [2] when the phase transition point is approached on its high-temperature side. Since nonlinear effects are significant in the vicinity of phase transitions, our theory seems better founded than that proposed in [2, 3], where nonlinear and correlation effects were ignored when calculating the correlation function. Our theoretical model allows the Raman spectra to be described without calculating the correlation function of polarization fluctuations; only a specific expression for their spectral density obtained by a statistical method is used. The theory developed in this paper is general and can be applied to various ferroelectrics in the vicinity of phase transition points.

### 2. THEORY OF THE SHAPE OF THE RAMAN SCATTERING PEAKS

#### 2.1. The Raman Scattering Intensity

The virtual ferroelectric  $\text{KTaO}_3$  doped with Li or Nb ions can undergo a phase transition to the ferroelectric phase, or the dipole-glass phase, or a mixed ferroelectric glass phase, depending on the temperature and the impurity concentration [8, 9]. These materials can be considered as model systems for disordered ferroelectrics. Their special features are associated with off-center Li and Nb ions, which replace  $\text{K}^+$  and  $\text{Ta}^{5+}$  ions, respectively. These off-center ions are also responsible for some anomalies of the Raman spectra. In particular, quasi-static polarization fluctuations caused by the off-center ions can reduce the cubic symmetry of  $\text{KTaO}_3$  and give rise to FORS above the phase transition temperature  $T_c$  [1, 3]. The most detailed description of the

appearance of one-phonon Raman lines above  $T_c$  can be found in [10], where polar-phase nuclei of a finite size characterized by slow dynamics are shown to be able to cause quasi-first-order Raman scattering above  $T_c$ .

As is known, Raman scattering in ferroelectrics with a perovskite structure is caused by variations in the electron polarizability of oxygen  $\delta\alpha(\mathbf{r}, t)$  associated with optical lattice vibrations. These variations can be written as

$$\delta\alpha(\mathbf{r}, t) = \mathbf{P}(\mathbf{r}, t) \cdot \hat{\Lambda} \cdot \mathbf{P}(\mathbf{r}, t), \quad (1)$$

where  $\mathbf{P}(\mathbf{r}, t)$  is a spatial and temporal fluctuation of the polarization and  $\hat{\Lambda}$  is a fourth-rank tensor. Generally, Eq. (1) describes second-order Raman scattering. However, if polarization fluctuations can be represented as the sum of two terms, one of which,  $P^h$ , is associated with hard polar modes and the other,  $P^\mu$ , represents slowly relaxing fluctuations, then mixed terms  $P^\mu P^h$  in Eq. (1) will describe one-phonon Raman scattering above  $T_c$ . It is these terms that are responsible for quasi-first-order scattering when there are slowly relaxing polarization fluctuations induced by off-center ions. The intensity of Raman scattering is determined by spatial-temporal Fourier transforms of the polarization fluctuation correlation function

$$I(\omega) \sim \left\{ \begin{array}{l} \langle \sigma\alpha(\mathbf{r}, t)\delta\alpha(0, 0) \rangle_{\mathbf{q}=0, \omega} \\ \sum_{\mathbf{q}'} \int d\omega' \langle P^\mu(\mathbf{r}, t)P^\mu(0, 0) \rangle_{\mathbf{q}', \omega'} \\ \times \langle P^h(\mathbf{r}, t)P^h(0, 0) \rangle_{-\mathbf{q}', \omega-\omega'} \end{array} \right. \quad (2)$$

The first correlation function has a sharp maximum near  $\omega' = 0$ , while the second is maximal near  $\Omega_{\mathbf{q}'}$ ; therefore, the intensity  $I(\omega)$  has a maximum at  $\omega = \Omega_{\mathbf{q}'}$ , i.e., near the frequency of the hard one-phonon mode. The correlator decoupling, which allows one to represent  $I(\omega)$  as the product of pair correlators in Eq. (2), is justified, because the relaxation frequencies of the polarization fluctuation components  $P^h$  and  $P^\mu$  differ greatly in value and Eq. (2) becomes asymptotically exact in the static limit of slowly relaxing dipoles. From Eq. (2), it follows that the intensity can be written as the convolution of two functions which describe inhomogeneous and homogeneous broadening associated with the first and second correlators, respectively:

$$I(\omega) = I_0 \int_{-\infty}^{\infty} J(\omega, \omega') f(\omega') d\omega'. \quad (3)$$

Specific expressions for the homogeneous  $J(\omega, \omega')$  and inhomogeneous  $f(\omega')$  contributions can be derived as follows. The polarization fluctuation correlation function associated with hard optical phonons (thermal lattice vibrations) is usually approximated by a so-called quadratic Lorentzian  $\Gamma/[\Gamma^2\Omega^2 + (\omega^2 - \Omega^2)^2]$ . For fre-

quencies  $\omega$  close to hard-phonon frequencies  $\Omega_{\mathbf{q}'}$ , this function can be approximated by a simple Lorentzian, because  $(\omega^2 - \Omega^2)^2 \approx 4\Omega^2(\omega - \Omega)^2$ . Therefore, the expression

$$\langle P^h(\mathbf{r}, t)P^h(0, 0) \rangle_{-\mathbf{q}', \omega-\omega'} \sim \frac{1}{\Omega_{\mathbf{q}'}\Gamma^2 + (\omega - \omega' - \Omega_{\mathbf{q}'})^2} \quad (4)$$

will be valid in the frequency range where the difference  $(\omega - \omega')$  is close to the hard-phonon frequency  $\Omega_{\mathbf{q}'}$ . On the other hand, the correlation function of quasi-static polarization fluctuations is written as

$$\langle P^\mu(\mathbf{r}, t)P^\mu(0, 0) \rangle_{\mathbf{q}', \omega'} = \langle P^\mu(\mathbf{r})P^\mu(0) \rangle_{\mathbf{q}'} \frac{v_{\mathbf{q}'}}{v_{\mathbf{q}'}^2 - \omega'^2}. \quad (5)$$

Here,  $v_{\mathbf{q}'}$  is the relaxation frequency of the  $q$ th Fourier transform of fluctuations. In the quasi-static limit, the second factor on the right-hand side of Eq. (5) can be approximated by the  $\delta$  function and the correlator in Eq. (5) takes the form

$$\langle P^\mu(\mathbf{r}, t)P^\mu(0, 0) \rangle_{\mathbf{q}', \omega'} = \langle P^\mu(\mathbf{r})P^\mu(0) \rangle_{\mathbf{q}'} \pi \delta(\omega'). \quad (6)$$

Substituting Eqs. (6) and (4) into Eq. (2) yields

$$I(\omega) \sim \sum_{\mathbf{q}'} \langle P^\mu(\mathbf{r})P^\mu(0) \rangle_{\mathbf{q}'} \frac{1}{\Omega_{\mathbf{q}'}\Gamma^2 + (\omega - \Omega_{\mathbf{q}'})^2}. \quad (7)$$

Let us formally introduce the delta function  $\delta(\omega' - \Omega_{\mathbf{q}'})$  and integration over  $\omega'$  by using the identity

$$\frac{\Gamma}{\Gamma^2 + (\omega - \Omega_{\mathbf{q}'})^2} \equiv \int d\omega' \frac{\Gamma \delta(\omega' - \Omega_{\mathbf{q}'})}{\Gamma^2 + (\omega - \omega')^2}. \quad (8)$$

In the long-wavelength approximation, the sum can be converted into an integral, namely,  $\sum_{\mathbf{q}'} \rightarrow \frac{V}{(2\pi)^3} \int d^3q'$ ; therefore, taking into account Eq. (8), we can represent Eq. (2) in the form

$$I(\omega) = I_0 \int_{-\infty}^{\infty} d\omega' \int dq' q'^2 \langle P^\mu(\mathbf{r})P^\mu(0) \rangle_{\mathbf{q}'} \times \delta(\omega' - \Omega_{\mathbf{q}'}) \frac{1}{\Omega_{\mathbf{q}'}\Gamma^2 + (\omega - \omega')^2}. \quad (9)$$

The expression in Eq. (9) is the convolution of two functions

$$J(\omega, \omega') = \frac{\Gamma}{\Gamma^2 + (\omega - \omega')^2}, \quad I_0 = \frac{V}{2\pi}, \quad (10)$$

$$f(\omega') = \int dq' q'^2 \langle P^\mu(r)P^\mu(0) \rangle_{\mathbf{q}'} \delta(\omega' - \Omega_{\mathbf{q}'}) \frac{1}{\Omega_{\mathbf{q}'}}. \quad (11)$$

Equations (10) and (11) describe the contributions from homogeneous and inhomogeneous broadening, respec-

tively, to the shape of the Raman line. However, in order to calculate  $f(\omega)$ , one should first find the polarization fluctuation correlation function, as can be seen from Eq. (11). In most cases (see, e.g., [1, 3]), some approximations and assumptions are made when calculating the correlation function. In our opinion, the function  $f(\omega)$  can be calculated by a more general method based on the statistical theory of the spectral line shape. This theory does not involve cumbersome calculations of the correlation function and has been successfully employed in optical, radio-frequency, and  $\gamma$ -resonance spectroscopies [6, 11].

## 2.2. Calculation of $f(\omega)$ by a Statistical Method

The function  $f(\omega)$  has been calculated in the framework of statistical theory for the cases where the frequency shift of the spectral line is a linear [5, 6] or a nonlinear [7, 11] function of random fields. The latter case is of particular importance for disordered ferroelectrics at temperatures  $T = T_c \pm \Delta T$  with  $\Delta T \approx 10\text{--}20$  K, where the nonlinear and correlation effects are significant. In actuality, the distribution function that includes these effects can be expressed through the distribution function that takes into account only the linear terms in the frequency shift, because the probability theory allows one to express the distribution of a random variable in terms of the distribution of another variable if the latter variable is a function of the former [12]. For example, in the simplest case where a random variable  $x$  is a single-valued monotonic function of a random variable  $h$ , the relationship between their distributions  $g(h)$  and  $f(x)$  has the form [12]

$$g(h) = f[x(h)] \left| \frac{dx(h)}{dh} \right|. \quad (12)$$

In the general case, where several different values of  $x$  correspond to a value of  $h(x)$ , we can divide the  $x$  space into regions in which the function  $h(x)$  is monotonic and find the total distribution function  $g(h)$  as the sum of terms similar to that in Eq. (12) [7, 11, 12]. With this in mind, let us express the distribution function of the contributions nonlinear in the random field in terms of the distribution function of contributions linear in the random field (the latter function can be found analytically in statistical theory [5, 6]). We assume that the shift  $\Delta\omega = \omega - \omega_0 \equiv \omega$  of the frequency  $\omega_0$  (at which the scattering intensity is a maximum) caused by a random field  $\omega'$  can be written in the form of a power series

$$\omega = \omega' - \alpha_2(\omega')^2 - \dots - \alpha_m(\omega')^m. \quad (13)$$

Using Eq. (13), one can express the distribution function  $f_m(\omega)$  in terms of the distribution  $f_1(\omega')$ . The result is

$$f_m(\omega) = \sum_{k=1}^{-m} f_1(\omega' = \omega_k) \left| \frac{d\phi(\omega, \omega')}{d\omega'} \right|_{\omega' = \omega_k}, \quad (14)$$

$$\phi(\omega, \omega') = \omega - \omega' - \alpha_2(\omega')^2 - \dots - \alpha_m(\omega')^m, \quad (15)$$

where  $\omega_k$  is a real root of the equation

$$\phi(\omega, \omega_k) = 0. \quad (16)$$

Thus, the distribution function  $f_m(\omega)$  is expressed through the function calculated in the linear approximation, i.e., in the case where all coefficients characterizing nonlinearity are zero,  $\alpha_2 = \alpha_3 = \dots = \alpha_m = 0$ . The function  $f_1(\omega)$  as calculated in statistical theory can be a Gaussian, a Lorentzian, or a Holtmarkian, depending on the nature of the sources of random fields, and its parameters are determined by the concentration and other characteristics of these sources [6, 9].

In the simplest case where the contribution from the first nonlinear term in Eqs. (13) and (15) is dominant ( $\alpha_2 \neq 0$ ,  $\alpha_3 = \dots = \alpha_m = 0$ ), Eqs. (14)–(16) lead to the normalized second-order distribution function of the form

$$f_2(\omega) = \frac{\Theta\left(\omega + \frac{1}{4\alpha_2}\right)}{\sqrt{1 + 4\alpha_2\omega}} \times \left[ f_1\left(\frac{\sqrt{1 + 4\alpha_2\omega} - 1}{2\alpha_2}\right) + f_1\left(-\frac{\sqrt{1 + 4\alpha_2\omega} + 1}{2\alpha_2}\right) \right], \quad (17)$$

where  $\Theta$  is the step function. Therefore,  $f_2 \neq 0$  only in the range  $\omega_c \leq \omega \leq \infty$  (for  $\alpha_2 > 0$ ) or  $-\infty \leq \omega \leq \omega_c$  (for  $\alpha_2 < 0$ ), where

$$\omega_c = -\frac{1}{4\alpha_2} \quad (18)$$

is the critical frequency at which the function  $f_2(\omega)$  becomes divergent. Thus, the function  $f_2(\omega)$  is highly asymmetric and its wing for  $\omega \gg \omega_c$  is described by

$$f_2(\omega) \rightarrow 1/\sqrt{1 + 4\alpha_2\omega}. \quad (19)$$

In reality, the functions describing the line shapes have no divergences because of homogeneous broadening, the mechanisms of which always operate. We assume that homogeneous broadening leads to a Lorentzian shape. In this case, the integration in Eq. (3) is equivalent to the substitution of  $\omega \pm (i/\tau)$  for  $\omega$  in Eq. (17), where  $1/\tau \equiv \Gamma$  is the half-width at the half-maximum. If several mechanisms of homogeneous broadening operate, leading to a Lorentzian shape, then  $1/\tau = \sum_i 1/\tau_i$ , where  $i$  specifies the mechanisms.

Under the assumption that  $f_1(\omega)$  is a Gaussian, i.e.,

$$f_1(\omega) = \frac{1}{\sqrt{2\pi}} \exp\left[-\frac{\omega^2}{2\Delta^2}\right], \quad (20)$$

the procedure proposed above [or the integration in Eq. (3)] with the corresponding function  $f_2(\omega)$  in Eq. (17) leads to the following shape of the spectral

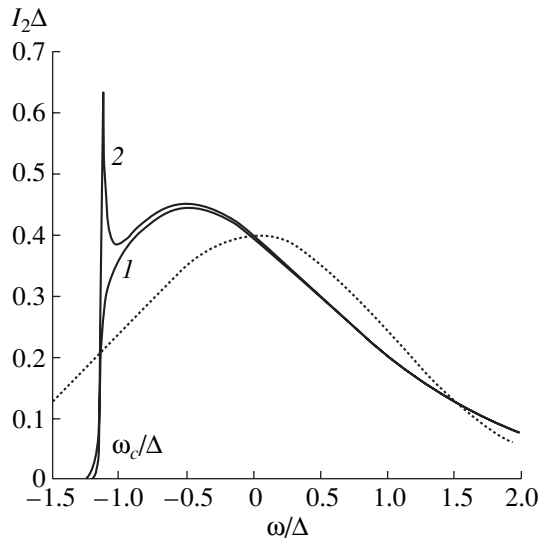


**Fig. 1.** Line shape calculated by Eq. (21) for  $\alpha_2\Delta = 0.22$  and  $(\tau\Delta)^{-1}$  equal to (1) 0.3 and (2) 0.01. The dotted curve is a Gaussian.

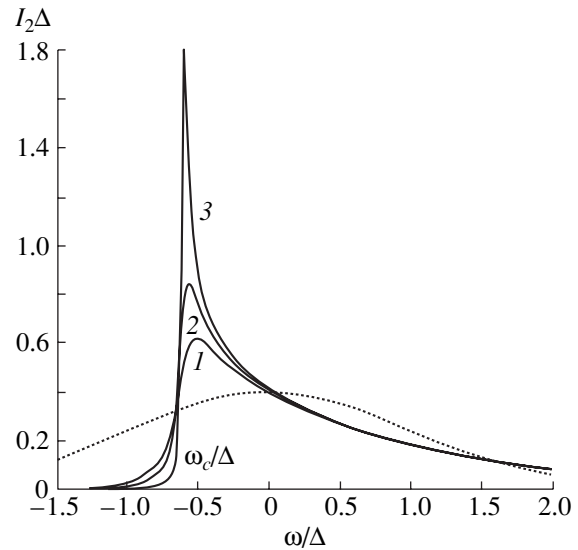


**Fig. 2.** Line shape calculated by Eq. (21) for  $\alpha_2\Delta = 0.4$  and  $(\tau\Delta)^{-1}$  equal to (1) 0.1, (2) 0.05, and (3) 0.01. The dotted curve is a Gaussian.

line:

$$I_2(\omega) = \frac{1/2 + \frac{1}{\pi} \arctan \tau(\omega - \omega_c)}{\Delta \sqrt{2\pi(\varphi(\omega))^{1/2}}} \times \left( \exp \left[ \frac{S_1(\omega) - 2(1 + 2\alpha_2\omega)}{8\alpha_2^2\Delta^2} \right] \cos \frac{4\alpha_2/\tau - S_2(\omega)}{8\alpha_2^2\Delta^2} + \exp \left[ \frac{-S_1(\omega) - 2(1 + 2\alpha_2\omega)}{8\alpha_2^2\Delta^2} \right] \cos \frac{4\alpha_2/\tau + S_2(\omega)}{8\alpha_2^2\Delta^2} \right), \quad (21)$$

where

$$\varphi(\omega) = \sqrt{(1 + 4\alpha_2\omega)^2 + (4\alpha_2/\tau)^2},$$

$$S_{1,2}(\omega) = \sqrt{2} \sqrt{\varphi(\omega) \pm (1 + 4\alpha_2\omega)}.$$

Figures 1 and 2 show the numerically calculated line shape for several values of the parameters  $\alpha_2\Delta$  and  $(\tau\Delta)^{-1}$ . It can be seen that the divergence of  $f_2(\omega)$  at  $\omega = \omega_c$  is transformed into a sharp maximum in the presence of homogeneous broadening, so that the spectral line has two maxima (Fig. 1) rather than one associated with the Gaussian, as in the linear case. The separation between the two maxima is approximately equal to  $\omega_c$  (Fig. 1). If the nonlinear contribution is large enough, only the sharp peak at  $\omega = \omega_c$  survives and its width increases with  $1/\tau$  (Fig. 2). The width of the left-hand part of the low-frequency peak is entirely due to homogeneous broadening, whereas its right-hand part ( $\omega > \omega_c$ ) is determined fundamentally by inhomogeneous broadening.

### 3. RAMAN SPECTRA OF KLT AND KTN

The theory developed above is used to interpret the first-order Raman spectra observed in KLT with 1 and 4% Li [3] and in KTN with 15.7% Nb [2].

#### 3.1. Raman Spectra of KLT

The measurements on KLT have been performed at  $T = 10$  K for  $x_{\text{Li}} = 0.01$  and at 55 K for  $x_{\text{Li}} = 0.04$  [3]. For both samples, the observed line shapes were highly asymmetric, with their maximum being at  $\omega \approx 198$   $\text{cm}^{-1}$ . These line shapes are described by Eqs. (20) and (21) with dimensionless parameters equal to  $\alpha_2\Delta = 0.38$ ,  $(\tau\Delta)^{-1} = 0.06$  (Fig. 3) and  $\alpha_2\Delta = 0.55$ ,  $(\tau\Delta)^{-1} = 0.15$  (Fig. 4) for the respective Li concentrations indicated above.

The position of the peaks  $\omega_m - \omega_0 = \omega_c$  is determined by the nonlinearity parameter in accordance with Eq. (18). By fitting Eq. (19) to the high-frequency tail of the line, we obtained  $\alpha_2 \approx 0.1$   $\text{cm}$ , which gives  $\omega_m = \omega_c + \omega_0 \approx 197.6$   $\text{cm}^{-1}$  and  $\omega_0 = 199$   $\text{cm}^{-1}$ . We note that Eq. (19) adequately describes the shape of the entire tail of the line with this value of  $\alpha_2$ . From the dimensionless parameter  $\alpha_2\Delta$ , the width of the Gaussian is estimated to be  $\Delta = 3.8$   $\text{cm}^{-1}$  for  $x_{\text{Li}} = 0.01$  and  $\Delta = 5.5$   $\text{cm}^{-1}$  for  $x_{\text{Li}} = 0.04$ .

According to our theory, the line shape at  $\omega < \omega_c$  is entirely determined by the homogeneous broadening described by Eq. (4) and the width of the low-frequency part of the line  $1/\tau$  is related to the lifetime of hard phonons  $\Gamma^{-1}$ . From the values of  $(\tau\Delta)^{-1} \equiv \Gamma/\Delta$  and  $\Delta$  found above, we obtain  $\Gamma(T = 10 \text{ K}) \approx 0.25$  and  $\Gamma(T = 55 \text{ K}) \approx 0.8$   $\text{cm}^{-1}$ . These values agree satisfactorily with the typical values of the lifetime of hard phonons and with the observed linewidth (Figs. 3, 4).

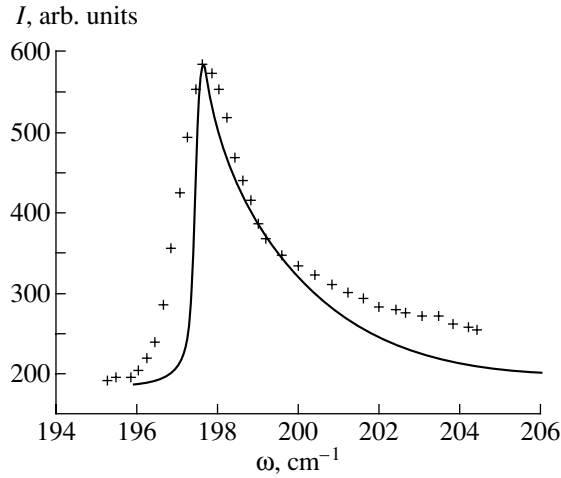


**Fig. 3.** Profile of the FORS line. The solid curve is a calculation for  $\alpha_2\Delta = 0.38$  and  $(\tau\Delta)^{-1} = 0.06$ , and dots are the experimental data obtained for KLT with 1% Li at  $T = 10$  K [3].

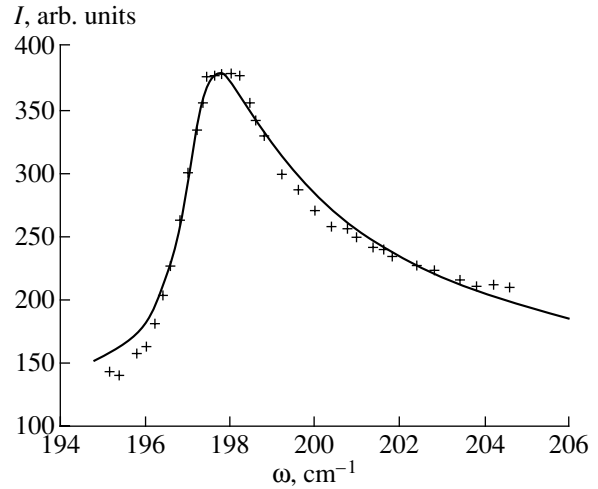


**Fig. 4.** Profile of the FORS line. The solid curve is a calculation for  $\alpha_2\Delta = 0.55$  and  $(\tau\Delta)^{-1} = 0.15$ , and dots are the experimental data obtained for KLT with 4% Li at  $T = 55$  K [3].

### 3.2. Raman Spectra of KTN

KTN with 15.7% Nb undergoes a phase transition from the cubic to the tetragonal phase at  $T_c = 138.6$  K. Measurements have been performed at several temperatures near  $T_c$ , namely,  $T = 160, 150, 146,$  and  $142$  K [2]. At all these temperatures, lines with two maxima were observed, one of which was near  $\omega_1 \approx 200$   $\text{cm}^{-1}$  and the other was near  $\omega_2 \approx 220$   $\text{cm}^{-1}$ . The intensity of the low-frequency maximum greatly increased with decreasing temperature, while the intensity of the high-frequency maximum became small at  $T = 142$  K. This can be explained by the fact that the nonlinearity parameter  $\alpha_2$  increases as  $T_c$  is approached [11]; therefore, nonlinear effects are more pronounced near  $T = 142$  K. The disappearance of the high-frequency maximum with the nonlinearity parameter increasing agrees qualitatively with our theory (Figs. 1, 2). The increase in the intensity of the low-frequency maximum with decreasing temperature can be due to an increase in the lifetime of phonons  $\tau$ .

In order to verify the conclusion that the nonlinear effects are responsible for the observed evolution of the Raman spectrum, we fitted the curves described by Eqs. (17)–(19) to the experimental spectra. The tail of the Raman line ( $\omega \geq 230$   $\text{cm}^{-1}$ ) at  $T = 142$  K is found to be described well by Eq. (19) with  $\alpha_2 \approx 0.015$  cm, which gives  $\omega_c \approx 20$   $\text{cm}^{-1}$  [see Eq. (18)]. The spacing between the two maxima of the Raman line is estimated to be rather close to its experimental value (Fig. 5), which also shows that nonlinear effects are significant. Figure 5b shows the spectrum calculated from Eq. (21) with  $\alpha_2 = 0.012$  cm and  $\Delta \approx 17$   $\text{cm}^{-1}$ . These values are determined from the width of the high-frequency peak. We note that knowing the absolute value of  $\Delta$  allowed us to relate the dimensionless scale of  $\omega/\Delta$  used for the-

oretical estimations to the scale of frequency  $\omega$  in Figs. 5 and 6.

The values of the homogeneous-broadening parameter  $1/\tau$  for different temperatures  $T$  are obtained under the assumption that they are fundamentally determined by the reorientation frequency of “elastic dipoles” formed by off-center Nb ions. The temperature dependence of this frequency was found earlier [13]; it follows from Arrhenius’ law that

$$\frac{1}{\tau} = \frac{1}{\tau_0} \exp(-U/T) \quad (22)$$

with  $U = 200$  K and  $1/\tau_0 = 7 \times 10^9$  Hz. At  $T = 150$  K, Eq. (22) gives  $(\tau\Delta)^{-1} \approx 0.004$ , which is used in calculating the line shape shown in Fig. 5b. The calculated (Fig. 5b) and experimentally observed (Fig. 5a) line shapes are qualitatively similar. A more detailed comparison of the theory and experiment is made for the Raman spectrum at  $T = 142$  K (Fig. 6). The theoretical curve is calculated for  $\alpha_2 = 0.015$  cm [which is found by fitting Eq. (19) to the wings of the experimental curve] and for  $1/\tau$  determined from Eq. (22). The good agreement between the theoretical and experimental line shapes substantiates the conclusion that the asymmetry of the line shape and its change with approaching the phase transition are due to nonlinear effects in KTN with 15.7% Nb. The theory predicts that the great enhancement of the intensity of the low-frequency peak in the range of  $142 \text{ K} > T > T_c$  is caused by the increased nonlinearity parameter and by the decreased  $1/\tau$  under the assumption that there are no temperature-independent contributions to  $1/\tau$ .

Comparing the data obtained for KLT and KTN, we note that, due to the great difference in the reorientation rate of the dipole moments of Nb and Li, homogeneous broadening of the Raman lines in KLT is determined by

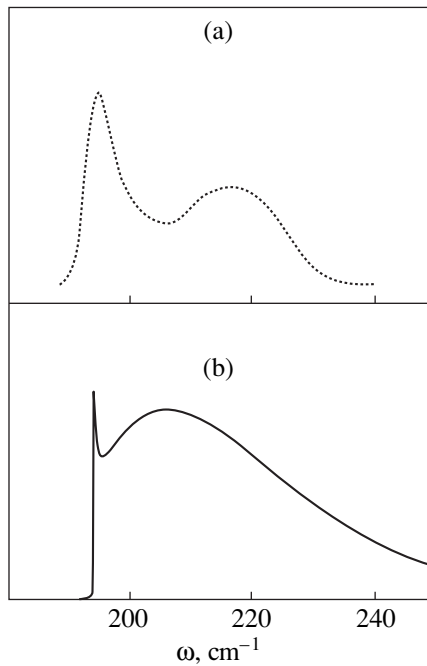


**Fig. 5.** Profile of the FORS line (a) as observed in KTN with 15.7% Nb at  $T = 150$  K [2] and (b) calculated for  $\alpha_2\Delta = 0.21$  and  $(\tau\Delta)^{-1} = 0.004$ .

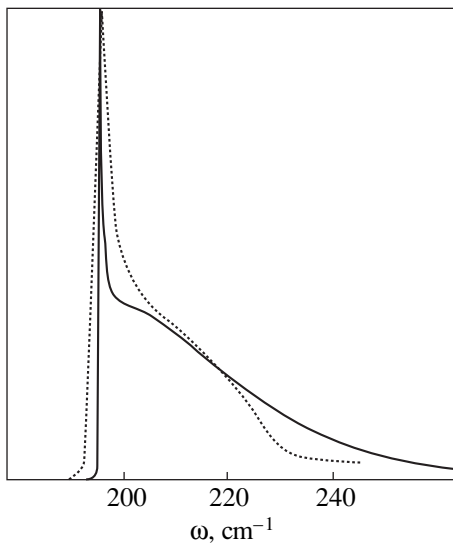


**Fig. 6.** Profile of the FORS line. The solid curve is a calculation for  $\alpha_2\Delta = 0.25$  and  $(\tau\Delta)^{-1} = 0.0036$ , and the dotted curve represents the experimental data obtained for KTN with 15.7% Nb at  $T = 142$  K [2].

the dynamics of hard phonons, whereas in KTN it is due to fast reorientation of the “elastic moments” of Nb ions. It should be noted that in [2, 3] it was assumed that homogeneous broadening of spectral lines is due to reorientation of the electric dipole moment of Nb.

However, the parameters of the electric dipoles and their reorientation rate found by fitting the theory to the experimental data differ markedly from their values determined earlier from independent experiments [14].

#### 4. DISCUSSION OF RESULTS

The theoretical description of the Raman spectra performed in this paper does not involve a calculation of the correlation function of quasi-static polarization fluctuations. A comparison with the Raman spectra calculated from the correlation function shows that the parameter  $\alpha_2\Delta$  corresponds to  $v_h^2/\omega_0^2 r_c^2$ , where  $v_h$ ,  $\omega_0$ , and  $r_c$  are the velocity of sound, the frequency of the hard mode at  $q = 0$ , and the polarization correlation length in the undoped lattice, respectively. These physical quantities determine the temperature and concentration dependences of  $\alpha_2\Delta$ . The parameter  $R_c/r_c$  (where  $R_c$  is the correlation length in a doped lattice) is equal to the ratio between the inhomogeneous and homogeneous contributions; at  $T \rightarrow T_c$ , we have  $R_c \rightarrow \infty$  and, therefore, the line broadening becomes purely inhomogeneous [3]. In terms of our theory, the nonlinearity parameter increases greatly as  $T \rightarrow T_c$  and its effect on the line shape becomes much larger than the decrease in the intensity of the maximum of the Raman line caused by the homogeneous contribution. Therefore, our results agree qualitatively with those obtained in [3].

However, the frequency dependence of  $J(\omega)$  obtained in [3] for large values of  $\omega$  is  $J(\omega) \sim (\omega - \Omega_0)^{-3/2}$ , whereas in our theory, this dependence has the form  $(1 + 4\alpha_2\omega)^{-1/2}$ . Which of them is more adequate can be clarified by more precise measurements. In addition, our theory predicts that the line shape can have two maxima for intermediate values of the parameter  $\alpha_2\Delta$ , which agrees with the Raman spectra observed in KTN (Fig. 5). In the theoretical model proposed in [3], the line shape has only one maximum and the appearance of a second maximum is associated in [3] with a forbidden transition which involves mixed optical and acoustic modes.

The theory proposed in this paper also provides an explanation for some other features of first-order Raman scattering. In particular, it is shown that nonlinearity leads to a highly asymmetric line shape and to the appearance of a low-frequency peak, whose low-frequency slope is determined by the dynamic properties of the system. The effects of the dynamical and static characteristics of the system on the shape of the spectrum are separated in our theory, which allows one to investigate them separately by Raman spectroscopy.

## REFERENCES

1. H. Uwe, K. B. Lyons, H. L. Carter, and P. A. Fleury, *Phys. Rev. B* **33**, 6436 (1986).
2. B. E. Vugmeister, P. Di Antonio, and J. Toulouse, *Phys. Rev. Lett.* **75**, 1646 (1995).
3. P. Di Antonio, B. E. Vugmeister, J. Toulouse, and L. A. Boatner, *Phys. Rev. B* **47**, 5629 (1993).
4. I. P. Sokoloff, L. L. Chase, and L. A. Boatner, *Phys. Rev. B* **41**, 2398 (1990).
5. A. U. Stoneham, *Rev. Mod. Phys.* **41**, 82 (1969).
6. M. D. Glinchuk, V. G. Grachev, M. F. Roïtsin, and L. A. Suslin, *Electric Effects in Radiospectroscopy* (Nauka, Moscow, 1981).
7. M. D. Glinchuk and I. V. Kondakova, *Fiz. Tverd. Tela* (St. Petersburg) **40**, 340 (1998) [*Phys. Solid State* **40**, 311 (1998)].
8. M. D. Glinchuk and V. A. Stephanovich, *J. Phys.: Condens. Matter* **6**, 6317 (1994).
9. M. D. Glinchuk and V. A. Stephanovich, *Ferroelectrics* **169**, 281 (1995).
10. A. D. Bruce, W. Taylor, and A. F. Murray, *J. Phys. C: Solid State Phys.* **13**, 483 (1980).
11. M. D. Glinchuk and I. V. Kondakova, *Mol. Phys. Rep.* **18/19**, 27 (1997).
12. D. J. Hudson, *Statistics* (Geneva, 1964).
13. T. V. Antimirova, M. D. Glinchuk, A. P. Pechenyĭ, and I. M. Smolyaninov, *Fiz. Tverd. Tela* (Leningrad) **32**, 208 (1990) [*Sov. Phys. Solid State* **32**, 116 (1990)].
14. U. T. Höchli, K. Knorr, and A. Loidl, *Adv. Phys.* **39**, 405 (1990).

*Translated by Yu. Epifanov*

---

## MAGNETISM AND FERROELECTRICITY

---

# To the Theory of Phase Transitions in Relaxors

R. F. Mamin

Zavoiskii Physicotechnical Institute, Russian Academy of Sciences, Sibirskii trakt 10/7, Kazan, Tatarstan, 420029 Russia  
e-mail: mamin@dionis.kfti.knc.ru

Received July 27, 2000; in final form, November 30, 2000

**Abstract**—It is shown that the process of charge carrier localization on impurity centers is of importance. Localized carriers produce local electric fields, thereby stimulating the appearance of an induced polarization near the phase transition point. The direction of this polarization is dictated by the spatial distribution of the centers occupied by charge carriers. The temperature dependence of the dielectric constant is determined by the dynamics of the local-center occupation with decreasing temperature. The dispersion of the dielectric constant is determined by the vibrational characteristics of the local states forming near a localized charge. The phase transitions in relaxors are considered in the framework of the thermodynamic approach. © 2001 MAIK “Nauka/Interperiodica”.

### 1. INTRODUCTION

Ferroelectric compounds undergoing diffuse phase transitions, which are frequently referred to as relaxors, have been studied intensively [1–33]. The first studies in which the broadened maximum of the dielectric constant was discovered were performed on polycrystalline solid solutions  $\text{Ba}(\text{Ti},\text{Sn})\text{O}_3$  [1, 2] and  $\text{Ba}(\text{Ti},\text{Zr})\text{O}_3$  [3]. The compounds  $\text{Pb}(\text{Mg}_{1/3}\text{Nb}_{2/3})\text{O}_3$  [PMN] [4–6] and  $\text{Pb}_{1-y}\text{La}_y(\text{Zr}_{1-x}\text{Ti}_x)\text{O}_3$  [PLZT( $y/1-x/x$ )] [11, 18] are the best known members of this family of materials. These compounds exhibit interesting ferroelectric, piezoelectric, and optical properties and show promise for electronic engineering. In particular, optically transparent relaxors can accumulate information recorded by light. This effect is a result of the capture of photoexcited carriers by local centers.

Although these compounds have been investigated for a long time, the physical mechanisms of the processes proceeding in them and the phenomena observed are still not completely understood. The main problem is an adequate description of the temperature and frequency dependences of the dielectric constant. Numerous experimental data also indicate that the properties of the low-temperature phase depend on the previous history of the sample; therefore, these compounds show nonergodic behavior in the low-temperature phase. The nature of this phase is still not completely understood. At the same time, some of these problems can be treated rather simply in terms of thermodynamic consideration. In this paper, we present a corresponding thermodynamic description. Since the localization of carriers on local centers is of importance in this description, we also discuss the properties of these centers. It is known that the relaxor behavior is associated with disorder in the positions of atoms [3–10]. In PMN, the disorder in the *B* positions of magnesium and niobium atoms is of importance. However, as

can be seen on the example of PMN, PLZT, and all other known relaxors, the disorder leads to relaxor behavior only if it is accompanied by disorder in the charge distribution. Furthermore, we believe that there is one more condition for relaxor behavior: the phase transition temperature must lie in the range where the number of occupied local centers is temperature-dependent. It is known that the relaxor properties can be significantly changed by introducing even a small amount of impurities, which affect the charge state of the compound. In this case, the temperature shift of the maximum of the dielectric constant can be as large as 50 K and more. The addition of lanthanum, which produces an excess charge, is known to lead to the relaxor behavior of PLZT. Furthermore, even at the earlier stage of the studies of barium titanate, it was found that the exposure of samples to light, which significantly changes the occupancy of the local centers, and other analogous external actions can shift the phase transition point to lower temperatures, by 10 K and more in some cases. A theoretical model in which the shift of the phase transition temperature is assumed to be due to occupation of energy levels is well known; it was developed to describe the effect of illumination on the structural phase transitions. In [34], this model was proposed for use in describing diffuse phase transitions in ferroelectrics. Thus, it is clear that the effects mentioned above are of importance in all perovskites, including the compounds undergoing diffuse phase transitions. The model taking these effects into account is employed in this paper.

### 2. MODEL

The features of structural phase transitions in semiconductors are determined to a large extent by the mutual influence of the electron and lattice subsystems. Because of this influence, a phase transition affects the



electronic energy spectrum and the phase transition temperature is shifted when the occupancy of traps is changed [35].

As the temperature is decreased, the trapping-center energy levels are gradually occupied and the effective width of the temperature range within which this occurs is equal to 10 to 40 K. In this temperature range, some specific features can appear in the structure of the system, especially if this range lies near a phase transition point. It is this situation that is considered in this paper.

As is known, when localized on a center, a carrier produces a deformation and a local polarization around the center; that is, it becomes a localized polaron. It is significant that the characteristic vibration frequency of this object will be generally determined by the characteristic times of both the lattice and electron subsystems. The localized charges produce local electric fields, which, in turn, induce an electric polarization. The direction of this polarization is determined by the spatial distribution of the local energy levels occupied by carriers. The spontaneous polarization arising at  $T_c$  will be aligned with these local fields (Fig. 1).

### 3. BASIC EQUATIONS

Let us consider a ferroelectric with impurity centers in the vicinity of a phase transition. The thermodynamic potential, which describes the behavior of the order parameter (polarization)  $\eta$  of this system near the phase transition point, has the form (allowing for the influence of the electron subsystem) [34–36]

$$\Phi = \Phi_0 + \alpha\eta^2 + \beta\eta^4 + \gamma\eta^6 + \tilde{E}_g m - E\eta. \quad (1)$$

Here,  $\Phi_0$  is the thermodynamic potential of the paraelectric phase;  $\alpha$ ,  $\beta$ , and  $\gamma$  are the expansion coefficients of the lattice part of the thermodynamic potential in a power series in the order parameter;  $\tilde{E}_g m$  is the contribution from the electron subsystem [35], with  $\tilde{E}_g$  being the energy of a trapped electron (which is of the order of the band gap  $E_g$ ) and  $m$  being the concentration of trapped electrons; and  $E$  is an external electric field. In what follows, we assume that only weak measuring fields are applied ( $E \approx 10$  V/cm) and, therefore, the last term in Eq. (1) can be ignored. Near the phase transition, the energy of a trapped electron can be expanded in powers of the components of the order parameter identical to that in the expansion of the lattice part of the thermodynamic potential:

$$\tilde{E}_g = \tilde{E}_{g0} + a\eta^2 + b\eta^4 + \dots \quad (2)$$

Here,  $\tilde{E}_{g0}$  is the energy of a trapped electron in the paraelectric phase and  $a$  and  $b$  are the expansion coefficients of the trapped-electron energy in a power series in the order parameter. Substituting Eq. (2) into Eq. (1) and retaining the first two terms in the expansion in

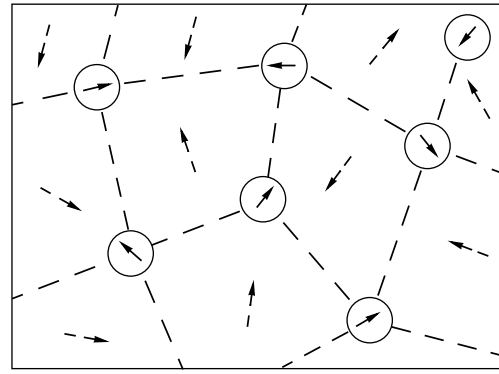


**Fig. 1.** Separation of a sample into microregions differing in the direction of the induced polarization (schematic). Circles with arrows inside them are polarized regions around localized carriers. Dashed arrows indicate the preferred directions of the induced polarization in the microregions.

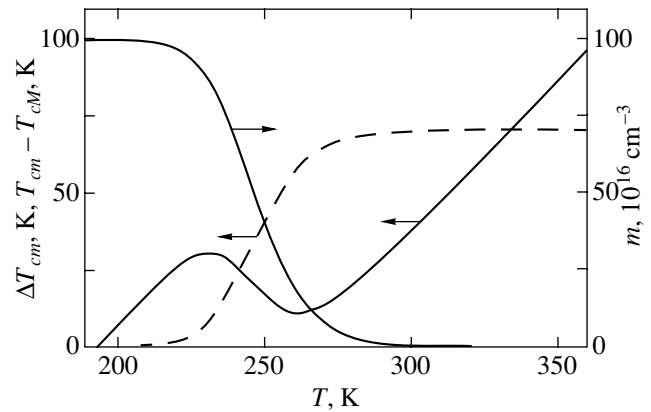


**Fig. 2.** Temperature dependences of the effective phase transition temperature  $T_{cm}$  in Eq. (4) reckoned from the temperature  $T_{cm}$  (dashed curve), of the actual departure  $\Delta T_{cm}$  from the effective phase transition temperature ( $\Delta T_{cm} = T - T_{cm}$ , solid curve), and of the concentration of trapped electrons  $m$  given by Eq. (7).

Eq. (2), we represent the thermodynamic potential in the form

$$\Phi = \Phi_0 + (\alpha + am)\eta^2 + \beta\eta^4 + \gamma\eta^6. \quad (3)$$

Here,  $\Phi_0$  is the thermodynamic potential of the paraelectric phase, including the energy of the electron subsystem.

Thus, the expansion coefficients of the thermodynamic potential depend on the concentration of trapped electrons and the term  $am$  determines the shift of the phase transition point caused by the trapped electrons [35]. The occupancy of the trapping centers can be changed under illumination and also because of localization of electrons on the trapping centers with decreasing temperature. Therefore, in the latter case, the influence of the electron subsystem on the phase transition should also be taken into account. The localization of electrons with decreasing temperature affects

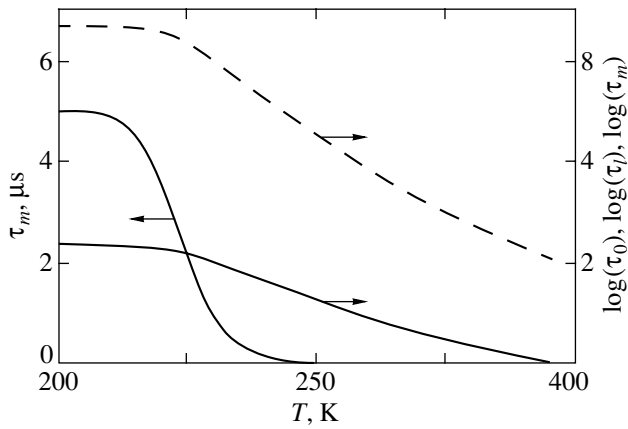


**Fig. 3.** Temperature dependences of the relaxation time of localized charges (concentration of trapped electrons)  $\tau_m$  in Eq. (8), of the logarithm of the relaxation time  $\tau_0$  in Eq. (10), and of the logarithm of  $\tau_m$  (dashed curve).

the distribution of electric fields over the sample, thereby changing all characteristics of the phase transition. Thermodynamically, the effect of the electron subsystem on the phase transition shows itself as a continuous shift of the phase transition point  $T_{cm}$  with progressive occupation of the traps (Fig. 2) [34]

$$T_{cm} = T_c - \frac{am}{\alpha'}, \quad (4)$$

where  $T_c$  is the phase transition temperature in the absence of the electron subsystem, i.e., in the case where the traps are empty [ $\alpha = \alpha'(T - T_c)$ ,  $\alpha' = 2\pi/C$ , where  $C$  is the Curie–Weiss constant].

The dynamics of the order parameter  $\eta$  can be described by the Landau–Khalatnikov relaxation equation

$$\frac{d\eta}{dt} = -\Gamma \left[ (\alpha + am)\eta + \beta\eta^3 + \gamma\eta^5 - \delta \frac{\partial^2 \eta}{\partial x^2} \right]. \quad (5)$$

The time dependence of the concentration of trapped electrons  $m$  involving the order parameter is described by the equation [36]

$$\frac{dm}{dt} = \gamma_n n_0 (M - m) - \gamma_n m N_c \exp\left(-\frac{u}{kT}\right). \quad (6)$$

Here,  $n_0$  is the equilibrium carrier concentration in the conduction band at relatively low temperatures,  $M$  is the concentration of trapping centers,  $\gamma_n$  is the kinetic coefficient,  $N_c$  is the effective density of states in the conduction band, and  $u$  is the spacing between the trapping center energy level and the bottom of the conduction band (this spacing is actually dependent on the order parameter,  $u = u_0 + \tilde{a}\eta^2(x)$  [35], but we can ignore this fact in this paper).

## 4. RESULTS

The dynamics of the system is determined by the fact that the relaxation times of the order parameter  $\eta$  and of the concentration of trapped electrons  $m$  are significantly different ( $\tau_\eta/\tau_m \ll 1$ ). This makes it possible to separate fast and slow processes. The order parameter depends on the concentration of trapped electrons at the specific point and on its spatial distribution. The equilibrium concentration of trapped electrons at a given temperature is found from Eq. (6) to be [34, 35]

$$m = \frac{n_0 M}{n_0 + N_c \exp(-u/kT)}. \quad (7)$$

The relaxation time  $\tau_m$  of trapped electrons is given by

$$\tau_m = [\gamma_n (n_0 + N_c \exp(-u/kT))]^{-1}. \quad (8)$$

Near the phase transition, the relaxation time  $\tau_m$  is sufficiently long to describe the localization of carriers on the trapping centers and, as will be shown below, to describe the dispersion relation of the dielectric constant. The temperature dependence of the relaxation time of localized charges  $\tau_m$  in Eq. (8) is shown in Fig. 3.

In a weak field, the induced polarization is proportional to the field  $E$ . In this case, it follows from Eqs. (5) and (7) that at any temperature above the Curie point the dielectric constant (dielectric function) has the form [36]

$$\varepsilon(\omega, T) = \varepsilon_\infty + \frac{2\pi}{\alpha_m(T) + i\tau_0(T)\omega}, \quad T > T_{cm}. \quad (9)$$

Here,  $\alpha_m(T) = \alpha'[T - T_{cm}(T)]$ ; and  $T_{cm}(T)$ , given by Eq. (4), is the phase transition temperature of the real system, which depends on the temperature through the concentration of trapped electrons  $m(T)$  given by Eq. (7). It should be noted that  $\varepsilon_\infty$  is much less than  $\varepsilon$  ( $\varepsilon \gg \varepsilon_\infty$ ) in a temperature range in the vicinity of the phase transition point.

A characteristic feature of relaxors is that the relaxation time  $\tau_0$  of the induced polarization is determined not only by the lattice relaxation time  $\tau_l$  (as is the case with conventional ferroelectrics [36]), but also by the relaxation time  $\tau_m$  of the electron subsystem given by Eq. (8) [35, 37, 38]:  $\tau_0 = (\tau_l \tau_m)^{1/2}$ . Therefore, the temperature dependence of  $\tau_0$  has the form

$$\tau_0(T) = (\gamma_n \tau_l^{-1} [n_0 + N_c \exp(-u/kT)])^{-1/2}. \quad (10)$$

As the temperature is decreased, the concentration of electron-occupied traps given by Eq. (7) becomes close to  $M$  and the effective phase transition temperature  $T_{cm}$  in Eq. (4) becomes equal to  $T_{cM} = T_c - aM/\alpha'$ . At the temperature  $T_{cM}$ , the phase transition to the state with a spontaneous polarization occurs. Since localized charges produce local electric fields and the external field is weak, the spontaneous polarization in different microregions will have different directions dictated by

the spatial distribution of localized charges (Fig. 1). Therefore, no features of  $\epsilon$  characteristic of the phase transition at  $T_{cm}$  will be observed, just as the features of  $\epsilon(\omega, T)$  in Eq. (9) are not observed in a pyroelectric phase transition [36].

Thus, the  $\epsilon(\omega, T)$  that would be observed if the spontaneous polarization occurring at  $T_{cm}$  had the same direction everywhere over the sample should be subtracted from  $\epsilon(\omega, T)$  in Eq. (9). Taking into account the temperature dependence of the relaxation time in Eq. (10), we arrive at the following final expression for the temperature dependence and dispersion of  $\epsilon(\omega, T)$  of a real crystal in weak fields:

$$\epsilon(\omega, T) = \epsilon_\infty + \frac{2\pi}{\alpha_m(T) + i\tau_0(T)\omega} - \frac{2\pi}{\alpha_M + i\tau_0(T)\omega}. \quad (11)$$

Here,  $\alpha_M = \alpha'(T - T_{cm})$ . The dispersion and temperature dependence of the dielectric function described by Eq. (11) are similar to those observed in diffuse phase transitions.

The temperature and frequency dependences of the real  $\epsilon'$  and imaginary  $\epsilon''$  parts of the dielectric function  $\epsilon(\omega, T)$  in Eq. (11) are shown in Figs. 4–6. In Fig. 4, the dashed curve represents the temperature dependence of the inverse square root of the real part of the dielectric function,  $[\epsilon'(T)]^{-1/2}$ . It can be seen from Fig. 4 that our model adequately describes the experimental dependence of the form  $\epsilon'(T) \approx (T - T_{cm})^{-2}$ , which is frequently discussed in the context of diffuse phase transitions [9, 10]. Since the situation considered in this paper is close to that taking place in PMN and PLZT(8/65/35), we used the following values of the parameters:  $\gamma_n = 10^{-13} \text{ cm}^3/\text{s}$ ,  $n_0 = 10^6\text{--}10^9 \text{ cm}^{-3}$ ,  $N_c = 10^{19} \text{ cm}^{-3}$ ,  $M \approx 10^{16}\text{--}10^{19} \text{ cm}^{-3}$ ,  $a \approx 10^{-19}\text{--}10^{-15} \text{ cm}^3$ ,  $T_c = 260 \text{ K}$ , the Curie–Weiss constant  $C \approx 10^5 \text{ K}$ , and  $u \approx 0.7 \text{ eV}$ . In Figs. 4–6,  $T_{cm} \approx 200 \text{ K}$ . It can be seen from Figs. 5 and 6 that our model also adequately describes the behavior of the dielectric function without any additional assumptions such as a spread in the phase transition temperatures over the sample [9, 10] and a continuous set of relaxation times [23–26].

Since the processes of localization of charge carriers on local centers are of fundamental importance in our model, we will discuss various possible investigations of these centers and the available experimental data on local centers in relaxors.

## 5. DISCUSSION

From the results presented above, it follows that the localization of charge carriers on local centers is of primary importance in dispersion of the dielectric constant. However, despite the fact that investigations of local centers and of the processes of charge exchange of them are of considerable interest, the available information on these centers is limited. Of prime interest are investigations of light-induced processes, because they

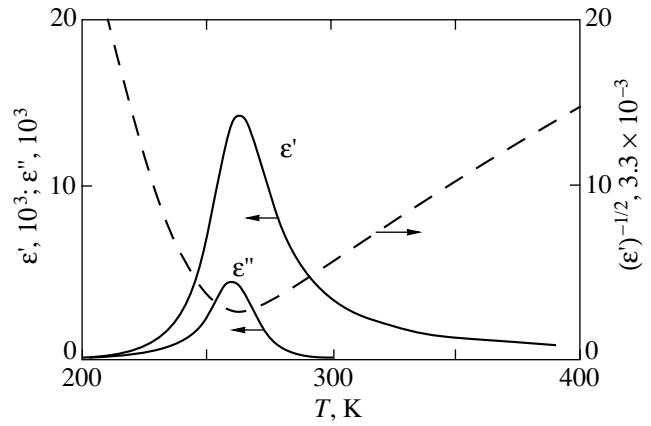


**Fig. 4.** Temperature dependences of the real  $\epsilon'$  and imaginary  $\epsilon''$  parts of the dielectric function  $\epsilon(\omega, T)$  in Eq. (11) and of the inverse square root of the real part of the dielectric function  $\epsilon'$  [dashed curve,  $\epsilon'(T) \approx (T - T_{cm})^{-2}$ ].

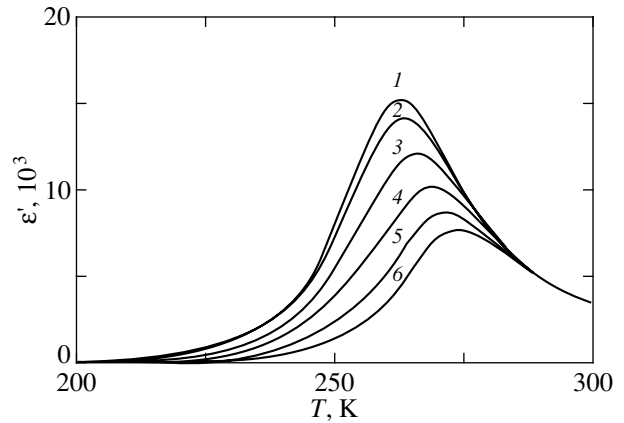


**Fig. 5.** Temperature dependence and dispersion of the real part  $\epsilon'$  of the dielectric function  $\epsilon(\omega, T)$  in Eq. (11) for different frequencies of the electromagnetic field  $\omega$ , kHz: (1) 0.001, (2) 1, (3) 2, (4) 3, (5) 4, and (6) 5.

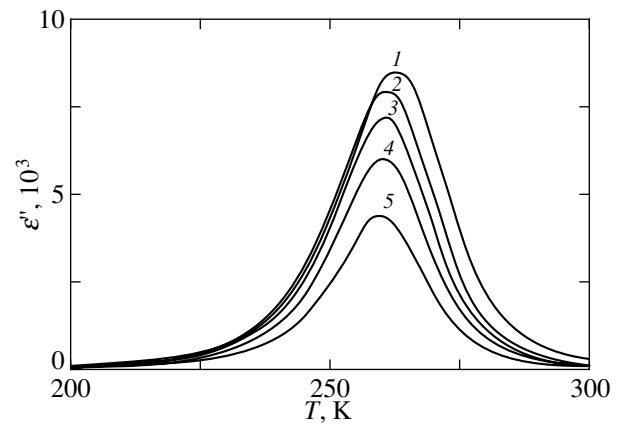


**Fig. 6.** Temperature dependence and dispersion of the imaginary part  $\epsilon''$  of the dielectric function  $\epsilon(\omega, T)$  in Eq. (11) for different frequencies of the electromagnetic field  $\omega$ , kHz: (1) 4, (2) 2.5, (3) 2, (4) 1.5, and (5) 1.

provide new data on local centers. Such investigations have been performed only in a few cases, and the samples in them were illuminated only before the measurements, rather than during them, or the intensity of illumination was low, which significantly affects the results obtained.

The nature of the local centers in PLZT can be judged from the data presented in [11], where it was found that when the samples were illuminated before the measurements at low temperatures, new resonance lines appeared in the ESR spectra, and they were shown to correspond to  $F$  centers. These lines did not appear when the samples were not illuminated or were exposed to light at room temperature. In our opinion, this is evidence that at room temperature the local centers are still thermally emptied and carriers cannot be localized on them. At low temperatures, the carriers are localized on these centers and the corresponding ESR lines are observed up to 200 K. It is at this temperature that the phase transition to the state with a local spontaneous polarization occurs. Therefore, one can assume that thermal detrapping of carriers from these local centers commences at 200 K and that these centers are responsible for the diffuseness of the phase transition and for dispersion of the dielectric constant. Unfortunately, ESR measurements under steady illumination were not made in [11], perhaps because they presented some technical difficulties. These measurements could undoubtedly provide qualitatively new results. ESR studies of these localized states on slow cooling of samples are also of considerable interest. One might expect a progressive increase in the intensity of the resonance lines of local centers with decreasing temperature and increasing occupancy of the centers. Let us discuss the nature of these centers. In [11], it is assumed that these centers are lead or oxygen vacancies. However, according to [12, 39], the PLZT is most likely to show hole conductivity. Therefore, it can be suggested that the local center is an oxygen vacancy that is localized near a lead vacancy. Such a defect acts as an acceptor, and a hole can be localized on it. It was shown in [40] that the activation energy of this level is roughly 0.7 eV, which agrees well with the theoretical model proposed above.

The activation energy and the temperature range in which charge carriers are being localized can easily be found from the temperature dependence of the conductivity. The values of the parameters we used in the calculations agree well with the experimental data on conductivity [39]. From the data of [12], it follows that the temperature range in which the carrier localization occurs is in the vicinity of the phase transition point.

## 6. CONCLUSION

Thus, we presented a thermodynamic description of diffuse phase transitions in ferroelectrics. The localization of carriers on local centers is shown to be of importance. The localized charges produce local electric fields and thereby stimulate the appearance of the

induced polarization. The direction of this polarization is determined by the spatial distribution of the local centers occupied by carriers. The spontaneous polarization that occurs in the phase transition is directed along these fields. The dispersion of the dielectric constant is determined by the vibrational characteristics of the local states and depends not only on the relaxation time of the lattice subsystem, but also on the dynamics of trapped electrons.

We hope that this paper will stimulate experimental investigations of the dynamics of the occupation of local centers and the nature of these centers.

## REFERENCES

1. G. A. Smolenskiĭ and V. A. Isupov, Dokl. Akad. Nauk SSSR **9**, 653 (1954).
2. G. A. Smolenskiĭ and V. A. Isupov, Zh. Tekh. Fiz. **24**, 1375 (1954).
3. G. A. Smolenskiĭ, N. P. Tarurtin, and N. P. Grutsin, Zh. Tekh. Fiz. **24**, 1584 (1954).
4. G. A. Smolenskiĭ, V. A. Isupov, A. I. Agranovskaya, and S. N. Popov, Fiz. Tverd. Tela (Leningrad) **2** (10), 2906 (1960) [Sov. Phys. Solid State **2**, 2584 (1960)].
5. G. A. Smolenskiĭ, N. K. Yushin, and S. I. Smirnov, Fiz. Tverd. Tela (Leningrad) **27** (3), 801 (1983) [Sov. Phys. Solid State **27**, 492 (1983)].
6. V. A. Bokov and I. N. Myl'nikova, Fiz. Tverd. Tela (Leningrad) **3** (3), 841 (1961) [Sov. Phys. Solid State **3**, 613 (1961)].
7. L. E. Cross, Ferroelectrics **76**, 241 (1987).
8. L. E. Cross, S. J. Jang, R. E. Newnham, *et al.*, Ferroelectrics **23**, 187 (1980).
9. N. Setter and L. E. Cross, J. Appl. Phys. **68**, 2916 (1990).
10. V. A. Isupov, Ferroelectrics **143**, 109 (1993).
11. Yu. L. Maksimenko, M. D. Glinchuk, and I. P. Bykov, Fiz. Tverd. Tela (St. Petersburg) **39**, 1833 (1997) [Phys. Solid State **39**, 1638 (1997)].
12. A. E. Krumin, U. I. Ilyin, and V. I. Dimza, Ferroelectrics **22**, 695 (1978).
13. E. V. Colla, E. Yu. Koroleva, N. M. Okuneva, and S. B. Vakhrushev, Phys. Rev. Lett. **74**, 1681 (1995).
14. D. Viehland, S. J. Jang, L. E. Cross, and M. Wuttig, Phys. Rev. B **43** (10), 8316 (1991).
15. D. Viehland, M. Wuttig, and L. E. Cross, Ferroelectrics **120**, 71 (1991).
16. R. Sommer, N. K. Yushin, and J. J. van der Klink, Phys. Rev. B **48** (18), 13230 (1993).
17. Z.-G. Ye and H. Schmid, Ferroelectrics **145**, 83 (1993).
18. V. I. Dimza, A. A. Strogis, A. E. Kapenieks, *et al.*, Ferroelectrics **90**, 45 (1989).
19. C. Boulesteix, F. Varnier, A. Llebaria, and E. Husson, J. Solid State Chem. **108**, 141 (1994).
20. S. N. Dorogovtsev and N. K. Yushin, Ferroelectrics **112**, 18 (1990).
21. A. A. Bokov, Ferroelectrics **131**, 49 (1992).
22. G. Schmidt, Ferroelectrics **78**, 199 (1988).
23. G. Burns and F. H. Dacol, Solid State Commun. **48** (10), 853 (1983).

24. G. Burns and F. H. Dacol, *Ferroelectrics* **104**, 25 (1990).
25. G. Burns and F. H. Dacol, *Solid State Commun.* **42**, 9 (1982).
26. A. Levstik, Z. Kutnjak, C. Filipic, and R. Pirc, *Phys. Rev. B* **57**, 11204 (1998).
27. W. Kleemann, *Int. J. Mod. Phys. B* **7**, 2469 (1993).
28. V. Westphal, W. Kleemann, and M. D. Glinchuk, *Phys. Rev. Lett.* **68** (6), 847 (1992).
29. W. Kleemann and A. Klossner, *Ferroelectrics* **150**, 35 (1993).
30. H. M. Christen, R. Sommer, N. K. Yushin, and J. J. van der Klink, *J. Phys.: Condens. Matter* **6**, 2631 (1994).
31. Z.-G. Ye, P. Tissot, and H. Schmid, *Mater. Res. Bull.* **25**, 739 (1990).
32. Z.-G. Ye, *Ferroelectrics* **184**, 513 (1996).
33. R. Blinc, J. Dolinsek, R. Pirc, *et al.*, *Phys. Rev. Lett.* **63**, 2248 (1989).
34. R. F. Mamin, *Pis'ma Zh. Éksp. Teor. Fiz.* **58** (7), 534 (1993) [*JETP Lett.* **58**, 538 (1993)].
35. R. F. Mamin and G. B. Teitel'baum, *Pis'ma Zh. Éksp. Teor. Fiz.* **44** (7), 326 (1986) [*JETP Lett.* **44**, 420 (1986)].
36. V. L. Ginzburg, *Usp. Fiz. Nauk* **37**, 490 (1949).
37. B. S. Kerner and V. V. Osipov, *Zh. Éksp. Teor. Fiz.* **83**, 2201 (1982) [*Sov. Phys. JETP* **56**, 1275 (1982)].
38. R. F. Mamin, *Zh. Éksp. Teor. Fiz.* **111** (4), 1 (1997) [*JETP* **84**, 808 (1997)].
39. M. Takahashi, *J. Appl. Phys.* **10**, 643 (1971).
40. V. V. Prisedskiĭ and Yu. D. Tret'yakov, *Izv. Akad. Nauk SSSR, Neorg. Mater.* **21**, 1389 (1982).

*Translated by Yu. Epifanov*

## MAGNETISM AND FERROELECTRICITY

# General Features of the Intrinsic Ferroelectric Coercive Field

V. M. Fridkin<sup>1,2</sup> and S. Ducharme<sup>1\*</sup>

<sup>1</sup> Department of Physics and Astronomy, Center for Material Research and Analysis University of Nebraska,  
68588-0111 Lincoln, USA  
e-mail: sducharme1@unl.edu

<sup>2</sup> Shubnikov Institute of Crystallography, Russian Academy of Sciences, Leninskii pr. 59, Moscow, 117333 Russia  
e-mail: fridkin@ns.crys.ras.ru

Received December 14, 2000

**Abstract**—The value of the intrinsic ferroelectric coercive field is obtained independently, from general energy considerations and from the predictions of several models of the ferroelectric state. All predictions yield a value of the order of the depolarization field, which is equal to the spontaneous polarization divided by the dielectric permittivity, and are consistent with the recent measurements of the intrinsic ferroelectric coercive field in ultrathin Langmuir–Blodgett films of copolymers of polyvinylidene fluoride with trifluoroethylene. Prior studies succeeded only in measuring the much smaller extrinsic coercive fields, which are limited by nucleation processes and domain motion. © 2001 MAIK “Nauka/Interperiodica”.

The characteristic feature of a ferroelectric is the ability of its polarization to be reversed or switched repeatedly through the application of a sufficiently large external electric field, as illustrated by the hysteresis loops in Fig. 1. However, since the discovery of ferroelectricity 80 years ago by Valasek, few published reports have considered the value of the intrinsic coercive field connected with collective polarization reversal, a consequence of the instability of the macroscopic polarization state in an opposing electric field. This is because the measured value of the ferroelectric coercive field was invariably much smaller than the intrinsic value predicted by theory, such as the Landau–Ginzburg (LG) mean-field model [1] and the ferroelectric Ising model [2, 3]. The low extrinsic coercive field observed in real ferroelectric crystals and films is caused by nucleation of domains with reversed polarization, which then grow and coalesce by domain wall motion [2, 4, 5]. Nucleation can occur at fixed defects in the crystal or due to a passive (nonferroelectric) surface layer [6]. Nucleation mechanisms and domain wall dynamics must be arbitrarily inserted into these models in order to explain the experimental observations of switching kinetics with much lower coercive fields in real ferroelectric materials [2]. In fact, the study and modeling of extrinsic switching is of great importance and is central to the application of ferroelectric films to nonvolatile random-access memories [7].

It has proven difficult to prevent extrinsic switching by eliminating defects or by pinning domain walls. Another way to achieve intrinsic switching is to make a particle small enough or a film thin enough to inhibit nucleation [5, 8–10]. Several mechanisms for this

finite-size effect have been proposed, including reduction of the nucleation volume, introduction of a space charge near the electrodes, elimination of passive layers, and domain-wall pinning [4, 6, 10, 11]. Even in the thinnest ferroelectric films obtained previously, the measured extrinsic coercive field is much smaller than the expected intrinsic value calculated from theoretical models, and, consequently, there has been relatively little published discussion of intrinsic switching, except to note that it remained out of reach. Thin ferroelectric

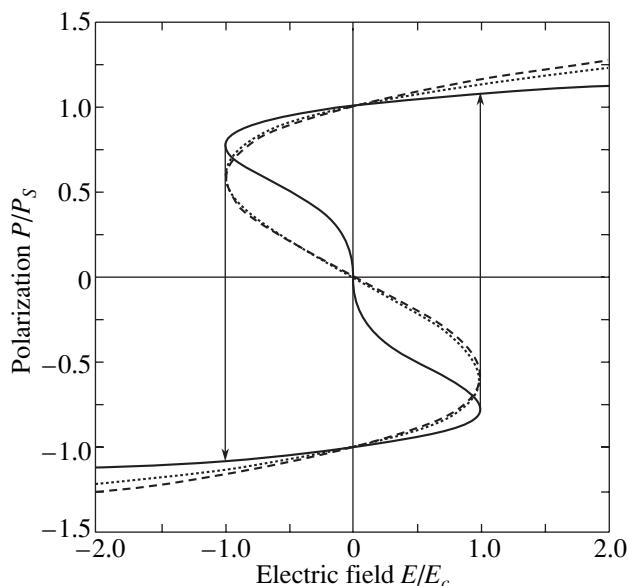


**Fig. 1.** Theoretical ferroelectric hysteresis loops from the first-order Landau–Ginzburg model (solid line), second-order Landau–Ginzburg model (dashed line), and Ising–Devonshire model (dotted line).

\* This article was submitted by the authors in English.

films have indeed shown the nucleation-inhibition finite-size effect, an increase in the coercive field with a decrease in thickness, but the value of the measured coercive field was still much lower than the intrinsic one, and, correspondingly, the switching was still controlled by nucleation and domains. Recently [12], we succeeded in finding the limiting intrinsic coercive field in films as thin as 1 nm made by Langmuir–Blodgett (LB) deposition of a two-dimensional ferroelectric copolymer [13].

The measured values of the intrinsic coercive field were in good agreement with the predictions of the LG mean-field theory [1, 14]. Here, we analyze the calculation of the intrinsic coercive field from a more general perspective and from several specific models of ferroelectricity.

We can estimate the intrinsic ferroelectric coercive field  $E_c$  by calculating the external electric field necessary to overcome the depolarization field  $P_S/\epsilon\epsilon_0$ , where  $P_S$  is the spontaneous polarization,  $\epsilon$  is the dielectric constant (more precisely, the contribution to the dielectric constant from ferroelectricity; the total dielectric constant of the medium  $\epsilon_T = \epsilon_B + \epsilon$  contains contributions from the background polarizability and the ferroelectric polarizability) along the direction of spontaneous polarization, and  $\epsilon_0$  is the permittivity of free space. The energy density associated with the spontaneous polarization is  $u_P = (1/2)P_S^2/\epsilon\epsilon_0$ . Application of an external field  $E$  in a direction opposite to the spontaneous polarization would contribute to the energy density  $u_E = \mathbf{E} \cdot \mathbf{P}_S = -EP_S$ .<sup>1</sup> The intrinsic coercive field  $E_c$  is then approximately the value of the applied field that produces an energy comparable to the polarization energy,  $u_E \approx u_P$ , so that the intrinsic coercive field is approximately half the depolarization field:

$$E_c \approx \frac{1}{2} \frac{P_S}{\epsilon\epsilon_0} \quad (\text{from energy}). \quad (1)$$

The intrinsic coercive field for a continuous ferroelectric–paraelectric first-order (close to second-order) phase transition can be calculated from the Landau–Ginzburg phenomenology (LG1) [15, 16]. The LG1 Gibbs free energy of a uniaxial material is  $G = G_0 + (1/2)\alpha P^2 + (1/4)\beta P^4 + (1/6)\gamma P^6 - PE$ , where the first coefficient has the Curie–Weiss form  $\alpha = (T - T_0)/(\epsilon_0 C)$ ,  $T_0$  is the Curie temperature,  $C$  is the Curie constant, and the second coefficient obeys the condition  $\beta < 0$ , whereas the condition for the necessary third coefficient is  $\gamma > 0$ . The parameters  $C$ ,  $T_0$ ,  $\beta$ , and  $\gamma$  are assumed independent of temperature and the electric

<sup>1</sup> This contribution applies to all kinds of ferroelectrics, whether displacive, order–disorder, or other. For example, in ferroelectric materials consisting of fixed dipoles with the dipole moment  $\mu$  and density  $N$ , as in ferroelectric polymers, the macroscopic polarization is  $\mathbf{P}_S = -N\langle\boldsymbol{\mu}\rangle$  and the energy density of the dipoles in the applied field is  $u_E = -N\langle\mathbf{E} \cdot \boldsymbol{\mu}\rangle$ , which leads to the same result.

field. From the minimum of the free energy density, it is possible to calculate the properties of the ferroelectric phase that exists just below the zero-field transition temperature  $T_C = T_0 + (3/16)\epsilon_0 C \beta^2/\gamma$ . In the ferroelectric phase, the spontaneous polarization is  $P_S = \pm\sqrt{-\beta(1 + \sqrt{1-t})/2\gamma}$ , where  $t = 4\alpha\gamma/\beta^2$  and the ferroelectric contribution to the dielectric constant is given by  $1/\epsilon\epsilon_0 = -8(T - T_C)/C\epsilon_0 + (9/4)(\beta^2/\gamma)$ . The LG1 intrinsic coercive field in the temperature range from just below  $T_0(t = 0)$  up to  $T_C(t = 3/4)$  is closely approximated by  $E_c \approx 2\beta(3|\beta|/5\gamma)^{3/2}(1 - (25/24)t)$  [12, 17], so the coercive field can be written as

$$E_c \approx \frac{3\sqrt{3}}{25\sqrt{5}} \frac{P_S}{\epsilon\epsilon_0} \left(1 - \frac{1}{6}t\right) \quad (\text{from LG1}). \quad (2)$$

The value of the intrinsic coercive field  $E_c$  near the Curie temperature  $T_0$  is about one-tenth of the depolarization field.

The Landau–Ginzburg continuous ferroelectric phase transition of the second order (LG2) [1] is modeled with a free energy  $G = G_0 + (1/2)\alpha P^2 + (1/4)\beta P^4 - PE$ , where the first coefficient is again  $\alpha = (T - T_0)/(\epsilon_0 C)$ , and the second coefficient  $\beta > 0$ . The ferroelectric phase in a zero electric field exists below the transition temperature  $T_C = T_0$ , where the spontaneous polarization  $P_S = \pm\sqrt{-\alpha/\beta}$  and the ferroelectric contribution to the dielectric constant is given by  $1/\epsilon\epsilon_0 = -2\alpha$ . The intrinsic coercive field  $E_c = 2\beta(-\alpha/3\beta)^{3/2}$  as calculated from the LG2 free energy can be written [17]

$$E_c = \frac{1}{3\sqrt{3}} \frac{P_S}{\epsilon\epsilon_0} \quad (\text{from LG2}). \quad (3)$$

Devonshire [16] applied the Ising model to ferroelectrics consisting of electric dipoles with dipole moment  $p_0$ , which can achieve a collective ordered state. The two-level (spin-1/2) Ising–Devonshire (ID) model describes a uniaxial ferroelectric that undergoes an order–disorder phase transition with the order parameter equal to the normalized spontaneous polarization  $S = P_S/P_{S0}$ , where  $P_{S0} = Np_0$ . The order parameter is obtained from the transcendental equation [2, 3, 16]  $S = \tanh[(J_0 S + Ep_0)/kT]$ , where  $k$  is the Boltzmann constant and  $J_0$  is the pseudospin Ising interaction constant. In the ferroelectric phase near (but below)  $T_C = T_0 = J_0/k$ , the zero-field spontaneous polarization follows a simple 1/2 power scaling  $S \approx \pm\sqrt{3(1 - T/T_C)}$  and the dielectric constant is given by  $1/\epsilon\epsilon_0 \approx 2[(kT_0)/(Np_0^2)][1 - T/T_0]$ . The ID intrinsic coercive field near  $T_C$  is approximately

Typical experimental values of the coercive field  $E_c^{\text{exp}}$  compared to the depolarization field  $E_d$  for BaTiO<sub>3</sub>, TGS, and BL copolymer films (all values were obtained near  $T_0$ )

Material	$\epsilon$	$P_S$ , C/m <sup>2</sup>	$E_c^{\text{exp}}$ , MV/m	$E_d = P_S/\epsilon\epsilon_0$ , MV/m	$E_c^{\text{exp}}/(1/2)E_d$
BaTiO <sub>3</sub> [18]	150	0.26	0.20	196	0.0020
Triglycine sulphate (TGS) [19]	43	0.028	0.011	74	0.00030
KD <sub>2</sub> PO <sub>4</sub> [20]	43	0.062	0.34	163	0.0042
PZr <sub>0.25</sub> Ti <sub>0.75</sub> O <sub>3</sub> (PZT) 100 nm thin film [21]	200	0.38	10	215	0.093
Polyvinylidene fluoride (PVDF) [22]	11	0.065	55	667	0.16
$P(\text{VDF} : \text{TrFE} 65 : 35)$ [23]	9.5	0.090	45	1070	0.084
$P(\text{VDF} : \text{TrFE} 75 : 25)$ 60 nm thin film [24]	10	0.10	125	1129	0.22
$P(\text{VDF}-\text{TrFE} 70 : 30) \leq 15$ nm thin film [13, 17]	8	0.10	480	1412	0.68
Ratio $E_c/(1/2)E_d$ (at $T_0$ ) predicted by model					
				LG1	0.18
				LG2	0.38
				ID	0.38

$E_c \approx [(2kT_0)/(3p_0)][1 - T/T_0]^{3/2}$ , so the coercive field near  $T_C$  can be written as

$$E_c \approx \frac{1}{3\sqrt{3}} \frac{P_S}{\epsilon\epsilon_0} \quad (\text{ID}). \quad (4)$$

Note that the ID and LG2 models are equivalent near  $T_0$  and predict the same temperature dependences for the spontaneous polarization, dielectric constant, and coercive field, because near  $T_C$ , the ID order parameter  $S$  is small and the free energy of the ID model can be expanded in powers of  $P_S$  to reproduce the LG2 free energy.

The value of the coercive field near the Curie temperature  $T_0$  obtained from the three mean-field models (Eqs. 2–4) ranges from 10 to 20% of the depolarization

field  $P_S/\epsilon\epsilon_0$ , a little less than the value of 50% estimated from basic energy considerations (Eq. 1), even as the spontaneous polarization and dielectric constant vary strongly with temperature. The predictions hold well near  $T_0$  for all models, as shown in Fig. 2. Therefore, the essential existence and approximate value of the intrinsic coercive field does not depend on the nature of the ferroelectric transition, whether it is first order or second order, displacive or order–disorder, from permanent dipoles or induced dipoles. However, the measured dielectric constant includes the background contribution and, near  $T_C$ , the ferroelectric contribution is typically larger than the equilibrium value because of thermal hysteresis, particularly in ferroelectrics with a first-order phase transition. Therefore, the value of the depolarization field  $P_S/\epsilon\epsilon_0$  obtained from direct measurements near  $T_C$  will likely be somewhat less than the intrinsic value.

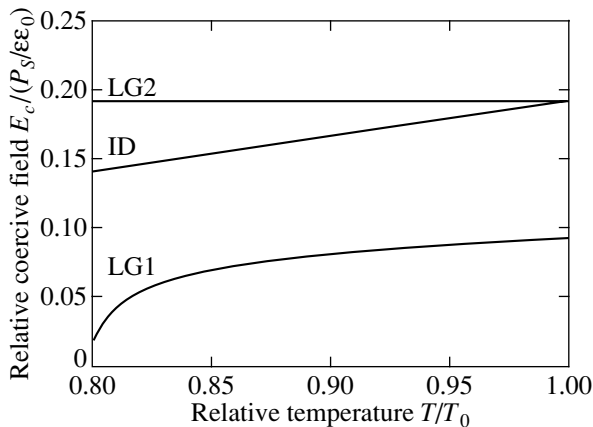


**Fig. 2.** Intrinsic coercive field  $E_c$  normalized to the depolarization field  $P_S/\epsilon\epsilon_0$  calculated from the LG2 model, LG1 model, and ID model.

Measurements of the coercive field in bulk ferroelectric crystals have invariably yielded values much smaller than the intrinsic value, as summarized in the table. While the traditional ferroelectrics have extremely low coercive fields, the ferroelectric polymer polyvinylidene fluoride (PVDF) and its copolymers show considerably higher coercive fields, typically 50 MV/m in “bulk” films, approaching the intrinsic value predicted by various models. By 1986, Kimura and Ohigashi [24] reported that copolymer films thinner than 1  $\mu\text{m}$  showed increasing coercive fields with decreasing thickness (Fig. 3) up to a then-record coercive field of 125 MV/m in a copolymer film 60 nm thick [24]. But the solvent-spinning techniques used would not yield thinner films of sufficient quality and dielectric strength, so the measurement of the intrinsic coercive field lay just beyond reach.



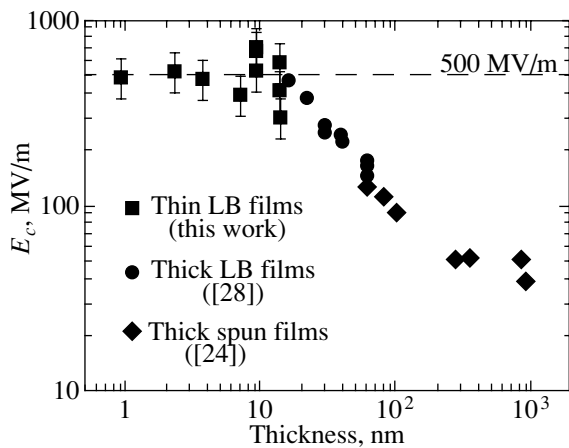


**Fig. 3.** Scaling of the coercive field with film thickness, measured at or near 25°C, from ferroelectric vinylidene fluoride-trifluoroethylene copolymer films. Adapted from [12].

The successful fabrication by LB deposition of ultrathin films of PVDF and copolymers with trifluoroethylene (TrFE) beginning in 1995 [25–27] presented us with highly crystalline films with polymer chains lying in the film plane and with the polarization axis perpendicular to the film. These films, ranging in thickness from 1 nm to over 100 nm, allowed us to study ferroelectricity down to the monolayer level [12, 13, 25–30]. One of the surprising results of these studies was the discovery of two-dimensional ferroelectricity [13], as the ferroelectric phase persisted in the thinnest films, with no significant decrease in the transition temperature, contrary to the common expectation that finite-size scaling would suppress ferroelectricity. But finite-size effects did appear to suppress nucleation in films thinner than 1  $\mu\text{m}$  [24, 28]. As Fig. 3 shows, the rising coercive field with decreasing thickness  $d$  observed by Kimura and Ohigashi continues with the thinner LB films to follow a  $d^{-0.7}$  power law scaling down to a thickness of 15 nm [28], consistent with a finite-thickness suppression of nucleation or domain wall motion.

The films of a thickness of 15 nm (30 monolayers) or less, on the other hand, had coercive fields of about 500 MV/m at 25°C, which is comparable to the theoretical intrinsic value [12] calculated with the LG1 model with free-energy coefficients determined in prior studies [30, 31]. Because of uncertainties in the LG1 parameters, the good coincidence between the measured and expected coercive fields did not ensure that it was indeed the intrinsic value. However, cessation of finite-size scaling below 15 nm implies that polarization reversal is no longer initiated by nucleation; that is, nucleation is inhibited and polarization reversal depends only on the intrinsic ferroelectric properties. Detailed measurements of the temperature dependence of the coercive field confirmed the specific predictions of the LG1 model [12] and thus established that the measurements coincided with the intrinsic coercive

field. Though nucleation and domains do not limit the value of the coercive field, they could play a key role in switching dynamics. Preliminary imaging of the polarization through pyroelectric scanning microscopy has not revealed domains larger than the 2  $\mu\text{m}$  resolution of our current system, but further study is necessary before something can be said about domain and crystallite properties.

It is not clear whether or not the two-dimensional nature of ferroelectricity in the vinylidene fluoride copolymers was essential for this achievement to be made. There may soon be results bearing on this question as several groups have reported good films with thicknesses less than 10 nm made from several known bulk ferroelectric materials [21, 32–34]. Recent improvements in the quality of solvent-crystallized vinylidene fluoride copolymers should help elucidate the effects of nucleation and domain-wall motion in bulk crystals [35–37].

#### ACKNOWLEDGMENTS

This work was supported by the USA National Science Foundation and the Nebraska Research Initiative.

#### REFERENCES

1. V. L. Ginzburg, *Zh. Éksp. Teor. Fiz.* **15**, 739 (1945).
2. M. E. Lines and A. M. Glass, *Principles and Applications of Ferroelectrics and Related Materials* (Clarendon, Oxford, 1977; Mir, Moscow, 1981).
3. B. A. Strukov and A. P. Levanyuk, *Ferroelectric Phenomena in Crystals* (Nauka, Moscow, 1995; Springer-Verlag, Berlin, 1998).
4. W. J. Merz, *Phys. Rev.* **95**, 690 (1954).
5. W. J. Merz, *J. Appl. Phys.* **27**, 938 (1956).
6. A. M. Bratkovsky and A. P. Levanyuk, *Phys. Rev. Lett.* **84**, 3177 (2000).
7. O. Auciello, J. F. Scott, and R. Ramesh, *Phys. Today* **51**, 22 (1998).
8. K. Dimmler, M. Parris, D. Butler, *et al.*, *J. Appl. Phys.* **61**, 5467 (1987).
9. J. F. Scott, *Phase Transit.* **30**, 107 (1991).
10. Y. Ishibashi, in *Ferroelectric Thin Films: Synthesis and Basic Properties*, Ed. by C. Paz de Araujo, J. F. Scott, and G. W. Taylor (Gordon and Breach, Amsterdam, 1996), p. 135.
11. A. K. Tagantsev, *Integr. Ferroelectr.* **16**, 237 (1997).
12. S. Ducharme, V. M. Fridkin, A. V. Bune, *et al.*, *Phys. Rev. Lett.* **84**, 175 (2000).
13. A. V. Bune, V. M. Fridkin, S. Ducharme, *et al.*, *Nature* **391**, 874 (1998).
14. V. L. Ginzburg, *J. Phys. USSR* **10**, 107 (1946).
15. V. L. Ginzburg, *Zh. Éksp. Teor. Fiz.* **19**, 39 (1949).
16. A. F. Devonshire, *Adv. Phys.* **3**, 85 (1954).
17. L. M. Blinov, V. M. Fridkin, S. P. Palto, *et al.*, *Usp. Fiz. Nauk* **170**, 247 (2000).
18. F. Jona and G. Shirane, *Ferroelectric Crystals* (Macmillan, New York, 1962; Mir, Moscow, 1965).
19. P. J. Lock, *Appl. Phys. Lett.* **19**, 390 (1971).

20. G. A. Samara, *Ferroelectrics* **5**, 25 (1973).
21. T. Maruyama, M. Saitoh, I. Sakai, *et al.*, *Appl. Phys. Lett.* **73**, 3524 (1998).
22. M. A. Marcus, *Ferroelectrics* **40**, 29 (1982).
23. T. Fukukawa, *Ferroelectrics* **57**, 63 (1984).
24. K. Kimura and H. Ohigashi, *Jpn. J. Appl. Phys.* **25**, 383 (1986).
25. S. Palto, L. Blinov, A. Bune, *et al.*, *Ferroelectr. Lett. Sect.* **19**, 65 (1995).
26. A. Bune, S. Ducharme, V. M. Fridkin, *et al.*, *Appl. Phys. Lett.* **67**, 3975 (1995).
27. S. Palto, L. Blinov, E. Dubovik, *et al.*, *Europhys. Lett.* **34**, 465 (1996).
28. L. M. Blinov, V. M. Fridkin, S. P. Palto, *et al.*, *Thin Solid Films* **284–285**, 474 (1996).
29. S. Ducharme, S. P. Palto, L. M. Blinov, and V. M. Fridkin, in *Proceedings of the 6th Williamsburg Workshop on Fundamental Physics of Ferroelectrics*, Ed. by R. Cohen and K. Rabe (American Inst. of Physics, Melville, 2000), p. 354.
30. S. Ducharme, A. V. Bune, V. M. Fridkin, *et al.*, *Phys. Rev. B* **57**, 25 (1998).
31. A. V. Bune, C. Zhu, S. Ducharme, *et al.*, *J. Appl. Phys.* **85**, 7869 (1999).
32. T. Tybell, C. H. Ahn, and J.-M. Triscone, *Appl. Phys. Lett.* **75**, 856 (1999).
33. E. D. Specht, H.-M. Christen, D. P. Norton, and L. A. Boatner, *Phys. Rev. Lett.* **80**, 4317 (1998).
34. J. F. M. Cillessen, M. W. J. Prins, and R. M. Wolf, *J. Appl. Phys.* **81**, 2777 (1997).
35. H. Ohigashi, K. Omote, H. Abe, and K. Koga, *Jpn. J. Appl. Phys.* **68**, 1824 (1999).
36. H. Ohigashi, K. Omote, and T. Gomyo, *Appl. Phys. Lett.* **66**, 3281 (1995).
37. M. Hikosaka, K. Sakurai, H. Ohigashi, and T. Koizumi, *Jpn. J. Appl. Phys.* **32**, 2029 (1993).

---

**MAGNETISM  
AND FERROELECTRICITY**

---

# Thermostimulated Electron Emission from Polar Cleavage of a Triglycine Sulfate Crystal

**O. V. Rogazinskaya, S. D. Milovidova, A. S. Sidorkin, and A. A. Sidorkin**

*Voronezh State University, Universitetskaya pl. 1, Voronezh, 394693 Russia*

*e-mail: sidorkin@dom.vsu.ru*

Received December 19, 2000

**Abstract**—This paper reports the results of experimental investigations into thermostimulated electron emission from the positive and negative cleavage surfaces of a ferroelectric triglycine sulfate crystal. It is shown that the current density  $j$  of emission from the negative surface is universally higher than that from the positive surface over the entire range from room temperature to the Curie point. The shape of the  $j(T)$  curves substantially depends on the degree of natural unipolarity of the studied samples. The results obtained are discussed in the framework of the mechanism of field electron emission from the surface electronic states. © 2001 MAIK “Nauka/Interperiodica”.

## 1. INTRODUCTION

Electron emission has been extensively used in practice as a highly sensitive method of testing the surface condition of different materials. In ferroelectrics, the electron emission can be stimulated by any action that produces a change in the polar state of the surface of a material: application of an electric field, a variation in the temperature, or a mechanical action on the sample. Traditionally, the first two stimulation methods are widely covered in the literature [1–4]. The electron emission stimulated by a mechanical deformation in a ferroelectric material has not been adequately investigated. In particular, Minakova *et al.* [5] demonstrated that the high-energy electron emission current, which was measured immediately after the cleavage of a crystal under vacuum at room temperature, depends on the sign of the polar cleavage surface of the ferroelectric triglycine sulfate crystal.

Earlier [6–8], we proved that the emission properties of ferroelectric crystals are primarily determined by different-type defects (for example, growth defects and radiation damages of the material). Their effect can manifest itself in the generation of emission-active centers, the blocking of domain boundaries providing the polarization switching of ferroelectric materials [6, 7], and the formation of the unipolar state [9], which is characterized by the so-called internal field in the material [10].

The purpose of the present work was to investigate thermostimulated electron emission from positively and negatively charged surfaces (positive and negative cleavages) obtained by cleaving triglycine sulfate crystal samples. We have determined and analyzed the dependence of the emission current on the degree of initial unipolarity of the sample, which is governed by the defect concentration in the material.

## 2. EXPERIMENTAL TECHNIQUE AND RESULTS

Electron emission was investigated using samples prepared from a nominally pure triglycine sulfate crystal grown in the ferroelectric phase by decreasing the saturation temperature of the solution. A rectangular bar, with the largest side along the polar axis, was sawed out from the grown crystal. Then, the bar was cleaved along the cleavage planes into samples according to the procedure described in [10]. The sample thickness was approximately equal to 1.5 mm, and the sample area was  $\sim 50 \text{ mm}^2$ . Prior to and after the emission measurements (which were finished in the paraphase after passing the Curie point), the domain structure was examined for all the studied samples and the degree of natural unipolarity of each sample was estimated from the ratio between the areas of domains with different signs [10]. The sign of domains emerging on the surface of the material was checked for each pair of mirror cleavage samples.

The electron emission current density was measured according to the standard procedure [1] under a vacuum of  $\sim 10^{-5} \text{ mmHg}$ . The experiments were performed in the range from room temperature to the Curie point. The temperature of a sample was determined by a copper–constantan thermocouple and was controlled by the simultaneous measurement of the capacitance of another pure triglycine sulfate crystal sample. The error in the temperature measurement did not exceed 5%. The heating rate was equal to  $\sim 1\text{--}1.2 \text{ K/min}$ . All the data obtained were recorded and processed using a computer.

The curve plotted in Fig. 1a illustrates the change in the degree of initial unipolarity  $\phi$  of the samples located at different distances from the seed. The growth temperatures that correspond to the location of the samples in the grown crystal are shown in Fig. 1b.

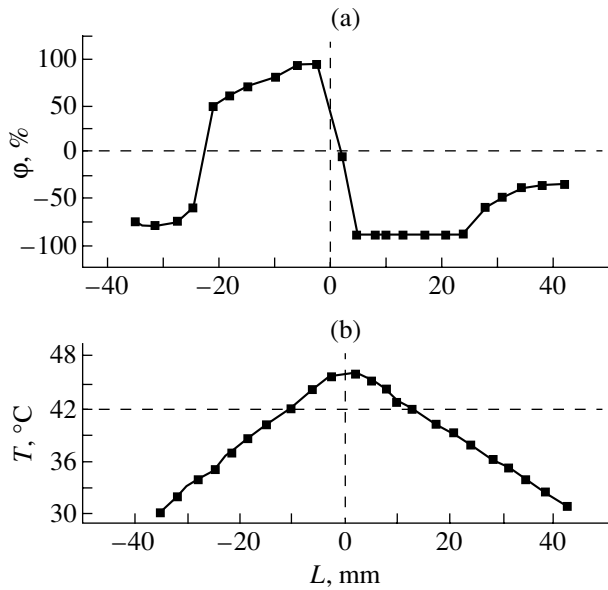


**Fig. 1.** Dependences of (a) the unipolarity and (b) the growth temperature of triglycine sulfate crystal samples on their distance from the seed.

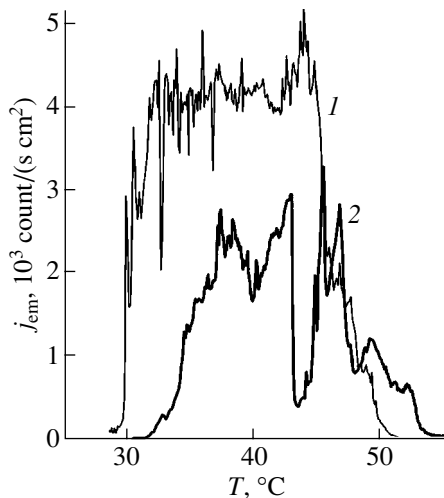


**Fig. 2.** Temperature dependences of the current density of emission from the (1) negative and (2) positive surfaces of pure triglycine sulfate crystal samples with the unipolarity coefficient  $\phi = 90\%$ .

It is worth noting that, on one side of the seed, the degree of unipolarity for the majority of samples is rather high ( $\sim 90\%$ ) and drastically decreases to a value corresponding to a virtually nonunipolar state ( $\sim 40\text{--}50\%$ ) when the crystal growth temperature passes through a temperature of  $37^\circ\text{C}$ , i.e., the temperature that corresponds to the domain structure transformation in a triglycine sulfate crystal [11]. On the other side of the seed, the degree of unipolarity near the seed is also high ( $+95\%$ ) but has the opposite sign. This correlates with the experimental data obtained for the internal dis-

placement field [10]. As the distance between the sample and the seed increases, the unipolarity  $\phi$  gradually decreases and changes sign at the same temperature of domain structure transformation ( $37^\circ\text{C}$ ).

Note that all the above values of  $\phi$  were measured at the initial (room) temperature. After even a single measurement resulting in the transition of the studied sample to the paraphase, all the samples became completely nonunipolar.

The samples located on opposite sides of the seed are characterized by different domain structures. The samples whose location corresponds to the positive direction of the polar axis in Fig. 1 have a lens-shaped domain structure with domains uniformly distributed over the studied surface. Strip extended domains are observed in the samples located on the opposite side of the seed. The difference in the domain structures in the aforementioned samples correlates with the difference in the temperatures of their formation. For samples of the former group, the domain structure was formed during the growth at a temperature of about  $38^\circ\text{C}$ , which corresponds to the temperature range of the domain structure transformation. For samples of the latter group, the onset of the unipolarity formation was observed at a considerably lower temperature ( $32^\circ\text{C}$ ).

The measurements of the electron emission current in the triglycine sulfate crystal demonstrated that the electron emission changes in magnitude and character with an increase in the distance from the seed. It should be noted that, over the entire temperature range studied, the current density  $j_{em}$  of emission from the negatively charged cleavage surface is universally higher than that from the positively charged surface.

Figure 2 displays typical temperature dependences  $j_{em}(T)$  for the mirror cleavage samples with a high degree of unipolarity. It is interesting to note that the temperature of the onset of electron emission from the positive cleavage (Fig. 2, curve 2) is  $3\text{--}5\text{ K}$  higher than that of the onset of electron emission from the negative cleavage (Fig. 2, curve 1).

A decrease in the unipolarity with an increase in the distance between the sample and the seed leads to a decrease in the mean emission current density from  $4\text{--}5 \times 10^3\text{ count}/(\text{s cm}^2)$  for samples with  $\phi = 80\text{--}90\%$  to  $2.5\text{--}3.5 \times 10^3\text{ count}/(\text{s cm}^2)$  for samples with  $\phi = 60\%$ . It is characteristic that, for the negative cleavage surface of the samples with a low degree of unipolarity, the maximum emission current in the range of the domain structure transformation is always larger than that in the phase transition range.

### 3. DISCUSSION

The possible reasons for the formation of the internal displacement field and the unipolar state in ferroelectric materials were analyzed in our earlier work [10]. Owing to the difference in the trapping coefficients of impurities and their mobilities, which are

related to the impurity size, the crystallization front can be considered a surface that efficiently separates charges of opposite signs. The charge separation induces the effective electric field in the direction perpendicular to the crystallization front. This field orients newly trapped dipole complexes consisting of oppositely charged impurities. The difference in the energies of the oriented polar defects in domains of different signs gives rise to a preferred polarization direction, i.e., brings about the formation of a unipolar domain structure [12].

It is evident that the above mechanism of the formation of the internal displacement field works well not only during the growth of crystals with special dopants but also in the case of the so-called nominally pure crystals, which always contain a certain amount of uncontrollable impurities.

All the results obtained indicate that the observed emission effect essentially depends on the degree of natural unipolarity of the samples. As was noted above, the emission current density for the negative cleavage surface is universally higher than that for the positive cleavage surface. This is in agreement with the experimental data obtained by Biedrzycki [4], who revealed that the emission stimulated by an external electric field is observed only during the half-cycles of an external ac field when a negative charge is formed at the active surface. Moreover, the results obtained agree well with the data reported in [5], according to which the high-energy electron emission from an as-prepared cleavage under vacuum is more efficient for the negatively charged surface of ferroelectric materials.

The thermoionic emission activity observed for the studied ferroelectrics and the available experimental data [1–4] can be explained by the field emission of electrons from surface electronic states in the field of charges of spontaneous polarization screening. At the equilibrium state, the field of spontaneous polarization charges is usually compensated for by charges trapped from air, so that the ferroelectric surface is electrically nonactive. As the Curie point is approached, the balance between these fields is disturbed due to the decrease in spontaneous polarization, which results in the formation of a nonzero total field whose direction is determined by the field of compensation charges. It is this nonzero field that is responsible for the escape of electrons from traps of surface electronic states.

In the framework of the proposed mechanism, it is clear that only the net negative charge at the surface of materials favors the escape of electrons from the sample surface. It is also evident that the higher the degree of unipolarity of the sample, the stronger the field  $E$  (active in the electron emission) and, therefore, the higher the emission current density  $j$  observed experimentally.

The electron emission from the positive cleavage surface in the samples can be explained as follows. The unipolarity implies that there is a preferred orientation

of the spontaneous polarization vector in the corresponding domains and, hence, a dominant charge at the surface of the sample. At the same time, it is obvious that the positive cleavage surface involves local regions with a negative charge that can also be active in the electron emission. An increase in the degree of unipolarity leads to a decrease in the fraction of these regions, which, in turn, brings about a decrease in the electron emission.

The observed change in the temperature of the onset of the electron emission in samples with positive cleavage toward the high-temperature range can be associated with the fact that the escape of electrons from the positively charged surface requires a higher initial energy, which results in an increase in temperature of the onset of the electron emission in these samples.

#### ACKNOWLEDGMENTS

This work was supported by the “Nonlinear Dielectric Films for Nanotechnology” Grant of the Netherlands Research Organization (NWO).

#### REFERENCES

1. A. M. Kostsov, A. S. Sidorkin, V. S. Zal'tsberg, and S. P. Gribkov, *Fiz. Tverd. Tela (Leningrad)* **24** (11), 3436 (1982) [*Sov. Phys. Solid State* **24**, 1952 (1982)].
2. A. S. Sidorkin, A. M. Kostsov, and V. S. Zal'tsberg, *Fiz. Tverd. Tela (Leningrad)* **27** (7), 2200 (1985) [*Sov. Phys. Solid State* **27**, 1320 (1985)].
3. A. S. Sidorkin, P. V. Loginov, A. M. Savvinov, *et al.*, *Fiz. Tverd. Tela (St. Petersburg)* **38** (2), 624 (1996) [*Phys. Solid State* **38**, 344 (1996)].
4. K. Biedrzycki, *Phys. Status Solidi A* **109**, K79 (1988).
5. E. V. Minakova, N. A. Tikhomirova, and Yu. A. Khrustalev, *Poverkhnost* **7**, 135 (1986).
6. A. S. Sidorkin and A. M. Kostsov, *Fiz. Tverd. Tela (Leningrad)* **33** (8), 2458 (1991) [*Sov. Phys. Solid State* **33**, 1383 (1991)].
7. A. S. Sidorkin and B. M. Darinskii, *Appl. Surf. Sci.* **111**, 325 (1997).
8. A. A. Sidorkin, S. D. Milovidova, O. V. Rogazinskaya, and A. S. Sidorkin, *Fiz. Tverd. Tela (St. Petersburg)* **42** (4), 725 (2000) [*Phys. Solid State* **42**, 743 (2000)].
9. A. S. Sidorkin and A. M. Kostsov, in *Emission and Scattering of Electrons in Solids* (Leningr. Gos. Politekh. Inst., Leningrad, 1988), p. 19.
10. B. M. Darinskii, A. S. Sidorkin, and S. D. Milovidova, *Ferroelectrics* **142**, 45 (1993).
11. V. A. Kopsik, N. D. Gavrilova, and V. K. Novik, *J. Phys. Soc. Jpn.* **28**, 382 (1970).
12. A. P. Levanyuk, V. V. Osipov, A. S. Sigov, and A. A. Sobyanin, *Zh. Éksp. Teor. Fiz.* **76**, 345 (1979) [*Sov. Phys. JETP* **49**, 176 (1979)].

*Translated by O. Borovik-Romanova*

## MAGNETISM AND FERROELECTRICITY

# Acoustic and Dielectric Anomalies in the Temperature Range of a Ferroelectric Phase Transition in Glycine Phosphite Crystals

E. V. Balashova\*, V. V. Lemanov\*, and G. A. Pankova\*\*

\* Ioffe Physicotechnical Institute, Russian Academy of Sciences, Politekhnicheskaya ul. 26, St. Petersburg, 194021 Russia

\*\* Institute of High-Molecular Compounds, Russian Academy of Sciences, St. Petersburg, 190034 Russia

Received December 19, 2000

**Abstract**—The acoustical and dielectric properties of glycine phosphite crystals are investigated in the temperature range of a ferroelectric phase transition. The acoustic anomalies for longitudinal waves along the  $X$ ,  $Y$ , and  $Z$  crystallographic axes (where  $Y$  is the spontaneous polarization axis) are analyzed in the framework of the Landau theory. It is shown that pronounced acoustic anomalies of the velocity can be quantitatively described within the pseudoproper ferroelectric phase transition model with due regard for the long-range dipole–dipole interaction. For longitudinal acoustic waves propagating along the polar crystal axis, the striction anomaly of the velocity is only partly suppressed by the long-range dipole–dipole forces and an abrupt jump in the velocity is observed in the vicinity of the phase transition. The temperature coefficients of the velocity in the paraphase are determined. The striction contribution and the contributions biquadratic in the order parameter and in the strain to the velocity anomaly are separated. © 2001 MAIK “Nauka/Interperiodica”.

### 1. INTRODUCTION

A new compound—glycine phosphite  $(\text{NH}_3^+\text{CH}_2\text{COOH})(\text{H}_2\text{PO}_3^-)$ —has been recently synthesized from glycine amino acid  $\text{NH}_3^+\text{CH}_2\text{COO}^-$  and phosphorous acid  $\text{H}_3\text{PO}_3$ . Glycine phosphite crystals have a monoclinic symmetry  $P2_1/a$  ( $Z = 4$ ) at  $T > T_c \cong 224$  K [1] and undergo a phase transition to the ferroelectric state at  $T = T_c$ , in which the direction of the spontaneous polarization  $P_s$  is parallel to a twofold axis [2]. The permittivity of crystals is characterized by relatively small Curie–Weiss constants ( $C \approx 200$ – $400$  K for different samples [2, 3]) and the spontaneous polarization  $P_s = 0.5$   $\mu\text{C}/\text{cm}^2$  at  $T \cong 200$  K [2].

Furtak *et al.* [4] carried out the acoustic investigation in the vicinity of the ferroelectric phase transition in glycine phosphite and revealed jumps in the velocity of longitudinal waves along the  $X$  and  $Z$  crystallographic axes and also along the  $Y$  axis—the direction of the spontaneous polarization  $\mathbf{P}_s$ . Note that, in proper ferroelectrics, the velocity anomalies (due to the electrostriction coupling of the order parameter and the strain) for longitudinal acoustic waves propagating along  $\mathbf{P}_s$  are usually suppressed by the long-range dipole–dipole interaction [5]. The effect of the long-range dipole–dipole interaction on the acoustic anomalies at the ferroelectric phase transition is primarily determined by the Curie–Weiss constant. In this respect, it is of interest to analyze quantitatively the velocity anomalies for a longitudinal wave along the  $Y$  axis in glycine phosphite crystals. On the one hand, the Curie–Weiss constants for these crystals are approximately one order of magnitude less than those

for triglycine sulfate crystals and two orders of magnitude less than those for betaine phosphite crystals—proper amino acid ferroelectrics in which acoustic anomalies for longitudinal waves along the polar axis are completely suppressed by the long-range dipole–dipole interaction. On the other hand, the Curie–Weiss constant for glycine phosphite crystals is approximately two orders of magnitude larger than those for weak ferroelectrics, such as calcium trisarcosine chloride and lithium germanate ( $\text{Li}_2\text{Ge}_7\text{O}_{15}$ ) crystals in which the acoustic anomalies are virtually not suppressed [6, 7].

The relatively small Curie–Weiss constants, small values of spontaneous polarization, and an abrupt jump in the velocity of longitudinal waves along the spontaneous polarization axis suggest that the ferroelectric phase transition in glycine phosphite crystals has a pseudoproper character [4]. However, as far as we know, the effect of long-range dipole–dipole forces has never been evaluated quantitatively. In our opinion, this is a topical problem, because its solution can provide a deeper insight into the mechanism of the formation of the ferroelectric state.

In this work, we examined the temperature dependences of the longitudinal acoustic wave velocity and the permittivity along three crystallographic directions ( $X$ ,  $Y$ , and  $Z$ ) for glycine phosphite crystals in the range of the ferroelectric phase transition. Within the pseudoproper ferroelectric phase transition model, the acoustic and dielectric anomalies were quantitatively analyzed on the basis of the thermodynamic potential accounting for the interaction of different modes.

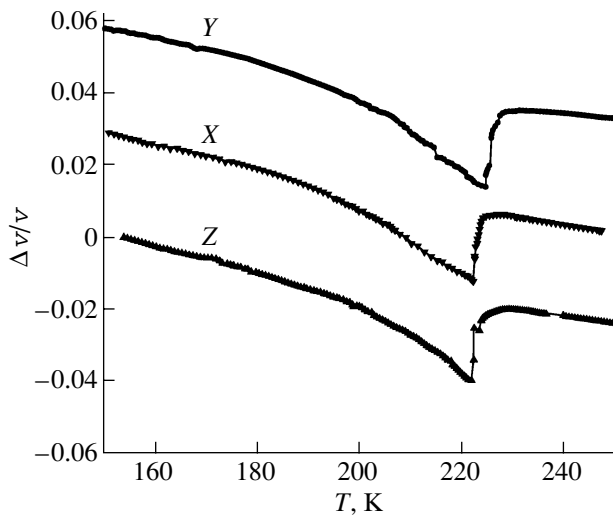


**Fig. 1.** Temperature dependences of the relative change in the longitudinal acoustic wave velocity along three crystallographic directions  $X$ ,  $Y$ , and  $Z$  at a frequency of 15 MHz.

## 2. CRYSTAL GROWTH AND EXPERIMENTAL TECHNIQUE

The glycine phosphite crystals were grown by the slow cooling method from an aqueous solution containing glycine amino and phosphorous acids. The temperature changed from 25 to 8°C at a rate of 1°C/day. The acoustic measurements were performed with samples  $5 \times 8 \times 3.5$  mm in size along the  $X$ ,  $Y$ , and  $Z$  axes, respectively (where  $X \parallel a$ ,  $Y \parallel b$ , and  $Z \perp (ab)$ ). The dielectric measurements were carried out with the samples which were cut from the same crystal and measured  $3 \times 1.5 \times 3.5$  mm along the  $X$ ,  $Y$ , and  $Z$  axes, respectively.

The acoustic waves were excited by lithium niobate crystal transducers at a frequency of 15 MHz. The relative measurements of the velocity were performed by the ultrasonic pulse-echo-overlap technique (the Papadakis method) with a sensitivity of  $\sim 10^{-4}$ . The absolute velocities were measured accurate to several percent. The attenuation was measured by the exponent method from the decay of pulse echoes with an accuracy of 0.2 dB/ $\mu$ s.

## 3. EXPERIMENTAL RESULTS

Figure 1 shows the temperature dependences of the relative change in the longitudinal acoustic wave velocity (shifted with respect to each other) along three crystallographic directions  $X$ ,  $Y$ , and  $Z$ . The velocity anomalies in the range of the ferroelectric phase transition ( $T_c \cong 225$  K) for all the directions manifest themselves in a jumpwise decrease in the velocity by 1.8–2.2% and a substantial increase in the velocity with a further decrease in the temperature, so that the velocity corre-

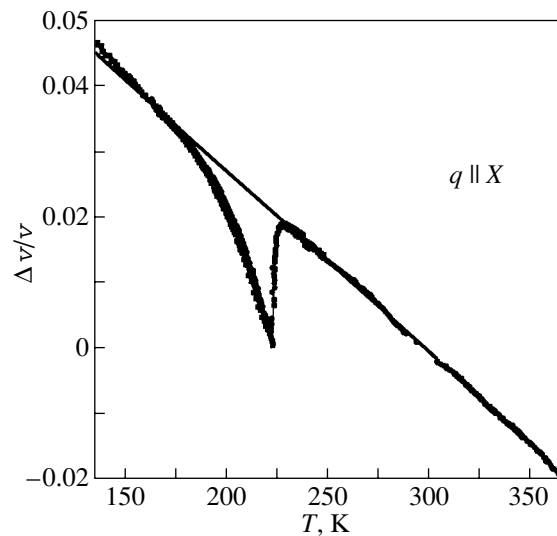


**Fig. 2.** Temperature dependence of the relative change in the longitudinal acoustic wave velocity along the  $X$  axis at a frequency of 15 MHz.

sponding to the paraphase has already been reached at  $T \approx 200$  K.

For the  $X$  direction, the velocity was measured in the range covering temperatures above room temperature (Fig. 2). It is seen from Fig. 2 that the temperature dependence of the velocity in the paraphase is well approximated by a linear dependence. The longitudinal wave velocities along the  $X$ ,  $Y$ , and  $Z$  directions at room temperature and their temperature coefficients in the paraphase are presented in Table 1. As follows from Table 1, the longitudinal wave velocity along the  $Y$  direction is maximum, whereas its temperature coefficient in the paraphase is minimum. For the  $X$  and  $Z$  directions, the velocities and their temperature coefficients differ to a smaller extent.

The temperature dependences of the permittivity  $\epsilon_b$  and the reciprocal of the permittivity  $1/\epsilon_b$  along the  $Y$  axis at a frequency of 1 MHz are displayed in Fig. 3. The temperature dependence of  $\epsilon_b$  exhibits a pronounced maximum in the vicinity of the ferroelectric phase transition. Because of the considerable dielectric losses, which appear in the ferroelectric phase and contribute to the permittivity [2], the order of the phase

**Table 1.** Longitudinal wave velocities at room temperature and temperature coefficients of velocity in the paraphase for three crystallographic directions  $X$ ,  $Y$ , and  $Z$  in a glycine phosphite crystal

Direction	Velocity, $10^3$ m/s	Temperature coefficient of velocity, $10^{-4}$ K $^{-1}$
$Y$	5.3	1.61
$X$	4.0	2.77
$Z$	3.7	2.15

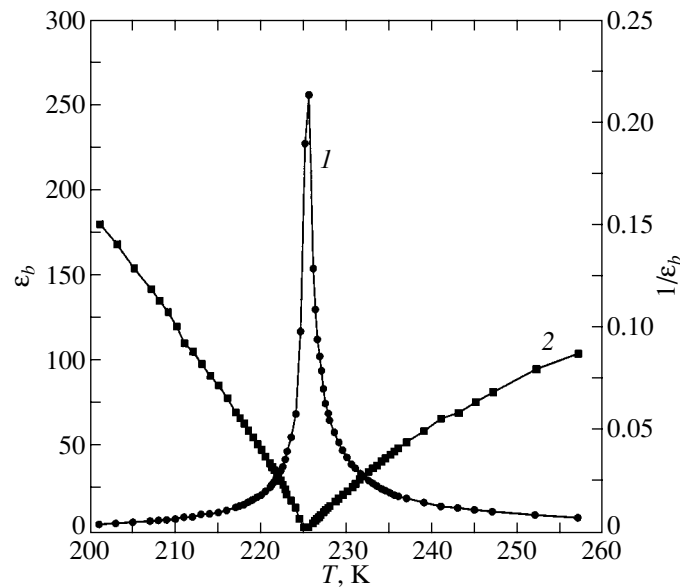


**Fig. 3.** Temperature dependences of (1) the permittivity and (2) the reciprocal of the permittivity along the  $Y$  axis at a frequency of 1 MHz.

transition is difficult to determine from the slope of the reciprocal of the permittivity in the paraphase and ferroelectric phase.

The temperature dependence of the attenuation of longitudinal waves along the  $Z$  axis in the vicinity of the phase transition is plotted in Fig. 4. The attenuation in the phase transition range is characterized by an asymmetric maximum, which is associated with the contribution of the Landau–Khalatnikov relaxation mechanism in the ferroelectric phase. The maximum attenuation at a frequency of 15 MHz is approximately equal to 2.5 dB/ $\mu$ s.

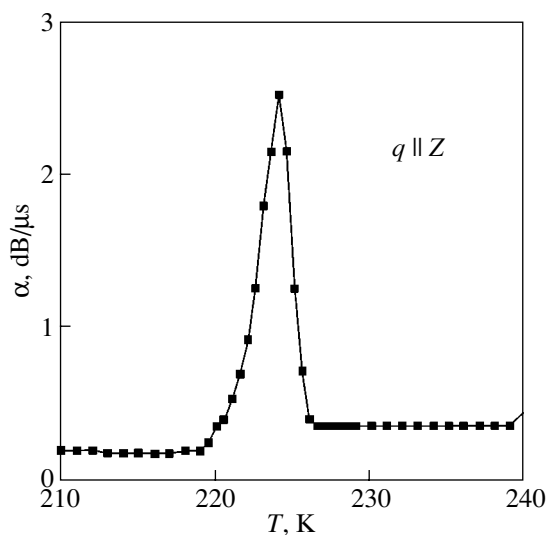


**Fig. 4.** Temperature dependence of the attenuation of longitudinal acoustic waves along the  $Z$  axis at a frequency of 15 MHz in the vicinity of a ferroelectric phase transition.

#### 4. ANALYSIS OF EXPERIMENTAL RESULTS

The specific feature of the acoustical properties of glycine phosphite crystals is a pronounced anomaly in the velocity of longitudinal waves propagating along the polar axis  $Y$  in the vicinity of the ferroelectric phase transition (Fig. 1). As a rule, this anomaly in ferroelectrics is suppressed by long-range dipole–dipole forces [5], except when the ferroelectric phase of crystals has a domain structure with polar domain sizes considerably less than the acoustic wavelength. In this case, the formation of a single-domain sample leads to the suppression of the acoustic anomaly. Since the formation of single-domain glycine phosphite samples virtually does not affect the character of the anomaly [4], it is necessary to analyze quantitatively the role of the long-range dipole–dipole interaction in these crystals.

Let us consider the acoustical and dielectric properties of the glycine phosphite crystals within the pseudoproper ferroelectric phase transition model. The free energy can be written in the following form [8]:

$$F = \frac{1}{2}\alpha\eta^2 + \frac{1}{4}\beta\eta^4 + \frac{1}{6}\gamma\eta^6 + h\eta P + \frac{1}{2\chi_0}P^2 + d\eta^2S + g\eta^2S^2 + \frac{1}{2}c_0S^2, \quad (1)$$

where  $\alpha = \lambda(T - T_c)$ ,  $\gamma > 0$ ,  $\eta$  is the nonpolar order parameter that possesses the transformation properties identical to those of the polarization  $P$ ,  $S$  is the strain,  $\chi_0$  is the background permittivity, and  $c_0$  is the background elastic modulus. The  $\xi\eta^3P$ -type invariant whose role will be considered below can also be included in potential (1).



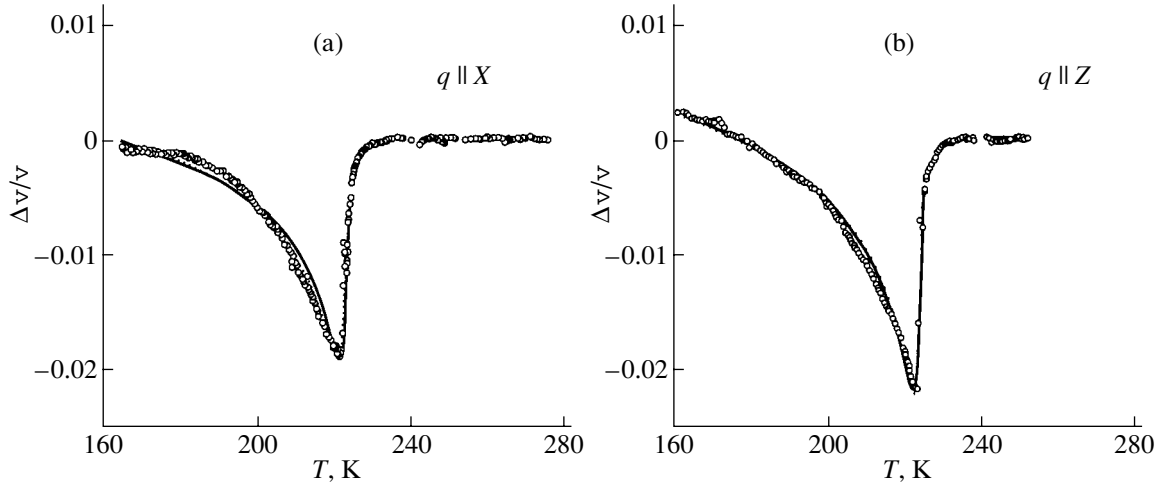


**Fig. 5.** Anomalies of the longitudinal wave velocity along the (a) X and (b) Z axes ( $\mathbf{q} \perp \mathbf{P}_s$ ) in the temperature range of a ferroelectric phase transition. The graphs are plotted as the difference between the velocity and the linear contribution (extrapolated from the data for the parapse) to the velocity. Solid lines correspond to the results of calculations by formula (17). The calculation according to formula (16) gives virtually the same dependences on this scale.

The acoustic anomalies obtained as the difference between the velocity and the linear contribution (extrapolated from the data for the parapse) to the velocity are shown in Fig. 5. As follows from the character of the acoustic dependences (a pronounced nonlinear temperature dependence of the velocity in the ferroelectric phase), the ferroelectric phase transition is close to a tricritical point. A similar inference was made by Dacko *et al.* [2] from the analysis of the temperature dependence of the spontaneous polarization.

Now, we analyze the following two cases: (i) the second-order phase transition close to the tricritical point and the tricritical point and (ii) the first-order phase transition close to the tricritical point.

#### 4.1. The second-order phase transition close to the tricritical point and the tricritical point ( $\beta^* = \beta -$

$\frac{2d^2}{c_0} \geq 0$ ). The equations of state have the form

$$\begin{aligned} \frac{\partial F}{\partial \eta} &= \alpha\eta + \beta\eta^3 + \gamma\eta^5 + hP + 2d\eta S = 0, \\ \frac{\partial F}{\partial P} &= h\eta + \frac{1}{\chi_0}P = 0, \\ \frac{\partial F}{\partial S} &= d\eta^2 + c_0S = 0 \end{aligned} \quad (2)$$

(without regard for the  $g\eta^2S^2$  invariant).

From relationships (2), we can obtain the following expressions for the spontaneous quantities  $\eta$ ,  $P$ , and  $S$

in the ferroelectric phase at  $T < T'_c$ :

$$\begin{aligned} \eta_s^2 &= \frac{\beta^*}{2\gamma} \left[ \left( \frac{T'_c - T + \Delta T}{\Delta T} \right)^{1/2} - 1 \right], \\ P_s^2 &= h^2 \chi_0^2 \eta_s^2, \\ S_s &= -\frac{d}{c_0} \eta_s^2, \end{aligned} \quad (3)$$

where  $T'_c = T_c + \frac{h^2 \chi_0}{\lambda}$  is the temperature of the ferro-

electric phase transition and the quantity  $\Delta T = \frac{(\beta^*)^2}{4\lambda\gamma}$  characterizes the closeness of the phase transition to the tricritical point.

For the permittivity in the paraelectric and ferroelectric phases, we have the expressions

$$\epsilon_b = \epsilon_\infty + \frac{C_+}{T - T'_c}, \quad T > T'_c, \quad (4)$$

$$\epsilon_b = \epsilon_\infty + \frac{C_+/4}{(\Theta_1^{1/2} - \Delta T^{1/2})(\Theta_1^{1/2} + \Delta T_1^{1/2})}, \quad T < T'_c, \quad (5)$$

where  $\Theta_1 = T'_c - T + \Delta T$ ,  $C_+ = (4\pi\chi_0^2 h^2)/\lambda$  is the effective Curie–Weiss constant in the paraelectric phase, the quantity  $\Delta T_1 = d^4/(c_0^2 \lambda \gamma)$  determines the strength of coupling between the order parameter and the strain, and  $\epsilon_\infty = 1 + 4\pi\chi_0$ .

The fitting of the experimental temperature dependence of the permittivity for the parapse (Fig. 3) with

the use of relationship (4) gives the Curie–Weiss constant  $C_+ = 190$  K and  $\epsilon_\infty = 6.5$  for the studied samples.

The effective elastic modulus for quasi-longitudinal waves propagating perpendicular to the spontaneous polarization axis ( $\mathbf{q} \perp \mathbf{P}_s$ ) in the ferroelectric phase ( $T < T_c'$ ) and the elastic modulus  $c \equiv c_{22}$  for pure longitudinal waves along the twofold axis ( $\mathbf{q} \parallel \mathbf{P}_s$ ) in the limit  $\omega\tau \ll 1$  (where  $\omega$  is the acoustic wave frequency and  $\tau$  is the order parameter relaxation time) are defined by the relationships

$$c = c_0 - \frac{c_0 \Delta T_1^{1/2}}{\Theta_1^{1/2} + \Delta T_1^{1/2}}, \quad \mathbf{q} \perp \mathbf{P}_s, \quad (6)$$

$$c = c_0 - \frac{c_0 \Delta T_1^{1/2} (\Theta_1^{1/2} - \Delta T_1^{1/2})}{(\Theta_1^{1/2} + \Delta T_1^{1/2})(\Theta_1^{1/2} - \Delta T_1^{1/2}) + C_+/4\epsilon_\infty}, \quad \mathbf{q} \parallel \mathbf{P}_s. \quad (7)$$

The appearance of the ratio  $C_+/4\epsilon_\infty$  (accounting for the long-range field  $E = -4\pi P$  [5–7]) in the denominator of expression (7) substantially changes the form of the acoustic anomaly, which, in the absence of the long-range dipole–dipole interaction, is described by expression (6).

At the phase transition temperature, the temperature dependence of the elastic modulus shows a jump for the directions perpendicular to  $P_s$  [see formula (6)] and a minimum for the direction along  $P_s$  [see formula (7)]. In this case, the temperature at a minimum of the elastic modulus is represented as

$$T_{\min} = T_c' - A \left[ 1 + \left( \frac{\Delta T}{A} \right)^{1/2} \right], \quad (8)$$

where  $A = C_+/4\epsilon_\infty$ . It is seen that this temperature for phase transitions close to the tricritical point ( $\Delta T \ll A$ ) is primarily determined by the  $A$  parameter and shifts toward the low-temperature range with an increase in the Curie–Weiss constant  $C_+$ .

Expression (7) also allows us to derive the relationship for the depth of the minimum of the elastic modulus

$$(c - c_0)_{\min} = -\frac{c_0 \Delta T_1^{1/2}}{\Delta T_1^{1/2} + \Delta T_1^{1/2} + 2A^{1/2}}. \quad (9)$$

From formula (9), it follows that the stronger the coupling of the order parameter and the strain, i.e., the larger the quantity  $\Delta T_1$ , the deeper the minimum ( $\Delta T, \Delta T \ll A$ ).

For the tricritical point ( $\beta^* = 0$ ), the expressions for the permittivity and the elastic modulus can be obtained from formulas (4)–(7) by setting  $\Delta T = 0$ . It follows from relationship (8) that, for the tricritical point, the temperature of the elastic modulus at a minimum is closest to the phase transition temperature. For our glycine phosphite crystals, the parameter  $A$  is equal to

$\approx 7$  K. According to formula (8), we obtain for the tricritical point that the minimum of the elastic modulus and, correspondingly, the velocity of sound should be observed at the temperature 7 K below the ferroelectric phase transition temperature.

**4.2. The first-order phase transition close to the tricritical point ( $\beta^* \leq 0$ ).** The equilibrium quantities  $\eta$ ,  $P$ , and  $S$  in the ferroelectric phase at  $T < T_0$  (where  $T_0$  is the first-order ferroelectric phase transition temperature at which the energies of the paraelectric and ferroelectric phases are equal to each other) are given by

$$\begin{aligned} \eta_s^2 &= -\frac{\beta^*}{2\gamma} \left[ \left( \frac{T_c' - T + \Delta T}{\Delta T} \right)^{1/2} + 1 \right], \\ P_s^2 &= h^2 \chi_0^2 \eta_s^2, \\ S_s &= -\frac{d}{c_0} \eta_s^2. \end{aligned} \quad (10)$$

In the low-frequency limit ( $\omega\tau \ll 1$ ), the elastic moduli in the ferroelectric phase at  $T < T_0$  for longitudinal waves propagating perpendicular and parallel to  $\mathbf{P}_s$  are described by the relationships

$$c = c_0 - \frac{c_0 \Delta T_1^{1/2}}{\Theta_2^{1/2} + \Delta T_1^{1/2}}, \quad \mathbf{q} \perp \mathbf{P}_s, \quad (11)$$

$$c = c_0 - \frac{c_0 \Delta T_1^{1/2} (\Theta_2^{1/2} + \Delta T_1^{1/2})}{(\Theta_2^{1/2} + \Delta T_1^{1/2})(\Theta_2^{1/2} + \Delta T_1^{1/2}) + A}, \quad \mathbf{q} \parallel \mathbf{P}_s. \quad (12)$$

Here,  $\Theta_2 = T_0 - T + (1/4)\Delta T$  and  $T_0 = T_c' + (3/4)\Delta T$  is the first-order phase transition temperature, which is determined from the equality of the energies for the paraelectric and ferroelectric phases.

The jumps in the elastic modulus at  $T = T_0$  are defined as

$$\begin{aligned} \frac{\Delta c}{c_0} &= -\frac{\Delta T_1^{1/2}}{\Delta T_1^{1/2} + \frac{1}{2}\Delta T^{1/2}} \\ &= -\frac{2d^2}{\beta^* c_0} \frac{\Delta T^{1/2}}{\left( \Delta T_1^{1/2} + \frac{1}{2}\Delta T^{1/2} \right)}, \quad \mathbf{q} \perp \mathbf{P}_s, \end{aligned} \quad (13)$$

$$\begin{aligned} \frac{\Delta c}{c_0} &= -\frac{\Delta T_1^{1/2}}{\Delta T_1^{1/2} + \frac{1}{2}\Delta T^{1/2} + \frac{2A}{3\Delta T^{1/2}}} \\ &= -\frac{2d^2}{\beta^* c_0} \frac{\Delta T^{1/2}}{\left( \Delta T_1^{1/2} + \frac{1}{2}\Delta T^{1/2} + \frac{2A}{3\Delta T^{1/2}} \right)}, \quad \mathbf{q} \parallel \mathbf{P}_s. \end{aligned} \quad (14)$$

It follows from formula (14) that, upon first-order phase transition, despite the suppression of the anom-

ally by the long-range field, the jump in the elastic modulus is retained and its magnitude appreciably depends on the parameters of the thermodynamic potential. The larger the parameter  $A$  and the closer the first-order phase transition to the tricritical point (at the same striction strength of the coupling between the order parameter and the strain), the smaller the jump.

First, we quantitatively analyze the acoustic anomalies in the vicinity of the ferroelectric phase transition for longitudinal waves propagating along directions perpendicular to the spontaneous polarization ( $\mathbf{q} \perp \mathbf{P}_s$ ) by using relationship (6) for the tricritical point and relationship (11) for the first-order phase transition close to the second-order transition. The acoustic wave velocity in the ferroelectric phase at  $T \leq 200$  K is higher than that in the paraphase. Therefore, in addition to the  $d\eta^2 S$ -type striction coupling of the order parameter and the strain, it is necessary to take into account the contribution quadratic in the order parameter and strain (of the  $g\eta^2 S^2$  type) to the acoustic anomalies of the interaction energy. This contribution is included in the form of a static term (proportional to the order parameter squared) in the elastic modulus

$$c = c_0 + 2g\eta^2. \quad (15)$$

From the Landau–Khalatnikov equation for the order parameter and the equation of motion of elastic displacements, we deduce the expressions for the longitudinal wave velocity in the case of the tricritical point and the first-order phase transition. With due regard for the biquadratic coupling of the order parameter and the strain, these expressions take the following form:

$$\frac{\Delta v}{v_0} = \left\{ 1 - \frac{\Delta T_1^{1/2}}{[(T'_c - T)^{1/2} + \Delta T_1^{1/2}]1 + \omega^2 \tau^2} \right\}^{1/2} - 1 + \left( \frac{T'_c - T}{G} \right)^{1/2} \quad (16)$$

(where  $\tau = \tau_0 \{ (T'_c - T)^{1/2} [(T'_c - T)^{1/2} + \Delta T_1^{1/2}] \}^{-1}$ ,  $\tau_0 = (4L\lambda)^{-1}$ ,  $L$  is the kinetic coefficient, and  $G = c_0^2 \gamma / g^2 \lambda$ ) for the tricritical point ( $\mathbf{q} \perp \mathbf{P}_s$ ) at  $T < T'_c$  and

$$\frac{\Delta v}{v_0} = -\frac{1}{2} \frac{\Delta T_1^{1/2}}{\Theta_2^{1/2} + \Delta T_1^{1/2}} \frac{1}{1 + \omega^2 \tau^2} + \frac{\Theta_2^{1/2} + \Delta T_1^{1/2}}{G^{1/2}}, \quad (17)$$

(where  $\tau = \tau_0 [(\Theta_2^{1/2} + \Delta T_1^{1/2})(\Theta_2^{1/2} + \Delta T_1^{1/2})]^{-1}$ ) for the first-order phase transition ( $\mathbf{q} \perp \mathbf{P}_s$ ) at  $T < T_0$ .

A comparison of the experimental data with relationships (16) and (17) enables us to find the  $\Delta T_1$  and  $G$  parameters, which determine the striction and biquadratic contributions to the velocity along the  $X$  and  $Z$  directions (Table 2).

As is seen from Fig. 5, the experimental dependences of the velocity are equally well described by the theoret-

**Table 2.** Contributions of the striction energy  $d\eta^2 S$  and the energy  $g\eta^2 S^2$  (quadratic in the order parameter and the strain) described by the parameters  $\Delta T_1 = d^4 / c_0^2 \lambda \gamma$  and  $G = c_0^2 \gamma / g^2 \lambda$  to anomalies of the longitudinal acoustic wave velocity along the  $X$ ,  $Y$ , and  $Z$  directions in a glycine phosphite crystal

Direction	Tricritical point ( $\Delta T = 0$ )		First-order phase transition ( $\Delta T \cong 0.6$ K)	
	$(\Delta T_1)^{1/2}$ , K <sup>1/2</sup>	$G^{1/2}$ , 10 <sup>3</sup> K <sup>1/2</sup>	$(\Delta T_1)^{1/2}$ , K <sup>1/2</sup>	$G^{1/2}$ , 10 <sup>3</sup> K <sup>1/2</sup>
$X$	0.10	1.1	0.13	0.90
$Y$ ( $A = 7$ )	0.29	0.27	0.26	0.33
$Z$	0.12	0.83	0.14	0.80

ical expressions (16) and (17) with the use of the parameters given in Table 2. It should be noted that, in the case of a weak first-order phase transition ( $\Delta T \cong 0.6$  K), the calculated parameters  $\Delta T_1$  and  $G$  insignificantly differ for the tricritical point and the first-order phase transition.

The description of the velocity anomaly in the immediate vicinity of the phase transition temperature by using formulas (16) and (17) requires the introduction of rather long times of the order parameter relaxation  $\tau_0 \cong 10^{-8}$  s K. The dynamic properties of the order parameter can be estimated from the anomaly of the acoustic wave attenuation due to the striction coupling of the order parameter and the strain in the phase transition range. This attenuation along the directions perpendicular to the spontaneous polarization axis ( $\mathbf{q} \perp \mathbf{P}_s$ ) is defined by the relationships

$$\alpha = \frac{1}{2} \frac{\Delta T_1^{1/2}}{(T'_c - T)^{1/2} + \Delta T_1^{1/2}} \frac{\omega^2 \tau}{1 + \omega^2 \tau^2}, \quad T < T'_c \quad (18)$$

for the tricritical point and

$$\alpha = \frac{1}{2} \frac{\Delta T_1^{1/2}}{\left( T_0 - T + \frac{1}{4} \Delta T \right)^{1/2} + \Delta T_1^{1/2}} \frac{\omega^2 \tau}{1 + \omega^2 \tau^2}, \quad T < T_0 \quad (19)$$

for the first-order phase transition. Substitution of the experimental data on the attenuation of longitudinal acoustic waves along the  $Z$  direction (Fig. 4) into relationships (18) and (19) gives  $\tau_0 \cong 10^{-9}$  s K, which is one order of magnitude less than the time  $\tau_0$  obtained from the velocity data processing. This can be associated with the fact that the change in the velocity near the  $T_c$  temperature decreases owing to static defects [9]. In this case, the order parameter relaxation times determined from the acoustic wave attenuation and dielectric measurements [3] coincide.

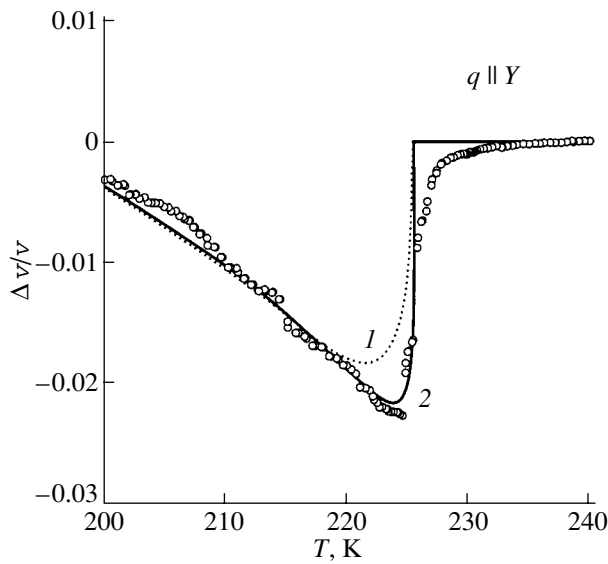


**Fig. 6.** Temperature dependences of the relative change in the longitudinal wave velocity along the spontaneous polarization axis  $Y(\mathbf{q} \parallel \mathbf{P}_s)$  in the vicinity of a ferroelectric phase transition. The graphs are plotted as the difference between the velocity and the linear contribution (extrapolated from the data for the parapsase) to the velocity. Curves 1 and 2 are the dependences calculated according to formulas (20) (the tricritical point) and (21) (the first-order phase transition). Points are the experimental data.

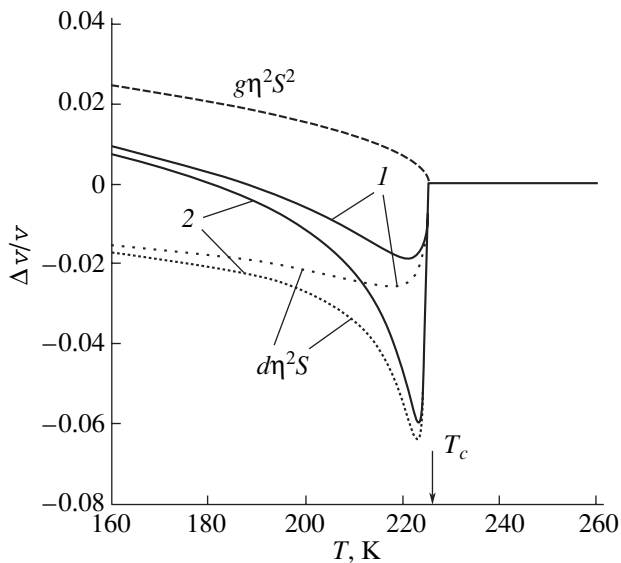


**Fig. 7.** Calculated dependences of the anomaly in the velocity at the phase transition at the tricritical point (solid lines) and the separated contributions of the striction energy  $d\eta^2 S$  and the energy  $g\eta^2 S^2$  (1) with ( $A = 7$ ) and (2) without inclusion of the long-range dipole-dipole interaction.

Now, we quantitatively analyze the velocity anomalies for longitudinal waves along the polar axis ( $\mathbf{q} \parallel \mathbf{P}_s$ ). The expressions for the velocity with allowance made for the biquadratic interaction of the order parameter

with the strain have the form

$$\frac{\Delta v}{v_0} = \left\{ 1 - \frac{\Delta T_1^{1/2} (T'_c - T)^{1/2}}{[(T'_c - T)^{1/2} + \Delta T_1^{1/2}](T'_c - T)^{1/2} + A} \right. \\ \left. \times \frac{1}{1 + \omega^2 \tau^2} \right\}^{1/2} - 1 + \left( \frac{T'_c - T}{G} \right)^{1/2} \quad (20)$$

(where  $\tau = \tau_0 \{ [(T'_c - T)^{1/2}][(T'_c - T)^{1/2} + \Delta T_1^{1/2}] + A \}^{-1}$ ) for the tricritical point ( $\mathbf{q} \parallel \mathbf{P}_s$ ) at  $T < T'_c$  and

$$\frac{\Delta v}{v_0} = -\frac{1}{2} \frac{\Delta T_1^{1/2} (\Theta_2^{1/2} + \Delta T^{1/2})}{(\Theta_2^{1/2} + \Delta T_1^{1/2})(\Theta_2^{1/2} + \Delta T^{1/2}) + A} \\ \times \frac{1}{1 + \omega^2 \tau^2} + \frac{\Theta_2^{1/2} + \Delta T^{1/2}}{G^{1/2}} \quad (21)$$

(where  $\tau = \tau_0 [(\Theta_2^{1/2} + \Delta T^{1/2})(\Theta_2^{1/2} + \Delta T_1^{1/2}) + A]^{-1}$ ) for the first-order phase transition ( $\mathbf{q} \parallel \mathbf{P}_s$ ) at  $T < T_0$ .

The fitting of the experimental data of the velocity along the  $Y$  axis by using relationships (20) and (21) permits us to determine the  $\Delta T_1$  and  $G$  parameters listed in Table 2.

The theoretical temperature dependences of the velocity along the  $Y$  axis in the ferroelectric phase were calculated by expressions (20) and (21) for the tricritical point and the first-order phase transition. The results of calculations and the experimental data are shown in Fig. 6. As can be seen, the theoretical dependences for the first-order phase transition (solid line 2) are in better agreement with the experimental data in the vicinity of the phase transition. The velocity jump for longitudinal waves along the  $Y$  axis due to the first-order phase transition can be determined by formula (14) with the parameters given in Table 2. The velocity jump is equal to approximately 2.5% and agrees well with the experimental data.

Using the phase transition at the tricritical point as an example, we consider the effect of the long-range field on the anomalies of the velocity along the polar axis (the  $c_{22}$  elastic modulus). Figure 7 displays the calculated velocity anomalies at the phase transition and the contributions from the striction energy  $d\eta^2 S$  and the energy  $g\eta^2 S^2$  with ( $A = 7$ ) and without regard for the long-range dipole-dipole interaction. This interaction leads to a decrease in the striction contribution and a partial suppression of the velocity anomaly. The inclusion of the biquadratic contribution leads to a shift of the minimum of the velocity toward the  $T'_c$  temperature. In this case, the total velocity anomaly along the polar axis with due regard for the dipole-dipole interaction appears to be approximately four times less than that without regard for the dipole-dipole forces and is almost identical in form and magnitude to the velocity

anomaly observed in the direction perpendicular to the polar axis. A clear anomaly of the velocity along the  $Y$  axis (similar to the anomalies along the  $X$  and  $Z$  axes) is explained by a relatively large contribution from the energy of the  $g\eta^2S^2$  type to the velocity along this direction, which is not suppressed by the long-range field.

Since the velocity anomalies along the  $Y$  axis are better described under the assumption of the weak first-order phase transition (with the maximum thermodynamic hysteresis  $\Delta T \cong 0.6$  K), let us estimate the jump in the spontaneous polarization in this case and compare it with the results obtained by Dacko *et al.* [2].

According to [2], the temperature dependences of the polarization are characterized by a saturation at  $T < 200$  K. The polarization saturation can be taken into account by introducing the  $\xi\eta^3P$  ( $\xi > 0$ ) invariant into the thermodynamic potential. In this case, the equilibrium values of  $\eta$  are described by expression (10), where  $\beta^* \equiv \beta^{**}$  and  $\gamma \equiv \gamma^*$  ( $\beta^{**} < 0$  and  $\gamma^*$  are the con-

stants renormalized upon introduction of the  $\xi\eta^3P$  invariant) and the relationship for the spontaneous polarization takes the form

$$P_s = -\chi_0 h \eta \left( 1 + \frac{\xi}{h} \eta^2 \right), \quad (22)$$

where  $h < 0$ . By substituting relationship (10) for the order parameter  $\eta$  at  $\Delta T \cong 0.6$  K into formula (22), from the experimental dependence  $P(T)$  taken from [2], we derive the parameter  $(\xi\beta^{**})/(2h\gamma) = 0.025$ . In this case, the relative jump in the polarization  $P(T_0)/P(150 \text{ K})$  is equal to 0.17 or (in absolute units)  $\Delta P = 0.085 \mu\text{C}/\text{cm}^2$  [ $P_s(150 \text{ K}) = 0.5 \mu\text{C}/\text{cm}^2$ ]. This polarization is less than the sensitivity of measurements near the phase transition.

Note that the  $\xi\eta^3P$  invariant was ignored in the analysis of the acoustic data. Its inclusion leads to the following relationship for the elastic modulus along the  $Y$  axis in the low-frequency limit at the tricritical point:

$$c = c_0 - \frac{c_0 \Delta T_1^{1/2} (T'_c - T)^{1/2}}{[(T'_c - T)^{1/2} + \Delta T_1^{1/2}](T'_c - T)^{1/2} + A \left[ 1 + 6 \left( \frac{\xi}{h} \right) \eta^2 + 9 \left( \frac{\xi}{h} \right)^2 \eta^4 \right]}. \quad (23)$$

According to the calculations, the  $\xi\eta^3P$  invariant at experimental values of the parameter  $(\xi\lambda^{1/2})/(h\gamma^{1/2}) \cong -0.025$  contributes insignificantly to the acoustic anomalies.

## 5. CONCLUSION

Thus, the acoustical and dielectric properties of the glycine phosphite crystals are consistently described within the pseudoproper ferroelectric phase transition model. Formally, the use of this model is not limited by any parameters of the system (for example, the case of small Curie–Weiss constants) and is determined by the mechanism of the formation of the ferroelectric state. The model adequately describes the crystal properties. A complex character of the displacements upon ferroelectric phase transition in glycine phosphite crystals [10] also indicates that these crystals can undergo a pseudoproper ferroelectric ordering.

## ACKNOWLEDGMENTS

We would like to thank N.V. Zaitseva for orienting the crystals and V.A. Yankovskaya for preparing the samples.

This work was supported by the State Program of Support for Leading Scientific Schools of the Russian Federation (project no. 00-15-96754) and in part by the Russian Foundation for Basic Research (project no. 99-02-18307).

## REFERENCES

1. M.-Th. Averbuch-Pouchot, *Acta Crystallogr. C* **C49**, 85 (1993).
2. S. Dacko, Z. Czapla, J. Baran, and M. Drozd, *Phys. Lett. A* **223**, 217 (1996).
3. R. Tchukvinskyi, Z. Czapla, R. Sobiestankas, *et al.*, *Acta Phys. Pol. A* **92** (6), 1191 (1997).
4. J. Furtak, Z. Czapla, and A. V. Kityk, *Z. Naturforsch. A* **52**, 778 (1997).
5. S. Ya. Geguzina and M. A. Krivoglaz, *Fiz. Tverd. Tela (Leningrad)* **9** (11), 3095 (1967) [*Sov. Phys. Solid State* **9**, 2441 (1967)].
6. G. A. Smolenskiĭ, I. G. Siniĭ, A. K. Tagantsev, *et al.*, *Zh. Éksp. Teor. Fiz.* **88**, 1020 (1985) [*Sov. Phys. JETP* **61**, 599 (1985)].
7. I. G. Siny, G. O. Andrianov, A. I. Fedoseev, *et al.*, *J. Phys. C* **7**, 4283 (1995).
8. B. A. Strukov and A. P. Levanyuk, *Ferroelectric Phenomena in Crystals* (Nauka, Moscow, 1995; Springer-Verlag, Berlin, 1998).
9. A. P. Levanyuk and A. S. Sigov, *Defects and Structural Phase Transitions* (Gordon and Breach, New York, 1987).
10. P. Morawski, M. Gramza, J. Goslar, *et al.*, *Ferroelectr. Lett. Sect.* **23**, 121 (1998).

*Translated by O. Borovik-Romanova*

## MAGNETISM AND FERROELECTRICITY

# Diserine Sulfate Monohydrate: Symmetry, Piezoelectric Properties, and Phase Transitions

V. V. Lemanov, S. N. Popov, V. V. Bakhurin, and N. V. Zaitseva

Ioffe Physicotechnical Institute, Russian Academy of Sciences, Politekhnikeskaya ul. 26, St. Petersburg, 194021 Russia

Received December 26, 2000

**Abstract**—A new compound, diserine sulfate monohydrate, was synthesized, and single crystals of this compound were grown. X-ray diffraction studies were carried out, and the temperature dependences of the piezoelectric response of these crystals were measured. A conclusion was drawn that the crystals are orthorhombic with the space symmetry group  $C_{1v}^-Pmm2$  and that they apparently undergo phase transitions at 340 and 255 K. © 2001 MAIK “Nauka/Interperiodica”.

Investigation of protein aminoacids and of related compounds is of considerable interest in the search for new ferroelectric materials, as well as in connection with the possibility of learning the part played by the piezo-, pyro-, and ferroelectric properties of protein aminoacids in the functioning of living organisms [1, 2].

This communication reports on the synthesis of a new compound, diserine sulfate monohydrate (DSSM), growth of single crystals of this compound, x-ray diffraction characterization of the single crystals, and a study of the temperature dependences of their piezoelectric response.

The serine (ser) aminoacid belongs to protein aminoacids containing an oxygroup  $NH_2CHCH_2OHCOOH$  [3]. The structural formulas of the serine molecule in its *L* and *D* configurations is presented in Fig. 1.

To obtain a serine compound with sulfuric acid, the Ch-grade *DL*-serine (racemate) was mixed with ChDA-grade concentrated sulfuric acid in a 2 : 1 molar ratio. The single crystals were seed-pulled from a water solution under slow cooling from 35 to 30°C. The single crystals thus grown were predominantly prism-shaped with maximum dimensions of  $20 \times 10 \times 7$  mm (Fig. 2).

Elemental analysis showed the single crystals to have the  $(Ser)_2H_2SO_4 \cdot H_2O$  composition, which corresponds to diserine sulfate monohydrate (DSSM).

The x-ray structural analysis of the single crystals was performed diffractometrically ( $CuK_\alpha$  radiation, Ni filter) and by the photographic technique (with W radiation). The photographic method revealed the existence in the single crystal of three mutually perpendicular twofold axes with symmetry planes, which indicates that the DSSM crystals belong to the  $D_{2h}-mmm$  class of the orthorhombic system. This class also includes the  $D_2-222$  and  $C_{2v}-mm2$  point-symmetry groups.

The lattice parameters were determined by rocking about each of the three symmetry axes and were subsequently refined by x-ray diffraction:

$$a = 21.260 \pm 0.002 \text{ \AA}, \quad b = 10.580 \pm 0.002 \text{ \AA}, \\ c = 5.8470 \pm 0.0006 \text{ \AA}.$$

The diffraction method was also used to study the DSSM powder. Figure 3 presents a typical diffraction pattern of the powder, with the indices of the various reflections specified. An analysis of the diffractograms suggests that the reflections observed do not have extinctions of the general *hkl* kind. No extinctions are found also among the *hk0*, *0kl*, *h0l* and *h00*, *0k0*, and *00l* kinds. This means [4] that DSSM crystals belong to one of the  $D_{2h}^1-Pmmm$ ,  $D_{2h}^1-P222$ , or  $C_{2v}^1-Pmm2$  space groups. We shall show below that the most probable point symmetry group of these crystals is  $C_{2v}-mm2$ ; i.e., they belong to the  $C_{2v}^1-Pmm2$  space symmetry group.

The x-ray density calculated for four DSSM molecules per unit cell ( $\rho_x = 1.636 \text{ g/cm}^3$ ) coincides within experimental error with the measured value of the density ( $\rho = 1.638 \text{ g/cm}^3$ ). Thus, for DSSM crystals,  $Z = 4$  and the optical vibration spectrum contain 453 branches.

The piezoelectric response of the crystals was studied on an IS-2 nuclear quadrupole resonance setup. The

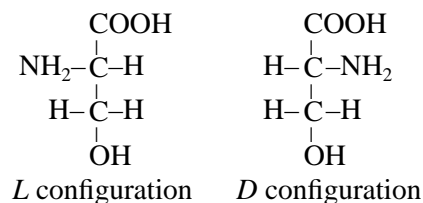


**Fig. 1.** Structure of the serine molecule in the *L* and *D* configurations.

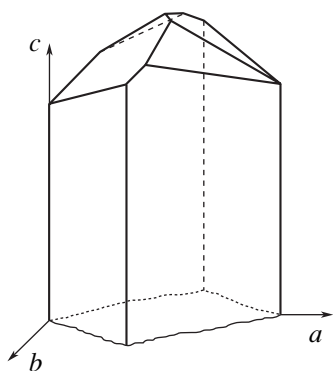


**Fig. 2.** Diserine sulfate monohydrate single crystal (only the upper part of the crystal is shown).

sample was placed in the capacitor of a circuit to which 10-MHz, 4- $\mu$ s long voltage pulses were applied at a repetition frequency of 12 Hz. The maximum circuit voltage amplitude was 4 kV, which corresponded to an electric field of about 1 kV/cm applied to the sample. The piezoelectric response signals were measured with an AI-1024 multichannel analyzer. RF pulses excite elastic vibrations in a piezoelectric crystal through the inverse piezoelectric effect. Elastic vibrations persist

after the end of a pulse for a time of about  $\Delta t$  ( $\mu$ s)  $\approx 10/\alpha$  (dB/ $\mu$ s), where  $\alpha$  is the elastic-wave damping. This “ringing” of the sample is recorded by a detector through the direct piezoelectric effect. Measured at room temperature and at a frequency of 10 MHz, the elastic-wave damping in “soft” crystals is typically of the order of  $\alpha \approx 10^{-1}$  dB/ $\mu$ s. This means that the sample ringing time is  $\Delta t \approx 100$   $\mu$ s. The damping can be estimated by measuring this time, and the magnitude of the piezoelectric response signal at  $\Delta t \approx 0$  is determined by the electromechanical coupling constant; i.e., it depends on the piezoelectric coefficients.

Measurements showed diserine sulfate monohydrate to be a piezoelectric at room temperature. Note that the original *DL*-serine aminoacid belongs to the holohedral class  $C_{2h}$  of the monoclinic system and does not exhibit a piezoelectric effect. Measurements of the piezoelectric effect with an rf electric field  $\mathbf{E}$  oriented differently relative to the crystallographic axes revealed that the response is maximum for  $\mathbf{E} \parallel \mathbf{c}$ , decreases about tenfold for  $\mathbf{E} \parallel \mathbf{a}$ , and drops further by more than an order of magnitude for  $\mathbf{E} \parallel \mathbf{b}$ .

As already mentioned, x-ray diffraction data suggest that the point symmetry group of the crystals under study can be  $D_{2h}-mmm$ ,  $D_2-222$ , or  $C_{2v}-mm2$ . Because

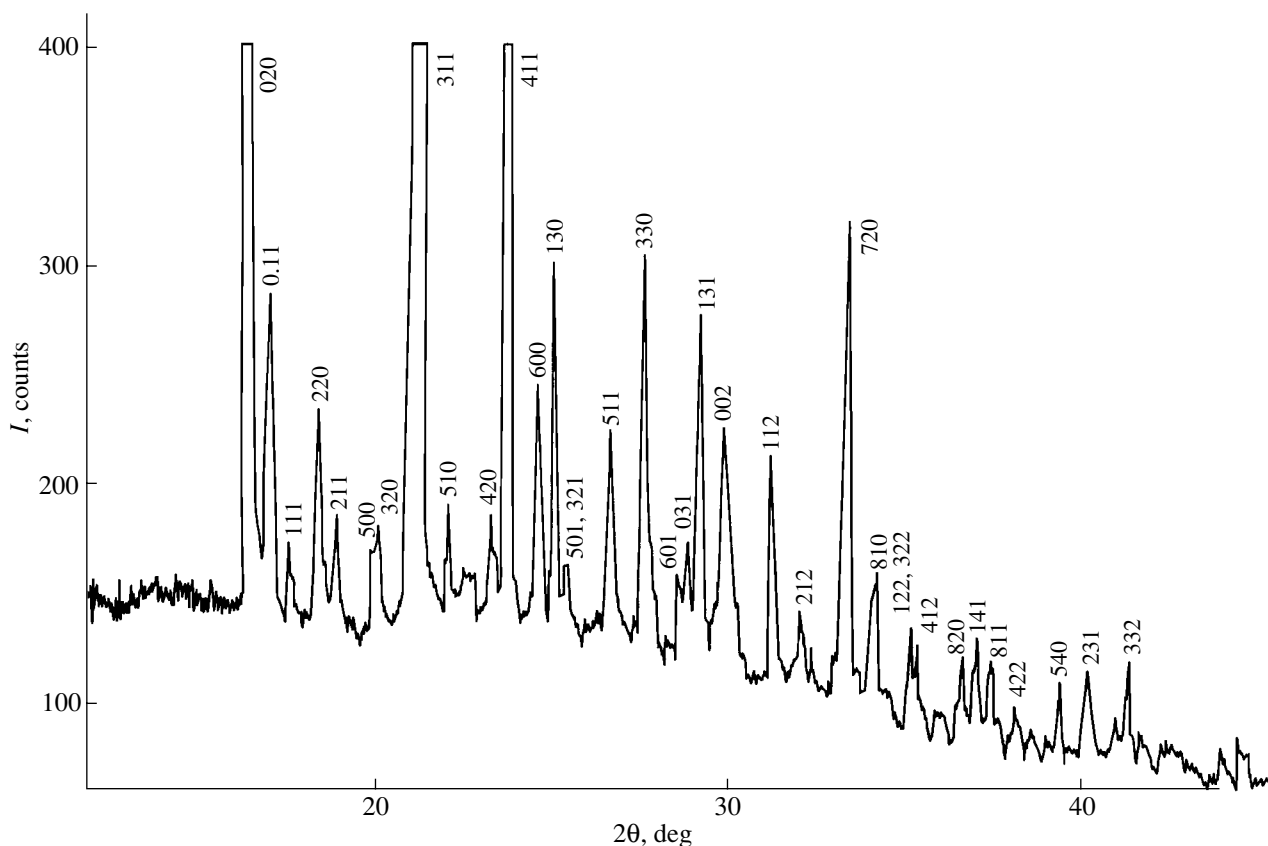


**Fig. 3.** Powder diffraction pattern of the diserine sulfate monohydrate.

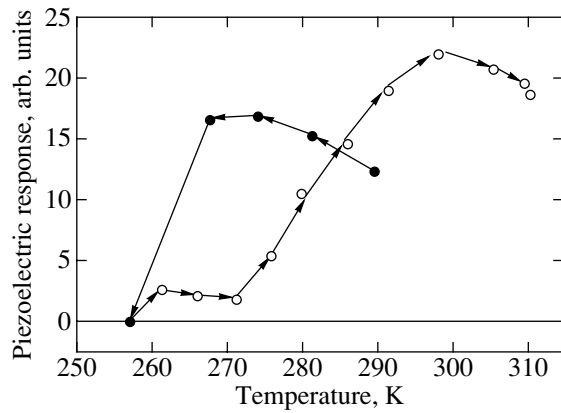


**Fig. 4.** Temperature dependence of the piezoelectric response.

these crystals are piezoelectric, they must belong to the  $D_2-222$  or  $C_{2v}-mm2$  symmetry groups. In the  $D_2$  class, the nonzero piezoelectric coefficients are  $xyz$ ,  $yxz$ , and  $zxy$ . In the  $C_{2v}$  class, they are  $xxz$ ,  $yyz$ ,  $zxx$ ,  $zyy$ , and  $zzz$ . Hence it follows that in the case of an rf field  $\mathbf{E}$  applied along the  $a(x)$ ,  $b(y)$ , and  $c(z)$  crystallographic axes, no elastic vibrations with a wave vector  $\mathbf{q} \parallel \mathbf{E}$  can be excited in the  $D_2$  class. As for the  $C_{2v}$  class, for  $\mathbf{E} \parallel \mathbf{c}(z)$ , longitudinal  $zz$  vibrations can be excited, while electric fields  $\mathbf{E} \parallel \mathbf{a}(x)$  and  $\mathbf{E} \parallel \mathbf{b}(y)$  excite the  $xz$  and  $yz$  transverse vibrations, respectively. The experiment shows the piezoelectric coefficients to range in magnitude as  $zzz > xxz > yyz$ .

Thus, x-ray structural and piezoelectric studies permit the conclusion that disirine sulfate crystals belong to the  $C_{2v}^1-Pmm2$  space symmetry group; i.e., they are pyroelectrics and, possibly, ferroelectrics as well.

Measurements of the temperature dependence of the piezoelectric response showed that as the temperature increases from room temperature to 335 K, the piezoelectric response signal drops rapidly to vanish at  $T_{c1} \approx 340$  K. On the other hand, under cooling, the piezoelectric response vanishes at  $T_{c2} \approx 255$  K. The behavior of the piezoelectric response in this temperature region under heating depends on the extent to

which the crystal was cooled. The temperature dependence of the piezoelectric response under heating obtained on a crystal cooled preliminarily to  $T_{c2} \approx 255$  K reproduces qualitatively the temperature dependence measured in the cooling run, but with a large temperature hysteresis of about 30 K. If, however, the sample was cooled to 240 K, then no piezoelectric response was detected under heating. The room-temperature piezoelectric response recovered from zero to the original level in only a few days. Figure 4 presents typical temperature dependences of the piezoelectric response. Thus, one can suggest that crystalline disirine sulfate monohydrate undergoes phase transitions at  $T_{c1} \approx 340$  K and  $T_{c2} \approx 255$  K, the lower-temperature one being a strong first-order transformation. Establishment of the nature of these transitions and, more specifically, of the nature of the piezoelectric anomalies would certainly require a more comprehensive investigation.

#### ACKNOWLEDGMENTS

The authors are indebted to A.S. Kolosova for assistance in the x-ray diffraction studies and to N.F. Kartenko for fruitful discussions.

This work was supported by the Russian Foundation for Basic Research (project no. 99-02-18307) and the leading scientific school program (project 00-15-96754).

#### REFERENCES

1. V. V. Lemanov, in *Piezoelectric Materials: Advances in Science, Technology and Applications*, Ed. by C. Galassi *et al.* (Kluwer, Dordrecht, 2000), p. 1.
2. V. V. Lemanov, *Ferroelectrics* **238**, 211 (2000).
3. G. V. Gurskaya, *Structure of Amino Acids* (Nauka, Moscow, 1966).
4. *International Tables for X-ray Crystallography* (Kynoch Press, Birmingham, 1952).

*Translated by G. Skrebtsov*



---

## LATTICE DYNAMICS AND PHASE TRANSITIONS

---

# Martensitic Transformations in a Thin Layer of a Shape Memory Alloy on an Elastic Substrate

G. A. Malygin

*Ioffe Physicotechnical Institute, Russian Academy of Sciences, Politekhnikeskaya ul. 26, St. Petersburg, 194021 Russia*

*e-mail: malygin.ga@pop.ioffe.rssi.ru*

Received November 22, 2000

**Abstract**—A martensitic transformation (MT) in a thin ( $10\text{--}10^3$  nm thick) layer of a shape memory alloy on an elastic substrate is analyzed theoretically in terms of the theory of diffuse MTs. The relaxation of thermoelastic stresses associated with the MT is considered, and the size effects that accompany this relaxation are analyzed; stresses arise in the layer because of the difference in the coefficients of thermal expansion of the materials of the microcomposite. It is found that nonlinear and hysteretic properties are imparted by the MT to microdrives (actuators) and temperature-sensitive microelements based on such composites. © 2001 MAIK “Nauka/Interperiodica”.

## 1. INTRODUCTION

In the past few decades, microsensors and microdrives (actuators) have found wide application [1, 2]. These devices make use, in particular, of bilayer or multilayer microcomposites, which consist of thin ( $10\text{--}10^3$  nm thick) layers of an active material sensitive to specific action on it and of passive substrate layers. As active elements for such devices, shape memory alloys have currently been of progressively more frequent use. These alloys undergo a diffusionless structural martensitic transformation (MT) in some temperature range [2–5]. The reversible (pseudoelastic) plastic deformations associated with this transformation are sensitive to mechanical stresses [2–4], hydrostatic pressure [5], and magnetic and electric fields [6] applied to the alloy. Therefore, these materials have the potential to be used for adaptable and smart functional microdevices. A calculation of the parameters of such devices should be based on the theory of diffusionless MTs with allowance for their sensitivity to the external factors mentioned above and to internal factors, in particular, structural ones associated with the presence of various defects in the crystal. At the present time, such a full-scale theory of MTs is absent. For this reason, the MT in a thin shape-memory alloy layer on a substrate is calculated using piecewise linear approximations to the temperature dependences of the experimentally measured amounts of martensite and austenite in the material [7].

Recently [8–10], we developed a theory of diffuse MTs in shape memory alloys in terms of the general theory of diffuse phase transitions of the first order [10]. This is a thermodynamic theory, but a heterophase (martensite–austenite) state of a material is considered

as a result of a kinetic transition from its one state to another.

According to this theory, the spatially inhomogeneous (heterophase) states of an alloy in kinetic equilibrium are determined by the balance of the thermodynamic force acting on the interphase boundaries and the interaction force between the interphase boundaries and various obstacles in the material. External action on the material increases or decreases the thermodynamic component of the force, thereby changing the relationship between the amounts of austenite and martensite in the material.

Thus, the theory of diffuse MTs takes into account the influence of both external and internal factors on the parameters of the MT and allows one to describe this influence analytically; in particular, it allows one to find the temperature dependence of the volume fraction of martensite or austenite in a material undergoing a diffusionless MT.

In this paper, we present this theory in Section 2 and then, in Section 3, the theory is used to calculate numerically the thermoelastic stresses arising because of the difference in the coefficients of thermal expansion of the materials of a bilayer microcomposite (a thin layer of a shape memory alloy on an elastic substrate) with allowance for relaxation of these stresses in the temperature range over which the phase transformation occurs. The size effects associated with this transformation are discussed in Section 4.

## 2. DIFFUSE MARTENSITIC TRANSFORMATIONS

In this section, we present the main relations derived in the theory of diffuse transformations, which enable one to calculate the martensitic relaxation of ther-

moelastic stresses in a thin layer of a shape memory alloy.

According to the theory, the relative volume fraction of martensite  $\varphi_M$  in a crystalline alloy undergoing a diffusionless MT is given by [9, 10]

$$\varphi_M(T, \{I\}, \{s\}) = \left[ 1 + \exp\left(\frac{\Delta U}{kT}\right) \right]^{-1}. \quad (1a)$$

Here,  $T$  is the temperature;  $k$  is the Boltzmann constant;  $\Delta U = \omega \Delta u$  is the change in the internal energy of the crystal due to the transformation of its elementary element  $\omega$  from the austenite to the martensite state;

$$\Delta u = q \frac{T - T_{c0}}{T_{c0}} - \xi_{ik} \tau_{ik} - \delta_0 P - p_i E_i - m_i H_i - [u_d] n_d \quad (1b)$$

is the change in the internal energy of a unit volume undergoing the transformation;  $q$  is the specific heat of the phase transformation;  $T_{c0}$  is the critical (characteristic) transformation temperature in the absence of any external action on the material;  $\{I\} \equiv \tau_{ik}, P, E_i, H_i$  is a set of parameters characterizing external actions, namely, mechanical stress  $\tau_{ik}$ , hydrostatic pressure  $P$ , and electric  $E_i$  and magnetic  $H_i$  fields;  $\xi_{ik}$  and  $\delta_0$  are the spontaneous shear strain and dilatation of the lattice associated with its structural rearrangement, respectively;  $p_i$  and  $m_i$  are the electric and magnetic dipole moments induced by the lattice rearrangement;  $\{s\}$  is a collection of structural factors which affect the transformation;  $[u_d]$  is the change in the energy of the lattice defects upon transformation; and  $n_d$  is the concentration of the defects.

From Eqs. (1a) and (1b), it is seen that the amount of martensite in the crystal depends on the value and sign of the energy  $\Delta u$ . The crystal is dominated by austenite at  $\Delta u > 0$  and by martensite at  $\Delta u < 0$ . At  $\Delta u = 0$ , the amounts of austenite and martensite in the crystal are equal, which defines the characteristic transformation temperature

$$T_c = T_{c0} + \frac{T_{c0}}{q} (\xi_{ik} \tau_{ik} + \delta_0 P + p_i E_i + m_i H_i + [u_d] n_d). \quad (2)$$

This relation is a generalized Clausius–Clapeyron equation, according to which external fields applied to the crystal will cause the critical transformation temperature to increase or decrease, depending on the values and signs of the spontaneous strain and electric and magnetic dipole moments induced by the lattice rearrangement. The presence of defects in the crystal also affects the critical transformation temperature.

The strain associated with the MT in the crystal is equal to

$$\varepsilon_{ik} = \sum_{a=1}^N \varepsilon_{ik}^a, \quad \varepsilon_{ik}^a = m_{il}^a \xi_{ik}^a \varphi_M^a(T, \sigma_{ik}), \quad (3)$$

$$\tau_{lk}^a = m_{il}^a \sigma_{ik},$$

where  $\sigma_{ik}$  is the stress applied to the crystal, the index  $a$  specifies possible variants of martensite,  $N$  is the total number of variants, and  $m_{il}^a$  are the crystallographic orientation factors of the variants of martensite. From Eqs. (1) and (3), it follows that the amount of the specified variant of martensite varies exponentially with its orientation factor. Therefore, in the presence of stress applied to the crystal, the variant of martensite with a maximum value of the orientation factor ( $m_{ik} = m \approx 0.5$ ,  $\xi_{ik} = \xi$ ) is dominant and, in the case of a uniaxial loading ( $\sigma_{ik} = \sigma$ ), the crystal strain is found from Eqs. (1) and (3) to be

$$\varepsilon_M(T, \sigma) = \varepsilon_m \varphi_M(T, \sigma),$$

$$\varphi_M(T, \sigma) = \left[ 1 + \exp\left( B \left( \frac{T - T_{c0}}{T_{c0}} - \frac{m\sigma \pm \tau_f}{\tau_M} \right) \right) \right]^{-1}. \quad (4)$$

Here,  $\varepsilon_m = m\xi$ ,  $\tau_M = q/\xi$ , and  $\tau_f$  and  $B$  are the dry-friction stress characterizing the interaction of interphase boundaries with lattice defects and the structure-sensitive parameter, which determine force hysteresis during the MT and the broadening of the transformation in temperature  $\Delta T_{M0}$ , respectively:

$$B = \frac{\omega q}{kT_{c0}}, \quad (5)$$

$$\Delta T_{M0} = \left| \frac{d\varphi}{dT} \right|_{T=T_{c0}}^{-1} = \frac{4T_{c0}}{B} = \left( \frac{4T_{c0}}{\omega q} \right) T_{c0}.$$

For instance, in a crystal with dislocations (of density  $\rho$ ) presenting obstacles to the motion of interphase boundaries, the elementary transformation volume is  $\omega = r/\rho$ , where  $r$  is the height of steps of atomic size on the interphase boundaries. In this case, the temperature width of the transformation is equal to  $\Delta T_{M0} = (4T_{c0}^2/q\rho)\rho$ ; that is, the broadening of the transformation increases with dislocation density in the crystal.

Figure 1a shows the temperature dependences of the relative volume fraction of martensite in the crystal for the forward and reverse MTs according to Eq. (4) in the absence of stresses ( $\sigma = 0$ ,  $B = 50$ ,  $\tau_f/\tau_M = 0.1$ ). The temperature dependence in the absence of force hysteresis during the transformation ( $\tau_f = 0$ ) is represented by the dashed curve and, in the presence of this hysteresis [ $2\Delta T_f = 2(\tau_f/\tau_M)T_{c0}$ ], by curves 1 and 2. The slope of the dashed curve at  $T = T_{c0}$  determines the width (broadening) of the transformation in temperature. When the  $\varphi_M(T)$  curves are approximated by straight lines, the

starting and finishing points of the martensitic transformation are denoted by  $M_s$  and  $M_f$ ; the respective points of the austenitic transformation, by  $A_s$  and  $A_f$ . In the notation introduced above for the parameters of diffuse transformations, we have, for example,  $M_s \approx T_{c0} + \Delta T_{M0} - \Delta T_f$ . The other starting and finishing points of transformations can also be expressed in a similar way.

### 3. MARTENSITIC RELAXATION OF THERMOELASTIC STRESSES IN A THIN LAYER

Let us consider a microcomposite in the form of a plate with length  $l$ , width  $w \ll l$ , and thickness  $h$ , consisting of a thin layer of a shape memory alloy and a substrate with thickness  $H \gg h$  which undergoes no phase transformation in the temperature range in question. As the plate was cooled from the diffusion-coating temperature  $T_0$ , longitudinal thermoelastic stresses  $\sigma_\alpha = Y_1 \Delta \alpha (T - T_0)$  arose in the thin layer because of the difference in the coefficients of thermal expansion  $\Delta \alpha$  of the materials of the thin layer and substrate ( $Y_1 = E_1 / (1 - \nu_1)$ , where  $E_1$  and  $\nu_1$  are the elastic modulus and the Poisson ratio of the material of the thin layer, respectively; both materials are assumed to be isotropic). The stresses caused the plate to bend. For the radius of curvature  $R$  of the plate and for the departure  $z$  of its ends from the horizontal plane (this quantity is measured experimentally), we can write [11]

$$R = \frac{H^2 (Y_2)}{6h (\sigma_\alpha)}, \quad z = \frac{l^2}{8R} = \frac{3h}{4} \left( \frac{l}{H} \right)^2 \left( \frac{\sigma_\alpha}{Y_2} \right), \quad (6)$$

where  $Y_2 = E_2 / (1 - \nu_2)$  and  $E_2$  and  $\nu_2$  are the corresponding material parameters of the substrate. From Eq. (6), it follows that the radius of curvature of the plate decreases and the departure of its ends from the horizontal plane increases with increasing stresses in the thin layer.

When the temperature of the plate decreases to the starting point of the MT in the shape-memory alloy layer, the strain due to the phase transformation given by Eq. (4) arises in the layer and the thermoelastic stress relaxes by the amount  $\delta_M(T) = Y_1 \epsilon_M(T, \sigma)$ , where  $\sigma = \sigma_\alpha - \sigma_M$  is the total stress in the thin alloy layer. Equation (4) for the volume fraction of martensite involves the total stress  $\sigma$ . Therefore, in order to find the stress  $\sigma_M$ , one should solve the transcendental equation (with the temperature being a parameter)

$$\sigma_M(T) = Y_1 \epsilon_m \left[ 1 + \exp \left( B \left( \frac{T - T_{c0}}{T_{c0}} - \frac{m Y_1 \Delta \alpha (T - T_0) - m \sigma_M(T) \pm \tau_f}{\tau_M} \right) \right) \right]^{-1}. \quad (7a)$$

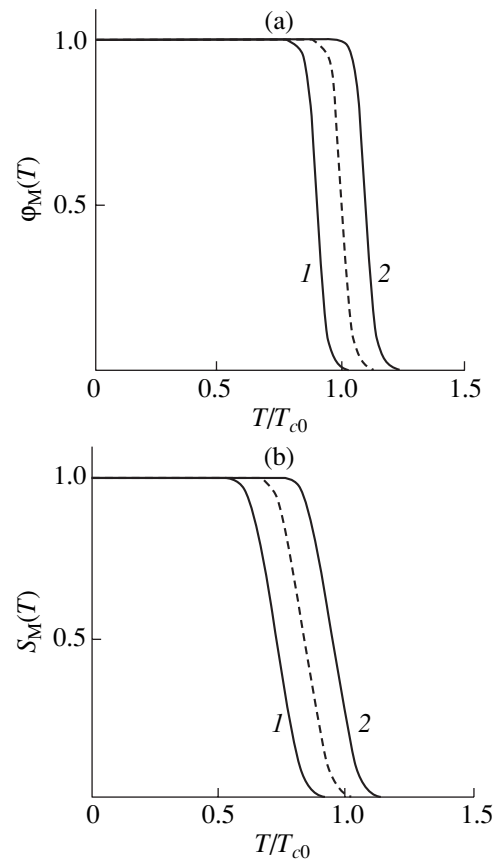


**Fig. 1.** Temperature dependences of the relative volume fraction of martensite for the forward (curve 1) and reverse (curve 2) martensitic transformations under (a) zero-stress and (b) stress conditions. The dashed curves correspond to the case where there is no transformation hysteresis.

In dimensionless variables, this equation takes the form

$$S_M(t) = \left[ 1 + \exp \left( B \left( t - 1 - a(t - t_0) + b S_M(t) \pm \frac{\tau_f}{\tau_M} \right) \right) \right]^{-1}, \quad (7b)$$

where

$$t_0 = \frac{T_0}{T_{c0}}, \quad a = m \left( \frac{Y_1}{\tau_M} \right) \Delta \alpha T_{c0}, \quad (7c)$$

$$b = m \left( \frac{Y_1}{\tau_M} \right) \epsilon_m, \quad \frac{a}{b} = \frac{\Delta \alpha}{\epsilon_m} T_{c0}.$$

Figure 2 shows the dependences of the left-hand side  $L(T)$  (straight line 1) and right-hand side  $R(T)$  (curves 2–5) of Eq. (7b) on the dimensionless stress  $S_M = \sigma_M / Y_1 \epsilon_m$  for various values of the dimensionless temperature  $t = T / T_{c0}$  and  $B = 50$ ,  $a = b = 0.1$ ,  $t_0 = 2$ , and  $\tau_f = 0$ . The intersection of straight line 1 and curves 2–5 determines the amount by which the thermoelastic stress relaxes at the given temperature due to the MT.

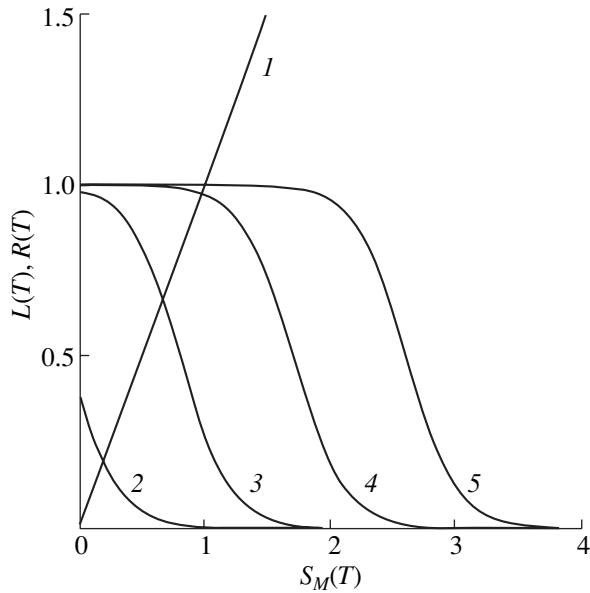


**Fig. 2.** Dependences of (1) the left-hand side and (2–5) right-hand side of Eq. (7b) on the stress  $S_M(t) = \sigma_M(t)/Y_1 \epsilon_m$  for different values of the relative temperature  $t = T/T_{c0}$ : (2) 0.9, (3) 0.8, (4) 0.7, and (5) 0.6.

Figure 1b shows self-consistent solutions of Eq. (7b) for forward (curve 1) and reverse (curve 2) phase transformations with allowance for transformation hysteresis ( $\tau_f/\tau_M = 0.1$ ). The curves represent the temperature dependences of  $S_M(t) \equiv \phi_M(t)$ , i.e., the variations in the amount of martensite in the alloy in the process of its MT under stress conditions. A comparison of Figs. 1a and 1b reveals that, under stress conditions, (i) the  $\phi_M(T)$  curves are shifted to lower temperatures and (ii) the MT extends over a larger temperature range; i.e., it is more diffuse than the MT under zero-stress conditions (Fig. 1a).

Indeed, by differentiating Eq. (7b) with respect to  $t$ , we find that the critical (characteristic) transformation temperature  $T_c$  and the temperature range  $\Delta T_M$  of the transformation under stress conditions are

$$T_c = \frac{1 - 0.5b - at_0}{1 - a} T_{c0}, \quad \Delta T_M = \frac{\Delta T_{M0} + bT_{c0}}{1 - a}, \quad (8)$$

respectively, where  $T_{c0}$  and  $\Delta T_{M0}$  are the respective parameters of the MT under zero-stress conditions. From the first expression in Eq. (8), it follows that if the initial temperature  $t_0 > 1 - b/2a$  and  $a > 0$  ( $\Delta\alpha > 0$ ), then the critical temperature  $T_c < T_{c0}$ . From the second expression in Eq. (8), it immediately follows that  $\Delta T_M > \Delta T_{M0}$ . At  $a < 0$  ( $\Delta\alpha < 0$ ), the critical transformation temperature is higher under stress conditions than under zero-stress conditions.

The total stress in the alloy layer at a specific temperature is equal to the sum of thermoelastic stresses minus the relaxation of the stress associated with the

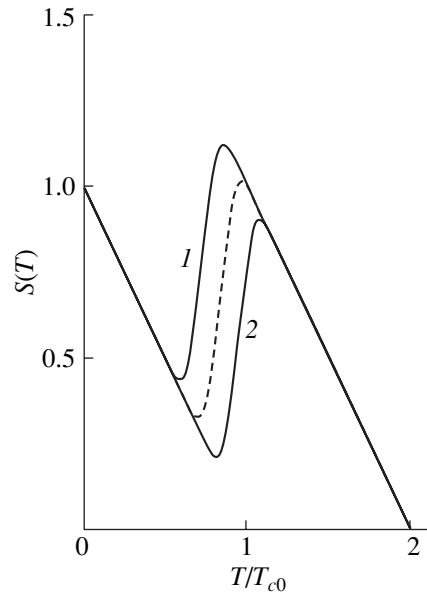


**Fig. 3.** Temperature dependences of the thermoelastic stress in the alloy layer for (1) the forward and (2) reverse MTs. The dashed curve corresponds to the absence of transformation hysteresis.

transformation. In dimensionless variables, the total stress takes the form

$$\frac{\sigma(t)}{Y_1 \epsilon_m} = S(t), \quad S(t) = \frac{a}{b}(t_0 - t) - S_M(t). \quad (9)$$

Figure 3 shows the temperature dependence of this total stress for the forward and reverse MTs (curves 1, 2) and the temperature dependence of the total stress in the absence of transformation hysteresis (dashed curve). It can be seen that the sensitivity of the temperature-sensitive element containing a thin active layer of an alloy undergoing the MT is greatly enhanced in the transformation temperature range in comparison with the sensitivity of this element without the active layer. According to Eq. (9), the temperature sensitivity of the total stress in the alloy layer is

$$\left. \frac{d\sigma}{dT} \right|_{T=T_c} = \left( \frac{\epsilon_m}{\Delta\alpha \Delta T_M} - 1 \right) Y_1 \Delta\alpha, \quad (10)$$

where  $\Delta T_M$  is the MT temperature range under the stress conditions given by Eq. (8). In the absence of the transformation ( $\epsilon_m = 0$ ), the sensitivity of the element [the departure  $z$  in Eq. (6)] to variations in temperature is determined, according to Eq. (10), by the quantity  $Y_1 \Delta\alpha$ , whereas in the case of the MT, it is determined by  $(\epsilon_m/\Delta T_M) Y_1$ .

Roytburd *et al.* [7] reported measurements on NiTi alloy films 50 nm and 1–3  $\mu\text{m}$  thick coated by diffusion on 90–100  $\mu\text{m}$  thick silicon substrates at 600 K. This alloy undergoes an MT over the temperature range 230–320 K. The stress versus temperature curve for the

NiTi layer had an S-shaped bend as in Fig. 3 because of the phase transformation. When the bilayer was cooled immediately after layer deposition by diffusion and then heated, the transformation temperature range (broadening) was much larger upon cooling than upon heating. This difference in the parameters of the forward and reverse transformations can be due to the plastic deformation of the alloy caused by the phase transformation upon cooling. For  $\Delta\alpha = 10^{-4} \text{ K}^{-1}$ , from the data presented in [7, Fig. 7] and Eq. (10), we obtain  $d\sigma/dT = 3 \text{ MPa K}^{-1}$ ,  $Y_1 = 26 \text{ GPa}$ ,  $\Delta T_M = 100 \text{ K}$ , and  $\epsilon_m = 2.2 \times 10^{-2}$ .

#### 4. SIZE EFFECTS

In [7], it was found that a decrease in the NiTi layer thickness from  $1 \mu\text{m}$  to  $50 \text{ nm}$  produces a decrease in the temperature sensitivity of stresses in Eq. (10) and a decrease in the amount of relaxation of the stress in the layer, i.e., in the total amount of change in the stress in the process of the MT. The theory of diffuse MTs allows one to identify the mechanism of these size effects.

For this purpose, we differentiate the dimensionless stress in Eq. (9) with respect to the dimensionless temperature  $t$  and, using the relation  $d\sigma/dT = (Y_1/T_c)\epsilon_m(dS/dt)$ , obtain the following expression at the critical temperature  $T_c$ :

$$\left. \frac{dS}{dt} \right|_{T=T_c} = Q = \frac{B - 4(a/b)}{bB + 4}. \quad (11)$$

Thus, the temperature sensitivity of the stress depends on the parameter  $B$ , i.e., according to Eq. (5), on the elementary volume  $\omega$  undergoing the MT. In a thick layer, we have  $\omega = r\lambda_m^2$ , where  $\lambda_m$  is the average spacing between obstacles in the plane of the interphase boundary. In a thin ( $h < \lambda_m$ ), but fairly wide layer ( $w \gg \lambda_m$ ), the elementary transformed volume is  $\omega = r\lambda_m\lambda_*(h)$ ,

where  $\lambda_*(h) = (\lambda_m^{-1} + h^{-1})^{-1}$ . Therefore, in a very thin layer ( $h \ll \lambda_m$ ), the elementary transformed volume decreases in proportion to the layer thickness,  $\omega \sim h$ . Thus, for the parameter  $B$ , which determines the broadening of the phase transformation and the sensitivity  $Q$  in Eq. (11), the dependence on the layer thickness has the form

$$B(h) = B_m \frac{h/\lambda_m}{1 + h/\lambda_m}, \quad (12)$$

where  $B_m$  is the value of this parameter in a thick layer.

Figure 4 shows the temperature dependences of the stress in the layer for  $B_m = 50$ ,  $a = b = 0.1$ , and values of  $B$  equal to 50, 20, and 6, which correspond to  $h/\lambda_m = \infty$ , 0.4, and 0.14, respectively. It can be seen that the sensitivity  $Q(h)$  in Eq. (11) (curve 3 in Fig. 5, where  $Q_m$  is the sensitivity for a thick layer), as well as the amount

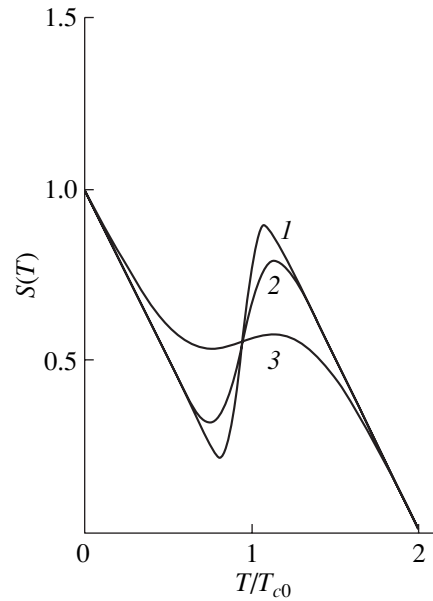


Fig. 4. Temperature dependences of the thermoelastic stress in the alloy layer for different values of the relative layer thickness  $h/\lambda_m$ : (1)  $\infty$ , (2) 0.4, and (3) 0.14.

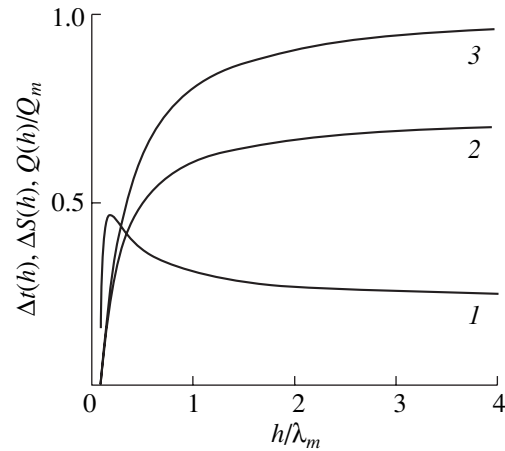


Fig. 5. Dependences of (1) the temperature range  $\Delta t$ , (2) the amount of stress relaxation  $\Delta S$ , and (3) sensitivity  $Q$  on the relative layer thickness  $h/\lambda_m$ .

of relaxation of the stress in the layer caused by the phase transformation, decreases with decreasing layer thickness.

The relaxation of the stress is equal to  $\Delta\sigma = \sigma_1 - \sigma_2$ , where  $\sigma_1 = \sigma(T_1)$  and  $\sigma_2 = \sigma(T_2)$  are the maximum and minimum stresses in Fig. 4, respectively, and  $T_1$  and  $T_2$  are their respective temperatures. In order to find these quantities, we differentiate Eq. (9) with respect to  $t$  [taking into account Eq. (7b)] and equate the derivative of the total stress to zero,  $dS/dt = 0$ . With this condition, we solve the system of equations (7b) and (9) and find the dimensionless stresses and temperatures corre-

sponding to the maximum and minimum of the curves in Fig. 4:

$$S_{1,2} = \left[ \frac{a}{b} \left( t_0 - 1 - B^{-1} \ln(z_{1,2}) \pm \frac{\tau_f}{\tau_M} \right) - \frac{1}{1 + z_{1,2}} \right] (1 + a)^{-1}, \quad (13a)$$

$$t_{1,2} = \left[ 1 + at_0 + B^{-1} \ln(z_{1,2}) - \frac{b}{1 + z_{1,2}} \mp \frac{\tau_f}{\tau_M} \right] (1 + a)^{-1}, \quad (13b)$$

where

$$z_{1,2} = \frac{bB}{2a} - 1 \pm \left[ \left( \frac{bB}{2a} - 1 \right)^2 - 1 \right]^{1/2}. \quad (13c)$$

The differences of the stresses and of the temperatures corresponding to these maximum and minimum are found to be

$$\Delta S = S_1 - S_2 = \left[ \left( 1 - \frac{4a}{bB} \right)^{1/2} - \frac{a}{bB} \ln \frac{z_1}{z_2} \right] (1 + a)^{-1}, \quad (14a)$$

$$\Delta t = t_1 - t_2 = \left[ b \left( 1 - \frac{4a}{bB} \right)^{1/2} + B^{-1} \ln \frac{z_1}{z_2} \right] (1 + a)^{-1}, \quad (14b)$$

$$\frac{z_1}{z_2} = \frac{1 - 2a/bB + (1 - 4a/bB)^{1/2}}{1 - 2a/bB - (1 - 4a/bB)^{1/2}}. \quad (14c)$$

These quantities depend on the layer thickness  $h$  through  $B = B(h)$  given by Eq. (12).

Figure 5 shows these dependences (curves 1, 2) for  $B_m = 50$  and  $a = b = 0.1$ . It can be seen that for (relatively large)  $h > 2\lambda_m$ , the relaxation of thermoelastic stresses in the process of the MT virtually does not depend on the layer thickness. In the range  $h < \lambda_m$ , this relaxation decreases sharply with decreasing layer thickness. At a critical value  $h_c = (B_c/(B_m - B_c))\lambda_m$ , where

$B_c = 4a/b$ , the temperature sensitivity of stresses  $Q$  in Eq. (12) and the difference between the maximum and minimum stresses vanish. From the data presented in [7, Fig. 8], it follows that in the NiTi alloy in question, the average spacing between obstacles is  $\lambda_m \approx 200$  nm. This can correspond, for example, to the case where the dislocation density in the alloy is  $\rho \approx \lambda_m^{-2} \approx 2.5 \times 10^9$  cm<sup>-2</sup>.

In summary, the theory of diffuse MTs developed in [8–10] is shown to describe adequately the experimental data on martensitic transformations in a thin layer of a shape memory alloy under stress conditions and the relaxation of thermoelastic stresses caused by these phase transformations.

## REFERENCES

1. S. M. Spearing, *Acta Mater.* **48** (1), 179 (2000).
2. *Materials for Smart Systems II: Symposium, Boston, 1996*, Ed. by E. P. George, R. Gotthardt, K. Otsuka, *et al.* (Materials Research Society, Pittsburg, 1997); *Mater. Res. Soc. Symp. Proc.* **459** (1997).
3. K. Shimizu and K. Otsuka, *Shape Memory Effects in Alloys* (Nauka, Moscow, 1979).
4. J. E. Bidaux, W. J. Yu, R. Gotthardt, and J. A. Manson, *J. Phys. IV* **5** (C-2), 453 (1995).
5. S. P. Belyaev, S. A. Egorov, V. A. Likhachev, and O. E. Ol'khovik, *Zh. Tekh. Fiz.* **66** (11), 36 (1996) [*Tech. Phys.* **41**, 1102 (1996)].
6. R. D. James and K. F. Hane, *Acta Mater.* **48** (1), 197 (2000).
7. A. L. Roytburd, T. S. Kim, Q. Su, *et al.*, *Acta Mater.* **46** (14), 5095 (2000).
8. G. A. Malygin, *Fiz. Tverd. Tela* (St. Petersburg) **36** (5), 1489 (1994) [*Phys. Solid State* **36**, 815 (1994)].
9. G. A. Malygin, *Zh. Tekh. Fiz.* **66** (11), 112 (1996) [*Tech. Phys.* **41**, 1145 (1996)].
10. G. A. Malygin, *Usp. Fiz. Nauk* **171** (2), 187 (2001).
11. G. G. Stoney, *Proc. R. Soc. London, Ser. A* **82**, 172 (1909).

*Translated by Yu. Epifanov*

---

## LATTICE DYNAMICS AND PHASE TRANSITIONS

---

# Equation of State of Rare-Gas Crystals near Their Metallization

E. V. Zarochentsev and E. P. Troitskaya

Donetsk Physicotechnical Institute, National Academy of Sciences of Ukraine, Donetsk, 83114 Ukraine

e-mail: zero@host.dipt.donetsk.ua

Received December 15, 2000

**Abstract**—A nonempirical equation of state of a crystal is found in the framework of the finite-deformation theory. The adiabatic potential is calculated from first principles by using a set of localized functions which are exactly orthogonalized to one another, with the orthogonalizing matrix being calculated by the cluster expansion method. The most essential part of the equation of state which corresponds to short-range repulsion involves no experimentally determined parameters. Comparison of the theory and experimental data in the range of large compressive deformations shows that the terms of higher orders in the overlap integral are of importance for neon, whereas it suffices to use the quadratic approximation for xenon. The reason for this is discussed. © 2001 MAIK “Nauka/Interperiodica”.

## 1. INTRODUCTION

Recent attention has been focused on the insulator–metal transition (metallization) under the action of external forces. This transition is believed to occur under compression; because of this, the energy gap between the filled and empty bands is closed. Of considerable interest are the value of the metallization pressure, the law according to which the band gap vanishes, and the properties of a material under these conditions.

In order to discuss the experimental data on the state of a crystal subjected to a high pressure, one should consider the following two aspects of this problem. First of all, the theory of the energy band structure of a crystal subjected to finite deformations should be constructed, for the most part, from first principles. Then, a general equation of state should be found in which the finite deformations are related to the externally applied stresses. The theory of the band structure should be based on a well-founded approach (in this paper, we use the Hartree–Fock method).

In [1], the overlap integrals  $S$  are considered control parameters for crystals of all rare gases. One can approach the problem of determining the atomic and electronic properties in two stages. First, the parameters  $S$  are calculated very accurately and then the specific problem is solved within appropriate approximations. In [1], the electronic structure was calculated using an exactly calculated orthogonalizing matrix; this was attained by summing certain subsequences in the power series in  $S$  (see also [2]), which made it possible to lift the restriction  $S \ll 1$  and to find the energy spectra in the case where the relative amount of compression of the crystal  $u = \Delta V/V_0$  is close to unity. Since the insulator–metal transition is expected to occur in this range of

compressions, this calculation method is of considerable interest.<sup>1</sup>

In recent years, isotherms have been frequently described in a wide pressure range by using semiempirical equations of state in which adjustable parameters are determined at normal pressure [4–9]. These equations were initially derived and applied to a wide range of materials in the range of kilobar pressures. Therefore, these equations are reliable only in the pressure range where the experimental data and the relationships used in their derivation are adequate. In the range of pressures in which the relevant experiments have not yet been performed, it is more appropriate to use equations of state that are derived from first principles in the framework of the nonlinear elasticity theory [10].

In this paper, the equation of state is derived using the microscopic interatomic-potential theory, which we develop according to [11, 12]. The short-range repulsion energy in the Hartree–Fock approximation is calculated from first principles on the basis of the entire power series in the overlap integrals of the atomic orbitals at different sites of the crystal. The contributions that are not included in the Hartree–Fock approximation are effectively taken into account in the long-range attractive potential, which contains three parameters.

The relevant fundamentals of the finite-deformation theory and the derivation of the equation of state are presented in Section 2 of this paper. The method for calculating the adiabatic potential of the crystal and the approximations made in this method are described in Section 3. In Section 4, the calculated interatomic pairwise potential is approximated by a simple analytical expression. With this expression, an equation of state is derived and discussed in Section 5, where we also com-

<sup>1</sup> Metallization of rare-gas crystals occurs when the indirect band gap is closed [3].

pare our findings with experimental data and with semiempirical equations of state in the range of megabar pressures. Conclusions are made in Section 6.

## 2. THE GENERAL EQUATION OF STATE

In this paper, the equation of state in the most general case is considered to mean the relation between the stress  $t_{ij}$  and the distortion tensor  $u_{ij}$  at a given temperature (or entropy; see, e.g., [10]):

$$t_{ij}(x) = \rho(x) \left[ \frac{\partial F(T, x')}{\partial u'_{ij}} \right]_{T, u'=0}, \quad (1)$$

where  $\rho(x)$  is the density of the substance in an arbitrary stressed state  $\{x\}$  and  $F(T, x')$  is the free energy (per unit mass) in the state  $x'$  at temperature  $T$ .

The free energy  $F(x)$  is a function of the distortion tensor,  $F(T, x) = F(T, X, u_{ij})$ ; the distortion characterizes the transition from the initial  $\{X\}$  to the final state  $\{x\}$ . In any microscopic model, the free energy is, in general, a function of the volume of the unit cell  $\Omega$  and the vectors of the direct ( $\mathbf{R}$ ) and the reciprocal lattice ( $\mathbf{g}$ ):  $F(T, x) = F(\Omega, \mathbf{R}, \mathbf{g})$ . Therefore, the equation of state (1) can be written as

$$\Omega \frac{\partial F}{\partial \Omega} - \sum_{\mathbf{g}} g_{\alpha} \frac{\partial F}{\partial g_{\alpha}} + \sum_{\mathbf{R}} R_{\alpha} \frac{\partial F}{\partial R_{\alpha}} = \Omega t_{\alpha\alpha}. \quad (2)$$

For hcp (or fct) crystals, the free energy is a function of two parameters, namely, the unit-cell volume  $\Omega$  and the  $c/a$  ratio. In this case, the equation of state takes the form

$$p = -\frac{\partial F(T, \Omega, c/a)}{\partial \Omega}, \quad \frac{\partial F(T, \Omega, c/a)}{\partial (c/a)} = 0. \quad (3)$$

For a cubic crystal,  $c/a \equiv 1$  and the second equation in Eq. (3) becomes an identity.

We will derive the equation of state  $p(u)$  that is valid for crystals at high hydrostatic pressures at  $T = 0$ . The crystal energy, the individual terms of which were derived in [11, 12], has the form

$$E = \sum_{\mathbf{l}} \left\{ \frac{(D^{\mathbf{l}})^2}{2\alpha} + \beta^{\mathbf{l}} D^{\mathbf{l}} + \frac{1}{2} \sum_{\mathbf{l}' \neq \mathbf{l}} \mathcal{K}(D^{\mathbf{l}}, D^{\mathbf{l}'}) + E^{(1)} + E^{(2)} \right\}. \quad (4)$$

Here,  $D^{\mathbf{l}}$  is the dipole moment of an atom at site  $\mathbf{l}$  induced by moving nuclei (higher multiple moments are neglected). The term  $\beta^{\mathbf{l}} D^{\mathbf{l}}$  is the exchange dipole interaction, and the third term is the dipole-dipole interaction. The first three terms are associated with fluctuating deformations of the electron shells and describe nonadiabatic effects (electron-phonon interaction). These terms make no contribution to the first-

and second-order elastic constants [10]. As can be seen from Eq. (4), the contributions from the electron-phonon interaction to the elastic constants are of the fourth and higher orders in the nuclear displacements  $u_{\alpha}$ . Indeed, from the self-consistency condition

$$\frac{\partial E}{\partial D^{\mathbf{l}}} = 0,$$

it follows that  $D_{\alpha} \sim \beta u_{\alpha}$ . The lowest order term in the expansion of the exchange dipole interaction constant in the power series in  $ak_{\alpha}$  is proportional to  $\sim k_{\alpha}$ . Therefore,  $D_{\alpha} \sim k u_{\alpha}$  and the energy of nonadiabatic motion of the electrons is proportional to  $\sim k^4$ . For the deformation tensor, we have  $u_{ij} \sim k_i u_j$ ; therefore, the nonadiabatic terms mentioned above contribute only to the fourth- and higher order elastic constants. For this reason, nonadiabatic effects will not be considered in this paper.

The last two terms in Eq. (4) are the energies of short-range repulsion of atoms and of long-range attraction due to many-particle effects, respectively [11]. They are expressed in terms of the pairwise interaction potentials between the atoms:

$$E^{(1)} = T_e + E_{sr}, \quad E_{sr} = \frac{1}{2} \sum_{\mathbf{l}' \neq \mathbf{l}} V_{sr}(R^{\mathbf{l}''}), \quad (5)$$

$$E^{(2)} = \frac{1}{2} \sum_{\mathbf{l}' \neq \mathbf{l}} V_{lr}(R^{\mathbf{l}''}). \quad (6)$$

The term  $E^{(2)}$  describes the attraction between the atoms; it is not allowed for in the one-electron (Hartree-Fock) approximation [12] and corresponds to virtual transitions of two electrons from states  $v_1$  and  $v_2$  of the valence band to states  $c_1$  and  $c_2$  of the empty conduction band under the action of the electron-electron interaction operator. In the particular case of atomic shells which do not overlap (at large interatomic spacings), the energy  $E^{(2)}$  reduces to the well-known van der Waals energy. The attraction energy between two atoms was calculated in [11] and can be written in the form

$$V_{lr}(R) = -\frac{C}{R^6} [1 + f(x)], \quad (7)$$

$$f(x) = A \exp(-\beta(x-1)), \quad x = R/R_0,$$

where  $C$  is the van der Waals constant,  $f(x)$  is a function associated with atomic electron shell overlapping, and  $R_0$  is the spacing between the nearest neighbors in the crystal before compression.

The fourth term  $E^{(1)}$  in Eq. (4) is the energy of the electron subsystem of the crystal, which includes the interaction energy between nuclei in the one-electron approximation.



### 3. INTERATOMIC INTERACTION AT SMALL DISTANCES

The energy of the crystal is a functional of the two-electron density matrix  $\rho(\mathbf{r}_1, \mathbf{r}_2 | \mathbf{r}'_1, \mathbf{r}'_2; \{\mathbf{I}\})$ , where  $\mathbf{r}_1$  and  $\mathbf{r}_2$  are the position vectors of electrons and  $\{\mathbf{I}\}$  are the position vectors of nuclei. We consider only the case of hydrostatic compression, in which the crystal remains cubic up to the structural phase transition. In the one-electron approximation, the two-electron density matrix is the sum of two terms, each of which is the product of two one-electron density matrices; these terms correspond to the Coulomb and exchange interactions.

Let us consider a crystal with closed electron shells. In the basis of localized Wannier functions  $\chi_v(\mathbf{r} - \mathbf{I})$ , the one-electron density matrix has the form (see [13])

$$\rho(\mathbf{r} | \mathbf{r}'; \{\mathbf{I}\}) = 2 \sum_{\mathbf{I}v} \chi_v(\mathbf{r} - \mathbf{I}) \chi_v^*(\mathbf{r}' - \mathbf{I}) \quad (8)$$

(the density is normalized to the number of electrons). In Eq. (8), the sum is over all occupied one-electron states  $v$ .

The original expression for  $E^{(1)}$  in terms of the one-electron density matrix  $\rho(\mathbf{r} | \mathbf{r}'; \{\mathbf{I}\})$  has the form

$$E^{(1)} = T_e + U_C + U_{ex} + U_{en} + U_{nn}, \quad (9)$$

where

$$T_e(\{\mathbf{I}\}) = -\hbar^2/(2m) \int d\mathbf{r} [\Delta_r \rho(\mathbf{r} | \mathbf{r}'; \{\mathbf{I}\})]_{\mathbf{r}=\mathbf{r}'}$$

is the kinetic energy of the electrons of the crystal,

$$U_C(\{\mathbf{I}\}) = \frac{1}{2} e^2 \int d\mathbf{r} d\mathbf{r}' \frac{\rho(\mathbf{r} | \mathbf{r}; \{\mathbf{I}\}) \rho(\mathbf{r}' | \mathbf{r}'; \{\mathbf{I}\})}{|\mathbf{r} - \mathbf{r}'|}$$

is the electron–electron Coulomb interaction energy,

$$U_{ex}(\{\mathbf{I}\}) = -\frac{1}{4} e^2 \int d\mathbf{r} d\mathbf{r}' \frac{\rho(\mathbf{r} | \mathbf{r}'; \{\mathbf{I}\}) \rho(\mathbf{r}' | \mathbf{r}; \{\mathbf{I}\})}{|\mathbf{r} - \mathbf{r}'|}$$

is the electron–electron exchange interaction energy, and

$$U_{en} = -Ze^2 \int d\mathbf{r} \rho(\mathbf{r} | \mathbf{r}; \{\mathbf{I}\}) \sum_{\mathbf{I}} \frac{1}{|\mathbf{r} - \mathbf{I}|},$$

$$U_{nn} = Z^2 e^2 \sum_{\mathbf{I}\mathbf{I}'} \frac{1}{|\mathbf{I} - \mathbf{I}'|}$$

is the electron–nucleus and nucleus–nucleus interaction energy.

Following [13], the density matrix  $\rho$  in Eq. (9) can be expressed in terms of the electron functions  $\varphi_s(\mathbf{r} - \mathbf{I})$

(atomic orbitals) of an isolated atom  $\mathbf{I}$ :

$$\rho(\mathbf{r} | \mathbf{r}') = \sum_{\mathbf{I}s} \left\{ \varphi_s(\mathbf{r} - \mathbf{I}) \varphi_s^*(\mathbf{r}' - \mathbf{I}) - \sum_{\mathbf{I}'s'} \varphi_{s'}(\mathbf{r} - \mathbf{I}') P_{s's'}^{II'} \varphi_s^*(\mathbf{r}' - \mathbf{I}) \right\}, \quad (10)$$

where the matrix  $P = I - (I + S)^{-1}$  ( $I$  is the identity matrix). The elements of the matrix  $S$  are the overlap integrals between two atomic orbitals centered at different sites:

$$S_{ss'}^{II'} = \int \varphi_s^*(\mathbf{r} - \mathbf{I}) \varphi_{s'}(\mathbf{r} - \mathbf{I}') d\mathbf{r}. \quad (11)$$

The matrix  $P$  can be calculated using a cluster expansion (CE); for details, see [13]. Using Eq. (10) for the matrix  $\rho(\mathbf{r} | \mathbf{r}')$  and Eq. (9), the short-range potential in Eq. (5) in the pair approximation is found to be

$$V_{sr}(R^{II'}) = 2 \sum_{\alpha\beta} \left\{ 4 \mathcal{P}_{\alpha\beta}^{II'} \left[ -\langle l'\beta | V^l | l\alpha \rangle + \sum_{\gamma} \langle l'\gamma, l'\beta | v_C | l'\gamma, l\alpha \rangle \right] + \sum_{\gamma} (\mathcal{P}_{\beta\alpha}^{II'} \mathcal{P}_{\gamma\alpha}^{II'} - 2 \mathcal{P}_{\alpha\beta}^{II'}) \right. \\ \left. \times \left( 2 \langle l'\beta | V^l | l'\gamma \rangle - \sum_{\delta} \langle l\delta, l'\beta | v_C | l'\gamma, l\delta \rangle \right) \right\}. \quad (12)$$

Here,  $V^l$  is the potential of the neutral atom  $l$ ,  $v_C = 1/|\mathbf{r} - \mathbf{r}'|$ ,  $\langle l'\gamma, l'\beta | v_C | l'\gamma, l\alpha \rangle = \int [(\varphi_{\gamma}^{l'}(\mathbf{r}) \varphi_{\beta}^{l'}(\mathbf{r}') \varphi_{\gamma}^{l'}(\mathbf{r}) \varphi_{\alpha}^{l'}(\mathbf{r}')) / |\mathbf{r} - \mathbf{r}'|] d\tau d\tau'$ , and the Cartesian components are indexed using Greek letters. From Eq. (10), it follows that  $V_{sr}$  is expressed in terms of the matrix  $P_{\alpha\beta}^{II'}$ , which we represented in Eq. (12) in the form

$$P = 2I\mathcal{P} - \mathcal{P}^2, \quad \mathcal{P} = I - (I + S)^{-1/2}, \quad (13)$$

which follows from the definitions of the matrices  $P$  and  $\mathcal{P}$  [2]. Equation (12) reduces to a well-known expression for the pairwise potential (first obtained in [14]) in the limit of small  $S \ll 1$ ; that is, if we substitute  $\mathcal{P}_{\alpha\beta}^{II'} = \frac{1}{2} S_{\alpha\beta}^{II'} + O(S^2)$  into Eq. (12)

$$\mathcal{P}_{\alpha\beta}^{II'} = -\frac{3}{8} \sum_{m\alpha} S_{\gamma\alpha}^{lm} S_{\beta\alpha}^{lm} + O(S^4). \quad (14)$$

#### 4. A SIMPLE EXPRESSION FOR THE INTERATOMIC POTENTIAL

In [12], the energy  $E^{(1)}$  and the potential  $V_{sr}$  in Eq. (5) were calculated in real space in the following approximations: (i) the atomic orbitals at different sites are orthogonalized to within the terms of the order  $S^2$ ; (ii) only the largest overlap integral  $S_{\sigma} = S_{n p_x, n p_z}$  (with  $n = 2, 3, 4$ , and  $5$  for Ne, Ar, Kr, and Xe, respectively) is assumed to be nonzero; (iii) all multicenter matrix elements are expressed through the two-center matrix elements and the interatomic pairwise interaction potential; and (iv) all calculations are performed in the nearest neighbor approximation.

One can go beyond approximation (i) by using an exact orthogonalization procedure after Levdin.

In this paper, the short-range repulsive potential  $V_{sr}$  is calculated from first principles within the Hartree–Fock approximation on the basis of exactly orthogonalized atomic orbitals, using the atomic orbitals listed in the Clementi–Roetti tables [15].

In what follows, we use a simple expression

$$V_{sr}(y) = (A_4 y^4 + A_3 y^3 + A_2 y^2 + A_1 y + A_0) \exp(-\alpha y), \quad (15)$$

where  $y = R/R_0 - 1$ .

As before, the parameters of the dependence of  $V_{sr}$  in Eq. (15) on the interatomic spacing in the crystal are found by the least square technique (with an accuracy of 1%). For example, the parameters  $A_i$  and  $\alpha$  in Eq. (15) for Ne are determined to be  $A_4 = 24.80 \times 10^{-4}$ ,  $A_3 = 11.52 \times 10^{-4}$ ,  $A_2 = 2.27 \times 10^{-4}$ ,  $A_1 = 0.42 \times 10^{-4}$ ,  $A_0 = 0.50 \times 10^{-4}$  a.u., and  $\alpha = 13.31$ .

With increasing compressive deformation of the crystal, the short-range repulsive potential varies (increases) much more greatly than the potential  $V_{lr}$  and the repulsive potential becomes dominant at high pressures. Therefore, the attractive potential is significant only in the range of small amounts of compression, where the model of the potential  $V_{lr}$  proposed in [11, 12] is adequate. This is the reason why the parameters  $C$ ,  $\beta$ , and  $A$  of the potential  $V_{lr}$  in Eq. (7) found in [11] are used in this paper for all rare-gas crystals.

#### 5. CALCULATION AND DISCUSSION OF THE EQUATION OF STATE

In the general case, the equation of state (3) at a finite temperature  $T$  can be represented in the form

$$p(T, V) = p_{\text{stat}}(V) + p_e^*(T, V) + p^*(T, V) + p_{zp}(V) + p_{na}(T, V). \quad (16)$$

Here,  $p_{\text{stat}}$  is the pressure in the static lattice (without

phonons):

$$p_{\text{stat}} = p_{sr} + p_{lr},$$

where  $p_{sr}$  and  $p_{lr}$  are the derivatives (with the minus sign) of the short-range energy  $E_{sr}$  and the long-range energy  $E^{(2)}$  with respect to the volume, respectively. The pressure of the conduction electron gas  $p_e^*$  is low, since the temperature  $T$  is small in comparison with the fundamental band gap. The thermal phonon pressure  $p^* \sim (T/\theta)^2$  [where  $\theta = \theta(p)$  is the Debye temperature] is also low. The  $(T/\theta)$  ratio is always small at high pressures, because  $\theta$  increases greatly with pressure. This is also the reason for the smallness of the electron–phonon and anharmonic interactions, which contribute to the nonadiabatic part  $p_{na}$  of the pressure.

Now, we consider the temperature-independent contributions  $p_{zp}$  and  $p_{na}(T = 0)$  corresponding to the zero-point harmonic and anharmonic energies, respectively. By definition [10],

$$p_{zp} = -\frac{\partial}{\partial \Omega} \sum_{\mathbf{q}\lambda} \hbar \omega_{\mathbf{q}\lambda} = \frac{\hbar}{2\Omega N} \sum_{\mathbf{q}\lambda} \omega_{\mathbf{q}\lambda} \gamma_{\mathbf{q}\lambda},$$

where  $\omega_{\mathbf{q}\lambda}$  and  $\gamma_{\mathbf{q}\lambda}$  are the frequency and the microscopic Grüneisen constant, respectively, of phonons with wave vector  $\mathbf{q}$  and polarization  $\lambda$ . Estimates show (see the approximate formula for  $\gamma$  in [16]) that the Grüneisen constant is small (in comparison with the scale of changes in pressure) and varies logarithmically with volume. The phonon frequencies are changed more greatly than  $\gamma_{\mathbf{q}\lambda}$ , but their dependence is weaker than linear [10]. Therefore, the zero-point pressure is small in comparison with  $p_{\text{stat}}$  and its relative contribution decreases with increasing pressure applied to the crystal. This is supported by the fact that isotherms approach each other as the pressure is increased, which has been observed experimentally in many materials (see, e.g., [16]). The behavior of the pressure  $p_{na}(T = 0)$  is similar, but this pressure is even smaller because of the phonon frequencies being in the denominators of the relevant integrals [10].

Thus, it may be concluded that the static-lattice pressure at  $T = 0$  is dominant at high pressures. For a cubic crystal, the equation of state takes the form [11]

$$p = -\frac{\partial E}{\partial \Omega} = \frac{e^2}{2a^4} [H(a) + 0.301123D(a)],$$

$$D(a) = \frac{6C}{e^2 a^5}, \quad (17)$$

$$H(a) = \frac{2ax^2 dV_{sr}}{e^2 dx} - AD \frac{6 + \beta x}{24} \exp[-\beta(x - 1)],$$

where  $x = a/a_0$ ,  $a$  is the lattice parameter of the crystal under compression,  $H(a)$  is the lattice-parameter derivative of the sum of the short-range potentials  $V_{sr}$  and the

**Table 1.** Dimensionless parameters  $H$  and  $D$  given by Eq. (17) for neon

$\Delta V/V_0$		0	0.3	0.7	0.77	0.8
$H, 10^{-2}$	CE	1.32	4.16	48.26	102.70	151.95
	$S^2$ [11]	1.28	4.54	68.15	140.09	199.56
$D, 10^{-2}$ [11]		4.25	7.70	31.61	49.22	62.13

**Table 2.** Equation of state of a neon crystal under compression

$\Delta V/V_0$	$p$ , kbar			$\delta$ , %	
	experiment [18]	theory [3], $S^2$	theory CE	[3]	CE
0.686	743	1113	732	50	1.5
0.690	783	1178	775	50	1.0
0.692	823	1212	798	47	3.0
0.695	835	1265	834	51	0.1
0.698	875	1321	872	51	0.5
0.701	911	1379	912	51	0.1
0.704	945	1441	954	52	1.0
0.707	977	1506	998	54	2.0
0.710	1010	1575	1045	56	3.0

Note:  $\delta = \frac{|p_{\text{theor}} - p_{\text{exp}}|}{p_{\text{exp}}} 100\%$ .

potential  $V_{lr}$  from which the van der Waals potential is subtracted,  $D$  is the dimensionless van der Waals constant, and the factor of 0.301123 is the value of a slowly convergent lattice sum.

Table 1 lists the values of  $H$  and  $D$  for Ne for various amounts of compression, which are found by two different methods: (i) by taking into account the terms of all orders in  $S$  in the potential  $V_{sr}$  in Eq. (15) (CE method) and (ii) by calculating to within the terms of the order  $S^2$  [11]. For compressive deformations up to  $u \approx 0.3$ ,  $H$  is roughly the same in both cases, but for  $u \approx 0.7$ , the value of  $H$  found by the CE method is 30% smaller. For crystals of other rare gases (Ar, Kr, and Xe), we made use of the values of the parameters  $H$  and  $D$  from [11, 12] in calculating isotherms for large compressive deformations.

The calculations correct to the second order in  $S$  agree very closely with the experimental data for crystals of all rare gases in the range of  $u \leq 0.3$  (Figs. 1–4, curve 1). However, for  $u \sim 0.65$ – $0.7$  for neon (and, to a smaller extent, for argon), the calculated pressure is higher than the experimental value. The calculations

for krypton and xenon correlate well with the experimental data (the difference for Xe is about 7% near the metallization point).

Since the logarithmic scale in Figs. 1–4 makes the difference between the values less evident, Table 2 compares some values of the pressure calculated to the second order in  $S$  in [3] and the values found in this paper by the CE method (taking into account the terms of all orders in  $S$ ) from the universal formula (12). From Table 2, it can be seen that, in the former case, the calculations agree with the experimental data to within 50%, while in the latter case, the difference is, on the average, about 2%.

Let us discuss the applicability of the semiempirical equations of state to crystals of rare gases in the range of megabar pressures (curves 2–5 in Figs. 1–4).

The existing semiempirical equations of state can be divided into three groups: (1) equations based on expansion of the crystal energy in a power series in the deformation parameters [4, 5], (2) equations based on empirical assumptions as to the dependence of the crystal energy on the interatomic spacing [6, 7], and (3) equa-

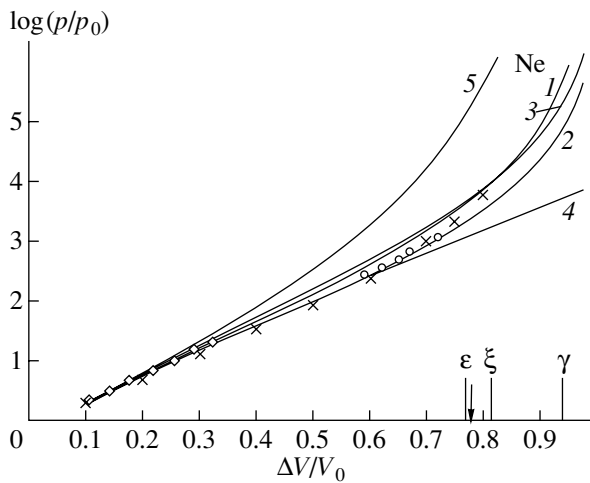


**Fig. 1.** Zero-temperature isotherms for neon ( $p_0 = 1 \text{ kbar} = 0.1 \text{ GPa}$ ). Solid curves are calculations: (1) [3], (2) [6], (3) [7], (4) [9], and (5) [8]. Crosses are calculations from this paper in the two-particle cluster approximation, diamonds are from experiment [17], and dots are from experiment [18]. The vertical arrow indicates the metallization point according to our calculations [19], and vertical bars are the calculations  $\epsilon$  [3],  $\xi$  [20], and  $\gamma$  [21].

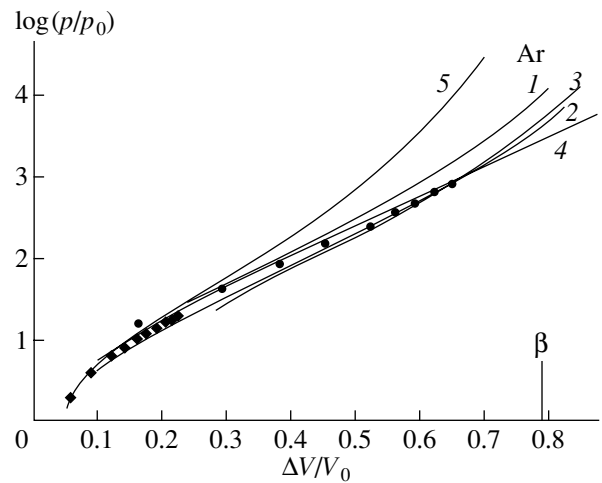


**Fig. 2.** Zero-temperature isotherms for argon. Diamonds and dots are experimental data from [22] and [23], respectively, and the vertical bar  $\beta$  indicates the metallization point calculated in [24]. The remainder of the interpretation is as in Fig. 1.

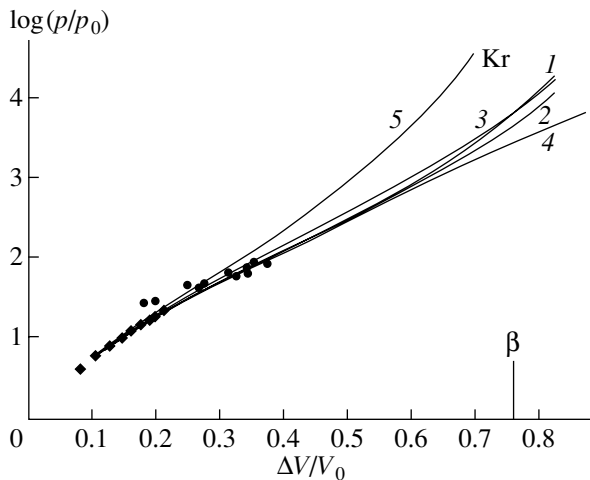


**Fig. 3.** Zero-temperature isotherms for krypton. Diamonds and dots are experimental data from [22] and [25], respectively. The remainder of the interpretation is as in Figs. 1 and 2.

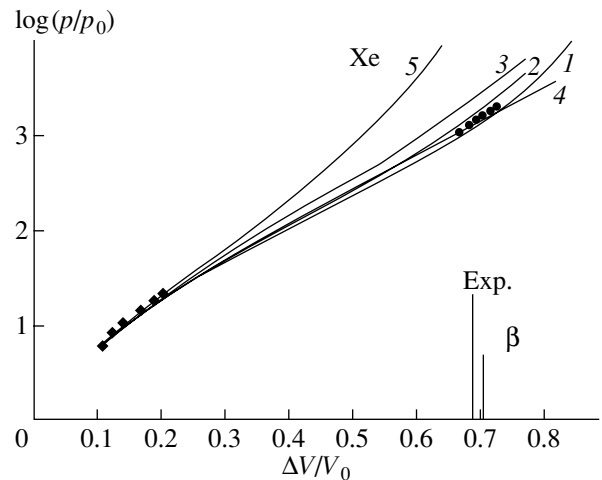


**Fig. 4.** Zero-temperature isotherms for xenon. Diamonds and dots are experimental data from [22] and [26], respectively; the vertical bar labeled "exp" indicates the experimental insulator-metal phase transition point [26]. The remainder of the interpretation is as in Figs. 1 and 2.

tions based on experimentally determined relations between various thermodynamic quantities [8, 9].

Figures 1–4 show isotherms calculated from semiempirical equations of state in different papers [4–9]. In our opinion, the Vinet equation of state [6] is the most appropriate; it agrees with the experimental data for  $u \sim 0.65$ – $0.7$  for Ne, Ar, and Xe to within 10%. The Vinet equation

of state was extended to the case of phase transitions by Fang [7]. The Fang equation of state allows one to adjust the parameters not only at  $p = 0$ , but also at any other point ( $p, V$ ) at which experimental values of the bulk modulus  $B$  and its derivative  $B'$  are available. The Murnaghan equation of state [8] ( $B' = \text{const}$ ) of crystals of rare gases gives highly overestimated values for the pressure even at small compressive deformations

(curve 5 in Figs. 1–4). Clearly, this is due to the fact that  $B'$  is assumed to be pressure-independent, which is not the case regardless of the amount of compression. For instance, in the case of neon,  $B'$  varies from 7.8 at  $p = 0$  to 5.5 at  $p = 17$  kbar [22]. The Kumar equation of state [9] underestimates the pressure at  $u = 0.65$ – $0.7$  for neon by 50% in comparison with the experimental value. The agreement is better for Ar and Xe (to within 7%). However, for larger amounts of compression, this equation underestimates the pressure in comparison with the experimental values for crystals of all rare gases.

## 6. CONCLUSION

In this paper, we analyzed a number of semiempirical equations of state as applied to highly compressed crystals (in the range of megabar pressures). The Vinet equation of state [6] gives the best fit to the available experimental data (up to 1–1.5 Mbar). The equation of state derived in this paper takes into account the Hartree–Fock short-range interatomic repulsion and is in good agreement with the available experimental data.

We did not take into account noncentral interaction forces, deformation of electron shells of atoms caused by motion of the nuclei, and terms involving higher multipoles. Nonetheless, the equation of state derived in this paper adequately describes the properties of Ne, Ar, Kr, and Xe. When constructing the potential for Ne, one should retain the pairwise terms of higher orders in  $S$  (Fig. 1), whereas for crystals of other rare gases, it suffices to take into account only the terms of the order  $\sim S^2$  (Figs. 2–4). This is because the potential  $V_{sr}$ , which consists of a large number of both positive and negative terms,

$$V_{sr} = V_{sr}^+ + V_{sr}^-$$

is as large as 40–50% of  $V_{sr}^+$  for crystals of Ar, Kr, and Xe, whereas for neon, the ratio  $V_{sr}/V_{sr}^+$  is equal to 0.20–0.25. Therefore, for crystals of Ar, Kr, and Xe, the terms of higher orders in  $S$  compensate each other and lead to small corrections, whereas their contribution to the potential for Ne is comparable to the terms of the order  $S^2$ .

The interatomic spacing (or relative compressive deformation of the crystal) is a physical parameter which is of prime importance in studying metallization and is measured experimentally. Theoretically, as well as experimentally, the pressure is calculated from an equation of state. Our theory [1] allows the metallization compressive deformation to be calculated fairly accurately. For example, for neon, the most adequate model [19] gives  $u_m = 0.78 \pm 0.01$  and the average value over all models is  $u_m = 0.80 \pm 0.03$ . However, since the pressure  $p$  increases rapidly (almost exponentially) with compressive deformation,  $p_m$  is determined less accurately. For  $u_m = 0.80 \pm 0.03$ , the pressure lies in the range  $2.9 \leq p_m \leq 10.5$  Mbar [ $p(u = 0.8) = 5.3$  Mbar], and for  $u_m = 0.78 \pm$

0.01, the metallization pressure is  $p_m = 3.5 \pm 0.7$  Mbar. However, even if the uncertainty is taken into account, this result is inconsistent with the anomalously large value  $p_m \sim 1300$ – $1500$  Mbar, predicted in [21], but agrees with the predicted values  $5 \pm 2$  [3] and 10 Mbar [20] (Fig. 1). A discussion of metallization will be published elsewhere.

## ACKNOWLEDGMENTS

The authors are grateful to V.G. Bar'yakhtar for his continued interest in this work and to Yu.V. Ereimeichenkova and A.V. Chaika for their help with the computations.

This work was supported by the International Scientific Foundation, grant no. QSU 082067.

## REFERENCES

1. V. G. Bar'yakhtar, E. V. Zarochentsev, E. P. Troitskaya, and Yu. V. Ereimeichenkova, *Fiz. Tverd. Tela* (St. Petersburg) **40** (8), 1464 (1998) [*Phys. Solid State* **40**, 1330 (1998)].
2. Yu. V. Ereimeichenkova, E. V. Zarochentsev, and E. P. Troitskaya, *Teor. Mat. Fiz.* **102** (3), 498 (1996).
3. E. V. Zarochentsev and E. P. Troitskaya, *Fiz. Tverd. Tela* (Leningrad) **27** (8), 2474 (1985) [*Sov. Phys. Solid State* **27**, 1480 (1985)].
4. F. Birch, *J. Geophys. Res.* **57**, 227 (1952).
5. R. E. Cohen, O. Gulseren, and R. J. Hemley, *condmat/9905389*.
6. P. Vinet, J. H. Rose, J. Ferrante, and L. R. Smidth, *J. Phys.: Condens. Matter* **1**, 1941 (1989).
7. Z. H. Fang, *Phys. Rev. B* **58**, 20 (1998).
8. F. D. Murnaghan, *Finite Deformation of Elastic Solids* (Wiley, New York, 1951).
9. M. Kumar, *Physica B* (Amsterdam) **212**, 391 (1995).
10. V. G. Bar'yakhtar, E. V. Zarochentsev, and E. P. Troitskaya, *Theory of Adiabatic Potential and Atomic Properties of Simple Metals* (Gordon and Breach, London, 1999).
11. V. L. Dorman, E. V. Zarochentsev, and E. P. Troitskaya, *Fiz. Nizk. Temp.* **8** (1), 94 (1982) [*Sov. J. Low Temp. Phys.* **8**, 47 (1982)].
12. V. L. Dorman, E. V. Zarochentsev, and E. P. Troitskaya, *Fiz. Tverd. Tela* (Leningrad) **23** (6), 1581 (1981) [*Sov. Phys. Solid State* **23**, 925 (1981)].
13. I. V. Abarenkov, I. M. Antonova, V. G. Bar'yakhtar, V. L. Bulatov, and E. V. Zarochentsev, *Methods of Computer Physics in Theory of Solid States. Electron Structure of Perfect and Imperfect Crystals* (Naukova Dumka, Kiev, 1991).
14. K. B. Tolpygo and E. P. Troitskaya, *Fiz. Tverd. Tela* (Leningrad) **17**, 102 (1975) [*Sov. Phys. Solid State* **17**, 58 (1975)].

15. F. Clementi and C. Roetti, *At. Data Nucl. Data Tables* **14** (3–4), 177 (1974).
16. M. Taravillo, V. G. Baonza, J. Nunez, and M. Caceres, *Phys. Rev. B* **54**, 7034 (1996).
17. M. S. Anderson, R. O. Fugate, and C. A. Swenson, *J. Low Temp. Phys.* **10**, 345 (1973).
18. R. J. Hemley, C. S. Zha, H. K. Mao, *et al.*, *Phys. Rev. B* **39** (16), 11820 (1989).
19. E. V. Zarochentsev, E. P. Troitskaya, and Yu. V. Ere-meichenkova, *Metallofiz. Novejšie Tekhnol.* **21**, 3 (1999).
20. N. H. March, in *Advances in High Pressure Research*, Ed. by R. S. Bradley (Academic, New York, 1969), Vol. 3, p. 241.
21. J. C. Boettger, *Phys. Rev. B* **33** (8), 6788 (1986).
22. M. S. Anderson and C. A. Swenson, *J. Phys. Chem. Solids* **36**, 145 (1975).
23. M. Ross, H. K. Mao, J. A. Hu, and P. M. Bell, *J. Chem. Phys.* **85**, 1028 (1986).
24. A. V. Tulub, V. F. Brattsev, and M. V. Pak, *Opt. Spektrosk.* **74**, 464 (1993) [*Opt. Spectrosc.* **74**, 279 (1993)].
25. H. Shimizu, N. Saitoh, and S. Sasaki, *Phys. Rev. B* **57**, 230 (1998).
26. K. A. Goettel, J. H. Eggert, J. F. Silvera, and M. C. Moss, *Phys. Rev. Lett.* **62**, 665 (1989).

*Translated by Yu. Epifanov*

---

## LATTICE DYNAMICS AND PHASE TRANSITIONS

---

# Tricritical Behavior of Compressible Systems with Frozen-In Structure Defects

S. V. Belim and V. V. Prudnikov

*Omsk State University, pr. Mira 55, Omsk, 644077 Russia*

Received October 10, 2000; in final form, December 20, 2000

**Abstract**—A field-theoretical description of phase transformations in weakly disordered elastically isotropic compressible systems is given. For three-dimensional Ising-like systems in a two-loop approximation, renormalization-group equations were analyzed using the Padé–Borel technique of summing and fixed points were distinguished that correspond to various types of critical and tricritical behavior under various macroscopic conditions imposed on the system. It is shown that a significant effect on the critical and tricritical behavior of compressible systems is exerted by structural defects, which manifests itself in both a change in the magnitudes of critical exponents and a decrease in the number of various types of multicritical behavior in comparison with uniform compressible systems. © 2001 MAIK “Nauka/Interperiodica”.

### 1. INTRODUCTION

Tricritical behavior that arises in condensed media upon a change in the type of the phase transition under the effect of an external field that is thermodynamically conjugated with the order parameter of the system, as well as upon changes in pressure, solution composition, etc., was revealed in studies of phase transformations in various types of solids, e.g., ferromagnets, ferroelectrics, and various crystals that suffer structural phase transitions [1]. From a variety of systems that exhibit tricritical behavior, we will be interested in this work in compressible magnets and solids that suffer structural phase transitions, in which an external pressure causes a second-order phase transition to pass into a first-order one. Most detailed experimental investigations of tricritical anomalies and measurements of tricritical exponents were performed on Ising-like crystals of  $\text{NH}_4\text{Cl}$ ,  $\text{ND}_4\text{Cl}$ , and single-crystal solid solutions on their basis [2, 3].

In compressible systems, of great importance is the connection of the order parameter with elastic deformations. As was first shown by Larkin and Pikin in [4], in elastoisotropic solids, the critical behavior of compressible systems with a quadratic striction is unstable with respect to the connection of the order parameter with acoustic modes; a first-order phase transition close to a second-order transition occurs in such systems. However, the conclusions of [4] are only valid at low pressures. It was shown in [5] that in the region of high pressures, beginning from a certain critical value of pressure  $P = P_t$  corresponding to a tricritical point, a more fundamental influence on the system is exerted by deformational effects induced by the external pressure,

leading to a change in the sign of the effective constant of interaction between the fluctuations of the order parameter and, as a consequence, to a change in the type of the phase transition. For uniform compressible systems, two types of tricritical behavior and the existence of a tetracritical point at which two tricritical curves meet were predicted in [5]. The allowance for the elastic anisotropy of crystals [6–9] complicates the problem but does not lead to qualitatively new results.

All solids inevitably contain impurities and other lattice defects. According to the Harris criterion, the presence of randomly distributed frozen-in structural point defects can especially strongly manifest itself in the thermodynamics of the system at the tricritical point, since the critical exponent of heat capacity for uniform systems in this case is positive and by no means small ( $\alpha_t^{(0)} = 1/2$ ). At the same time, along the curve of second-order phase transitions which ends at the tricritical point, the effect of lattice defects should be pronounced (because of the smallness of the exponent  $\alpha_c^{(0)}$ ) much weaker at  $\alpha_c^{(0)} > 0$  or be absent at all at  $\alpha_c^{(0)} < 0$ . A renormalization-group investigation of the effect of weak disorder on the tricritical behavior of systems without allowance for deformation effects was performed in [10–12]. The most systematic analysis of the solutions to the renormalization-group equations for a five-vertex model of a disordered crystal in the vicinity of the tricritical point performed in [12] revealed the effect of the “runaway” of phase trajectories from the tricritical region of the bare vertices into the region of large vertex magnitudes, where the perturbation theory ceases to be valid. This effect was inter-

puted as evidence for the smearing of phase transitions and the instability of tricritical behavior with respect to the configurational disorder. The investigation of the vicinity of the tricritical point performed in [13] using the strong-disorder model permitted the authors to predict that the tricritical point of a disordered system is preceded by a percolation-type phase transition related to the formation of localized droplets and their interaction, although the fluctuational behavior at the tricritical point itself has not been clarified.

In structural phase transitions without a piezoelectric effect in the paraelectric phase, elastic deformations play the role of a secondary order parameter, whose fluctuations in most cases are not critical. In [14, 15], based on the general concepts of phase transitions in systems in which the order parameter is connected with additional nonfluctuating displacements, the authors considered (to a lower order in  $\epsilon$ ) the effect of frozen-in impurities on the possible types of phase transformations depending on the macroscopic conditions imposed on the system. It was revealed that, under a constant "stress," the phase trajectories, when they go out from the vicinity of the tricritical impurity point, escape from the region of the stability of second-order phase transitions (region of smeared phase transitions); at the same time, in the absence of a constant stress, the system exhibits no tricritical behavior, and the phase transformations have a character of second-order transitions with a significant effect of impurities on the critical behavior of systems with the number of components of the order parameter  $n < 4$  and the absence of the effects of disorder for systems with  $n > 4$ , which is typical of approaches of lower orders in  $\epsilon$ . However, it is well known that, in the lower order perturbation theory, the renormalization-group equations for renormalized vertices of the model, which describe the self-action of the order-parameter fluctuations and their interaction through the field of impurities, are characterized by random degeneracy and cannot be used to analyze the most interesting case of a disordered Ising model.

In this paper, we extended the model of phase transformations in a disordered system with a coupling between nonfluctuating variables [14, 15] to the case (physically important for structural phase transitions) of a compressible three-dimensional Ising model with frozen-in lattice defects that is considered by the renormalization-group methods in the two-loop approximation. The main attention is paid to the investigation of the conditions of realization of tricritical behavior due to effects of long-range interaction of the order-parameter fluctuations caused by long-wavelength acoustic modes. To simplify the analysis, we assume that the systems considered are elastically isotropic.

## 2. RESULTS AND DISCUSSION

The Hamiltonian of a disordered Ising model with allowance for elastic deformations can be written as follows:

$$\begin{aligned}
 H_0 = & \int d^d x \left[ \frac{\tau_0}{2} S(x)^2 + \frac{1}{2} (\nabla S(x))^2 + u_0 (S(x)^2)^2 \right] \\
 & + \int d^d x [\Delta\tau(x) S(x)^2] + \int d^d x \left[ \frac{a_1}{2} \sum_{\alpha=1}^d u_{\alpha\alpha}^2(x) \right. \\
 & \left. + a_2 \sum_{\alpha, \beta=1}^d u_{\alpha\beta}^2(x) \right] + a_3 \int d^d x S(x)^2 \sum_{\alpha=1}^d u_{\alpha\alpha}(x) \\
 & + \int d^d x \sum_{\alpha, \beta=1}^d h_{\alpha\beta}(x) u_{\alpha\beta}(x),
 \end{aligned} \tag{1}$$

where  $S(x)$  is the order parameter;  $u_0$  is a positive constant;  $\tau_0 \sim |T - T_c|/T_c$ ;  $T_c$  is the phase-transition temperature;  $\Delta\tau(x)$  is the random field of impurities of the random-temperature type;  $u_{\alpha\beta}$  is the tensor of deformations;  $a_1 = K - 2\mu/d$  and  $a_2 = \mu$  are the elastic constants of the crystal ( $K$  and  $\mu$  are the compression and shear moduli, respectively); and  $a_3$  is the quadratic-striction parameter. The interaction of impurities with the nonfluctuating order parameter, i.e., with the deformation tensor  $u_{\alpha\beta}(x)$ , is given by the quantity  $h_{\alpha\beta}(x)$  that represents a random field that is thermodynamically conjugated to  $u_{\alpha\beta}(x)$ . Passing in Eq. (1) to Fourier transforms and introducing

$$u_{\alpha\beta}(x) = u_{\alpha\beta}^{(0)} + \Omega^{-1/2} \sum_{q \neq 0} u_{\alpha\beta}(q) \exp(iqx)$$

with  $u_{\alpha\beta}(q) = i/2[q_\alpha u_\beta + q_\beta u_\alpha]$ , after integration in the partition function with respect to the nondiagonal components of the uniform part of the deformation tensor  $u_{\alpha\beta}^{(0)}$  that are insignificant for the critical behavior of the system in an elastically isotropic medium, we obtain the Hamiltonian of the system in the following form:

$$\begin{aligned}
 H_0 = & \frac{1}{2} \int d^d q (\tau_0 + q^2) S_q S_{-q} + \frac{1}{2} \int d^d q \Delta\tau_q S_q S_{-q} \\
 & + u_0 \int d^d q S_{q1} S_{q2} S_{q3} S_{-q1-q2-q3} \\
 & + a_3 \int d^d q u_{\alpha\alpha}(q_1) S_{q2} S_{-q1-q2} + \frac{a_3^{(0)}}{\Omega} u_{\alpha\alpha}^{(0)} \int d^d q S_q S_{-q} \tag{2} \\
 & + \frac{\tilde{a}_1}{2} \int d^d q u_{\alpha\beta}(q) u_{\alpha\beta}(-q) + \frac{\tilde{a}_1^{(0)}}{2\Omega} (u_{\alpha\alpha}^{(0)})^2 \\
 & + \int d^d q h_{\alpha\beta}(q) u_{\alpha\beta}(-q) + \frac{h_{\alpha\alpha}^{(0)}}{\Omega} u_{\alpha\alpha}^{(0)},
 \end{aligned}$$



where  $\tilde{a}_1 = K + 2(d-1)\mu/d$  and  $\tilde{a}_1^{(0)} = K$ . In Eq. (2), the terms that describe the effect of uniform and nonuniform deformation are separated. As was shown in [4], such a separation is necessary, since the nonuniform deformations  $u_{\alpha\beta}(q)$  are responsible for the exchange by acoustic phonons and lead to long-range effects that are absent upon uniform deformations.

At small impurity concentrations, the distribution of random fields  $\Delta\tau_q$ ,  $h_{\alpha\beta}(q)$ , and  $h_{\alpha\alpha}^{(0)}$  can be considered to be Gaussian and specified by the function

$$P[\Delta\tau, h, h^{(0)}] = A \exp \left[ -\frac{1}{8b_1} \int \Delta\tau_q^2 d^d q - \frac{1}{8b_2} \int h_{\alpha\beta}^2(q) d^d q - \frac{(h_{\alpha\alpha}^{(0)})^2}{8b_3} - \frac{1}{4b_4} \int \Delta\tau_q h_{\alpha\alpha}(-q) d^d q - \frac{1}{4b_5} \int \Delta\tau_q h_{\alpha\alpha}^{(0)} d^d q \right], \quad (3)$$

where  $A$  is the normalization constant and  $b_i$  are positive constants that are proportional to the concentration of the frozen-in lattice defects.

By employing the replica procedure for averaging over random fields that are specified by the frozen-in structural defects, we obtain the following effective Hamiltonian of the system:

$$\begin{aligned} H_R = & \frac{1}{2} \int d^d q (\tau_0 + q^2) \sum_{a=1}^m S_q^a S_{-q}^a \\ & - \frac{\delta_0}{2} \sum_{a,b=1}^m \int d^d q (S_{q_1}^a S_{q_2}^a) (S_{q_3}^b S_{-q_1-q_2-q_3}^b) \\ & + u_0 \sum_{a=1}^m \int d^d q S_{q_1}^a S_{q_2}^a S_{q_3}^a S_{-q_1-q_2-q_3}^a \\ & + g_0 \sum_{a=1}^m \int d^d q u_{\alpha\alpha}^a(q_1) S_{q_2}^a S_{-q_1-q_2}^a \\ & + \frac{g_0^{(0)}}{\Omega} \sum_{a=1}^m u_{\alpha\alpha}^{(0)a} \int d^d q S_q^a S_{-q}^a \\ & + \frac{\lambda}{2} \sum_{a=1}^m \int d^d q u_{\alpha\beta}^a(q) u_{\alpha\beta}^a(-q) + \frac{\lambda_0}{2\Omega} \sum_{q=1}^m (u_{\alpha\alpha}^{(0)a})^2. \end{aligned} \quad (4)$$

Here,  $\delta_0$ ,  $g_0$ ,  $g_0^{(0)}$ ,  $\lambda = \tilde{K} + 2\tilde{\mu}(d-1)/d$ , and  $\lambda_0 = \tilde{K}$  are positive constants that are expressed through the constants  $a_i$  and  $b_i$ ;  $\delta_0$  has an impurity origin; and the quantities  $g_0$ ,  $g_0^{(0)}$ ,  $\tilde{K}$ , and  $\tilde{\mu}$  characterize the parameter of striction interaction and the elastic moduli of the crystal changed due to the influence of lattice defects. The properties of the initial system can be obtained in

the limit where the number of replicas (images)  $m \rightarrow 0$ ; therefore, the cubic anisotropy that arises in the Hamiltonian (4) due to the influence of defects is fictitious.

Let us determine the Hamiltonian of the system that depends only on the strongly fluctuating order parameter  $S$  in the following way:

$$\exp\{-H[S]\} = B \int \exp\{-H_R[S, u_{\alpha\beta}]\} \Pi du_{\alpha\beta}. \quad (5)$$

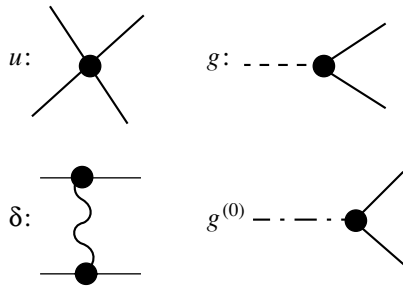
For experiments at a constant volume,  $u_{\alpha\alpha}^{(0)}$  is a constant, the integration in Eq. (5) is performed only over nonuniform deformations  $u_{\alpha\beta}(q)$ , and the uniform deformations do not contribute to the effective Hamiltonian. At a constant pressure, the Hamiltonian is only added with a term  $P\Omega$ ; the volume  $\Omega$  is expressed through the components of the deformation tensor as

$$\Omega = \Omega_0 \left[ 1 + \sum_{\alpha=1} u_{\alpha\alpha}^{(0)} + \sum_{\alpha \neq \beta} u_{\alpha\alpha}^{(0)} u_{\beta\beta}^{(0)} + O(u^3) \right] \quad (6)$$

and the integration in Eq. (5) is performed over both nonuniform and uniform deformations. As was noted in [5], the allowance for quadratic terms in Eq. (6) can be important in the case of high pressures and crystals with large striction effects. The neglect of quadratic terms in [4] restricts the application of the results of Larkin and Pikin's work to only the region of low pressures. As a result, we have

$$\begin{aligned} H = & \frac{1}{2} \int d^d q (\tau_0 + q^2) \sum_{a=1}^m S_q^a S_{-q}^a \\ & + \left( u_0 - \frac{z_0}{2} \right) \sum_{a=1}^m \int d^d \{q_i\} S_{q_1}^a S_{q_2}^a S_{q_3}^a S_{-q_1-q_2-q_3}^a \\ & + \frac{(z_0 - w_0)}{2\Omega} \sum_{a=1}^m \int d^d \{q_i\} (S_{q_1}^a S_{-q_1}^a) (S_{q_2}^a S_{-q_2}^a) \\ & - \frac{\delta}{2} \sum_{a,b=1}^m \int d^d \{q_i\} (S_{q_1}^a S_{q_2}^a) (S_{q_3}^b S_{-q_1-q_2-q_3}^b), \\ z_0 = & g_0^2/\lambda, \quad w_0 = g_0^{(0)2}/\lambda_0, \quad \lambda = \tilde{K} + 2\tilde{\mu}(d-1)/d, \\ & \lambda_0 = \tilde{K} + 2P(d-1)/d. \end{aligned} \quad (7)$$

The effective interaction parameter  $v_0 = u_0 - g_0^2/(2\lambda)$ , which arises due to the influence of striction effects that are determined by the parameter  $g_0$  and depend in the general case on the external pressure, can take on not only positive but also negative values. As a result, this Hamiltonian describes both first- and second-order phase transitions. At  $v_0 = 0$ , a tricritical behavior is realized in the system. In turn, the effective interaction in Eq. (7) that is determined by the difference of the



Graphical representation for the vertices of the interactions  $u$ ,  $\delta$ ,  $g$ , and  $g^{(0)}$ :  $\delta$  characterizes the interaction of fluctuations of the order parameter through the field of frozen-in point defects;  $g$  characterizes the interaction of fluctuations of the order parameter with nonuniform deformations of the crystal, and  $g^{(0)}$ , with uniform deformations of the crystal.

parameters  $z_0 - w_0$  can lead at pressures  $P > P_t = \tilde{\mu}$  to a phase transition of the second order and at pressures below  $P_t$ , to a first-order phase transition. The model predicts a relatively high value of the “tricritical pressure”  $P_t$  specified by the shear modulus  $\tilde{\mu}$ , which is a result of neglecting the contribution of anharmonic terms and terms that are of a higher order in the fluctuations of the order parameter and striction interaction, which are insignificant in the renormalization-group sense for the description of critical properties but can cause a significant change in the magnitude of the tricritical pressure [7]. The effective Hamiltonian of this type indicates that a critical point of a higher order can exist, at which tricritical curves intersect if the conditions  $v_0 = 0$  and  $z_0 = w_0$  are fulfilled simultaneously [5]. Note that at the tricritical condition  $z_0 = w_0$  the Hamiltonian of the model (7) is isomorphic to the Hamiltonian of the disordered Ising model.

In terms of the field-theoretical approach [16], the asymptotic critical behavior and the structure of phase diagrams in the fluctuational region are determined by the renormalization-group Callan–Symanzyk equation for the vertex parts of the irreducible Green’s functions. In order to calculate the  $\beta$  and  $\gamma$  functions as functions of renormalized vertices of the interactions  $u$ ,  $\delta$ ,  $g$ , and  $g^{(0)}$  that enter into the Callan–Symanzyk equation (a graphical representation for the introduced vertices is given in figure) or as functions of complex vertices  $z = g^2/\lambda$ ,  $w = g^{(0)2}/\lambda_0$ , and  $v = (v - z/2)$ , which are more suitable for determining the critical and tricritical behavior of the model, we applied the standard method based on Feynman’s diagrammatic technique and the renormalization procedure [17]. As a result, in terms of the two-loop approximation, we obtained the following expressions for the  $\beta$  functions:

$$\beta_v = -v(1 - 36v + 24\delta + 547.555556v^2 - 739.555556v\delta + 219.259259\delta^2),$$

$$\beta_\delta = -\delta(1 + 16\delta - 24v + 163.555556v^2)$$

$$-355.555556v\delta + 112.592593\delta^2), \tag{8}$$

$$\beta_z = (-z1 - 24v + 8\delta - 2z + 163.555556v^2 - 99.555556v\delta + 27.259259\delta^2),$$

$$\beta_w = -w(1 - 24v + 8\delta - 4z + 2w + 163.555556v^2 - 99.555556v\delta + 27.259259\delta^2).$$

It is known that the perturbation-theory expansions are asymptotic and the vertices of the interaction of order-parameter fluctuations in the fluctuational region are sufficiently large, so that Eqs. (8) can be applied directly. Therefore, in order to derive the necessary physical information from the expressions obtained, we used the Padé–Borel method extended to a four-parameter case. In this case, the direct and inverse Borel transformations have the following form:

$$f(v, \delta, z, w) = \sum_{i_1, \dots, i_4} c_{i_1, \dots, i_4} v^{i_1} \delta^{i_2} z^{i_3} w^{i_4}$$

$$= \int_0^\infty e^{-t} F(vt, \delta t, zt, wt) dt, \tag{9}$$

$$F(v, \delta, z, w) = \sum_{i_1, \dots, i_4} \frac{c_{i_1, \dots, i_4}}{(i_1 + \dots + i_4)!} v^{i_1} \delta^{i_2} z^{i_3} w^{i_4}.$$

To obtain an analytical continuation of the Borel transform of a function, we introduce a series in auxiliary variable  $\theta$

$$\tilde{F}(v, \delta, z, w, \theta)$$

$$= \sum_{k=0}^\infty \theta^k \sum_{i_1, \dots, i_4} \frac{c_{i_1, \dots, i_4}}{k!} v^{i_1} \delta^{i_2} z^{i_3} w^{i_4} \delta_{i_1 + \dots + i_4, k}, \tag{10}$$

to which we apply the Padé approximation  $[L/M]$  at the point  $\theta = 1$ . This technique was suggested and tested in [18] for describing the critical behavior of a number of systems characterized by several vertices of the interaction of order-parameter fluctuations. The property of symmetry preservation upon the application of the Padé approximants in variable  $\theta$ , which was revealed in [18], becomes significant upon the description of multivertex models.

In the two-loop approximation, we used the  $[2/1]$  approximant for calculating the  $\beta$  function. The nature of the critical behavior is determined in this case by the existence of a stable fixed point that satisfies the set of equations

$$\beta_i(v^*, \delta^*, z^*, w^*) = 0 \quad (i = 1, \dots, 4). \tag{11}$$

Magnitudes of fixed points of a disordered system and of eigenvalues of the stability matrix (magnitudes labeled by asterisks represent the real parts of complex eigenvalues; their imaginary parts are not given in the table)

No.	$v^*$	$\delta^*$	$z^*$	$w^*$	$\lambda_1$	$\lambda_2$	$\lambda_3$	$\lambda_4$
1	0	0	0	0	-1	-1	-1	-1
2	0.044353	0	0	0	0.65355	-0.16923	-0.16923	-0.16923
3	0.044353	0	0.089187	0	0.65355	-0.16923	0.17020	0.17098
4	0.044353	0	0.089187	0.089187	0.65355	-1.16923	-0.17098	-0.17098
5	0	0	0.5	0	-1	-1	1	1
6	0	0	0.5	0.5	-1	-1	1	-1
7	0.066205	0.034478	0	0	0.43130*	0.43130*	-0.03754	-0.03754
8	0.066205	0.034478	0.020432	0	0.43130*	0.43130*	0.03760	0.03767
9	0.066205	0.034478	0.020432	0.020432	0.43130*	0.43130*	0.03760	0.03760
10	0	-0.102000	0.201672	0	0.35678	0.64147	0.38753	0.39067
11	0	-0.102000	0.201672	0.201672	0.35678	0.64147	0.38753	-0.38753

The requirement for a fixed point to be stable reduces to the condition that the eigenvalues  $\lambda_i$  of the matrix

$$B_{i,j} = \frac{\partial \beta_i(u_1^*, u_2^*, u_3^*, u_4^*)}{\partial u_j} \quad (u_i, u_j \equiv v, \delta, z, w) \quad (12)$$

lay in the right-hand complex half-plane. The fixed point with  $v^* = 0$ , corresponding to the tricritical behavior, is a saddle point and should be stable in the directions specified by the variables  $\delta$ ,  $z$ , and  $w$  and unstable in the direction determined by the variable  $v$ . The stabilization of the tricritical fixed point in the direction specified by the variable  $v$  is effected as a result of allowance for the terms of the sixth order in order-parameter fluctuations in the effective Hamiltonian. The fixed point with  $z^* = w^*$ , which corresponds to the tricritical behavior of the second type, is also a saddle point and should be stable in the directions specified by the variables  $v$ ,  $\delta$ , and  $z$  and unstable in the direction determined by the variable  $w$ . Its stabilization can be due to anharmonic effects.

The thus-obtained set of summed  $\beta$  functions contains a wide variety of fixed points. The table contains fixed points of the model, which are most interesting for the description of the critical and tricritical behavior, that lie in the physical region of the values of vertices with  $v, \delta, z$ , and  $w \geq 0$ . Exceptions are fixed points nos. 10 and 11 with  $\delta^* < 0$ , which are given for a more detailed analysis of the effect of lattice defects on some types of multicritical behavior. The table also contains the eigenvalues of the stability matrix for corresponding fixed points.

An analysis of the magnitudes of fixed points and their stability permits us to make the following conclusions: fixed points nos. 1–6 for the uniform systems (with  $\delta^* = 0$ ) are unstable with respect to the effect of disorder produced by structural point defects. The Gaussian fixed point no. 1, being tricritical for the uniform incompressible systems, becomes unstable with

respect to deformation effects. Fixed point no. 2, corresponding to the critical behavior of uniform incompressible systems, also proves to be unstable with respect to the effect of elastic deformations. Fixed point no. 3 determines the critical behavior in uniform compressible systems that are investigated at a constant deformation ( $z^* \neq 0, w^* = 0$ ) or at high constant pressures  $P > P_t = \mu$ . Point no. 3 is unstable with respect to the introduction of disorder but is stable with respect to deformation effects and, according to Fisher's theory of the effect of additional thermodynamic variables [19], the critical behavior at this point is characterized by a renormalization of critical exponents. Point no. 4 is a tricritical point for uniform compressible systems that are investigated at a constant pressure. At this point, the effective Hamiltonian (7) is isomorphic to the Hamiltonian of the uniform incompressible model; therefore, the tricritical exponents should be determined by the values of the corresponding critical exponents of the incompressible Ising model. Point no. 5 is a tricritical point for uniform compressible systems that are investigated at a constant volume or at  $P > P_t$ . This point corresponds to the fixed point of the spherical model, and the tricritical behavior is determined by the critical exponents of this model. Point no. 6 is a tetracritical point for uniform compressible systems; at this point, two tricritical lines meet. This fixed point corresponds to a Gaussian fixed point for incompressible systems; therefore, the system is characterized at this point by mean-field values of the critical exponents.

The fixed points nos. 7–11 in the table correspond to the critical and tricritical behavior of the disordered Ising model with allowance for the compressibility effect. Point no. 7 is a standard impurity fixed point of the incompressible Ising model; however, as was shown by investigations, it is unstable with respect to fluctuational effects induced by elastic deformations. For the disordered compressible Ising model, the criti-

cal behavior at a constant volume or at  $P > P_t^{(\text{imp})}$  is determined by the stable fixed point no. 8. Point no. 9 is a tricritical point for disordered compressible systems. At this point, at the pressure  $P = P_t^{(\text{imp})} = \tilde{\mu}$  the Hamiltonian of the disordered compressible model (7) is isomorphic to the Hamiltonian of the disordered “rigid” Ising model, in which the critical exponents acquire in this case the status of tricritical exponents. For disordered systems, the pressure at the tricritical point  $P_t^{(\text{imp})}$  becomes changed due to the influence of impurities on the elastic moduli of the crystal. Fixed points nos. 10 and 11, which could specify the behavior of disordered compressible systems at the tricritical and tetracritical points, respectively, are characterized, however, by nonphysical negative values of the impurity vertex  $\delta^*$ . This indicates the instability of these types of behavior with respect to the perturbation introduced by lattice defects.

The magnitudes of the vertices obtained in the two-loop approximation for the fixed points corresponding to the critical and tricritical behavior of the compressible Ising model permit one to calculate the critical exponents for the given systems on the basis of the expressions (summed by the Padé–Borel method) for the exponents  $\nu$  and  $\eta$ :

$$\begin{aligned} \nu &= \frac{1}{2}(1 + 6\nu^* + z^* - 2\delta^* - w^* - 4.888889\nu^{*2} \\ &\quad + 16.888889\nu^*\delta^* - 2.814814\delta^{*2}), \\ \eta &= \frac{128}{27}(3\nu^{*2} - 3\nu^*\delta^* + 0.5\delta^{*2}). \end{aligned} \quad (13)$$

The values of the other critical exponents can be obtained from scaling relationships that link them to the exponents  $\nu$  and  $\eta$ . As a result, we obtained the following magnitudes of tricritical exponents for uniform compressible systems at the tricritical point of the first type (fixed point no. 5,  $\nu^* = 0$ )

$$\nu_t = 1, \quad \eta_t = 0, \quad \alpha_t = -1, \quad \beta_t = 0.5, \quad \gamma_t = 2,$$

and at the tricritical point of the second type (fixed point no. 4,  $z^* = w^*$ )

$$\begin{aligned} \nu_t &= 0.63, \quad \eta_t = 0.03, \quad \alpha_t = 0.10, \\ \beta_t &= 0.32, \quad \gamma_t = 1.25. \end{aligned}$$

It is interesting that, at the tricritical point of the first type for the uniform compressible systems, the spherical model is physically realized. However, as was shown in our investigations, the behavior of compressible systems at the given tricritical point is unstable with respect to the influence of lattice defects. Therefore, in the vicinity of the tricritical point, where impurities and other structure defects (inevitably present in the crystal) begin to manifest themselves, their presence leads to a smearing of the tricritical behavior.

The critical behavior of disordered compressible systems that is determined by fixed point no. 8 is characterized by the following critical exponents:

$$\begin{aligned} \nu^{(\text{imp})} &= 0.70, \quad \eta^{(\text{imp})} = 0.03, \quad \alpha^{(\text{imp})} = -0.08, \\ \beta^{(\text{imp})} &= 0.36, \quad \gamma^{(\text{imp})} = 1.37. \end{aligned}$$

In turn, the tricritical exponents for disordered compressible systems at the tricritical point of the second point (fixed point no. 9) have the following values:

$$\begin{aligned} \nu_t^{(\text{imp})} &= 0.68, \quad \eta_t^{(\text{imp})} = 0.03, \quad \alpha_t^{(\text{imp})} = -0.03, \\ \beta_t^{(\text{imp})} &= 0.35, \quad \gamma_t^{(\text{imp})} = 1.33, \end{aligned}$$

which correspond to the critical exponents of the disordered “rigid” Ising model.

### 3. CONCLUSION

The investigations performed show a significant influence of lattice defects on the critical and tricritical behavior of compressible Ising-like systems, which manifests itself both in a change in the magnitudes of critical exponents and in a decrease in the number of types of various multicritical behavior in comparison with uniform compressible systems. As a result, the critical behavior is characterized by renormalized (due to deformation effects) magnitudes of critical exponents of the disordered compressible Ising model, and the tricritical behavior is characterized by critical exponents of the incompressible Ising model. We hope that the effects revealed and the magnitudes of the exponents found will be confirmed in experimental investigations.

### ACKNOWLEDGMENTS

This work was supported in part by the Russian Foundation for Basic Research, project no. 00-02-16455.

### REFERENCES

1. M. A. Anisimov, E. E. Gorodetskiĭ, and V. M. Zaprudskii, *Usp. Fiz. Nauk* **133** (3), 103 (1981) [*Sov. Phys. Usp.* **24**, 57 (1981)].
2. E. B. Amitin, O. A. Nabutovskaya, I. E. Paukov, and K. S. Sukhovey, *J. Chem. Thermodyn.* **16** (3), 719 (1984).
3. E. B. Amitin and O. A. Nabutovskaya, *Fiz. Tverd. Tela (Leningrad)* **26** (4), 1159 (1984) [*Sov. Phys. Solid State* **26**, 702 (1984)].
4. A. I. Larkin and S. A. Pikin, *Zh. Éksp. Teor. Fiz.* **56**, 1664 (1969) [*Sov. Phys. JETP* **29**, 891 (1969)].
5. Y. Imry, *Phys. Rev. Lett.* **33** (21), 1304 (1974).
6. D. J. Bergman and B. I. Halperin, *Phys. Rev. B* **13** (4), 2145 (1976).
7. M. A. de Maura, T. C. Lubensky, Y. Imry, and A. Aharony, *Phys. Rev. B* **13** (4), 2177 (1976).

8. D. E. Khmel'nitskiĭ and V. L. Shneerson, *Zh. Éksp. Teor. Fiz.* **69**, 1100 (1975) [*Sov. Phys. JETP* **42**, 560 (1975)].
9. I. F. Lyuksyutov, *Zh. Éksp. Teor. Fiz.* **73**, 734 (1977) [*Sov. Phys. JETP* **46**, 383 (1977)].
10. M. J. Stephen, *Phys. Rev. B* **13** (5), 2007 (1976).
11. G. Busiello, L. De Cesare, and D. I. Usunov, *J. Phys. A* **17** (8), L441 (1984).
12. A. I. Sokolov, *Fiz. Tverd. Tela (Leningrad)* **29** (9), 2787 (1987) [*Sov. Phys. Solid State* **29**, 1600 (1987)].
13. V. I. Pentegov and M. V. Feĭgel'man, *Zh. Éksp. Teor. Fiz.* **94** (10), 345 (1988) [*Sov. Phys. JETP* **67**, 2154 (1988)].
14. V. M. Lapt'ev and Yu. N. Skryabin, *Phys. Status Solidi B* **91**, K143 (1979).
15. Y. N. Skryabin and A. V. Shchanov, *Phys. Lett. A* **234** (1), 147 (1997).
16. D. J. Amit, *Field Theory, the Renormalization Group, and Critical Phenomena* (McGraw-Hill, London, 1976).
17. J. Zinn-Justin, *Quantum Field Theory and Critical Phenomena* (Clarendon, Oxford, 1989).
18. S. A. Antonenko and A. I. Sokolov, *Phys. Rev. B* **49**, 15901 (1994); K. B. Varnashev and A. I. Sokolov, *Fiz. Tverd. Tela (St. Petersburg)* **38**, 3665 (1996) [*Phys. Solid State* **38**, 1996 (1996)]; A. I. Sokolov, K. B. Varnashev, and A. I. Mudrov, *Int. J. Mod. Phys. B* **12** (12/13), 1365 (1998); A. I. Sokolov and K. B. Varnashev, *Phys. Rev. B* **59** (13), 8363 (1999).
19. M. E. Fisher, *Phys. Rev.* **176** (1), 257 (1968).

*Translated by S. Gorin*

---

LATTICE DYNAMICS  
AND PHASE TRANSITIONS

---

## Diffuse X-ray Scattering in the $\text{Hg}_2\text{I}_2$ Model Incipient Ferroelastics

Yu. F. Markov\*, K. Knorr\*\*, and E. M. Roginskiĭ\*\*\*

\*Ioffe Physicotechnical Institute, Russian Academy of Sciences, ul. Politekhnikeskaya 26, St. Petersburg, 194021 Russia  
e-mail: Yu.Markov@pop.ioffe.rssi.ru

\*\*Universität des Saarlandes, Saarbrücken-6600, Germany

\*\*\*St. Petersburg State Technical University, ul. Politekhnikeskaya 29, St. Petersburg, 195251 Russia

Received December 22, 2000

**Abstract**—This paper reports the first detection and study of diffuse maxima in x-ray scattering in  $\text{Hg}_2\text{I}_2$  incipient ferroelastics. These maxima originate from the formation of clusters of the incipient orthorhombic phase in the paraelastic tetragonal matrix. The nucleation and growth of the clusters are caused by spatial and temporal fluctuations of the order parameter (which correspond to the TA soft mode at the  $X$  point of the Brillouin zone edge) and are induced by the incipient phase transition. Information is obtained on the temperature behavior of the susceptibility and correlation length and on the shape and anisotropy of clusters, and the critical indices are determined. © 2001 MAIK “Nauka/Interperiodica”.

### 1. INTRODUCTION

Crystals of the  $\text{Hg}_2\text{Hal}_2$  univalent-mercury halides (Hal = Cl, Br, I) are isomorphic at room temperature and have a structure consisting of parallel chains of linear molecules, Hal–Hg–Hg–Hal, weakly bound and forming a body-centered tetragonal lattice  $D_{4h}^{17}$  with two formula units in the cell [1]. The chain structure of these crystals accounts for the very strong anisotropy of their physical properties, in particular, a strong elastic anisotropy. For instance,  $\text{Hg}_2\text{I}_2$  crystals have a record-low transverse (TA) sound velocity  $V_{[110]}^{[1\bar{1}0]} = 254$  m/s among solids, and record-high birefringence  $\Delta n = +1.5$  and acoustooptical constants ( $M_2 = 4284 \times 10^{-18}$  s<sup>3</sup>/g) [2]. These crystals are used to an advantage in technology as the main components in acoustic delay lines, acoustooptical filters, polarizers, etc.

When cooled, these crystals undergo improper ferroelastic phase transitions from the tetragonal to the orthorhombic phase ( $D_{4h}^{17} \rightarrow D_{2h}^{17}$ ) at  $T_c = 186$  K ( $\text{Hg}_2\text{Cl}_2$ ) and 144 K ( $\text{Hg}_2\text{Br}_2$ ), which are driven by the condensation of the slowest TA branch at the  $X$  point of the Brillouin zone (BZ) edge in the tetragonal paraelastic phase and are accompanied for  $T \leq T_c$  by unit cell doubling, the  $X \rightarrow \Gamma$  Brillouin zone folding, and the onset of spontaneous deformation [3]. However, attempts at inducing the phase transition in isomorphic  $\text{Hg}_2\text{I}_2$  crystals met with failure down to very low temperatures ( $\sim 1.5$  K). The temperature of the incipient phase transition ( $T_c \cong -20$  K) for these crystals was derived from an extrapolation of the temperature dependence of the soft-mode overtone frequency from

the BZ edge (the  $X$  point) [4, 5]. We succeeded in driving the phase transition in  $\text{Hg}_2\text{I}_2$  only at a high hydrostatic pressure ( $P_c = 9$  kbar at room temperature) [6]. Crystals of the univalent-mercury halides possessing a very simple structure and strongly pronounced phase-transition effects serve as model objects in studies of general problems of structural phase transitions.

This paper reports on an x-ray structural study of the incipient phase transition in  $\text{Hg}_2\text{I}_2$  crystals. The study was carried out at various high-symmetry reciprocal-lattice points of the crystals over a broad temperature range (10–150 K). The attention was primarily focused on the  $X$  points at the BZ edge. Fundamental Bragg reflections at these points in the tetragonal phase ( $D_{4h}^{17}$ ) are forbidden by selection rules but could appear in the incipient phase ( $D_{2h}^{17}$ ) as a result of the phase transition, unit cell doubling, and the  $X \rightarrow \Gamma$  folding of the BZ. However, in the high-temperature paraelastic phase, one can also observe diffuse, usually weak reflections at the BZ edge (in our case, at the  $X$  points), which are related to spatial and temporal fluctuations of the order parameter induced by real or incipient phase transitions and giving rise to the nucleation of low-temperature clusters. This paper presents new information on the temperature behavior of the diffuse x-ray reflections at the  $X$  points of the BZ, on clusters of the incipient orthorhombic phase in the tetragonal paraelastic phase matrix, and on the temperature behavior of their shape and sizes; it also reports on the determination of the values of the critical indices.

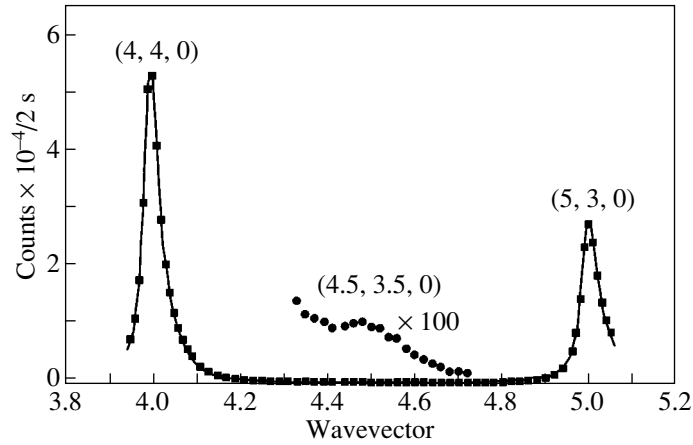


**Fig. 1.** Fundamental Bragg reflections (4, 4, 0) and (5, 3, 0) and a diffuse maximum at the BZ edge point  $X$  (4.5, 3.5, 0) obtained in an extended  $\Gamma$ - $X$ - $\Gamma$  scan at  $T = 15$  K (points are experiment and the solid line is drawn to aid the eye).

## 2. EXPERIMENT

The x-ray diffraction measurements were carried out on a double-circle diffractometer with the  $K_\alpha$  radiation of the copper anode. The low-temperature studies were made using a closed-cycle Cryogenics cryostat with a high temperature stability ( $\approx 0.1$  K). The samples were high-quality single crystals of univalent-mercury iodide,  $3 \times 3 \times 3$  mm in size, cleaved along the (110) and  $(1\bar{1}0)$  planes and cut along (001), which, prior to the measurements, were etched for a few minutes in a solution of aqua regia in distilled water. All the measurements were performed on the  $\{110\}$  planes.

## 3. EXPERIMENTAL RESULTS

We detected and studied a weak diffuse x-ray scattering at the various BZ  $X$  points, primarily at (4.5, 3.5, 0), (3.5, 2.5, 0), and (2.5, 1.5, 0). Because all the main results obtained for these  $X$  points are identical within experimental error, this paper presents only the data obtained in the measurements at the  $X$  point with the maximum indices  $h$  and  $k$  and at  $l = 0$ . Figure 1 displays a typical  $\Gamma$ - $X$ - $\Gamma$  (4.5 +  $\eta$ , 3.5 -  $\eta$ , 0) extended scan over the reciprocal lattice with the (4, 4, 0) and (5, 3, 0) Bragg reflections and a diffuse reflection at the  $X$  point (4.5, 3.5, 0), made at  $T = 15$  K. This scan coincides in direction with the soft-TA-mode propagation in  $\text{Hg}_2\text{I}_2$  crystals. The  $\Gamma$ - $X$ - $\Gamma$  scan offers a possibility to observe, simultaneously with the very weak diffuse maximum, the strong fundamental (Bragg) even ( $h + k + l = 2n$ ) reflections at (4, 4, 0) and (5, 3, 0), which are allowed in the case of the bcc tetragonal lattice ( $D_{4h}^{17}$ ) of these crystals. The odd Bragg reflections ( $h + k + l = 2n + 1$ ) are forbidden for this structure by selection rules and were not detected in extended scans of the  $\text{ZE-X-EZ}$  type [for instance, for (4.5 +  $\eta$ , 3.5 +  $\eta$ , 0), (3.5 +  $\eta$ , 2.5 +  $\eta$ , 0), (2.5 +  $\eta$ , 1.5 +  $\eta$ , 0)].

In Fig. 2, one can see the above diffuse (4.5, 3.5, 0) reflections (maxima) obtained at some fixed temperatures in two mutually perpendicular scans  $\Gamma$ - $X$ - $\Gamma$  and  $\text{ZE-X-EZ}$ . The amplitude and integrated intensity of these reflections increase under cooling and as one approaches the fictitious temperature  $T_c \cong -20$  K of the incipient transition, while their FWHM decreases. The profile of these reflections can be satisfactorily approximated by a Lorentzian (the thick solid lines in Fig. 2)

$$I(\mathbf{K}) = A\Delta^2 / \{\Delta^2 + 4(\mathbf{K} - \mathbf{K}_x)^2\}, \quad (1)$$

where  $A$  is the reflection intensity (amplitude);  $\mathbf{K}$  and  $\mathbf{K}_x$  are the wave vectors; and  $\Delta$  is the reflection half-width. This description permits one to obtain important characteristics (amplitude, integrated intensity, etc.) of these reflections. The large half-width of these diffuse reflections observed in the  $\Gamma$ - $X$ - $\Gamma$  scans is due primarily to interaction with the soft TA branch (wave) near the  $X$  point of the Brillouin zone, which, by analogy with the  $\text{Hg}_2\text{Cl}_2$  crystals, should have a small dispersion in this direction, compared to the large dispersion of this TA branch in the  $\text{ZE-X-EZ}$  scans (for the  $\text{Hg}_2\text{Cl}_2$  crystals, these dispersions are 8 and 255  $\text{meV}^2 \text{\AA}^2$ , respectively) [7].

Figure 3a presents temperature dependences of the integrated diffuse-reflection intensities for  $\text{Hg}_2\text{I}_2$  crystals. In a cooling run, one can observe only a smooth growth of the diffuse reflections in intensity, which is accounted for by the measurements being made far from the phase-transition temperature. There should naturally be no anomalous rise associated with  $T_c$ , because  $T \gg T_c$ . Figure 3b displays the temperature dependence of the half-width of the diffuse reflections. We readily see that this half-width depends strongly on temperature, namely, it decreases with cooling. It is known that the main parameter characterizing structural phase transitions, the correlation length, varies

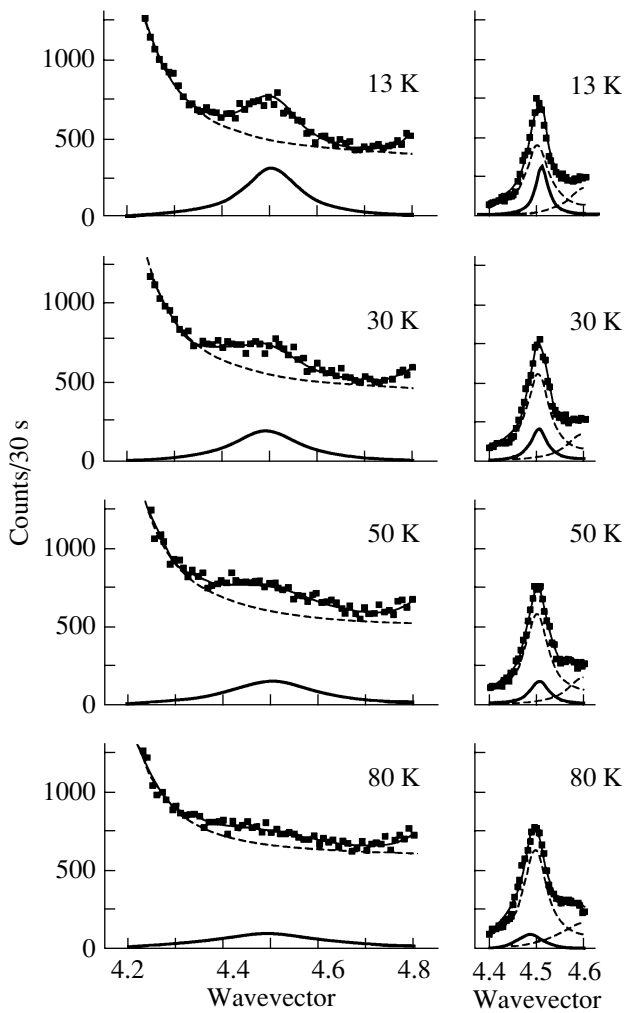


**Fig. 2.** Diffuse maxima (4.5, 3.5, 0) obtained at various temperatures ( $T > T_c$ ) in  $\Gamma$ -X- $\Gamma$  (left) and ZE-X-EZ (right) scans. Points are experiment, the thin solid lines illustrate the results of computer simulation, the dashed lines are the background induced by the tails of the fundamental reflections, and the thick solid lines are the true Lorentzian-shaped diffuse maxima.

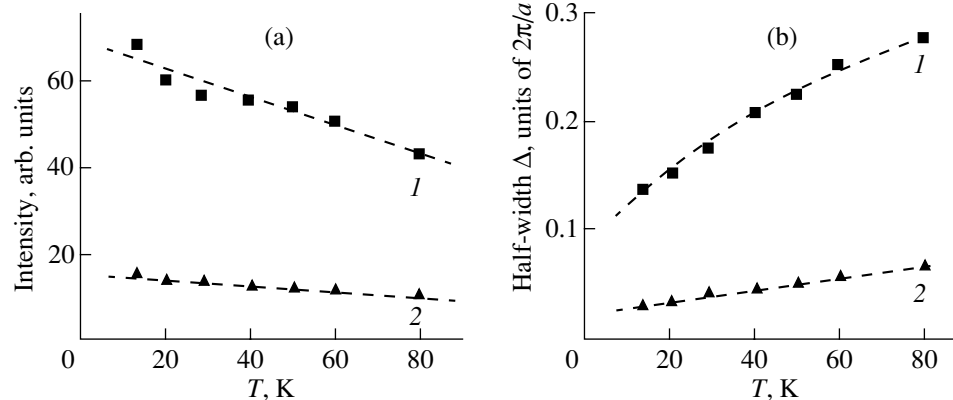


**Fig. 3.** Temperature dependences of (a) the integrated intensities and (b) half-widths of the diffuse reflections at the X point (4.5, 3.5, 0) at the BZ edge obtained in (1)  $\Gamma$ -X- $\Gamma$  and (2) ZE-X-EZ scans. Points are experiment and the dashed lines are drawn to aid the eye.

inversely proportional to the half-width of the diffuse maximum

$$\xi = 2/\Delta, \quad (2)$$

where  $\xi$  is the correlation length and  $\Delta$  is the reflection half-width; the factor 2 in this relation comes from the necessity of using one-half of the FWHM.

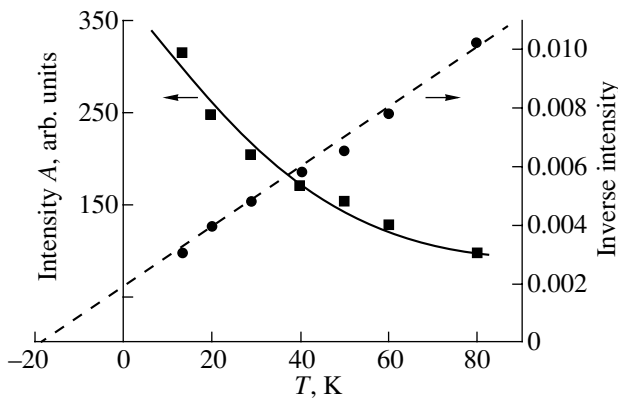
The correlation length is actually the cluster size. Thus, we can extract the temperature dependence of the cluster dimensions and their magnitude from the measured dependence of the diffuse reflection half-width. The correlation lengths measured in the two mutually perpendicular directions used in the experiment are seen to differ by a few times. At 80 K, the correlation lengths are  $\sim 60$  and  $\sim 250$  Å for the  $\Gamma$ -X- $\Gamma$  and ZE-X-EZ directions, respectively. These dimensions increase monotonically as the  $\text{Hg}_2\text{I}_2$  samples are cooled still further.

An important characteristic of diffuse x-ray scattering is the amplitude of the diffraction maxima. By fitting the profile of the diffuse maxima with a Lorentzian (Fig. 2), we obtained the temperature dependence of the amplitude (static susceptibility), which grows under cooling, as the integrated intensity does. Figure 4 presents the temperature dependences of the amplitude of the diffuse maxima and of the inverse intensity for the  $\text{Hg}_2\text{I}_2$  crystals. It is readily seen that under cooling ( $T \rightarrow T_c$ ) the amplitude grows rapidly and that extrapolating the inverse intensity to zero (the dashed line in Fig. 4) yields the fictitious temperature of the incipient phase transition  $T_c \approx -20$  K, which proves to coincide with its value derived by extrapolation of the temperature dependence of the soft-mode overtone at the BZ edge (the X point) [4]. It is known that

$$A \sim t^{-\gamma}, \quad (3)$$

where  $t = (T - T_c)/T_c$  is the reduced temperature and  $\gamma$  is the critical index.





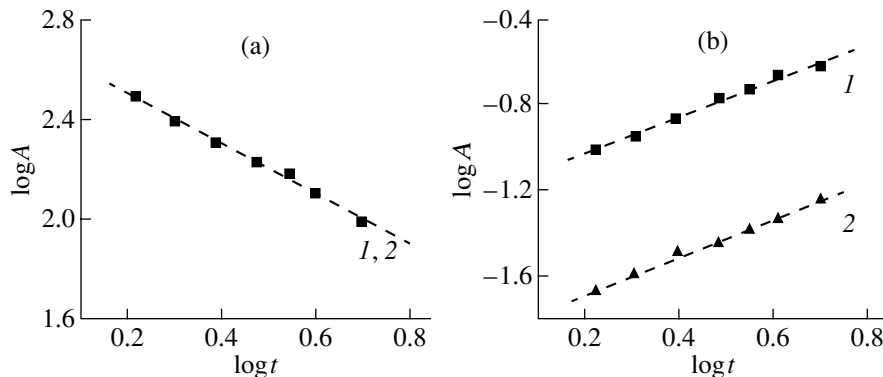
**Fig. 4.** Temperature dependences of the intensity (amplitude) and inverse intensity of the diffuse maxima at the X point (4.5, 3.5, 0) at the BZ edge. Points are experiment, the solid line is drawn to aid the eye, and the dashed straight line is a linear approximation.

Figure 5a plots this relation on a log–log scale; the approximation of this relation by a straight line yielded the critical index  $\gamma$ . Within the temperature range studied (10–100 K), the critical index remains constant,  $1.0 \pm 0.1$  (the values of  $\gamma$  obtained in the two orthogonal scans used in this work are naturally the same).

The dependence of the inverse correlation length on the reduced temperature  $t$  has the form

$$\Delta \sim t^\nu, \tag{4}$$

where  $\nu$  is a critical index. To determine the critical indices  $\nu$  for the two orthogonal scan directions, the experimental temperature dependences of the half-widths of the maxima (Fig. 3b), when subtracting of the instrumental resolution, were replotted on a log–log scale (Fig. 5b). The experimental points of these relations were approximated by straight lines whose slopes yielded the average values of the critical indices,  $0.83 \pm 0.1$  and  $0.87 \pm 0.1$  for the  $\Gamma$ –X– $\Gamma$  and ZE–X–EZ directions, respectively. The difference between these values is within the experimental accuracy.



**Fig. 5.** Log–log dependences of (a) the amplitude  $A$  and (b) the inverse correlation length  $\Delta$  of the diffuse maxima at the X point (4.5, 3.5, 0) at the BZ edge obtained in (1)  $\Gamma$ –X– $\Gamma$  and (2) ZE–X–EZ scans on reduced temperature  $t$ . Points are experiment and dashed lines are linear approximations.

#### 4. DISCUSSION

This is the first time that in the case of an incipient ferroelastic phase transition we have succeeded in observing, considerably above  $T_c$  ( $T \gg T_c$ ), the effects of this transition, namely, diffuse x-ray scattering at the X points at the BZ edge, which is induced by spatial and temporal order-parameter fluctuations and originates from the nucleation of clusters of the incipient ferroelastic phase in the paraelastic tetragonal matrix.

Studies of this diffuse scattering carried out on single crystals of the incipient ferroelastic  $\text{Hg}_2\text{I}_2$  revealed the existence of order-parameter fluctuations (the order parameter corresponds to the opposite shifts of the centers of gravity of the nearest  $\text{Hg}_2\text{I}_2$  molecules in adjacent (110) planes in the [110] direction) [3], which are associated with condensation of the TA soft mode at the X point at the BZ edge. Our studies also showed that the incipient phase transition should be accompanied by unit cell doubling in the basal plane and by the  $X \rightarrow \Gamma$  folding of the BZ. The appearance of the diffuse reflections and the monotonic increase in their intensity under cooling, which is caused by the nucleation and subsequent growth of clusters of the incipient phase, argues for the model of the above-mentioned ferroelastic phase transition. The diffuse scattering observed and studied at high enough temperatures ( $T \gg T_c$ ) originates primarily from the nucleation of static clusters; however, as the temperature is lowered and one approaches  $T_c$ , the dynamic effects associated with spatial and temporal fluctuations of the order parameter should increase, which should become manifest in an increase in the contribution of the dynamic clusters to the diffuse scattering. The latter effect apparently does exist; however, attempts at separating the static and dynamic contributions have failed. The large anisotropy in the correlation length and in the corresponding cluster dimensions (for instance,  $\sim 60$  and  $\sim 250$  Å at  $T = 80$  K) observed in the two orthogonal directions,  $\Gamma$ –X– $\Gamma$  and ZE–X–EZ, can also be determined because, in addition to the above reason (the interaction with the TA soft

wave (branch) at the BZ  $X$  point) but to a lesser degree, of an elastic anisotropy near the surface of these crystals (the average x-ray penetration depth is about 5  $\mu\text{m}$ ).

At the  $X$  points of the BZ one succeeds in observing, even at temperatures of the order of 100 K, broad weak maxima, whose comparison with the nearest Bragg reflections (see, for instance, Fig. 1) permits evaluation of the amount of the orthorhombic ferroelastic phase present in the tetragonal paraelastic phase matrix, which at temperatures of  $\sim 10$  K constitutes a few hundredths of a percent. Our experiments suggest, however, a general conclusion that, even in the case of incipient phase transitions, at real temperatures there exist clusters of the incipient phase, which represent volume defects degrading the crystal quality and narrowing the area of their practical application.

It appears only natural to associate the nucleation of static clusters with the presence of various growth-induced defects, such as dislocations, residual elastic strain fields, and point defects, in the crystals under study. We may recall that these crystals exhibit a strong dependence (increase) of the phase-transition temperature  $T_c$  on the hydrostatic pressure (35 K/kbar) [6]; i.e., various defects creating elastic strain fields around them may induce nucleation of the incipient orthorhombic phase. Additionally, considered from the standpoint of the minimum of the elastic and surface energies, the formation of nuclei of the ferroelastic phase in the paraelastic phase matrix in the form of extended small-radius cylinders or very thin plates is preferable. Theoretical estimates made for the  $\text{Hg}_2\text{I}_2$  crystals suggest that the nuclei can be created only in the form of plates parallel to the  $\{110\}$  planes and that the cross section of these nuclei may have two different dimensions, the thickness and the width along  $[110]$  and  $[1\bar{1}0]$ . It is the corresponding anisotropy (different correlation lengths) that was revealed in our x-ray scans made in the  $\Gamma-X-\Gamma$  and  $\text{ZE}-X-\text{EZ}$  directions (Figs. 2, 3).

It is of interest to compare the critical indices thus obtained with similar characteristics of model ferroelectric perovskites undergoing first-order (close to second order) phase transitions with a soft-mode condensation at the BZ-edge  $R$  point. The critical index  $\gamma$  of  $\text{Hg}_2\text{I}_2$ , which describes the temperature dependence of the diffuse-reflection amplitude (the static suscepti-

bility) well enough, is constant and equal to 1.0. The model perovskites  $\text{KMnF}_3$ ,  $\text{RbCaF}_3$ , and  $\text{SrTiO}_3$  are characterized by  $\gamma = 1.19$ , 1.34, and 1.40, respectively [8]. The average values of the critical index  $\nu$  derived from the temperature dependence of the reciprocal correlation length in  $\text{Hg}_2\text{I}_2$  are 0.83 and 0.87 for the  $\Gamma-X-\Gamma$  and  $\text{ZE}-X-\text{EZ}$  scan directions, respectively. These values are somewhat larger than the corresponding indices for the perovskite crystals ( $\nu = 0.62$  for  $\text{KMnF}_3$ , 0.64 for  $\text{RbCaF}_3$ , and 0.83 for  $\text{SrTiO}_3$ ) [8]. The above differences among the indices may possibly be accounted for by the various extents to which the first-order phase transitions under consideration are close to second-order ones and by defects.

#### ACKNOWLEDGMENTS

The authors are indebted to A.A. Kaplyanskiĭ for assistance and useful discussions.

This study was supported by the Russian Foundation for Basic Research, grant nos. 98-02-16144 and 01-02-17599.

#### REFERENCES

1. H. Mark and J. Steinbach, *Z. Krystallogr.* **64**, 78 (1926).
2. *Proceedings of the 2nd International Symposium on Univalent Mercury Halides, Trutnov, 1989.*
3. A. A. Kaplyanskiĭ, Yu. F. Markov, and C. Barta, *Izv. Akad. Nauk SSSR, Ser. Fiz.* **43** (8), 1641 (1979).
4. B. S. Zadokhin, A. A. Kaplyanskiĭ, Yu. F. Markov, and C. Barta, *Fiz. Tverd. Tela (Leningrad)* **20** (10), 3121 (1978) [*Sov. Phys. Solid State* **20**, 1800 (1978)].
5. A. A. Kaplyanskiĭ, K. Knorr, Yu. F. Markov, and A. Sh. Turaev, *Fiz. Tverd. Tela (St. Petersburg)* **36** (9), 2744 (1994) [*Phys. Solid State* **36**, 1497 (1994)].
6. C. Barta, A. A. Kaplyanskiĭ, Yu. F. Markov, and V. Yu. Mirovitskiĭ, *Fiz. Tverd. Tela (Leningrad)* **27** (8), 2500 (1985) [*Sov. Phys. Solid State* **27**, 1497 (1985)].
7. J. P. Benoit, G. Hauret, and J. Levebvre, *J. Phys. (Paris)* **43**, 641 (1982).
8. U. J. Nicholls and R. A. Cowley, *J. Phys. C* **20**, 3417 (1987).

*Translated by G. Skrebtsov*

# Lattice IR Reflection Spectra of ZnSe/Zn<sub>1-x</sub>Cd<sub>x</sub>Se Strained Superlattices Grown on a GaAs Substrate by Molecular Beam Epitaxy

V. S. Vinogradov, L. K. Vodop'yanov, S. P. Kozyrev, and Yu. G. Sadof'ev

Lebedev Institute of Physics, Russian Academy of Sciences, Leninskii pr. 53, Moscow, 117924 Russia

e-mail: vodopian@sci.Lebedev.ru

Received November 21, 2000

**Abstract**—This paper reports the results of measurements of the lattice IR reflection spectra for the ZnSe/Zn<sub>1-x</sub>Cd<sub>x</sub>Se ( $x = 0.20, 0.40,$  and  $0.47$ ) superlattices grown on a GaAs(001) substrate by molecular beam epitaxy. Mathematical analysis of the experimental spectra has revealed the presence of only one lattice mode rather than the two expected IR-active lattice modes of the ZnSe and Zn<sub>1-x</sub>Cd<sub>x</sub>Se layers. This result is explained by the fact that the frequencies of the lattice modes of these layers become closer in magnitude under the effect of internal elastic stresses. © 2001 MAIK “Nauka/Interperiodica”.

## 1. INTRODUCTION

Superlattices based on II–VI semiconductor compounds have attracted considerable attention of researchers owing to their interesting physical properties and possible practical applications (for example, in light emitters operating in the green and blue spectral ranges). However, the optical properties of these superlattices have not been adequately investigated. The ZnSe/Zn<sub>1-x</sub>Cd<sub>x</sub>Se superlattices are of particular interest, because the ZnCdSe solid solution forming quantum wells is characterized by a single-mode transformation of the phonon spectrum [1], which is very unusual for alloys of II–VI compounds. In earlier works, thin layers of this alloy were used to construct and investigate different structures with quantum wells [2] and quantum dots [3]. As far as we know, research dealing with the lattice vibrations in ZnSe/ZnCdSe superlattices has never been published.

Unlike the well-known superlattices based on the GaAs–AlAs pair with matched lattice parameters, the ZnSe/ZnCdSe superlattices (in which the lattice matching is rather imperfect) are characterized by internal elastic stresses that substantially affect their physical properties.

The effect of internal stresses on the superlattice properties can be judged from the shift of the lattice modes by using optical vibrational spectroscopic methods, such as Raman and IR spectroscopy. Raman spectroscopy provides information on thin near-surface layers, whereas IR spectroscopy makes it possible to investigate the microstructure in the bulk of the material. In particular, the lattice IR reflection technique is very sensitive to internal stresses arising in superlattices.

According to recent publications, the strained state of quantum-size structures has a complex nature. These structures are characterized by several critical thicknesses: the minimum critical thickness corresponds to the onset of the formation of misfit dislocations, and the maximum critical thickness is associated with the attainment of the relaxed state at large distances [4]. There is experimental evidence obtained by different methods that strained states in the same samples but at different depths manifest themselves in various ways. For example, Hernandez-Corderon *et al.* [5] studied ZnSe films on a GaAs(001) substrate by Raman spectroscopy (the data were obtained for a thin surface layer) and found that elastic stresses completely relax when the film thickness exceeds the critical value ( $\sim 0.1 \mu\text{m}$ ). On the other hand, investigation of the same samples by x-ray diffraction (the data were obtained in the bulk of the material) revealed that residual stresses in the studied films are observed at a thickness of larger than  $2 \mu\text{m}$ .

Earlier [1, 6], we studied the Zn<sub>1-x</sub>Cd<sub>x</sub>Se films on a GaAs(001) substrate by lattice IR reflection spectroscopy, which also provided information for large depths. In these works, we examined the shift in the frequencies of the IR-active modes and revealed that residual stresses can occur up to film thicknesses of the order of  $1 \mu\text{m}$ . In the present work, the vibrational spectra of ZnSe/Zn<sub>1-x</sub>Cd<sub>x</sub>Se superlattices on a GaAs(001) substrate were measured by the lattice IR reflection method for the first time. It was found that the IR spectra of the superlattices exhibit only one lattice mode at an intermediate frequency rather than the two expected IR-active modes of the ZnSe and Zn<sub>1-x</sub>Cd<sub>x</sub>Se layers. This result was explained by the fact that the lattice modes of the layers approach each other in frequency under the effect of internal elastic stresses.

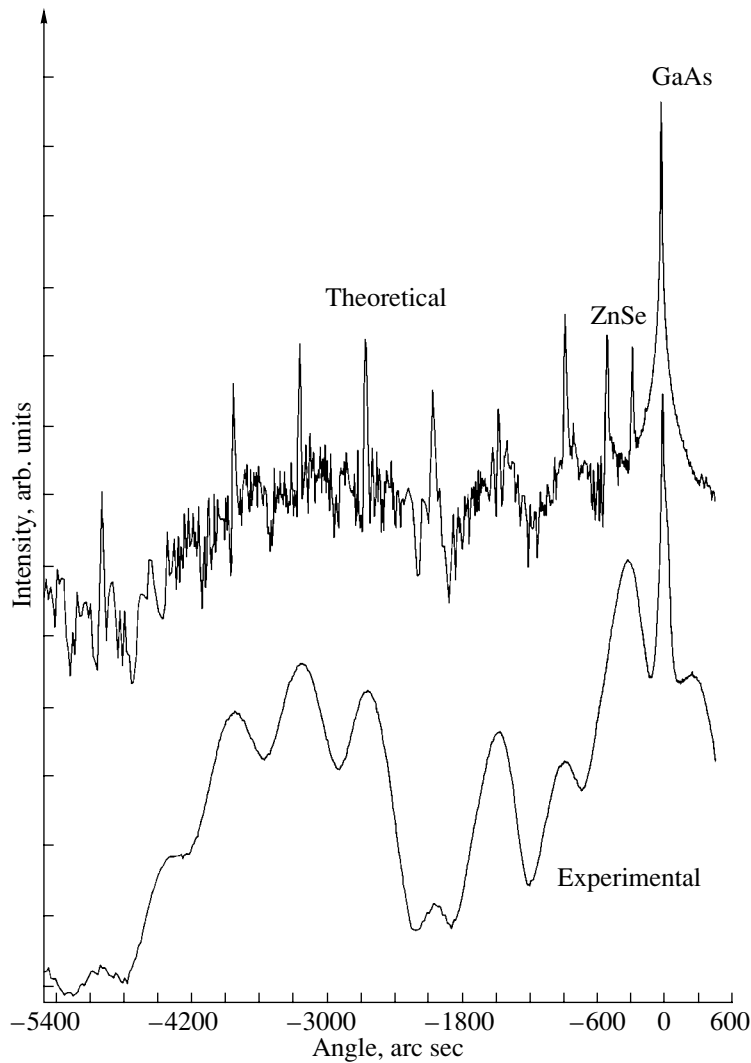


**Fig. 1.** X-ray diffraction patterns of the ZnSe/Zn<sub>0.53</sub>Cd<sub>0.47</sub>Se//GaAs superlattice. The thicknesses of barriers (ZnSe) and wells (Zn<sub>0.53</sub>Cd<sub>0.47</sub>Se) are equal to 65 and 50 Å, respectively; the thickness of the buffer layer (ZnSe) is 0.6 μm; and the number of periods is 95. The upper curve represents the theoretical calculation. The peaks attributed to the substrate (GaAs) and the buffer layer (ZnSe) are labeled. The other peaks located to the left correspond to different diffraction orders of the superlattice.

## 2. GROWTH OF SUPERLATTICES AND MEASUREMENTS

The ZnSe/Zn<sub>1-x</sub>Cd<sub>x</sub>Se ( $x = 0.20, 0.40,$  and  $0.47$ ) superlattices on a GaAs substrate were grown by molecular beam epitaxy. The epitaxy was performed on chromium-terminated GaAs(100) substrates with a misorientation of  $3^\circ$  with respect to the  $\{110\}$  direction by the evaporation of Zn, Cd, and Se special-purity (6N) elements from individual molecular sources. The substrate surface was cleaned from a layer of natural oxides by heating at  $580^\circ\text{C}$  under vacuum in the absence of selenium and zinc vapors. After cooling to the epitaxial growth temperature ( $280\text{--}320^\circ\text{C}$ ), the substrate was held in zinc vapors at an equivalent pressure of  $3 \times 10^{-5}$  Pa for 100 s in order to prevent the formation of chemical compounds of selenium with gallium which is present in excess on the GaAs substrate sur-

face due to incongruent evaporation during heating under vacuum.

In the course of the superlattice growth, the ratio between the equivalent pressure of the Se molecular beam and the total pressure of the Zn and Cd molecular beams was chosen close to two in order to ensure the coexistence of the superstructure consisting of a mixture of  $(1 \times 2)$  and  $c(2 \times 2)$  reconstructions and the superstructure corresponding to the conditions of the stoichiometric growth on the surface. As the cadmium content in the growing films increased, the epitaxy temperature decreased. The growth rate was maintained equal to  $0.3\text{--}0.5$  μm/h. The composition of the grown layers was checked against both the intensity ratio of the Zn *LMM* and Se *LMM* Auger lines and the location of the emission lines of quantum wells in the cathodoluminescence spectra.

Figure 1 shows the experimental x-ray diffraction pattern and the calculated curve for one of the superlattices (sample no. 237). The x-ray diffraction pattern was measured on a DRON diffractometer. The large number of equidistant peaks shown in the x-ray diffraction pattern corresponds to different diffraction orders. This indicates that the studied structure has a superlattice.

The long-wavelength IR reflection spectra were recorded on a laboratory grating infrared spectrometer with an OAP-5 optoacoustic receiver as an infrared detector with a spectral resolution of no worse than  $1 \text{ cm}^{-1}$ .

### 3. DISPERSION ANALYSIS OF IR REFLECTION SPECTRA

We studied the IR reflection spectra of three  $\text{ZnSe}/\text{Zn}_{1-x}\text{Cd}_x\text{Se}$  ( $x = 0.20, 0.40, \text{ and } 0.47$ ) superlattices. Figure 2 displays the lattice IR reflection spectrum measured for the  $\text{ZnSe}/\text{Zn}_{1-x}\text{Cd}_x\text{Se}$  ( $x = 0.20$ ) superlattice at 300 K (curve 1), the calculated spectrum (curve 2), and the IR reflection spectrum of the GaAs substrate (curve 3). As can be seen from this figure, the lattice IR reflection spectrum of the superlattice contains only one band. This is confirmed by the subsequent mathematical analysis. The other superlattices have similar lattice reflection spectra, but the band that corresponds to the lattice mode of the superlattice is shifted in frequency. All the reflection spectra exhibit frequent oscillations associated with the interference from the GaAs substrate 400–500  $\mu\text{m}$  thick. The inset shows these oscillations together with the experimental points on an enlarged scale of the wave numbers. The oscillation period is approximately equal to  $2.5 \text{ cm}^{-1}$  (or  $0.8 \mu\text{m}$ ). The experimental points depicted in the inset indicate a high spectral resolution (better than  $1 \text{ cm}^{-1}$ ) of the instrument used for recording the reflection spectra.

In order to perform the dispersion analysis of the lattice reflection spectra of the superlattices, let us consider a model structure formed by a thin film (superlattice + buffer layer) on a bulk (semi-infinite) substrate. In the framework of this model structure for a film of thickness  $L$  with a dielectric function  $\epsilon_f(\omega)$  and a substrate with a dielectric function  $\epsilon_s(\omega)$  in normally incident light, the amplitude reflectivity has the following form [7]:

$$r_{1f_s}(\omega) = \frac{r_{1f}(\omega) + r_{f_s}(\omega) \exp(i2\beta)}{1 + r_{1f}(\omega)r_{f_s}(\omega) \exp(i2\beta)}, \quad (1)$$

where

$$r_{1f}(\omega) = \frac{1 - \sqrt{\epsilon_f(\omega)}}{1 + \sqrt{\epsilon_f(\omega)}}, \quad r_{f_s}(\omega) = \frac{\sqrt{\epsilon_f(\omega)} - \sqrt{\epsilon_s(\omega)}}{\sqrt{\epsilon_f(\omega)} + \sqrt{\epsilon_s(\omega)}},$$

$$\beta = \frac{2\pi L \sqrt{\epsilon_f(\omega)}}{\lambda}.$$

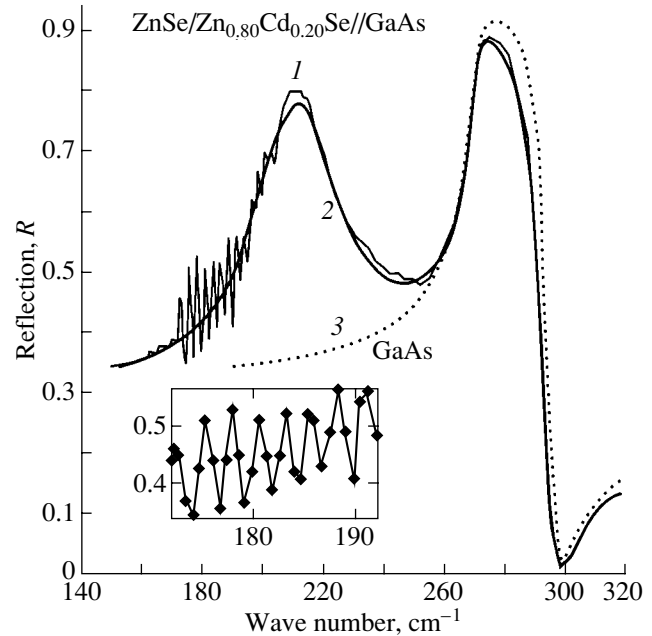


**Fig. 2.** (1) Experimental and (2) calculated IR reflection spectra of the  $\text{ZnSe}/\text{Zn}_{0.80}\text{Cd}_{0.20}\text{Se}/\text{GaAs}$  superlattice. The thicknesses of barriers ( $\text{ZnSe}$ ) and wells ( $\text{Zn}_{0.80}\text{Cd}_{0.20}\text{Se}$ ) are equal to 110 and 70  $\text{\AA}$ , respectively, and the number of periods is 90. (3) IR reflection spectrum of the GaAs substrate. The inset shows the experimental points on an enlarged scale in the wave number range 170–190  $\text{cm}^{-1}$ . The oscillation period is approximately equal to  $2.5 \text{ cm}^{-1}$ .

Here,  $\lambda = 10^4/\omega$  is the wavelength. The reflectivity is defined as  $R(\omega) = |r_{1f_s}(\omega)|^2$ . The specific features in the reflection spectra of thin films and superlattices on a substrate in the range of lattice vibrations and their interpretation were discussed in more detail in our earlier work [8].

The dielectric function  $\epsilon_f(\omega)$  of the film was considered in the classical additive form

$$\epsilon_f(\omega) = \epsilon_\infty + \sum_j \frac{S_j \omega_{ij}^2}{\omega_{ij}^2 - \omega^2 - i\omega\gamma_j}. \quad (2)$$

In calculations of the reflectivity  $R(\omega)$ , we varied the following parameters in the formula for  $\omega_{ij}$ : the frequency  $S_j$  of the  $j$ th TO-phonon mode, the oscillator strength  $S_j$  of the  $j$ th TO-phonon mode, and the attenuation parameter  $\gamma_j$ .

The dispersion analysis of the lattice reflection spectra of the superlattices on the substrate revealed the presence (to within the spectral resolution of the instrument) of only one lattice mode rather than the expected modes of the  $\text{ZnSe}$  and  $\text{Zn}_{1-x}\text{Cd}_x\text{Se}$  layers forming the superlattice. The characteristics of the  $\text{ZnSe}/\text{Zn}_{1-x}\text{Cd}_x\text{Se}$  ( $x = 0.20, 0.40, \text{ and } 0.47$ ) superlattices and the results of the dispersion analysis of the experimental IR reflection spectra are listed in Table 1.

4. CALCULATION OF THE CHANGE  
IN THE FREQUENCIES OF IR-ACTIVE MODES  
OF A SUPERLATTICE  
UNDER THE EFFECT OF ELASTIC STRESSES:  
RESULTS AND DISCUSSION

Let us now explain the presence of the sole transverse mode in the spectrum. We assume that the transverse modes of the superlattice layers approach each other in frequency due to internal stresses so that the difference in their frequencies becomes less than their width and, hence, these modes become indistinguishable in the experimental spectra.

In order to verify this assumption, we calculated the shifts in the frequencies of the transverse modes under

**Table 1.** Characteristics of the studied samples and dispersion analysis data for IR reflection spectra of ZnSe/ZnCdSe superlattices

Sample no.	243	178	237
$x$	0.20	0.40	0.47
$l_b, \text{\AA}$	110	100	65
$l_w, \text{\AA}$	70	50	50
$N_p$	90	100	95
$l_{\text{buf}}, \mu\text{m}$	0.5	1.0	0.6
$\omega_t, \text{cm}^{-1}$	204.5	202.0	202.0
$S$	3.2	3.1	2.9
$\Gamma, \text{cm}^{-1}$	4.5	6.5	6.5
$\epsilon_\infty$	5.5	5.5	5.5
$l_{SL}, \mu\text{m}$	1.6	1.5	1.09

Note:  $x$  is the composition;  $l_b$  and  $l_w$  are the thicknesses of the barrier (ZnSe) and the well (ZnCdSe), respectively;  $N_p$  is the number of superlattice periods;  $l_{\text{buf}}$  is the thickness of the buffer (ZnSe);  $\omega_t$ ,  $S$ , and  $\Gamma$  are the characteristics of a transverse optical phonon: the frequency, oscillator strength, and attenuation parameter, respectively;  $\epsilon_\infty$  is the high-frequency part of the dielectric function; and  $l_{SL}$  is the thickness of the superlattice, including the thickness of the buffer layer.

**Table 2.** Elastic constants and their combinations  $C(x)$  (in terms of  $10^{10} \text{ dyn cm}^{-2}$ ) for  $\text{Zn}_{1-x}\text{Cd}_x\text{Se}$

$x$	0	0.2	0.4	0.47	1
$C_{11}$	85.9	83.7/83.2	81.5/80.1	80.7/–	74.9
$C_{12}$	50.6	49.7/49.2	48.8/47.2	48.5/–	46.1
$C(x)$	76.9	74.43/74.5	71.9/71.1	70.9/–	64.3

Note: In columns 3–5, the first value was obtained by interpolation of the boundary elastic constants and the second value was derived by extrapolation of the constants for the composition  $x = 0$  (ZnSe).

the effect of stresses in the superlattice layers. The calculation was performed using the relationship [6]

$$\frac{\Delta\omega_t}{\omega_t} = k\left(-\frac{\Delta a}{a}\right),$$

$$k = \frac{1}{3}(1-\gamma)^{-1}\left[\left(1-2\frac{\rho}{R_0}\right)^{-1}\left(\frac{R_0}{\rho}\left(1-\frac{C_{12}}{C_{11}}\right)\right.\right. \quad (3)$$

$$\left.\left.-\left(1+2\frac{C_{12}}{C_{11}}\right)-3\frac{\rho}{R_0}\right)-\frac{9}{5}\gamma\left(2-\frac{C_{12}}{C_{11}}\right)\right],$$

where  $a$  and  $\Delta a$  are the lattice constant and its change along the layer plane, respectively;  $C_{11}$  and  $C_{12}$  are the elastic constants;  $\rho/R_0$  is the ratio of the repulsive potential parameter to the distance between the neighboring anion and cation;  $\gamma = ((\omega_l/\omega_t)^2 - 1)((\omega_l/\omega_t)^2 + 2)^{-1}$ ; and  $\omega_l$  and  $\omega_t$  are the frequencies of longitudinal and transverse long-wavelength phonons, respectively.

The value of  $k = k(0) = 3.33$  for ZnSe was calculated in [6]. This constant for CdSe in the cubic phase was determined from the quantities  $\omega_l$ ,  $\omega_t$ ,  $C_{11}$ , and  $C_{12}$  for the wurtzite phase (because their values for the cubic phase are unavailable) and the lattice constant  $a = 6.052 \text{ \AA}$ , which was obtained by extrapolation [9]. As a result, we obtained  $k = k(1) = 3.67$  for CdSe. For the solid solution of composition  $x$ , the  $k(x)$  quantity was calculated according to the formula  $k(x) = (1-x)k(0) + xk(1)$ .

The lattice constant  $a'$  for layers in the lateral direction was determined from the equilibrium condition for two elastic layers that are stretched over each other and have free surfaces, i.e., under the assumption that the superlattice “separates” from the substrate. The expression for  $a'$  has the form

$$a' = \frac{d_2 C_2 + d_3 C_3}{d_2 C_2/a_2 + d_3 C_3/a_3}, \quad (4)$$

where  $a_i$ ,  $d_i$ , and  $C_i$  are the lattice constants, the total thicknesses of layers, and the combinations of elastic constants  $C(x) = C_{11} + C_{12} - 2C_{12}^2/C_{11}$  for the binary ( $i = 2$ , ZnSe) and ternary ( $i = 3$ ,  $\text{Cd}_x\text{Zn}_{1-x}\text{Se}$ ) materials, respectively.

For lack of reliable information on the elastic constants for the cubic  $\text{Zn}_{1-x}\text{Cd}_x\text{Se}$  phase, their values were determined by the interpolation or extrapolation of the available data for the boundary components. For the interpolation, we used the formula  $C_{ik}(x) = (1-x)C_{ik}(0) + xC_{ik}(1)$ . The elastic constants  $C_{ik}(0)$  (for ZnSe) and  $C_{ik}(1)$  (for CdSe in the wurtzite phase) were taken from [9]. The extrapolation was performed using the relationship  $C_{ik}(x) = C_{ik}(0)[a(0)/a(x)]^3$ , in which the values of  $a(x)$  were taken from [10].

The elastic constants and their combinations  $C(x)$  are given in Table 2. It is seen from this table that the elastic constants obtained by the two methods are close

to each other. Henceforth, we will use the elastic constants obtained by the first method. Now, we determine the frequencies of transverse optical phonons in the superlattice layers for sample no. 243 ( $x = 0.20$ ). By using the data on the layer thickness and the combination  $C(x)$  (Tables 1, 2) and the lattice constants  $a_2 = 5.6686$  Å for ZnSe [9] and  $a_3 = 5.729$  Å for the  $\text{Cd}_{0.2}\text{Zn}_{0.8}\text{Se}$  solid solution [10], we obtain the lattice constant for the layers in the lateral direction  $a' = 5.692$  Å. In this case, the tensile and compressive strains for the ZnSe and  $\text{Cd}_{0.2}\text{Zn}_{0.8}\text{Se}$  layers are found to be  $(\Delta a/a)_2 = (a' - a_2)/a_2 = 0.4\%$  and  $(\Delta a/a)_3 = (a' - a_3)/a_3 = -0.65\%$ .

Substitution of these strains and the constants  $k(0) = 3.33$  and  $k(0.2) = 3.4$  into formula (3) gives the relative changes of the frequencies in the layers:  $(\Delta\omega_i/\omega_i)_2 = -1.33\%$  and  $(\Delta\omega_i/\omega_i)_3 = 2.21\%$ . Then, using the frequencies of transverse phonons in the ZnSe and  $\text{Cd}_{0.2}\text{Zn}_{0.8}\text{Se}$  unstrained materials, namely,  $\omega_{i2} = 206.5$   $\text{cm}^{-1}$  and  $\omega_{i3} = 200$   $\text{cm}^{-1}$ , we derive the corresponding frequencies in the strained superlattice layers:  $\omega'_{i2} = 203.7$   $\text{cm}^{-1}$  and  $\omega'_{i3} = 204.4$   $\text{cm}^{-1}$ .

The calculations for the other samples were carried out in a similar way. The lattice constant for the sample with  $x = 0.35$ – $0.40$  was also taken from [10], and the lattice constant for the sample with  $x = 0.47$  was determined by a linear interpolation of the available data for ZnSe and CdSe in the cubic phase. The results of calculations are summarized in Table 3. Analysis of the tabulated data shows that the transverse modes of the ZnSe and  $\text{Zn}_{1-x}\text{Cd}_x\text{Se}$  layers in the superlattice substantially approach each other in frequency. Under the effect of internal elastic stresses, the difference between the mode frequencies decreases by a factor of 5–9 depending on the sample and becomes two to six times less than the width  $\gamma_i$ .

Thus, the presence of the sole transverse mode in the IR reflection spectrum of the  $\text{ZnSe}/\text{Zn}_{1-x}\text{Cd}_x\text{Se}$  superlattice is explained by the fact that the lattice modes of the layers become closer in frequency due to internal elastic stresses. This inference remains valid with allowance made for the effect of the buffer. The upper estimate of the buffer effect can be obtained by assuming that the buffer is in the unrelaxed state and has no elastic contact with the substrate. In this case, the lattice constant  $a'$  should be calculated according to formula (4) in which the thickness  $d_2$  includes the buffer thickness. Then, the difference between the frequencies  $|\omega'_{i2} - \omega'_{i3}|$  only decreases; however, the additional effect itself appears insignificant.

An interesting question now arises as to why the buffer layer does not manifest itself in the IR spectrum (as well as in the x-ray diffraction pattern). This can be explained by the smaller thickness of the buffer layer as compared to the superlattice and also by the structural

**Table 3.** Frequencies  $\omega'_{i2}$  and  $\omega'_{i3}$  (in  $\text{cm}^{-1}$ ) of IR-active phonons in ZnSe and  $\text{Zn}_{1-x}\text{Cd}_x\text{Se}$  strained superlattice layers, their frequencies  $\omega_{i2}$  and  $\omega_{i3}$  in the unstrained materials, lattice parameters  $a'$  for layers in the lateral direction, and lattice parameters  $a_2$  and  $a_3$  for the unstrained materials

Sample no.	243	178	237
$x$	0.20	0.40	0.47
$a_2$ , Å	5.6687	5.6687	5.6687
$a_3$ , Å	5.729	5.802	5.8489
$a'$ , Å	5.692	5.711	5.742
$\omega_{i2}$ , $\text{cm}^{-1}$	206.5	206.5	206.5
$\omega_{i3}$ , $\text{cm}^{-1}$	200	193	189
$\omega'_{i2}$ , $\text{cm}^{-1}$	203.7	201.3	197.6
$\omega'_{i3}$ , $\text{cm}^{-1}$	204.4	203.5	201.1

Note: Frequencies  $\omega'_{i2}$  and  $\omega'_{i3}$  were calculated by formula (3), and the parameter  $a'$  was determined according to formula (4).

imperfection that leads to a large broadening of the IR-active modes of this layer.

#### ACKNOWLEDGMENTS

This work was supported by the Russian Foundation for Basic Research, project no. 00-2-16571.

#### REFERENCES

1. L. K. Vodop'yanov, S. P. Kozyrev, and Yu. G. Sadof'ev, *Fiz. Tverd. Tela (St. Petersburg)* **41** (6), 982 (1999) [*Phys. Solid State* **41**, 893 (1999)].
2. P. Gingo, M. de Vittorio, R. Rinald, and R. Cingolani, *Phys. Rev. B* **54** (23), 16934 (1996).
3. M. Strassberd, V. Kutzer, U. Pohl, *et al.*, *Appl. Phys. Lett.* **72** (8), 972 (1998).
4. J. S. Milnes, C. Morhain, S. A. Telfer, *et al.*, *Appl. Phys. Lett.* **73** (21), 3141 (1998).
5. I. Hernández-Corderon, E. López-Luna, J. Luyo, *et al.*, *J. Cryst. Growth* **175/176**, 571 (1997).
6. V. S. Vinogradov, L. K. Vodop'yanov, S. P. Kozyrev, and Yu. G. Sadof'ev, *Fiz. Tverd. Tela (St. Petersburg)* **41** (11), 1948 (1999) [*Phys. Solid State* **41**, 1786 (1999)].
7. H. W. Verleur, *J. Opt. Soc. Am.* **58**, 1356 (1968).
8. S. P. Kozyrev, *Fiz. Tverd. Tela (St. Petersburg)* **36** (10), 3008 (1994) [*Phys. Solid State* **36**, 1601 (1994)].
9. *Landolt-Börnstein: Numerical Data and Functional Relationship in Science and Technology*, Ed. by K.-H. Hellwege (Springer-Verlag, Berlin, 1982), Vol. 178, pp. 139, 202.
10. N. N. Berchenko, V. E. Krevs, and V. G. Sredin, *Semiconductor Solid Solutions  $A^2B^6$  and Their Application* (Voenizdat, Moscow, 1982).

*Translated by O. Borovik-Romanova*

---

LOW-DIMENSIONAL SYSTEMS  
AND SURFACE PHYSICS

---

# Renormalization of the Electron Spectrum by Confined and Interface Phonons in a Spherical Nanoheterosystem ( $\beta$ -HgS/CdS)

N. V. Tkach, V. A. Golovatskiĭ, O. M. Voitsekhivskaya,  
M. Ya. Mikhal'ova, and R. B. Fartushinskiĭ

*Chernivtsi National University, Chernivtsi, 58012 Ukraine*

*e-mail: theormyk@chdu.cv.ua*

Received August 10, 2000; in final form, December 5, 2000

**Abstract**—The mechanisms of the electron spectrum renormalization by confined ( $L$ ) and interface ( $I$ ) phonons in a spherical quantum dot (QD) embedded in a semiconducting sphere are studied for the specific case of the  $\beta$ -HgS/CdS nanosystem. It is shown that, in view of the absence of interaction between an electron in spherically symmetric states and interface phonons forming only one bound state in a small-size QD, the shift  $\Delta$  of this single level is formed only by confined phonons. As the size of the QD increases, the contribution of  $L$  and  $I$  phonons to  $\Delta$  changes accordingly ( $L$  phonons slightly dominate), and the shift varies from  $\Delta_{\text{CdS}}^{3D}$  to  $\Delta_{\text{HgS}}^{3D}$ . © 2001 MAIK “Nauka/Interperiodica”.

## 1. INTRODUCTION

The electron–phonon interaction in low-dimensional nanoheterosystems is studied with the help of various theoretical models, which sometimes lead to different results. A detailed analysis of the advantages and drawbacks of the three main models of the electron–phonon interaction is given by Wong and Lei [1] for a quasi-one-dimensional cylindrical quantum wire. They proved that the semimicroscopic Huang–Zhy (HZ) model and the dielectric continuum (DC) model give close results, which are better than those obtained in the hydrodynamic continuum (HC) model.

Since the DC model is much simpler than the HZ model, it is not surprising that this model forms the basis of the study of the electron–phonon interaction in simple semiconducting nanoheterosystems such as quantum dots (QDs) [2–5], quantum wires [1, 6–10], and 2D quantum wells (QWs) [11–15]. However, in spite of the relative simplicity of the DC model (as compared to the HZ model), an analysis of the electron–phonon interaction on its basis is a complicated problem even in the case of the simplest heterosystems mentioned above. The main reasons behind the mathematical difficulties are due to the presence of several phonon branches in the system and especially the multiple levels (in QDs) and multiple bands (in quantum wires and QWs) in the electronic systems.

Some authors [1, 2, 6, 9] who studied the renormalization of the electron spectrum by polarization phonons in low-dimensional heterosystems used the approximation of an infinitely deep potential well. In this case, cumbersome mathematical computations

were simplified but the interaction between an electron and phonons of the ambient medium (barrier) was disregarded automatically and the real contribution from interface phonons was decreased since the potential field corresponding to these phonons has a peak only at the potential barrier of an infinitely large height.

The role of various phonon mechanisms in the renormalization of the fundamental energy band in a quasi-two-dimensional QW GaAs/Al<sub>x</sub>Ga<sub>1-x</sub>As was investigated most comprehensively and consistently by Hai *et al.* [15]. They proved, using the approximation of effective mass and finite depth of the quantum well in the DC model, that, as the QW width increases from zero to infinity, the shift of the bottom of the well and the electron effective mass vary smoothly in the limits close to their 3D analogs.

This work aims at studying all phonon mechanisms of the renormalization of the electron spectrum of a spherical QD for the specific case of the HgS/CdS system by using the Green’s function method. We use the DC model for phonons and the approximation of effective mass and a finite mass of the potential well for the electron. The potentialities of the Green’s function method [16, 17] on the basis of the Hamiltonian of the system in the second-quantization representation [15] not only enabled us to solve the problem formulated above but will make it possible in the future to analyze the effects of multiphonon processes and temperature on the renormalized spectrum of the electron–phonon system of a quantum dot.



## 2. ELECTRON-PHONON SYSTEM OF A SPHERICAL QUANTUM DOT EMBEDDED IN A BULK SPHERE: HAMILTONIAN

We will study the electron-phonon system of a semiconducting spherical QD of radius  $r_0$  which is placed in a bulk semiconducting medium (Fig. 1). In the approximation of effective mass and a rectangular potential

$$m(r) = \begin{cases} m_0, & r \leq r_0 \\ m_1, & r \geq r_0, \end{cases} \quad U(r) = \begin{cases} -U, & r \leq r_0 \\ 0, & r \geq r_0, \end{cases} \quad (1)$$

the Schrödinger equation can be solved exactly [5]. As a result, the Hamiltonian of an electron in the second-quantization representation has the form

$$\hat{H} = \sum_{nlm} E_{nlm} \hat{a}_{nlm}^+ \hat{a}_{nlm}, \quad (2)$$

where  $\hat{a}_{nlm}^+$  and  $\hat{a}_{nlm}$  are the Fermi creation and annihilation operators. The energy levels  $E_{nlm}$  of degenerate stationary states ( $nlm$ ) can be determined from the equations

$$\frac{l}{kr_0} - \frac{j_{l+1}(kr_0)}{j_l(kr_0)} = i \frac{\chi m_0}{k m_1} \left[ \frac{l}{i\chi r_0} - \frac{h_{l+1}^+(i\chi r_0)}{h_l^+(i\chi r_0)} \right], \quad (3)$$

$$(l = 0, 1, 2, \dots),$$

where

$$k = \hbar^{-1} \sqrt{2m_0(U - |E|)}; \quad \chi = \hbar^{-1} \sqrt{2m_0|E|}; \quad (4) \quad \text{where}$$

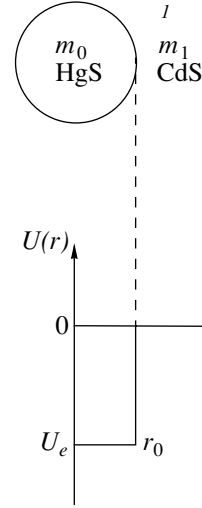


**Fig. 1.** Geometry and the potential of the HgS/CdS nano-system.

and  $j_l$ ,  $h_l^+$ , and  $h_l^-$  are the spherical Bessel and Hankel functions.

The orthonormal system of wave functions ( $nlm$ ) in the spherical system of coordinates has the form

$$|nlm\rangle = \Psi_{nlm}(\mathbf{r}) = R_{nl}(r) Y_{lm}(\theta, \varphi), \quad (5)$$

$$R_{nl}(r) = R_{nl}^0(r)|_{r \leq r_0} + R_{nl}^1(r)|_{r \geq r_0} = \frac{j_l(k_0 r)/j_l(k_0 r_0)|_{r \leq r_0} + h_l^+(i\chi_1 r)/h_l^+(i\chi_1 r_0)|_{r \geq r_0}}{\sqrt{\frac{r_0^3}{2} \left[ 1 + \left| \frac{j_{l+1}(k_0 r_0)}{j_l(k_0 r_0)} \right|^2 \right] + |h_l^+(i\chi r_0)|^{-2} \int_0^\infty r^2 |h_l^+(i\chi r)|^2 dr}}. \quad (6)$$

The phonon spectrum and the potential of the polarization field of the system are determined in the dielectric continuum model [5], in which it is assumed that the QD (0) and the external medium (1) are characterized by known values of the permittivities  $\epsilon_{00}$ ,  $\epsilon_{0\infty}$ ,  $\epsilon_{10}$ , and  $\epsilon_{1\infty}$  and by the energies  $\Omega_{L0}$  and  $\Omega_{L1}$  of optical phonons. In such a model, the Hamiltonian of the phonon system in the occupation number representation has the form

$$\hat{H}_{\text{ph}} = \hat{H}_L + \hat{H}_I, \quad (7)$$

where

$$\hat{H}_L = \sum_{i=0}^1 \sum_{s,lm} \Omega_{Li} (\hat{b}_{s,lm}^+ \hat{b}_{s,lm} + 1/2) \quad (8)$$

is the Hamiltonian of confined phonons and

$$\hat{H}_I = \sum_{lms=\pm} \Omega_l^{(s)} (\hat{b}_{s,lm}^+ \hat{b}_{s,lm} + 1/2) \quad (9)$$

is the Hamiltonian of interface phonons. The energies ( $\Omega_l^{(s)}$ ) of the two branches ( $s = \pm$ ) of these phonons are determined by the dispersion equations

$$l\epsilon_{0\infty} \frac{\Omega^2 - \Omega_{L0}^2}{\Omega^2 - \Omega_{T0}^2} + (l+1)\epsilon_{0\infty} \frac{\Omega^2 - \Omega_{L1}^2}{\Omega^2 - \Omega_{T1}^2} = 0, \quad (10)$$

$$(l = 1, 2, \dots, \infty),$$

where

$$\Omega_{Ti} = \Omega_{Li} \sqrt{\frac{\epsilon_{i\infty}}{\epsilon_{i0}}}, \quad (i = 0, 1) \quad (11)$$

are the energies of the longitudinal optical phonons in the bulk materials of the  $i$ th spheres.

The Hamiltonian of the electron–phonon interaction in the second-quantization representation in all variables of the system can be determined in terms of the polarization field potential by using the orthonormal system of wave functions of bound stationary states [5]:

$$\hat{H}_{\text{int}} = \hat{H}_{e-L} + \hat{H}_{e-I}. \quad (12)$$

Here, the interaction Hamiltonian of the electron with confined phonons

$$\begin{aligned} \hat{H}_{e-L} = & \sum_{i=0}^1 \sum_{n_1 l_1 m_1} \sum_{s_l m} \Phi_{n_1 l_1 m_1}^{n_2 l_2 m_2}(s_l m) \\ & \times \hat{a}_{n_2 l_2 m_2}^+ \hat{a}_{n_1 l_1 m_1} (\hat{b}_{s_l m}^+ + \hat{b}_{s_l - m}^+) \end{aligned} \quad (13)$$

contains coupling functions

$$\Phi_{n_1 l_1 m_1}^{n_2 l_2 m_2}(s_l m) = (Y_{lm})_{l_1 m_1}^{l_2 m_2} (F_{ls})_{n_1 l_1}^{n_2 l_2}, \quad (i = 0, 1), \quad (14)$$

where

$$\begin{aligned} & (Y_{lm})_{l_1 m_1}^{l_2 m_2} \\ & = \int_0^\infty \sin \theta d\theta \int_0^{2\pi} d\varphi Y_{l_2 m_2}^*(\theta, \varphi) Y_{lm}(\theta, \varphi) Y_{l_1 m_1}(\theta, \varphi), \end{aligned} \quad (15)$$

$$\begin{aligned} (F_{ls_0})_{n_1 l_1}^{n_2 l_2} = & \sqrt{\frac{4\pi\Omega_{L0} e^2}{r_0} \left( \frac{1}{\varepsilon_{0\infty}} - \frac{1}{\varepsilon_{00}} \right)} (k_{s_0} r_0 j_{l-1}(k_{s_0} r_0))^{-1} \\ & \times \int_0^{r_0} r^2 j_l(k_{s_0} r) R_{n_2 l_2}^{0*}(r) R_{n_1 l_1}^0(r) dr, \end{aligned} \quad (16)$$

$$\begin{aligned} (F_{ls_1})_{n_1 l_1}^{n_2 l_2} = & \sqrt{\frac{4\pi\Omega_{L1} e^2}{r_1} \left( \frac{1}{\varepsilon_{1\infty}} - \frac{1}{\varepsilon_{10}} \right)} \\ & \times \frac{k_{s_1} r_1}{\sqrt{|1 - r_1 n_l^2(k_{s_1} r_1)/r_0 n_l^2(k_{s_1} r_0)|}} \int_{r_0}^\infty R_{n_2 l_2}^*(r) R_{n_1 l_1}(r) r^2 \\ & \times [n_l(k_{s_1} r_1) j_l(k_{s_1} r) - j_l(k_{s_1} r_1) n_l(k_{s_1} r)] dr. \end{aligned} \quad (17)$$

The values of the coefficients  $k_{s_0}$  and  $k_{s_1}$  can be determined from equations

$$j_l(k_{s_0} r_0) = 0, \quad \frac{j_l(k_{s_1} r_0)}{n_l(k_{s_1} r_0)} = \lim_{n \rightarrow \infty} \frac{j_l(k_{s_1} r_1)}{n_l(k_{s_1} r_1)}, \quad (18)$$

in which the quantities  $s_0$  and  $s_1$  label the roots of the corresponding equations.

The interaction Hamiltonian between the electron and interface phonons

$$\begin{aligned} \hat{H}_{e-I} = & \sum_{i=0}^1 \sum_{n_1 l_1 m_1} \sum_{s_l m} \Phi_{n_1 l_1 m_1}^{n_2 l_2 m_2}(s_l m) \\ & \times \hat{a}_{n_2 l_2 m_2}^+ \hat{a}_{n_1 l_1 m_1} (\hat{b}_{s_l m}^+ + \hat{b}_{s_l - m}^+) \end{aligned} \quad (19)$$

contains the coupling functions

$$\Phi_{n_1 l_1 m_1}^{n_2 l_2 m_2}(s_l m) = (Y_{lm})_{l_1 m_1}^{l_2 m_2} (F_l^s)_{n_1 l_1}^{n_2 l_2}, \quad (20)$$

where

$$\begin{aligned} (F_l^s)_{n_1 l_1}^{n_2 l_2} = & \sqrt{\frac{4\pi e^2 \Omega_{ls}}{r_0 Y_{ls}}} \left\{ \int_0^{r_0} R_{n_2 l_2}^{0*}(r) R_{n_1 l_1}^0(r) (r/r_0)^l r^2 dr \right. \\ & \left. + \int_{r_0}^\infty R_{n_2 l_2}^{1*}(r) R_{n_1 l_1}^1(r) (r/r_0)^{l+1} r^2 dr \right\}, \end{aligned} \quad (21)$$

$$Y_{ls} = \frac{l(\varepsilon_{00} - \varepsilon_{0\infty})}{\left( \frac{\Omega_l^s}{\Omega_{T0}} - \frac{\Omega_{T0}}{\Omega_l^s} \right)^2} + \frac{(l+1)(\varepsilon_{10} - \varepsilon_{1\infty})}{\left( \frac{\Omega_l^s}{\Omega_{T1}} - \frac{\Omega_{T1}}{\Omega_l^s} \right)^2}. \quad (22)$$

Thus, the Hamiltonian of the electron–phonon system in the spherical quantum dot embedded in the external medium has a quite definite form

$$\hat{H} = \hat{H}_e + \hat{H}_L + \hat{H}_I + \hat{H}_{e-L} + \hat{H}_{e-I}, \quad (23)$$

which enables us to apply the Green's function method for determining the electron spectrum renormalized by phonons.

### 3. RENORMALIZATION OF THE ELECTRON SPECTRUM BY PHONONS WITH ALLOWANCE FOR THE INTERACTION BETWEEN ENERGY LEVELS

Since the electron spectrum of the QD contains many energy levels, it is convenient to use the Green's function method for calculating its renormalization by the interaction between an electron and phonons.

It is well known [16, 17] that, in the case of a multi-level system of electrons interacting with phonons and described by Hamiltonian (23), the Fourier transform of the electron's Green's function is connected with the mass operator (MO) at  $T = 0$  through the Dyson equation

$$G_{\mu\mu'}(\omega) = G_{\mu\mu'}^0(\omega) \delta_{\mu\mu'} + G_{\mu\mu'}^0(\omega) \sum_{\mu_1} M_{\mu\mu_1} G_{\mu_1\mu'}(\omega), \quad (24)$$

Parameters of crystals

Crystal	$m_e, m_0$	$m_h, m_0$	$a, \text{\AA}$	$E_g, \text{eV}$	$V_e, \text{eV}$	$\Omega_L, \text{meV}$	$\epsilon_0$	$\epsilon_\infty$
CdS	0.2	0.7	5.818	2.5	3.8	57.2	9.1	5.5
HgS	0.036	0.044	5.851	0.5	5.0	27.8	18.2	11.36

where

$$G_\mu^0(\omega) = \{\omega - E_\mu + i\eta\}^{-1}, \quad (25)$$

and  $\mu = \{n, l, m\}$  is the set of all quantum numbers characterizing the electron state.

System (25) can be used for determining the exact diagonal Fourier transforms of the Green's functions:

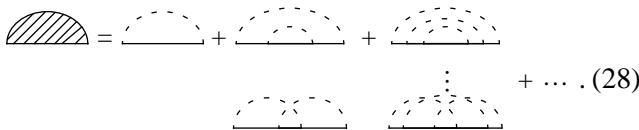
$$G_{\mu\mu}(\omega) = \left\{ \omega - E_\mu - M_{\mu\mu} - \frac{1}{d_{\mu\mu}(\omega)} \times \sum_{\mu_1 \neq \mu}^{\tau} (-1)^{\mu + \mu_1} M_{\mu\mu_1}(\omega) d_{\mu_1\mu}(\omega) \right\}^{-1}, \quad (26)$$

where matrix  $d_{\mu_1\mu_2}$  is given in the Appendix.

According to estimates, the moduli of the diagonal coupling functions for the  $\beta$ -HgS/CdS system exceed the moduli of the off-diagonal coupling functions by more than an order of magnitude. This circumstance and the alternation of the sum in Eq. (26) ensure the smallness of the last term as compared to the diagonal component  $M_{\mu\mu}$  of the mass operator. Thus, we obtain the following expression for  $G_{\mu\mu}(\omega)$ :

$$G_{\mu\mu}(\omega) = \{\omega - E_\mu - M_{\mu\mu}(\omega)\}^{-1}, \quad (27)$$

where the mass operator  $M_{\mu\mu}(\omega)$  is defined by the following diagrammatic representation [17]:



$$+ \dots \quad (28)$$

In view of the weakness of the electron-phonon interaction in the  $\beta$ -HgS/CdS system, the main contribution to the MO comes from the first diagram in Eq. (28). In accordance with the rules for Feynman's diagrams, we obtain the following mass operator for the system with Hamiltonian (23), which describes the renormalization of the ground state:

$$M(\omega) = M_L(\omega) + M_I(\omega). \quad (29)$$

Here,

$$M_L(\omega) = M_L^{(0)}(\omega) + M_L^{(1)}(\omega) = \sum_{lm} \frac{2l+1}{4\pi} \frac{\sum_{s_0} |(F_{s_0 l})_{10}|^{2l}}{\omega - E_{nl} - \Omega_{L_0}} + \sum_{nl} \frac{2l+1}{4\pi} \frac{\sum_{s_1} |(F_{s_1 l})_{10}|^{2l}}{\omega - E_{nl} - \Omega_{L_1}} \quad (30)$$

is the MO term describing the contribution of confined ( $M_L^{(0)}(\omega)$ ) and semiconfined ( $M_L^{(1)}(\omega)$ ) polarization phonons, while

$$M_I(\omega) = M_{I^+}(\omega) + M_{I^-}(\omega) = \sum_{nl=1} \frac{2l+1}{4\pi} \frac{\sum_{s_0} |(F_{I^+}^+)_{10}|^{2l}}{\omega - E_{nl} - \Omega_{I^+}} + \sum_{nl \neq 1} \frac{2l+1}{4\pi} \frac{\sum_{s_1} |(F_{I^-})_{10}|^{2l}}{\omega - E_{nl} - \Omega_{I^-}} \quad (31)$$

is the MO term describing the contributions of both ( $\pm$ ) interface branches of phonons.

The energy  $\tilde{E}_{10}$  of the electron ground level renormalized by phonons is defined by the equation

$$\omega - E_{10} - M(\omega) = 0. \quad (32)$$

The renormalized energy

$$\tilde{E}_{10} = E_{10} + \Delta \quad (33)$$

taking into account the shift ( $\Delta$ ) of the ground level is calculated on a computer.

#### 4. ANALYSIS OF THE MECHANISMS OF FORMATION OF THE ELECTRON GROUND LEVEL SHIFT IN THE $\beta$ -HgS/CdS SYSTEM

The energy shift  $\Delta$  was calculated using the physical parameters of the nanoheterosystem  $\beta$ -HgS/CdS presented in the table. Considering that the MO in Eq. (29) contains four terms describing different mechanisms of the electron-phonon interaction, it is natural to present

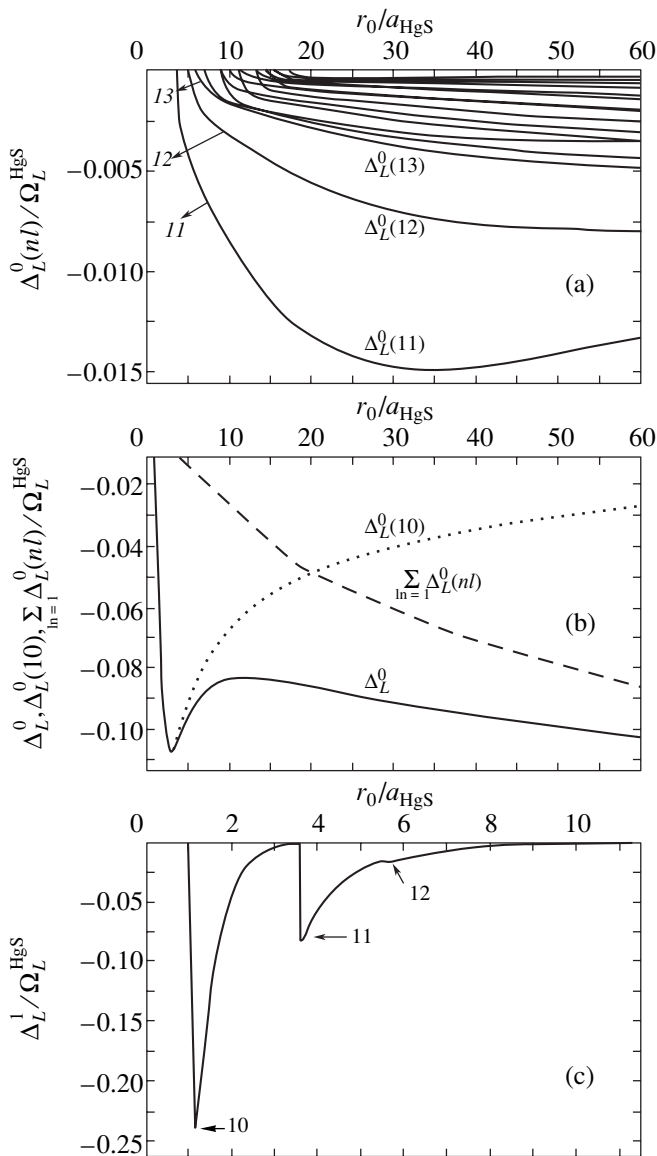


**Fig. 2.** Dependences of the partial shifts formed by confined phonons ( $L_0, L_1$ ) on the size ( $r_0/a_{\text{HgS}}$ ) of the QD. Here and in Fig. 3,  $n$  and  $l$  are the principal and orbital quantum numbers.

the shift  $\Delta$  as the sum of the corresponding partial shifts:

$$\Delta = \Delta_{eL}^0 + \Delta_{eL}^1 + \Delta_{eL^+} + \Delta_{eL^-}. \quad (34)$$

An analysis of the results of calculation of the dependence of partial and total shifts on the QD radius  $r_0$  in units of the HgS lattice constant leads to the following conclusions. Since the system at  $T = 0$  contains only virtual phonons, an electron interacts with them only in processes involving their emission; consequently, all partial shifts (and, hence, the total shift) are negative.

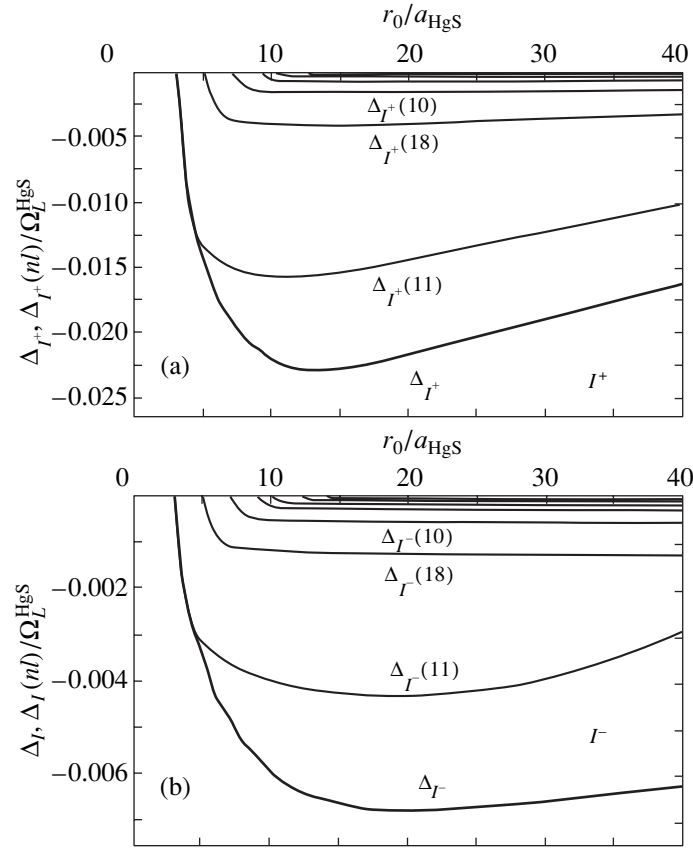
Figure 2 illustrates the formation of the energy shifts in the internal ( $\Delta_{eL}^0$ ) and external ( $\Delta_{eL}^1$ ) media of the nanoheterosystem, which are induced by confined phonons. From Fig. 2a, it can be seen that when the energy level is formed in the HgS well (for  $r_0 \approx 1a_{\text{HgS}}$ ) its shift  $\Delta_{eL}^0$  is formed by the intralevel interaction with confined photons. As the QD radius increases, the contribution of the intralevel interaction to the absolute value of  $\Delta_{eL}^0$  increases rapidly, attains its maximum value (for  $r_0 \approx 5a_{\text{HgS}}$ ), and then decreases slowly.

Figure 2b shows that, as the size of the quantum dot increases, higher excited energy levels appear in the potential well and kinematic interaction with them through  $L_0$  phonons forms the corresponding partial contributions to  $\Delta_{eL}^0$ . The dependence of these contributions on  $r_0$  is qualitatively the same: after the emergence of each level, its contribution to  $\Delta_{eL}^0$  first increases slowly upon an increase in  $r_0$ , attains its peak value, and then decreases slowly.

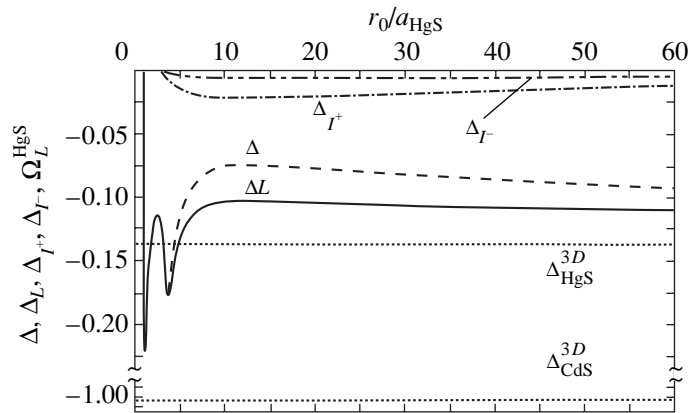
It can be seen from Fig. 2b that the partial shift  $\Delta_{eL}^0$  for small values of  $r_0$  ( $a_{\text{HgS}} \leq r_0 \leq 3a_{\text{HgS}}$ ), such that the HgS well contains only one bound state, is formed by the intralevel interaction with  $L_0$  phonons. Then the interlevel interaction appears, which increases with  $r_0$ ; attains the value of the intralevel interaction (for  $r_0 \approx 20a_{\text{HgS}}$ ); and then gradually becomes dominant. Thus, the dependence of  $\Delta_{eL}^0$  on  $r_0$  turns out to be quite complicated (Fig. 2a).

Figure 2c shows the dependence of the partial contribution  $\Delta_{eL}^1$  on the QD radius. It can be seen that the value of  $\Delta_{eL}^1$  is very significant only for small values of the radius  $r_0$ . This is not surprising since the electron penetrates in the barrier medium CdS with a high probability only for a very small QD radius and, hence, its interaction with  $L_1$  phonons of this medium is significant. The  $\Delta_{eL}^1$  curve contains three well-defined peaks corresponding to the contributions of intralevel (10) and interlevel (11, 12) interactions through  $L_1$  phonons. The remaining levels appear at values of  $r_0$  for which the electron does not penetrate in CdS in view of the large size of the well and, hence, virtually does not interact with  $L_1$  phonons. For this reason, the value of  $\Delta_{eL}^1$  rapidly tends to zero upon an increase in  $r_0$ .

As follows from the general theory [5], the intralevel interaction of the electron with interface phonons in spherically symmetric states ( $l = 0$ ) is absent. For this reason, as can be seen from Figs 3a and 3b, the partial shifts  $\Delta_{eL^+}$  and  $\Delta_{eL^-}$  are formed only by the interlevel interaction (of the ground state with the remaining states) through  $I^+$  and  $I^-$  phonons, respectively. For all



**Fig. 3.** Dependence of the partial shifts formed by interface phonons ( $I^+$ ,  $I^-$ ) on the size ( $r_0/a_{\text{HgS}}$ ) of the QD.



**Fig. 4.** Dependence of the total and partial shifts on the size ( $r_0/a_{\text{HgS}}$ ) of the QD.

values of the QD radius,  $\Delta_{I^+}$  exceeds (in absolute value)  $\Delta_{I^-}$ . As  $r_0$  increases, the absolute values of both partial shifts first increase gradually and then decrease smoothly.

The dependences of the partial and total shifts of the electron ground level on the radius  $r_0$  of the well are presented in Fig. 4. From the figure, it can be seen that

for all values of  $r_0$ , the main contribution to  $\Delta$  comes from confined phonons (belonging to the external medium for small values of the QD radius and to the internal medium for large values of the QD radius). Interface phonons of both branches make a considerable contribution to  $\Delta$  only for the comparatively small QD size (up to  $r_0 \approx 40a_{\text{HgS}}$ ), and then their contribution decreases gradually.

For very small sizes of QD ( $r_0 \leq 5a_{\text{HgS}}$ ),  $\Delta$  exceeds the energy shift in a bulk HgS crystal ( $\Delta_{\text{HgS}}^{3D} \approx 0.137\Omega_{\text{HgS}}$ ) but remains smaller than the energy shift in a bulk CdS crystal ( $\Delta_{\text{CdS}}^{3D} \approx 1.02\Omega_{\text{HgS}}$ ). Although the effective mass approximation and the dielectric continuum model lose their rigorous meaning for such small QD radii, the general tendency in the behavior of  $\Delta$  as a function of  $r_0$  remains realistic from the physical point of view.

A decrease in the value of the QD radius (starting from  $r_0 \approx 10a_{\text{HgS}}$ ) leads to a slow increase in  $\Delta$ , and it approaches  $\Delta_{\text{HgS}}^{3D}$ . The difference between  $\lim_{n_0 \rightarrow \infty} \Delta(r_0)$  and  $\Delta_{\text{HgS}}^{3D}$ , amounting to  $\approx 8\%$ , is due to the fact that the electron–phonon interaction through continual states, as well as a higher order terms in the interlevel interaction, is disregarded while calculating  $\Delta$ .

Finally, it should be noted that the role of the mechanisms of the electron–phonon interaction responsible for the shift in the ground level in the spherical QD of  $\beta$ -HgS/CdS, which was determined in this work, correlates well with the role of similar mechanisms in a 2D QW of GaAs/Al<sub>x</sub>Ga<sub>1-x</sub>As, which were determined in [15]. The obtained results indicate the applicability of the model, on the one hand, and, on the other hand, make it possible to apply the Green’s function method for studying a wider class of problems in the theory of electron–phonon interaction. Among other things, it is proposed to investigate bound electron–phonon states and to study the temperature genesis in the electron spectrum in simple and multilayered quantum dots.

## APPENDIX

Matrix  $d_{\mu_1\mu_2}$  has the form

$$d_{\mu_1\mu_2}(\omega) = \begin{vmatrix} \omega - \varepsilon_1 - M_{11} & \dots & -M_{1\mu_2-1} & & -M_{1\mu_2+1} & \dots & -M_{1\tau} \\ \dots & \dots & \dots & & \dots & \dots & \dots \\ -M_{\mu_1-11} & \dots & \omega - \varepsilon_{\mu_1-1} M_{\mu_1-1\mu_2+1} & & -M_{\mu_1-1\mu_2+1} & & -M_{\mu_1-1\tau} \\ -M_{\mu_1+11} & \dots & -M_{\mu_1+1\mu_2-1} & & \omega - \varepsilon_{\mu_1+1} M_{\mu_1+1\mu_2-1} & \dots & -M_{\mu_1+1\tau} \\ \dots & \dots & \dots & & \dots & \dots & \dots \\ -M_{\tau 1} & \dots & -M_{\tau\mu_2-1} & & -M_{\tau\mu_2+1} & \dots & \omega - \varepsilon_{\tau} M_{\tau\tau} \end{vmatrix}.$$

Here,  $\tau$  is the maximum number of discrete energy levels in the system.

## REFERENCES

1. X. F. Wong and X. L. Lei, Phys. Rev. B **49** (7), 4780 (1994).
2. M. C. Klein, F. Hache, D. Ricard, and C. Flytzanis, Phys. Rev. B **42** (17), 11 123 (1990).
3. S. Nomura and T. Kobayashi, Phys. Rev. B **45** (2), 1305 (1992).
4. J. C. Marini, B. Stebe, and E. Kartheuser, Phys. Rev. B **50** (19), 14 302 (1994).
5. N. V. Tkach, Fiz. Tverd. Tela (St. Petersburg) **39** (6), 1109 (1997) [Phys. Solid State **39**, 995 (1997)].
6. M. A. Stroschio, K. W. Kim, M. A. Littlejohn, and H. Chnang, Phys. Rev. B **42** (2), 1488 (1990).
7. P. A. Knipp and T. L. Reineke, Phys. Rev. B **45** (2), 9091 (1992).
8. A. Ercelebi and R. T. Senger, Phys. Rev. B **53** (2), 11 008 (1996).
9. B. Tanatar, K. Güven, C. R. Bennett, and N. C. Constantinou, Phys. Rev. B **53** (16), 10 866 (1996).
10. N. V. Tkach, J. Phys. Stud. **3** (3), 377 (1999).
11. L. Wendler and R. Pechstedt, Phys. Status Solidi B **141** (1), 129 (1987).
12. K. Huang and B. F. Zhu, Phys. Rev. B **38** (20), 13 377 (1988).
13. N. Mori and T. Ando, Phys. Rev. B **40** (9), 6175 (1989).
14. G. Q. Hai, F. M. Peeters, and J. T. Devreese, Phys. Rev. B **42** (16), 11 063 (1990).
15. G. Q. Hai, F. M. Peeters, and J. T. Devreese, Phys. Rev. B **48** (7), 4666 (1993).
16. A. A. Abrikosov, L. P. Gor’kov, and I. E. Dzyaloshinskiĭ, *Methods of Quantum Field Theory in Statistical Physics* (Fizmatgiz, Moscow, 1962; Prentice-Hall, Englewood Cliffs, 1963).
17. V. M. Agranovich, *The Theory of Excitons* (Nauka, Moscow, 1968).

Translated by N. Wadhwa

---

**LOW-DIMENSIONAL SYSTEMS  
AND SURFACE PHYSICS**

---

# Pseudosurface Dispersion Polaritons and Their Resonance Excitation

V. I. Alshits, V. N. Lyubimov, and L. A. Shuvalov

*Shubnikov Institute of Crystallography, Russian Academy of Sciences, Leninskiĭ pr. 59, Moscow, 117333 Russia*

Received September 18, 2000; in final form, January 9, 2001

**Abstract**—The conditions for the transformation of surface polaritons (surface electromagnetic waves) into pseudosurface polaritons under the influence of perturbations are investigated. The transformation occurs because of the appearance of a weak energy loss flow typical of pseudosurface polaritons, which carries energy away from the surface of the solid. The dispersion polaritons existing at negative values of the dielectric constant are considered. The domain of existence of the pseudosurface polaritons is studied; their main characteristics and the parameters of the resonance excitation of these polaritons by a pumping wave are investigated. © 2001 MAIK “Nauka/Interperiodica”.

## 1. INTRODUCTION

The electromagnetic wave fields localized near the boundaries between different continuous media are called surface polaritons [1–5]. In this paper, the greatest attention is paid to pseudosurface polaritons, which, in contrast to surface polaritons, possess not only components localized near the boundary of the continuous medium, but also a bulk component, namely, a weak loss current carrying energy away from the boundary. Due to this characteristic feature, the resonance excitation of the localized components of the wave field is possible; the reflection of the bulk pumping wave from the boundary amplifies the loss current and simultaneously enhances the localized components of the wave field [6, 7]. Due to this feature, it is especially interesting to investigate pseudosurface polaritons. It should be noted that this method of resonance amplification of wave fields, as applied to waveguide structures, was described in [8, 9].

In the present paper, we consider surface and pseudosurface polaritons existing at negative values of the dielectric constant of a solid, which takes place near resonance frequencies. The speed of these polaritons depends essentially on the frequency; for this reason, we call them dispersion polaritons in order to distinguish them from the dispersionless ones [10, 11], which exist at positive values of the dielectric constant.

## 2. STATEMENT OF THE PROBLEM

Pseudosurface polaritons arise from surface polaritons because of a certain small modification of the solid-state structure in which ordinary polaritons exist. Such a modification results in a weak energy loss current which carries energy away from the surface of the solid. For example, let us consider one of the possible

situations in which the pseudosurface polaritons appear.

The simplest surface polariton exists on the boundary between a vacuum and a semi-infinite isotropic medium whose dielectric constant  $\epsilon < -1$  (the dielectric constant and refraction index of the vacuum are equal to unity:  $\epsilon_v = n_v = 1$ ). The wave field of this polariton decays exponentially with distance from the boundary on both sides of it.

Now, let us suppose that the isotropic medium is not semi-infinite but is a sufficiently thick layer of thickness  $h$ , which is much larger than the wavelength of the polariton  $\lambda$  ( $h \gg \lambda$ ). If the layer is placed on another isotropic medium (see Fig. 1a), this leads to small changes in the speed  $v_s$  and structure of the wave field of the polariton. In this case, depending on the relationship between  $v_s$  and the speed  $v_b$  of the bulk electromagnetic wave in the attached medium, the polariton either remains a slightly modified surface polariton (at  $v_b > v_s$ ) or transforms into a pseudosurface polariton (at  $v_b < v_s$ ) due to the appearance of a weak energy loss in the attached medium. The speed  $v_b$  is determined by the dielectric constant of the attached medium  $\tilde{\epsilon}$ , because  $v_b = c/\tilde{n}$  (here,  $\tilde{n} = \sqrt{\tilde{\epsilon}}$  is the refraction index and  $c$  is the speed of light in a vacuum). Thus, if the attached medium is such that  $\tilde{\epsilon} > (c/v_s)^2$ , the polariton becomes a pseudosurface polariton, slightly damped due to the appearance of the energy loss.

## 3. PSEUDOSURFACE DISPERSION POLARITONS IN THE LAYER ON A SUBSTRATE

All properties of the pseudosurface polaritons under study follow from the Maxwell equations and standard boundary conditions for the electromagnetic fields.

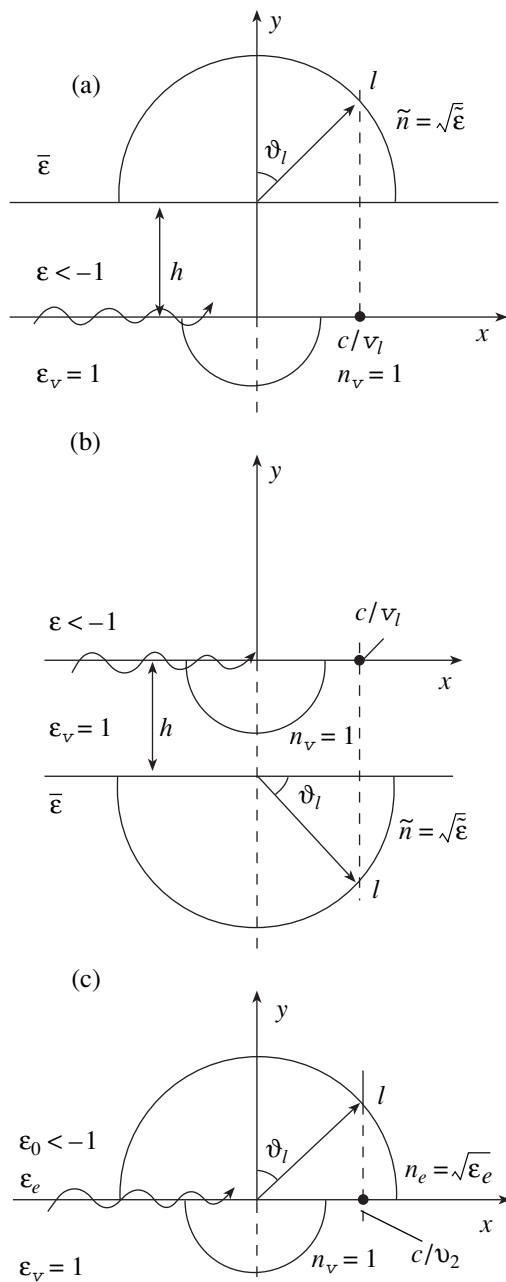


**Fig. 1.** Schemes of the appearance of the pseudosurface dispersion polaritons: (a) the layer on the substrate; (b) two semi-infinite media separated by a vacuum gap; and (c) an optically uniaxial crystal. The semicircles are the cross sections of the refraction-index surface by the sagittal plane, the wavy lines show the components of the wave field localized near the boundary, and the arrows ( $l$ ) indicate the directions of energy loss currents making an angle  $\vartheta_l$  with the perpendicular to the boundary.

Omitting rather cumbersome calculations, we present the final results.

The dependence of the wave field of the polariton under consideration on the coordinates  $x$  and  $y$  and time

$t$  can be represented in the form

$$\mathbf{H}(x, y; t) = \mathbf{H}(y) \exp[i\omega(N_l x/c - t)]. \quad (1)$$

Here,  $N_l \equiv (c/\omega)K_l$ , where  $\omega$  is the frequency and  $K_l = k_l + ik'_l$  is a complex number; the complex parameter  $N_l = n_l + in'_l$  determines the complex speed of the polariton propagation  $V_l \equiv v_l - iv'_l = c/N_l$ . Small imaginary parts of the characteristics introduced here describe weak damping of the polariton as it propagates along the  $x$  axis. We presented the magnetic component of the wave field; the formulas for the electric field and induction are analogous to it.

The vector amplitude  $\mathbf{H}(y) = (0, 0, 1)H(y)$  is assumed to be

$$H(y) = \begin{cases} H_v \exp(i\omega p_v y/c), & y \leq 0, \\ H \exp(i\omega p y/c), & 0 \leq y \leq h, \\ \tilde{H} \exp[i\omega \tilde{p}(y-h)/c], & y \geq h. \end{cases} \quad (2)$$

It is supposed here that the layer is sufficiently thick,  $h \gg \lambda$ ; the parameters  $p_v, p$ , and  $\tilde{p}$  in Eq. (2) determine the dependence of the wave field on the coordinate  $y$ . These parameters depend on the dielectric constants

$$p_v = -i\sqrt{|\epsilon + 1|}, \quad (3)$$

$$p = i|\epsilon|\sqrt{|\epsilon + 1|}, \quad (4)$$

$$\tilde{p} = \sqrt{\tilde{\epsilon} - \epsilon/(\epsilon + 1)}. \quad (5)$$

It is supposed that the dielectric constant of the layer satisfies the inequality  $\epsilon < -1$  and, hence, the parameters  $p_v$  and  $p$  are purely imaginary, which ensures the localization of the polariton wave field near the boundary  $y = 0$ . At the same time, the dielectric constant of the attached medium is positive; it can ensure the reality of the parameter  $\tilde{p}$  only if  $\tilde{\epsilon} > 1$ . In this case, the energy loss current appears and the polariton becomes a pseudosurface polariton. It exists in the region

$$\epsilon < \tilde{\epsilon} \equiv -\tilde{\epsilon}/(\tilde{\epsilon} - 1), \quad (6)$$

where  $\tilde{\epsilon} > 1$ , and, hence,  $\tilde{\epsilon} < -1$  (see Fig. 2a). In the adjacent region, we have

$$\tilde{\epsilon} < \epsilon < -1 \quad (7)$$

and an ordinary surface polariton exists. Thus, at  $\tilde{\epsilon} > 1$ , the entire region of existence of polaritons  $\tilde{\epsilon} < -1$  is divided into two parts. In one of them, defined by Eq. (6), the pseudosurface polaritons arise, while in the other, Eq. (7), the ordinary polaritons exist. As was already mentioned, the condition for existence of the pseudosurface polariton in Eq. (6) can be written as

$v_b < v_s$  (where  $v_b = c/\sqrt{\tilde{\epsilon}}$  is the speed of the bulk wave in the attached medium) and condition (7) can be written as  $v_b > v_s$ .



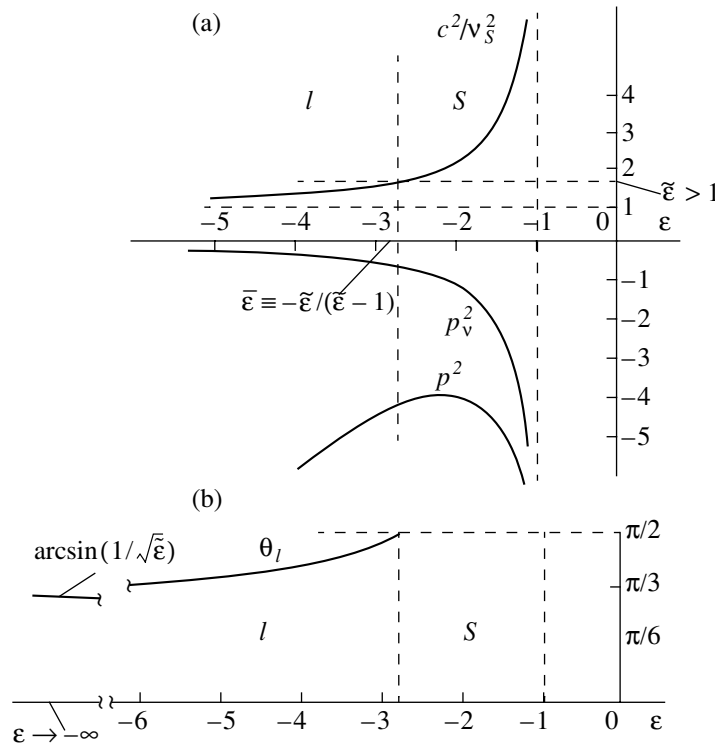


**Fig. 2.** Characteristics of the wave fields of the polaritons as functions of the dielectric constants: (a) the regions of the existence of the surface polaritons (s) and pseudosurface polaritons (l) and their parameters and (b) the direction of the energy loss current in the pseudosurface polaritons defined by the angle  $\vartheta_l$ .

If the perturbation of the medium is absent (the limit  $h \rightarrow \infty$  corresponds to this case), they remain surface polaritons and their speed is [1–5, 12, 13]

$$v_s = c\sqrt{(\epsilon + 1)/\epsilon}. \quad (8)$$

At large finite values of  $h$  ( $h \gg \lambda$ ), when the polariton becomes a pseudosurface polariton due to the attached substrate, the speed in Eq. (8) changes by a small complex value with a real and an imaginary part:  $v_s \rightarrow v_l - i v_l'$ . Here,  $v_l = v_s + \Delta v_l$ , where

$$\Delta v_l = 2v_s \frac{\epsilon \tan^2 \vartheta_l + \tilde{\epsilon}^2}{(\epsilon^2 - 1)(\tan^2 \vartheta_l - \tilde{\epsilon}^2/\epsilon)} \exp(-2\gamma h), \quad (9)$$

$$v_l' = 4v_s \frac{\tilde{\epsilon} \sqrt{|\epsilon|} \tan \vartheta_l}{(\epsilon^2 - 1)(\tan^2 \vartheta_l - \tilde{\epsilon}^2/\epsilon)} \exp(-2\gamma h), \quad (10)$$

and  $\gamma = \omega|p|/c$ . If condition (6) is fulfilled, it can be verified that  $v_l' > 0$ , as it should be since the intensity of the pseudosurface polariton is decreased during its propagation because of energy loss.

As is seen from Fig. 1a, the direction of the energy loss current arising under condition (6) is defined by the angle  $\vartheta_l$ , which is determined by the relationship

$$\sin \vartheta_l = c/v_s \sqrt{\tilde{\epsilon}} = \sqrt{\epsilon/(\epsilon + 1)} \tilde{\epsilon}. \quad (11)$$

It can easily be verified that the right-hand side of Eq. (11) is smaller than unity under condition (6). The dependence given by Eq. (11) is shown in Fig. 2b.

If condition (7) is fulfilled, then the radical in Eq. (11) becomes purely imaginary and the value  $i v_l'$  is real. In this case, in spite of the perturbation, the polariton speed remains real and the polariton remains an ordinary surface polariton. The perturbation also leaves the polariton to be a surface polariton in the whole range  $\epsilon < -1$  at  $\tilde{\epsilon} < 1$  (that is, at  $v_b > v_s$ ).

#### 4. RESONANCE EXCITATION OF THE SURFACE COMPONENTS OF THE WAVE FIELD

Let us consider the reflection of a bulk pumping wave, propagating through the attached medium, from the boundary  $y = h$  under the condition that the reflection occurs in the vicinity of the angle  $\vartheta_l$  in Eq. (11) and, therefore, the direction of the reflected wave is close to that of the energy loss current of the pseudosurface polariton. In this case, the wave field can be described by Eq. (1), in which the complex parameter  $N_l$  should be replaced by the real parameter  $n_x \equiv n_l + \Delta n$ , where  $\Delta n = 2(n_l/\sin 2\vartheta_l)\Delta\vartheta$ . The speed of the wave-field propagation along the  $x$  axis also becomes real,  $v = v_l + \Delta v = c/n_x$ . In this case, the amplitude of the

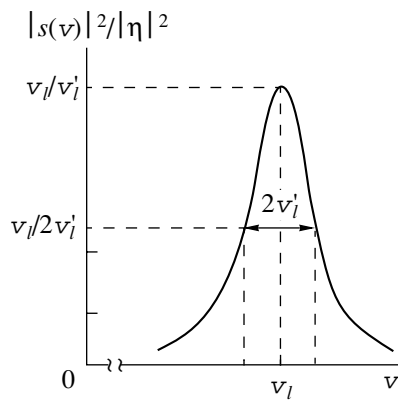


**Fig. 3.** Coefficient of the excitation of the components of the wave field localized near the boundary as a function of the velocity  $v$  determined by the incident pumping wave.

wave field in the attached medium ( $y \geq h$ ) in Eq. (2) should be written as

$$H_i \exp[-i\omega \tilde{p}(y-h)/c] + H_r \exp[i\omega \tilde{p}(y-h)/c]. \quad (12)$$

Here, the coefficients  $H_i$  and  $H_r$  define the amplitudes of the incident and reflected waves, respectively. The incident pumping wave excites the components of the wave field localized near the boundary  $y=0$ . The excitation is resonant and can be described by the following ratio between the amplitudes (see Fig. 3):

$$s(v) = \frac{H}{H_i} = \eta \frac{\sqrt{v_l v_l'}}{v - v_l + i v_l'} \quad (13)$$

Here, the coefficient  $\eta$  depends on the dielectric constants:

$$\eta = -2 \frac{\sqrt{|\epsilon| \sqrt{|\epsilon|} \tan \vartheta_l (\sqrt{|\epsilon|} \tan \vartheta_l + i \tilde{\epsilon})}}{\tilde{\epsilon} (\epsilon^2 - 1) (\sqrt{|\epsilon|} \tan \vartheta_l - i \tilde{\epsilon})}. \quad (14)$$

At resonance, the excitation coefficient of the localized components of the wave field in Eq. (13) becomes anomalously large,

$$s(v_l) = -i\eta \sqrt{v_l/v_l'} \sim \exp(\gamma h) \rightarrow \infty \quad (15)$$

at  $h \rightarrow \infty$ , when  $v_l' \rightarrow 0$ .

The width of the resonance peak is determined by the value  $v_l'$  and, according to the general theory [6], the ratio  $s(v)$  in Eq. (13) transforms into a  $\delta$  function at  $v_l' \rightarrow 0$ .

The intrinsic absorption (energy dissipation) is a factor limiting this exponential growth. The dissipation is taken into account phenomenologically by introducing a small imaginary part in the speed  $v_l$  [14]:  $v_l \rightarrow v_l - i v_l'$  (it is assumed that  $v_l' \ll v_l$ ). This essentially

affects the behavior of the function  $s(v)$  in Eq. (13) at resonance. Indeed, at  $v \rightarrow v_l$ , we have

$$s(v_l) = -i\eta \frac{\sqrt{v_l v_l'}}{v_l' + v_l'} \quad (16)$$

and, instead of Eq. (15), we have

$$s(v_l) = 0 \text{ at } v_l' \rightarrow 0. \quad (17)$$

At the same time, the function in Eq. (16) reaches its maximum at  $v_l' = v_l'$ :

$$s(v_l) = -i(\eta/2) \sqrt{v_l/v_l'} \ll 1. \quad (18)$$

Another factor limiting the resonant amplification is the divergence of a real acoustical pumping beam, since not all waves forming the beam can be near resonance.

## 5. DISPERSION PROPERTIES OF POLARITONS

Now, let us discuss the questions about the frequencies at which the polaritons under consideration exist and what the dependences of their main characteristics on the frequencies are. In the simplest case, the dielectric constant of an isotropic medium as a function of frequency can be written in the form [13]

$$\epsilon(\omega) = \epsilon^{(0)} - \frac{2A\omega_R^2}{\omega^2 - \omega_R^2}, \quad (19)$$

where  $\omega_R$  is a resonance frequency (it is supposed that the other resonance frequencies are far from this one) and the parameters  $\epsilon^{(0)}$  and  $A$  are frequency-independent. In this case, the condition  $\epsilon(\omega) < -1$  is fulfilled in the following range of frequencies:

$$\omega_R < \omega < \omega_C \equiv \omega_R \sqrt{1 + 2A/(\epsilon^{(0)} + 1)}. \quad (20)$$

Here,  $\omega_C$  is the critical frequency, for which  $\epsilon(\omega_C) = -1$ . At  $\tilde{\epsilon} > 1$ , the frequency range in Eq. (20) is divided into the following two frequency domains:

$$\omega_R < \omega < \bar{\omega} \quad (21)$$

and

$$\bar{\omega} < \omega < \omega_C \quad (22)$$

The pseudosurface polaritons arise in the range defined by Eq. (21), while the ordinary surface polaritons exist in the range in Eq. (22). Here, the frequency  $\bar{\omega}$  is defined by the relationship  $\epsilon(\bar{\omega}) = \tilde{\epsilon} \equiv -\tilde{\epsilon}/(\tilde{\epsilon} - 1)$ . Obviously, conditions (21) and (22) are equivalent to conditions (6) and (7), respectively.

## 6. DISCUSSION

In other structures, the appearance of the pseudosurface polaritons is also possible (see Figs. 1b and 1c). Figure 1b illustrates a structure consisting of two semi-

infinite media. In one of them,  $\epsilon < -1$ , and in the other,  $\tilde{\epsilon} > 1$ . The media are separated by a vacuum gap of thickness  $h$  ( $h \gg \lambda$ ). The situation is qualitatively similar to the case considered. The most essential thing is that the parameter  $p$  defined in Eq. (4) should be replaced by  $p_v$  defined in Eq. (3) in the exponent factors in the relationships analogous to Eqs. (9), (10), and (15). The other changes are not so important.

Finally, one more example is the boundary between an optically uniaxial crystal and a vacuum, when the optical axis is slightly inclined from the perpendicular to the sagittal plane (the plane of propagation); see Fig. 1c. The smallness of the inclination determines the weakness of the energy loss. As is known [15], the optical properties of uniaxial crystals are determined by two dielectric constants,  $\epsilon_0$  and  $\epsilon_e$ . For the appearance of pseudosurface polaritons in the structure under consideration, the condition  $\epsilon_0 < -1$  should be fulfilled and the speed of a bulk extraordinary wave  $v_e$  (the energy loss current is due to this wave) should satisfy the inequality  $v_e < v_s$  ( $v_e = c/n_e$ ,  $n_e = \sqrt{\epsilon_e}$ ). The possibility of the appearance of the pseudosurface polaritons in the system under consideration is demonstrated in [12].

The principle difference of this scheme from the previous ones is that the smallness of  $\Delta v_l$  and  $v_l'$  is determined not by the exponential factor but by the angle of deviation  $\alpha$  from the perpendicular to the sagittal plane  $\Delta v_l \sim \alpha^2$ . Thus, instead of the estimate in Eq. (15), at resonance, we have

$$s(v_l) \sim 1/|\alpha| \rightarrow \infty \text{ at } \alpha \rightarrow 0. \quad (23)$$

Based on the experimental data for an optically uniaxial  $\text{MgF}_2$  crystal [2], we consider a particular example as an illustration. If the optical axis of the crystal is exactly perpendicular to the sagittal plane, then a surface polariton exists on the boundary between the crystal and the vacuum and the properties of the polariton are determined only by the dielectric constant  $\epsilon_0$ . In this case, the properties of the crystal are similar to those of an optically isotropic medium. The surface polariton exists in the frequency range ( $\approx 275 \text{ cm}^{-1}$ )  $< \omega < (\approx 290 \text{ cm}^{-1})$ . In this case, the value  $c/v_s$  varies in the range ( $\approx 1.2$ )  $< c/v_s < (\approx 2.9)$ . Now, let us consider the realization of the situations presented in Figs. 1a and 1b. If the refraction index of the attached medium  $\tilde{n} = \sqrt{\tilde{\epsilon}}$  lies in the range  $\tilde{n} = c/v_s$ , then the polariton remains an ordinary surface polariton at the frequencies  $\bar{\omega} < \omega < (\approx 290 \text{ cm}^{-1})$ , where the frequency  $\bar{\omega}$  was already determined above (it corresponds to the condition  $\tilde{n} = c/v_s$ ). On the other hand, if  $c/v_s < \tilde{n}$ , then the polariton transforms into a pseudosurface polariton in the frequency range ( $\approx 275 \text{ cm}^{-1}$ )  $< \omega < \bar{\omega}$ .

On the basis of the crystal under consideration, the scheme shown in Fig. 1c can also be realized by slightly inclining the optical axis from the sagittal plane. In this

case, a weak energy loss appears if the dielectric constant  $\epsilon_e$  is such that  $\sqrt{\epsilon_e} < c/v_s$ . In  $\text{MgF}_2$  crystals, we have  $\sqrt{\epsilon_e} \approx 2.8$  [2] and the surface polariton transforms into a pseudosurface polariton in almost the entire frequency range of its existence except for a small part of the range adjacent to the limiting frequency  $\approx 290 \text{ cm}^{-1}$ . In this frequency range, the polariton remains a surface polariton.

## ACKNOWLEDGMENTS

This work was supported by the Russian Foundation for Basic Research, grant no. 98-02-16069.

## REFERENCES

1. *Surface Polaritons: Electromagnetic Waves at Surfaces and Interfaces*, Ed. by V. M. Agranovich and D. L. Mills (North-Holland, Amsterdam, 1982; Nauka, Moscow, 1985).
2. V. V. Bryksin, D. N. Mirlin, and Yu. A. Firsov, *Usp. Fiz. Nauk* **113** (1), 29 (1974) [*Sov. Phys. Usp.* **17**, 305 (1974)].
3. V. M. Agranovich, *Usp. Fiz. Nauk* **115** (2), 199 (1975) [*Sov. Phys. Usp.* **18**, 99 (1975)]; *Usp. Fiz. Nauk* **126** (4), 677 (1978) [*Sov. Phys. Usp.* **21**, 995 (1978)].
4. V. N. Lyubimov and D. G. Sannikov, *Fiz. Tverd. Tela (Leningrad)* **14** (3), 675 (1972) [*Sov. Phys. Solid State* **14**, 575 (1972)].
5. G. A. Puchkovskaya, V. L. Strizhevskii, Yu. A. Frolkov, *et al.*, *Phys. Status Solidi B* **89** (1), 27 (1978).
6. V. I. Alshits and J. Lothe, *Wave Motion* **3** (4), 297 (1981).
7. V. I. Alshits, A. S. Gorkunova, V. N. Lyubimov, *et al.*, in *Proceedings of the International Symposium on Trends in Continuum Physics* (World Scientific, Singapore, 1999), p. 28.
8. L. V. Iogansen, *Zh. Éksp. Teor. Fiz.* **40** (6), 1838 (1961) [*Sov. Phys. JETP* **13**, 1291 (1961)].
9. L. V. Iogansen, *Zh. Tekh. Fiz.* **32** (4), 406 (1962) [*Sov. Phys. Tech. Phys.* **7**, 295 (1962)]; *Zh. Tekh. Fiz.* **33** (11), 1323 (1963) [*Sov. Phys. Tech. Phys.* **8**, 985 (1964)]; *Zh. Tekh. Fiz.* **36** (11), 2056 (1966) [*Sov. Phys. Tech. Phys.* **11**, 1529 (1967)]; *Zh. Tekh. Fiz.* **38** (5), 781 (1968) [*Sov. Phys. Tech. Phys.* **13**, 589 (1968)].
10. M. I. D'yakonov, *Zh. Éksp. Teor. Fiz.* **94** (4), 119 (1988) [*Sov. Phys. JETP* **67**, 714 (1988)].
11. F. N. Marchevskii, V. L. Strizhevskii, and S. V. Strizhevskii, *Fiz. Tverd. Tela (Leningrad)* **26** (5), 1501 (1984) [*Sov. Phys. Solid State* **26**, 911 (1984)].
12. V. N. Lyubimov, *Zh. Prikl. Spektrosk.* **33** (5), 913 (1980).
13. V. M. Agranovich and V. L. Ginzburg, *Crystal Optics with Spatial Dispersion, and Excitons* (Nauka, Moscow, 1965; Springer-Verlag, New York, 1984).
14. V. I. Al'shits and V. N. Lyubimov, *Fiz. Tverd. Tela (St. Petersburg)* **37** (6), 1862 (1995) [*Phys. Solid State* **37**, 1014 (1995)].
15. Yu. I. Sirotin and M. P. Shaskolskaya, *Fundamentals of Crystal Physics* (Nauka, Moscow, 1975; Mir, Moscow, 1982).

Translated by A. Poushnov

---

## POLYMERS AND LIQUID CRYSTALS

---

# Mechanisms of Reversible Thermal Deformation of Oriented Polymers

A. I. Slutsker\*, L. A. Laius\*\*, I. V. Gofman\*\*, V. L. Gilyarov\*, and Yu. I. Polikarpov\*\*\*

\* Ioffe Physicotechnical Institute, Russian Academy of Sciences, Politekhnicheskaya ul. 26, St. Petersburg, 194021 Russia  
e-mail: Alexander.Slutsker@pop.ioffe.rssi.ru

\*\* Institute of Macromolecular Compounds, Russian Academy of Sciences, Bol'shoĭ pr. 31, St. Petersburg, 199004 Russia

\*\*\* St. Petersburg State Technical University, Politekhnicheskaya ul. 29, St. Petersburg, 195251 Russia

Received December 29, 2000

**Abstract**—Reversible thermal deformation coefficients (TDCs) of oriented samples of a flexible-chain polymer (polyethylene) and of a number of rigid-chain polymers were measured in the longitudinal and transverse directions near room temperature. The same samples were used to measure the TDCs of crystallites by x-ray diffraction. The magnitudes of the TDCs of macroscopic oriented samples and of constituting crystallites and the characteristics of the thermal deformation of flexible-chain and rigid-chain polymers are compared. A conclusion is made that the mechanisms that determine thermal deformation in the longitudinal and transverse directions for the flexible-chain and rigid-chain polymers are different. © 2001 MAIK “Nauka/Interperiodica”.

## 1. INTRODUCTION

By the reversible thermal deformation, a reversible change in the dimensions of a solid due to changes in temperature is meant. It is difficult to use the conventional term “thermal expansion” when considering polymers, since various anomalies such as negative thermal expansion coefficients (TEC), i.e., an increase rather than a decrease in the dimensions of a heated body, are frequently encountered in them [1]. These anomalies, just as some other features of the thermal deformation of polymers, are naturally due to the chainlike structure of their molecules and the strong difference in the forces of intramolecular and intermolecular interaction characteristic of solids with such a molecular structure. For this reason, the polymers differ from low-molecular solids also in the modes of internal dynamics, as well as in the mechanisms of thermal deformation.

For low-molecular solids, a single mechanism of thermal deformation (expansion), which can be called vibrational anharmonic, is dominating. In this case, particle vibrations in asymmetric potential wells that occur with changing temperature lead to a change in the average distances between particles. The TECs are, as a rule, positive; the anomalies in the sign of the TEC are quite rare [2]. As an example, graphite can be noted, whose crystals exhibit a significant anisotropy of thermal deformation in both the sign and magnitude [2]. However, graphite can be regarded as a transition to the so-called layered structures, which have some common features with the chain structure of polymers.

The thermal deformation of polymers was studied in numerous experimental and theoretical works. A com-

prehensive review of the available data and their analysis can be found in the monograph by Godovskii [1].

As the main mechanisms of the thermal deformation of polymers, we can indicate the following: (i) a vibrational anharmonic mechanism, which is inherent in any condensed system of atoms; (ii) a “membrane” mechanism [1, 3], which is characteristic of solids of chain (or layered) structure and consists in the effect of transverse vibrations on the longitudinal dimensions of the chains (or layers); and (iii) a conformational mechanism (specific of polymers), which is related to changes in the axial length of segments of chain molecules under the effect of jumpwise transitions of some conformation isomers from one type into another (gauche–trans and trans–gauche transitions) [4].

In polymeric bodies, depending on their morphology and the temperature range, various combinations of the above mechanisms of thermal deformation with different relationships between their contributions to the total thermal deformation can be encountered. The particular roles of these mechanisms need to be clarified in more detail.

The aim of this work is to perform comparative investigations of the thermal deformation of polymers on macroscopic and microscopic levels with the purpose to concretize the contributions of the various mechanisms to the total magnitude of thermal deformation of a polymer body.

## 2. OBJECTS OF INVESTIGATION

As the objects for the investigation, we chose polymers differing in the rigidity of their chains.

As a typical representative of flexible-chain polymers, low-density polyethylene (PE) was selected. It has an amorphous–crystalline structure, with the amorphous phase in the room-temperature range being in the devitrified state.

As a representative of polymers with an enhanced rigidity, we studied typical rigid-chain polymers such as poly(paraphenyleneterephthalamide) (Kevlar K-49) and poly(amidobenzimidazole) (PABI) and a closely related to them (in this characteristic) poly(pyromellitimide) (PM), which has a mesomorphic structure with a degree of crystallinity to about 10%. Note that all these polymers have high glass-transition temperatures  $T_g$  (much greater than room temperature).

A comparison of data for PE, which is characterized by an intense conformation dynamics above the transition temperature  $T_g$ , with that for the polymers in the glassy state, in which the conformation transitions are hindered, should permit one to reveal the role of the conformational mechanism in the process of thermal deformation. At the same time, the investigations of rigid-chain polymers are of interest from the viewpoint of revealing the role of the membrane mechanism in the processes studied.

The investigations were performed on polymer samples that were in a uniaxially oriented state. In this state, the samples possess a pronounced anisotropy of thermal deformation, which makes them suitable objects for comparing their properties with the thermodeformational properties of crystallites of the same polymers.

The oriented samples of PE were prepared from the initial isotropic samples in the form of rods ~16 mm in diameter by orientational drawing at room temperature to degrees of drawing (the ratios of the final length of the sample to its initial length)  $\lambda \cong 3$ –4.

The oriented samples of PM were prepared from a commercial film 100  $\mu\text{m}$  thick. The film was cut into strips 20 mm wide and 200 mm long, which then were subjected to a uniaxial orienting drawing at  $T = 400^\circ\text{C}$  to the drawing degrees  $\lambda \cong 2$ .

The samples of K-49 and PABI were taken in the form of oriented fibers.

### 3. EXPERIMENTAL

The longitudinal (along the orientation axis) thermal deformation for all the objects and the transverse deformation for the film samples were measured on a laboratory setup with a sensitivity to deformation of 3  $\mu\text{m}$ .

The temperature range of measurements of thermal deformation was chosen to ensure the reversibility of deformation (absence of remanent deformation) in short-term heating of the samples and was 293–323 K for PE and 293–573 K for the other polymers.

Under the above conditions, we measured the longitudinal ( $\epsilon_{\parallel}$ ) and transverse ( $\epsilon_{\perp}$ ) thermal deformations.

From these data, we found the magnitudes of the thermal-deformation coefficients (TDCs)  $\alpha_{\parallel} = \Delta\epsilon_{\parallel}/\Delta T$  and  $\alpha_{\perp} = \Delta\epsilon_{\perp}/\Delta T$ .

The thermal deformation on a microscopic level, namely, the lattice thermal deformation of crystallites of these polymers, was measured by x-ray diffraction from the angular shifts of reflections caused by changes in temperature. The measurements were carried out on a DRON-1.0 diffractometer using filtered  $\text{CuK}\alpha$  radiation ( $\lambda = 1.54 \text{ \AA}$ ). The samples were placed in a thermal chamber whose temperature could be varied in a range of 100–600 K. The profiles of meridional and equatorial large-angle reflections were recorded with the temperature being varied in a range of 212–360 K for PE and 110–418 K for the other polymers.

The relative lattice thermal deformations of crystallites ( $\epsilon^{\mu}$ ) along various crystallographic directions were determined from an expression that was obtained by differentiating the Bragg formula:

$$\epsilon^{\mu} = \frac{\Delta d}{d} = -\frac{\Delta\varphi}{2 \tan(\varphi_m/2)}, \quad (1)$$

where  $d$  and  $\Delta d$  are the interplanar distance and its change, respectively;  $\varphi_m$  is the center of gravity of the reflection at the initial temperature; and  $\Delta\varphi$  is the shift of the reflection due to a change in the temperature.

### 4. MEASUREMENT RESULTS

The results of the measurements of the thermal deformation of oriented samples are shown in Fig. 1 for the flexible-chain polymer (PE) and in Fig. 2 for the rigid-chain polymers.

In the temperature ranges studied, the thermal deformations were virtually reversible; no remanent structural changes were observed under these conditions.

The general character of temperature deformations shown in the graphs is the same: the deformation is negative (contraction) for all the samples in the longitudinal (along the orientation axis) direction and positive (expansion) in the transverse direction. In spite of the similar general form of these temperature dependences, we can note a significant difference in the magnitudes of the deformation. The thermal deformation is significantly higher for PE than for the other objects studied.

From the slopes of the graphs in Figs. 1 and 2, we determined the magnitudes of the TDCs near room temperature. These values are given in the table.

Now, we consider thermal microdeformation, i.e., the lattice deformation of crystallites of these polymers. Figures 3 and 4 display examples of thermally stimulated shifts of the angular positions of both equatorial and meridional x-ray diffraction reflections for the flexible-chain and one of the rigid-chain polymers, respectively. (The shifts of the equatorial reflections

Coefficients of thermal deformation (near 293 K)

Polymer	For oriented samples		For crystallites	
	$\alpha_{\perp}, \text{K}^{-1}$	$\alpha_{\parallel}, \text{K}^{-1}$	$\alpha_{\perp}^{\mu}, \text{K}^{-1}$	$\alpha_{\parallel}^{\mu}, \text{K}^{-1}$
PE	$4.8 \times 10^{-4}$	$-2.1 \times 10^{-4}$	$2.0 \times 10^{-4}$	$-1.2 \times 10^{-5}$
PM	$0.9 \times 10^{-4}$	$-7.0 \times 10^{-6}$	—	—
K-49	—	$-5.6 \times 10^{-6}$	$1.1 \times 10^{-4}$	$-6.0 \times 10^{-6}$
PABI	—	$-7.8 \times 10^{-6}$	$1.1 \times 10^{-4}$	$-7.7 \times 10^{-6}$

permit one to determine the temperature deformation in the direction that is perpendicular to the macromolecule axes; the shifts of the meridional reflections make it possible to determine temperature deformation in the longitudinal direction, along the macromolecule axes.) Changes in the deformation patterns observed for the other rigid-chain polymers are similar to those shown in Fig. 4.

In Figs. 3 and 4, line profiles for only three temperatures are shown in order to simply demonstrate the magnitudes of the shifts in the temperature range studied. In the experiment, reflections at a number of intermediate temperatures were also recorded.

It is seen from these figures that the angular shifts of the reflections differ in sign: with increasing temperature, the equatorial reflections are shifted toward smaller angles, while the meridional reflections toward the greater angles. According to Eq. (1), this indicates the well-known (for polymer crystals) situation: as the

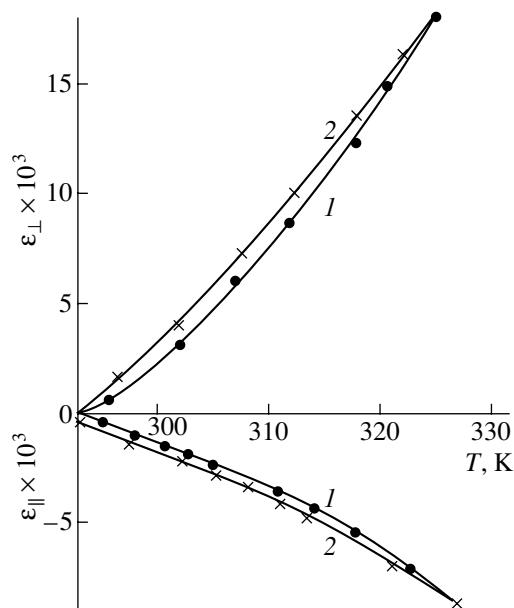


**Fig. 1.** Thermal deformation of an oriented polyethylene sample in the transverse ( $\epsilon_{\perp}$ ) and longitudinal ( $\epsilon_{\parallel}$ ) directions: (1) upon heating and (2) upon subsequent cooling of the sample.

temperature increases, the polymer lattice expands in the transverse direction and contracts in the longitudinal direction [1].

The use of Eq. (1) permitted us to determine the temperature dependences of the relative thermal deformation of the crystallite lattices in the transverse ( $\epsilon_{\perp}^{\mu}$ ) and longitudinal ( $\epsilon_{\parallel}^{\mu}$ ) directions. These dependences are given in Figs. 5 and 6, respectively.

From the slopes of the  $\epsilon^{\mu}(T)$  dependences near 293 K, we found the magnitudes of the TDCs of the crystallite lattices for room temperatures (see table).

The data obtained permit us to compare the magnitudes of the TDCs of the objects studied, i.e., of flexible-chain and rigid-chain polymers on macroscopic oriented samples and microscopic crystallites of the same polymer in the transverse and longitudinal directions.

## 5. DISCUSSION OF THE RESULTS

First of all, note that from the viewpoint of the signs of the TDCs, the oriented samples of the polymers and the crystallites that constitute them give qualitatively similar results: the TDCs are positive in the transverse directions and are negative in the longitudinal directions.

As to the quantitative results, the TDCs of different polymers differ significantly. For the rigid-chain polymers, the values of both the transverse and longitudinal TDCs are close for the macroscopic oriented samples

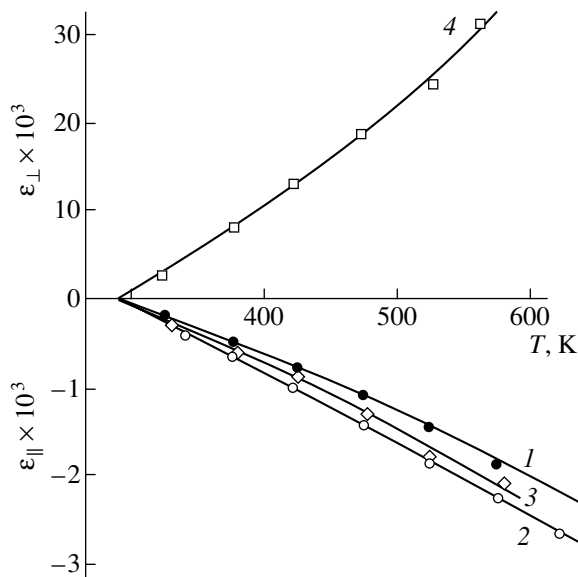


**Fig. 2.** Thermal deformation in the longitudinal direction of (1) PABI and (2) K-49 fibers and the deformation of PM films in (3) longitudinal and (4) transverse directions.

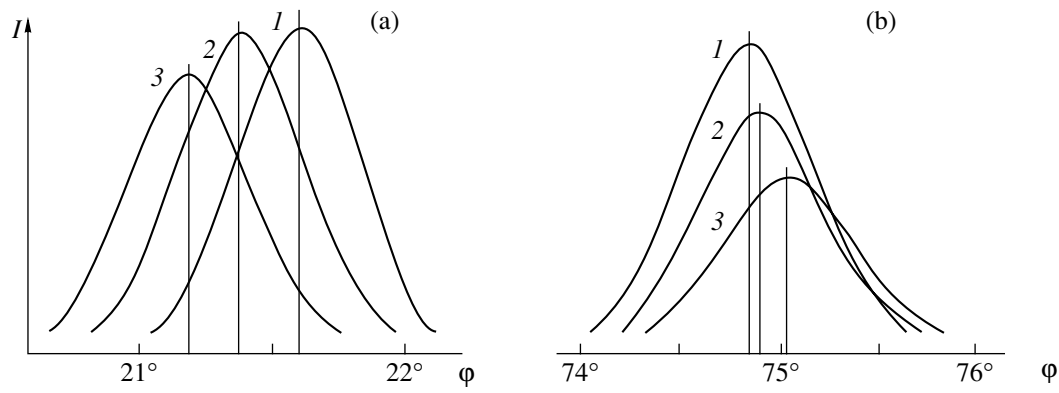


**Fig. 3.** Profiles of x-ray diffraction lines of oriented polyethylene at various temperatures: (a) equatorial reflection [110], (1)  $T = 212$ , (2) 293, and (3) 352 K; (b) meridional reflection [002], (1)  $T = 218$ , (2) 293, and (3) 347 K.

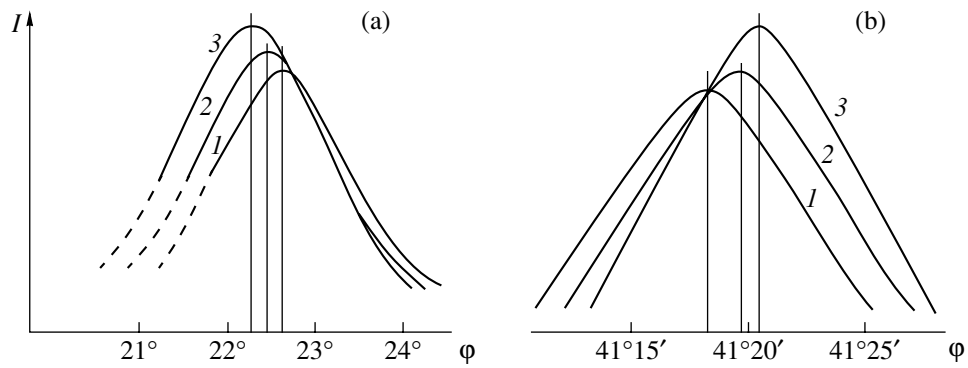


**Fig. 4.** Profiles of x-ray diffraction lines of K-49 fibers at various temperatures: (a) equatorial reflection, (1)  $T = 247$ , (2) 343, and (3) 418 K; (b) meridional reflection, (1) 110, (2) 293, and (3) 400 K.

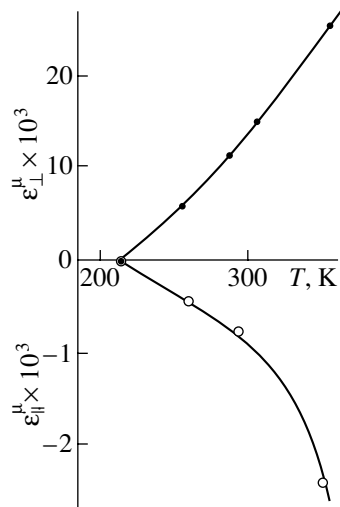


**Fig. 5.** Thermal deformation of polyethylene crystallites in the transverse ( $\epsilon_{\perp}^{\mu}$ ) and longitudinal ( $\epsilon_{\parallel}^{\mu}$ ) directions.

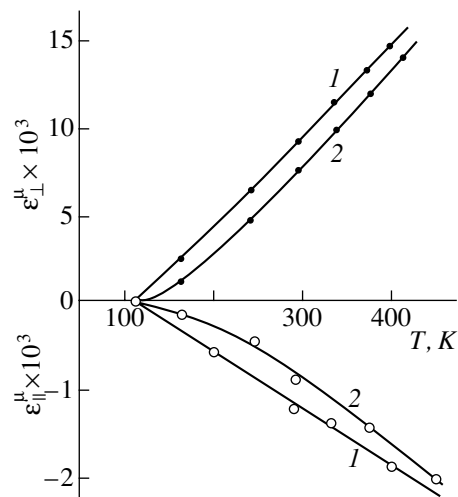


**Fig. 6.** Thermal deformation of crystallites of (1) K-49 and (2) PABI in the transverse ( $\epsilon_{\perp}^{\mu}$ ) and longitudinal ( $\epsilon_{\parallel}^{\mu}$ ) directions.

and the constituting crystallites (they are almost coincide). As to the flexible-chain polymer (PE), the TDC of the oriented samples significantly exceeds that of crystallites (especially, in the longitudinal direction).

We first consider the thermal deformation of crystallites. This problem has been studied to date in much detail in both the experimental and theoretical plan [1, 3, 5].

In polymer crystals, the macromolecules are in a straightened state and are located in parallel with one another. Almost all the molecules (to be precise, their segments that enter into crystallites) contain only transverse conformers. Up to temperatures close to the melting point, the conformation dynamics is virtually absent. The dominating and the virtually single form of dynamics in crystals is vibrational dynamics. Because of the high, as a rule, longitudinal rigidity of macromolecules caused by strong covalent bonds in the skeletons of chain molecules, the longitudinal vibrations are characterized by high frequencies and, as a consequence, by high characteristic (Debye) temperatures such as 1000 K or higher [1]. Therefore, in the room-temperature range, the longitudinal vibrations, which in the case of normal anharmonicity would lead to a longitudinal expansion (elongation) of the molecules, prove to be almost unexcited. This prevents a noticeable manifestation of the vibrational anharmonic mechanism of the thermal expansion of macromolecules in the longitudinal direction.

The situation is different for the transverse direction. The bending (as well as the twisting) rigidity of macromolecules is small in comparison with the longitudinal rigidity (it is smaller by 1.5–2 orders of magnitude). The intermolecular interactions (hydrogen, van der Waals, and other dispersion bonds) are significantly (by 1–2 orders of magnitude) weaker than the intramolecular (covalent) bonds. For this reason, the frequencies of transverse (bending and torsional) vibrations of the macromolecules are much lower than the frequencies of longitudinal vibrations and, correspondingly, the characteristic temperatures for them are much smaller than those for longitudinal vibrations; namely, they are on the level of ~100 K [1]. Therefore, in the room-temperature range, the transverse vibrations are already excited sufficiently strongly. This results in the following effects.

(a) A decrease in the axial length of macromolecules (the “membrane” effect). This effect can vividly be explained by the bending of a longitudinally inextensible chain, which leads to a decrease in the projection of the contour length of the macromolecule onto its axis (i.e., to a decrease in the axial length of the macromolecule). A theoretical analysis of this effect for layered and chain structures was performed in [1, 3, 5]. The anharmonicity of the intramolecular and intermolecular atomic interactions is not of a decisive importance for this effect.

(b) Expansion of the crystallite lattice in the transverse direction. This expansion is due to the anharmonicity of the intermolecular interaction.

Thus, in polymer crystallites, two mechanisms of thermal deformation are operative: (1) the membrane mechanism (which is not related to the anharmonicity) in the longitudinal direction and (2) the vibrational anharmonic mechanism in the transverse direction.

Let us compare the TDCs of the crystallites and oriented samples for rigid-chain polymers. It is seen from the table that the TDCs of crystallites and oriented samples in the longitudinal direction are virtually coincident. For all these polymers, the glass-transition temperatures  $T_g$  are much higher than room temperature. Note that the magnitude of  $\alpha_{\perp}$  for the oriented film of PM is close to the magnitude of  $\alpha_{\perp}^{\mu}$  for K-49 and PABI.

The data presented in the table permit us to conclude that the same two mechanisms are dominating at room temperatures in the macroscopic thermal deformation of the samples of oriented rigid-chain polymers as in the deformation of crystallites, i.e., the membrane mechanism in the longitudinal direction and the vibrational anharmonic mechanism in the transverse direction.

Now, we turn to oriented samples of the flexible-chain polymer (polyethylene) which at room temperature is in the devitrified state. First, we consider the longitudinal thermal deformation. As can be seen from the table, the negative longitudinal TDC of the oriented sample  $\alpha_{\parallel}$  significantly (by an order of magnitude) exceeds the negative longitudinal TDC of crystallites  $\alpha_{\parallel}^{\mu}$ . Undoubtedly, this difference is due to the fact that in the oriented samples of PE, amorphous regions exist apart from crystallites (the volume fraction of crystallites is ~60% [6]). These regions are located both inside fibrils (enter into the “long periods”) and between fibrils [6]. The macromolecules in the amorphous regions of the oriented PE samples are also oriented (this follows from a texture that is observed in the amorphous halo in the x-ray diffraction patterns of oriented PE [6]), although certainly in a smaller degree than in the crystallites.

Note that since the amorphous regions occupy only part of the oriented-sample volume (about 40%), the local longitudinal TDC of intrafibril amorphous regions is significantly (by a factor of 2 or 3) higher than the longitudinal TDC of the oriented sample as a whole; i.e., it is higher by about two orders of magnitude than the longitudinal TDC of the crystallites. As for the TDC of amorphous interfibril regions, it appears to be close to the longitudinal TDC of the oriented sample.

What can cause the high value of the TDC of amorphous regions? We think that it is difficult to explain such a value of the TDC by an increase in the amplitude of transverse vibrations of macromolecules and the related enhancement of the membrane effect. In this



case, we had to assume that at the same temperature the amplitude of transverse vibrations of macromolecules in amorphous regions is greater than the amplitude of similar vibrations in crystallites by more than an order of magnitude.

Thus, we may think of the existence of one more mechanism (apart from the "membrane" one), which leads to a contraction of the axial length of oriented macromolecules with increasing temperature. For the amorphous regions of the polymer being in a devitrified state, conformational (isomeric) trans-gauche transitions in macromolecules can serve as such a mechanism. The axial length of a gauche isomer is smaller than that of the trans isomer; therefore, the transitions of trans isomers into gauche isomers should cause a contraction of the axial length of oriented macromolecules.

Let us approximately estimate the longitudinal TDC of the oriented amorphous region of PE proceeding from the statistics of the isomers.

Introduce a quantity  $\Delta l$ , i.e., the difference of the axial lengths of trans and gauche isomers. The longitudinal TDC of an amorphous polymers is defined through this quantity as follows:

$$\alpha_{\parallel}^{\text{am}} \approx \Delta l \frac{dN_{\text{tr}}}{dT} n_s^{-1}, \quad (2)$$

where  $N_{\text{tr}}$  is the number of trans isomers per unit volume and  $n_s$  is the number of molecules passing through a unit area of the cross section of the sample ( $n_s \cong S_m^{-1}$ , where  $S_m$  is the cross-sectional area of a chain molecule).

In order to estimate  $dN_{\text{tr}}/dT$ , we use the formula that determines the equilibrium concentration of trans isomers at a temperature  $T$  [4]:

$$N_{\text{tr}}(T) = N \left[ 1 + \exp\left(-\frac{\Delta U}{kT}\right) \right]^{-1}, \quad (3)$$

where  $N$  is the total concentration of isomers and  $\Delta U$  is the difference of the potential energies of the gauche and trans isomers. For PE,  $\Delta U = 2.1 \text{ kJ/mol} = 3.5 \times 10^{-21} \text{ J}$  per conformation [1].

Equation (2) refers to a free polymer molecule. The retention of an oriented state of devitrified amorphous regions in PE is due to the existence of a rigid oriented "framework" consisting of crystallites. This, certainly, changes the conditions of the equilibrium state of chain molecules in amorphous regions. However, since the above calculations were performed differentially, i.e., by considering the change in the concentration of trans isomers upon temperature variations, the use of Eq. (3) for an approximate estimation of the magnitude of  $dN_{\text{tr}}/dT$  seems to be justified.

Then, it follows from Eqs. (2) and (3) that

$$\alpha_{\parallel}^{\text{am}} \approx -N\Delta l n_s^{-1} \frac{\Delta U}{kT^2} \exp\left(-\frac{\Delta U}{kT}\right) \left[ 1 + \exp\left(-\frac{\Delta U}{kT}\right) \right]^{-2}. \quad (4)$$

For the longitudinal TDC of the oriented sample of PE with allowance for its degree of crystallinity  $q \cong 0.6$ , we may write the following approximate expression:

$$\alpha_{\parallel} \cong \alpha_{\parallel}^{\text{am}} (1 - q). \quad (5)$$

Let us perform a qualitative estimation. Assume that  $\Delta l \cong 1 \text{ \AA} \cong 1 \times 10^{-10} \text{ m}$ ,  $n_s \cong 4 \times 10^{18} \text{ m}^{-2}$ , and  $N \cong 4 \times 10^{28} \text{ m}^{-3}$  (the number of  $\text{CH}_2$  groups per unit volume of amorphous PE). Then, we have from Eqs. (4) and (5) that

$$\alpha_{\parallel} \cong -2.1 \times 10^{-4} \text{ K}^{-1}.$$

It is seen that the calculated value of  $\alpha_{\parallel}$  is very close to the measured value (see table). This coincidence of the calculated and experimental values of  $\alpha_{\parallel}$  suggests that the longitudinal thermal deformation of oriented PE is indeed caused by the conformational dynamics, i.e., by trans-gauche transitions. The anharmonicity of the interparticle interaction does not contribute to the longitudinal thermal deformation in this case (just as in the case of the membrane mechanism).

Thus, the longitudinal thermal deformation of oriented PE is dominated by the conformational mechanism, since the contribution of the membrane component to the thermal deformation of crystallites and amorphous regions is small.

Now, we briefly consider the transverse thermal deformation of oriented PE. As is seen from the table, the transverse TDC of the oriented sample significantly (by a factor of 2–2.5) exceeds the transverse TDC of crystallites, although the difference between the transverse TDCs of the oriented sample and crystallites is not so large as in the longitudinal direction.

It may be supposed that the thermal deformation of the oriented sample in the transverse direction is affected by the conformation dynamics. Actually, the trans-gauche transitions, causing a contraction of the axial lengths of macromolecules, lead to an increase in the average transverse dimensions of macromolecules, which in itself contributes to the transverse thermal expansion of the oriented sample. However, naturally, the vibrational-anharmonic mechanism also continues to be operative in this case and makes its contribution to expansion. As a result, the transverse TDC of the oriented sample proves to be higher than that of crystallites. It is evident that in the case of macrodeformation of the sample we cannot discriminate the dominating mechanism of transverse expansion. It is possible that the contributions of the vibrational anharmonic and conformational mechanisms are comparable. A quantitative estimation of the relationship between these contributions is a difficult problem and requires a more detailed consideration. Such a consideration permits

one to approach the problem of the analysis of thermal expansion of unoriented samples of flexible-chain polymers.

## 6. CONCLUSION

The main results of this work consist in that we revealed various mechanisms (of both anharmonic and nonanharmonic origin) in the thermal deformation of oriented polymers.

## ACKNOWLEDGMENTS

This work was supported in part by the Russian Foundation for Basic Research, project no. 00-03-33064a.

## REFERENCES

1. Yu. K. Godovskii, *Thermal Physics of Polymers* (Khimiya, Moscow, 1982).
2. S. I. Novikova, *Thermal Expansion of Solids* (Nauka, Moscow, 1974).
3. I. M. Lifshits, *Zh. Éksp. Teor. Fiz.* **22** (4), 475 (1952).
4. M. V. Vol'kenshtein, *Configurational Statistics of Polymer Chains* (Akad. Nauk SSSR, Moscow, 1959).
5. F. C. Chen, C. L. Choy, and K. Young, *J. Polym. Sci., Part B: Polym. Phys.* **18** (12), 2313 (1980).
6. V. A. Marikhin and L. P. Myasnikova, *Supramolecular Structure of Polymers* (Khimiya, Moscow, 1977).

*Translated by S. Gorin*

---

## FULLERENES AND ATOMIC CLUSTERS

---

# Sign Reversal of the Magnetoplastic Effect in C<sub>60</sub> Single Crystals during the sc–fcc Phase Transition

Yu. A. Osip'yan\*, Yu. I. Golovin\*\*, R. B. Morgunov\*\*,  
R. K. Nikolaev\*, I. A. Pushnin\*\*, and S. Z. Shmurak\*

\* Institute of Solid-State Physics, Russian Academy of Sciences, Chernogolovka, Moscow oblast, 132432 Russia

\*\* Derzhavin State University, Tambov, 392622 Russia

e-mail: golovin@tsu.tmb.ru

Received November 27, 2000

**Abstract**—It is found that the magnetoplastic effect in C<sub>60</sub> single crystals in a pulsed magnetic field with induction larger than 10 T changes its sign in the vicinity of the phase transition at  $T_c = 250$ – $260$  K: crystal strengthening is observed for  $T < T_c$ , and softening occurs for  $T > T_c$ . This indicates a change in the crystal lattice structure in the magnetic field. © 2001 MAIK “Nauka/Interperiodica”.

## 1. INTRODUCTION

In our earlier publication [1], we reported the observation of the magnetoplastic effect in C<sub>60</sub> single crystals at room temperature. The effect consists in a long-term variation of the microhardness  $H$  of crystals exposed to a pulsed magnetic field (MF). Residual changes in  $H$  can reach 10% in a pulsed MF with amplitude  $B = 25$  T and duration  $\sim 100$   $\mu$ s and can be observed both immediately after the exposure of the crystal to the MF and for 24 h following the exposure. The reasons for the softening of C<sub>60</sub> crystals have not been established. At the same time, an understanding of the relation between the magnetic and plastic properties of C<sub>60</sub> could stimulate the development of the theory describing the microscopic mechanisms of plastic deformation of fullerenes.

Many physical parameters of C<sub>60</sub> crystals (heat capacity, volume, x-ray diffraction spectra [2], velocity of sound [3], Raman spectra [4]) are known to experience a jumplike change in the phase transition region at  $T_c = 252$  K. The mechanical properties (internal friction [5], Young's modulus [6], temperature spectra of deformation rates [7, 8], microhardness [9]) also display sharp variations in the vicinity of  $T_c$ . In order to determine the reasons behind the effect of an MF on the plasticity of fullerenes, we must obviously find out how the above-mentioned phase transition, in which the simple cubic (sc) lattice is transformed into a face-centered cubic (fcc) lattice at  $T > T_c$ , influences the magnetoplastic effect. The present work is devoted to an analysis of the magnetoplastic effect in fullerenes placed in an MF in the temperature range including the sc–fcc phase transition region.

## 2. EXPERIMENTAL TECHNIQUE

In order to study the sensitivity of microhardness to an MF, we used high-purity (99.95%) C<sub>60</sub> single crystals grown from the vapor phase with the natural faceting typical of fcc crystals and a mean linear size of  $\sim 2$ – $3$  mm. The crystals were fixed to glass with the help of picein so that the face under investigation was accessible for indentation and parallel to the table of a PMT-3 microhardness tester. Each indentation was carried out for 5 s at the same temperature  $T = 298$  K and under a load of 20 g on the indenter. The temperature variations required for studying the temperature dependence of the relaxation kinetics of the crystals after their exposure to the MF took place in the time intervals between indentations.

The microhardness of C<sub>60</sub> is known to change in the process of the sample ageing in air as a result of photo-stimulated oxidation and polymerization of the surface [10]. In order to slow down the oxidation, all experimental procedures were made in the dark (except the measurements of imprints carried out in dim red light). This allowed us to preserve the value of microhardness in zero MF for  $\sim 10$  days at the same level as immediately after the extraction of the crystals from the evacuated capsule. Each point on the graphs (Figs. 1, 2) was obtained by averaging the size of 15–20 imprints created under identical conditions. The MF pulses had a shape close to that of a positive half-cycle of the sinusoid, amplitude  $B = 24$  T, and duration 140  $\mu$ s; they were generated in a coil with a small number of turns as a result of a discharge of a capacitor bank. It should be emphasized once again that we studied the possible manifestations of residual changes in the microhardness of fullerenes after their preliminary exposure to an MF. The exposure to the MF and the measurement of microhardness were carried out in different setups with

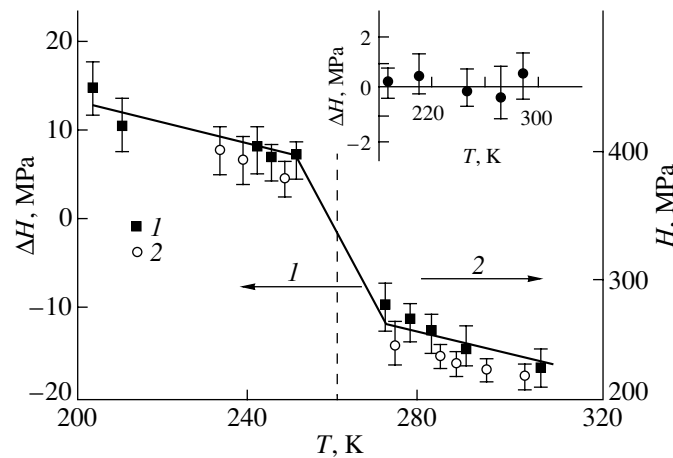


**Fig. 1.** Dependences (1) of the variation of microhardness  $\Delta H$  of a  $C_{60}$  crystal, induced by a magnetic field pulse, on the temperature  $T$  at which the samples were exposed to the magnetic field and (2) of microhardness  $H$  of  $C_{60}$  crystals on the temperature  $T$  at which it was measured according to [9]. The inset shows the dependence of  $\Delta H$  in a test series of experiments on the temperature  $T$  at which the samples were held in zero magnetic field prior to the measurements of  $H$ .

a time interval required for moving the sample ( $\sim 1$  min), so that the effect of the MF on the procedure of variation of  $H$  was completely precluded in the experimental setup.

### 3. DISCUSSION OF EXPERIMENTAL RESULTS

It was found that the microhardness of crystals subjected to the action of an MF at a temperature  $T < T_c$  increases as compared to the value obtained prior to the exposure of fullerite in the MF. For  $T > T_c$ , an MF pulse

causes a decrease in  $H$  (see Fig. 1). Thus, the sign of the magnetoplastic effect is reversed at the phase transition point  $T_c$  and the temperature interval in which this phenomenon is observed is close to that observed in [9] while measuring the  $H(T)$  dependence (see Fig. 1).

Under certain conditions, heating and cooling of the crystals can cause the emergence of metastable “quenching” defects associated with the excess concentrations of molecules that are in the so-called hexagonal ( $h$ ) and pentagonal ( $p$ ) mutual orientations [7]. In a series of test experiments, it was found that the procedure of cooling and subsequent heating carried out in zero MF does not lead to a change in  $H$  (see the inset to Fig. 1) and the variation of the mean rate of cooling (heating) in the range 0.02–1.2 K/s does not change the value of the magnetoplastic effect  $\Delta H$ . It is hardly probable that the metastable “quenching” defects influence the magnetoplastic effect in any way.

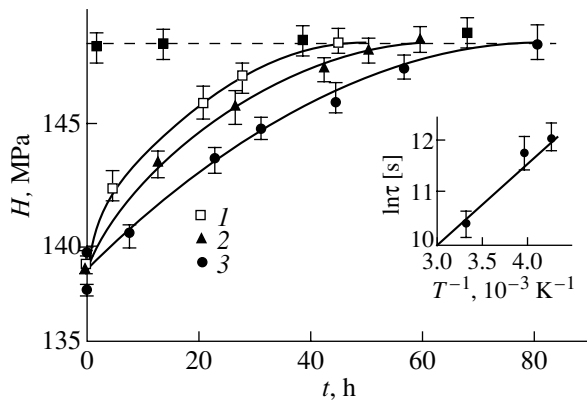


**Fig. 2.** Dependence of the microhardness  $H$  of the crystals subjected to the action of the magnetic field at  $T = 298$  K on the time  $t$  elapsed after the sample exposure to the magnetic field in the case when  $H$  was measured at  $T = 298$  K, while in the interval between the magnetic field pulse and the  $H$  measurements, the samples were at the temperature (1) 298, (2) 258, and (3) 248 K. The dashed line indicates the value of  $H$  prior to the exposure of crystals to the magnetic field. The inset shows the dependence of the time constant  $\tau$  of microhardness recovery on the reciprocal temperature  $T$  at which the relaxation occurred.

In our earlier publication [1], it was reported that the change in the value of  $H$  induced by the MF in fullerite gradually disappears with the time  $t$  elapsed after the exposure of the sample to the field but it can be induced again many times by repeated application of the MF. This apparently indicates that the MF imparts excess energy to certain elements of the fullerite structure, exciting them to a metastable state. The transition rate from this state is characterized by a certain kinetics of restoration of  $H$  after the action of an MF pulse (Fig. 2). One can assume that the relaxation occurs through the thermally activated surmounting of the potential barrier. In order to estimate the barrier height  $U$ , the crystal was held at three different temperatures (298, 258, and 248 K) after the exposure to the MF (occurring at  $T = 298$  K in this series of experiments). In the latter two cases, its temperature was periodically brought to room temperature, required for the next measurement of  $H$

for a short time (as compared to the duration of the recovery of  $H$ ) ( $\sim 30$  min), and then restored to its previous value. A comparison of the slopes of the initial segments of  $H$  relaxation (Fig. 2) shows that an increase in temperature accelerates the process. Consequently, the thermodynamic role of the MF lies in the initiation of the transition of the crystal to the metastable state which is separated from the ground state by a potential barrier and the relaxation of this excited state occurs through thermal activation with an activation energy  $\sim 0.18 \pm 0.02$  eV (see the inset to Fig. 2).

We note that the local deformation conditions were identical in the course of variation of hardness (mechanical loading and temperature) in all the experiments. This means that the sensitivity of the sign of the magnetoplastic effect under investigation to temperature cannot be attributed to the variation of the thermal-activation and orientation relaxation times for molecules in the vicinity of moving dislocation cores, although the inclusion of these factors by Natsik *et al.* [11] enabled them to explain the nonmonotonic temperature dependence of plastic properties of fullerites. In our experiments, the action of the MF could change only the state of the crystal lattice itself or of the defects contained in it. The coincidence of the temperature at which the sign inversion of the magnetoplastic effect was observed in our experiments with the known value of  $T_c$  may indicate that the effect of the MF involves a change in the structure of the crystal lattice itself rather than of the point defects, as is the case in ionic crystals [12, 13].

The energy  $E$  imparted to a  $C_{60}$  molecule from the MF with induction 24 T amounts to  $E \sim \mu B \sim 10^{-2}$  eV irrespective of the assumptions concerning the origin of the magnetic moment of a molecule  $\mu \sim \mu_B \approx 9 \times 10^{-24}$  A m ( $\mu_B$  is Bohr's magneton), whose presence can be due to both an uncompensated spin and the magnetic susceptibility anisotropy of chemical bonds. The value of  $E$  is equal to the difference  $\Delta$  between the energies of  $h$  and  $p$  configurations of  $C_{60}$  molecules [7, 8, 11]. According to the above estimate, the height of the potential barrier that hinders the recovery of  $H$  is much smaller than the known energy value  $U^* = 0.3$  eV required for surmounting the potential barrier through the rotation of molecules around the threefold axis and for a transition between  $h$  and  $p$  configurations [11]. In our opinion, the difference may be due to the fact that the crystal had to be periodically heated for measuring  $H$ , which could lead to an increase in the hardness restoration rate of  $H$  and, hence, to a lower estimate of  $U$ . Another explanation may be that the relaxation following an MF pulse occurs through the rotation of  $C_{60}$  molecules around the twofold axis with an activation energy  $\sim 0.245$  eV [11], which is closer to the value of  $U$  obtained by us.

According to the results obtained by Tachibana *et al.* [9], the hardness decreases jumpwise as the phase-transition point is approached from the low-temperature side (Fig. 1). This might indicate that the hardness of

the low-temperature sc phase is higher than the hardness of the fcc phase. If, in compliance with the above estimates, we accept the hypothesis that the MF changes the population of the  $h$  and  $p$  states of  $C_{60}$  molecules (for example, by inducing their reorientation), we can assume that its role might be the initiation of the change in the size of cooperative regions of the sc and fcc phases. In this case, the MF reduces the size of metastable sc-phase regions by transforming them to the fcc phase for  $T > T_c$  and increases the size of these regions for  $T < T_c$ . It should be noted that the effect of the sc-fcc phase transition on the plasticity can be explained by the fact that the process of polymerization of  $C_{60}$ , which is sensitive to the temperature and phase composition [14] and can occur in the vicinity of dislocation cores, can change after the exposure of the crystals to the MF. As a result, the structure of dislocation cores and, hence, their mobility might change. Another reason for the observed sign inversion of the magnetoplastic effect can be that the MF changes the kinetics of the phase transition during heating of the crystal subjected to the action of the MF at  $T < T_c$ .

#### 4. CONCLUSION

Thus, we have established a relation between the phase composition of the fullerite  $C_{60}$  and the sensitivity of its plastic properties to the action of a pulsed MF. The observed sign inversion of the magnetoplastic effect upon a transition through the phase-transition point can be explained by the effect of this phase transition on the sensitivity of the plastic parameters to the MF, as well as by the opposite effect of the MF on the phase-transition kinetics.

#### ACKNOWLEDGMENTS

This work was supported by the Russian Scientific and Technical Program "Fullerenes and Atomic Clusters," project no. 2008.

#### REFERENCES

1. B. A. Osip'yan, B. I. Golovin, D. V. Lopatin, *et al.*, Pis'ma Zh. Éksp. Teor. Fiz. **69** (2), 110 (1999) [JETP Lett. **69**, 123 (1999)].
2. I. O. Bashkin, V. I. Rashchupkin, A. F. Gurov, *et al.*, J. Phys.: Condens. Matter **6**, 7491 (1994).
3. X. D. Shi, A. R. Kortan, J. M. Williams, *et al.*, Phys. Rev. Lett. **68**, 827 (1992).
4. K. Matsuishi, K. Tada, S. Onari, and T. Arai, Philos. Mag. **70** (3), 795 (1994).
5. W. Shranz, A. Fuith, P. Dolinar, *et al.*, Phys. Rev. Lett. **71**, 1561 (1993).
6. N. P. Kobelev, A. P. Moravskii, Ya. M. Soifer, *et al.*, Fiz. Tverd. Tela (St. Petersburg) **36** (9), 2732 (1994) [Phys. Solid State **36**, 1491 (1994)].

7. V. M. Egorov, R. K. Nikolaev, B. I. Smirnov, and V. V. Shpeĭzman, *Fiz. Tverd. Tela (St. Petersburg)* **42** (9), 1716 (2000) [*Phys. Solid State* **42**, 1766 (2000)].
8. V. V. Shpeĭzman, N. N. Peschanskaya, V. M. Egorov, *et al.*, *Fiz. Tverd. Tela (St. Petersburg)* **42** (9), 1721 (2000) [*Phys. Solid State* **42**, 1771 (2000)].
9. M. Tachibana, M. Michiyama, K. Kikuchi, *et al.*, *Phys. Rev. B* **49** (21), 14945 (1994).
10. I. Manika and J. Maniks, *Fullerene Sci. Technol.* **5** (1), 149 (1997).
11. V. D. Natsik, S. L. Lubenets, and L. S. Fomenko, *Fiz. Nizk. Temp.* **22** (3), 337 (1996) [*Low Temp. Phys.* **22**, 264 (1996)].
12. Yu. I. Golovin, R. B. Morgunov, V. E. Ivanov, and A. A. Dmitrievskĭĭ, *Zh. Ėksp. Teor. Fiz.* **116** (6), 1 (2000) [*JETP* **90**, 939 (2000)].
13. Yu. I. Golovin and R. B. Morgunov, *Zh. Ėksp. Teor. Fiz.* **115** (2), 605 (1999) [*JETP* **88**, 332 (1999)].
14. M. Nuñez-Regueiro, L. Margues, J. L. Hodeau, C. H. Xu, and G. E. Scuseria, in *Fullerene Polymers and Fullerene Polymer Composites*, Ed. by P. C. Eklund and A. M. Rao (Springer-Verlag, Berlin, 2000); *Springer Ser. Mater. Sci.* **38**, 241 (2000).

*Translated by N. Wadhwa*

## FULLERENES AND ATOMIC CLUSTERS

# Optical and Electrical Properties of $C_{60}Te_x$ Films

T. L. Makarova\*, V. G. Melekhin\*, I. T. Serenkov\*, V. I. Sakharov\*,  
I. B. Zakharova\*\*, and V. É. Gasumyants\*\*

\* Ioffe Physicotechnical Institute, Russian Academy of Sciences, Politekhnikeskaya ul. 26, St. Petersburg, 194021 Russia

\*\* St. Petersburg State Technical University, Politekhnikeskaya ul. 29, St. Petersburg, 195251 Russia

e-mail: zakharova@rphf.spbstu.ru

Received December 9, 2000

**Abstract**—The structure, composition, and electrical and optical properties of thin tellurium-intercalated fullerene films  $C_{60}Te_x$  are investigated. The samples of compositions from  $C_{60}Te_{0.1}$  to  $C_{60}Te_6$  are prepared by thermal evaporation. The sample composition and the impurity distribution are controlled by the Rutherford backscattering technique. The Raman vibrational spectra indicate changes in the symmetry of a  $C_{60}$  molecule: the strain of the molecule increases with a decrease in the tellurium concentration and decreases as the tellurium impurity concentration increases. The evolution of the optical absorption spectra and the electrical conductivity suggests that intercalation of a tellurium impurity leads to modification of the electronic structure of the material. This process is accompanied by a shift and change in shape of the optical absorption edge and a change in the electrical conductivity of films by several orders of magnitude depending on the composition. The electrical conductivity is minimum at a low tellurium impurity content. © 2001 MAIK “Nauka/Interperiodica”.

### 1. INTRODUCTION

The incorporation of impurity atoms into a fullerene film can occur in two ways. In the first case, impurity atoms are distributed in a crystal in the form of microinclusions or impurity clusters. In the second case, impurity atoms are intercalated into the compound; i.e., they occupy holes in the crystal lattice of fullerite. The equilibrium solid phase of  $C_{60}$  at room temperature is a molecular crystal with a face-centered cubic lattice (the lattice constant is equal to 1.417 nm) [1]. The unit cell involves eight tetrahedral and four octahedral holes which can be occupied by impurity atoms. The intercalation can substantially affect the physical and electronic properties of the material. For example, the intercalation of an alkali metal impurity into fullerite is accompanied by the charge transfer to  $C_{60}$  due to the low ionization potential of alkali metal atoms. The electrical properties of these compounds depend on the number of metal atoms per  $C_{60}$  unit cell [2, 3]. The term doped fullerenes, as applied to the incorporation of impurities into a fullerene matrix, is often used in the literature; however, in the majority of cases, these works actually dealt with intercalation compounds.

At present, alkali, alkaline-earth, and rare-earth elements are predominantly used for doping of fullerenes. However, materials whose fullerene matrix is intercalated with semiconductor compounds remain virtually unexplored. The interaction of intercalated semiconductor atoms with fullerene molecules should bring about a radical change in the electronic properties of the material, and the change in the composition and concentration of impurities makes it possible to modify the electrical and optical properties in a controlled way.

The purpose of this work was to prepare tellurium-intercalated fullerene films and to investigate experimentally their electrical and optical properties as functions of the structure, composition, and concentration of the intercalated impurity.

### 2. EXPERIMENTAL TECHNIQUE

Samples of  $C_{60}Te_x$  films on glass and silicon substrates were prepared by the thermal evaporation technique under vacuum from a mechanical mixture of two components, namely, a microcrystalline  $C_{60}$  powder (99.98%) and a spectroscopically pure Te powder. The evaporation temperature was equal to 400–450°C, and the condensation temperature was 100–200°C. The thickness of the films prepared varied in the range 200–400 nm. The composition of the samples was calculated from the batch composition with due regard for the saturation vapor pressure of the components at different evaporation temperatures. The actual tellurium content in the films produced was controlled by the Rutherford backscattering method. Compared to the as-batched composition, the as-analyzed composition was characterized by a higher tellurium content. The reference samples of  $C_{60}$  films were prepared under similar conditions.

The films thus prepared can either be a composite material in which impurities are distributed in the matrix in the form of individual clusters (as in the case of  $Cu_nC_{60}$  films produced by evaporation of a mechanical mixture of the components [4]) or have an intercalated structure. In the former case, the material can be considered a system of two components and its permit-

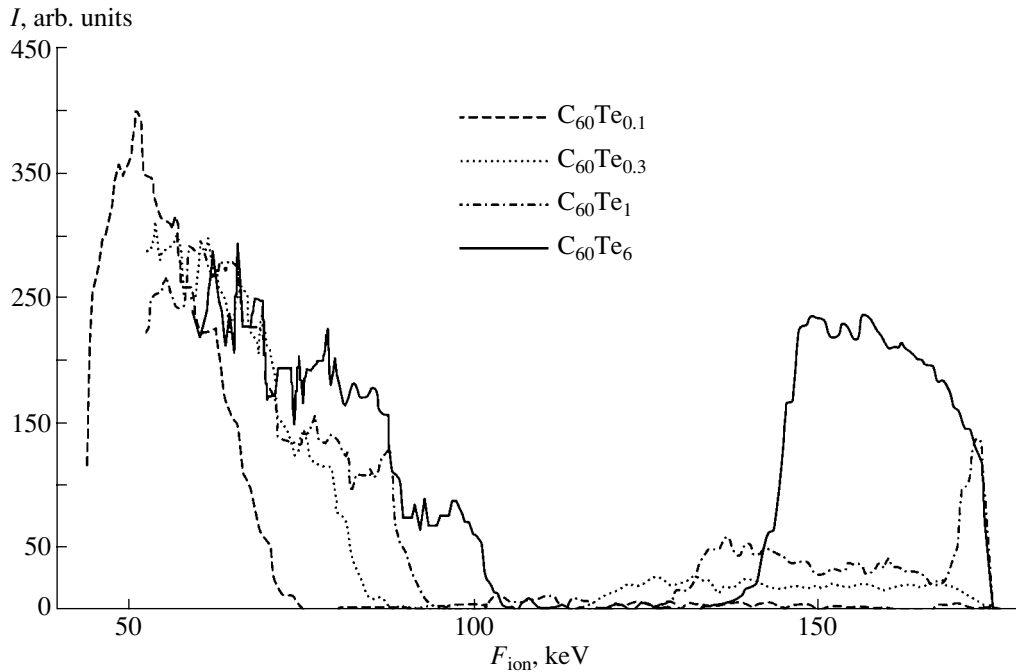


Fig. 1. Rutherford backscattering spectra of  $C_{60}Te_x$  samples. The energy of  $He^+$  ions is equal to 190 keV.

tivity can be evaluated within the effective medium model [5]. In the framework of this model, we calculated the real ( $\epsilon_1$ ) and imaginary ( $\epsilon_2$ ) parts of the permittivity ( $\epsilon = \epsilon_1 + i\epsilon_2$ ) for the  $C_{60}Te_x$  materials. The results of these calculations disagree with the experimental values of  $\epsilon_1$  and  $\epsilon_2$ , which were determined from ellipsometric measurements of samples containing up to six tellurium atoms per  $C_{60}$  molecule. This indicates a low degree of clustering in the films. This inference is confirmed by the Rutherford backscattering data. Therefore, the samples prepared most likely have an intercalated structure.

### 3. INVESTIGATION OF THE ELEMENTAL COMPOSITION OF FILMS BY RUTHERFORD BACKSCATTERING

Rutherford backscattering measurements were carried out by probing the films with a beam of  $He^+$  ions at an energy of 190 keV. Figure 1 displays the Rutherford backscattering spectra of  $C_{60}Te_x$  films. The spectra exhibit two peaks in the ranges of high and low energies. Heavier tellurium atoms are characterized by a higher energy of scattered ions. A decrease in the energy leads to the appearance of a threshold, which corresponds to carbon atoms forming fullerene molecules. The second threshold, which is observed down to the lowest energies, corresponds to silicon atoms and can be associated with the scattering of  $He^+$  ions by the substrate. Reasoning from the intensity ratio of the peaks and their width and shape, we can evaluate the

quantitative ratio of the elements and the composition distribution over the film depth. Analysis of the Rutherford backscattering spectra revealed that the concentrations of tellurium atoms are uniformly distributed over the sample depth and comprise 0.1, 0.3, 1, 3, and 6 tellurium atoms per  $C_{60}$  molecule with a sufficiently high accuracy. For sample no. 3, the tellurium impurity concentration in a thin (of the order of 20 nm) surface layer corresponds to the  $C_{60}Te_3$  composition. Below this layer, there is a subsurface 10-nm-thick layer characterized by the  $C_{60}Te_{0.3}$  composition. The remaining part of the sample is uniformly doped and has the  $C_{60}Te_1$  composition. It is assumed that, at a total film thickness of about 400 nm, this inhomogeneity has a negligible effect on the electrical and optical properties of the sample. Hence, in the subsequent discussion, this sample will correspond to the  $C_{60}Te_1$  composition.

### 4. RAMAN SCATTERING SPECTRA OF $C_{60}Te_x$ FILMS

Figure 2 shows the Raman scattering spectra of  $C_{60}Te_x$  films in the wave number range 50–1600  $cm^{-1}$ . Figures 3 and 4 display the characteristic spectral features in the vicinity of two fundamental Raman-active vibrations of  $C_{60}$  for samples with different tellurium contents.

Let us compare the vibrational modes in the Raman spectra of the pure  $C_{60}$  fullerene films with those of the  $C_{60}Te_x$  samples. The line at 272  $cm^{-1}$  (Fig. 3), which is assigned to the so-called squashing mode that corre-



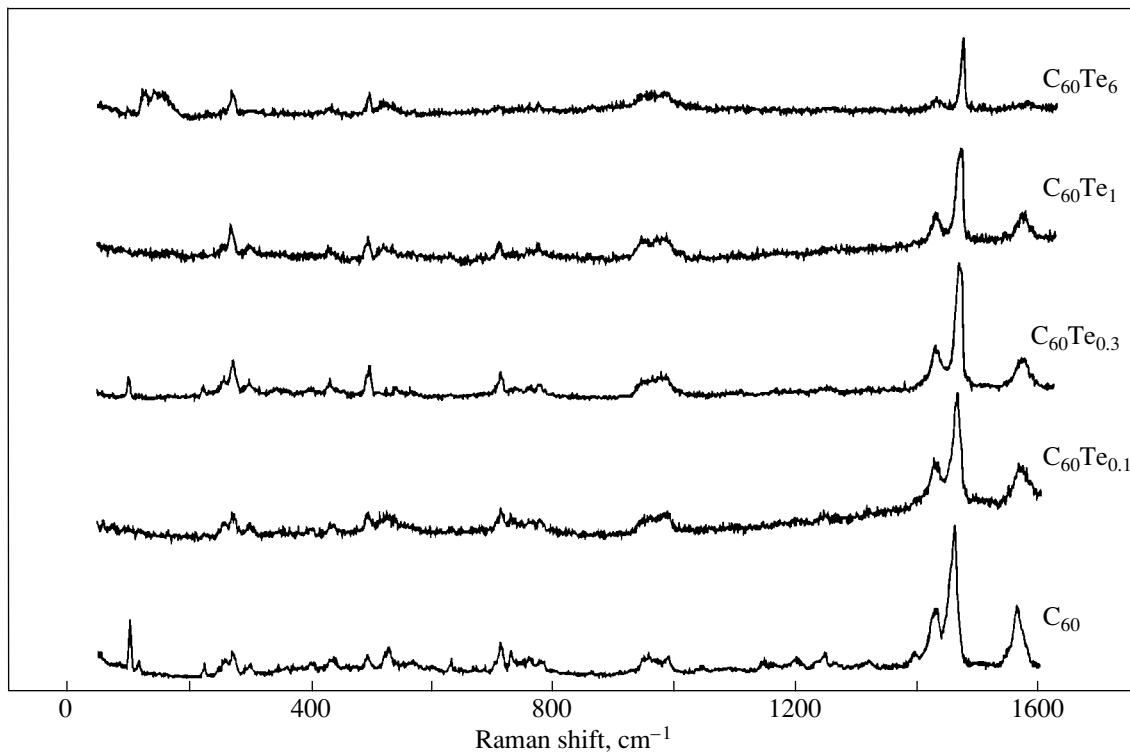


Fig. 2. Total Raman spectra of  $C_{60}Te_x$  samples.

sponds to the one-sided oblateness of a fullerene molecule, is shifted toward the low-frequency range: 270, 268, 264, and 266  $cm^{-1}$  at  $x = 0.1, 0.3, 1.0,$  and  $6.0,$  respectively. Moreover, this line is split into three components; i.e., there appear two (low- and high-frequency) satellites. This indicates that the fullerene molecules become strained, that the bond lengths are changed along all three directions, and that the degeneracy of vibrations is relieved. The satellite height is maximum at a low tellurium content and decreases with an increase in  $x$ . When the impurity concentration reaches six tellurium atoms per  $C_{60}$  molecule, the satellites disappear and, therefore, the molecular asymmetry becomes insignificant. This is consistent with a symmetrical distribution of impurities over holes in the  $C_{60}$  lattice.

The line at  $1468\text{ cm}^{-1}$ , which is attributed to the pentagonal pinch mode, corresponds to vibrations of pentagons in a  $C_{60}$  molecule. The observed change in the location of this line is often considered an indication of the polymerized states of the fullerene, because the pentagonal mode is sensitive even to a slight distortion of pentagonal faces of the molecule upon deformation of  $C_{60}$  fullerene. In the Raman spectra (Fig. 4), the line associated with the pentagonal pinch mode is shifted toward the low-frequency range compared to that for pure  $C_{60}$  fullerene:  $1461, 1465, 1465,$  and  $1467\text{ cm}^{-1}$  at  $x = 0.1, 0.3, 1.0,$  and  $6.0,$  respectively.

It is seen that the spectra contain an additional peak. This peak can be associated with a change in the shape of a  $C_{60}$  molecule due to its deformation. The location of this satellite coincides with that of the additional line observed upon fullerene polymerization. However, much more research must be done in order to either validate or disprove the assumption regarding the possible polymerization of the  $C_{60}$  fullerene upon tellurium intercalation. The intensity of the additional line is maximum for  $x = 0.3$  and decreases with an increase in the tellurium content. It should be noted that the spectrum of the tellurium-intercalated fullerene film with  $x = 0.1$  contains one more line at  $1451\text{ cm}^{-1}$ , which corresponds to the stronger strain of a  $C_{60}$  molecule. The absence of this peak in the spectrum of the fullerene film with  $x = 6$  indicates an insignificant strain of the  $C_{60}$  molecule.

In the Raman spectra of  $C_{60}Te_x$  samples, the lines attributed to the squashing modes are slightly shifted with respect to those observed for pure  $C_{60}$  fullerene at frequencies of  $709, 771, 1424,$  and  $1574\text{ cm}^{-1}$ . An increase in the tellurium content leads to a decrease in the intensity of the squashing mode at  $1574\text{ cm}^{-1}$ , which virtually disappears in the spectrum of the  $C_{60}Te_6$  film. The other squashing modes (at  $485, 1100,$  and  $1250\text{ cm}^{-1}$ ) are very weak. The breathing mode, which corresponds to the uniform tension and compression of a fullerene molecule and is observed at  $496\text{ cm}^{-1}$  for  $C_{60}$ , is also shifted and varies only

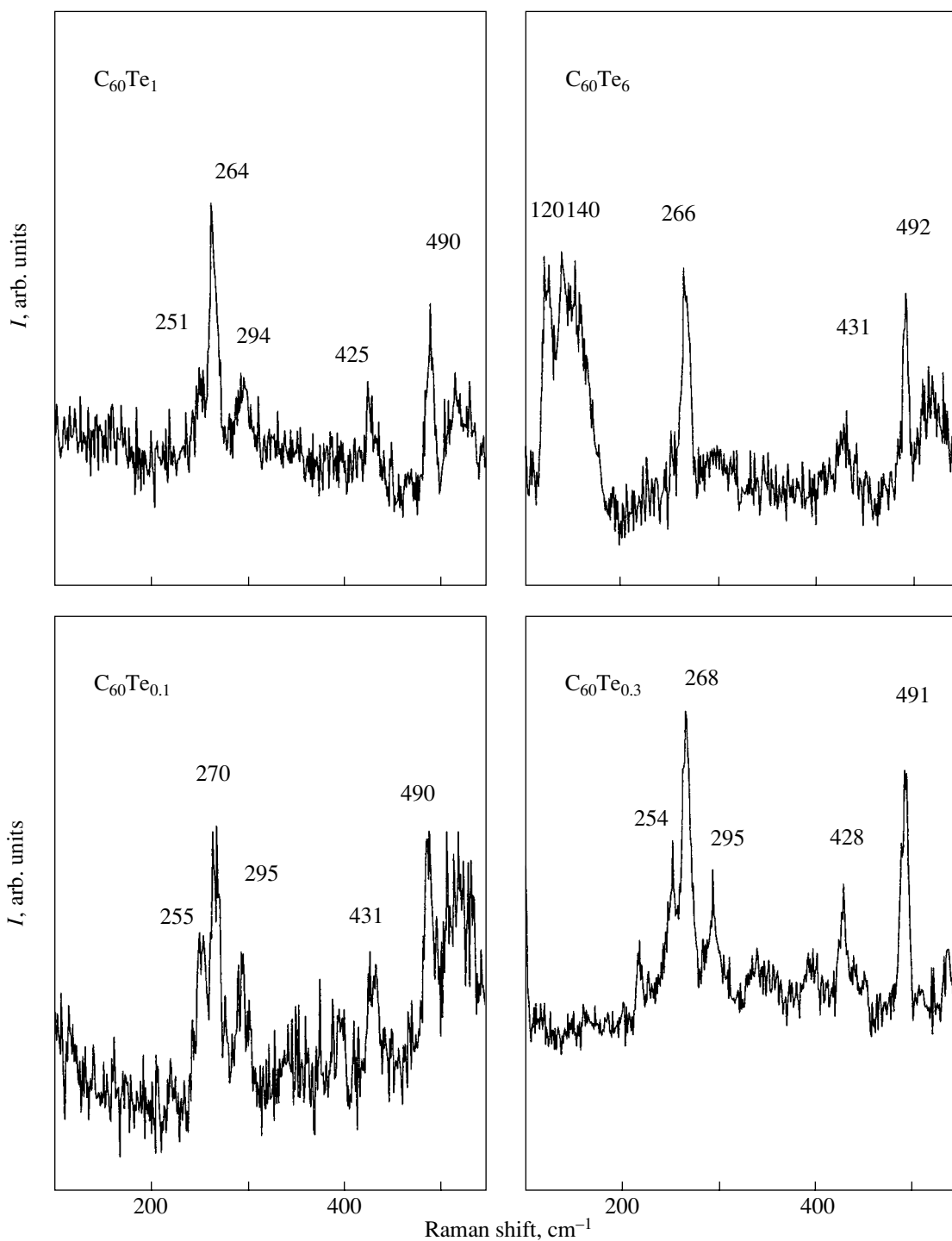


**Fig. 3.** Raman spectra of  $C_{60}Te_x$  samples near the “squashing” vibrational mode of a  $C_{60}$  molecule.

slightly from sample to sample. All the spectra contain a line (at 431, 428, 425, and 431  $\text{cm}^{-1}$  for  $x = 0.1$ , 0.3, 1.0, and 6.0, respectively) whose nature remains unclear. The shift of all the lines toward the low-frequency range as compared to those in the spectrum of

the pure  $C_{60}$  fullerene film can be explained by the fact that a partial transfer of the electron density from intercalated tellurium atoms to the  $C_{60}$  molecule brings about a slight increase in the bond lengths of the fullerene molecule.

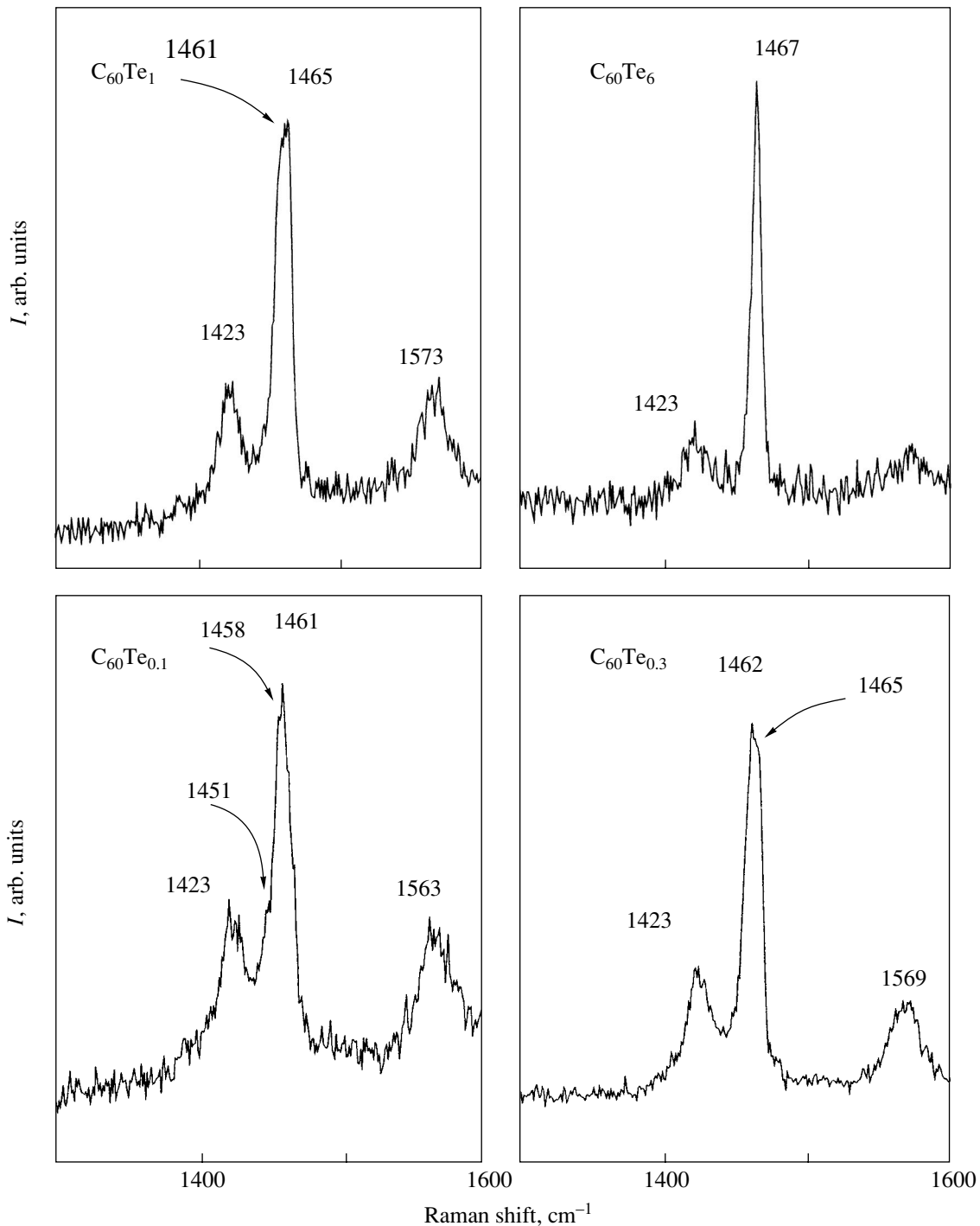
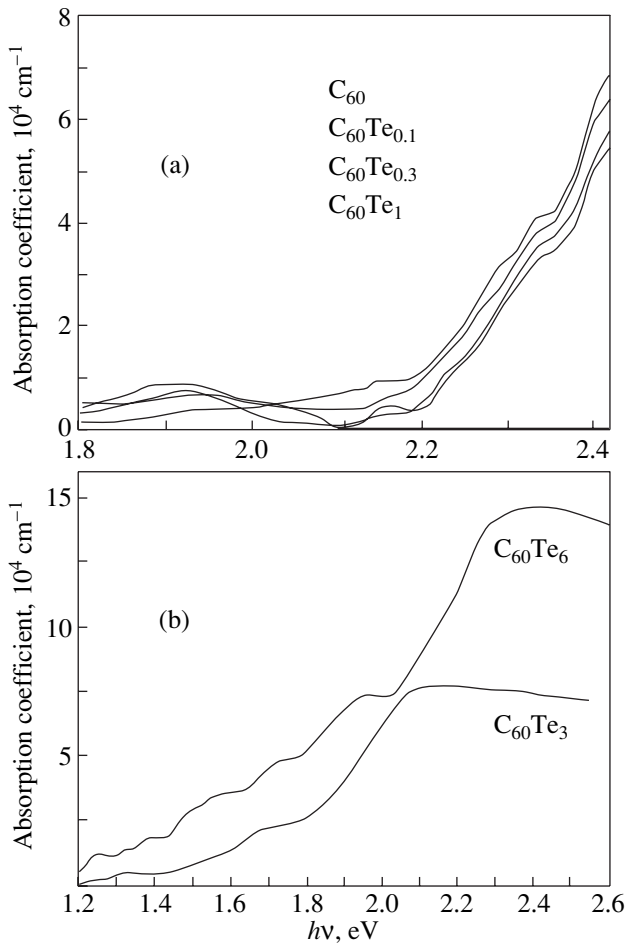


Fig. 4. Raman spectra of  $C_{60}Te_x$  samples near the pentagonal pinch vibrational mode of a  $C_{60}$  molecule.

### 5. OPTICAL SPECTRA OF $C_{60}Te_x$ FILMS

The optical absorption spectra were measured in the range 500–1000 nm. The absorption spectra are represented by curves with the absorption edge near 2 eV (Fig. 5). In the range of the absorption edge, the curves are sufficiently well linearized in the coordinates  $(\alpha h\nu)^2 = f(h\nu)$ . The value of  $E_g$  for pure  $C_{60}$  fullerene is

equal to 2.16 eV, which agrees with the data available in the literature [6]. For samples with a low tellurium content,  $E_g$  increases insignificantly with an increase in the tellurium content in films up to the  $C_{60}Te_1$  composition ( $E_g = 2.17, 2.19,$  and  $2.20$  eV at  $x = 0.1, 0.3,$  and  $1.0,$  respectively) (Fig. 5a). The slight increase in  $E_g$  at low tellurium concentrations can be caused by the low-



**Fig. 5.** Energy dependences of the optical absorption coefficient for  $C_{60}Te_x$  films near the absorption edge.

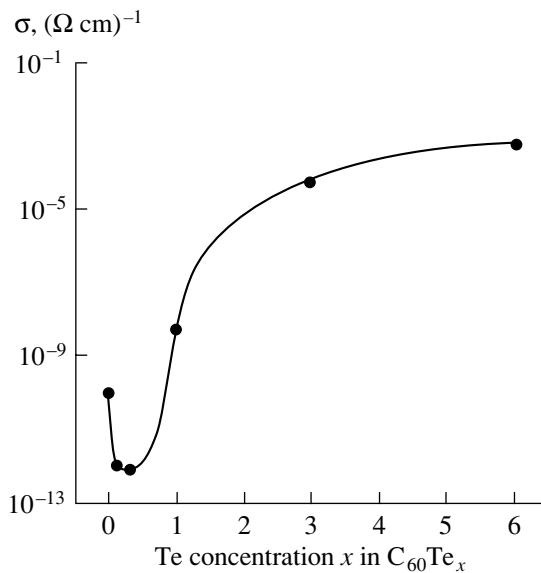


**Fig. 6.** Dependence of the electrical conductivity of  $C_{60}Te_x$  films on the tellurium content (per  $C_{60}$  molecule).

ering of the crystal symmetry and, as a consequence, the decrease in the overlap integral of fullerene molecules. The absorption edge is substantially shifted when the impurity concentrations are equal to three and six tellurium atoms per  $C_{60}$  molecule (Fig. 5b). Attempts to determine the band gap have failed because of the presence of several strong-absorption bands which extend to the infrared region. The strongest absorption is observed in the range 1.70–1.75 eV. These findings can be explained by the appearance of additional electronic levels created by intercalated impurity atoms and the energy levels of defects arising at a high tellurium content.

## 6. ELECTRICAL CONDUCTIVITY OF $C_{60}Te_x$ FILMS

The temperature dependences of the dc electrical conductivity for samples of different compositions were measured in the temperature range from 4.2 to 300 K.

Figure 6 shows the dependence of the electrical conductivity on the tellurium content in the  $C_{60}Te_x$  compounds at room temperature. In the case when  $x$  is less than unity, the incorporation of tellurium impurities leads to a decrease in the electrical conductivity by almost two orders of magnitude compared to the conductivity of pure  $C_{60}$  fullerene. This can be explained by either the lowering of the crystal symmetry (which is confirmed by the Rutherford backscattering spectra) or the disordering of the material (due to a random distribution of tellurium atoms in lattice holes) and an increase in the scattering of charge carriers. The temperature dependence of the electrical conductivity for

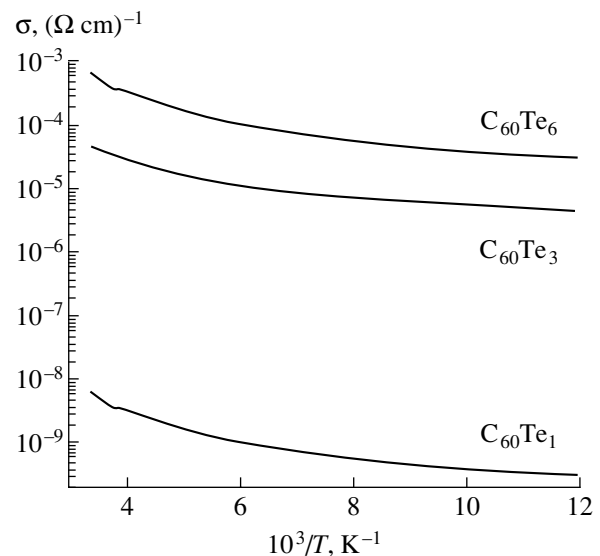


**Fig. 7.** Temperature dependences of the electrical conductivity of  $C_{60}Te_x$  films.

films with a low tellurium content could not be measured because of the extremely high resistance of the samples. An increase in the tellurium content brings about an increase in the electrical conductivity by several orders of magnitude. This can be caused by the formation of a channel for current passage through the impurities. Moreover, the charge can be transferred from impurities to  $C_{60}$  molecules, which leads to an increase in the overlap integral of the fullerene molecules and the concentration of conducting chains in the crystal. The exponential character of the temperature dependences (Fig. 7) implies that the fullerene films for all the tellurium concentrations have a semiconductor-type conduction. It is possible to distinguish several mechanisms of conduction with different activation energies (from  $E_A = 0.05$  eV at low temperatures to 0.3 eV at high temperatures). At temperatures close to liquid-helium temperatures, the conduction most likely occurs through the hopping mechanism. At a temperature close to 250 K, there are features associated with the orientational phase transition in the  $C_{60}$  fullerene [1]. At this temperature, the activation energy is characterized by a small jump, which is especially pronounced for  $C_{60}Te_6$ .

## 7. CONCLUSION

Thus, in the present work, the technique for preparing  $C_{60}Te_x$  fullerene films intercalated with tellurium at different concentrations was devised for the first time. Analysis of the Raman vibrational spectra revealed the change in the symmetry of the  $C_{60}$  cluster. It was found that the change in the tellurium impurity content leads to a change in the electrical conductivity of films by several orders of magnitude. The conductivity is minimum at  $x = 0.1$ . The change in the conductivity and the

evolution of the spectral dependence of optical absorption proved that the incorporation of tellurium impurities results in the modification of the electronic structure of the material. The extra optical absorption at photon energies of less than 2 eV in the  $C_{60}Te_x$  films with a high impurity content indicates the appearance of electronic levels created by intercalated impurity atoms or energy levels of defects formed at a high tellurium content.

## ACKNOWLEDGMENTS

We are grateful to O.E. Kvyatkovskii for helpful discussions.

This work was supported by the Russian Foundation for Basic Research (project no. 99-02-18170) and the State Scientific and Technical Program "Fullerenes and Atomic Clusters" (project "Film").

## REFERENCES

1. A. V. Eletskiĭ and B. M. Smirnov, *Usp. Fiz. Nauk* **165** (9), 977 (1995) [*Phys. Usp.* **38**, 935 (1995)].
2. R. C. Haddon, A. F. Hebard, M. J. Rossinsky, *et al.*, *Nature* **350**, 320 (1991).
3. O. Gunnarson, *Rev. Mod. Phys.* **69**, 575 (1997).
4. V. F. Masterov, A. V. Prikhod'ko, T. R. Stepanova, *et al.*, *Fiz. Tverd. Tela (St. Petersburg)* **40** (3), 580 (1998) [*Phys. Solid State* **40**, 535 (1998)].
5. D. A. G. Bruggeman, *Ann. Phys.* **24**, 636 (1935).
6. M. S. Dresselhaus, G. Dresselhaus, A. M. Rao, and P. C. Eklund, *Synth. Met.* **78**, 313 (1996).

*Translated by O. Borovik-Romanova*